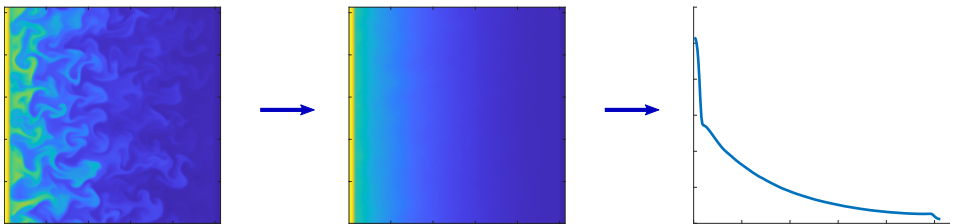# Turbulence Closure Models for Plasma Edge Simulations of Magnetically Confined Fusion Reactors

**Reinart Coosemans**

Supervisors:
Prof. dr. ir. Martine Baelmans
Dr. ir. Wouter Dekeyser

Dissertation presented in partial fulfillment of the requirements for the degree of Doctor of Engineering Science (PhD): Mechanical Engineering

June 2022

# Turbulence Closure Models for Plasma Edge Simulations of Magnetically Confined Fusion Reactors

**Reinart COOSEMANS**

Examination committee:
em. Prof. dr. ir. Jean-Pierre Celis, chair
Prof. dr. ir. Martine Baelmans, supervisor
Dr. ir. Wouter Dekeyser, supervisor
Prof. dr. ir. Johan. Meyers
Prof. dr. Rony Keppens
Dr. Patrick Tamain
  (IRFM-CEA Cadarache, France)
Prof. dr. Bruce Lipschultz
  (University of York, United Kingdom)

June 2022

# Preface

Wat begon met een eenvoudige mail naar Tine, relatief onwetend over wat er uiteindelijk uit zou volgen, leidde uiteindelijk tot dit doctoraat. Net als turbulentie, is het leven onvoorspelbaar en kunnen kleine dingen grote gevolgen hebben over een langere tijdshorizon. Dat vind ik best een mooie manier om naar het leven te kijken: ook al lijkt iets weinig bij te dragen, uiteindelijk kan het toch grotere zaken teweeg brengen. Bovendien maakt dat ook overdreven piekeren overbodig vermits je toch maar in beperkte mate kan voorspellen waartoe keuzes zullen leiden. Beide gelden ook tot op zekere hoogte voor een doctoraat.

Het is niet altijd makkelijk vliegen onder de turbulente omstandigheden van een doctoraat. Gelukkig waren er in het algemeen meer mooie zonnige vlieguren en fijne tussenstops dan periodes van hevige turbulentie. Desondanks ben ik blij dat ik nu (even) geland ben. Hoewel ik de piloot was van mijn eigen vliegtuig, waren er vele copiloten, bemanningsleden, controletorens en grondpersoneel die ik niet genoeg kan bedanken om mij te ondersteunen bij deze uitdagende reis.

Ten eerste wil ik mijn promotor Tine Baelmans bedanken. In de eerste plaats om mij de kans te geven om aan dit enorm interessante onderwerp te beginnen en vervolgens voor de begeleiding en de brede blik op mijn werk. Ik had steeds het gevoel dat je mij steunde en dat ik bij je terecht kon in geval van problemen, ondanks je meer dan goed gevulde agenda.

Ten tweede wil ik ook mijn copromotor Wouter Dekeyser bedanken voor de begeleiding van iets dichterbij. In het bijzonder voor de fantastische besprekingen waar ik altijd uit kwam met een duidelijker beeld van waar ik naartoe moest, met veel nieuwe ideeën en, misschien wel nog belangrijker, meer motivatie dan tevoren. De gedeelde interesse in dit onderwerp leidde steeds tot heel fijne gedachtewisselingen.

I'm also thankful to Patrick for the genuine, easy-going collaboration we had. I really appreciated your sincere interest in my research and the openness with which you received my sometimes unexpected results. I would also like to thank both you and William for sharing your expertise as well as detailed simulation data I could analyse. I'm grateful to William for patiently answering all the question I came up with regarding this simulation data as well.

Next, I would like to sincerely thank all members of the jury for carefully and critically reviewing my manuscript and for the interesting discussions. I'm convinced that your valuable suggestions have significantly improved my dissertation.

I'm very grateful to my TME colleagues for creating the excellent atmosphere at work. I quite enjoyed the bonding-through-shared-suffering event that was organised weekly, i.e. Alma day. Of course the TME weekends were also unforgettable. In particular, I would like to thank everyone I had the pleasure of sharing an office with during my TME-carreer: Dieter, Damien, Sarah, Andreas, Bart, Kristof, Sander, Javier, Yannick, Nathan and Kenneth. Besides concentrated working, you were always there for a nice chat or a good laugh. Sander deserves a special mention, not only for being a source of practical information running one year ahead of me, but also for providing some guidance during my start at TME, and for providing good advice in general. A special thanks also goes out to Kristel and Wim for the unforgettable holidays after my only in-person conference. I would also like to thank Stefano, Ján, Geert and Michiel for the great conversations we had.

Verder wil ik ook graag iedereen die meewerkte aan de ondersteunende functies vanuit het departement bedanken. Bedankt om alles wat vlotter te doen verlopen en voor de administratieve ondersteuning Valérie, Marina, Cindy, Nele en Karin. Ook Hans wil ik graag bedanken voor zijn inzet om alle machines in het thermotechnisch instituut te onderhouden en op te waarderen, en voor de fijne gesprekken over uiteenlopende onderwerpen.

Ik ben heel blij dat ik ook buiten het werk steeds omringd was door fantastische mensen. Bedankt aan al mijn vrienden voor alle leuke gesprekken, ontspannende momenten, fijne uitstappen en geweldige reizen,... Ik hoop samen met jullie dat we dit kunnen verderzetten met slechts een beperkte hoeveelheid minder geslaagde nachtelijke wandelingen naar willekeurige heuveltoppen over twijfelachtige padjes ;)

Ten laatste wil ik zeker ook mijn familie, ouders, grootouders en broer bedanken om mij altijd te ondersteunen, altijd naar mij te luisteren en goede raad te geven. Bedankt Papa om steeds een rots in de branding te zijn, een referentiepunt en een voorbeeld. Bedankt Mama om er altijd met zo veel liefde voor mij te zijn en zonder aan jezelf te denken mij altijd te helpen. Bedankt Sander om zo vaak leuke dingen samen te doen, maar ook voor de goede gesprekken en om als een klankbord te fungeren wanneer ik dat nodig had.

<div align="right">

Reinart Coosemans
Leuven, Juni 2022

</div>

# Abstract

The absence of greenhouse gas emissions, the widely available fuel, the inherent safety and the limited nuclear waste make nuclear fusion an attractive option for our future electricity supply. However, a number of technological challenges still stand, one of which is the high heat and particle load on the divertor. Turbulent transport processes largely determine the outward heat and particle fluxes and thus the efficiency of the plasma confinement. Taking the turbulence into account is of crucial importance to predict the load on the divertor.

Mean-field transport codes remain a key tool for designing the plasma facing components and the divertor. However, the description of turbulent transport in these codes remains lacking. Typically, the turbulent fluxes are described via an ad hoc diffusive approximation, in which the diffusion coefficients are determined for a particular experiment. This poses severe limitations on the predictive capabilities of these mean-field codes. As a solution to this, this thesis proposes an approach for modelling the turbulent fluxes that is inspired by the Reynolds-Averaged Navier-Stokes methods commonly used in hydrodynamic turbulence modelling. In this approach, still only the average of the turbulent flow field is resolved to maintain a tractable computational cost, but the turbulent fluxes are modelled by relating them to quantities characteristic of the turbulence.

Firstly, this thesis establishes an analytical framework by deriving the mean-field equations through a rigorous averaging procedure. This provides an exact interpretation for the quantities in the mean-field equations and identifies the closure terms. The turbulent E×B fluxes of heat and particles are demonstrated to be the crucial closure terms to be modelled. It is proposed to retain the diffusive model structure commonly used in mean-field codes, but to relate the transport coefficients to averaged quantities characterising the turbulence. In particular, it is found that the average kinetic energy ($k_\perp$) and enstrophy ($\zeta_\perp$) in the E×B drift fluctuations, which are exactly the fluctuations causing the E×B turbulent transport, can be used to robustly capture the turbulent transport coefficients. Hence, to complete the analytical framework, equations

for $k_\perp$ and $\zeta_\perp$ are derived. This allows to pinpoint and physically interpret their sources, sinks and transport terms. Most of these terms are in turn closure terms which require modelling.

To develop a practical, self-consistent model, this analytical framework is subsequently applied to the basic case of 2D electrostatic plasma edge turbulence, for which reference data is provided by the TOKAM2D turbulence code. The focus lies on the interchange-dominated sheath-connected scrape-off layer case. The extension to a core region with drift wave-like dynamics is likewise considered. A Bayesian inference framework for model comparison and parameter estimation supports the development of models for important closure terms. In particular, these Bayesian inference methods are used to select the best performing model for the relation between $k_\perp$ (and $\zeta_\perp$) and the transport coefficients.

With the above methodology, a self-consistent model for the turbulent E×B fluxes is established. The physics of this model is that mean-field density and temperature gradients lead to turbulent heat fluxes down the gradient. If this flux is in the direction opposite to the magnetic field strength gradient, this drives the interchange source of $k_\perp$ (through a generally valid analytical relation), which in turn leads to increased transport, etc. The turbulence saturates when the mean-field gradients are such that a balance is established between this interchange source and the sheath losses, which were found to provide the dominant sink of $k_\perp$. Note that all elements of this model derive from specific terms in the analytical framework, giving a clear analytical basis and physical meaning to the model. Forward 1D mean-field simulations with this $k_\perp$ model are capable of reproducing the profiles of the averaged TOKAM2D reference data very well. While it is shown that including the enstrophy has the potential to further improve the turbulent transport description, it is found that the additional complexity of closing the enstrophy equation may render the resulting mean-field model less accurate at present.

Even though important physics ingredients such as drift waves, flow shear and neutrals are still missing and extensive testing is required to establish its predictive capabilities, the model already provides a large improvement over the current practise for modelling the turbulent transport in mean-field codes. Its implementation in SOLPS-ITER shows that transport patterns which are novel for mean-field codes can be achieved. The results of this thesis directly lead to ballooned transport combined with fast parallel spreading of it due to fast "anomalous" transport of $k_\perp$ through parallel current fluctuations. In this way, this work provides a crucial stepping stone for the development of self-consistent turbulent transport models for mean-field simulations, both in terms of analytical mean-field equations as background and by suggesting a concrete model for a subset of the dynamics involved in future fusion reactors.

# Beknopte samenvatting

Kernfusie is een veelbelovende optie voor onze toekomstige elektriciteitsvoorziening, aangezien het geen broeikasgassen uitstoot, de brandstof overvloedig voorhanden is, het proces inherent veilig is en weinig radioactief afval produceert. Echter, een aantal technologische uitdagingen verhinderen momenteel nog het gebruik van deze technologie. Eén hiervan is de enorme warmtebelasting van de divertor. Turbulente transportprocessen bepalen grotendeels de uitstroom van deeltjes en warmte en dus de efficiëntie van de magnetische opsluiting. Bijgevolg is het van cruciaal belang om deze turbulentie in rekening te nemen om de belasting van de divertor te voorspellen.

Voor het ontwerpen van de divertor worden gewoonlijk transportcodes gebruikt. Deze codes maken gebruik van een ad-hoc beschrijving van het turbulent transport, waarbij eenvoudige diffusiemodellen gebruikt worden met modelcoëfficiënten afgesteld voor specifieke experimenten. Dit plaatst sterke beperkingen op het voorspellende vermogen van de modellen. Als oplossing hiervoor stelt deze thesis een aanpak voor geïnspireerd op Reynolds-Averaged Navier-Stokes methodes die veelvuldig gebruikt worden in hydrodynamische turbulentiemodellering. Nog steeds wordt enkel het gemiddelde van het turbulente stromingsveld berekend teneinde de rekenkost te beperken, maar de turbulente fluxen worden nu gemodelleerd door ze te relateren aan grootheden die de turbulentie karakteriseren.

Eerst wordt een analytisch kader opgebouwd door de gemiddelde transportvergelijking af te leiden via een rigoureuze uitmiddelingsprocedure. Dit laat een exacte interpretatie toe van de grootheden in transportcodes en identificeert de sluitingstermen. Er wordt geïllustreerd dat de turbulente E×B fluxen van deeltjes en warmte cruciale sluitingstermen zijn die gemodelleerd moeten worden. De diffusieve modelstructuur van de transportcodes wordt behouden voor deze termen, echter, de transportcoëfficiënten worden gerelateerd aan karakteristieke grootheden van de turbulentie. In het bijzonder wordt er aangetoond dat de gemiddelde kinetische energie ($k_\perp$) en enstrofie ($\zeta_\perp$) in de E×B fluctuaties,

dewelke het turbulent transport veroorzaken, gebruikt kunnen worden om een robuuste voorspelling van de transportcoëfficiënten te maken. Het analytische kader wordt dan vervolledigd door ook transportvergelijkingen voor $k_\perp$ en $\zeta_\perp$ af te leiden. Dit maakt het mogelijk om hun bronnen, verliezen en transporttermen éénduidig aan te duiden en fysisch te interpreteren. De meeste van van deze termen zijn op hun beurt opnieuw sluitingstermen.

Om concrete, zelf-consistente modellen te ontwikkelen, wordt dit analytische kader dan toegepast op het geval van 2D elektrostatische plasmarandturbulentie, waarvoor de TOKAM2D turbulentiecode gedetailleerde referentiedata levert. De focus ligt op het interchange-gedomineerde sheath-geconnecteerde regime in de plasmarand. De uitbreidingen naar de kernregio met drift wave-achtig gedrag wordt eveneens gemaakt. Bayesiaanse methoden voor modelvergelijking en parameterschatting ondersteunen de ontwikkeling van modellen voor belangrijke sluitingstermen. Deze methodologie wordt bijvoorbeeld gebruikt om de exacte relatie tussen $k_\perp$ (en $\zeta_\perp$) en de transportcoëfficiënten te bepalen.

Met behulp van de bovenstaande methodologie wordt een zelf-consistent model opgesteld voor de turbulente E×B fluxen. Dit model impliceert dat gemiddelde gradiënten van dichtheid en temperatuur leiden tot turbulente warmtefluxen. Indien de richting van deze warmteflux tegengesteld is aan die van de magnetische veldgradiënt, drijft dit de interchange bron van de turbulentie aan (volgens een analytisch verband), hetgeen op zijn beurt tot een verhoogd transport leidt, etc. De turbulentie verzadigt wanneer de gemiddelde gradiënten een niveau aannemen waarop een evenwicht ontstaat tussen de interchange bron en het sheath verlies dat werd geïdentificeerd als het dominante verlies van $k_\perp$. Gezien alle elementen van dit model voortkomen uit de analytische transportvergelijkingen, krijgt dit model een duidelijke fysische interpretatie. Voorwaartse 1D transportsimulaties slagen er zeer goed in om de profielen van de TOKAM2D referentiedata te reproduceren. Hoewel er wordt aangetoond dat het toevoegen van de enstrofie in principe de prestaties van het transportmodel kan verbeteren, blijkt de toegenomen modelcomplexiteit nefast voor de nauwkeurigheid.

Hoewel verdere ontwikkelingen nodig zijn om effecten als drift waves, afschuifstroming en neutralen in rekening te brengen en het nog uitgebreid getest moet worden, is het huidige model reeds een grote stap voorwaarts ten opzichte van de bestaande aanpak voor het modelleren van het turbulente transport in transportcodes. De implementatie ervan in SOLPS-ITER toont aan dat dit nieuwe transportpatronen introduceert, zoals asymmetrische gedrag in combinatie met snel parallel transport van $k_\perp$. Op deze manier vormt dit werk een cruciaal steunpunt in de ontwikkeling van zelf-consistente turbulente transportmodellen voor transportsimulaties, zowel door het analytische kader van gemiddelde transportvergelijkingen als door het voorstellen van een concreet model voor een subset van de fenomenen die in realistische gevallen optreden.

# List of Abbreviations

**AMH** Adaptive Metropolis-Hastings. 92, 93

**DHD** drift hydrodynamic , 1D in-house mean-field code. 28, 30, 31

**DNS** direct numerical simulations. 19, 23

**DOL** DivOptLight, 1D in-house mean-field code. xxii, xxiii, 187–190, 208–211, 281, 282

**DW** drift wave. xxiii, 9, 10, 13, 75, 98, 149, 154, 156, 157, 159, 164, 167–170, 191, 213, 217, 226, 227, 230, 231, 237, 239, 240, 242, 245, 247, 248, 255, 263

**HFS** high-field side. 10, 235, 236, 240

**KH** Kelvin-Helmholtz. 74, 237, 238

**LCFS** last closed flux surface. 4

**LES** large eddy simulations. 19, 20, 23

**LFS** low-field side. 10, 235, 237

**LHS** left hand side. 22, 32–34, 41–44, 48, 63, 68, 73, 75, 76, 80, 107, 108, 111, 112, 128, 129, 139, 144, 157, 173, 195, 208, 212, 224, 226, 235, 252, 253, 264, 265, 272, 290, 292, 295, 296

**LS** least squares. 83, 84, 89, 91, 142, 143

**MAP** maximum a posteriori. xxiii, 91, 143, 145–147, 162–164, 184, 201, 206

**MCMC** Markov chain Monte Carlo. 91, 92

**MHD** magneto hydrodynamic , 1D in-house mean-field code. 28

**OMP** outer mid-plane. 46, 99, 212, 236, 258

**PDE** partial differential equation. 22, 48

**RANS** Reynolds-averaged Navier-Stokes. 18–23, 37, 38, 49, 50, 53, 56, 93, 122, 139, 140, 151, 242

**RHS** right hand side. 19, 25, 32, 35, 42–44, 48, 65, 67, 69, 74–77, 80, 82, 100, 104, 107, 108, 111, 112, 114, 137, 139, 152, 155, 180, 195, 196, 199, 228, 252, 255, 261, 265, 267, 268, 271, 274, 290, 291

**RS** Reynolds stress. 9, 10, 20–22, 68, 74, 80, 112, 157, 175, 237, 238, 242

**SCW** sheath-driven conducting-wall. xxii, 193, 194, 198–200, 204, 211, 213, 214, 216–218, 246, 248, 283

**SOL** scrape-off layer. xxi, xxii, 4, 10, 13, 14, 52, 75, 94, 95, 98, 99, 101, 103, 107, 113, 147–149, 151–153, 155, 156, 158, 159, 164, 168–173, 191, 193, 194, 199, 203, 212, 214, 220, 226, 228, 230, 233–237, 239, 240, 243, 245, 247, 248, 258, 259, 263, 275, 278, 280, 288, 297

**TW** total vorticity. xxii, xxiii, 172–175, 178, 180–191, 223, 227–233, 237, 238, 245

# List of Symbols

**Parameter estimation and model validation**

$\mathcal{D}$       data

$\epsilon$       model error

$\mathcal{L}(\mathcal{D}|\mathcal{M})$   Bayesian evidence

$I$       input quantity of a model

$\mathcal{L}(\mathcal{D}|\theta, \mathcal{M})$   Bayesian likelihood function

$\mathcal{M}$       mathematical model

$O$       output quantity to be modelled

$\mathcal{P}(\theta|\mathcal{D}, \mathcal{M})$   Bayesian posterior function

$\pi(\theta|\mathcal{M})$   Bayesian prior

$\Sigma$       model error covariance matrix

$\sigma$       model error standard deviation

$\theta$       unknown parameter

$B_{ij}$       Bayes factor for models $\mathcal{M}_i$ and $\mathcal{M}_j$

$R^2$       coefficient of determination

**Fluid properties**

$\mu$       dynamic viscosity

$\nu$       kinematic viscosity

$\Pi$       viscous stress tensor

$\rho$      mass density

$\boldsymbol{\omega}$      vorticity vector

$\mathbf{V}$      velocity vector

$n$      particle density

$p$      pressure

$S$      shearing rate

$T$      temperature

**General**

$L_{||}$      parallel connection length

$L_{\perp}$      perpendicular length scale

$\mathbf{e}$      unit vector

$\tau$      time scale

$a$      tokamak minor radius

$C$      Constant

$g$      effective gravity

$I$      unit tensor

$R$      tokamak major radius

$S$      source term

$t$      time

$x$      radial coordinate

$y$      diamagnetic coordinate

$z$      parallel coordinate

**Plasma quantities**

$\mathbf{A}$      magnetic vector potential field

$\mathbf{B}$      magnetic field

$\mathbf{b}$      magnetic field direction (unit vector)

$\mathbf{E}$      electric field

$\gamma$      sheath heat transmission coefficient

$\mathbf{J}$      current density

$\Lambda$      sheath potential drop

$\mu$      magnetic permeability

$\Omega$      ion gyro-frequency

$\phi$      electrostatic potential

$Q_{\mathrm{ei}}$      electron-ion heat transfer

$\eta_{||}$      parallel resistivity

$\rho$      ion gyro-radius

$\mathbf{R}_{ei}$      electron-ion friction force

$\mathbf{U}_0$      $\mathbf{V}_0 \times \mathbf{b}$

$W$      pseudo-vorticity

$\mathbf{V}_0$      Dominant plasma velocity

$c_s$      plasma sound speed

$e$      electron charge

$m$      ion mass

$q$      particle charge

$Z$      charge state

**Transport**

$\chi$      diffusion transport coefficient

$\boldsymbol{\Gamma}$      flux

$\mathbf{q}$      heat flux

$\theta$      Prandtl number

$D$      (particle) diffusion coefficient

**Subscripts, superscripts, and accentuation**

| | |
|---|---|
| $'$ | Reynolds fluctuating component |
| $''$ | Favre fluctuating component |
| $*$ | diamagnetic |
| $0$ | refence value or dominant contributions |
| $^-$ | Reynolds average component |
| $\hat{}$ | magnitude of complex quantity |
| $\lambda$ or $y$ | diamagnetic |
| $\perp$ | perpendicular |
| $\phi$ | toroidal |
| $\theta$ | poloidal |
| $\sim$ | Favre average component |
| $E$ | E×B |
| $e$ | electron |
| $i$ | ion |
| $m$ | mean-field |
| $p$ | polarisation |
| $r$ or $x$ | radial |
| $t$ | turbulent |
| $Z$ | zonal flow |

**Turbulence**

| | |
|---|---|
| $\gamma$ | (linear) growth rate |
| $G_k$ | interchange drive term of $k_\perp$ |
| $\mathbf{K}$ | wave number |
| $\nu_t$ | turbulent viscosity |
| $\mathcal{P}$ | turbulent kinetic energy production |
| $\psi$ | fase difference |

$S_k$       sheath sink term of $k_\perp$

$\mathcal{T}$       turbulent kinetic energy transport

$\varepsilon$       turbulent kinetic energy dissipation

$\varepsilon_k$       viscous sink of $k_\perp$

$\zeta$       enstrophy

$E$       kinetic energy

$I$       turbulence intensity

$k$       turbulent kinetic energy

$l_m$       mixing length

# Contents

# List of Figures

# List of Tables

# Chapter 1

# Introduction

It has become abundantly clear that mankind's emissions of greenhouse gases and other pollutants have to drop drastically to preserve Earth's ecosystems. The absence of greenhouse gas emissions, the widely available fuel, the inherent safety and the limited, short-lived nuclear waste make nuclear fusion a formidable option for sustainable electricity generation in the future. However, harnessing the power of nuclear fusion has presented an equally formidable challenge and a number of technological problems still stand.

In the effort of working towards controlled electricity generation by nuclear fusion, several test reactors of increasing size have already been built. Currently the full-size ITER reactor is under construction in France. Next, DEMO will supply energy from a fusion reaction to the electricity grid for the first time. The exhaust functions of these test reactors are becoming ever more important as the problem of large scale stability of the magnetic confinement for the plasma has virtually been solved. Hence, the focus of this thesis will be on obtaining a more realistic description of the turbulent heat and particle transport processes that play a crucial role in determining the load on the exhaust system.

## 1.1 Nuclear fusion, the tokamak concept and power exhaust

In classical power plants for electricity generation, fossil fuels are combusted by means of a chemical reaction, releasing energy in the form of heat. For the combustion of methane for example, the principal component of natural gas,

the reaction can be written as follows.

$$CH_4 + 2O_2 \rightarrow CO_2 + 2H_2O + 9.24\,eV \tag{1.1}$$

Through a classical thermodynamic cycle, the 9.24eV of heat that is generated per reaction is converted into useful work and then into electricity.

In nuclear fusion-based electricity generation, these last steps are envisaged to remain unchanged. There as well the generated heat will be converted in electricity through a well known steam cycle and by driving an electrical generator. However, the heat will now be generated by a nuclear reaction instead. In the nuclear reaction that will be used, two hydrogen isotopes, deuterium (D) and tritium (T), are fused to create a helium (He) particle and a neutron [71, 165], while releasing a large amount of energy:

$$D + T \rightarrow He + n + 17.6\,MeV. \tag{1.2}$$

This energy is released in the form of kinetic energy of the resulting helium and neutron particles, and is converted into heat by collisions, either with other particles or with the reactor walls. Notice that contrary to the combustion of methane, no carbon dioxide (or other greenhouse gases) is formed in this reaction. Furthermore, the D-T nuclear reaction releases an enormous amount of energy per fuel particle, almost two million times more than for the combustion of a methane molecule. Hence, very low quantities of deuterium and tritium suffice to generate the same heat as a gas-fired power plant does.

However, in order for the D-T fusion reaction to take place, the deuterium and tritium particles need to have sufficient energy to overcome the repulsive Coulomb barrier between their nuclei. In the thermonuclear fusion concept considered in this thesis, this requires a mixture of D and T at enormously high temperatures (order of magnitude $100,000,000\,K$ [165, 71]). At these temperatures, the D, T and He particles are present in the aggregation state known as a plasma, i.e. the electrons have detached from the atomic nuclei resulting in a collection of unbound charged particles. Note that while individual particles are charged, the plasma as collection of charged particles remains quasi-neutral on length scales larger than the Debye length, which is typically very small in fusion plasmas (see table 1.1). This is because plasma particles arrange themselves in such a way that the charge of each particle is shielded by those around it such that no net space charge remains on larger length scales [82, 165]. Nonetheless, the individual charged particles are affected by electromagnetic forces. In the presence of a strong magnetic field, charged particles in the plasma can move almost unhindered along magnetic field lines, while particle motion perpendicular to it is greatly hindered by the Lorentz force. This behaviour
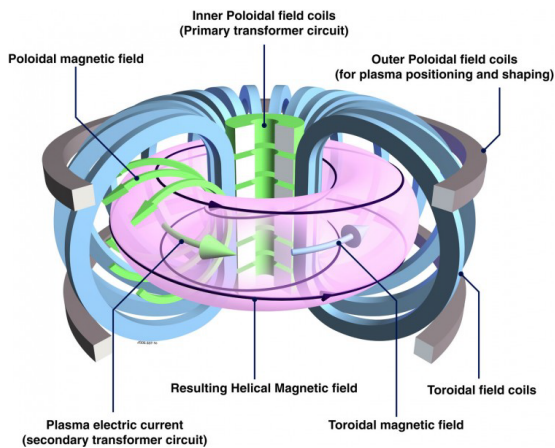
Figure 1.1: Magnetic field structure in a tokamak. Figure reproduced from [124].

is exploited to confine the plasma in the most advanced concept for achieving nuclear fusion to date: the tokamak.

In a tokamak, the plasma is kept in a toroidal vessel. To minimise the contact between the hot plasma and the walls, the plasma is confined by a magnetic field, see figure 1.1. This magnetic field has a toroidal and a poloidal component resulting in magnetic field lines that are helically shaped and form nested flux surfaces [165]. Since plasma particles tend to gyrate around magnetic field lines in orbits much smaller than the system size (see table 1.1), this magnetic field structure largely confines the plasma particles to their magnetic flux surface. However, the magnetic fields cannot confine the plasma particles indefinitely. Several mechanisms exist by which particles do move across flux surfaces. Moreover, reaction products need to be removed to sustain conditions favourable for the fusion reaction and the generated heat[1] needs to be transferred to a secondary circuit to use it for electricity generation. To achieve this, a potent exhaust system is required.

To this end, the magnetic configuration at the wall is changed by a divertor in most test reactors. The resulting magnetic configuration comprises an X-point

---

[1] Of the 17.6 MeV generated per fusion reaction in equation 1.2, only the 3.5 MeV carried by the kinetic energy of the helium particle is typically absorbed by the plasma and contributes to the exhaust problem sensu stricto. As the neutrons hardly interact with the plasma, the remaining 14.1 MeV carried by them is deposited roughly uniformly over the vessel wall.

Table 1.1: Typical values for characteristic tokamak edge plasma quantities. Evaluated for a deuterium plasma (charge number $Z = 1$), magnetic field $B = 5T$, density $n = 5 \times 10^{19}/m^3$, temperature $T = 50eV$, $\ln \Lambda = 20$ safety factor $q = 4$.

| quantity | formula | typical value |
|---|---|---|
| major radius | | $\sim 2\text{m}$ |
| minor radius | | $\sim 1\text{m}$ |
| parallel connection length | $L_{\|} = 2\pi q R$ | $\sim 50\text{m}$ |
| speed of sound | $c_s = \sqrt{\frac{T}{m}}$ | $4.9 \times 10^4 \text{m/s}$ |
| gyro-frequency | $\Omega = \frac{eB}{m}$ | $2.4 \times 10^8 \text{Hz}$ |
| gyro-radius | $\rho = \frac{c_s}{\Omega}$ | $2.0 \times 10^{-4}\text{m}$ |
| Debye length [82, 165] | $L_{Debye} = \sqrt{\frac{\epsilon_0 T}{ne^2}}$ | $7.4 \times 10^{-6}\text{m}$ |
| SOL dwell time [153] | $\tau_{SOL} \sim L_{\|}/c_s$ | $\sim 1.0 \times 10^{-3}\text{s}$ |
| SOL width [14, 81] | $L_{SOL} = \frac{p}{\nabla p} \sim 4q\rho$ | $\sim 3.3 \times 10^{-3}\text{m}$ |
| typical parallel length scale [165] | $\sim L_{\|}$ | $\sim 50\text{m}$ |
| smallest turbulent time scale [71] | $\tau_{t,min}^{-1} \sim \frac{\rho}{L_{SOL}}\Omega$ | $\sim 1.5 \times 10^7 \text{Hz}$ |
| smallest turbulent perpendicular length scale [71] | $L_{t,\perp,min} \sim \rho$ | $\sim 2.0 \times 10^{-4}\text{m}$ |
| ion-ion collision frequency [165] | $\nu_{ii} = \frac{nZ^4 e^4 \ln \Lambda}{12\pi^{3/2}\epsilon_0^2 m_i T^{3/2}}$ | $9.6 \times 10^4 \text{Hz}$ |
| electron-electron collision frequency [165] | $\nu_{ee} = \frac{\sqrt{2}ne^4 \ln \Lambda}{12\pi^{3/2}\epsilon_0^2 m_e T^{3/2}}$ | $8.2 \times 10^6 \text{Hz}$ |
| ion-electron collision frequency [165] | $\nu_{ei} = \frac{\sqrt{2}nZ^2 e^4 \ln \Lambda}{12\pi^{3/2}\epsilon_0^2 m_e T^{3/2}}$ | $8.2 \times 10^6 \text{Hz}$ |
| ion mean-free path [165] | $L_{mfp,i} \sim \frac{c_s}{\nu_{ii}}$ | $\sim 0.51\text{m}$ |
| electron mean-free path [165] | $L_{mfp,e} \sim \frac{\sqrt{T}}{\sqrt{m_e}\nu_{ee}}$ | $\sim 0.36\text{m}$ |
| plasma $\beta$ | $\beta = 2\mu p/B^2$ | $4.0 \times 10^{-5}$ |

that lies on the last closed flux surface (LCFS), also called the separatrix. The region outside of this LCFS is called the scrape-off layer (SOL) or open field line region. Flux surfaces in this region are in contact with the divertor target plates. The plasma edge is formed by the SOL and the plasma that lies just inside the LCFS [153]. Figure 1.2 shows a cross section in the poloidal plane of a tokamak with a divertor.

At a material surface in contact with the plasma, charged plasma particles recombine to form neutral atoms and molecules again. As a result, the material surface acts like a sink of plasma particles such that the plasma accelerates to sound speed towards this surface. The details of these plasma-wall interactions are governed by a layer as thin as a couple Debye lengths that forms in front of
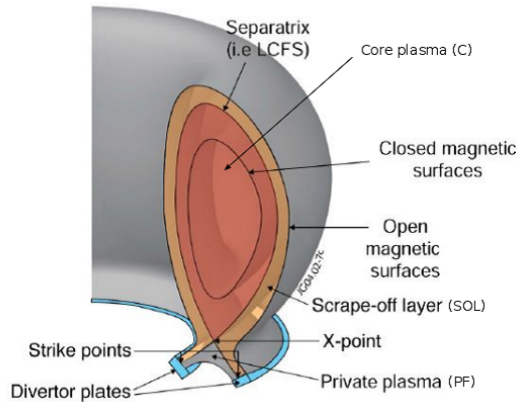
Figure 1.2: Schematic of a tokamak with divertor configuration. ©EFDA-JET

the surface, which is known as the sheath. The neutral particles formed at the surface are released again and enter the plasma. Furthermore, the impact of plasma particles on the material surface tends to knock particles loose, leading to impurities (particles other than fuel or exhaust species) entering the plasma. Consequently, a certain concentration of neutral particles and impurities is typically present in the plasma edge, especially close to the divertor targets. These plasma-wall interactions are described in detail in Ref. [153] for example. A divertor configuration shifts the main place of contact between the plasma and the wall away from the core plasma, limiting the amount of impurities that enter the core plasma as well as protecting the walls of the main chamber from excessive heat loads. As a result of this configuration, heat and particle loads are concentrated on the divertor plates [153]. The full-size ITER reactor is designed to handle a steady state heat flux of $10\,\mathrm{MW/m^2}$ impinging on the target plates. However, depending on the exact operating parameters and modelling assumptions, this value may be exceeded [123].

Overcoming the difficulties posed by these peaked heat and particle loads at the divertor targets is crucial in the development of commercially viable nuclear fusion power plants. The magnitude and location of these heat and particle loads depend both on the quickness of heat and particle removal along magnetic field lines toward the target plates and on the rate at which they are transported outward across magnetic flux surfaces in the plasma edge. Furthermore, the outward transport in the plasma edge also contributes to the energy confinement time, which is an important performance characteristic for the reactor efficiency and operation. While self-consistent models based on collisional closures exist
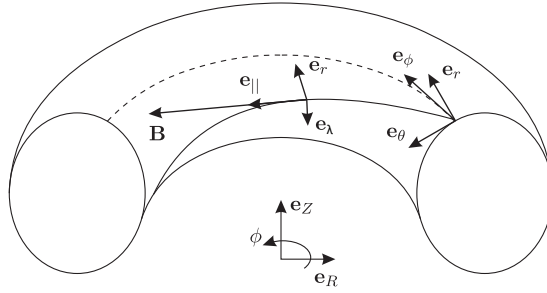
Figure 1.3: Illustration of the radial ($\mathbf{e}_r$), diamagnetic ($\mathbf{e}_\lambda$), parallel ($\mathbf{e}_{||}$) and radial ($\mathbf{e}_r$), poloidal ($\mathbf{e}_\theta$), toroidal ($\mathbf{e}_\phi$) axis systems used for the description of the plasma edge in tokamak geometry. Figure reproduced from Ref. [52].

for the transport in the parallel direction, the outward transport perpendicular to the magnetic field is poorly understood. This outward transport is known to be dominated by turbulent processes [71, 143, 165] for which accurate yet computationally affordable models are still being developed. The next section will introduce the basic mechanisms driving this turbulent transport.

## 1.2    Plasma drifts and turbulence

As mentioned in the previous section, plasma particles in a strong magnetic field tend to move along the magnetic flux lines. In the direction perpendicular to the magnetic field line, the charged plasma particles are confined by the Lorentz force and trace circular orbits. This is called the gyro-motion of the particles [82, 165]. Different mechanisms breaking this perfectly confined gyro-motion exist though.

In order to facilitate the upcoming discussion, figure 1.3 introduces the directions and coordinate systems that will be used. Mostly the radial, diamagnetic, parallel ($\mathbf{e}_{||}$) system will be used in this thesis. The radial $\mathbf{e}_r$ direction points outwards, out of the flux surface. The parallel direction $\mathbf{e}_{||}$ is perpendicular to it and points in the direction of the magnetic field. The diamagnetic direction $\mathbf{e}_\lambda$ lays in the magnetic flux surface, perpendicular to the former two and completes the right handed axes system. Alternatively, the radial, poloidal, toroidal coordinate system could be used. Here, the toroidal axis $\mathbf{e}_\phi$ is aligned with the toroidal direction of the tokamak, while the poloidal direction $\mathbf{e}_\theta$ is perpendicular to both the radial and the toroidal directions completing this right handed axis system. Note that the same radial axis is used in both systems.

## 1.2.1  Mechanisms of perpendicular transport in the plasma edge

Classical particle transport is due to collisions on the scale of the collision mean free path in the direction parallel to the magnetic field and the gyro-radius in the directions perpendicular to it. Typical values for the collision frequencies and mean-free paths (in the parallel direction) are shown in table 1.1. This classical transport theory does not take toroidal effects that lead to gradients in the magnetic field into account. These gradients lead to different kinds of particle motions that induce neoclassical transport effects in the collisional transport, enhancing the transport compared to classical theory [165]. Comparing experimental results to neoclassical predictions, it was found that the perpendicular transport is much larger than theory predicts [165, 143, 165]. This *anomalous* transport is generally known to be caused by turbulent fluctuations which are not included in the neoclassical predictions. This turbulence is due to fluctuating drift flows [71, 143, 165]. Table 1.1 also shows typical length and time scales for the turbulent fluctuations.

In general, plasma drift flows are the effect of the gyro-motion of plasma particles being distorted either by forces acting on plasma particles or due to spatial and temporal changes of the magnetic field. As a result, the particles no longer trace perfect circles around the field lines, but instead "drift" across magnetic field lines. These drifts occur in the plane perpendicular to the magnetic field. In tokamak plasmas, the dominant plasma drift is usually the E×B drift due to the presence of an electric field. The resulting drift velocity $\mathbf{V}_E$ is

$$\mathbf{V}_E = \frac{\mathbf{E} \times \mathbf{B}}{B^2}. \tag{1.3}$$

In this equation, $\mathbf{E}$ is the electric field vector, $\mathbf{B}$ the magnetic vector field and $B$ the magnetic field strength. As can be seen from this formula, the E×B velocity is indeed perpendicular to the magnetic field, and purely due to the part of the electric field perpendicular to the magnetic field. The E×B drift velocity and the other drift velocities add to the circular gyro-motions. The drift velocities are thus the velocity of the so called *guiding centres*, the location of the particle averaged over many gyro-periods (which are much shorter than the length scales of the turbulence and the transport of interest in this thesis). Looking not at the guiding centres of individual particles but at the plasma as a whole, equivalent drifts for the plasma fluid are found. A detailed description and derivation of guiding centre and fluid drifts can be found in, for example, Refs. [82, 165].

E×B drift flows occur due to an electric field that persists on long time and length

scales as part of the plasma equilibrium in the reactor, but arises in response to small scale fluctuations of the electric field just as well. The latter kind of drift flows constitute the main mechanism of the turbulence. The correlation of electric field fluctuations with density and temperature fluctuations leads to turbulent fluxes of particles and heat. Note that fluctuations of the magnetic field typically play a less important role for the transport in the plasma edge and are often neglected in an electrostatic treatment [71, 143, 153]. What happens is that in the plane perpendicular to the magnetic field, an electric field with many small perturbations arises. Under effect of the E×B drift, plasma fluid elements trace orbits around local maxima an minima of the electrostatic potential ($\phi$). More precisely, perpendicular to the magnetic field, the plasma elements move along lines of constant electrostatic potential. This motion convects thermal energy and particles, which in turn changes the structure of the electric field. The continuous interactions between both leads to a chaotic structure of both the electric field and the flow which evolves over a range of time and length scales, and hence to turbulence.

These small scale E×B convection cells of the turbulence constitute the dominant mechanism by which heat and particles are transported across magnetic flux surfaces in modern tokamaks [153, 165, 143, 71]. This mechanism is illustrated in figure 1.4. It shows that a local maximum in the electrostatic potential ($\phi$), indicated by the "+" symbol, leads to a convection cell around it. In the presence of a density ($n$) gradient perpendicular to the magnetic field, this causes a particle flux ($\mathbf{\Gamma}$) in the direction perpendicular to the magnetic field. Note that while the figure depicts a simple quadratic-like potential structure resulting in elliptical E×B orbits, the picture is much more irregular in real plasma edge turbulence. Many local maxima and minima occur and change in time, such that the lines of constant electrostatic potential which are followed by the plasma elements may be much more tortuous and complex.

Since the drift flows occur in the plane perpendicular to the magnetic field and motion in the parallel direction is largely unhindered by the magnetic field, the flow field takes the form of small scale structures in the plane perpendicular to the magnetic field (of the order of the ion gyro-radius) that are highly elongated in the direction parallel to it. As a result turbulence in the plasma edge is typically quasi-2D with fluctuations in the parallel direction occurring on much larger scales than those in the perpendicular plane [131, 141, 153, 143].

## 1.2.2 Phenomenology of plasma edge turbulence

In general, turbulence arises when strong thermal gradients are present in the plasma. As a way of diminishing this thermodynamic inequilibrium, turbulent
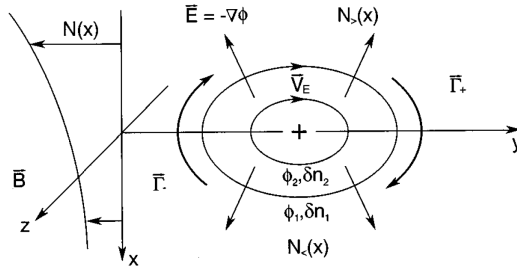
Figure 1.4: Schematic representation of an E×B convection cell. E×B drift velocities cause fluid elements to trace orbits around maxima and minima of the electrostatic potential. Figure reproduced from Ref. [94].

flow structures develop that cause strong heat and particle fluxes to counteract this. As such, it is the energy present in the background thermal energy and its inequilibrium which provides the energy for the turbulence to develop [36, 94, 117, 143, 145]. A plethora of instabilities can occur in the plasma edge by which perturbations can grow and feed the turbulence. While the structure of the developed turbulence is nonlinear and cannot be determined from the linear instability only [71, 143, 145], some characteristics of the linear drive may still shine through. Here, we will take the energy transfer channels into the turbulence as a viewpoint though. These transfer channels correspond to sources and sinks of the energy in the turbulent fluctuations, which exchange energy with other energy forms in the plasma (see section 3.2.5). While several more channels exist, the drift wave (DW), interchange and Reynolds stress (RS) channels are assumed to dominate the dynamics [143].

The DW transfer channel allows energy to be exchanged with the turbulence through dynamics parallel to the magnetic field. Hence, this transfer channel can only be active when fluctuations in the parallel direction are allowed [143]. For this reason, the DW channel is expected to be more important in the closed field line region inside the separatrix where parallel fluctuations are not constrained by the magnetic field lines ending at the sheath [131]. The DW instability related to this channel originates from the wave which propagates in the direction perpendicular to both the (electron) pressure gradient and the magnetic field when electron parallel dynamics are allowed for. When the parallel electron response to density perturbations is not infinitely fast, this wave grows in amplitude and can induce turbulence [94, 95, 164].

Next, the interchange channel allows energy exchange with the turbulence in the presence of gradients in the magnetic field strength. This channel purely relies

on dynamics perpendicular to the magnetic field and can function without any fluctuations in the parallel direction. As such, this channel tends to be dominant in the SOL where the parallel dynamics are modified by the magnetic field lines being in contact with material surfaces, hindering the DW channel [131]. The larger resistivity (due to lower temperatures) and the strong gradients in this region further facilitate the interchange channel over the DW channel. This transfer channel is related to the "interchange" of fluid elements by which the heavier fluid element moves radially outward due magnetic field gradients acting like an effective gravity in that direction. Equivalently, this can be explained as an interaction between the E×B drift and the pressure-gradient-induced drift [82, 164]. Since the interchange mechanism is only unstable when the pressure gradient ($\nabla p$) points in the opposite direction of the effective gravity ($g = -2p\kappa/\rho$, with $\kappa$ the local magnetic field line curvature and $\rho$ the density [82]), interchange turbulence is normally strongest on the outboard side of the tokamak. This is illustrated in figure 1.5, where also the magnetic field strength is indicated for future reference. As such, interchange is believed to explain the experimental observation that the turbulence is usually much stronger at the outboard side (or low field side, LFS) of the tokamak than at the inboard side (or high field side, HFS), an effect which is called "ballooning" [34, 66, 74, 85, 158].

The interchange mechanism is also responsible for the propagation of blob-filaments aligned with magnetic field lines in the plasma edge. High density perturbations known as "blobs" propagate outwards, while low density "holes" propagate inwards. This induces a pronounced ballistic character into the small scale dynamics of the turbulent transport. A significant fraction of the radial transport in the plasma edge is due to these blob-filaments, such that this mechanism should be considered as an important addition to the picture of convection cells moving thermal energy and particles gradually outwards sketched above [76, 78, 61, 101, 106, 125].

Another phenomenon of interest are large scale shear flows which tend to develop around the separatrix. These are plasma flows in the poloidal/diamagnetic direction which are sheared in the radial direction. Typically, these flow structures are largely uniform on magnetic flux surfaces. A distinction can be made between the stationary mean-field component due to the plasma equilibrium and the so-called "zonal flow" component which varies in time (typically on a time scale larger than that of the turbulence). These shear flows act to break up turbulent eddies and thus reduce the intensity of the turbulence and the transport. Moreover, these shear flows are partly fed by absorbing the energy of the turbulence through the RS energy transfer channel. As a result, strong shear flows can create a "transport barrier" which improves the confinement, leading to the operating regime called H-mode, as opposed to the lower confinement regime called L-mode [56, 58, 144, 146, 163]. The formation
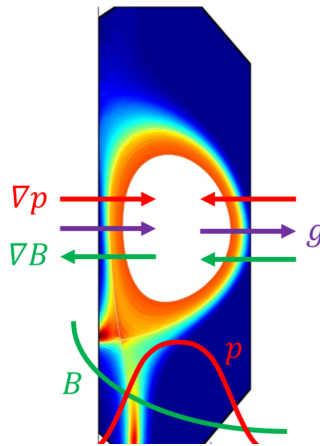
Figure 1.5: Cross-section of a tokamak showing the density profile in the radial-poloidal plane. A schematic representation of quantities relevant to the stability of the interchange mode has been overlaid. Figure adapted from Ref. [12].

process of these strong shear flows can be understood as a manifestation of the inverse energy cascade by which energy is transferred from small to large scales in 2D turbulent systems [4, 36, 71, 169].

## 1.3 Simulating turbulent transport

As experimental tokamaks are extremely expensive, numerical simulations of the plasma edge are vital to predict the performance of future reactors and to obtain improved designs. The detailed models solved in these simulations allow to extrapolate knowledge obtained from smaller-scale test machines to operating regimes of future full-scale reactors. While the turbulent transport processes introduced in the previous section are of crucial importance to predict the load on the divertor, simulating this transport remains challenging.

A first approach is to explicitly resolve all the fine length and time scales of the turbulence, which yields a very accurate representation of the turbulent transport. This is done in turbulence codes which solve a set of fluid equations governing the plasma dynamics, see for example Refs. [132, 157, 154, 33]. Gyrokinetic codes go a step further by using a gyro-averaged 5D kinetic description of the plasma, see for example [86]. However, the fine spatio-temporal resolution that these approaches require, leads to an exceedingly

high computational cost for large devices and inhibits their use for routine design simulations. Hence, despite the availability of advanced super computer infrastructure, the applications of these approaches remains largely limited to the plasma edge of medium-size tokamaks.

Instead, plasma facing-components and the exhaust system are typically designed using mean-field plasma edge transport codes. Since these codes only calculate averaged, macroscopic values of quantities and usually assume toroidal symmetry, their computation cost is much more affordable. Running a simulation for the plasma edge of an ITER-scale machines typically takes around a month in wall time on dedicated computational infrastructure [102]. SOLPS-ITER, which is the reference code for the design of the ITER divertor, is a prime example of such a mean-field code [29, 167]. The main transport code in SOLPS-ITER is B2.5-EIRENE. The EIRENE code solves the Boltzmann equation for the neutrals based on a Monte-Carlo approach [130, 142]. The B2.5 code models the ion and electron transport, using a finite volume discretisation. Fluid equations for the plasma are used to model the parallel transport, while ad-hoc diffusion-type equations approximate the turbulent transport in the perpendicular directions. The reason why these ad-hoc diffusion models are used is that the turbulent fluctuations appear as closure terms consisting of correlations between fluctuating quantities in the averaged mean-field equations. These closure terms cannot be calculated from first principles based on mean-field quantities.

However, at present these diffusive models contain no information on the underlying turbulence. Instead, these models employ experimentally determined profiles for the diffusion coefficient featuring a large amount of parameters as the profiles are a function of the radial (and sometimes the poloidal) coordinate [3, 53, 128]. The resulting diffusion coefficients are typically found to vary significantly between machines and operating conditions, even varying by several orders of magnitude within a single discharge [103]. Moreover, in the current "best practices", there is no framework for evaluating these models and issues such as overfitting are not taken into account. Therefore, these diffusive approximations pose severe limitations on the predictive capabilities of the codes.

## 1.4 Goals and outline

At present, the mean-field transport codes used for divertor design are not capable of properly modelling turbulent transport. This thesis aims to develop self-consistent models for the turbulent transport in the plasma edge which can

be used in mean-field codes without exceedingly increasing the computational cost. The resulting models should depend on fewer and more universal parameters than the ad-hoc diffusive models that are presently used. Such model should be able to predict the anomalous transport phenomena based on a physical description of the underlying mechanisms. The improved predictive capabilities of the model are envisaged to enhance the reliability of simulation-based design of future fusion reactors.

To achieve this goal, a theoretical model is derived first. This includes rigorously averaging the equations governing the plasma dynamics taking turbulent fluctuations into account. The averaged equations include closure terms that depend on the correlation of multiple fluctuating quantities [143]. Appropriate models for the relevant closure terms will be developed. Inspiration can be found in the methodology and models employed for hydrodynamic turbulence. However, these models have to be carefully analysed and adapted to the specific nature of edge plasma turbulence.

The development of models for the important closure terms proceeds by an analysis of detailed reference data provided by (averaged) data from turbulence code simulations. A systematic approach is followed by the use of reference data from increasingly complex turbulence models that gradually take additional physical effects into account. This gradual approach allows to build a reduced model starting from the basic physics of plasma edge turbulence, to subsequently determine the impact of the refinements in the turbulence model, and integrate it into the reduced model. This thesis will mostly consider 2D interchange-dominated electrostatic turbulence in the SOL where flow shear is limited. Preliminary extensions will be made to cases with DW dynamics and strong flow shear, as well as fully-3D configurations. The effect of neutrals will largely be neglected in the analysis.

An important element in this data driven model development process is the estimation of the model parameters and the selection of the most suited model variant. Appropriate values for the parameters can be determined by optimising the fit between the reference data and the mean-field models that are developed. A Bayesian framework will be applied in order to not only estimate the single "best" value of the model parameters, but also the uncertainty on the model parameters and their mutual correlations. Furthermore, this Bayesian approach allows to compare different models in a statistically relevant way, while inherently taking differences in model complexity and the issue of overfitting into account.

The remainder of this thesis works towards the objective with the following structure. Chapter 2 first reviews the basics of hydrodynamic turbulence and the Reynolds-averaging approach followed to solve the closure problem in hydrodynamic turbulence. Then, the commonly used fluid equations governing

the plasma behaviour in the plasma edge are formulated and averaged to obtain their mean-field equivalent. This already allows to identify the exact form of the perpendicular turbulent heat and particle fluxes that need to be closed. Next, the treatment of these fluxes in mean-field codes as well as a number of models recently proposed in literature to self-consistently determine these fluxes are discussed.

Chapter 3 explains the basic ansatz that will be followed in this thesis for developing mean-field turbulent transport models and provides a physical argumentation for it. The closure strategy that is followed relies on relating the effective turbulent transport coefficients to characteristic quantities of the turbulence, in particular the perpendicular turbulent kinetic energy $k_\perp$ and enstrophy $\zeta_\perp$. Next, analytical transport equations for these quantities are presented. These equations provide insight in the dynamics of the turbulence, in the form of new closure terms that appear as sources and sinks of the turbulence. Notably, an analytical relation for the interchange source of the turbulent kinetic energy is identified. Finally, the Bayesian inference methodology that will be used for parameter estimation and model comparison is introduced.

Chapter 4 applies the framework developed earlier to the case of 2D isothermal electrostatic interchange-dominated E×B drift turbulence in the SOL. Reference data for this simplified flow case is obtained from the TOKAM2D turbulence code [109, 116, 141]. Two mean-field turbulent transport models, the $k_\perp$ and $k_\perp - \zeta_\perp$ model, will be developed and compared. A good match with the TOKAM2D reference data is achieved by both models. It is believed that these simple models already capture some of the basic physics of turbulent plasma edge transport.

The developed models are then further tested and extended for more challenging flow cases in chapters 5 and 6. First, a core region with drift-wave like dynamics is added in chapter 5, which also introduces strong flow shear in the simulations. Both elements are found to require adjustments in the particle transport model. Next, the effect of including the pressure gradient drift in the inertia is investigated. This is found to require adjustments to the model coefficients. Chapter 6 then investigates the anisothermal case in which not only the turbulent particle flux, but also the turbulent heat fluxes need to be modelled. Furthermore, this introduces a new instability capable of driving the turbulence. A natural extension of the previously developed $k_\perp$ model is found to reproduce the reference data with good accuracy, although the detailed dynamics of the new instability are not captured.

Chapter 7 provides a first step in the extension of the approach towards 3D turbulence (2D mean-field cases). This is guided by a preliminary analysis of 3D turbulence code data for isothermal slab cases generated with the TOKAM3X

[157] turbulence code. In particular, this enables a more detailed investigation of the parallel dynamics and their effect on the turbulent perpendicular kinetic energy.

Finally, chapter 8 summarises the main results of this thesis, presents a conclusion, and suggests tracks for future research.

# Chapter 2

# Plasma edge turbulence and state of the art in mean-field modelling

The previous chapter has established that turbulent transport processes largely determine the outward power and particle fluxes in the plasma edge. Thus, properly modelling these processes is crucial to correctly predict the load on the divertor. However, doing so using acceptable computational resources remains challenging. The aim of this chapter is to review the current state of the art in modelling the average turbulent transport.

There is a long history of studying 3D hydrodynamic turbulence, which has led to a good understanding of it, and a range of models have been developed. In view of this, section 2.1 will investigate how this related research field may serve as inspiration for plasma edge turbulence modelling. Particular attention will go to the Reynolds averaging methodology and the strategy to solve the closure problem in hydrodynamic turbulence.

Next, section 2.2 will present the instantaneous fluid equations governing the plasma edge turbulence. Similarities and differences with respect to the hydrodynamic case will be highlighted, to get an idea of the degree to which knowledge on hydrodynamic turbulence can be transferred to the plasma edge case at hand. Section 2.3 will then average the instantaneous equations derived in the previous section in order to obtain the corresponding mean-field equations. In these equations, the closure terms which require modelling will be identified. The lacking treatment of these closure terms in current mean-field codes, and

models suggested in literature to improve this will be discussed. Finally, section 2.4 will conclude this chapter.

## 2.1 Hydrodynamic turbulence and RANS approach

Turbulence is a ubiquitous feature of fluid flows which is commonly encountered in non-plasma applications as well. The standard setting that has been most often studied is that of 3D hydrodynamic turbulence. Even though there are very important differences between the plasma edge turbulence of interest in this work and this 3D hydrodynamic turbulence, it is worthwhile to take the state of the art in this related field into account and to draw inspiration from it. Especially the Reynolds-averaged Navier-Stokes (RANS) models to calculate the average of the turbulent flow field are of interest since the goal of this thesis is to advance the development of equivalent models for the plasma edge, which are only in their infancy at the time of writing.

Hydrodynamic fluid flow can be described by the Navier-Stokes equations:

$$\frac{\partial \rho}{\partial t} + \nabla \cdot (\rho \mathbf{V}) = 0, \tag{2.1}$$

$$\frac{\partial \rho \mathbf{V}}{\partial t} + \nabla \cdot (\rho \mathbf{V} \mathbf{V}) = -\nabla p - \nabla \cdot \Pi. \tag{2.2}$$

In these equations, $t$ is time, $\rho$ is the mass density, $\mathbf{V}$ the fluid velocity, $p$ the pressure and $\Pi$ the viscous stress tensor. Particle sources and body forces are assumed to be zero in these equations. If we consider the archetypical example of Newtonian constant density flow in which $\rho$ is constant in space and time and the stress tensor is $\Pi = -\mu(\nabla \mathbf{V} + \nabla \mathbf{V}^T)$ with $\mu$ the dynamic viscosity, the equations reduce to

$$\nabla \cdot \mathbf{V} = 0, \tag{2.3}$$

$$\frac{\partial \mathbf{V}}{\partial t} + \nabla \cdot (\mathbf{V}\mathbf{V}) = -\frac{\nabla p}{\rho} + \nu \nabla^2 \mathbf{V}, \tag{2.4}$$

with $\nu = \mu/\rho$ the kinematic viscosity. Equation 2.3 can be used to rework equation 2.4 into a Poisson equation for the pressure

$$\nabla^2 p = -\rho \nabla \mathbf{V} : \nabla \mathbf{V}^T = -\rho \nabla \cdot (\nabla \cdot (\mathbf{V}\mathbf{V})). \tag{2.5}$$

This way, equations 2.4 and 2.5 form a closed set of equations for the velocity and pressure fields.

In 3D constant-density hydrodynamic turbulence as described above, the general picture is the following. Energy is injected into the turbulence at some macroscopic length scale. Eddies of this size having absorbed this energy tend to break down into smaller eddies, transferring the energy to smaller length scales. This process of eddy break-up is dominated by inertial forces and goes on until the energy reaches the Kolmogorov length scale at which viscous effects become important and the energy is taken out of the turbulence and dissipated into heat. The energy is said to follow a direct cascade, being transferred from large to ever smaller length scales [126]. The basic mechanism responsible for the eddies becoming smaller and smaller is vortex stretching. According to Helmholtz theorem [126] for inviscid constant-density hydrodynamic flow, lines of vorticity are conserved in fluid elements, i.e. they could be imagined to be "frozen-in" the flow. Now in general, the end points of a vortex tube in a turbulent flow will move away from each other (following the random walk principle) such that vortex tubes are stretched. Due to the incompressibility, this stretching leads to the thinning of the vortex tube. Moreover, due to the conservation of angular momentum, this thinning leads to an increase of the vorticity of the tubes. Thus, this vortex stretching leads to a reduction of the scales of the turbulence and an increase of the vorticity. Note that vortex stretching is inherently a 3D effect. A third direction is required in order for the end points of a vortex tube to be able to move away from each other [9, 126].

Vortex stretching can also be identified in the vorticity equation, which can be obtained by taking the curl of equation 2.4:

$$\frac{D\boldsymbol{\omega}}{Dt} = \boldsymbol{\omega} \cdot \nabla \mathbf{V} + \nu \nabla^2 \boldsymbol{\omega}, \tag{2.6}$$

where $\boldsymbol{\omega} = \nabla \times \mathbf{V}$ is the vorticity vector. The first term to the RHS of this equation is the vortex stretching term leading to the creation of vorticity in fluid elements (and, losely speaking, of turbulence), while the second term leads to viscous dissipation of it. It can be remarked here as well that the vortex stretching term can only be nonzero if a velocity gradient along the direction of the vorticity vector can exist [126].

In hydrodynamic turbulence, an extensive framework for turbulence modelling has been developed over the past decades. Three modelling approaches can be distinguished: DNS, LES and RANS modelling. In direct numerical simulations (DNS), the Navier-Stokes fluid equations (2.1-2.2 or 2.3-2.4) are solved on a very fine grid, such that even the smallest turbulent length and time scales are explicitly simulated. This generally requires significant computational efforts,

but yields a very accurate description of the flow. In large eddy simulations (LES), only large scale turbulent structures are resolved, while the small scale turbulent fluctuations are approximated using models. This approach reduces the computational cost at the expense of the accuracy and requires accurate models for the fine scales. Lastly, in Reynolds-averaged Navier-Stokes (RANS) modelling, the Navier-Stokes equations are averaged such that only macroscopic quantities of the flow are calculated. The effects of turbulent fluctuations appear as closure terms consisting of correlations between fluctuating quantities. In this RANS approach, each turbulent quantity $u$ (which can vary chaotically in space and time) is decomposed in an average component $\bar{u}$ and a fluctuating component $u'$ according to [126]

$$u = \bar{u} + u', \tag{2.7}$$

$$\bar{u} \triangleq \lim_{N \to \infty} \frac{1}{N} \sum_{i=1}^{N} u^{(i)}. \tag{2.8}$$

The latter formula defines the ensemble average where $u^{(i)}$ is an individual realisation of the flow. Applying this averaging operator to the incompressible NS equations 2.3-2.4 yields

$$\nabla \cdot \bar{\mathbf{V}} = 0, \tag{2.9}$$

$$\frac{\partial \bar{\mathbf{V}}}{\partial t} + \nabla \cdot (\bar{\mathbf{V}}\bar{\mathbf{V}} + \overline{\mathbf{V}'\mathbf{V}'}) = -\frac{\nabla \bar{p}}{\rho} + \nu \nabla^2 \bar{\mathbf{V}}, \tag{2.10}$$

Equation 2.9 could again be replaced by a Poisson equation for the average pressure:

$$\nabla^2 \bar{p} = -\rho \nabla \cdot (\nabla \cdot (\bar{\mathbf{V}}\bar{\mathbf{V}} + \overline{\mathbf{V}'\mathbf{V}'})). \tag{2.11}$$

In these equations, the Reynolds stresses (RS) $\overline{\mathbf{V}'\mathbf{V}'}$ appear, which depend on the correlation between fluctuating velocity components. They cannot be calculated self-consistently from the average velocity $\bar{\mathbf{V}}$ that is obtained from equations 2.10-2.11. As such, this is a closure term for which an external model is needed in order to solve the system of averaged Navier-Stokes equations. The RS are the primary closure terms that needs to be modelled in RANS modelling. Various models for these closure terms have been developed. Most of these models solve additional partial differential equations for higher order moments of the fluctuations such as turbulent kinetic energy ($k$) or Reynolds stresses

themselves. Some well-known examples are the $k$, $k - \varepsilon$ and $k - \omega$ models, which are widely used for industrial applications today [126].

In the remainder of this section, we will discuss the $k$ model in some more detail to give insight in the way RANS models tackle the closure problem for the RS. To start of with, the turbulent kinetic energy is defined as

$$k \triangleq \frac{1}{2}\mathrm{tr}(\overline{\mathbf{V}'\mathbf{V}'}) = \frac{\overline{\mathbf{V}'^2}}{2}. \tag{2.12}$$

It is thus that part of the kinetic energy of the flow that is present in the fluctuating part of the velocity field. As such, it is an interesting measure for the intensity of the turbulence and can be used to construct a characteristic velocity scale for it.

The $k$ model, like the $k - \varepsilon$ and $k - \omega$ models, makes use of the turbulent viscosity hypothesis, which assumes the RS to behave similarly to the viscous stress tensor. Thus, in analogy with the total pressure tensor, the RS are modelled as

$$\overline{\mathbf{V}'\mathbf{V}'} = \frac{2}{3}kI - \nu_t(\nabla\bar{\mathbf{V}} + \nabla\bar{\mathbf{V}}^T) \tag{2.13}$$

In this equation, $\nu_t$ is the turbulent viscosity, which is to be interpreted as some kind of effective turbulent viscosity acting on the averaged flow field. This turbulent viscosity now needs to be modelled still. The $k$ model does so by taking $\nu_t = C_\nu l_m \sqrt{k}$, where $l_m$ is a characteristic mixing length scale to be chosen and $C_\nu$ a model coefficient. This expression has the same dimensions as a viscosity, and it seems sensible to relate the strength of the RS to the turbulent intensity as characterised by $k$. This now shifts the closure problem to modelling $k$. Manipulating the momentum equation 2.4, a transport equation for $k$ can be derived:

$$\frac{\partial k}{\partial t} + \nabla \cdot (k\bar{\mathbf{V}} + \mathcal{T}) = \mathcal{P} - \varepsilon, \tag{2.14}$$

$$\mathcal{P} = -\overline{\mathbf{V}'\mathbf{V}'} : \nabla\bar{\mathbf{V}}, \tag{2.15}$$

$$\varepsilon = \frac{\nu}{2}\overline{(\nabla\mathbf{V}' + \nabla\mathbf{V}'^T) : (\nabla\mathbf{V}' + \nabla\mathbf{V}'^T)}, \tag{2.16}$$

$$\mathcal{T} = \frac{\overline{\mathbf{V}'^2\mathbf{V}'}}{2} + \frac{\overline{p'\mathbf{V}'}}{\rho} - \nu\overline{\mathbf{V}' \cdot (\nabla\mathbf{V}' + \nabla\mathbf{V}'^T)}. \tag{2.17}$$

This provides yet another way of looking at the energy cascade. Energy is injected into the turbulence by the production term $\mathcal{P}$ through the RS acting on the average flow shear. This turbulent kinetic energy is then either dissipated locally at the fine scales by viscous effects through the dissipation $\varepsilon$, or transported in space by the transport terms on the LHS (to be dissipated by $\varepsilon$ elsewhere). However, equation 2.14 still needs closures for $\varepsilon$ and $\mathcal{T}$ before it can be used to model $k$. The understanding of the energy cascade and dimensional arguments are used to provide a closure for $\varepsilon$, while transport $\mathcal{T}$ is modelled using a gradient diffusion hypothesis (see later in this section). All this together leads to the following $k$ model:

$$\frac{\partial k}{\partial t} + \nabla \cdot (k\bar{\mathbf{V}} - \frac{\nu_t}{\theta_k}\nabla k) = -\overline{\mathbf{V}'\mathbf{V}'} : \nabla\bar{\mathbf{V}} - \frac{C_\varepsilon}{l_m}k^{3/2} \tag{2.18}$$

$$\overline{\mathbf{V}'\mathbf{V}'} = \nu_t(\frac{2}{3}kI - \nu_t(\nabla\bar{\mathbf{V}} + \nabla\bar{\mathbf{V}}^T) \tag{2.19}$$

$$\nu_t = C_\nu l_m \sqrt{k} \tag{2.20}$$

In these equations, $\theta_k$ is the turbulent Prandtl number and $C_\nu$ and $C_\varepsilon$ are coefficients to be determined. Hence, together with the averaged Navier-Stokes equation 2.10-2.11, this leads to a closed set of equations for the averaged flow field. In summary, the $k$ model allows solving the averaged Navier-Stokes equations by closing the RS. A model for these is constructed based on $k$, for which an additional PDE is solved.

As mentioned above, extensions of this $k$ model also exist, e.g. the $k - \varepsilon$ and $k - \omega$ models. In the $k - \varepsilon$ model, the dissipation $\varepsilon$ is no longer modelled as a scaling law based on $k$, but by a separate transport equation. This equation is typically taken ad-hoc, based on dimensional arguments and trying to replicate the energy cascade. The additional field for $\varepsilon$ that is now available is used to complete the scaling for $\nu_t = C_\nu k^2/\varepsilon$ such that the mixing length $l_m$ is no longer needed.

Another noteworthy topic is the treatment of the transport of a (passive) scalar in RANS modelling. The total flux $\mathbf{\Gamma}_u$ of a scalar $u$ can be written as

$$\mathbf{\Gamma}_u = \overline{u\mathbf{V}} = \bar{u}\bar{\mathbf{V}} + \overline{u'\mathbf{V}'}. \tag{2.21}$$

Here, the first term represents transport by the mean velocity, while the second term governs turbulent transport. This second term again requires closure. A typical way to model it is to make use of the gradient-diffusion hypothesis

$$\overline{u'\mathbf{V}'} = -D_u\nabla\bar{u}, \tag{2.22}$$

with $D_u$ an effective turbulent diffusion coefficient. Hence, the "random" turbulent fluctuations are expected to produce a flux of $u$ down the gradient of its average, much like regular molecular diffusion would. The turbulent diffusion coefficient $D_u$ in this expression has the same dimensions as the turbulent viscosity $\nu_t$ and a similar interpretation as well. As such, both are typically modelled similarly, i.e. $D_u = \nu_t/\theta_u$, where $\theta_u$ is a turbulent Prandtl number. Hence, if the $k$ model is used, the turbulent flux of $u$ would typically be modelled as

$$\overline{u'V'} = -D_u \nabla \bar{u} = -\frac{C_\nu l_m}{\theta_u} \sqrt{k} \nabla \bar{u}. \tag{2.23}$$

## 2.2  Plasma edge turbulence: governing equations

While the approach followed by plasma turbulence codes is similar to the approach followed by DNS, mature LES- or RANS-like equivalents for plasma turbulence are missing to date. It is possible to average the fluid-like Braginskii equations governing the turbulence, taking the turbulent fluctuations into account though, as was done in [143]. Some first steps towards a RANS-like model for plasmas have been set only recently in [11, 12, 13, 14, 34, 44, 45, 46, 47, 113]. This section will first discuss the full turbulence equations governing the plasma edge. Next, section 2.3 will present their averaged, mean-field equivalent as well as the treatment of these averaged equations in mean-field transport codes.

Plasma edge turbulence codes solve fluid equations describing the dominant dynamics in the plasma edge on very fine time and length scales to resolve the turbulent flow field, as is done in a DNS approach for hydrodynamic turbulence. Examples of such plasma edge turbulence codes capable of resolving the whole 3D flow field self-consistently (without assuming a scale separation between turbulence and the background plasma) are TOKAM3X [157], GBS [90, 132], GRILLIX [154] and SOLEDGE3X [33]. Simulations with such turbulence codes require substantial computational resources. Turbulence codes that resolve the flow field under a 2D approximation also exist, e.g. TOKAM2D [141, 109, 116], HESEL [119, 159] and SOLT [139, 140]. These are significantly more affordable, but are typically only reliable to model a small region of the reactor.

While some concepts and methodologies can presumably be transferred, plasma edge turbulence is inherently different from the familiar 3D constant-density hydrodynamic case discussed in the previous section. Some elements leading to significantly different dynamics are the following. The strong magnetic field present in the tokamak plasma edge and its interaction with the plasma
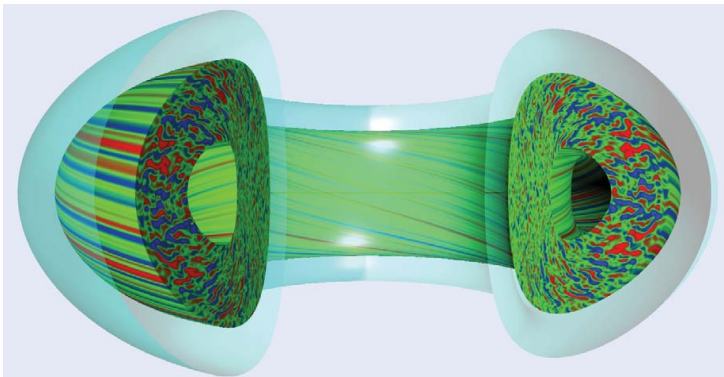
Figure 2.1: Visualisation of the instantaneous plasma density in a tokamak. Figure reproduced from Ref. [48].

fluid leads to a strong anisotropy of the turbulence. Plasma particles can move almost unhindered in the direction parallel to the magnetic field (the parallel direction), while these charged particles are strongly constrained in their movement perpendicular to the magnetic field line due to Lorentz forces. As a result of this, the turbulent structures are elongated along the magnetic field lines, i.e. the length scale of the turbulent structures is much larger in the parallel direction than in the perpendicular direction. This leads to a quasi-2D structure of turbulence. Figure 2.1 illustrates this instantaneous structure based on a detailed numerical simulation.[1]

Chapters 4 to 6 will almost exclusively consider the turbulence as fully 2D according to the commonly made flute approximation [36, 71, 92, 119, 141]. In such 2D turbulence, the vortex stretching mechanism is no longer active, completely changing the dynamics of the turbulence. Indeed, in 2D inviscid hydrodynamic turbulence the energy cascade is reversed with energy now being transferred from small to large length scales in an inverse cascade instead [4, 71, 169]. Similar characteristics are also expected in 2D plasma edge turbulence [36, 71]. In the absence of vortex stretching, other mechanisms are required in order to create turbulence. This can again be shown in the vorticity equation (for a plasma this time) [51]:

$$\frac{D\boldsymbol{\omega}}{Dt} = \boldsymbol{\omega} \cdot \nabla \mathbf{V} - \boldsymbol{\omega} \nabla \cdot \mathbf{V} + \frac{\nabla \rho \times \nabla p}{\rho^2} + \nabla \times (\frac{\mathbf{J} \times \mathbf{B}}{\rho}) - \nabla \times (\frac{\nabla \cdot \Pi}{\rho}) \quad (2.24)$$

_____

[1] Note this figure does not show the plasma edge in particular, but the general, qualitative picture it paints is representative for the plasma edge as well.

In this equation, $p$ is the plasma pressure, $\mathbf{J}$ the plasma current density and $\mathbf{B}$ the magnetic field. The first term on the RHS is still the vortex stretching term, but will be zero in the 2D case. The second term is a new term due to the compressibility of the plasma. The third term enters because the plasma density is not constant. In this case, the pressure gradient can give rise to a drive for the turbulence. This term is not plasma-specific and also occurs in hydrodynamic flows with variable density, see for example the case of Rayleigh-Taylor-driven turbulence [2, 27, 134]. The fourth term is then the effect of the Lorentz forces acting on the plasma and introduces electromagnetic effects into the vorticity generation. The last term represents viscous dissipation. In this work, it will be shown that the pressure gradient term and the Lorentz term are the most important ones for the dynamics of the turbulence.

Apart from these rather general considerations, some more specific features of the plasma edge case could be expected to influence the dynamics. First of all there is the specific magnetic geometry and the very strong flow to the plasma sheath along the magnetic field in the third direction. Also, the ionisation of neutrals into plasma particles leads to significant sources of particles, momentum and energy [153]. Next, the temperature in the plasma edge varies by orders of magnitude such that an energy equation needs to be coupled to the system.

## 2.2.1   Fluid turbulence equations for the plasma edge

Having briefly established a qualitative description of plasma edge turbulence and highlighted the differences with 3D constant density hydrodynamic turbulence, a systematic overview of the equation set used to describe plasma edge turbulence will now be given. The equations presented in this section are largely based on the internal technical report by Dekeyser [51].

To start of with, the plasma under consideration will be assumed to behave as a continuum, such that the fluid approximation can be used and kinetic effects for the plasma can be neglected. This fluid assumption is often made in plasma edge modelling despite the fact that edge plasmas are in practice often just marginally collisional [153], limiting the strict validity of the fluid treatment. Especially in the parallel direction, the particle mean-free path can be longer than the mean-field gradient lengths, in particular close to the plasma sheath. Nonetheless, fluid treatments do predict similar values for the main quantities of interest as fully kinetic treatments [153]. Hence, collisional closures are still widely used, also in modern plasma edge turbulence codes [33, 90, 132, 154, 157]. Furthermore, kinetic correction for the fluid approach have been suggested in literature [7, 82, 153]. As an illustration, table 1.1 shows typical orders of magnitude for collisional time and length scales.

It will also be assumed that the length scales of interest for the transport and the turbulence are much larger than the Debye length $L_{Debye}$, which is typically well satisfied in the plasma edge (see table 1.1). At this condition, the plasma can be assumed to be quasi-neutral since the charged ion and electron particles organise themselves in such a way that the net space charge remaining in a control volume on the length scales of interest is negligible [82]. The result of quasi-neutrality is that Gauss's law cannot be used to calculate the electric field $\mathbf{E}$, because the net space charge is assumed to be zero. Instead, the charge balance equation specifying that no charges can build up in the plasma will be used for this, as will be discussed in section 2.2.2.

When such a quasi-neutral fluid approach is adopted, the plasma can be described by the Braginskii equations [32, 71]. The continuity equations for the ions and electrons then take the following form:

$$\frac{\partial n_\mathrm{i}}{\partial t} + \nabla \cdot (n\mathbf{V}_i) = S_{n_\mathrm{i}}, \tag{2.25}$$

$$\frac{\partial n_\mathrm{e}}{\partial t} + \nabla \cdot (n_e\mathbf{V}_e) = S_{n_\mathrm{e}}. \tag{2.26}$$

In these equations $n_i$ and $n_e$ are the ion and electron particle densities, $\mathbf{V}_i$ and $\mathbf{V}_e$ the ion and electron velocities, and $S_{n_\mathrm{i}}$ and $S_{n_\mathrm{e}}$ the ion and electron particle sources. Under quasi-neutrality, the densities are related as $n_e = \sum_i Z_i n_i$ with $Z_i$ the charge state of ionic species $i$. In the remainder of this manuscript we consider plasmas consisting of only a single hydrogen isotope ($Z_i = 1$) such that $n_i = n_e$. Hence, only one continuity equation, 2.25 or 2.26 needs to be used, not both. For simplicity of notation, we will drop the subscript on the density $n = n_i = n_e$ and on the ion velocity $\mathbf{V}_i = \mathbf{V}$. Note that using these definitions, the mass density is equal to $\rho = mn$, with $m$ the ion mass (and neglecting the electron mass).

In order for quasi-neutrality to be maintained, the condition

$$\nabla \cdot \mathbf{J} = 0 \tag{2.27}$$

is applied such that no net charge can build up in the plasma. This is called the charge balance equation. In this equation, the plasma current density is defined as $\mathbf{J} = en(\mathbf{V} - \mathbf{V}_e)$.

The momentum equation for the ions is written as

$$\frac{\partial mn\mathbf{V}}{\partial t} + \nabla \cdot (mn\mathbf{V}\mathbf{V})$$

$$= -\nabla p_i - \nabla \cdot \Pi + en\mathbf{E} + en\mathbf{V} \times \mathbf{B} - \mathbf{R}_{ei} + \mathbf{S}_m. \tag{2.28}$$

In this equation, $\Pi$ is the ion viscous stress tensor, $\mathbf{E}$ the electric field, $\mathbf{B}$ the magnetic field, $\mathbf{R}_{ei}$ the friction force between ions and electrons and $\mathbf{S}_m$ sources of ion momentum (e.g. due to ion-neutral collisions).

The electron momentum equation has a similar form:

$$-\nabla p_e - en\mathbf{E} - en\mathbf{V}_e \times \mathbf{B} + \mathbf{R}_{ei} = 0, \tag{2.29}$$

with $p_e$ the electron pressure. Notice that the terms scaling with electron inertia have been neglected because of the very low electron mass [149]. The momentum equations of ions and electrons can be added to obtain the plasma momentum equation:

$$\frac{\partial mn\mathbf{V}}{\partial t} + \nabla \cdot (mn\mathbf{V}\mathbf{V}) = -\nabla p - \nabla \cdot \Pi + \mathbf{J} \times \mathbf{B} + \mathbf{S}_m, \tag{2.30}$$

where $p = p_i + p_e$ is the total pressure. The ion and electron thermal energy equations are

$$\frac{3}{2}\frac{\partial p_i}{\partial t} + \nabla \cdot (\frac{5}{2}p_i\mathbf{V} + \mathbf{q}_i) = \mathbf{V} \cdot \nabla p_i - \Pi : \nabla \mathbf{V}^T - Q_{ei} + \frac{3}{2}S_{p_i}, \tag{2.31}$$

$$\frac{3}{2}\frac{\partial p_e}{\partial t} + \nabla \cdot (\frac{5}{2}p_e\mathbf{V}_e + \mathbf{q}_e) = \mathbf{V}_e \cdot \nabla p_e + \frac{\mathbf{J}}{en} \cdot \mathbf{R}_{ei} + Q_{ei} + \frac{3}{2}S_{p_e}, \tag{2.32}$$

Here, the internal energy of the fluid is $3p_{i/e}/2 = 3nT_{i/e}/2$, with $T_{i/e}$ respectively the ion or electron temperature. $Q_{ei}$ is the collisional heat transfer from ions to electrons, $\mathbf{q}_{i/e}$ the conductive heat flux and $S_{pi/e}$ the sources of thermal energy.

In theory, equations 2.25-2.32 could be solved for $n$, $\mathbf{V}$, $\mathbf{V}_e$, $p_i$ and $p_e$. This still requires expressions for the sources $S_n$, $\mathbf{S}_m$, $S_{p_i}$, $S_{p_e}$, the viscous stress $\Pi$, the force $R_{ei}$, the heat fluxes $\mathbf{q}_i$ and $\mathbf{q}_e$, the electron-ion heat exchange $Q_{ei}$ as a function of the afore mentioned state variables. Such expressions can be found for example in Refs. [32, 71]. In addition, the electromagnetic quantities $\mathbf{E}$ and $\mathbf{B}$ have to be treated. The treatment of the coupling with the electric and magnetic fields will be discussed in more detail in the next section. Direct

numerical solution of the equations presented here is very difficult, in particular for the perpendicular components of the momentum equation 2.30 which are strongly dominated by the force terms on the right-hand side, with the inertial terms being much smaller. Instead, the equations are usually reformulated as discussed in the next section.

## 2.2.2 Drift formulation through charge balance equation

In order to arrive at a more workable equation set, the equations are first rewritten in such a way that the fluxes parallel to the magnetic field (in the magnetic field direction $\mathbf{b} = \mathbf{B}/B$) and the fluxes perpendicular to it are decoupled. Next, a drift ordering is followed to identify the dominant velocity components. The equations presented in this section are largely based on the internal technical report by Dekeyser [51] and the 2003 paper by Scott [143].

The drift ordering that will be used relies on the assumption that strong magnetic fields are present in the plasma edge such that the (ion) gyration time and length scales are much smaller than those of the plasma as a fluid (see table 1.1) [71, 82, 149]. Note that the strict validity of the drift ordering is limited by the fact that the smallest length scales of the turbulent dynamics are comparable to the ion gyro-radius [71, 143, 147]. While formally it may be needed to take finite larmor radius effects into account, it is assumed here that a regular drift description still captures the dominant dynamics of the turbulence. Note that this is also the route taken by modern plasma edge turbulence codes [33, 90, 132, 154, 157].

In this thesis, drift hydrodynamic dynamics (DHD) will be considered, which is suitable to describe plasma edge transport. Compared to magnetohydrodynamics (MHD), the fast time scale used in this ordering is relatively slow. As a result, slower dynamics are retained in DHD, while it excludes some fast dynamics present in MHD. In particular, electrodynamic induction is small in DHD leading to dominantly electrostatic dynamics [71]. Moreover, the ratio between the plasma pressure and the magnetic pressure is typically very small in the plasma edge, i.e. $\beta \triangleq 2\mu p/B^2 \ll 1$ with $\mu$ the plasma magnetic permeability. Such a low $\beta$ plasma justifies the assumption that $\nabla \times \mathbf{B} \approx 0$ (sometimes called "vacuum field" assumption) where the plasma current is small and thus plays a negligible role in Ampère's law [82]. This assumption likewise differs strongly from the (ideal) MHD description. The reader interested in MHD and MHD turbulence is referred to Refs. [26, 80].

The main idea in reformulating the plasma edge fluid equations presented in section 2.2.1 is to exploit the cross product with the magnetic field $\mathbf{B}$ in the Lorentz force term in the momentum equations to find expressions for the ion

and electron fluxes. This relies on using the identity $(\mathbf{V} \times \mathbf{B}) \times \mathbf{B} = -\mathbf{V}_\perp$, with $\mathbf{V}_\perp$ the velocity in the plane perpendicular to the magnetic field direction. Hence, taking the cross product of $\mathbf{B}$ with the momentum equations 2.28, 2.29 and 2.30 and rewriting yields expressions for the perpendicular components of the ion and electron fluxes and currents:

$$\mathbf{\Gamma}_{\perp,i} = n\mathbf{V}_\perp = \underbrace{-\frac{m}{eB}(\frac{\partial n\mathbf{V}}{\partial t} + \nabla \cdot (n\mathbf{V}\mathbf{V})) \times \mathbf{b}}_{n\mathbf{V}_{p,0}} \underbrace{-\frac{\nabla p_i \times \mathbf{b}}{eB}}_{n\mathbf{V}_{*,i}}$$

$$+ \underbrace{\frac{n\mathbf{E} \times \mathbf{b}}{B}}_{n\mathbf{V}_E} \underbrace{-\frac{\nabla \cdot \Pi}{eB} \times \mathbf{b} + \frac{\mathbf{S}_m \times \mathbf{b}}{eB}}_{n\mathbf{V}_{p,\Pi}} - \frac{\mathbf{R}_{ei} \times \mathbf{b}}{eB}, \quad (2.33)$$

$$\mathbf{\Gamma}_{\perp,e} = n\mathbf{V}_{\perp,e} = \underbrace{\frac{\nabla p_e \times \mathbf{b}}{eB}}_{n\mathbf{V}_{*,e}} + \underbrace{\frac{n\mathbf{E} \times \mathbf{b}}{B}}_{n\mathbf{V}_E} - \frac{\mathbf{R}_{ei} \times \mathbf{b}}{eB}, \quad (2.34)$$

$$\mathbf{J}_\perp = e(\mathbf{\Gamma}_{\perp,i} - \mathbf{\Gamma}_{\perp,e}) = \underbrace{-\frac{m}{B}(\frac{\partial n\mathbf{V}}{\partial t} + \nabla \cdot (n\mathbf{V}\mathbf{V})) \times \mathbf{b}}_{\mathbf{J}_{p,0}} \underbrace{-\frac{\nabla p \times \mathbf{b}}{B}}_{\mathbf{J}_*}$$

$$\underbrace{-\frac{\nabla \cdot \Pi}{B} \times \mathbf{b} + \frac{\mathbf{S}_m \times \mathbf{b}}{B}}_{\mathbf{J}_{p,\Pi}}. \quad (2.35)$$

In these equations, the total particle flux is decomposed in a parallel and a perpendicular component as $\mathbf{\Gamma} = \mathbf{\Gamma}_{||} + \mathbf{\Gamma}_\perp$, where $\mathbf{\Gamma}_{||} \triangleq (\mathbf{\Gamma} \cdot \mathbf{b})\mathbf{b}$ and $\mathbf{\Gamma}_\perp \triangleq -\mathbf{b} \times (\mathbf{b} \times \mathbf{\Gamma})$.

The plasma drifts that were introduced in a mechanistic way in section 1.2.1 now appear in equations 2.33-2.35.[2] The first term on the RHS of equation 2.33 represents the flux due to the polarisation drift and can be seen to be due to inertial effects. The viscous term and the term due to momentum sources will likewise be included in this polarisation drift. Together, they will be denoted $\mathbf{V}_p = \mathbf{V}_{p,0} + \mathbf{V}_{p,\Pi}$ for the polarisation velocity and $\mathbf{J}_p = \mathbf{J}_{p,0} + \mathbf{J}_{p,\Pi}$ for the polarisation current. As there is no electron equivalent (because the electron inertia and viscosity have been neglected) for this drift, it also leads to a current in equation 2.35. The second term in equation 2.33 is the diamagnetic flux which is due to the pressure gradient force. This term has an analogue in the

---

[2]Note that the section 1.2.1 mainly introduced the drifts from a guiding center approach, while the drifts are here derived from the fluid approach.

electron flux, second term in equation 2.34. Since both depend on the particle charge, these fluxes also lead to a current, called diamagnetic current, second term in 2.35. The third term in 2.33 represents the E×B drift. It is also present in the electron flux, and since this one does not depend on either the mass or the charge of the particle, it does not lead to a current.

A rigorous ordering of the drift terms in these equations shows that the E×B and diamagnetic drifts are typically the dominant terms, while the polarization drift is of higher order [71, 82, 149]. Furthermore, the E×B drift is expected to be more important for the transport than the diamagnetic drift. The reason for this is that the only nonzero contribution to the divergences of the diamagnetic particle and heat fluxes (see later) can be shown to be due to gradients of the magnetic field, which typically have much larger length scales than the turbulent quantities [147, 162]. This is commonly used to write

$$\mathbf{V} \approx \mathbf{V}_0 = \mathbf{V}_{||} + \mathbf{V}_E + \mathbf{V}_*, \qquad (2.36)$$

with $\mathbf{V}_E \triangleq E \times \mathbf{b}/B$ the E×B velocity and $\mathbf{V}_{*,i/e} \triangleq -\nabla p \times \mathbf{b}/(qnB)$ the diamagnetic velocity, where $q$ is the particle charge, i.e. $e$ for the ion and $-e$ for the electron. For the reason given above, the diamagnetic contribution is also regularly neglected in this expression. Note that the inclusion of the diamagnetic current $\mathbf{J}_*$ in the charge balance equation 2.41 is of fundamental importance though (as there is no current due to ExB drifts). Hence, the dominant velocity in the perpendicular turbulent plasma transport that will be investigated in this work is the E×B velocity.

As the E×B drift velocity is of prime importance in the perpendicular direction, the treatment of the magnetic field and the electric field are crucial. From the DHD description and/or the low $\beta$ assumption, it follows that the externally imposed magnetic field (i.e. by the toroidal field coils and the plasma current in the core) and far exceeds the magnetic field fluctuations generated by electromagnetic effects in the plasma edge. The net transport as a result of magnetic field lines fluctuating around their equilibrium position (magnetic flutter transport) is also deemed to be negligible [71, 143, 153]. For these reasons, the magnetic field $\mathbf{B}$ will be assumed to be constant in time and externally imposed (with exception of its treatment in the parallel electric field).

The electric field can then be written as

$$\mathbf{E} = -\nabla\phi - \frac{\partial \mathbf{A}}{\partial t}. \qquad (2.37)$$

In this equation $\phi$ is the electrostatic potential and $\mathbf{A}$ is the magnetic vector potential defined as $\mathbf{B} \triangleq \nabla \times \mathbf{A}$ with $\nabla \cdot \mathbf{A} \triangleq 0$. The electrostatic contribution

to the electric field is widely accepted to be dominant in the plasma edge, and the electromagnetic contribution is often neglected (low $\beta$). In this text as well, it will be neglected in the turbulence model used in chapters 4-7. The inductive contribution due to $\mathbf{A}_\perp$ is found to be small because of the rather slow time scales assumed in the DHD ordering [71, 149]. Literature indicates however that the parallel magnetic vector potential $\mathbf{A}_{||}$ may play a role in the dynamics of the turbulence in the plasma edge through its presence in the electric field, where it may be of particular importance for the drift wave coupling (see section 3.2.5) [71, 131, 143, 145]. Thus, we retain it in the electric field for now:

$$\mathbf{E} = -\nabla\phi - \frac{\partial \mathbf{A}_{||}}{\partial t}. \tag{2.38}$$

The parallel magnetic vector potential can be solved from a Poisson equation stemming from Ampère's law:

$$\nabla_\perp^2 A_{||} = -\mu J_{||}. \tag{2.39}$$

Whether the parallel magnetic vector potential is taken into account or not, the E×B velocity can be written as

$$\mathbf{V}_E = \frac{\mathbf{b} \times \nabla\phi}{B}, \tag{2.40}$$

and is thus determined by the electrostatic potential (and the magnetic field that is assumed to be constant in time in this expression, i.e. without influence of $\mathbf{A}_{||}$). Then, an equation for the electrostatic potential is still needed to be able to calculate the E×B velocity. Since the plasma is assumed to be quasi-neutral, the net space charge is zero and Gauss' law cannot be used. Instead, the charge balance condition 2.27, which maintains the neutrality of the plasma, provides an equation for the electrostatic potential. The charge balance equation can be rewritten as $\nabla \cdot \mathbf{J}_{||} = -\nabla \cdot \mathbf{J}_\perp$, in which we can insert equation 2.35 for the perpendicular current density:

$$-\nabla \cdot \mathbf{J}_p = \nabla \cdot \mathbf{J}_{||} + \nabla \cdot \mathbf{J}_*. \tag{2.41}$$

In this equation, the dominant plasma velocities $\mathbf{V} \approx \mathbf{V}_0$ (see equation 2.36) can be filled out in the inertial part of the the polarisation current $\mathbf{J}_{p,0}$:

$$-\mathbf{J}_{p,0} \approx \frac{m}{B}(\frac{\partial n\mathbf{V}_0}{\partial t} + \nabla \cdot (n\mathbf{V}\mathbf{V}_0)) \times \mathbf{b} = \frac{m}{B}\frac{\partial}{\partial t}\left(\frac{n\nabla_\perp \phi}{B} + \frac{\nabla_\perp p_i}{eB}\right)$$

$$+ \frac{m}{B}\nabla \cdot \left(\mathbf{V}\left(\frac{n\nabla_\perp \phi}{B} + \frac{\nabla_\perp p_i}{eB}\right)\right) + \frac{D\mathbf{b}}{Dt} \times \frac{mn\mathbf{V}_0}{B} \quad (2.42)$$

The LHS of equation 2.41 then effectively includes a time change term for the electrostatic potential. Note that only perpendicular gradients of the electrostatic potential enter in the time-dependent term in this equation. Parallel gradients of the potential enter through the $\nabla \cdot \mathbf{J}_{||}$ term on the RHS of equation 2.41.

The parallel ion velocity and parallel current are computed from the parallel components of the momentum equations 2.29 and 2.30. Indeed, taking the scalar product of these equations with the unit vector along the magnetic field yields

$$-\nabla_{||}p_e - enE_{||} + R_{ei,||} = 0, \quad (2.43)$$

$$\frac{\partial mnV_{||}}{\partial t} + \nabla \cdot (mn\mathbf{V}V_{||}) = -\nabla_{||}p - (\nabla \cdot \Pi) \cdot b + mn\frac{D\mathbf{b}}{Dt} \cdot \mathbf{V}_{0,\perp} + S_{m,||}. \quad (2.44)$$

Note that in the last equation $\frac{D\mathbf{b}}{Dt} \cdot \mathbf{V}_0 = \frac{D\mathbf{b}}{Dt} \cdot \mathbf{V}_{0,\perp}$ since $\frac{D\mathbf{b}}{Dt} \cdot \mathbf{b} = 0$. Equation 2.43 is also referred to as "Ohm's law". Equation 2.38 and the Braginskii closure for the parallel friction force $R_{ei,||} = en\eta_{||}J_{||} - 0.71n\nabla_{||}T_e$ can be filled out in this equation to obtain

$$\nabla_{||}p_e - en\nabla_{||}\phi - en\frac{\partial A_{||}}{\partial t} - e\eta_{||}nJ_{||} + 0.71n\nabla_{||}T_e = 0, \quad (2.45)$$

with $\eta_{||}$ the parallel resistivity. This equation can readily be solved for $\mathbf{J}_{||}$ and then filled out in 2.41. Doing so, also the parallel gradient of the electrostatic potential enters in that equation, such that the full electrostatic potential can be solved for in the end.

Note that we have not made use of the so-called "gyro-viscous cancellation" in the charge balance equation 2.41-2.42 nor in the parallel momentum equation 2.44. This would allow to cancel part of the viscous stress tensor $\nabla \cdot \Pi$ with a part of the momentum transport (approximately $\nabla \cdot mn\mathbf{V}_{*,i}\mathbf{V}_0$). The details of this cancellation remain a topic of study in the community though [127, 136, 138].

As such, the stress tensor $\Pi$ represents the full Braginskii stress tensor and the convective velocity $\mathbf{V}$ (which could be approximated as $\mathbf{V}_0$) includes the diamagnetic velocity $\mathbf{V}_{*,i}$. This interpretation will be maintained in this chapter and the next. In view of later derivations, we will henceforth distinguish the velocity used in the ion convection operators and the velocity considered for the inertia. For this reason, we define the symbol $\mathbf{V}_C$ for the ion convective velocity and avoid writing specific velocity components for it in the plasma momentum equations (charge balance and plasma parallel momentum). It will be assumed that the ion convective velocity $\mathbf{V}_C$ is the same in the plasma momentum equations and in the ion continuity equation, as should be the case in theory. This notation might also facilitate the interpretation of the derivations that will follow in view of the gyro-viscous cancellation. The rigorous validation hereof is left for future work though.

### 2.2.3 Link between charge balance equation and vorticity equation

In plasma edge turbulence modelling, the charge balance equation 2.41 is commonly formulated as a transport equation for a quantity that approximates the (parallel component of the) vorticity. For this reason, the charge balance equation is often called the vorticity equation, even though strictly speaking this is somewhat of a misnomer. Appendix A.1 semi-quantitatively shows that the charge balance equation 2.41 is equivalent to the projection of the vorticity equation 2.24 onto the parallel direction $\mathbf{b}$ divided by $B$. The basic reason for the equivalence between both equations is that in essence they both derive from manipulation of the plasma momentum equation 2.30. Appendix A.1 illustrates that the LHS of the vorticity equation resembles the $\nabla \cdot \mathbf{J}_{p,0}$ term in the charge balance equation, the pressure gradient term in the vorticity equation gives rise to the diamagnetic current divergence in the charge balance equation, and the Lorentz force term to the parallel current divergence.

Having established the relation between the equation for the vorticity and the charge balance equation, the latter will now be reformulated as a transport equation for a quantity that approximates the parallel component of the vorticity, which we will call pseudo-vorticity. This is usually the form of the charge balance equation that is solved in plasma edge turbulence codes. This pseudo-vorticity, which will be denoted $W$ in this work, takes the form [116, 141, 157]

$$W \triangleq \nabla \cdot \left( \frac{\nabla_\perp \phi}{B^2} + \frac{\nabla_\perp p_i}{enB^2} \right) = \nabla \cdot \frac{\mathbf{U}_0}{B}. \tag{2.46}$$

In the last equality, the notation

$$\mathbf{U}_0 \triangleq -\mathbf{b} \times \mathbf{V}_0 = \frac{\nabla_\perp \phi}{B} + \frac{\nabla_\perp p_\mathrm{i}}{enB}. \tag{2.47}$$

has been introduced. Note that $\mathbf{U}_0$ naturally appears in the LHS of the charge balance equation as can be seen in expression 2.42. The pseudo-vorticity $W$ relates to the real vorticity $\boldsymbol{\omega}$ as

$$\boldsymbol{\omega} \cdot \frac{\mathbf{B}}{B^2} \approx W + \frac{\mathbf{U}_0}{B} \cdot \nabla \ln B. \tag{2.48}$$

Hence, the difference between the parallel component of the real vorticity and the pseudo-vorticity is proportional to magnetic field gradients which typically have a much larger length scale than turbulent quantities. Based on this result, it is expected that $W$ can function as a good proxy for the parallel component of $\boldsymbol{\omega}$. Remark that the parallel velocity component is no longer present in these expressions.

Next, the charge balance equation 2.41 is rewritten as a transport equation for $W$. This starts from the inertial part of the polarisation current $\mathbf{J}_{p,0}$, whose divergence can be written as

$$\nabla \cdot \mathbf{J}_{p,0} = en\nabla \cdot \mathbf{V}_{p,0} + e\nabla n \cdot \mathbf{V}_{p,0}. \tag{2.49}$$

Starting from equation 2.42, the inertial part of the polarisation velocity $\mathbf{V}_{p,0}$ can be manipulated as follows:

$$-\mathbf{V}_{p,0} = -\frac{\mathbf{J}_{p,0}}{ne} = \frac{m}{eB}\frac{D}{Dt}\mathbf{U}_0 + \frac{D\mathbf{b}}{Dt} \times \frac{m\mathbf{V}_0}{eB} + \frac{m}{enB}S_{n_\mathrm{i}}\mathbf{U}_0$$

$$= \frac{m}{e}\frac{D}{Dt}\frac{\mathbf{U}_0}{B} + \frac{m\mathbf{U}_0}{eB}\frac{D\ln B}{Dt} + \frac{D\mathbf{b}}{Dt} \times \frac{m\mathbf{V}_0}{eB} + \frac{m}{enB}S_{n_\mathrm{i}}\mathbf{U}_0. \tag{2.50}$$

Note that the ion continuity equation 2.25 is used to get to the last form in the first line of this equation. Moreover, it is assumed that the ion convective velocity $\mathbf{V}_C$ (which is implicitly present in the $D/Dt$ operator) is the same in the momentum equation and in the ion continuity equation. Differences between this ion convective velocity and the velocity $\mathbf{V}_0$ which is important for the (ion) flow inertia are allowed though.

Taking the divergence of the first term of equation 2.50 yields

$$\nabla \cdot \left(\frac{m}{e}\frac{D}{Dt}\frac{\mathbf{U}_0}{B}\right) = \frac{m}{e}\frac{DW}{Dt} + \frac{m}{e}\nabla \mathbf{V}_C : \nabla\frac{\mathbf{U}_0}{B}. \tag{2.51}$$

Taking the divergence of the second and last terms in 2.50 yields

$$\nabla \cdot \left(\frac{m\mathbf{U}_0}{eB}\frac{D\ln B}{Dt} + \frac{m}{enB}S_{n_i}\mathbf{U}_0\right)$$

$$= \frac{mW}{e}\left(\frac{D\ln B}{Dt} + \frac{S_{n_i}}{n}\right) + \frac{m\mathbf{U}_0}{eB}\cdot\nabla\left(\frac{D\ln B}{Dt} + \frac{S_{n_i}}{n}\right) \tag{2.52}$$

Combining equations 2.49-2.52, the charge balance equation 2.41 may be written as

$$m\frac{\partial nW}{\partial t} + \nabla \cdot mnW\mathbf{V}_C = \nabla \cdot \mathbf{J}_{||} + \nabla \cdot \mathbf{J}_* + \nabla \cdot \mathbf{J}_{p,\Pi} + S_{W,cor}, \tag{2.53}$$

$$S_{W,cor} \triangleq e\nabla n \cdot \mathbf{V}_{p,0} - mn\nabla\mathbf{V}_C : \nabla\frac{\mathbf{U}_0}{B} - mnW\frac{D\ln B}{Dt}$$

$$-\frac{mn\mathbf{U}_0}{B}\cdot\nabla\left(\frac{D\ln B}{Dt} + \frac{S_{n_i}}{n}\right) - mn\nabla\cdot\left(\frac{D\mathbf{b}}{Dt}\times\frac{\mathbf{V}_0}{B}\right). \tag{2.54}$$

The current divergence terms in the RHS of equation 2.53 can straightforwardly be traced back to the terms in the original charge balance equation 2.41. However, in order to obtain a vorticity-equation-like form of the equation, quite a number of "correction terms" appear as well, which are grouped in $S_{W,cor}$. These correction terms are often (implicitly) assumed to be small and neglected in turbulence code models [74, 119, 132, 141, 157, 170]. For generality, they will be retained here. In particular, evaluating the associated artefacts in the mean-field equations for the TOKAM2D and TOKAM3X codes will give some insight into how important they may or may not be.

**Model summary**

To summarise, the drift-reduced equations to be solved are the continuity equation for ions are electrons 2.25 or 2.26, the thermal energy equations for ions 2.31 and electrons 2.32, the parallel momentum equations for ions and electrons 2.44 and 2.45 and the charge balance equation 2.41 (or its vorticity equation-like equivalent 2.53). In all these equations, the dominant perpendicular drift velocities and currents in expressions 2.33-2.35 can be filled out where appropriate. If electromagnetic effects are not ignored, equation 2.45 needs to be solved for $\mathbf{A}_{||}$ and equation 2.39 is added for the parallel current. Finally, expressions for the sources $S_n$, $\mathbf{S}_m$, $S_{p_i}$, $S_{p_e}$, the viscous stress $\Pi$, the friction force $R_{ei}$, the heat fluxes $\mathbf{q}_i$ and $\mathbf{q}_e$ and the electron-ion heat exchange $Q_{ei}$ are still required. Such expressions can be found for example in Refs. [32, 71].

Having established these drift-reduced equations commonly used to describe plasma edge turbulence, the qualitative flow picture of the turbulence can be revisited. In the direction parallel to the magnetic field, the plasma can freely flow, it is not hindered by the magnetic field as can be seen from equations 2.44 and 2.45. As such, the classical, collisional transport along the magnetic field is very fast and turbulent structures are elongated in this direction. In the directions perpendicular to the field on the other hand, the particles are restrained. Mainly due to the plasma drifts, particles are however not perfectly confined to their field lines, see equations 2.33 and 2.34. The dominant one of these drifts is the E×B drift, which in equation 2.40 has been shown to be purely due to the electrostatic field that is present. Equation 2.53 shows that this E×B drift (included in $\mathbf{V}_C$) in turn convects the 2D pseudo-vorticity $W$, and as such the electrostatic potential itself. In this way, the E×B drift is coupled back to the electrostatic field that produces the drift. This readily yields a swirling chaotic flow field with eddies in the 2D plane perpendicular to the magnetic field. In this 2D flow field, density and energy are convected by the turbulence, mainly by the E×B drift. This then leads to a turbulent flux of particles and thermal energy across magnetic flux surfaces. In this quasi-2D turbulence picture, the vortex stretching effect that was the dominant mechanism for the creation of vorticity in hydrodynamic turbulence (see section 2.1) can be expected to play a minor role only. Instead, the sources and sinks of (pseudo-)vorticity on the right hand side of the charge balance equation 2.41 or 2.53 are due to the divergence of the diamagnetic current (related to pressure gradient), the divergence of the parallel current, and momentum sources. This is further complicated by diamagnetic contribution to the pseudo-vorticity, non-constant pressures and densities, fluctuations in the parallel magnetic vector potential etc.

## 2.3 Mean-field plasma edge transport equations and existing closure models

In the previous section, the fluid equations describing the instantaneous dynamics of the edge plasma have been presented. These equations tend to develop a chaotic, turbulent flow with large fluctuations. These fluctuations occur at very small time and length scales, typically of the order of $(\rho\Omega/L_\perp)^{-1}$ and $\rho$ respectively, with $\Omega = eB/m$ the ion gyro-frequency, $\rho = c_s\Omega$ the ion gyro-radius, $c_s = \sqrt{(T_i + T_e)/m}$ the plasma sound speed and $L_\perp$ a typical length scale of the average perpendicular gradients of the profiles [71, 143, 147]. Typical numerical values for these length and time scales are given in table 1.1. The details of these very fine scale dynamics are not really of interest to the design of future fusion reactors. Moreover, they are very expensive to resolve
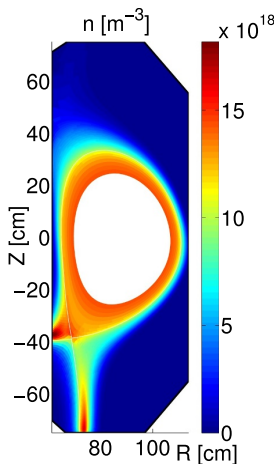
Figure 2.2: Mean-field plasma density in a poloidal cross section of the plasma edge of the TCV tokamak. Figure reproduced from Ref. [12].

computationally since very fine meshes and time steps are required. It is rather the average behaviour of the turbulence and the resulting average profiles of density and pressure that are of interest. These averaged or so-called mean-field quantities of the turbulent flow are calculated in mean-field transport codes such as SOLPS-ITER [29, 167], SOLEDGE2D [35], DivOpt [55, 52], UEDGE [136] and EDGE2D-EIRENE [129, 150, 166]. As an example, figure 2.2 shows the mean-field density as calculated by such a code. This is clearly very smooth, the turbulent fluctuations are not resolved in this code.

However, the turbulent fluctuations introduce a number of closure terms in the mean-field equations which need to be modelled. Typically, the treatment of these closure terms in mean-field codes is minimal and very ad-hoc. This severely limits the predictive capabilities of these codes. This work will develop a self-consistent model for these closure terms, drawing inspiration from the RANS methodology which is commonly used in hydrodynamic turbulence modelling (see section 2.1).

Section 2.3.1 derives the mean-field equations for the plasma edge based on the instantaneous equations presented in section 2.2. The main closure terms will be pointed out. Next, the typical treatment of these closure terms in mean-field codes is discussed in section 2.3.2, after which section 2.3.3 presents recent developments in literature proposing improved closure models.

### 2.3.1 Analytical mean-field equations

The current approach in mean-field modeling is basically to take the full turbulence equations from section 2.2 and to evaluate them with mean-field quantities. In addition to this, ad-hoc diffusion pieces are added to model the radial turbulent transport. Due to turbulent fluctuations, these equations are not equivalent to the turbulent equations and forego the actual dynamics of the turbulence. This section on the other hand derives mean-field equations that do correspond to the underlying turbulence equations analytically through a rigorous averaging methodology. The resulting equations will give more insight into which terms are being modelled and/or neglected in the mean-field codes. Furthermore, this will allow to evaluate the terms to be modelled using reference data in later chapters. The methodology followed for analytically deriving these mean-field equations is inspired by the 2003 paper by Scott [143] and by the internal report by Dekeyser [51].

In order to derive the averaged, mean-field equations, all quantities are split in a mean-field component and a fluctuating component, as is done in the RANS methodology for hydrodynamic turbulence. Both the Reynolds and the Favre decomposition of turbulent quantities (generally denoted by $u$) will be used. The Reynolds decomposition was already introduced in equations 2.7-2.8 and is repeated here for convenience [126]:

$$u = \bar{u} + u', \tag{2.55}$$

$$\bar{u} \triangleq \lim_{N \to \infty} \frac{1}{N} \sum_{i=1}^{N} u^{(i)}. \tag{2.56}$$

In this thesis, we assume the turbulent flows to be ergodic such that a long time statistical steady state of the flow exists, of which the time average converges to the ensemble average:

$$\bar{u} \triangleq \lim_{N \to \infty} \frac{1}{N} \sum_{i=1}^{N} u^{(i)} = \lim_{T \to \infty} \frac{1}{T} \int_0^T u \, dt. \tag{2.57}$$

In addition to the Reynolds average, the Favre or density weighted average will also be used. This is defined as follows [37]:

$$u = \tilde{u} + u'', \tag{2.58}$$

$$\tilde{u} \triangleq \frac{\overline{nu}}{\bar{n}}. \tag{2.59}$$

This Favre average is particularly useful when transport equations with variable density need to be averaged, as it allows to limit the number of closure terms in that case. The Reynolds and Favre decompositions imply the following relationships:

$$\overline{u'} = 0, \qquad \overline{nu''} = 0, \qquad \tilde{u} = \bar{u} + \frac{\overline{n'u'}}{\bar{n}}, \qquad \overline{nu_1 u_2} = \bar{n}\tilde{u}_1 \tilde{u}_2 + \overline{nu_1'' u_2''}. \tag{2.60}$$

Note also that the averaging operator $\bar{u}$ commutes with time and space derivatives, but the Favre operator $\tilde{u}$ does not:

$$\overline{\nabla u} = \nabla \bar{u}, \qquad \widetilde{\nabla u} = \nabla \tilde{u} - \frac{\overline{u'' \nabla n}}{\bar{n}} = \nabla \tilde{u} + \frac{\overline{n \nabla (u'')}}{\bar{n}}. \tag{2.61}$$

As discussed in section 2.2.2, this thesis only considers low $\beta$ plasmas. Hence, it is assumed that strong time-constant magnetic fields are externally applied and that fluctuations of the magnetic field can be neglected. As such, the magnetic fields can be brought out of the averaging operators. An exception to this is again the treatment of $A_{||}$ in the parallel momentum equations, which will be retained in this chapter and in chapter 3.

The remainder of this section will apply the above averaging operators to the drift ordered equations presented earlier. The resulting mean-field equations this yields are largely inspired on the internal report by Dekeyser [51].

**Mean-field continuity equation**

Averaging the continuity equation for the ions 2.25 and electrons 2.26 with the dominant plasma velocities filled out from equation 2.36 (including the polarisation current for the ions as well) yields

$$\frac{\partial \bar{n}}{\partial t} + \nabla \cdot (\Gamma_{n,||} + \mathbf{\Gamma}_{n,E} + \Gamma_{n,*,i} + \Gamma_{n,p}) = \bar{S}_{n_{\mathrm{i}}} \tag{2.62}$$

$$\frac{\partial \bar{n}}{\partial t} + \nabla \cdot (\Gamma_{n,||} - \bar{\mathbf{J}}_{||}/e + \mathbf{\Gamma}_{n,E} + \Gamma_{n,*,e}) = \bar{S}_{n_{\mathrm{e}}}, \tag{2.63}$$

with

$$\Gamma_{n,||} \triangleq \bar{n}\tilde{\mathbf{V}}_{||}, \tag{2.64}$$

$$\boldsymbol{\Gamma}_{n,E} \triangleq \overline{n\mathbf{V}_E} = \bar{n}\bar{\mathbf{V}}_E + \overline{n'\mathbf{V}'_E} \triangleq \boldsymbol{\Gamma}_{n,m,E} + \boldsymbol{\Gamma}_{n,t,E}, \tag{2.65}$$

$$\Gamma_{n,*,i} \triangleq \frac{\mathbf{b} \times \nabla \bar{p}_i}{eB}, \qquad \Gamma_{n,*,e} \triangleq -\frac{\mathbf{b} \times \nabla \bar{p}_e}{eB}, \tag{2.66}$$

$$\Gamma_{n,p} \triangleq \bar{n}\tilde{\mathbf{V}}_p = \bar{\mathbf{J}}_p/e. \tag{2.67}$$

These equations describe the time evolution of the average densities. As mentioned in section 2.2.1 already, it suffices to solve either equation 2.62 or 2.63 for a quasi-neutral single species hydrogenic plasma in which $n = n_e = n_i$.

In these equations the turbulent E×B particle flux $\boldsymbol{\Gamma}_{n,t,E} \triangleq \overline{n'\mathbf{V}'_E}$ constitutes a closure term as it depends on the correlation between fluctuations, which cannot directly be determined based on mean-field quantities only. Modelling $\boldsymbol{\Gamma}_{n,t,E}$ is important since this term is known to dominate the outward transport across magnetic flux surfaces [143, 165, 71].

Note that the parallel term is written with Favre averages in equation 2.64. In this way it can be solved from the average parallel plasma momentum equation 2.77, see later. Similarly, the average parallel current is available from the parallel electron momentum equation 2.75. Equation 2.66 shows that the diamagnetic fluxes can be calculated exactly from the mean-field pressures, which are available from thermal energy equations 2.68 and 2.69. Furthermore, the divergence of the diamagnetic fluxes can be shown to depend on gradients of the magnetic field strength, such that this term is expected to be rather small [147, 162]. The averaged polarisation flux also entails a number of closure terms, see charge balance equation 2.74. However, since the polarisation velocity is of higher order than the other velocities [71, 82, 149], it is usually neglected in the continuity equation (even for the ions).

For the E×B drift, a similar Favre average does not make sense, since in mean-field modelling, the Reynolds average potential $\bar{\phi}$ is solved for from the average charge balance equation 2.74 and not the Favre averaged potential (see later). Hence, the turbulent E×B particle flux $\overline{n'\mathbf{V}'_E}$ needs to be added next to the Reynolds average mean-field E×B particle flux $\bar{n}\bar{\mathbf{V}}_E$. Note that after modelling $\overline{n'\mathbf{V}'_E}$, the Favre averaged E×B velocity can be calculated following relation 2.60 as $\hat{\mathbf{V}}_E = \bar{\mathbf{V}}_E + \overline{n'\mathbf{V}'_E}/\bar{n}$.

**Mean-field thermal energy equations**

As for the continuity equation, mean-field equations can be derived for the ion and electron thermal energy from equations 2.31 and 2.32. Following Ref. [143] for the general form of the equation, but treating the averaging more rigorously we write

$$\frac{3}{2}\frac{\partial \bar{p}_i}{\partial t} + \nabla \cdot (\frac{3}{2}\mathbf{\Gamma}_{p_i,E} + \frac{5}{2}\mathbf{\Gamma}_{p_i,||} + \frac{5}{2}\mathbf{\Gamma}_{p_i,p} + \frac{5}{2}\frac{\mathbf{b} \times \overline{\nabla p_i T_i}}{eB} + \bar{\mathbf{q}}_{||,i}),$$

$$= -\overline{p_i \nabla \cdot \mathbf{V}_E} + \overline{\mathbf{V}_{||} \cdot \nabla p_i} + \overline{\mathbf{V}_p \cdot \nabla p_i} - \overline{\Pi : \nabla \mathbf{V}_0^T} - \bar{Q}_{\mathrm{ei}} + \frac{3}{2}\bar{S}_{p_i}, \qquad (2.68)$$

$$\frac{3}{2}\frac{\partial \bar{p}_e}{\partial t} + \nabla \cdot (\frac{3}{2}\mathbf{\Gamma}_{p_e,E} + \frac{5}{2}\mathbf{\Gamma}_{p_e,||} + \frac{5}{2}\frac{\mathbf{b} \times \overline{\nabla p_e T_e}}{eB} + \bar{\mathbf{q}}_{||,e}),$$

$$= -\overline{p_e \nabla \cdot \mathbf{V}_E} + \overline{\mathbf{V}_{||} \cdot \nabla p_e} - \overline{\frac{\mathbf{J}_{||}}{ne} \cdot \nabla p_e} + \overline{\frac{\mathbf{J}}{en} \cdot \mathbf{R}_{ei}} + \bar{Q}_{\mathrm{ei}} + \frac{3}{2}\bar{S}_{p_e}. \qquad (2.69)$$

with

$$\mathbf{\Gamma}_{pi/e,E} \triangleq \overline{nT_{i/e}\mathbf{V}_E} = \tilde{T}_{i/e}\mathbf{\Gamma}_{n,E} + \overline{nT_{i/e}''\mathbf{V}_E''} \triangleq \mathbf{\Gamma}_{pi/e,m,E} + \mathbf{\Gamma}_{pi/e,t,E}, (2.70)$$

$$\mathbf{\Gamma}_{p_i,||} \triangleq \overline{nT_i\mathbf{V}_{||}} = \tilde{T}_i\mathbf{\Gamma}_{n,||} + \overline{nT_i''\mathbf{V}_{||}''} (2.71)$$

$$\mathbf{\Gamma}_{p_e,||} \triangleq \overline{nT_e\mathbf{V}_{||}} - \overline{\frac{p_e\mathbf{J}_{||}}{en}} = \tilde{T}_e\mathbf{\Gamma}_{n,||} + \overline{nT_e''\mathbf{V}_{||}''} - \frac{\tilde{T}_e\bar{\mathbf{J}}_{||}}{e} - \frac{\overline{T_e''\mathbf{J}_{||}}}{e} (2.72)$$

$$\mathbf{\Gamma}_{p_i,p} \triangleq \overline{nT_i\mathbf{V}_p} = \bar{n}\tilde{T}_i\tilde{\mathbf{V}}_p + \overline{nT_i''\mathbf{V}_p''} (2.73)$$

In these equations, it was assumed that the only important conductive heat fluxes are the parallel ones $\mathbf{q}_{||}$ and the one due to the diamagnetic drift. The latter is combined with the diamagnetic heat convection and the pressure work on the diamagnetic velocity $\nabla p \cdot \mathbf{V}_*$ to obtain the one but last term in the LHS of equations 2.68 and 2.69 [143].

Note that the average pressure in the equations can be decomposed using Favre averages as $\bar{p} = \bar{n}\tilde{T}$. As shown in equations 2.70-2.73, the energy fluxes on the LHS of equations 2.68 and 2.69 can be decomposed into a mean-field convection term and a turbulent convection term. Assuming the mean-field particle fluxes $\mathbf{\Gamma}_n$ are available, this introduces a new closure term for each velocity component. The closure terms that are expected to be most important in the LHS are the turbulent E×B heat fluxes $\mathbf{\Gamma}_{p_i,t,E}$ and $\mathbf{\Gamma}_{pi/e,t,E}$ [71, 143, 165]. Next, there are

also parallel turbulent fluxes (see equations 2.71 and 2.72). However, due to the fast classical collisonal transport in the parallel direction, the length scale of the fluctuations is much longer in this direction than in the perpendicular directions. It can be expected that the transport by parallel velocity fluctuations will be small compared to the anyway very fast classical collisional transport in this direction. Hence, it is presumed that the mean-field convective fluxes and the conductive heat flux $\mathbf{q}_{||}$ dominate the turbulent one in the parallel direction. The careful validation of this hypothesis is left for future work though. Then, the contribution due to the polarisation velocity (in the ion thermal energy equation) is expected to be small as well because the polarisation drift itself is of higher order than the E×B drift [71, 82, 149]. Finally, the diamagnetic contribution to the transport terms in equations 2.68 and 2.69 (penultimate term in the LHS of both equations) is presumably rather small as well. The only nonzero contribution from this term can be shown to be through gradients of the magnetic field [147, 162] and to vanish exactly in a 1D mean-field geometry.

The terms in the RHS of equations 2.68 and 2.69 likewise contain closure terms. The turbulent contributions of these terms are not expected to play a large role in the thermal energy equations though. While these terms will briefly be revisited later on when dealing with the energetic couplings in section 3.2.5, their closure will only receive limited attention in this thesis.

**Mean-field charge balance and parallel momentum equations**

Averaging equation 2.41 with expression 2.42 filled out yields the averaged charge balance equation:

$$\nabla \cdot \frac{m}{B} \left[ \frac{\partial}{\partial t} \left( \overline{\frac{n\nabla_\perp \phi}{B} + \frac{\nabla_\perp \bar{p}_i}{eB}} \right) + \nabla \cdot \left( \overline{\mathbf{V}_C \left( \frac{n\nabla_\perp \phi}{B} + \frac{\nabla_\perp p_i}{eB} \right)} \right) \right]$$

$$= \nabla \cdot \bar{\mathbf{J}}_{||} + \nabla \cdot \bar{\mathbf{J}}_* - \nabla \cdot \left( \frac{\nabla \cdot \bar{\bar{\Pi}}}{B} \times \mathbf{b} \right) - \nabla \cdot \left( \frac{D\mathbf{b}}{Dt} \times \frac{mn\mathbf{V}_0}{B} \right)$$

$$+ \nabla \cdot \left( \frac{\bar{\mathbf{S}}_m \times \mathbf{b}}{B} \right). \quad (2.74)$$

In this equation, the divergences of parallel current and diamagnetic current on the RHS are typically dominant, since the other terms are of higher order [71, 82, 149]. As such, it is mostly important to treat the averages of these two terms with care. The average diamagnetic current $\bar{\mathbf{J}}_* = -\nabla \bar{p} \times \mathbf{b}/B$ does not lead to any closure terms. Dividing the Ohm's law 2.45 by the density and then

averaging yields following expression for the average parallel current:

$$\bar{\eta}_{||}\bar{J}_{||} = \frac{\overline{\nabla_{||}p_e}}{en} - \nabla_{||}\bar{\phi} - \frac{\partial \bar{A}_{||}}{\partial t} + \frac{0.71}{e}\nabla_{||}\bar{T}_e - \overline{\eta'_{||}J'_{||}}. \tag{2.75}$$

Clearly, the Reynolds averaged electrostatic potential $\bar{\phi}$ appears naturally in the Ohm's law 2.75 for the parallel current, and thus in the RHS of 2.74. For this reason, the average charge balance equation 2.74 is solved for $\bar{\phi}$ and a Reynolds average is used for the electrostatic potential. As a result, a Reynolds average also appears naturally for the mean-field E×B drift i.e. $\bar{\mathbf{V}}_E = \mathbf{b} \times \nabla\bar{\phi}/B$ and the $\overline{n'\mathbf{V}'_E}$ closure for the E×B flux is required in the average E×B particle flux in equation 2.65. Essentially the same closure also appears in the LHS of the charge balance equation 2.74 in the form of $\overline{n'\nabla_\perp\phi'}$, however, in this equation it presumably constitutes but a small correction. The second term on the LHS of equation 2.74 basically represents the convection of perpendicular momentum. This includes an additional closure term as well, which can be seen to consist of part of the Reynolds stresses. Apart from these closures, also the convective part of the second but last term in 2.74 requires closure.

Equation 2.75 likewise contains a number of closure terms. The first term on the RHS of this equation requires closure due to the nonlinear dependence on both $n$ and $p_e$. The third term on the RHS features the Reynolds average $\bar{T}_e$ of the electron temperature instead of the Favre average $\tilde{T}_e$ which follows from the electron thermal energy equation 2.69. Relation 2.60 has shown that a closure term enters in the relation between both averages. The last term in equation 2.75 is likewise a nonzero closure term since the resistivity depends on the plasma quantities ($\eta_{||} \sim T_e^{-3/2}$). Note that similar closure terms due to nonlinear plasma properties are likewise present in the viscous stress tensor $\bar{\bar{\Pi}}$ in equations 2.74 and 2.77, and in the collisional parallel heat fluxes $\bar{\mathbf{q}}_{||,i}$ and $\bar{\mathbf{q}}_{||,e}$ in the thermal energy equations 2.68 and 2.69.

Unless the magnetic vector potential is neglected, an equation for this is also required. From 2.39, rather straightforwardly one finds

$$\nabla_\perp^2 \bar{A}_{||} = -\mu\bar{J}_{||}. \tag{2.76}$$

Finally, by averaging equation 2.44, an equation for the Favre averaged parallel velocity is obtained:

$$\frac{\partial m\bar{n}\tilde{V}_{||}}{\partial t} + \nabla \cdot (m\bar{n}\tilde{\mathbf{V}}_C\tilde{V}_{||} + m\overline{n\mathbf{V}_C''V_{||}''})$$

$$= -\nabla_{||}\bar{p} - (\nabla \cdot \bar{\Pi}) \cdot b + mn\overline{\frac{D\mathbf{b}}{Dt} \cdot \mathbf{V}_{0,\perp}} + \bar{\mathbf{S}}_{m,||}. \tag{2.77}$$

The third term on the LHS represents the turbulent transport of parallel momentum, which is again a closure term to be modelled. Presumably, mostly the perpendicular part of the turbulent transport of parallel momentum is important, as the turbulence is mostly active in the plane perpendicular to the magnetic field. The third term on the RHS also entails a closure term, but this one is always neglected as far as the author is aware, both in turbulence and mean-field models.

### Mean-field equation summary

We briefly summarise the mean-field equations that have been derived and the closure terms which need modelling in order to solve them self-consistently. The main equations are the following: the continuity equation 2.62 or 2.63 is to be solved for the average density $\bar{n}$, the mean-field thermal energy equations 2.68 and 2.69 for the average pressures $\bar{p}_i$ and $\bar{p}_e$ (which allows to calculate the Favre averaged temperatures $\tilde{T}_i = \bar{p}_i/\bar{n}$ and $\tilde{T}_e = \bar{p}_e/\bar{n}$), the mean-field charge balance equation 2.74 for the average potential $\bar{\phi}$ and the mean-field plasma parallel momentum equation 2.77 for the Favre averaged parallel ion velocity $\tilde{V}_{||}$. Furthermore, the average parallel current $\bar{J}_{||}$ follows directly from equation 2.75 in the purely electrostatic case. In the electromagnetic case, equation 2.75 needs to be solved for $\bar{A}_{||}$, which then yields $\bar{J}_{||}$ through equation 2.76.

The closure terms remaining in these equations are the turbulent E×B fluxes of particles $(\overline{n'\mathbf{V}_E'})$ and heat $(\overline{nT''\mathbf{V}_E''})$, the parallel turbulent heat fluxes $(\overline{nT''\mathbf{V}_{||}''}$ and $\overline{T_e''\mathbf{J}_{||}''}/e)$, the diamagnetic contribution to the thermal energy equations $(\mathbf{b} \times \overline{\nabla p T}/eB)$, the turbulent heat flux due to the polarisation velocity $(\overline{nT_i''\mathbf{V}_p''})$ the Reynolds stresses $(\overline{n\mathbf{V}_C''\mathbf{V}_0''})$ and the turbulent contributions to the terms on the RHS of the mean-field thermal energy equations 2.68 and 2.69. Furthermore, $\bar{T}_e$ and $\overline{\nabla p_e/n}$ appear in 2.75, which can also not be determined from the mean-field quantities listed before. Lastly, any nonlinear dependence on the plasma state in the classical transport expressions ($\Pi$, $\mathbf{R}_{ei}$, $\mathbf{q}_{||}$, $Q_{ei}$) or source terms ($S_n$, $\mathbf{S}_m$, $S_p$) will likewise give rise to closure terms.

Hence, a considerable number of closure terms appear. This thesis will mostly consider the turbulent particle transport $\boldsymbol{\Gamma}_{n,t,E} \triangleq \overline{n'\mathbf{V}'_E}$ which is considered to be of crucial importance, and which is indeed known to be large compared to the mean-field flux $\bar{n}\bar{\mathbf{V}}_E$ [71, 143, 165]. The goal of chapters 4 and 5 is to develop a suitable closure model for this term in particular. Moreover, the information gained from modelling this relatively simple term could be used to further develop the applied methodology to assess the important terms and to elaborate models for the dominant closure terms. Indeed, chapter 6 will build upon the models for the particle flux to also model the E×B turbulent heat convection $\boldsymbol{\Gamma}_{pi/e,t,E} \triangleq \overline{nT''_{i/e}V''_E}$. These are again important closure terms which are large compared to the perpendicular mean-field thermal energy convection [71, 143, 165]. In addition, both the turbulent particle flux and heat flux are explicitly modelled in mean-field codes, as will be illustrated in the next section.

## 2.3.2  Treatment in mean-field transport codes

In mean-field codes, an equation set similar to 2.62-2.77 is typically solved. Assuming a toroidally-symmetric device, the equations are solved in a 2D radial-poloidal domain. Next to these equations for the plasma, mean-field transport codes usually also resolve the neutral particles using a kinetic treatment and couple this to the plasma solver. Usually, most of the nonlinear terms in the mean-field plasma equations are simply evaluated using the mean-field quantities involved, e.g. $\overline{V \cdot \nabla p}$ would simply be modelled as $\bar{V} \cdot \nabla \bar{p}$ (where the averaging symbols would have to be tacitly assumed to be there). As such, the turbulent closure terms are implicitly neglected [7, 29, 35, 55, 52, 129, 130, 136, 150, 166, 167]. The perpendicular turbulent fluxes of particles, heat and parallel momentum are typically taken into account, but through an ad-hoc treatment. Usually it is assumed that

$$\overline{n'\mathbf{V}'_\perp} = -D\nabla_\perp \bar{n} + \bar{n}\mathbf{V}_{conv}, \tag{2.78}$$

$$\overline{nT''_{i/e}\mathbf{V}''_\perp} = -\bar{n}\chi_{i/e}\nabla_\perp \tilde{T}_{i/e}, \tag{2.79}$$

$$m\overline{nV''_{||}\mathbf{V}''_\perp} = -\chi_{m,||}\bar{n}\nabla_\perp \tilde{V}_{||}. \tag{2.80}$$

where $D$, $\mathbf{V}_{conv}$, $\chi_{i/e}$ and $\chi_{m,||}$ are anomalous particle diffusion, convection, ion/-electron heat conductivities and parallel momentum conductivity respectively. They are typically determined empirically, from experimental observations. The convective contribution to the particle flux $\bar{n}\mathbf{V}_{conv}$ is often not included [3, 53, 103, 128]. It can be noted that the diffusive parts of these models are implicitly derived from a gradient diffusion hypothesis similar to that used

in hydrodynamic turbulence modelling, see section 2.1 and equation 2.22 in particular. The effective transport coefficients typically take the form of 1D or 2D profiles. Usually, in the analysis of experimental data the 1D profile of the transport coefficients at the outer mid-plane (OMP) is first manually tuned in order to achieve good agreement between the profile of the mean-field code simulation and the reference data at that location. Then further manual tuning is performed to achieve a better match between simulation and reference data at other locations, e.g. at the targets. In addition, ad-hoc corrections based on the magnetic field geometry can be used to further adjust the 2D profiles of the transport coefficients [1, 3]

While such a procedure may give a good match of data from a particular experiment by construction, the effective transport coefficients differ significantly from one machine to another, from one operating regime to another, and from one discharge to another [103]. Note also that all perpendicular velocities and fluxes are typically lumped in these models, while the careful averaging combined with the typical length scale assumptions outlined in section 2.3.1 has shown that mainly the E×B particle and heat fluxes require closure. Since the underlying dynamics of the turbulence driving the transport are not taken into account in this procedure, the resulting transport coefficients can hardly be extrapolated to different machines or operating conditions.

Another issue is that the parameter space available for this fitting procedure, allowing arbitrary 2D variations of the transport coefficients, is clearly very large, making the procedure prone to overfitting of the experimental data. Moreover, no framework for systematically assessing these models and issues such as overfitting is routinely used. Furthermore, this manual tuning procedure is very time consuming and laborious for the modeller and it effectively relies on expert judgement. Least squares regression approaches have been applied to alleviate this problem by automating this fitting procedure [8, 99, 118].

Due to the shortcomings sketched above, the predictive capability of such models calibrated to a particular experiment is rather limited. To address these issues, self-consistent models for the turbulent transport coefficients that do take information about the underlying characteristics of the turbulence into account have recently been proposed, as will be outlined in the next section.

### 2.3.3  Recent closure attempts

Two often used scalings to determine the order of magnitude of the turbulent transport coefficients are the Bohm and the gyro-Bohm scalings. In the Bohm scaling, it is assumed that the relevant length and time scales for the turbulence are the ion gyro-radius (evaluated at cold ion sound speed) and the ion gyro-

period. This leads to following scaling for the turbulent diffusion coefficient

$$D \sim \chi \sim \frac{T_e}{eB}. \tag{2.81}$$

Literature seems to indicate that the turbulent transport in tokamaks rather follows the gyro-Bohm scaling:

$$D \sim \chi \sim \frac{\rho_{T_e}}{L_\perp} \frac{T_e}{eB}, \tag{2.82}$$

where $L_\perp$ is the scale length of the perpendicular mean-field profiles and $\rho_{T_e}$ is the ion gyro-radius evaluated at the electron temperature. Often, the factor $\rho/L_\perp$ is assumed to scale as $\rho/L_\perp \sim \rho/a$, with $a$ the tokamak minor radius. As $\rho \ll L_\perp < a$, gyro-Bohm scaling predicts much lower turbulent transport than the Bohm scaling (assuming proportionality constants of order unity should be added to either scaling). However, these scalings might need to be viewed as order of magnitude estimates of global machine performance rather than detailed models for the local behaviour within a single machine [73, 94, 95, 71, 141]. Rather recently, a number of models has been proposed that relate the mean-field turbulent transport coefficients to the characteristics of the underlying turbulence. These models intend to capture both the global scaling of the turbulent transport across different tokamaks, and the important local variations within a single machine.

Miki *et al.* [113] pioneer in the development of such a model. They present a 1D (radial) model to explain the L-H transition (see section 1.2.2). The turbulent flux of particles ($\mathbf{\Gamma}_n$) and heat ($\mathbf{\Gamma}_p$) are modelled as in equations 2.78 and 2.79. However, both transport coefficients are assumed to scale with the local and time dependent turbulence intensity $I$:

$$D = \chi = \frac{\tau c_s^2 I}{1 + \alpha S_m^2}. \tag{2.83}$$

In this equation, $c_s$ is the plasma sound speed, $\tau$ is a time scale for the turbulence decorrelation, $S_m = \nabla_r V_{MF,\theta}$ is the mean flow shear with $V_{MF,\theta}$ the poloidal mean flow velocity, and $\alpha$ a coefficient determining how strongly mean flow shear reduces the transport coefficients. Hence, a mechanism for the suppression of the turbulent transport coefficient by flow shear breaking up the turbulent eddies is also included in these diffusion relations. All quantities in the equations of this model are to be interpreted as being averaged over fast time scales and short length scales.

The turbulence intensity is then solved from a separate PDE:

$$\frac{\partial I}{\partial t} - \chi_I \nabla_r (I \nabla_r I) = \gamma I - \delta I^2 - \alpha_Z S_Z^2 - \alpha_{MF} S_m^2. \tag{2.84}$$

The first term on the LHS of this equation is the time change of $I$, the second term represents transport of $I$, assumed to be diffusive with some coefficient $\chi_I$. The first term on the RHS is the linear growth of $I$ with linear growth rate $\gamma$ (which may be a function of the plasma state), the second term is a nonlinear damping term with $\delta$ a coefficient characterising its strength. The third and fourth terms on the RHS represent the suppression of the turbulence by zonal flow and mean flow shear, with $S_Z = \nabla_r V_{Z,\theta}$ in which $V_{Z,\theta}$ is the zonal flow velocity. $\alpha_Z$ and $\alpha_{MF}$ are coefficients determining the strength of both effects. As discussed in section 1.2.2, these shear flows evolve on time and length scales that are significantly larger than the smallest scales of the turbulence. They are partly driven by the fine scale turbulence [58]. Sometimes a distinction is made between mean-field shear flows that are not turbulence driven, and zonal flows that are, as is done in this paper.

The model presented by Miki *et al.* then suggests following equation for the zonal flow shear:

$$\frac{\partial S_Z^2}{\partial t} = \frac{\alpha_Z I S_Z^2}{1 + \beta S_m^2} - \gamma_{damp} S_Z^2. \tag{2.85}$$

Hence, the growth of the zonal flow shear is stronger as the zonal flow itself is stronger and when the turbulence intensity is higher. Mean flow shear hinders the growth of zonal flow on the other hand, the strength of this effect being characterised by the coefficient $\beta$. The $\gamma_{damp}$ characterises the linear damping of the zonal flow growth. Finally, the model would be complemented with an expression for the convective velocity $V_{conv}$ introduced in equation 2.78 and an equation for the mean flow velocity $V_{MF,\theta}$. An ad-hoc expression for a particle pinch $V_{conv}$ is used, while $V_{MF,\theta}$ is determined from a poloidal force balance equation in which some further closure assumptions are made.

Hence, the physics of the turbulence dynamics in this model is that the turbulence intensity is driven by the (linear) growth of some instability (typically depending on the mean-field gradients). A first mechanism to saturate the turbulence is through the nonlinear damping term $\delta I^2$. Secondly, it could be saturated by shear flows. The dynamics of the zonal flow is of particular interest. Zonal flow shear simultaneously leads to a sink of the turbulence intensity and a source of the zonal flow shear itself. In turn, the growth of the zonal flow also depends on the turbulence intensity itself, as it is inherently driven by the

turbulence. This leads to a kind of predator-prey dynamic, where the turbulence acts as the prey and the zonal flow shear as the predator, which can only grow if there is a prey present. Zonal flow dynamics are an active area of research, as they are believed to be at the basis of transport barrier formation around the separatrix and the L-H transition [14, 56, 58, 113, 144, 146].

The model summarized in equations 2.83-2.85 elegantly combines numerous physical mechanisms at play. However, it is a phenomenological model which specifically intends to explain the L-H transition. Hence, it has not been intended to be used in complete mean-field simulations as is the goal of this PhD. The turbulence intensity equation 2.84 is based on the wave kinetic equation [57], implicitly assuming weak wave turbulence, which may not be a valid paradigm for fully developed nonlinear plasma edge turbulence. Moreover, some ad-hoc additions and simplifications have been made to the analytically derived equation. Also, the meaning of the quantity turbulence intensity $I$ remains somewhat vague.

Using the work of Miki *et al.* as inspiration, Bufferand *et al.* [34] proposed for the first time a RANS-like model for mean-field transport simulations, based on an equation for the evolution of the turbulent kinetic energy. Firstly, Bufferand *et al.* identified the turbulence intensity with the turbulent kinetic energy of the ExB fluctuations, defined here as $k_\perp \triangleq \overline{\mathbf{V}_E'^2}/2$.[3] As is done in hydrodynamic turbulence modelling, the transport coefficient in the gradient diffusion hypothesis is modelled based on a dimensional scaling involving the turbulent kinetic energy. Following form is suggested in this work:

$$D \sim \chi_{i/e} \sim \chi_k \sim \frac{ak_\perp}{c_s}, \qquad (2.86)$$

with $a$ the tokamak minor radius and $\chi_k$ a transport coefficient for the transport of $k$. No convective contribution $\bar{n}\mathbf{V}_{conv}$ to the turbulent particle flux is used in this model. The proposed turbulent kinetic energy equation is written as

$$\frac{\partial nk_\perp}{\partial t} + \nabla \cdot (nk_\perp \mathbf{V}_{||} - \chi_k \nabla_\perp k_\perp) = \gamma nk_\perp - \delta nk_\perp^2. \qquad (2.87)$$

Bufferand *et al.* explicitly related the linear growth rate to that of the interchange instability:

$$\gamma = c_s \sqrt{\frac{\nabla B \cdot \nabla p}{Bp} - \frac{5}{R^2}(1 + \frac{T_i}{T_e})}, \qquad (2.88)$$

---

[3]The symbol $k_\perp$ here is not to be confused with the perpendicular wave number, which in plasma physics literature is often denoted with this symbol as well.

where $R$ is the tokamak major radius. Equations 2.86-2.88 yield a self-consistent model for the turbulent transport coefficient that can be used in a mean-field code. For completeness, it is to be remarked that all quantities in these equations are assumed to be mean-field quantities, but nothing is mentioned about the specific averaging operators used in the original publication.

The interchange growth rate (equation 2.88) immediately leads to "ballooned" characteristics of the transport with higher transport on the outboard side of the tokamak, as observed in experiments [34, 66, 74, 85, 158]. Indeed, the magnetic field strength generally decreases as the major radius coordinate increases, while the pressure decreases with the minor radius coordinate. As a result, the growth rate is only positive on the outboard side of the tokamak. Comparing to the model by Miki *et al.*, it can be seen that the effects of flow shear have been left out as a simplification, as well as the convective particle flux as mentioned earlier. Hence, in this model the linear drive of the turbulence causes the turbulent kinetic energy to increase initially. As $k_\perp$ increases, the nonlinear sink increases faster than the drive term and finally saturates the turbulence.

Baschetti *et al.* [11, 12, 13] refined the previous model by including information on experiments into the model. Ref. [11] calibrated the free model parameters by matching measurements of a set of discharges on the TCV tokamak to a 2D mean-field simulation using this model. Refs. [12, 13] on the other hand used a scaling law for the SOL width obtained from multimachine comparison to close the dissipation parameter $\delta$ in the $k_\perp$ equation. Not only does this fix the value of this parameter, it also introduces a new scaling with machine parameters into it.

Baschetti *et al.* [14] further extended these models by including an equation for $\varepsilon$, the dissipation of turbulent kinetic energy, taking the analogy with the $k - \varepsilon$ RANS approach for hydrodynamic turbulence a step further. The turbulent transport coefficients are then modelled as

$$D \sim \chi_{i/e} \sim \chi_k \sim \chi_\varepsilon \sim \frac{k_\perp^2}{\varepsilon}, \tag{2.89}$$

with $\chi_\varepsilon$ a transport coefficient for $\varepsilon$. Note that the local turbulent transport coefficient now only depends on local characteristics of the turbulence, and no longer on global machine parameters as the minor radius $a$. The equations for the turbulent kinetic energy and its dissipation take the following form:

$$\frac{\partial k_\perp}{\partial t} + \nabla \cdot (k_\perp \mathbf{V}_{||} - \chi_k \nabla_\perp k_\perp) = \gamma k_\perp - \delta_k k_\perp^2 - \varepsilon, \qquad (2.90)$$

$$\frac{\partial \varepsilon}{\partial t} + \nabla \cdot (\varepsilon \mathbf{V}_{||} - \chi_\varepsilon \nabla_\perp \varepsilon) = \gamma \varepsilon - \delta_\varepsilon \frac{\varepsilon^2}{k_\perp^{3/2}}. \qquad (2.91)$$

In this equation, $\delta_\varepsilon$ is a model coefficient characterising the nonlinear sink of the dissipation. $\gamma$ is again chosen to be the interchange growth rate. $\delta_k$ is taken to be very small, such that the dissipation of $k_\perp$ is almost purely due to $\varepsilon$. The parameter $\delta_\varepsilon$ is again chosen such that the same machine scaling law used in Refs. [12, 13] is obtained as an asymptotic solution. As an alternative it is proposed to take $\delta_\varepsilon$ as a function of the flow shear, such that suppression of the turbulence by flow shear could be taken into account.

The idea behind this model is that $k_\perp$ represents the kinetic energy of the part of the spectrum that strongly contributes to turbulent transport, while $\varepsilon$ is the rate at which this kinetic energy is transferred to regions of the spectrum that do not significantly contribute to transport. The latter regions can either be at very small scales where the energy is dissipated by viscous effects as in hydrodynamic turbulence, or at very large scales (in the zonal flows) through an inverse energy cascade. In order to model these cascades, the $k^{3/2}$ scaling is used in the sink of $\varepsilon$ in equation 2.91 to enforce an inertial range scaling in the model.

It is worth remarking that next to the extended mean-field models discussed above, different approaches have also been proposed. It has been suggested to couple turbulence codes to mean-field transport codes to provide transport coefficients self-consistently. In such an approach, the turbulence code can either resolve the turbulence locally in distinct parts of the mean-field domain as performed by for example Nishimura *et al.* [120], or it can globally solve the entire mean-field computational domain as performed by Zhang *et al.* [171]. Note that in the former approach non-local transport effects cannot be captured, while in the latter approach the computational cost is expected to remain a bottleneck due to the need for a 3D turbulence simulation resolving the relevant turbulent length and time scales.

Machine learning provides another approach to use turbulence codes in order to obtain an improved transport description in mean-field codes. In such an approach, a database of detailed reference data from turbulence codes is first constructed, after which machine learning techniques are used to train a reduced model. After the training phase, the reduced model can be used to quickly calculate the average turbulent fluxes from given mean-field information [42, 104, 111]. Note that this approach presents clear similarities with the method

that is suggested in this thesis, in the sense that it is based on studying detailed reference data. Moreover, the parameter estimation and model validation techniques suggested in this thesis can be seen as a step towards machine learning. While the machine learning approach certainly holds promise and may be complementary to the physics based approach suggested here, it remains to be proven that it can capture the physics needed to extrapolate to new cases out of the training data set.

Furthermore, quasilinear approaches have also been suggested, see for example Refs. [30, 31, 42]. The idea behind this is to linearise the system of equations and to calculate the mode structure and growth rates of the turbulence based on that. When the amplitude of the modes is known, the turbulent fluxes can then be calculated from this mode structure. However, the linearised system does not provide information on the amplitude of the modes in the saturated state. This information is calculated separately by means of ad-hoc "mixing length rules". Moreover, since the saturated state of the turbulence is manifestly nonlinear and since fluctuation levels in the plasma edge can be rather large, it is questionable whether a framework based on the linear characteristics of the turbulence can supply accurate predictions [71, 143, 145]. Hence, quasilinear models have mostly been used for the core region where turbulent fluctuations are typically smaller. Borrowing some elements from the quasilinear approach, Fedorczak *et al.* [68] and Peret *et al.* [122] recently proposed models for the turbulent transport in the SOL based on a spectral decomposition of the fluctuations.

While the extended mean-field models by Miki *et al.*, Bufferand *et al.* and Baschetti *et al.* discussed earlier certainly have their merits and contain numerous important physical effects, they tend to be rather ad-hoc still. To some extent, they rely on qualitative expectations of the turbulence and consist of a combination of mechanisms that have empirically been observed to be relevant. Little supporting evidence is available for the validity of some of the models used for these individual elements. Moreover, a clear view of the overarching picture and of the first principle equations governing the dynamics seems to be somewhat missing. In the work presented here however, we will start from a clear physical basis in the form of the governing turbulent equations (as presented in section 2.2) and the mean-field equations derived from these (see section 2.3.1). In addition, the closures used will be derived based on detailed reference data from turbulence code simulations and the developed models (both the complete models and the submodels for individual terms) will be rigorously compared to this reference data. In order to avoid being overly reliant on ad-hoc parameter tuning and expert judgement, a framework for rigorous parameter estimation and model validation will be set up as well.

## 2.4  Conclusion

This chapter has provided the analytical fluid equations that govern the plasma edge and the turbulence which tends to develop in it. The interpretation of these equations has provided insight into the structure of plasma edge turbulence and the main differences with hydrodynamic turbulence. Next, these instantaneous equations have been rigorously averaged to obtain their mean-field equivalent. This averaging procedure has introduced closure terms into the equations which depend on the correlation between turbulent fluctuations. Such closure terms cannot be calculated from mean-field quantities from first principles and require modelling instead. The importance of the turbulent E×B particle and heat fluxes for the continuity and thermal energy equations has been highlighted.

The lacking treatment of these perpendicular turbulent fluxes in currently used mean-field codes as well as recent self-consistent models presented in literature have been discussed. While these models proposed in literature contain interesting elements, the approach that will be followed for modelling these fluxes in this thesis will stay closer to the underlying governing equations and draw inspiration from the RANS techniques used in hydrodynamic turbulence modelling that have also been briefly summarised. This will further be discussed in the next chapter. Another deficiency in current approach of modelling the turbulent fluxes is that no systematic methodology for parameter estimation and model selection is consistently used. In the next chapter, a Bayesian inference framework to treat this will be suggested.

# Chapter 3

# Methodology for the development of mean-field models for the E×B turbulent fluxes

In the previous chapter it was argued that the E×B turbulent particle flux $\mathbf{\Gamma}_{n,t,E}$ and turbulent heat fluxes $\mathbf{\Gamma}_{p_{\mathrm{i}},t,E}$ and $\mathbf{\Gamma}_{p_{\mathrm{e}},t,E}$ are vital turbulent closure terms to be modelled. This chapter[1] outlines the main philosophy of the closure strategy that will be used for these terms. This will rely on relating the effective turbulent transport coefficients to turbulence characteristics — to the turbulent kinetic energy and enstrophy in particular. To support the application to particular plasma models in later chapters, a general analytical framework of equations for the turbulent kinetic energy and enstrophy will be developed here. Since many models for the turbulent closure terms will feature one or several parameters that need to be calibrated, a methodology to do so is also required. Furthermore, multiple competing models may exist which one may

---

[1]This chapter uses material that has been published in "Coosemans, R., Dekeyser, W., Baelmans, M. (2021). Turbulent kinetic energy in 2D isothermal interchange-dominated scrape-off layer E×B drift turbulence: Governing equation and relation to particle transport. *Physics of Plasmas*, 28:012302" [46], in "Coosemans, R., Dekeyser, W., Baelmans, M. (2020). A new mean-field plasma edge transport model based on turbulent kinetic energy and enstrophy. *Contributions to Plasma Physics*, 60:e201900156" [44], and in "Coosemans, R., Dekeyser, W., Baelmans, M. (2022). A self-consistent mean-field model for turbulent particle and heat transport in 2D interchange-dominated electrostatic ExB turbulence in a sheath-limited scrape-off layer. *Contributions to Plasma Physics*, e202100193" [47].

want to compare. To this end, the framework for parameter estimation and model comparison that is used as a tool in this thesis will also be presented. Both nonlinear regression and Bayessian inference are considered.

This chapter is organised as follows. Section 3.1 will sketch the general RANS-like approach that will be followed to close the turbulent E×B fluxes, and provide a physical argumentation for it. Analytical equations for the turbulent kinetic energy $k_\perp$ and the enstrophy $\zeta_\perp$, key quantities in the closure strategy that will be followed, are derived in sections 3.2 and 3.3. Next, section 3.4 will describe the framework for parameter estimation and model comparison employed in this thesis. Then, section 3.5 will conclude the main results presented in this chapter.

## 3.1 Ansatz of the $k_\perp$ model

As has been discussed in section 2.3.2, the standard approach to close the perpendicular turbulent fluxes in mean-field codes is to model them using ad-hoc (convection-)diffusion relations, in which transport coefficients are tuned in order to achieve a match with available experimental data. This reliance on experimental data, combined with the knowledge that these transport coefficients strongly vary in space, depend on the operating regime and on the reactor, strongly hampers the reliability of predictive mean-field code simulations.

In this thesis, it is instead proposed to relate the turbulent E×B particle flux $\mathbf{\Gamma}_{n,t,E} \triangleq \overline{n'\mathbf{V}'_E}$ and heat fluxes $\mathbf{\Gamma}_{p_i,t,E} \triangleq \overline{nT''_i\mathbf{V}''_E}$ and $\mathbf{\Gamma}_{p_e,t,E} \triangleq \overline{nT''_e\mathbf{V}''_E}$ that require closure to quantities that characterise the underlying turbulence that drives these fluxes. In addition to a relation between the closure terms and well-chosen turbulent quantities, a way to determine these turbulent quantities themselves is also required in order to establish a self-consistent model. To this end, transport equations for these turbulence characteristics will be derived. These transport equations in turn include additional closure terms, of which the dominant ones will be identified and modelled.

The proposed approach is inspired by RANS techniques used in hydrodynamic turbulence modelling (see section 2.1) and by recent literature on turbulent transport modelling in the plasma edge (see section 2.3.3). However, the latter tended to rely on ad-hoc assumptions and expert knowledge. Here, a clear analytical framework will first be established starting from the governing turbulence equations, after which the closure terms are modelled based on detailed data from turbulence code simulations with the aid of the parameter estimation and model comparison framework described in section 3.4.

While we certainly do not rule out convective models or more complex descriptions of the fluxes in general [107, 59], the diffusive structure of the turbulent fluxes which is commonly used in mean-field modelling will be maintained in the models developed here because they were found to work well for the cases investigated. Thus, similar to models 2.78 and 2.79, but now neglecting the convective contribution, and clearly stating that only the E×B fluxes are modelled, we use

$$\mathbf{\Gamma}_{n,t,E} \triangleq \overline{n'\mathbf{V}'_E} \approx -D\nabla_\perp \bar{n}, \tag{3.1}$$

$$\mathbf{\Gamma}_{pi/e,t,E} \triangleq \overline{nT''_{i/e}\mathbf{V}''_E} \approx -\chi_{i/e}\bar{n}\nabla_\perp \tilde{T}_{i/e}. \tag{3.2}$$

Hence, the closure problem is now moved to modelling the transport coefficients $D$, $\chi_i$ and $\chi_e$. In general, it is expected that these effective turbulent transport coefficients scale as $D \sim L^2/\tau \sim LV \sim V^2\tau$ and likewise for $\chi_i$ and $\chi_e$, with $L$, $\tau$ and $V$ characteristic length, time and velocity scales of the turbulence. In the approach followed here, the assumption is that such characteristic scales can be constructed from time-averaged turbulence quantities. By then deriving transport equations for these quantities, estimates of the relevant turbulent scales in the entire simulation domain are obtained.

Note that in writing equations 3.1-3.2, it is implicitly assumed that a scalar transport coefficient is capable of modelling the turbulent fluxes in both directions perpendicular to the magnetic field, as is also commonly done in mean-field codes. In general, it could however be envisaged to make the transport coefficients tensors to account for differences in the transport in both directions. Such generalisations might be required in view of the magnetic field gradients which play a role in the propagation of blob filaments and large-scale shear flows affecting the turbulent transport. For the practical cases that will be studied later in this thesis, this does not make a difference because mean-field plasma gradients, magnetic field gradients and transport will only occur in the radial direction and will be zero in the diamagnetic direction. This is a relevant starting point since mostly the radial turbulent transport is important in mean-field modelling.

While diffusion relations such as 3.1-3.2 are routinely used for the radial particle transport in mean-field modelling and despite the merits of the diffusive model that will be presented in this thesis, literature seems to indicate that the nature of the particle and heat transport in the plasma edge is not diffusive. Radially propagating structures such as avalanches and blob-filaments would rather induce intermittent convective/ballistic transport with a strong non-local character [76, 78, 101, 61, 117, 125], see also section 1.2.2. These blobs might be interpreted as a result of the gradient removal mechanism [114, 89, 133]: on

short timescales, density and temperature gradients build up and then suddenly decay as they become unstable and a blob-like outburst of particles occurs, resulting in a flattening of the gradient that becomes stable again.

It might however be expected that a well-chosen diffusion model can give a reasonable approximation of the long time scale average particle flux. To provide qualitative support for this idea, we make an analogy to collisional diffusion. Collisional diffusion in gases is the result of particles undergoing random collisions and tracing (ballistic) trajectories in between. If individual particles have an equal probability of moving in either direction, the presence of density gradient results in a net flux of particles, because more particles are present on one side. In plasma edge turbulence, as an approximation, the convection cells and/or plasma filaments could be assumed to cause seemingly random ballistic transport of plasma fluid elements in either direction. Likewise, density and temperature gradients will lead to particle and heat fluxes in the direction opposite to the gradients. Hence, even if the underlying particle transport physics may not be diffusive, its statistical average may be approximated as such to a certain extent. It could nonetheless be interesting to research particle transport models that better incorporate the underlying convective properties. Inspiration for such models might be drawn from characteristic blob propagation velocity models [74, 101, 106, 61].

Another perspective is that while a diffusion relation might not suffice to describe the intermittent, fast fine-scale dynamics, the transport coefficients can effectively be defined and calculated for any flow according to equations 3.1-3.2 based on the mean-field gradients and fluxes.[2] In that sense, all the complex non-local, fine-scale dynamics of the fine scales are implicitly incorporated in these transport coefficients. The only question is then how these effective transport coefficients can be modelled in a self-consistent way for predictive purposes. Note that the models for the transport coefficients do not need to use local quantities only. In particular, the transport of the quantities characterising the turbulence in the full transport models that are developed in this work (e.g. transport of $k_\perp$ in equations 6.17-6.21) introduces a non-local effect in the mean-field model. This transport allows turbulent kinetic energy created in one location to increase turbulent transport in another. In addition to that, the local density gradient in a mean-field model is not just the gradient of the instantaneous background density seen by the propagating blobs, but the gradient of the time-averaged density field including the averaged density of these blobs. This may partially help bridging the gap between non-local behaviour of (individual) blobs and a mean-field diffusive description.

---

[2]When fluxes would be in the direction opposite to the gradient, or when fluxes would occur without a gradient, the transport coefficients would need to become zero or infinity respectively. It is fair to say the diffusive model breaks down for these (exceptional) situations.

As $\mathbf{\Gamma}_{n,t,E}$, $\mathbf{\Gamma}_{p_\mathrm{i},t,E}$ and $\mathbf{\Gamma}_{p_\mathrm{e},t,E}$ have been shown to be governed by the correlations between density, temperature and potential fluctuations, we aim to find a measure for the intensity of these fluctuations, and relate it to the resulting fluxes and thus to the transport coefficients $D$, $\chi_i$ and $\chi_e$. To this end, we define the turbulent kinetic energy in the E×B drift velocity as

$$\bar{n}k_E \triangleq \frac{\overline{mn\mathbf{V}_E''^2}}{2}. \tag{3.3}$$

This turbulent kinetic energy provides a direct measure of the characteristic (density weighed) E×B drift velocity of particles in the fluctuating electrostatic field. The eddies and convection cells that this forms are exactly the motions that cause the anomalous transport observed in the SOL that is of interest here (see section 1.2.1) [10, 71, 143, 165]. Hence, a link between $k_E$ and the effective turbulent diffusion coefficient is expected. In the next chapters, it will be found that $D \sim \rho_0\sqrt{k_E/m}$. Thus, the velocity scale for the turbulence is indeed identified with the turbulent kinetic energy as $\sqrt{k_E/m}$ and the reference gyro-radius $\rho_0$ provides a length scale.

To further refine this basic scaling for the transport coefficients, the turbulent enstrophy will also be considered, which is defined as

$$\bar{n}\zeta_E \triangleq \frac{\overline{mn\omega_E''^2}}{2}, \tag{3.4}$$

with $\omega_E = \mathbf{b} \cdot (\nabla \times \mathbf{V}_E)$. Like the turbulent kinetic energy, the turbulent enstrophy provides a measure for the intensity of the turbulence. Also, in hydrodynamic, inviscid, 2D turbulence, both the kinetic energy and the enstrophy are conserved. While the kinetic energy follows an inverse cascade, transferring energy from smaller to larger scales, the enstrophy follows a direct cascade [4, 71, 169]. Similar characteristics are expected for E×B drift turbulence [36, 71]. Furthermore, it is also known from hydrodynamic turbulence that viscous dissipation of kinetic energy is closely related to the enstrophy. Tran *et al.* [160] have shown that the enstrophy is related to zonal flow formation in E×B drift turbulence. Hence, it is expected that the turbulent enstrophy will provide valuable additional information not contained in the turbulent kinetic energy.

In practical terms, the enstrophy allows to complete the scaling for the transport coefficients with a turbulent time scale as $D \sim k_E/\sqrt{m\zeta_E}$. Hence, in this scaling, the transport coefficient only depends on characteristics of the turbulence that drives the transport to be modelled. No (global) reference quantities such as the gyro-radius are required anymore. It could be argued that while $\sqrt{k_E/m}$

still defines a velocity scale for the particles in the eddies, $\sqrt{k_E/\zeta_E}$ now adds a length scale. For a given value of $k_E$ this length scale decreases as $\zeta_E$ increases, meaning that the particles move in smaller structures, leading to less transport at a velocity determined by $k_E$.

Another mechanism that is known to influence the turbulent transport is flow shear. As briefly discussed in section 1.2.2, strong flows in the poloidal direction are known to develop, which are sheared in the radial direction. These flows tend to break up turbulent eddies and as such reduce the turbulent transport. These shear flows are partly fed by the turbulence. Such shear flows decrease the turbulence intensity (and thus presumably $k_E$ and $\zeta_E$) but are also expected to decrease the turbulent transport at a given turbulence intensity [23, 58, 88, 113]. Hence, this phenomenon also needs to be accounted for in the turbulent transport relation. This could for example be done by including a time scale for how long it would take a shear flow to decorrelate turbulent eddies.

Lastly, corrections for the phase structure of the turbulence will also be investigated. Assuming a single, dominant wave number exists in the turbulent spectrum, the E×B transport could be approximated as $\boldsymbol{\Gamma}_{n,t,E} \approx \mathbf{K}_y \hat{n} \hat{\phi} sin(\psi)$, where $\hat{n}$ and $\hat{\phi}$ are the amplitude of the density and the potential of this mode, $\mathbf{K}_y$ the wavenumber in the diamagnetic direction and $\psi$ is the phase difference between the potential and the density fluctuations. While a diffusion relation with $k_E$ and $\zeta_E$ supposedly does well at representing the magnitude of the amplitudes, a further correction for the phase difference might be needed. This phase difference is expected to change significantly with the turbulence regime (e.g. interchange or drift wave dominated turbulence) [145].

## 3.2 Analytical derivation of $k_\perp$ equations and energy theorem

In order to use the above scalings for the transport coefficients for predictive purposes, expressions for the underlying turbulent quantities are required. To this end, equations for $k_E$ and $\zeta_E$, which are crucial quantities to the closure strategy, are analytically derived. This section derives equations for the kinetic energy, while section 3.3 considers the enstrophy equations. Next to the relevance for the models, a further investigation of these equations also provides a view into the dynamics of the turbulence and the interaction between various energy forms at play.

This section will first derive the total perpendicular turbulent kinetic energy equation in section 3.2.1. Next, this equation will further be manipulated to

obtain a transport equation for the turbulent kinetic energy of the E×B drift velocity only in section 3.2.2. Then, section 3.2.3 will consider the interchange term which acts as an important source term in these equations in more detail and derive an analytical expression for it. Section 3.2.4 will derive equations for the parallel turbulent kinetic energy. Finally, section 3.2.5 will put the equations derived previously in their physical context by discussing the channels by which energy can be exchanged between the turbulent kinetic energy and other forms of energy in the plasma.

## 3.2.1 Derivation of total perpendicular kinetic energy equations

We define the perpendicular total ($E_{\mathrm{k},\perp}$), mean-flow ($E_{\mathrm{k},m,\perp}$), and turbulent ($k_\perp$) kinetic energies as

$$E_{\mathrm{k},\perp} \triangleq \frac{m\mathbf{V}_{0,\perp}^2}{2}, \quad E_{\mathrm{k},m,\perp} \triangleq \frac{m\tilde{\mathbf{V}}_{0,\perp}^2}{2}, \quad \bar{n}k_\perp \triangleq \frac{\overline{mn\mathbf{V}_{0,\perp}''^2}}{2}, \tag{3.5}$$

where $\mathbf{V}_{0,\perp}$ contains the perpendicular velocity components that are relevant for the ion inertia. In this section, we will assume that $\mathbf{V}_{0,\perp} = \mathbf{V}_E + \mathbf{V}_{*,i}$. As in the previous chapter, the electron inertia and the related kinetic energy is neglected because the electron mass is much smaller than the ion mass. Note that $E_{\mathrm{k},\perp}$ varies rapidly in time and space as it follows the instantaneous fluctuations, while $E_{\mathrm{k},m,\perp}$ and $k_\perp$ are ensemble averaged quantities that do not change at these small scales. The latter two are constant in time in a statistical steady state, while the former is not. Note also that the sum of mean flow and turbulent kinetic energy per unit volume equals the averaged total kinetic energy per unit volume:

$$\overline{nE_{\mathrm{k},\perp}} = \bar{n}E_{\mathrm{k},m,\perp} + \bar{n}k_\perp. \tag{3.6}$$

The analytical derivation of the equation governing the transport of $k_\perp$ starts from the charge balance equation 2.41. We follow a procedure similar to Scott [143], Garcia *et al.* [76] and Tran *et al.* [160], but rigorously account for density fluctuations in the kinetic energy equation. The Favre averages demonstrated in equation 2.58 allow to reduce the number of closure terms that appear in the mean-field equations with respect to using Reynolds averages shown in equation 2.55. Similar Favre averaging techniques have been used to take density fluctuations into account to analyse zonal flow generation by Ref. Held *et al.* [93].

**Total perpendicular kinetic energy equation**

In order to derive equations for the turbulent kinetic energy, we start by deriving an equation for the total kinetic energy, and later on split this up in a mean-flow and a turbulent part. The basic trick to derive a turbulent energy equation is to multiply the charge balance equation 2.41 with $\phi$ and to rewrite the polarisation current term. We start from the polarisation current in equation 2.42 (where only its inertial contribution was shown):

$$-\mathbf{J}_p \triangleq \left(\frac{\partial n\mathbf{V}_0}{\partial t} + \nabla \cdot (n\mathbf{V}_C\mathbf{V}_0)\right) \times \frac{m\mathbf{b}}{B} + \frac{\nabla \cdot \Pi}{B} \times \mathbf{b} - \frac{\mathbf{S}_m \times \mathbf{b}}{B}$$

$$= \frac{m}{B}\frac{\partial}{\partial t}n\mathbf{U}_0 + \frac{m}{B}\nabla \cdot (n\mathbf{V}_C\mathbf{U}_0) + \frac{D\mathbf{b}}{Dt} \times \frac{mn\mathbf{V}_0}{B}$$

$$+\frac{\nabla \cdot \Pi}{B} \times \mathbf{b} - \frac{\mathbf{S}_m \times \mathbf{b}}{B}. \qquad (3.7)$$

In this expression, we have used the symbol $\mathbf{U}_0 \triangleq \mathbf{V}_0 \times \mathbf{b} = \frac{\nabla_\perp \phi}{B} + \frac{\nabla_\perp p_i}{enB}$ introduced in equations 2.47. Note that in the convective term, it is assumed that the velocity $\mathbf{V}_0$ that is important for the (ion) flow inertia might differ from the convective (ion) velocity $\mathbf{V}_C$ that is used in the second term. Typically, the convective velocity will be chosen to contain the dominant plasma velocities though, such that $\mathbf{V}_C = \mathbf{V}_0$ with $\mathbf{V}_0$ as in equation 2.36.

Multiplying the polarisation current with $(\nabla_\perp \phi + \frac{\nabla_\perp p_i}{en})$, leads to

$$-(\nabla_\perp \phi + \frac{\nabla_\perp p_i}{en}) \cdot \mathbf{J}_p = \mathbf{U}_0 \cdot \left(\frac{\partial}{\partial t}mn\mathbf{U}_0 + \nabla \cdot mn\mathbf{V}_C\mathbf{U}_0\right)$$

$$+\mathbf{U}_0 \cdot \left(\frac{D\mathbf{b}}{Dt} \times mn\mathbf{V}_0 + (\nabla \cdot \Pi) \times \mathbf{b} - \mathbf{S}_m \times \mathbf{b}\right)$$

$$= \frac{\partial nE_{k,\perp}}{\partial t} + \nabla \cdot (nE_{k,\perp}\mathbf{V}_C + \Pi \cdot \mathbf{V}_{0,\perp})$$

$$-\Pi : \nabla\mathbf{V}_{0,\perp}^T + mnV_{||}\frac{D\mathbf{b}}{Dt} \cdot \mathbf{V}_{0,\perp} + E_{k,\perp}S_{n,i} - \mathbf{S}_m \cdot \mathbf{V}_{0,\perp}. \qquad (3.8)$$

In this derivation, we made use of continuity equation 2.25 in which we assumed the convection velocity is also given by $\mathbf{V}_C$. Furthermore, we used the fact that $E_{k,\perp} = \mathbf{V}_{0,\perp}^2/2 = \mathbf{U}_0^2/2$ and some common vector calculus identities ($\frac{D\mathbf{b}}{Dt} \cdot \mathbf{b} = 0$ for the unit vector $\mathbf{b}$, $\nabla \cdot (\Pi \cdot \mathbf{V}) = (\nabla \cdot \Pi) \cdot \mathbf{V} + \Pi : \nabla\mathbf{V}^T$, $P \cdot (Q \times R) = Q \cdot (R \times P)$ and $(P \times Q) \cdot (R \times T) = (P \cdot R)(Q \cdot T) - (Q \cdot R)(P \cdot T)$ for arbitrary vectors $P$,

$Q$, $R$, and $T$). Thus, this way a relation for the time change and transport of the total perpendicular kinetic energy is found.

So far we have only performed algebraic manipulations involving the polarization current, relating it to the perpendicular kinetic energy. Note that we have not yet added any meaningful information other than its definition though. The critical piece of information to get to a proper transport equation is the charge balance equation 2.41. This is inserted by manipulating the LHS of equation 3.8 as follows:

$$-(\nabla_\perp \phi + \frac{\nabla_\perp p_i}{en}) \cdot \mathbf{J}_p = -\nabla \cdot \phi \mathbf{J}_p + \phi \nabla \cdot \mathbf{J}_p - \nabla_\perp p_i \cdot \mathbf{V}_p$$

$$= -\nabla \cdot \phi \mathbf{J}_p - \phi \nabla \cdot \mathbf{J}_{||} - \phi \nabla \cdot \mathbf{J}_* - \nabla_\perp p_i \cdot \mathbf{V}_p, \qquad (3.9)$$

where the charge balance equation $\nabla \cdot \mathbf{J}_p = -\nabla \cdot \mathbf{J}_{||} - \nabla \cdot \mathbf{J}_*$ has been used to get to the second line. Combining expressions 3.8 and 3.9 now yields the transport equation for $E_{k,\perp}$:

$$\frac{\partial n E_{k,\perp}}{\partial t} + \nabla \cdot (n E_{k,\perp} \mathbf{V}_C + \Pi \cdot \mathbf{V}_{0,\perp} + \phi \mathbf{J}_p)$$

$$= -\phi \nabla \cdot \mathbf{J}_{||} - \phi \nabla \cdot \mathbf{J}_* - \nabla_\perp p_i \cdot \mathbf{V}_p + \Pi : \nabla \mathbf{V}_{0,\perp}^T$$

$$-m n V_{||} \frac{D\mathbf{b}}{Dt} \cdot \mathbf{V}_{0,\perp} - E_{k,\perp} S_{n_i} + \mathbf{S}_m \cdot \mathbf{V}_{0,\perp}. \qquad (3.10)$$

**Mean-flow and turbulent kinetic energy equations**

To arrive at equations for $E_{k,m,\perp}$ and $k_\perp$ defined in equation 3.5, the $E_{k,\perp}$ equation 3.10 should be averaged and split in a contribution due to mean flows and a contribution due to fluctuations.

The procedure to obtain an equation for $E_{k,m,\perp}$ is rather similar to that used for $E_{k,\perp}$. An expression for the time rate of change of $E_{k,m,\perp}$ can now be obtained by taking the scalar product of the average polarisation current $\bar{\mathbf{J}}_p$ and $\tilde{\mathbf{U}}_0$. Taking the average of the polarisation current in equation 3.7 yields:

$$-\bar{\mathbf{J}}_p = \frac{m}{B} \frac{\partial}{\partial t} \bar{n} \tilde{\mathbf{U}}_0 + \frac{m}{B} \nabla \cdot (\bar{n} \tilde{\mathbf{V}}_C \tilde{\mathbf{U}}_0 + \overline{n \mathbf{V}_C'' \mathbf{U}_0''})$$

$$+ \overline{\frac{D\mathbf{b}}{Dt} \times \frac{m n \mathbf{V}_0}{B}} + \frac{\nabla \cdot \bar{\bar{\Pi}}}{B} \times \mathbf{b} - \frac{\bar{\mathbf{S}}_m \times \mathbf{b}}{B}. \qquad (3.11)$$

Multiplying this with $(\widetilde{\nabla_\perp \phi} + \frac{\nabla_\perp \bar{p}_i}{e\bar{n}})$,

$$-(\widetilde{\nabla_\perp \phi} + \frac{\nabla_\perp \bar{p}_i}{e\bar{n}}) \cdot \bar{\mathbf{J}}_p = \frac{\partial \bar{n} E_{k,m,\perp}}{\partial t}$$

$$+\nabla \cdot (\bar{n} E_{k,m,\perp} \tilde{\mathbf{V}}_C + m \overline{n \mathbf{V}_C'' \mathbf{V}_{0,\perp}''} \cdot \tilde{\mathbf{V}}_{0,\perp} + \bar{\bar{\Pi}} \cdot \tilde{\mathbf{V}}_{0,\perp}) - \bar{\bar{\Pi}} : \nabla \tilde{\mathbf{V}}_{0,\perp}^T$$

$$-m \overline{n \mathbf{V}_C'' \mathbf{V}_{0,\perp}''} : \nabla \tilde{\mathbf{V}}_{0,\perp}^T + m \overline{n V_{||} \frac{D\mathbf{b}}{Dt}} \cdot \tilde{\mathbf{V}}_{0,\perp} + E_{k,m,\perp} \bar{S}_{n_i} - \bar{\mathbf{S}}_m \cdot \tilde{\mathbf{V}}_{0,\perp} \quad (3.12)$$

is obtained, again making use of the ion continuity equation. This can be linked to the divergence of the average polarisation current as

$$-(\widetilde{\nabla_\perp \phi} + \frac{\nabla_\perp \bar{p}_i}{e\bar{n}}) \cdot \bar{\mathbf{J}}_p$$

$$= \bar{\phi} \nabla \cdot \bar{\mathbf{J}}_p - \nabla \cdot (\bar{\phi} \bar{\mathbf{J}}_p) - \frac{\bar{\mathbf{J}}_p}{\bar{n}} \cdot \overline{n' \nabla \phi'} - \nabla_\perp \bar{p}_i \cdot \tilde{\mathbf{V}}_p. \quad (3.13)$$

Note that this is more complicated than for the total kinetic energy case because Favre averages and gradients do not commute. As a result, an additional "Favre averaging term", which is the penultimate term in 3.13, originates.

Combining equations 3.12 and 3.13 and filling out the average charge balance equation as $-\nabla \cdot \bar{\mathbf{J}}_p = \nabla \cdot \bar{\mathbf{J}}_{||} + \nabla \cdot \bar{\mathbf{J}}_*$ then yields the mean-field kinetic energy equation:

$$\frac{\partial \bar{n} E_{k,m,\perp}}{\partial t} + \nabla \cdot (\bar{n} E_{k,m,\perp} \tilde{\mathbf{V}}_C + m \overline{n \mathbf{V}_C'' \mathbf{V}_0''} \cdot \tilde{\mathbf{V}}_{0,\perp} + \bar{\bar{\Pi}} \cdot \tilde{\mathbf{V}}_{0,\perp} + \bar{\phi} \bar{\mathbf{J}}_p)$$

$$= -\bar{\phi} \nabla \cdot \bar{\mathbf{J}}_{||} - \bar{\phi} \nabla \cdot \bar{\mathbf{J}}_* - \nabla_\perp \bar{p}_i \cdot \tilde{\mathbf{V}}_p + \bar{\bar{\Pi}} : \nabla \tilde{\mathbf{V}}_{0,\perp}^T$$

$$+m \overline{n \mathbf{V}_C'' \mathbf{V}_{0,\perp}''} : \nabla \tilde{\mathbf{V}}_{0,\perp}^T - \frac{\bar{\mathbf{J}}_p}{\bar{n}} \cdot \overline{n' \nabla \phi'} - m \overline{n V_{||} \frac{D\mathbf{b}}{Dt}} \cdot \tilde{\mathbf{V}}_{0,\perp}$$

$$-E_{k,m,\perp} \bar{S}_{n_i} + \bar{\mathbf{S}}_m \cdot \tilde{\mathbf{V}}_{0,\perp} \quad (3.14)$$

Since the average total kinetic energy equals the sum of the mean-field and turbulent kinetic energies (as illustrated in equation 3.6), an equation for the perpendicular turbulent kinetic energy can be derived by taking the difference between the average of the total perpendicular kinetic energy equation 3.10 and the mean-field perpendicular kinetic energy equation 3.14. This then leads to the following equation:

$$\frac{\partial \bar{n} k_\perp}{\partial t} + \nabla \cdot (\bar{n} k_\perp \tilde{\mathbf{V}}_C + \frac{m\overline{n \mathbf{V}_0''^2 \mathbf{V}_C''}}{2} + \overline{\Pi \cdot \mathbf{V}_{0,\perp}''} + \overline{\phi' \mathbf{J}_p'})$$

$$= -\overline{\phi' \nabla \cdot \mathbf{J}_{||}'} - \overline{\phi' \nabla \cdot \mathbf{J}_*'} - \overline{\nabla_\perp p_{\mathrm{i}} \cdot \mathbf{V}_p''} + \overline{\Pi : \nabla \mathbf{V}_{0,\perp}''^T}$$

$$-m\overline{n \mathbf{V}_C'' \mathbf{V}_{0,\perp}''} : \nabla \tilde{\mathbf{V}}_{0,\perp}^T + \frac{\bar{\mathbf{J}}_p}{\bar{n}} \cdot \overline{n' \nabla \phi'} - mn V_{||} \overline{\frac{D\mathbf{b}}{Dt} \cdot \mathbf{V}_{0,\perp}''}$$

$$-\frac{m\overline{S_{n_{\mathrm{i}}} \mathbf{V}_{0,\perp}''^2}}{2} - m\tilde{\mathbf{V}}_{0,\perp} \cdot \overline{\mathbf{V}_{0,\perp}'' S_{n_{\mathrm{i}}}} + \overline{\mathbf{S}_m \cdot \mathbf{V}_{0,\perp}''}. \tag{3.15}$$

The manipulations performed in this section and the equations in which they resulted have largely been based on the seminal paper by Scott [143]. However, a clearer definition of the averaging operators has been used here, which consistently includes density fluctuations. Next to changes in the exact form of some terms in terms of averages and fluctuations, this lead to the appearance of the "Favre term" in equations 3.14 and 3.15 (sixth term on the RHS). Furthermore, particle and momentum sources ($S_n$ and $\mathbf{S}_m$) have been retained in the equation set (including their possible fluctuations) as well as the $\frac{D\mathbf{b}}{Dt}$ term which were not included in the paper by Scott. Also, we chose to keep the general form of the viscous stress tensor $\Pi$ instead of assuming a particular model for it. On the other hand, magnetic field fluctuations have been neglected here, while they were (partly) maintained in the original paper.

We leave a discussion of the perpendicular kinetic energy equations 3.10, 3.14, and 3.15 and the physics they included for section 3.2.5.

### 3.2.2 Derivation of E×B kinetic energy equations

At this point, it is important to remember (cfr. section 2.3.1) that the turbulent fluxes $\boldsymbol{\Gamma}_{n,t,E}$, $\boldsymbol{\Gamma}_{p_{\mathrm{i}},t,E}$ and $\boldsymbol{\Gamma}_{p_{\mathrm{e}},t,E}$ (see equations 2.65 and 2.70) due to the E×B drift are the ones that require modelling. It could be expected that these E×B fluxes are more closely related to the turbulent kinetic energy in the E×B velocity fluctuation only than to the total turbulent kinetic energy due to the total perpendicular $\mathbf{V}_{0,\perp}$ consisting of both the E×B and the ion diamagnetic velocity. This would indeed be more in line with the underlying hypotheses of the $k_\perp$ transport models formulated in section 3.1. As such, this section will derive an equation for the kinetic energy in the E×B drift velocity only.

In analogy to the total kinetic energies, we define the E×B-only kinetic energies
as

$$E_{\mathrm{E}} \triangleq \frac{m\mathbf{V}_E^2}{2}, \quad E_{\mathrm{E},m} \triangleq \frac{m\tilde{\mathbf{V}}_E^2}{2}, \quad \bar{n}k_E \triangleq \frac{\overline{mn\mathbf{V}_E''^2}}{2}. \tag{3.16}$$

Note that the sum of this and the diamagnetic drift's kinetic energy which
could be defined as $m\mathbf{V}_{*,i}^2/2$ is not equal to the total drift kinetic energy $E_{\mathrm{k},\perp}$
as the $\mathbf{V}_E \cdot \mathbf{V}_{*,i}$ terms would then be overlooked, i.e. $E_{\mathrm{k},\perp} = m\mathbf{V}_{0,\perp}^2/2 =$
$m\mathbf{V}_E^2/2 + m\mathbf{V}_{*,i}^2/2 + m\mathbf{V}_E \cdot \mathbf{V}_{*,i}$. Equations for the latter two kinetic energy
components separately are derived in appendix A for completeness.

As a first step to derive equations for the E×B kinetic energies, we split the
polarisation current in a contribution due to the E×B velocity, a contribution
due to the ion diamagnetic velocity and a contribution due to viscosity and
momentum sources as follows:

$$\mathbf{J}_p \triangleq \underbrace{\frac{D\mathbf{b}}{Dt} \times \frac{mn\mathbf{V}_{||}}{B}}_{\mathbf{J}_{p,||}} + \underbrace{\left( \frac{\partial n\mathbf{V}_E}{\partial t} + \nabla \cdot n\mathbf{V}_C\mathbf{V}_E \right) \times \frac{m\mathbf{b}}{B}}_{\mathbf{J}_{p,E}}$$

$$+ \underbrace{\left( \frac{\partial n\mathbf{V}_{*,i}}{\partial t} + \nabla \cdot n\mathbf{V}_C\mathbf{V}_{*,i} \right) \times \frac{m\mathbf{b}}{B}}_{\mathbf{J}_{p,*}} \underbrace{- \frac{\nabla \cdot \Pi}{B} \times \mathbf{b} + \frac{\mathbf{S}_m \times \mathbf{b}}{B}}_{\mathbf{J}_{p,\Pi}}, \tag{3.17}$$

where

$$\mathbf{J}_{p,||} \triangleq \left( \frac{\partial n\mathbf{V}_{||}}{\partial t} + \nabla \cdot n\mathbf{V}_C\mathbf{V}_{||} \right) \times \frac{m\mathbf{b}}{B} = \frac{D\mathbf{b}}{Dt} \times \frac{mn\mathbf{V}_{||}}{B}. \tag{3.18}$$

By excluding the contribution of the ion diamagnetic velocity to the polarisation
current, transport equations for the E×B-only kinetic energy can be constructed.
The procedure to do this is very analogous to that used for the total kinetic
energy. The equivalent to equation 3.8 now becomes

$$-\nabla_\perp\phi\cdot(\mathbf{J}_{p,E}+\mathbf{J}_{p,\Pi}+\mathbf{J}_{p,||}) = m\mathbf{U}_E\cdot\left(\frac{\partial}{\partial t}n\mathbf{U}_E+\nabla\cdot n\mathbf{V}_C\mathbf{U}_E\right)$$

$$+\mathbf{U}_E\cdot\left(\frac{D\mathbf{b}}{Dt}\times mn\mathbf{V}_{||}+\nabla\cdot\Pi\times\mathbf{b}-\frac{\mathbf{S}_m\times\mathbf{b}}{B}\right)$$

$$=\frac{\partial nE_\mathrm{E}}{\partial t}+\nabla\cdot(nE_\mathrm{E}\mathbf{V}_C+\Pi\cdot\mathbf{V}_E)-\Pi:\nabla\mathbf{V}_E^T$$

$$+mnV_{||}\frac{D\mathbf{b}}{Dt}\cdot\mathbf{V}_E+E_\mathrm{E}S_{n_\mathrm{i}}-\mathbf{S}_m\cdot\mathbf{V}_E. \quad (3.19)$$

Note that the polarization current is only multiplied with the electrostatic field gradient to obtain the E×B-only kinetic energy. In equation 3.19, the following definition has been used:

$$\mathbf{U}_E\triangleq-\mathbf{b}\times\mathbf{V}_E=\frac{\nabla_\perp\phi}{B}. \quad (3.20)$$

Relating this to the charge balance equation as before yields

$$-\nabla_\perp\phi\cdot(\mathbf{J}_{p,E}+\mathbf{J}_{p,\Pi}+\mathbf{J}_{p,||})$$

$$=-\nabla\cdot\phi(\mathbf{J}_{p,E}+\mathbf{J}_{p,\Pi}+\mathbf{J}_{p,||})+\phi\nabla\cdot(\mathbf{J}_{p,E}+\mathbf{J}_{p,\Pi}+\mathbf{J}_{p,||})$$

$$=-\nabla\cdot\phi(\mathbf{J}_{p,E}+\mathbf{J}_{p,\Pi}+\mathbf{J}_{p,||})-\phi\nabla\cdot\mathbf{J}_{||}-\phi\nabla\cdot\mathbf{J}_*-\phi\nabla\cdot\mathbf{J}_{p,*}. \quad (3.21)$$

Combining equations 3.19 and 3.21, an equation for the E×B-only kinetic energy is readily obtained:

$$\frac{\partial nE_\mathrm{E}}{\partial t}+\nabla\cdot(nE_\mathrm{E}\mathbf{V}_C+\Pi\cdot\mathbf{V}_E+\phi\mathbf{J}_p)=-\phi\nabla\cdot\mathbf{J}_{||}-\phi\nabla\cdot\mathbf{J}_*$$

$$+\nabla\phi\cdot\mathbf{J}_{p,*}+\Pi:\nabla\mathbf{V}_E^T-mnV_{||}\frac{D\mathbf{b}}{Dt}\cdot\mathbf{V}_E-E_\mathrm{E}S_{n_\mathrm{i}}+\mathbf{S}_m\cdot\mathbf{V}_E. \quad (3.22)$$

The form of this equation is very similar to equation 3.10. However, $E_{\mathrm{k},\perp}$ is "replaced" by $E_\mathrm{E}$ and $\mathbf{V}_{0,\perp}$ by $\mathbf{V}_E$. Furthermore, the $\nabla p_\mathrm{i}\cdot\mathbf{V}_p$ term is no longer present in the equation, while the last term on the RHS of equation 3.21, rewritten as $-\phi\nabla\cdot\mathbf{J}_{p,*}=-\nabla\cdot\phi\mathbf{J}_{p,*}+\nabla\phi\cdot\mathbf{J}_{p,*}$, comes in to include the diamagnetic drift contribution to the polarisation current. Thus the latter is not

neglected. Instead, it is chosen to account for it as a current divergence term instead of including it in the kinetic energy in the LHS as was done in the total kinetic energy case in section 3.2.1. When the diamagnetic drift contribution to the polarisation current is small or is neglected the $\phi \nabla \cdot \mathbf{J}_{p,*}$ term can also be neglected. On the other hand, it is worth noting that the parallel and diamagnetic drift current divergence terms remain unchanged between the total perpendicular and the E×B-only kinetic energy equations. Note that equation 3.22 could of course also have been derived directly from equation 3.10 by algebraic manipulation. This derivation proved much more tortuous and tedious though.

Splitting the average polarisation current into an E×B, a diamagnetic and a viscous and source term contribution as well, multiplying with $\widetilde{\nabla \phi}$ and rewriting using the averaged charge balance equation as before, yields following equation for the E×B-only mean-field kinetic energy:

$$\frac{\partial \bar{n} E_{\mathrm{E},m}}{\partial t} + \nabla \cdot (\bar{n} E_{\mathrm{E},m} \tilde{\mathbf{V}}_C + m \overline{n \mathbf{V}_C'' \mathbf{V}_E''} \cdot \tilde{\mathbf{V}}_E + \bar{\bar{\Pi}} \cdot \tilde{\mathbf{V}}_E + \bar{\phi} \bar{\mathbf{J}}_p)$$

$$= -\bar{\phi} \nabla \cdot \bar{\mathbf{J}}_{||} - \bar{\phi} \nabla \cdot \bar{\mathbf{J}}_* + \nabla \bar{\phi} \cdot \bar{\mathbf{J}}_{p,*} + \bar{\bar{\Pi}} : \nabla \tilde{\mathbf{V}}_E^T + m \overline{n \mathbf{V}_C'' \mathbf{V}_E''} : \nabla \tilde{\mathbf{V}}_E^T$$

$$- (\frac{\bar{\mathbf{J}}_{p,E} + \bar{\mathbf{J}}_{p,\Pi}}{\bar{n}}) \cdot \overline{n' \nabla \phi'} - \overline{m n V_{||} \frac{D \mathbf{b}}{Dt}} \cdot \tilde{\mathbf{V}}_E - E_{\mathrm{E},m} \bar{S}_{n_{\mathrm{i}}} + \bar{\mathbf{S}}_m \cdot \tilde{\mathbf{V}}_E. \quad (3.23)$$

Taking the difference between the average of equation 3.22 and equation 3.23 again yields an equation for the turbulent kinetic energy, in the E×B drift fluctuations this time:

$$\frac{\partial \bar{n} k_E}{\partial t} + \nabla \cdot (\bar{n} k_E \tilde{\mathbf{V}}_C + \frac{m \overline{n \mathbf{V}_E''^2 \mathbf{V}_C''}}{2} + \overline{\bar{\bar{\Pi}} \cdot \mathbf{V}_E''} + \overline{\phi' \mathbf{J}_p'})$$

$$= -\overline{\phi' \nabla \cdot \mathbf{J}_{||}'} - \overline{\phi' \nabla \cdot \mathbf{J}_*'} + \overline{\nabla \phi' \cdot \mathbf{J}_{p,*}'} + \overline{\bar{\bar{\Pi}} : \nabla \mathbf{V}_E''^T}$$

$$- m \overline{n \mathbf{V}_C'' \mathbf{V}_E''} : \nabla \tilde{\mathbf{V}}_E^T + (\frac{\bar{\mathbf{J}}_{p,E} + \bar{\mathbf{J}}_{p,\Pi}}{\bar{n}}) \cdot \overline{n' \nabla \phi'} - \overline{m n V_{||} \frac{D \mathbf{b}}{Dt} \cdot \mathbf{V}_E''}$$

$$- \frac{m \overline{S_{n_{\mathrm{i}}} \mathbf{V}_E''^2}}{2} - m \tilde{\mathbf{V}}_E \cdot \overline{\mathbf{V}_E'' \cdot S_{n_{\mathrm{i}}}} + \overline{\mathbf{S}_m \cdot \mathbf{V}_E''}. \quad (3.24)$$

Comparing these E×B-only kinetic energy equations 3.23 and 3.24 to the total perpendicular kinetic energy equations 3.14 and 3.15, the same changes as for the total kinetic energy can be observed. In addition, it is worth remarking that the Reynolds stresses (RS) have also changed now, in the sense that these

now include only the E×B velocity (and $\mathbf{V}_C$). Likewise, in the Favre averaging term (sixth term on the RHS) the diamagnetic drift polarisation current is no longer present.

### 3.2.3 Analytical relation between interchange term and turbulent fluxes

The term involving $\phi\nabla\cdot\mathbf{J}_*$ in the perpendicular kinetic energy equations, which we will call interchange terms, will be shown to be an important source of kinetic energy in the next chapters. Moreover, they appear unchanged in the total perpendicular kinetic energy equations 3.10, 3.14, 3.15 and the E×B-only kinetic energy equations 3.22, 3.23, 3.24 respectively, indicating that they are a direct source of E×B kinetic energy. Hence, it is of crucial importance to model them correctly. Interestingly, an analytical expression is found that relates these important terms to the E×B energy flux.

Following Scott [143], the interchange term $G_{Ek}$ in the total kinetic energy equations 3.10 and 3.22 can be rewritten as

$$G_{Ek} \triangleq -\phi\nabla\cdot\mathbf{J}_* = -\nabla\cdot\phi\mathbf{J}_* + \nabla\phi\cdot\mathbf{J}_*$$

$$= -\nabla\cdot\phi\mathbf{J}_* + \nabla\phi\cdot\left(\frac{\mathbf{b}\times\nabla p}{B}\right) = -\nabla\cdot\phi\mathbf{J}_* - \nabla p\cdot\left(\frac{\mathbf{b}\times\nabla\phi}{B}\right)$$

$$= -\nabla\cdot\phi\mathbf{J}_* - \nabla p\cdot\mathbf{V}_E = -\nabla\cdot(\phi\mathbf{J}_* + p\mathbf{V}_E) + p\nabla\cdot\mathbf{V}_E \qquad (3.25)$$

In complete analogy, the interchange terms for the mean-field and turbulent kinetic energy can be written as

$$G_{Ekm} \triangleq -\bar{\phi}\nabla\cdot\bar{\mathbf{J}}_* = -\nabla\cdot(\bar{\phi}\bar{\mathbf{J}}_* + \bar{p}\bar{\mathbf{V}}_E) + \bar{p}\nabla\cdot\bar{\mathbf{V}}_E \qquad (3.26)$$

$$G_k \triangleq -\overline{\phi'\nabla\cdot\mathbf{J}'_*} = -\nabla\cdot(\overline{\phi'\mathbf{J}'_*} + \overline{p'\mathbf{V}'_E}) + \overline{p'\nabla\cdot\mathbf{V}'_E} \qquad (3.27)$$

These derivations clearly show that the first two terms in these expressions are actually transport terms that do not inject energy in the turbulence, but merely transport it. The sum of both terms is expected to be small [143], and their average can moreover be shown to vanish in 1D radial geometries (as will be considered in the next chapters of this thesis) [46]:

$$-\nabla\cdot(\overline{\phi\mathbf{J}_*} + \overline{p\mathbf{V}_E}) = \nabla\cdot\left(\frac{\nabla(\overline{p\phi})\times\mathbf{b}}{B}\right) \approx 0. \qquad (3.28)$$

Assuming symmetry in the diamagnetic direction on average, only the radial gradient of $\bar{p}\phi$ can be nonzero. The gradient of this in the diamagnetic direction which is taken in the divergence operator is zero. This also holds for the corresponding terms in the mean-field and turbulent kinetic energy interchange terms.

Hence, the last term in the interchange expressions 3.25-3.27 is expected to be the dominant contribution. The divergence in this term can be rewritten as [143]

$$\nabla \cdot \mathbf{V}_E = \nabla \cdot \left( \frac{\mathbf{b} \times \nabla \phi}{B} \right) = \frac{\nabla \phi}{B^2} \cdot \nabla \times B - \mathbf{V}_E \cdot \nabla \ln B^2. \tag{3.29}$$

In this equation, the first term is expected to be small because of the low $\beta$ approximation (cfr. section 2.2.2).

Largely independently from Scott [143], results equivalent to equations 3.25-3.29 were achieved in this thesis, and have been reported in Ref. [46]. Based on these derivations, it is found that the interchange term can be modelled as

$$G_{Ek} \approx -p\mathbf{V}_E \cdot \nabla \ln B^2, \tag{3.30}$$

$$G_{Ekm} \approx -\bar{p}\bar{\mathbf{V}}_E \cdot \nabla \ln B^2, \tag{3.31}$$

$$G_k \approx -\overline{p'\mathbf{V}'_E} \cdot \nabla \ln B^2. \tag{3.32}$$

These relations for the interchange term are similar to relations reported by Refs. [155, 74, 76]. They very clearly illustrate the link between the interchange source of kinetic energy and the E×B energy flux $3p\mathbf{V}_E/2$ (in equations 2.68 and 2.69 for example).

The interchange drive for the turbulent kinetic energy, $G_k$, can further be elaborated to deepen this link. Defining $T = T_i + T_e$ and writing $p' = n'\tilde{T} + nT''$, it is found that

$$\overline{p'\mathbf{V}'_E} = \tilde{T}\overline{n'\mathbf{V}'_E} + \overline{nT''\mathbf{V}'_E} = \tilde{T}\overline{n'\mathbf{V}'_E} + \overline{nT''\mathbf{V}''_E}. \tag{3.33}$$

Using equations 2.65 and 2.70, the expression for the interchange term becomes

$$G_k = -(\tilde{T}\overline{n'\mathbf{V}'_E} + \overline{nT''\mathbf{V}''_E}) \cdot \nabla \ln(B^2)$$

$$= -(\tilde{T}\mathbf{\Gamma}_{n,t,E} + \mathbf{\Gamma}_{p_i,t,E} + \mathbf{\Gamma}_{p_e,t,E}) \cdot \nabla \ln(B^2). \tag{3.34}$$

This shows that the interchange drive for the turbulent kinetic energy is purely due to turbulent fluctuations, and more in particular due to turbulent ion and electron energy fluxes. Furthermore, this expression directly explains the ballooning character of the turbulence (see also section 1.2.2) [74, 34, 158, 85, 66]. A radially outward turbulent E×B heat flux will lead to the generation of $k_\perp$ on the low field side of the tokamak where this flux is in the opposite direction of the magnetic field gradient. On the high field side on the other hand, such an outward flux leads to a sink of $k_\perp$ (not just the absence of a source). In real tokamaks, this effect may be reduced or compensated by the contributions from other sources of the turbulence. Note also that if the diffusive relations 3.1-3.2 are filled out in the interchange relation 3.34, a direct link is established between the drive of the turbulence and the mean-field gradients (in combination with the magnetic geometry). This is in accordance with the general principle that plasma turbulence originates from free energy that is available from the thermodynamic inequilibrium created by nonzero mean-field gradients [36, 94, 143, 145, 117].

Hence, when closures for the turbulent E×B particle and heat fluxes are available (possibly as a function of $k_\perp$), expression 3.34 can be directly used such that no additional closures are required for the interchange term $G_k$. Remember that this expression is analytically exact for a 1D (radial) geometry with zero plasma $\beta$ and under the assumption of electrostatic turbulence, such that there are no fluctuations in the magnetic field **B**. Moreover, this closure is expected to provide an accurate approximation for more general cases since the correction terms are expected to be rather small.

## 3.2.4  Derivation of parallel kinetic energy equations

There is also kinetic energy in the parallel ion plasma velocity, both in the mean-field and the fluctuating component. In analogy with the perpendicular kinetic energies, we write the parallel kinetic energies as

$$E_{\mathrm{k},||} \triangleq \frac{m\mathbf{V}_{||}^2}{2}, \quad E_{\mathrm{k},m,||} \triangleq \frac{m\tilde{\mathbf{V}}_{||}^2}{2}, \quad \bar{n}k_{||} \triangleq \frac{\overline{mn\mathbf{V}_{||}''^2}}{2}. \tag{3.35}$$

Remember from section 2.2 that because the plasma is not hindered by electromagnetic forces in the parallel direction, fluctuations along the parallel direction occur on longer length scales than those in the perpendicular direction. As mentioned in section 2.3.1, it might be expected that parallel velocity fluctuations are relatively small and only play a secondary role for the parallel particle and heat fluxes and for the (average) parallel kinetic energy. The rigorous validation of these hypotheses is left for future work though. Transport equations for the parallel kinetic energy can be obtained in a rather straightforward way

which is very similar to the typical procedure used in hydrodynamic turbulence. An equation for $E_{k,||}$ can be obtained by multiplying the parallel momentum equation 2.44 with $V_{||}$:

$$\frac{\partial}{\partial t}(nE_{k,||}) + \nabla \cdot (n\mathbf{V}_C E_{k,||} + \Pi \cdot \mathbf{V}_{||})$$

$$= \Pi : \nabla \mathbf{V}_{||}^T - \mathbf{V}_{||} \cdot \nabla_{||} p + m V_{||} \frac{D\mathbf{b}}{Dt} \cdot n\mathbf{V}_{0,\perp} - E_{k,||} S_{n_i} + \mathbf{V}_{||} \cdot \mathbf{S}_m. \quad (3.36)$$

In this derivation, the ion continuity equation 2.25 has been used, in which the convection velocity is assumed to be $\mathbf{V}_C$, as in the ion momentum equation. Likewise, a mean-field parallel kinetic energy equation is constructed by multiplying the average of equation 2.44 with $\tilde{\mathbf{V}}_{||}$. This yields

$$\frac{\partial}{\partial t}(\bar{n}E_{k,m,||}) + \nabla \cdot (m\bar{n}\tilde{\mathbf{V}}_C E_{k,m,||} + m\overline{n\mathbf{V}_C''\mathbf{V}_{||}''} \cdot \tilde{\mathbf{V}}_{||} + \overline{\overline{\Pi}} \cdot \tilde{\mathbf{V}}_{||})$$

$$= \overline{\overline{\Pi}} : \nabla \tilde{\mathbf{V}}_{||}^T + m\overline{n\mathbf{V}_C''\mathbf{V}_{||}''} : \nabla \tilde{\mathbf{V}}_{||}^T - \tilde{\mathbf{V}}_{||} \cdot \nabla_{||} \bar{p}$$

$$+ m\tilde{V}_{||} \overline{\frac{D\mathbf{b}}{Dt} \cdot n\mathbf{V}_{0,\perp}} - E_{k,m,||} \bar{S}_{n_i} + \tilde{\mathbf{V}}_{||} \cdot \bar{\mathbf{S}}_m. \quad (3.37)$$

Taking the difference between the average of the equation 3.37 and the previous equation, an equation for the parallel turbulent kinetic energy is found as

$$\frac{\partial}{\partial t}(\bar{n}k_{||}) + \nabla \cdot (\bar{n}\tilde{\mathbf{V}}_C k_{||} + \frac{m\overline{n\mathbf{V}_C''\mathbf{V}_{||}''^2}}{2} + \overline{\Pi \cdot \mathbf{V}_{||}''})$$

$$= \overline{\Pi : \nabla \mathbf{V}_{||}''^T} - m\overline{n\mathbf{V}_C''\mathbf{V}_{||}''} : \nabla \tilde{\mathbf{V}}_{||}^T - \overline{\mathbf{V}_{||}'' \cdot \nabla_{||} p}$$

$$+ m\overline{V_{||}'' \frac{D\mathbf{b}}{Dt} \cdot n\mathbf{V}_{0,\perp}} - \frac{\overline{S_{n_i} \mathbf{V}_{||}''^2}}{2} - \tilde{\mathbf{V}}_{||} \cdot \overline{\mathbf{V}_{||}'' \cdot S_{n_i}} + \overline{\mathbf{V}_{||}'' \cdot \mathbf{S}_m}. \quad (3.38)$$

Beside the $D\mathbf{b}/Dt$ terms, the interpretation of these equations is rather standard and deviates little from that for the kinetic energy in hydrodynamic turbulence. We will come back to this interpretation in the next section.

## 3.2.5 Energy theorem

Next to the perpendicular turbulent kinetic energy, supposedly driving the turbulent transport of heat and particles and thus our main interest, other

forms of energy are present in the plasma edge as well. These include mean-field kinetic energy, thermal energy and parallel kinentic energy (mean-field and turbulent) for which transport equations have already been derived, but also magnetic energy. This section illustrates the energetic couplings between these various kinds of energy and thus of the different pathways for the energy to get into and out of the turbulence. This discussion is largely based on the insight provided by Ref. [143]. To facilitate this analysis and to bring out the energetic couplings, we start by slightly rewriting the mean-field and turbulent kinetic energy equations 3.14 and 3.15:

$$\frac{\partial \bar{n}E_{\mathrm{k},m,\perp}}{\partial t}$$

$$+\nabla \cdot (\bar{n}E_{\mathrm{k},m,\perp}\tilde{\mathbf{V}}_C + m\overline{n\mathbf{V}_C''\mathbf{V}_0''} \cdot \tilde{\mathbf{V}}_{0,\perp} + \bar{\Pi} \cdot \tilde{\mathbf{V}}_{0,\perp} + \bar{\phi}\bar{\mathbf{J}} + \bar{p}\mathbf{V}_E)$$

$$= \nabla_{||}\bar{\phi} \cdot \bar{\mathbf{J}}_{||} + \bar{p}\nabla \cdot \bar{\mathbf{V}}_E + m\overline{n\mathbf{V}_C''\mathbf{V}_{0,\perp}''} : \nabla\tilde{\mathbf{V}}_{0,\perp}^T - \frac{\bar{\mathbf{J}}_p}{\bar{n}} \cdot \overline{n'\nabla\phi'}$$

$$+\bar{\Pi} : \nabla\tilde{\mathbf{V}}_{0,\perp}^T - \nabla_\perp\bar{p}_i \cdot \tilde{\mathbf{V}}_p - mnV_{||}\overline{\frac{D\mathbf{b}}{Dt}} \cdot \tilde{\mathbf{V}}_{0,\perp} - E_{\mathrm{k},m,\perp}\bar{S}_{n_i} + \bar{\mathbf{S}}_m \cdot \tilde{\mathbf{V}}_{0,\perp} \quad (3.39)$$

$$\frac{\partial \bar{n}k_\perp}{\partial t} + \nabla \cdot (\bar{n}k_\perp\tilde{\mathbf{V}}_C + \frac{m\overline{n\mathbf{V}_0''^2\mathbf{V}_C''}}{2} + \overline{\Pi \cdot \mathbf{V}_{0,\perp}''} + \overline{\phi'\mathbf{J}'} + \overline{p'\mathbf{V}_E'})$$

$$= \overline{\nabla_{||}\phi' \cdot \mathbf{J}_{||}'} + \overline{p'\nabla \cdot \mathbf{V}_E'} - m\overline{n\mathbf{V}_C''\mathbf{V}_{0,\perp}''} : \nabla\tilde{\mathbf{V}}_{0,\perp}^T + \frac{\bar{\mathbf{J}}_p}{\bar{n}} \cdot \overline{n'\nabla\phi'}$$

$$+\overline{\Pi : \nabla\mathbf{V}_{0,\perp}''^T} - \overline{\nabla_\perp p_i \cdot \mathbf{V}_p''} - mnV_{||}\overline{\frac{D\mathbf{b}}{Dt} \cdot \mathbf{V}_{0,\perp}''}$$

$$-\frac{m\overline{S_{n_i}\mathbf{V}_{0,\perp}''^2}}{2} - m\tilde{\mathbf{V}}_{0,\perp} \cdot \overline{\mathbf{V}_{0,\perp}'' \cdot S_{n_i}} + \overline{\mathbf{S}_m \cdot \mathbf{V}_{0,\perp}''}. \quad (3.40)$$

Here, interchange relations 3.26 and 3.27 were filled out, the parallel current term was written as $\phi\nabla \cdot \mathbf{J}_{||} = \nabla \cdot \mathbf{J}_{||} - \nabla_{||}\phi \cdot \mathbf{J}_{||}$ and all $\nabla \cdot \phi\mathbf{J}$ terms have been collected in the LHS.

We will first consider the LHS of 3.40. The first term is the time rate of change of the turbulent kinetic energy. Then, all terms under the divergence operator represent fluxes transporting turbulent kinetic energy from one location to another. The first flux is the convection of $k_\perp$ by the mean-field velocity, the second one the convection by turbulent fluctuations and the third one a flux due

to viscous stresses. These terms also appear in regular hydrodynamic turbulence, see for example equation 2.14. Next, a flux due to electrostatic potential and current fluctuations follows and then a flux of pressure due to E×B velocity fluctuations. In section 3.2.3, it has already been argued that the divergence $\nabla \cdot (\overline{\phi' \mathbf{J}'_* + p' \mathbf{V}'_E})$ is presumably small. Furthermore, Scott [143] argues that that $\nabla \cdot (\overline{\phi' \mathbf{J}' + p' \mathbf{V}'_E}) \approx \nabla \cdot \overline{\phi' \mathbf{J}'_{||}}$, since $p\mathbf{V}_E$ cancels with $\phi \mathbf{J}_\perp$ due to Pointing cancellation. The remaining term thus constitutes a non-convective parallel transport term that does not have an equivalent in hydrodynamic turbulence. Note that all these transport terms, except for mean-field convection, constitute closure terms, and that little quantitative information is available for them a priori. Ref. [151] focuses on the radial transport of turbulence intensity and investigates when the associated terms are important. As far as the author is aware, the $\overline{\phi' \mathbf{J}'_{||}}$ flux has received very little attention in literature. However, chapter 7 will show it may play an important role in plasma edge turbulence.

Next, the coupling between mean-field and turbulent kinetic energy is considered. As in hydrodynamic turbulence, the Reynolds stress term (RS, third term in the RHS of equations 3.39 and 3.40, different sign in both) exchanges energy between the turbulent and mean-field kinetic energy. While in 3D hydrodynamic turbulence this term typically drives the turbulence, in plasma edge physics it is expected to act like a sink of $k_\perp$ and thus a source of $E_{k,m,\perp}$ because of the inverse energy cascade (see section 2.2). Hence, this term is expected to be important close to the separatrix, where strong shear flows tend to develop, which are partly fed by the turbulent kinetic energy by tearing apart small eddies. Moreover, this term is also expected to play an important role in the generation of these shear flows [58, 108, 93]. However, when the turbulence is sufficiently damped and when the flow shear is sufficiently strong, the RS term may act like a source of $k_\perp$ through the Kelvin-Helmholtz (KH) instability [79, 115, 135]. In addition, the "Favre term", fourth term on the RHS in both equations, also exchanges energy between mean-field and turbulent kinetic energy. This term appeared due to the non-commutivity of the gradient and Favre averaging operators. Thus, this term only appeared in the equation because of the rigorous average techniques that have been applied and had not been identified in literature before as far as the author is aware. The RS clearly constitute a closure term. The Favre term contains closure terms in $\bar{\mathbf{J}}_p$ (see equation 3.11), while the $\overline{n' \nabla \phi'}$ factor can be calculated from $\mathbf{\Gamma}_{n,t,E}$.

Comparing the RHS of the thermal energy equations 2.68 and 2.69 to that of the kinetic energy equations 3.39 and 3.40 it can be seen that interchange terms involving $p\nabla \cdot \mathbf{V}_E$ appear in all of them. Hence, the fluctuations of this interchange term exchange energy between the turbulence and the thermal energy. From the discussion in section 3.2.3, it follows that this energy transfer could occur in both directions (from thermal energy to turbulence and vice versa).

However, it is expected that this interchange term will provide an important source of the turbulence on the outboard side of the tokamak, especially in the SOL [143, 145, 131]. This will be confirmed for the TOKAM2D cases that will be studied in chapters 4-6. While the interchange term is a closure term, an analytical model for it was already found in equation 3.34. The $\nabla_\perp p_{\mathrm{i}} \cdot \mathbf{V}_p$ and viscous stress terms likewise exchange energy between the kinetic energy (both mean-field and turbulent) and ion thermal energy. In chapters 5 and 7, the former will be shown to be a large sink in the $k_\perp$ equation, although some reservations about this result are in place. The viscous stress will be found to be of secondary importance for the $k_\perp$ balance in the next chapters. As would be expected, it acts like a sink dissipating kinetic energy into thermal energy. Again, both terms appear as closure terms in the $k_\perp$ equation.

Then, the $\overline{\nabla_{||}\phi' \cdot \mathbf{J}'_{||}}$ term in the $k_\perp$ equation can be shown to exchange energy with the fluctuating magnetic energy. As in chapter 2, it is assumed that the only relevant fluctuations of the magnetic field are those due to $\mathbf{A}_{||}$. An equation for the energy in magnetic fluctuations can be obtained by averaging the scalar product between $\mathbf{J}'_{||}$ and the parallel electron momentum equation 2.45 divided by $en$, which yields [143]

$$\frac{1}{2}\frac{\partial}{\partial t}\overline{\mathbf{B}'^2_\perp} + \nabla \cdot (\overline{\frac{\partial \mathbf{A}'_{||}}{\partial t} \times \mathbf{B}'_\perp}) = \overline{\mathbf{J}'_{||} \cdot (\frac{\nabla_{||} p_{\mathrm{e}}}{ne})'} - \overline{\mathbf{J}'_{||} \cdot \nabla_{||}\phi'} - \overline{\mathbf{J}'_{||} \cdot (\frac{\mathbf{R}_{ei}}{ne})'}. (3.41)$$

Hence, the $\overline{\nabla_{||}\phi' \cdot \mathbf{J}'_{||}}$ term does indeed allow energy transfer between $k_\perp$ and turbulent magnetic energy $\mathbf{B}'^2_\perp/2$. Furthermore, the other two terms on the RHS of equation 3.41 exchange energy between this magnetic energy and the electron thermal energy in equation 2.69. The last term in equation 3.41 is due to electron-ion friction and is expected to dissipate magnetic energy providing a unidirectional transfer to the thermal energy. The first term on the RHS of the equation is assumed to allow energy transfer from thermal energy to magnetic energy and from there to the turbulent kinetic energy. Hence, this constitutes a second channel by which energy can be injected from the thermal energy into the turbulence (next to the interchange channel) [143, 145]. This transfer channel is related to the dynamics parallel to the magnetic field and especially the drift wave (DW) instability is expected to act on this channel. Because parallel dynamics have more freedom to evolve in the closed field line region than in the SOL, it is expected to be especially important there [131, 143, 145]. The importance of this DW coupling will partly be confirmed in chapter 7. However, since the main part of this thesis will investigate simplified 2D cases, the DW coupling will not be studied in great detail here.

Note that in the electrostatic case (which will be studied in the next chapters) in which $\mathbf{A}'_{||} = 0$, the LHS of equation 3.41 vanishes. Nonetheless, the DW coupling

remains active, be it in a slightly simplified form. The terms $-\overline{\mathbf{J}_{||} \cdot \nabla_{||} p_{\mathrm{e}}/(ne)} + \overline{\mathbf{J}_{||} \cdot \mathbf{R}_{ei}/(ne)}$ in the electron thermal energy equation 2.69 could then be replaced by $-\overline{\mathbf{J}_{||} \nabla_{||} \phi}$, such that the coupling is directly between the thermal energy and the turbulent kinetic energy (without the mediation of the magnetic energy).

Next, the $D\mathbf{b}/Dt$ terms in the perpendicular kinetic energy equations 3.39 and 3.40 exchange energy with the parallel kinetic energies in equations 3.37 and 3.38. These terms are due to changes in the magnetic field direction. Notice that the $D\mathbf{b}/Dt$ term in the $k_\perp$ equation does not only exchange energy with $k_{||}$, but also with $E_{\mathrm{k},m,||}$. Likewise, this term allows energy transfer from $E_{\mathrm{k},m,\perp}$ to $E_{\mathrm{k},m,||}$ and $k_{||}$. The importance of these energy transfer channels is unknown (they were not included in Ref. [143]). It may be expected that their magnitude and sign depend on the direction of the magnetic field in the reactor (forward field or reverse field). Note that these terms represent the only direct coupling between parallel and perpendicular kinetic energies. However, energy could also be transferred between them by the mediation of the ion and electron thermal energy. Furthermore, it is very well possible that the parallel kinetic energy dynamics implicitly impact the turbulence, for example by their impact on or competition with other energy transfer channels.

The interpretation of the other terms in the parallel kinetic energy equations 3.37 and 3.38 is rather standard and deviates little from that for the kinetic energy in hydrodynamic turbulence. The terms on the LHS under the divergence represent kinetic energy fluxes due to mean-field convection, turbulent convection and viscous transport. On the RHS, the first term is the viscous dissipation of kinetic energy which is converted into ion thermal energy. The second term contains Reynolds stresses acting on the gradients of the parallel (ion) velocity and exchanges energy between turbulent and mean-field parallel kinetic energy again. The third term is the work done by the pressure gradient on the parallel velocity. Both for mean-field and turbulent energy this exchanges energy with the ion and electron thermal energy. This energy transfer might again take place in either direction. The last three terms are due to particle and momentum sources, which are expected to be mainly due to plasma-neutral interactions.

Finally, the last three terms in the RHS of the perpendicular turbulent kinetic energy equation 3.40 are due to particle and momentum sources in the plasma. The prime particle and momentum sources in the plasma are expected to be due to the ionisation of neutral particles and collisions with neutrals. These source terms are again closure terms, about which very limited information is available a priori. While neutrals are known to influence the turbulent dynamics (see for example Refs. [140, 159, 172]), they will not be explicitly considered in the remainder of this thesis.

The energetic couplings between the different energy forms in plasma edge
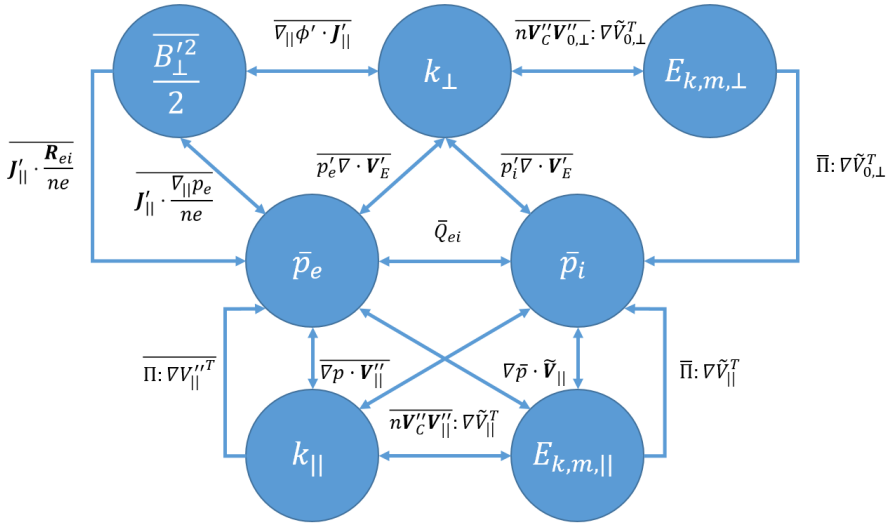
Figure 3.1: Schematic representation of the main energy transfer channels between the different energy forms in plasma edge turbulence. Adapted from Ref. [143].

turbulence are illustrated in figure 3.1. The figure aims to give an overview of some of the couplings which are expected to be important, but does not contain all the energy transfer channels. This figure is inspired by a similar figure in Ref. [143].

Now, almost all source/sink terms on the RHS of the energy equations 2.68, 2.69, 3.39, 3.40, 3.41, 3.37, 3.38 appear in two equations with opposite signs, hence conserving their total energy. The only terms to only appear once are the $\overline{\frac{\mathbf{J}_\perp}{en} \cdot \mathbf{R}_{ei}}$, $\bar{\mathbf{J}}_{||} \cdot \overline{\frac{\mathbf{R}_{ei}}{en}}$ and $\bar{\mathbf{J}}_{||} \cdot \overline{\frac{\nabla p_e}{ne}}$ terms in the electron thermal energy equation 2.69 and the $\nabla \bar{\phi} \cdot \bar{\mathbf{J}}_{||}$ term in the mean-field perpendicular kinetic energy equation 3.39. The latter three terms presumably exchange energy with the mean-field perpendicular magnetic energy (for which no equation is derived here). Moreover, if $\partial_t \bar{\mathbf{A}}_{||} = 0$ as should be the case for the mean-field magnetic field, the sum of these terms cancels exactly because of the electron momentum equation 2.43. Finally, the author expects the $\overline{\frac{\mathbf{J}_\perp}{en} \cdot \mathbf{R}_{ei}}$ in the electron thermal energy equation exchanges energy with the magnetic energy in the $\mathbf{A}_\perp$ component of the magnetic field, but this is not proven. However, this term is assumed to only be of minor importance [143, 149].

## 3.3   Analytical derivation of $\zeta_\perp$ equations

In section 3.1, the hypothesis that the perpendicular turbulent kinetic energy, which has been discussed in detail in the previous section, could be used to develop a scaling for the effective turbulent transport coefficients was put forward. In particular, $k_\perp$ could be used to provide a velocity scale for the turbulence. However, as also discussed in section 3.1, such a scaling for the turbulent transport coefficients might be further refined through the construction of a time scale, for which the (turbulent) enstrophy could be employed. This provides the motivation for this section, which derives transport equations for the enstrophy. Section 3.3.1 considers the total enstrophy, after which section 3.3.2 will consider the E×B-only enstrophy.

Theoretically the total, mean-field and turbulent enstrophies are defined as

$$\zeta_{tot} \triangleq \frac{m\boldsymbol{\omega}^2}{2}, \quad \zeta_{mean} \triangleq \frac{m\tilde{\boldsymbol{\omega}}^2}{2}, \quad \bar{n}\zeta_{turb} \triangleq \frac{m\overline{n\boldsymbol{\omega}''^2}}{2}, \tag{3.42}$$

where $\omega = \nabla \times \mathbf{V}$. In the variable density case considered here, density weighing with Favre averages is used in these definitions. In analogy to the definition of the turbulent kinetic energy in equation 3.5, the total enstrophy is defined as a fluctuating quantity, while the mean-field and turbulent enstrophies are defined as mean-field quantities. Also, the average total enstrophy per unit volume is again equal to the sum of mean-field and turbulent enstrophy per unit volume, i.e. $\overline{n\zeta_{tot}} = \bar{n}\zeta_{mean} + \bar{n}\zeta_{turb}$.

Since in plasma physics it is customary to work with a charge balance equation and since most numerical codes also use a charge balance equation, we will take that equation as a starting point rather than the vorticity equation. Both are however not exactly the same as discussed in section 2.2.3. Moreover, since plasma edge turbulence is mostly 2D, mainly the component of the vorticity in the parallel direction is of interest. For these reasons, we will consider the "pseudo-vorticity" $W$ defined in equation 2.46 as a proxy for the (parallel component of) the real vorticity. This pseudo-vorticity follows more naturally from the charge balance equation, see equation 2.53. Note that $W$ has a component due to the E×B drift and one due to the ion diamagnetic drift. Using this quantity, we define the enstrophies that will be used in this thesis as

$$\zeta_{tot} \triangleq \frac{mW^2}{2}, \quad \zeta_{mean} \triangleq \frac{m\tilde{W}^2}{2}, \quad \bar{n}\zeta_{turb} \triangleq \frac{m\overline{nW''^2}}{2}, \tag{3.43}$$

### 3.3.1   Total enstrophy equations

To analytically derive transport equations for the enstrophy, we follow a procedure similar to the work of Ref. [160], but allow independent density fluctuations, and we split the resulting equation into mean flow and turbulent contributions. An equation for the total enstrophy can readily be obtained by multiplying the vorticity-equation-like form of the charge balance equation 2.53 with the (pseudo-)vorticity $W$:

$$\frac{\partial n\zeta_{tot}}{\partial t} + \nabla \cdot n\zeta_{tot}\mathbf{V}_C = W\nabla \cdot \mathbf{J}_{||} + W\nabla \cdot \mathbf{J}_* + W\nabla \cdot \mathbf{J}_{p,\Pi}$$

$$+WS_{W,cor} - \zeta_{tot}S_{n_{\mathrm{i}}}. \qquad (3.44)$$

Note that in this derivation, the ion continuity equation 2.25 has been used, in which the convection velocity is assumed to be $\mathbf{V}_C$, as in the charge balance equation. Hence, like the total kinetic energy equation, the total enstrophy equation is mainly driven by the divergences of the plasma currents. In addition, the correction terms resulting from the vorticity equation formulation of the charge balance equation appear in this equation through the $WS_{W,cor}$ term. $S_{W,cor}$ has been defined in equation 2.54.

A mean-field enstrophy equation is then obtained by taking the product of $\tilde{W}$ and the average of the plasma vorticity equation 2.53:

$$\frac{\partial \bar{n}\zeta_{mean}}{\partial t} + \nabla \cdot (\bar{n}\zeta_{mean}\tilde{\mathbf{V}}_C + m\overline{n W''\mathbf{V}_C''} \cdot \tilde{W}) = \tilde{W}\nabla \cdot \bar{\mathbf{J}}_{||}$$

$$+\tilde{W}\nabla \cdot \bar{\mathbf{J}}_* + \tilde{W}\nabla \cdot \bar{\mathbf{J}}_{p,\Pi} + m\overline{n W''\mathbf{V}_C''} \cdot \nabla \tilde{W} + \tilde{W}\bar{S}_{W,cor} - \zeta_{mean}\bar{S}_{n_{\mathrm{i}}}. (3.45)$$

This derivation again involved the ion continuity equation. The difference between the average of equation 3.44 and equation 3.45 then allows to write the turbulent enstrophy equation as

$$\frac{\partial \bar{n}\zeta_{turb}}{\partial t} + \nabla \cdot (\bar{n}\zeta_{turb}\tilde{\mathbf{V}}_C + \frac{m\overline{n W''^2\mathbf{V}_C''}}{2})$$

$$= \overline{W''\nabla \cdot \mathbf{J}_{||}} + \overline{W''\nabla \cdot \mathbf{J}_*} + \overline{W''\nabla \cdot \mathbf{J}_{p,\Pi}} - m\overline{n W''\mathbf{V}_C''} \cdot \nabla \tilde{W}$$

$$+\overline{W''S_{W,cor}} - \frac{\overline{W''^2 S_{n_{\mathrm{i}}}}}{2} - \tilde{W}\overline{W''S_{n_{\mathrm{i}}}}. \qquad (3.46)$$

The structure of the mean-field and turbulent enstrophy equations 3.45 and 3.46 can be seen to be rather similar to that of the mean-field and turbulent

kinetic energy equations 3.14 and 3.15. Here as well, the main source terms in the RHS are due to current divergences and similar mean-field and turbulent convection terms appear in the LHS. Furthermore, the fourth term on the RHS of both equations seems to play a role similar to the RS term for the kinetic energy, allowing enstrophy transfer between mean-field and turbulence. Because a direct cascade of enstrophy is expected in 2D-like turbulence [4, 36, 71, 169], it is anticipated that this transfer will be from mean-field enstrophy to turbulent enstrophy.

Thus, both the $k_\perp$ equation and the $\zeta_{turb}$ equations have their origin in the charge balance equation and the form of both equations shows remarkable similarities. Nonetheless we expect both equations to behave differently and expect $k_\perp$ and $\zeta_{turb}$ to provide complementary information for the closure models that will be developed in the next chapters. Since the cascade directions are opposite for both quantities, it is anticipated that $\zeta_{turb}$ is concentrated on smaller length scales than $k_\perp$ for example. This can also be seen from a spectral decomposition of both quantities. This shows that $\zeta_{tot}(K_\perp) = K_\perp^2 E_{k,\perp}(K_\perp)$, with $E_{k,\perp}(K_\perp)$ and $\zeta_{tot}(K_\perp)$ the intensity of the spectrum of the kinetic energy and the enstrophy at a perpendicular wave number $K_\perp$. Hence, the enstrophy spectrum is larger at high $K_\perp$, at smaller spatial scales. In addition, the dimension of $k_\perp$ and $\zeta_\perp$ is different. Furthermore, it could be argued that in averaging the charge balance equation as is done in the mean-field approach followed here, an infinite amount of information on the instantaneous fluctuations is lost. The $k_\perp$ and $\zeta_{turb}$ equations represent but two different moments of the original instantaneous charge balance equation and should thus not be expected to be equivalent.

Note that derivations for the real enstrophies (based on the real vorticity $\boldsymbol{\omega}$) defined in equation 3.42 could be derived from vorticity equation 2.24 by a procedure very similar to that outlined here for the pseudo-enstrophies and pseudo-vorticity $W$ here.

### 3.3.2 E×B-only enstrophy equations

The main closure terms we want to model in this thesis are the turbulent E×B particle ($\boldsymbol{\Gamma}_{n,t,E}$) and heat ($\boldsymbol{\Gamma}_{p_i,t,E}$ and $\boldsymbol{\Gamma}_{p_e,t,E}$) fluxes. In line with the hypothesis formulated in section 3.1, these fluxes may be more closely related to turbulence quantifiers which are based on the E×B drift only. To this end, section 3.2.2 derived equations for the E×B-only kinetic energy $k_E$ already. This section will do the same for the enstrophy by deriving equations for the E×B-only enstrophy.

To arrive at equations for the E×B-only enstrophy, we first split the total vorticity defined in equation 2.46 into its contribution by the E×B drift and its contribution by the ion diamagnetic drift as

$$W = W_E + W_* \triangleq \nabla \cdot \frac{\nabla_\perp \phi}{B^2} + \nabla \cdot \frac{\nabla_\perp p_{\mathrm{i}}}{enB^2} \triangleq \nabla \cdot \frac{\mathbf{U}_E}{B} + \nabla \cdot \frac{\mathbf{U}_{*,i}}{B}. \quad (3.47)$$

The E×B-only enstrophies are then defined based on the E×B-only vorticity as

$$\zeta_{tot,E} \triangleq \frac{mW_E^2}{2}, \quad \zeta_{mean,E} \triangleq \frac{m\tilde{W}_E^2}{2}, \quad \bar{n}\zeta_{turb,E} \triangleq \overline{\frac{mnW_E''^2}{2}}. \quad (3.48)$$

Note that the sum of this E×B-only enstrophies and a diamagnetic enstrophy which could be defined as $mW_*^2/2$ is not equal to the total enstrophy, since $W_E W_*$ terms would then be ignored.

In order to derive transport equations for these E×B-only enstrophies, the charge balance equation is rewritten to explicitly bring out $W_E$. To this end, the procedure followed in section 2.2.3 in equations 2.49-2.54 to obtain a vorticity-like form of the charge balance equation is repeated for the E×B-part of the polarisation current $\mathbf{J}_{p,E}$ (see definition 3.17). This yields

$$m\frac{\partial nW_E}{\partial t} + \nabla \cdot mnW_E\mathbf{V}_C$$

$$= \nabla \cdot \mathbf{J}_{||} + \nabla \cdot \mathbf{J}_* + \nabla \cdot \mathbf{J}_{p,\Pi} + \nabla \cdot \mathbf{J}_{p,*} + \nabla \cdot \mathbf{J}_{p,||} + S_{W_E,cor} \quad (3.49)$$

$$S_{W_E,cor} \triangleq e\nabla n \cdot \mathbf{V}_{p,E} - mn\nabla\mathbf{V}_C : \nabla\frac{\mathbf{U}_E}{B} - mnW_E\frac{D\ln B}{Dt}$$

$$- \frac{mn\mathbf{U}_E}{B} \cdot \nabla(\frac{D\ln B}{Dt} + \frac{S_{n_{\mathrm{i}}}}{n}) - mn\nabla \cdot (\frac{D\mathbf{b}}{Dt} \times \frac{\mathbf{V}_E}{B}). \quad (3.50)$$

Equations for the total, mean-flow and turbulent E×B-only enstrophy can be obtained by multiplying equation 3.49 with $W_E$ following exactly the same procedure as that followed in section 3.3.1 for the total enstrophies. This leads to following equations:

$$\frac{\partial n\zeta_{tot,E}}{\partial t} + \nabla \cdot n\zeta_{tot,E}\mathbf{V}_C = W_E\nabla \cdot \mathbf{J}_{||} + W_E\nabla \cdot \mathbf{J}_* + W_E\nabla \cdot \mathbf{J}_{p,\Pi}$$

$$+ W_E\nabla \cdot \mathbf{J}_{p,*} + W_E\nabla \cdot \mathbf{J}_{p,||} + W_E S_{W_E,cor} - \zeta_{tot,E}S_{n_{\mathrm{i}}}, \quad (3.51)$$

$$\frac{\partial \bar{n}\zeta_{mean,E}}{\partial t} + \nabla \cdot (\bar{n}\zeta_{mean,E}\tilde{\mathbf{V}}_C + m\overline{n W_E'' \mathbf{V}_C''} \cdot \tilde{W}_E) = \tilde{W}_E \nabla \cdot \bar{\mathbf{J}}_{||}$$

$$+\tilde{W}_E \nabla \cdot \bar{\mathbf{J}}_* + \tilde{W}_E \nabla \cdot \bar{\mathbf{J}}_{p,\Pi} + \tilde{W}_E \nabla \cdot \bar{\mathbf{J}}_{p,*} + \tilde{W}_E \nabla \cdot \bar{\mathbf{J}}_{p,||}$$

$$+\overline{n W_E'' \mathbf{V}_C''} \cdot \nabla \tilde{W}_E + \tilde{W}_E \bar{S}_{W_E,cor} - \zeta_{mean,E}\bar{S}_{n_i}, \quad (3.52)$$

$$\frac{\partial \bar{n}\zeta_{turb,E}}{\partial t} + \nabla \cdot (\bar{n}\zeta_{turb,E}\tilde{\mathbf{V}}_C + \frac{m\overline{n W_E''^2 \mathbf{V}_C''}}{2}) = \overline{W_E'' \nabla \cdot \mathbf{J}_{||}}$$

$$+\overline{W_E'' \nabla \cdot \mathbf{J}_*} + \overline{W_E'' \nabla \cdot \mathbf{J}_{p,\Pi}} + \overline{W_E'' \nabla \cdot \mathbf{J}_{p,*}} + \overline{W_E'' \nabla \cdot \mathbf{J}_{p,||}}$$

$$-\overline{n W_E'' \mathbf{V}_C''} \cdot \nabla \tilde{W}_E + \overline{W_E'' S_{W_E,cor}} - \frac{\overline{W_E''^2 S_{n_i}}}{2} - \tilde{W}_E \overline{W_E'' S_{n_i}}. \quad (3.53)$$

These E×B-only enstrophy equations are very similar to the total enstrophy
equations 3.44-3.46. The only difference is that the total quantities (sum of
E×B-only and ion diamagnetic contributions) in all terms have been replaced
by E×B-only quantities where appropriate. In addition, terms proportional
to $W_E \nabla \cdot \mathbf{J}_{p,*}$ now also appear on the RHS. Contrary to the results for the
E×B-only kinetic energy in section 3.2.2, the form of the current divergences in
the RHS of these equations does change, as they are multiplied with the total
vorticity $W$ for the total enstrophy and only with the E×B-only vorticity $W_E$
for the E×B-only enstrophy.

If desired, the current divergences could be rewritten as follows

$$W_E \nabla \cdot \mathbf{J}_{||} + W_E \nabla \cdot \mathbf{J}_* + W_E \nabla \cdot \mathbf{J}_{p,\Pi} + W_E \nabla \cdot \mathbf{J}_{p,*} + W_E \nabla \cdot \mathbf{J}_{p,||}$$

$$= W(\nabla \cdot \mathbf{J}_{||} + \nabla \cdot \mathbf{J}_* + \nabla \cdot \mathbf{J}_{p,\Pi} + \nabla \cdot \mathbf{J}_{p,*} + \nabla \cdot \mathbf{J}_{p,||})$$

$$-W_*(\nabla \cdot \mathbf{J}_{||} + \nabla \cdot \mathbf{J}_* + \nabla \cdot \mathbf{J}_{p,\Pi} + \nabla \cdot \mathbf{J}_{p,*} + \nabla \cdot \mathbf{J}_{p,||})$$

$$= W(\nabla \cdot \mathbf{J}_{||} + \nabla \cdot \mathbf{J}_* + \nabla \cdot \mathbf{J}_{p,\Pi} + \nabla \cdot \mathbf{J}_{p,*} + \nabla \cdot \mathbf{J}_{p,||}) + W_* \nabla \cdot \mathbf{J}_{p,E}. \quad (3.54)$$

In the last line, the charge balance equation has been used. Hence, the equations
could be rewritten with the total vorticity multiplied with the current divergences
such that the terms become identical with those in the total enstrophy equations.
However, a correction term of the form $W_* \nabla \cdot \mathbf{J}_{p,E}$ needs to be added then (in
addition to the $\nabla \cdot \mathbf{J}_{p,*}$ term that already provided a first correction).

# 3.4 Parameter estimation and model validation framework

Mean-field models for the turbulent transport in the plasma edge are by definition a simplification of the underlying detailed fine-scale turbulent processes. As such, these models require calibration with respect to reference data in a first step. This is the case for the standard approach of imposing ad-hoc transport coefficient profiles to match particular experiments discussed in section 2.3.2, for the recent closure models proposed in literature that have been discussed in section 2.3.3 and for the closure models that will be discussed in this thesis following the ansatz presented in section 3.1. This comes down to a problem of parameter estimation, where the parameters $\theta$ of a model $f(I, \theta)$, with the model $I$ inputs, need to be chosen such that the model approximates the reference data $O$ as closely as possible. In addition different competitor models may exist of which the best one needs to be selected. To the extent of the model capabilities, the calibrated (best) model can then be used to extrapolate the reference data and to provide predictions in a next step.

This section[3] discusses two approaches for parameter estimation and model validation that will be used in this thesis. First the standard approach of least squares regression will briefly be discussed in section 3.4.1. Then, section 3.4.2 discusses the theory of Bayesian inference which provides an alternative framework for parameter estimation and model validation with a solid statistical basis. Section 3.4.3 then presents the computational methods that will be used to apply Bayesian inference in this thesis.

## 3.4.1 Least squares methodology for regression analysis

The non-linear least squares (LS) regression techniques presented here are based on Ref. [43]. It is assumed that a set of reference input $I$ and output $O$ data measurements are available, of which individual elements are denoted $I_i$ and $O_i$. In this thesis, these data points will come from the averaged data of detailed turbulence code simulations. The parameters $\theta$ in the model $f(I, \theta)$

---

[3]This section uses material that has been published in "Coosemans, R., Dekeyser, W., Baelmans, M. (2021). Turbulent kinetic energy in 2D isothermal interchange-dominated scrape-off layer E×B drift turbulence: Governing equation and relation to particle transport. *Physics of Plasmas*, 28:012302" [46], in "Coosemans, R., Dekeyser, W., Baelmans, M. (2021). Bayesian analysis of turbulent transport coefficients in 2D interchange dominated E×B turbulence involving flow shear. *Journal of Physics: Conference Series*, 1785:012001" [45], and in "De Wolf, R., Coosemans, R., Dekeyser, W., Baelmans, M. (2021). Bayesian approach to parameter estimation and model validation for nuclear fusion reactor mean-field edge turbulence modelling. *Nuclear Fusion*, 61:046048" [50].

approximating $O$ are tuned by minimising an objective function over these parameters of the model, resulting in the optimisation problem

$$\underset{\theta}{\text{minimize}} \quad \text{obj}(\theta) \tag{3.55}$$

$$\text{obj} = \sum_{i=1}^{N_d} \left( \frac{f(I_i, \theta)}{O_i} - 1 \right)^2 \tag{3.56}$$

In these formulae, $N_d$ is the number of available data points. The objective function 3.56 aims to minimize the relative error between model and data.

Within this approach, the coefficient of determination, or $R^2$ value, can be used as a figure of merit for the models that will be tested. This value is defined as

$$R^2 \triangleq 1 - \frac{\sum_{i=1}^{N_d} (f(I_i, \theta) - O_i)^2}{\sum_{i=1}^{N_d} (O_i - O_{mean})^2}, \tag{3.57}$$

where $O_{mean} \triangleq \sum_{i=1}^{N_d} O_i / N_d$. Thus, it quantifies to what extent the variance of the data can be explained by the model. Note that the $R^2$ value depends on the value of the parameters $\theta$ that is used.

While the LS method is rather straightforward and widely used, it suffers from several drawbacks. Firstly, the result does not provide any information about the uncertainty of the parameters, it merely finds a best fit for the model. Secondly, this approach is oblivious to possible correlations between the parameters, which might be of interest to the researcher. The largest drawback of the LS approach, however, is the danger of overfitting the data. It is generally known that adding more model parameters reduces the error of fit for a certain reference data set, even when said parameters are completely irrelevant. Therefore, it may be difficult to know whether a parameter is actually relevant for the model or merely improves the fit by stochastic coincidence. According to Occam's principle [5], models with fewer parameters should be preferred to models with more parameters, by penalizing the latter for every additional parameter. A possible way to overcome this issue would be to use a cross validation approach. In such an approach only part of the data is used to estimate the parameters, and the remainder to validate the model (e.g. the $R^2$ value). This process is repeated multiple times, always leaving out different subsets of the data for the parameter estimation [6, 69]. The Bayesian inference methodology discussed in the next section is capable of addressing all the issues outlined above.

## 3.4.2   Theory of Bayesian inference

The objective of a Bayesian analysis is to infer about the joint probability distribution of the model parameters, which provides much more information than a single parameter value resulting from a classical least squares regression. In addition, the Bayesian evidence provides a statistically rigorous methodology to rank different competing models. In this section, we aim to give a concise overview of the main features of Bayesian inference theory. We refer to De Wolf *et al.* [50] and the reference therein for a more detailed discussion of this topic.

The basic identity underlying Bayesian techniques is Bayes' rule:

$$\mathcal{P}(\theta|\mathcal{D}, \mathcal{M}) = \frac{\pi(\theta|\mathcal{M})\mathcal{L}(\mathcal{D}|\theta, \mathcal{M})}{\mathcal{L}(\mathcal{D}|\mathcal{M})}, \tag{3.58}$$

where the posterior $\mathcal{P}(\theta|\mathcal{D}, \mathcal{M})$ is the probability of the parameters $\theta$ after observing the data $\mathcal{D}$ for a certain model $\mathcal{M}$, the prior $\pi(\theta|\mathcal{M})$ is the probability of the parameters before observing the data for the model, the likelihood $\mathcal{L}(\mathcal{D}|\theta, \mathcal{M})$ indicates how likely it is to observe the data given a specific value of the parameters and the model, and the Bayesian evidence $\mathcal{L}(\mathcal{D}|\mathcal{M})$ is the marginal likelihood of observing the data given the model no matter the parameters [49, 50, 100, 121, 161]. The main objective of Bayesian analysis for parameter estimation is to infer the posterior distribution of the parameters $\mathcal{P}(\theta|\mathcal{D}, \mathcal{M})$ from the data.  Secondly, the model evidence $\mathcal{L}(\mathcal{D}|\mathcal{M})$ can be evaluated for model comparison, as it will be shown to be proportional to the probability of the model given the data. In order to achieve this, a likelihood function and a prior need to be constructed.

**Likelihood function and prior**

The likelihood function is basically a model for the probability distribution describing the error between the data and the model. If we consider a (physical) model $f(I, \theta)$ (which is a function of the input data $I$) that approximates the (output) data $\mathcal{D} : O$, the error is defined as

$$\epsilon \triangleq O - f(I, \theta) \tag{3.59}$$

Describing the model error $\epsilon$ is a delicate matter.  This error is not only composed of the statistical error that remains on the averaged output data $O$ but also includes the error on the model $f(I, \theta)$. The latter is composed of an error because the model form $f(I, \theta)$ is not perfect (model inadequacy), an

error caused by propagating the statistical error on the averaged input data $I$ through the model and a numerical error in solving the model [137]. Since very little is known about most of these error contributions in this work, we chose to aggregate them all. Due to this lack of knowledge, the true probability distribution of this aggregated error is also unknown. To acknowledge our ignorance, we choose to use an error distribution which is as uninformative as possible. Through the maximum entropy principle, it can be shown that a Gaussian distribution is the least informative distribution characterised by only a mean and a standard deviation [24, 50, 60, 84, 96, 121]. Based on this argumentation, we assume the error at every data point has a Gaussian distribution. Furthermore, the model error is assumed to have zero mean, such that $\epsilon_i \sim N(0, \sigma_i)$ for every data point $i$. The likelihood function is then this distribution expressed as a function of the parameters, yielding for a single data point:

$$\mathcal{L}(\mathcal{D}_i|\theta, \mathcal{M}) = \frac{1}{\sqrt{2\pi}\sigma_i} \exp\left(-\frac{(O_i - f(I_i, \theta))^2}{2\sigma_i^2}\right). \tag{3.60}$$

For a data set consisting of multiple points and allowing for possible correlations between the data, we get

$$\mathcal{L}(\mathcal{D}|\theta, \mathcal{M}) = \frac{1}{((2\pi)^{n/2} \det \Sigma^{1/2}} \exp(-\frac{1}{2}\epsilon^T \Sigma^{-1}\epsilon), \tag{3.61}$$

where it is understood that $\epsilon$ is now a vector grouping the errors $\epsilon_i$ of all individual data points and $\Sigma$ is the covariance matrix of the error [49, 50, 121]. Note that while the likelihood function is a proper probability density as a function of the model error $\epsilon$, it is not a probability density when viewed as a function of the parameters $\theta$. From equations 3.60 and 3.61, it is clear that in order to evaluate the likelihood function for a single value of the parameters $\theta$, a forward model evaluation of $f(I, \theta)$ is required for all data points.

In equations 3.61, the error covariance matrix still needs to be further specified. If the (spatial) data points are not statistically independent, it is important to account for this (spatial) correlation [40, 98]. This correlation can be taken into account by assigning nonzero values to the off-diagonal elements of the covariance matrix, in accordance with a chosen model for the correlation. In this work, we will assume the correlation to decay exponentially with the distance between the data points [62, 121, 168], yielding the following expression for the off-diagonal elements:

$$\Sigma_{ij} = \sigma_{ii}^2 \exp\left(-\frac{\Delta_{ij}}{\ell}\right), \tag{3.62}$$

where $\Delta_{ij}$ is the distance between two grid points at which data is available and $\ell$ is the characteristic correlation length of the exponential model. Note that $\ell$ might be different for different directions in case the data is anisotropic. Similarly, if the data would be time dependent, a correlation time would need to be added. Both would require generalisation of equation 3.62. For the diagonal elements of the error correlation matrix, two alternative assumptions will be used in this work. Either the standard deviation of the error will be assumed to be uniform over all data points

$$\sigma_{ii} = \sigma_{abs}, \tag{3.63}$$

or it will be assumed to scale with the magnitude of the considered data point

$$\sigma_{ii} = \sigma_{rel}O_i. \tag{3.64}$$

Through the definition of the model for the error 3.62 with 3.63 or 3.64, the additional parameters $\ell$ and $\sigma_{abs/rel}$ enter the likelihood function. If these are not known a priori, as will be the case in this thesis, they should be estimated during the Bayesian inference procedure just as the parameters of the physical model. These model parameters of the error model are called nuisance parameters. Note that the parameters $\theta$ include both the parameters used in the physical model $f(I, \theta)$, and the nuisance parameters.

At this point it is worth remarking that in a Bayesian analysis, the results (both the posterior and the evidence) do not only depend on the physical model $f(I, \theta)$ under consideration, but also on the statistical model that is used for the model error in the likelihood function, i.e. the model $\mathcal{M}$ includes both the physical model and the statistical model [168]. While characterising the (statistical) model error may provide relevant insights, we will mostly be interested in the physical model. However, as both cannot be decoupled in a Bayesian analysis we will try to select statistical models that properly represent the error, such that the results for the physical model are as accurate as possible and are not disturbed too much by deficiencies of the statistical model.

Next, we turn our attention to the model prior $\pi(\theta|\mathcal{M})$, which describes what is known about the parameters prior to observing the data. Note that not only the parameters of the physical models require a prior, but also the nuisance parameters. As the models developed in this thesis are novel such that no prior information is available, it is opted to use non-informative, wide prior distributions in order not to exclude any values of the parameters from the start. A number of methods have been proposed to construct so-called objective priors [22, 156, 18, 19], but it should be mentioned that a prior can never be truly non-informative and will always contain at least some subjectivity [28, 161].

As is evident from equation 3.58, the product of the likelihood and the prior $\mathcal{L}(\mathcal{D}|\theta, \mathcal{M})\pi(\theta|\mathcal{M})$ determines the shape of the posterior distribution $\mathcal{P}(\theta|\mathcal{D}, \mathcal{M})$, which is the end goal for the parameter estimation since the evidence $\mathcal{L}(\mathcal{D}|\mathcal{M})$ is a scalar which can be considered to be a normalisation factor in equation 3.58. This posterior provides a comprehensive description of the information the data provides on the parameters: the regions in parameter space that are most likely, how large the spread is on the parameters and the correlation between the different parameters of the model $\mathcal{M}$.

**Model evidence**

The evidence $\mathcal{L}(\mathcal{D}|\mathcal{M})$ on the other hand is of particular interest to compare different competing models $\mathcal{M}$ attempting to explain the data. Defined as

$$\mathcal{L}(\mathcal{D}|\mathcal{M}) \triangleq \int \pi(\theta|\mathcal{M})\mathcal{L}(\mathcal{D}|\theta, \mathcal{M})d\theta, \tag{3.65}$$

the evidence is independent of the value of the parameters. Note that the evidence is not a probability, since the likelihood is not a probability distribution in terms of the parameters. However, the Bayesian evidence is directly related to the probability of a model given the data. Applying the Bayes rule 3.58 again, but now reworking the conditionality on the model instead, it is found that

$$\mathcal{P}(\mathcal{M}|\mathcal{D}) = \frac{\mathcal{P}(\mathcal{M})\mathcal{L}(\mathcal{D}|\mathcal{M})}{\mathcal{L}(\mathcal{D})}, \tag{3.66}$$

where $\mathcal{P}(\mathcal{M})$ is the prior probability for the model before observing the data (independent of the parameters) and $\mathcal{L}(\mathcal{D})$ is a normalisation factor that purely depends on the data. Hence, if there is no prior information $\mathcal{P}(\mathcal{M})$ about which model is more probable, the ratio of the evidence of two models $\mathcal{M}_1$ and $\mathcal{M}_2$ is equal to the relative probability of both models given the data [100, 161]:

$$B_{12} \triangleq \frac{\mathcal{L}(\mathcal{D}|\mathcal{M}_1)}{\mathcal{L}(\mathcal{D}|\mathcal{M}_2)} = \frac{\mathcal{P}(\mathcal{M}_1|\mathcal{D})}{\mathcal{P}(\mathcal{M}_2|\mathcal{D})}. \tag{3.67}$$

This evidence ratio of $B_{12}$ is also called the Bayes factor. Thus, while the evidence for a single model does not have a clear meaning (as it is not a probability), the ratio of the evidence between competing models directly indicates which model is to be preferred. Note that this only holds for models trying to explain the same diagnostic output data, the evidence cannot be used

Table 3.1: Interpretation of the Bayes factor. Source: adapted from [96].

| $\log B_{12}$ | $B_{12}$ | Strength of evidence for hypothesis 1 |
|---|---|---|
| $< 0$ | $< 1$ | Negative (supports hypothesis 2) |
| $0 - 1.2$ | $1 - 3.2$ | Barely worth mentioning |
| $1.2 - 2.3$ | $3.2 - 10$ | Substantial |
| $2.3 - 3.5$ | $10 - 31.6$ | Strong |
| $3.5 - 4.6$ | $31.6 - 100$ | Very strong |
| $> 4.6$ | $> 100$ | Decisive |

to compare models that explain different (output) data sets. The reference input data $I$ that is implicitly included in $\mathcal{M}$ may be different. Guidelines for interpreting the value of $B_{12}$ have been included in table 3.1.

It needs to be kept in mind that just like the model posterior, also the model evidence does not only depend on the physical model $f(I, \theta)$, but also on the statistical model that is used for the error (included in $\mathcal{M}$) and on the prior. As such, the Bayesian evidence compares the combination of physical model and statistical model. As we are mostly interested in the physical model (for the average turbulent transport) in this thesis, we will try to select statistical models that properly represent the error, such that the results for the physical model are as accurate as possible. The other way around, different statistical models can be compared based on the evidence when the physical model is kept the same. This way, the most suitable statistical model can be selected (Gaussian distribution or not, scaled error or not, correlation length or not,...). While in theory different error models may be better suited for different physical models, we choose to use the same error model when comparing different physical models with each other in this thesis.

In order to highlight the main strength of the evidence in context of model comparison, recall that the LS approach is not a good method to compare models of different complexity due to the danger of overfitting. In contrast, the evidence provides a theoretically founded measure to compare such models, because it inherently penalizes more complex models. This is generally referred to as Occam's Razor [152] and is by no means limited to a Bayesian context. Next to the concept of model sparsity, the Bayesian evidence inherently includes the concept of predictive capability as well. It can be shown that under certain conditions, the result of a rigorous cross validation approach reduces to the Bayesian evidence [69]. In effect, there is no point in splitting the data into a data set for model calibration and another for testing the calibrated model.

To understand how the Bayesian evidence automatically applies Occam's Razor,

the reasoning of Ref. [100] is followed quite closely. Consider a model which features a single parameter $\theta$, given a uniform prior distribution in the range $\Delta\theta = \theta_{max} - \theta_{min}$. The effective width $\delta\theta \leq \Delta\theta$ of the likelihood function is then defined by

$$\delta\theta = \frac{1}{\mathcal{L}_{max}} \int_{\theta_{min}}^{\theta_{max}} \mathcal{L}(\mathcal{D}|\theta, \mathcal{M}) d\theta, \qquad (3.68)$$

where $\mathcal{L}_{max}$ is the dominant mode of the likelihood function, for which the goodness-of-fit of the model is maximized. The evidence can then be written as

$$\mathcal{L}(\mathcal{D}|\mathcal{M}) = \frac{1}{\Delta\theta} \int_{\theta_{min}}^{\theta_{max}} \mathcal{L}(\mathcal{D}|\theta, \mathcal{M}) d\theta, \qquad (3.69)$$

since the prior is a uniform distribution of height $1/\Delta\theta$. Upon substitution of equation 3.68 into this last equation, we obtain an intuitive expression for the evidence as

$$\mathcal{L}(\mathcal{D}|\mathcal{M}) = \mathcal{L}_{max} \frac{\delta\theta}{\Delta\theta}, \qquad (3.70)$$

where $\mathcal{L}_{max}$ is a goodness-of-fit indicator and $\delta\theta/\Delta\theta$ can be viewed as an Occam factor.

The above derivation can readily be extended to multidimensional evidence calculations. Physically, equation 3.70 shows that the evidence is maximized when the effective width (or volume in higher dimensions) of the likelihood function occupies the prior range to its maximum. When an additional parameter is introduced to a model, the evidence will only increase if the goodness-of-fit offsets the decreased occupied relative volume of the prior parameter space.[4]

Clearly, the evidence strongly depends on how the prior distributions are constructed. From equation 3.69 it can be seen that the evidence can be made arbitrarily small by increasing the range of the prior distributions. Moreover, it can be seen that improper priors are to be avoided due to the evidence becoming meaningless in an infinitely large prior parameter space. To deal with this issue, care should be taken to construct correct (i.e. proper) prior distributions. If this is not possible, e.g. when a non-informative Jeffreys prior is improper, upper boundaries of the evidence could be computed as comparative measure [148, 161].

To highlight the main features of Bayesian theory, we briefly review the main difference with a classical least square regression approach. If the model error $\epsilon$ is assumed to have a Gaussian distribution as in equation 3.60 and when the

---

[4]Note that more complex models with more parameters need not necessarily have a smaller volume ratio between posterior and prior. Nonetheless, this is the expected trend, since every parameter does lead to an additional dimension in which the data (have the potential to) constrain the values allowed by the prior.

covariance matrix only has diagonal elements that are uniform ($\boldsymbol{\Sigma} = \Sigma_{ii} = \sigma_{abs}^2$), it can be seen that maximising this likelihood is identical to a classical LS regression. Alternatively, when scaled errors are used such that $\boldsymbol{\Sigma} = \Sigma_{ii} = (\sigma_{rel}O_i)^2$, maximising the likelihood reduces to the objective in equation 3.56 presented in the regression analysis in section 3.4.1. So, a first generalisation is that the likelihood function also allows more complex distributions for the error if desired. In a second step, the likelihood function is multiplied with the prior distribution such that any available prior information could be self-consistently incorporated. Maximising this product yields the maximum a posteriori (MAP) estimate for the parameters. In addition, the distribution of the parameters formed by the product $\mathcal{L}(\mathcal{D}|\theta,\mathcal{M})\pi(\theta|\mathcal{M})$ is proportional to the probability density function for the parameters, hence including much more information than the MAP point-estimate itself. Comparing different models based on the value of $\mathcal{L}(\mathcal{D}|\theta,\mathcal{M})\pi(\theta|\mathcal{M})$ at MAP would still only compare models for a single parameter setting, as the LS comparison does. Instead, the Bayesian evidence $\mathcal{L}(\mathcal{D}|\mathcal{M})$ integrates this product of likelihood and prior over the parameter space of the models in order to effectively compare the models for any setting of the parameters allowed by the prior. This "prior-weighed" integration of the likelihood function over parameter space adds the Occam factor - penalizing more complex models - to the basic (LS-like) goodness of fit statistic included in the likelihood function [161, 100].

### 3.4.3 Computational methods for Bayesian inference

Computational techniques are required in order to infer about the complex posterior distribution $\mathcal{P}(\theta|\mathcal{D},\mathcal{M})$ and to determine the Bayesian evidence $\mathcal{L}(\mathcal{D}|\mathcal{M})$. In this work, we choose to employ Markov Chain Monte Carlo MCMC techniques to evaluate Bayes' theorem, which is widely used in the research community. In this section, we will only briefly treat the basics of this method, while a more complete description of it can be found in Refs. [49, 50] and the references therein. The framework developed in these references has been used for all Bayesian inferences reported in this thesis.

The idea of MCMC is to approximate a target distribution by generating a chain of samples which converges to a statistical steady state in which the samples are distributed as the target distribution. A typical step of the classical Metropolis-Hastings algorithm [112] for sampling from a generic target distribution $h(\theta)$ is schematically represented below:

- Given $\theta_i$, generate $\theta'$ according to the proposal distribution $q(\theta'|\theta_i)$

- Calculate the acceptance probability $\alpha = \min\left(\frac{h(\theta')q(\theta'|\theta_i)}{h(\theta_i)q(\theta_i|\theta')}, 1\right)$

- generate a sample from the uniform distribution $u \sim U(0,1)$
  if $\alpha > u$ accept sample, $\theta_{i+1} = \theta'$
  if $\alpha < u$ reject sample, $\theta_{i+1} = \theta_i$

In this algorithm, $q(\theta'|\theta_i)$ is the proposal distribution describing the probability of where the next proposal parameter will be located given the previous accepted sample. Thus, in each iteration, a random step is taken, which is more likely to go to a point of higher probability than to one of lower probability. This brings the great advantage that the Markov chain will automatically move to high density regions of the target distribution. Hence, the regions of interest and the locations were samples need to be taken do not need to be specified a priori.

The choice of the proposal distribution $q(\theta'|\theta_i)$ distribution is crucial to the efficiency of the algorithm. If this distribution is very narrow, samples will easily be accepted as they are likely to be close to the previous accepted sample, however, it will take a long time for the chain to move to other regions and explore the whole target distribution. If the proposal distribution is very wide on the other hand, the accepted samples will quickly cover the entire target distribution, but a high number proposal samples will be rejected before one is accepted since they are likely to be far off in low probability regions.

A typical choice for the proposal density is a multivariate Gaussian probability distribution centered around the last accepted sample, i.e. $q(\theta'|\theta_i) \sim N(\theta_i, \Sigma_q)$. In order to increase the efficiency of the algorithm, the Adaptive Metropolis-Hastings (AMH) algorithm [87, 49, 50] which adjusts the proposal distribution during runtime will be used in this thesis. The previously accepted samples are used to estimate the covariance matrix of the target distribution $\Sigma_T$, which is then optimally scaled and used as the covariance matrix of the Gaussian proposal function, i.e. $\Sigma_q \sim 2.4\Sigma_T/\sqrt{d}$ where $d$ is the dimension of $\theta$ [49, 50, 77, 87].

This algorithm is used for Bayesian inference by sampling for $h(\theta) \sim \pi(\theta|\mathcal{M})\mathcal{L}(\mathcal{D}|\theta, \mathcal{M})$. Remark that the second step of this algorithm requires a forward evaluation of the model $f(I, \theta)$ in order to calculate the likelihood, making it the most expensive step of the algorithm in most cases. An optimal choice for the initial conditions of the AMH algorithm (the initial sample and covariance matrix of the proposal distribution) can significantly reduce the number of required model evaluations before convergence. This can be achieved by starting from the results from a cheaper simplified analysis such as the Laplace approximation [50, 121, 161].

While MCMC offers a very complete framework for Bayesian inference, the evidence is by default not an output of the analysis and has to be estimated separately. Several methods of varying complexity and accuracy can be employed for this [91, 70]. In this thesis, Chib's method [41, 49] is used. This method

uses the Bayes rule 3.58 to calculate the evidence as the ratio

$$\mathcal{L}(\mathcal{D}|\mathcal{M}) = \frac{\mathcal{L}(\mathcal{D}|\theta^*, \mathcal{M})\pi(\theta^*|\mathcal{M})}{\pi(\theta^*|\mathcal{D}, \mathcal{M})}. \tag{3.71}$$

at a single parameter value $\theta^*$. In theory, any choice of $\theta^*$ is admitted, but in order for the estimate to be accurate the method requires a point in the high density region of the posterior. The numerator of expression 3.71 can readily be calculated since the value of the likelihood and the prior can be calculated for any parameter value. Obtaining the denominator is more difficult though. Chib et. al [41] prove that it can be calculated as

$$\pi(\theta^*|\mathcal{D}, \mathcal{M}) = \frac{M^{-1}\sum_{g=1}^{M} \alpha(\theta^*|\theta^{(g)})q(\theta^*|\theta^{(g)})}{J^{-1}\sum_{j=1}^{J} \alpha(\theta^{(j)}|\theta^*)}, \tag{3.72}$$

where $\theta^{(g)}$ are samples of the posterior distribution, $\theta^{(j)}$ are samples of the proposal density, $\alpha$ is the acceptance ratio and $q$ is the proposal density. $M$ and $J$ are the number of samples drawn for the numerator and the denominator, respectively. Note that for $\theta^{(g)}$, the samples from the AMH algorithm can be used, while new samples are required for $\theta^{(j)}$. However, as the proposal density is normally much less complicated, this is typically much less computationally demanding.

## 3.5 Conclusion

In chapter 2, it has been established that the turbulent E×B particle and heat fluxes for the continuity and thermal energy equations play an important role for the plasma edge transport. Since the average of these fluxes depends on the correlation of turbulent fluctuations of the density, electrostatic potential and temperature, closure models are required to include them in mean-field codes. A closure strategy based on the RANS techniques that are widely used in hydrodynamic turbulence modelling is outlined in this chapter.

It is proposed to base such closure models on average quantities that characterise the E×B drift turbulence driving the transport. It is argued that the turbulent kinetic energy $k_\perp$ and turbulent enstrophy $\zeta_\perp$ offer attractive choices for such quantities as they contain relevant information on the turbulent eddies providing the mechanism for the transport. Furthermore, they can be used to construct a velocity and a time scale for the turbulence respectively. Despite the knowledge that the fine-scale phenomena leading to turbulent transport have a clear

convective nature, it is suggested that a diffusive model may provide an adequate description of their statistical average. Thus, it is proposed that $k_\perp$ and $\zeta_\perp$ can be used to model the effective turbulent transport coefficients in these diffusion relations. This ansatz will be proven to be fruitful in the next chapters.

In order to construct a self-consistent model for these turbulent fluxes, model equations for these quantifiers of the turbulence, $k_\perp$ and $\zeta_\perp$, are required. To this end, transport equations for both are derived analytically. Variants have been obtained for the total quantities including contributions due to the E×B drift and the diamagnetic ion drift, and for the E×B-only variant. Since the fluxes to be modelled feature only the E×B velocity, the latter may be more relevant. However, most terms in the transport equations for $k_\perp$ and $\zeta_\perp$ are closure terms that depend on correlations between turbulent fluctuations. Hence, in order to obtain a self-consistent model, these transport equations in turn require modelling. To this end, the next chapters will evaluate the different terms based on turbulence code data for reduced flow cases. This will allow to identify the dominant terms and to model these.

Literature does already provide some direction though. A detailed analysis of the perpendicular turbulent kinetic energy equation and how it couples to other energy equations (thermal energy, mean-field perpendicular kinetic energy, parallel kinetic energy, magnetic energy) provide insight in how energy can be injected into the turbulence and extracted from it. Two main channels are the interchange coupling and the drift wave coupling. The interchange channel exchanges energy between $k_\perp$ and thermal energy in the presence of magnetic field gradients. This is expected to be particularly important in the SOL. An analytical relation has been found to model this source of the turbulence, which links it to the turbulent E×B heat fluxes themselves. The drift wave channel transfers energy between electron thermal energy and $k_\perp$ through a coupling involving parallel current dynamics. Because of this link with fluctuations in the direction parallel to the magnetic field, this channel is expected to be more important in the closed field line region. Furthermore, the Reynolds stresses allow energy transfer between $k_\perp$ and the mean-field perpendicular kinetic energy. It is expected that this will act as a strong sink of the turbulence around the separatrix where strong shear flows tend to occur. Lastly, spatial transport of $k_\perp$ might also play a significant role. In particular, a transport term related to parallel current fluctuations is identified. The results in the next chapters suggest that this term enables fast transport of $k_\perp$ along the magnetic field lines to the plasma sheath, hence acting as a sink of $k_\perp$.

The mean-field turbulent transport models that will be developed in this thesis will feature a number of free parameters to be estimated. Furthermore, multiple competitor models (of different complexity) will be developed, which need to be compared. For this purpose, a framework for parameter estimation and model

comparison has been presented in this chapter. Both the simple least-squares method and the Bayesian inference methodology are discussed.

In the next chapters, the hypotheses formulated in this chapter will be checked systematically and the broad picture strategy for developing closure models will be put in practice. This will be done by applying the framework developed here to detailed turbulence code simulation data. Detailed analysis of the resulting averaged data will allow to suggest a number of closure models.

In order to gradually develop closure models starting from the basic dynamics, strongly simplified cases will be studied first, after which the complexity of the considered cases is gradually increased. First, the case of an isothermal, interchange-dominated, SOL in 2D with dominant E×B drifts will be considered in chapter 4. Chapter 5 will extend this case to also investigate the outer core region, where drift wave dynamics and flow shear also come into play. In addition, the influence of the ion diamagnetic drift in the inertia will be studied. Then, 6 will generalise the developed models to consider the anisothermal 2D SOL. Finally, chapter 7 will provide a look ahead by an exploratory analysis of fully 3D turbulence code data.

# Chapter 4

# 2D isothermal interchange-dominated E×B drift turbulence in the SOL

Chapters 2 and 3 considered fluid equations for the plasma edge in general, making a limited amount of assumptions on effects to be neglected. This led to a rather extensive set of equations containing a lot of physics. In this chapter[1], we will first reduce the complexity of the physics under consideration in order to be able to better disentangle the different effects at play. We start from a simplified case and try to understand this. Later on, assumptions can gradually be removed to build up a model for more realistic cases. This methodology allows to systematically construct a model based on a good understanding of the basic elements as well as any further additions.

This chapter will consider the simplified case of 2D isothermal, interchange-dominated, electrostatic E×B drift turbulence in the SOL. While simplified, this already contains some of the basic physics of plasma edge turbulence

---

[1]Parts of this chapter have been published in "Coosemans, R., Dekeyser, W., Baelmans, M. (2021). Turbulent kinetic energy in 2D isothermal interchange-dominated scrape-off layer E×B drift turbulence: Governing equation and relation to particle transport. *Physics of Plasmas*, 28:012302" [46], in "Coosemans, R., Dekeyser, W., Baelmans, M. (2020). A new mean-field plasma edge transport model based on turbulent kinetic energy and enstrophy. *Contributions to Plasma Physics*, 60:e201900156" [44], and in "Coosemans, R., Dekeyser, W., Baelmans, M. (2022). A self-consistent mean-field model for turbulent particle and heat transport in 2D interchange-dominated electrostatic ExB turbulence in a sheath-limited scrape-off layer. *Contributions to Plasma Physics*, e202100193" [47].

(e.g. blob-like structures, intermittency,...). Usually, the interchange coupling provides the main source of the turbulence in the SOL. In contrast, the drift wave (DW) coupling, requiring parallel fluctuations, plays a less important role in the SOL since fluctuations without a parallel component can exist in this region [89, 131, 133]. DW dynamics are not considered in the present chapter. Mean-field models for the average particle transport will be constructed based on a rigourous analysis of reference data obtained from the TOKAM2D turbulence code described in detail in Refs. [109, 116, 141]. This code fully resolves turbulent time and length scales in a plane perpendicular to the magnetic field. Section 4.1 first describes the 2D equation set modelling this turbulence and the TOKAM2D code setup used to simulate it. Next, section 4.2 derives the mean-field equations for this 2D model, including equations for $k_\perp$ and $\zeta_\perp$. Then, a mean field model for the transport is constructed that relates the turbulent diffusion coefficient to the turbulent kinetic energy in section 4.3. Section 4.4 further refines this model by also taking the turbulent enstrophy $\zeta_\perp$ into account. Finally, section 4.5 compares both models by means of a Bayesian analysis.

## 4.1    TOKAM2D setup and equations

Section 2.2 has presented the equations commonly used to describe the instantaneous dynamics of plasma edge turbulence. Appendix B.1 simplifies these equations to the case of 2D interchange-dominated electrostatic E×B drift turbulence in a sheath-limited SOL. This yields the equation set that is solved in the TOKAM2D turbulence code described in detail in Refs. [109, 116, 141]. TOKAM2D will be used to obtain detailed reference data for the turbulence in this chapter and in chapters 5 and 6. In this chapter, the TOKAM2D equations are simplified to the very basics of plasma edge turbulence and consider the isothermal E×B-vorticity-only case.

TOKAM2D considers a collection of flux tubes in the SOL connecting two plasma sheaths. As discussed in detail in section 2.2, plasma edge turbulence has much smaller length scales in the direction perpendicular to the magnetic field than in the direction parallel to it, especially in the SOL. In view of this, a flute approximation is made in TOKAM2D to neglect fluctuations along the parallel direction and an infinite conductivity is assumed such that plasma quantities are constant in this direction. Under these assumptions, the geometry reduces from 3D to 2D. Formally, the TOKAM2D equations are derived by averaging over the uniform parallel direction of these flux tubes. The fluxes out of this flux tube in the parallel direction are incorporated as artificial volumetric sinks. The form of these sinks is inspired by Bohm-like sheath

conditions. The assumptions above effectively imply a sheath-limited regime. The TOKAM2D equations are expected to be representative for the dynamics under such a sheath-limited regime in the outer midplane (OMP) region, the region on the outboard side of the tokamak around the horizontal midplane where the turbulence is strongest. While these assumptions do not hold for SOLs under all plasma edge conditions, it is a reasonable approximation and already allows to capture some of the dominant mechanisms at play in plasma edge turbulence [65, 67, 68, 122, 141].

The TOKAM2D equations are solved on a rectangular 2D domain, which is schematically represented in figure 4.1. $x$ is the radial direction and $y$ is the diamagnetic direction perpendicular to $x$ and to the magnetic field direction $\mathbf{b}$, such that the three form a right handed coordinate system. Hence, $y$ points in the electron diamagnetic direction. The direction along $\mathbf{b}$ is assumed to be uniform and is not resolved. In TOKAM2D, the magnetic field is assumed to be constant in time and uniform in space (except for magnetic field gradients in the $\nabla \cdot \mathbf{J}_*$ term in the charge balance equation which act as effective gravity). Furthermore, TOKAM2D uses quantities which are normalised with the ion mass $m$, reference ion gyro-frequency $\Omega_0 = eB_0/m$ and reference gyro-radius $\rho_0 = c_{s,0}\Omega_0$, with $B_0$ the reference magnetic field strength, $c_{s,0} = \sqrt{T_0/m_i}$ the reference sound speed and $T_0$ the reference temperature. The density is normalised to the reference density $n_0$. Note that the reference temperatures are defined in energy units of [J] or equivalently [eV]. This normalisation procedure is illustrated for typical tokamak SOL conditions in appendix C. Note that for clarity of notation, we choose to keep using the same symbols after the normalisation. In the remainder of this chapter and in chapter 5 and 6, the plasma quantities are all normalised, unless explicitly stated otherwise. Likewise, almost all figure showing TOKAM2D data in this thesis plot nondimensional, normalised data. For clarity, the "units" are indicated in terms of ion mass, reference density, gyro-frequency, gyro-radius and reference sound speed. Dimensional quantities can be obtained by filling out values for these reference quantities (which can be freely chosen).

Using this notation, the equations solved by TOKAM2D for the isothermal SOL case are the following:

$$\frac{\partial n}{\partial t} + \mathbf{V}_E \cdot \nabla n - D_0 \nabla_\perp^2 n = S_n - \frac{nc_s}{L_{||}} \exp(\Lambda - \frac{\phi}{T_e}), \qquad (4.1)$$

$$\frac{\partial W}{\partial t} + \mathbf{V}_E \cdot \nabla W - \nu_0 \nabla_\perp^2 W = -\frac{g}{n}\frac{\partial p}{\partial y} + \frac{c_s}{L_{||}}(1 - \exp(\Lambda - \frac{\phi}{T_e})), \qquad (4.2)$$

$$W \triangleq \nabla_\perp^2 \phi, \qquad \mathbf{V}_E \triangleq \mathbf{b} \times \nabla\phi. \qquad (4.3)$$

These equations correspond to the minimal subset of the full TOKAM2D equations B.21-B.25 presented in appendix B.1. In these equations, it is assumed that only the E×B velocity is relevant for convection in the perpendicular plane, i.e. $\mathbf{V}_C \triangleq \mathbf{V}_E$. Moreover, the divergence of the E×B drift $\nabla \cdot \mathbf{V}_E$ vanishes exactly since the magnetic field strength is assumed to be uniform over the whole domain (see equation 3.29). The perpendicular classical particle flux and the viscous stresses are modelled using simple diffusion models with $D_0$ and $\nu_0$ as a constant transport coefficient. Next to their physical meaning of classical transport, these terms are likewise required for numerical stability of the TOKAM2D code as they stop the direct cascade to length scales smaller than the gyro-radius, which would be unphysical in a drift-reduced fluid approach.

The divergences of the parallel fluxes are retained. These terms represent the flow of particles out of the flux tube at the parallel ends of it, i.e. at the plasma sheath. Using Bohm conditions for the plasma sheath, this leads to [153]

$$\nabla \cdot n\mathbf{V}_{e,||} \approx \frac{nc_s}{L_{||}} \exp(\Lambda - \frac{\phi}{T_e}), \quad \nabla \cdot \mathbf{J}_{||} \approx \frac{enc_s}{L_{||}}(1 - \exp(\Lambda - \frac{\phi}{T_e})). \quad (4.4)$$

In these expressions $\Lambda = \frac{1}{2}\ln(\frac{m_i}{2\pi m_e})$ [116] is the sheath potential drop. $L_{||}$ represents half the connection length, the distance along the field line between the intersections with the solid surface, i.e. the parallel length of the flux tube considered here. Hence, the expressions in 4.4 give rise to the last terms on the RHS of equations 4.1 and 4.2.

In the vorticity equation 4.2, only the contribution of the E×B velocity to the polarisation current is considered, meaning that the contribution from the diamagnetic ion drift is neglected. Furthermore, the $S_{W,cor}$ term (see equation 2.54) is neglected, which in this reduced case mainly implies the commonly made Boussinesq approximation is used [74, 132, 141, 170]. In addition, particle and momentum sources are also neglected in the vorticity equation. Since neutrals are not treated in TOKAM2D, the only particle source is an imposed source close the domain boundary, a region which will be excluded from the analysis in this thesis. Hence, neglecting the particle source terms can be justified. Finally, the first term in equation 4.2 represents the diamagnetic current divergence, where $g = -\partial \ln(B^2)/\partial x$ and a low $\beta$ approximation is made (see equation B.18 in appendix for details). Note that spatial variations of the magnetic field are retained in this term specifically in TOKAM2D in order to be able to represent the important interchange drive for the turbulence. Moreover, the parameter $g$ is to be interpreted as the average magnetic field curvature along the parallel extent of the considered flux tube. It is worth remarking that in this 2D case with a constant magnetic field, the pseudo-vorticity $W$ and (the parallel component of) the real vorticity are equivalent, see equation 2.48.

For the isothermal SOL case, TOKAM2D only solves the equations 4.1-4.3 and assumes spatio-temporally constant ion and electron temperatures $T_i$ and $T_e$ (instead of solving thermal energy equations). These equations are solved for a rectangular Cartesian $x, y$-coordinate system representing the plane perpendicular to the magnetic field. In this thesis the finite volume version of the TOKAM2D code [109, 116] is used.

On radial ($x$) boundaries of the domain, the radial fluxes of all quantities are forced to zero.[2] This is done by applying Neumann boundary conditions on radial boundaries combined with fringe regions near the radial boundaries to drive fluctuations in the diamagnetic ($y$) direction to zero in those regions. The latter are required because gradients in the $y$-direction would otherwise lead to ExB fluxes over the radial boundaries. Periodic boundary conditions are used on diamagnetic boundaries. The particle source $S_n$ has a Gaussian profile in the $x$-direction and is constant both in the $y$-direction and in time. In the simulations performed for this thesis, the particle source is situated towards the inner boundary of the domain. Figure 4.1 shows a sketch of the different regions in the TOKAM2D computational domain. Note that in this thesis only the physical middle part of the computational domain will be considered where the influence of the fringe region and the particle source is negligible. More details regarding the TOKAM2D simulation parameters used in the various sets of simulations reported here can be found in appendix D.

## 4.2 Mean-field equations

As discussed in chapters 1-3, the goal of this thesis is to a model the average turbulent E×B transport, drawing inspiration from RANS techniques for hydrodynamic turbulence. Hence, this section will construct mean-field equation from the instantaneous, turbulent equations for isothermal electrostatic interchange-dominated E×B drift turbulence SOL described in the previous section. To this end, all turbulent quantities in the governing equations 4.1-4.2 and 4.3-4.3 are split into a mean flow and a fluctuating component, either using a Reynolds or a Favre decomposition, see equation 2.55 and 2.58. Averaging the equations then yields equations describing the evolution of the average density

---

[2]Particles enter the domain through the source term instead.
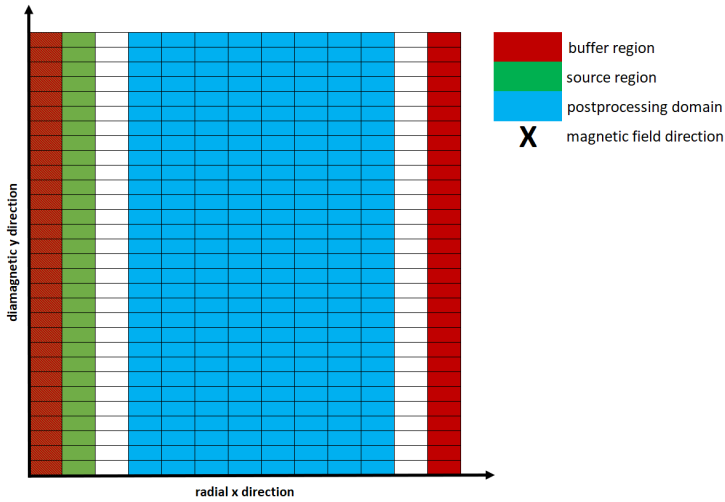
Figure 4.1: Sketch of the computational domain of the TOKAM2D turbulence code and the various regions in it.

$\bar{n}$, vorticity $\bar{W}$ and electrostatic potential $\bar{\phi}$:

$$\frac{\partial \bar{n}}{\partial t} + \nabla \cdot (\bar{n}\bar{\mathbf{V}}_E + \overline{n'\mathbf{V}'_E}) = \bar{S}_n - \frac{c_s}{L_{||}}\overline{n\exp(\Lambda - \frac{\phi}{T_e})} + D_0\nabla_\perp^2\bar{n}, \qquad (4.5)$$

$$\frac{\partial \bar{n}\tilde{W}}{\partial t} + \nabla \cdot (\bar{n}\tilde{W}\tilde{\mathbf{V}}_E + \overline{nW''\mathbf{V}''_E})$$

$$= -gT\frac{\partial \bar{n}}{\partial y} + \frac{c_s}{L_{||}}(\bar{n} - \overline{n\exp(\Lambda - \frac{\phi}{T_e})}) + \nu\overline{n\nabla_\perp^2 W}, \qquad (4.6)$$

$$\tilde{W} = \widetilde{\nabla_\perp^2\phi}, \qquad \bar{\mathbf{V}}_E = \mathbf{b} \times \nabla\bar{\phi}, \qquad (4.7)$$

where $T = T_i + T_e$. The terms in these equation can be compared to the corresponding terms in the turbulent equations 4.1-4.2. Linear terms, such as the time derivative and diffusive terms, retain the same form as in the original equation. Nonlinear terms, such as the convective terms and the sheath loss terms, lead to correlations between fluctuations, and give rise to terms that require closure. $\bar{S}_n$ represents the averaged source term of particles. As the particle source in the TOKAM2D code is constant in time, this overbar notation is not strictly necessary, but is used for generality and possible future extensions of the model. Note that in writing the above mean-field equations, the
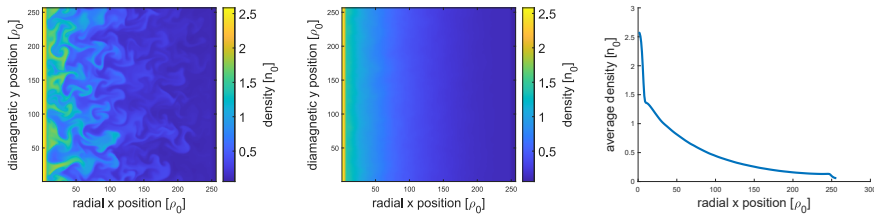
Figure 4.2: Typical results for the TOKAM2D density field. Snapshot of the turbulent density field (left), time averaged density field (middle) and radial profile (averaged in time and diamagnetic direction, right) .

original convective operator $\mathbf{V}_E \cdot \nabla u$ was rewritten as $\nabla \cdot u\mathbf{V}_E$, for an arbitrary convected quantity $u$. Given the definition 4.7, hence without taking variations of the magnetic field strength into account, both are exactly equivalent since $\nabla \cdot \mathbf{V}_E = 0$. We write the equations in this chapter in the conservative form using the divergence operator to allow easier generalisation to more complex models. It is also to be remarked that a Reynolds average for the E×B velocity is used in the continuity equation in analogy to the treatment in current mean-field transport models and codes, as discussed in section 2.3.

Figure 4.2 illustrates the concrete averaging procedure that is applied to TOKAM2D data. The density field as obtained for the default isothermal SOL TOKAM2D simulation (see appendix D.1.1 for detailed parameters) is considered as an example. The raw data consist of the evolution of the 2D density field in time, which feature strong turbulent fluctuations as illustrated in the left panel of figure 4.2. The middle panel is obtained by averaging the data in time from the onset of steady state. Since the diamagnetic $y$-direction in TOKAM2D is periodic and there are no inhomogeneities in this direction (in geometry, parameters, or sources), averaged quantities should only vary in the radial $x$-direction. For this reason, the TOKAM2D data will not only be averaged over time as indicated in the average in equation 2.57, but also over this periodic $y$-direction. This then yields the right panel of figure 4.2. Hence, the mean-field models for the turbulence developed in this chapter will be 1D, radial models. Note that the diamagnetic averaging is not a necessary part of the methodology, but is only used to obtain more data points for the averaging.

Figure 4.3 illustrates how the finite time average $\langle u \rangle_T = \frac{1}{T} \int_0^T u \, dt$ varies with the averaging time $T$. For this default TOKAM2D case, $\langle u(x,y) \rangle_T$ clearly reaches a quasi-constant value when $T$ becomes sufficiently high. The figure also illustrates the diamagnetic symmetry at longer averaging times. Small variations of $\langle u(x,y) \rangle_T$ for different $y$ values at the same $x$ do persist even for

(a) density $n$

(b) electrostatic potential $\phi$
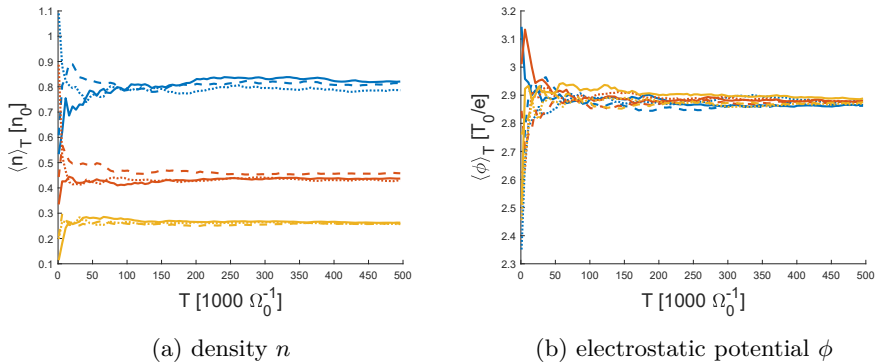
Figure 4.3: Dependence of selected quantities on the averaging time horizon $T$ for a representative TOKAM2D simulation. Results are plotted for three radial locations ($x = 50\rho_0$ in blue line, $x = 100\rho_0$ in red line, $x = 150\rho_0$ in yellow line) at three diamagnetic locations ($y = 1\rho_0$ in solid line, $y = 100\rho_0$ in dashed line, $y = 200\rho_0$ in dotted line).

large averaging times $T$ though.[3] This may be due to a certain hysteris in the flow field leading to large scale flow structures remaining on long time scales.

Figure 4.4 then illustrates the variations of quantities averaged in time and over the diamagnetic direction for varying initial conditions. TOKAM2D simulations are initialised with random seeding for a selected set of diamagnetic modes ($K_y$). Figure 4.4 shows the radial profile (at selected locations) for 25 simulations with different seeding. These 25 simulations consist of sets of 5 simulations with different (preselected) modes in the initial state. Results are shown for the density divided by the average density in all simulations in figure 4.4a and for the effective turbulent diffusion coefficient in figure 4.4b. These results seem to indicate that the same average state is achieved independently of the initial conditions, although noise does remain on the averages. As such, this figure gives an idea of the noise level on the averaged data. This noise level can be very different for different quantities, i.e. the density variations seem to lay within 1%, while the diffusion coefficient varies by over 10%. While figures 4.3 and 4.4 do not provide a formal proof of ergodicity at infinite time (see equation 2.57), ergodicity will be assumed in this thesis based on these qualitative observation.

Because the average quantities only vary in the $x$ direction, only the turbulent E×B particle flux $\mathbf{\Gamma}_{n,E,t,x} = \overline{n'\mathbf{V}'_{E,x}}$ contributes to the averaged radial total

---

[3]For the electrostatic potential, there is little variation in the radial direction as well for this isothermal case. The reason is that the potential is driven to a value $\phi = \Lambda T_e$ by the exponential terms on the RHS of equations 4.1-4.2.

(a) density ratio

(b) Effective turbulent diffusion coefficient
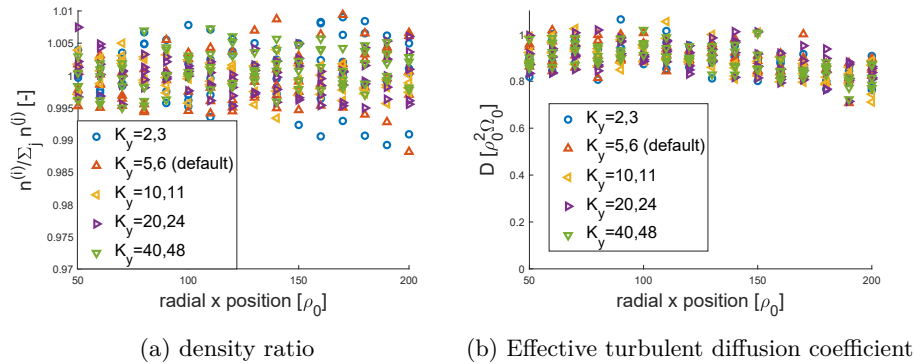
Figure 4.4: Dependence of averaged TOKAM2D quantities on the initial conditions for representative parameters. Radial profiles are shown for a reduced number of radial points to preserve readability. Different colours represent different modes in the initial conditions. Five different simulations with random seeds (for the selected modes) are shown for each colour.

E×B particle flux because the mean field E×B particle flux $\mathbf{\Gamma}_{n,E,m,x} = \bar{n}\bar{\mathbf{V}}_{E,x}$ is zero (since gradients in the $y$-direction of averaged quantities are zero). For this reason the term $\nabla \cdot \bar{n}\bar{\mathbf{V}}_E = \nabla \cdot \mathbf{\Gamma}_{n,m,E}$ drops from equation 4.5. Hence, the remainder of this chapter will look for models to close the turbulent E×B particle flux $\mathbf{\Gamma}_{n,E,t,x} = \overline{n'\mathbf{V}'_{E,x}}$ in mean-field transport models. Note however that in more general (non-1D) models, solving equations 4.6 and 4.7 for $\bar{n}$ and $\bar{\phi}$ would allow to calculate the mean-field E×B particle transport $\mathbf{\Gamma}_{n,m,E}$. Note also that this requires additional closures for the nonlinear terms in the averaged vorticity equation.

According to the hypothesis formulated in section 3.1, the turbulent E×B particle flux is assumed to be related to the turbulence characteristics. Sections 4.3 and 4.4 will relate this closure term to the turbulent kinetic energy $k_\perp$ and the turbulent enstrophy $\zeta_\perp$ in particular. To that end, sections 4.2.1 and 4.2.2 will first present the analytically derived transport equations for these two quantities themselves.

## 4.2.1 Discussion of the kinetic energy equations

In this chapter it is assumed that the E×B drift is the dominant perpendicular velocity, and the only one relevant for the inertia, as assumed in the basic isothermal TOKAM2D model in equations 4.1-4.3. As a result, only the E×B

velocity appears in the vorticity $W = \nabla_\perp^2 \phi$. Consequently, we also define the (perpendicular) kinetic energy based on this E×B drift. Hence, we define the total ($E_{k,\perp}$), mean flow ($E_{k,m,\perp}$), and turbulent ($k_\perp$) perpendicular kinetic energies as in equation 3.16[4]:

$$E_{k,\perp} \triangleq \frac{\mathbf{V}_E^2}{2}, \quad E_{k,m,\perp} \triangleq \frac{\tilde{\mathbf{V}}_E^2}{2}, \quad \bar{n}k_\perp \triangleq \overline{\frac{n\mathbf{V}_E''^2}{2}}. \tag{4.8}$$

As before, $E_{k,\perp}$ varies rapidly in time and space as it follows the instantaneous fluctuations, while $E_{k,m,\perp}$ and $k_\perp$ are time averaged quantities that do not change at these small scales. Note also that the sum of mean flow and turbulent kinetic energy per unit volume equals the averaged total kinetic energy per unit volume, as shown in equation 3.6. Figure 4.5 shows the radial profile of the turbulent kinetic energy for the default isothermal TOKAM2D simulation. For future reference, it also shows the radial profiles of the turbulent diffusion coefficient and the turbulent enstrophy. The profiles of all three quantities can be seen to be rather flat. Note that the profile of the diffusion coefficient remains rather noisy, while those of $k_\perp$ and $\zeta_\perp$ are much smoother. This complies with the results in figure 4.4, which also showed that the diffusion coefficient is a quantity on which significant noise tends to remain. This may be due to the persistence of certain flow structures on long time scales and/or hysteresis in the density profile.

Transport equations for the perpendicular kinetic energy are derived in appendix B.2.2. This derivation is largely similar to that presented for the general case in section 3.2.2 and the resulting equation are very similar to the E×B-only kinetic energy equations 3.22-3.24. The differences are due to model assumptions in TOKAM2D: only E×B convection is considered, the Boussinesq approximation is made, $\mathbf{J}_{p,*}$ has been neglected, source terms have been neglected in 4.2 and specific forms of the currents $\mathbf{J}_{||}$ and $\mathbf{J}_*$ have been used. Furthermore, it is opted to keep the viscous contribution to the polarisation current $\mathbf{J}_{p,\Pi}$ completely separately from the inertial part of it ($\mathbf{J}_{p,0}$). This leads to slight differences in the exact formulation of the equations. As in chapter 3, the density fluctuations are rigorously taken into account in these derivations and in the resulting equations. However, this may not bring a large benefit for the present analysis of incompressible flow. Nonetheless, we decided not to neglect density fluctuation a priori, for generality, and in anticipation of future extensions of the model presented in this manuscript where they may be more important.

---

[4]In this chapter, we use the notation subscript $\perp$ to denote the perpendicular kinetic energy. In the present chapter, this includes only the E×B drift such that subscripts $E$ could equivalently be used. We opt to use the more general notation $\perp$ since no other perpendicular velocities come into play and there can thus be little confusion. The same comment goes for the subscripts on the vorticity, the enstrophy and the inertial part of the polarisation current.
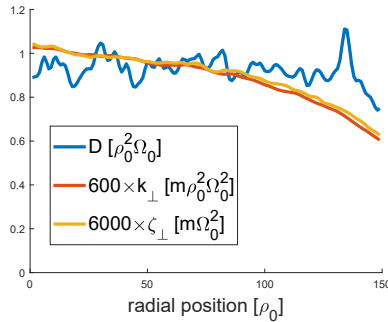
Figure 4.5: Radial profiles of the turbulent diffusion coefficient (D), the turbulent kinetic energy $(k_\perp)$ and the turbulent enstrophy $(\zeta_\perp)$ for a representative isothermal TOKAM2D simulation for the SOL.

Retaining these density fluctuations does render the derivation and the final expressions more complicated though, but the Favre averages demonstrated in equation 2.58 allow to reduce the number of closure terms that appear in the mean-field equations with respect to using Reynolds averages shown in equation 2.55.

The total kinetic energy equation is found to be (see equation B.49 in appendix)

$$\frac{\partial}{\partial t} n E_{\mathrm{k},\perp} + \nabla \cdot \mathbf{\Gamma}_{E_{\mathrm{k},\perp}} = g\phi \frac{\partial p}{\partial y} - \frac{c_s n \phi}{L_{||}} (1 - \exp(\Lambda - \frac{\phi}{T_e}))$$

$$-\nu n \phi \nabla_\perp^2 W + S_{E_{\mathrm{k},\perp},n} + \phi \mathbf{V}_{p,0} \cdot \nabla n, \tag{4.9}$$

$$\mathbf{\Gamma}_{E_{\mathrm{k},\perp}} = n E_{\mathrm{k},\perp} \mathbf{V}_E + \phi \mathbf{J}_{p,0}, \tag{4.10}$$

$$S_{E_{\mathrm{k},\perp},n} = E_{\mathrm{k},\perp} S_n + D_0 E_{\mathrm{k},\perp} \nabla_\perp^2 n - E_{\mathrm{k},\perp} \frac{c_s n}{L_{||}} \exp(\Lambda - \frac{\phi}{T_e}), \tag{4.11}$$

$$\mathbf{J}_{p,0} = n \mathbf{V}_{p,0} = n \mathbf{b} \times \frac{D \mathbf{V}_E}{Dt}. \tag{4.12}$$

The terms on the LHS of this equation represent the time rate of change and transport of $E_{\mathrm{k},\perp}$, with the transport terms written in conservative form. In equation 4.9, only the E×B velocity appears in the convective transport term on the LHS. The contributions of the parallel and diffusive flow components appear on the RHS of the equation, as part of the source term 4.11. In more complete models, these two flow components would naturally be moved to the transport

term on the LHS of the equation to ensure particle and energy conservation. The RHS of the equation groups sources and sinks of $E_{\mathrm{k},\perp}$. The first two are the interchange source and loss to the sheath through divergence of the parallel current, which will turn out to be the dominant ones. The following term is a dissipation term due to the viscosity. The last term on the RHS is a "Boussinesq correction term" introduced by bringing $n$ in the divergence in $n\nabla\cdot(\phi\mathbf{V}_p)$. This term would not have been present if the Boussinesq approximation had not been made in the vorticity equation 4.2, i.e. if the corresponding term had not been dropped in equation B.15.

In order to arrive at equations for $E_{\mathrm{k},m,\perp}$ and $k_\perp$ defined in equation 3.5, the $E_{\mathrm{k},\perp}$ equation 4.9 should be split in a contribution due to mean flows and a contribution due to fluctuations. Appendix B.2.2 applies a rigorous methodology to do so, obtaining the mean-field kinetic energy equation (see equation B.54 in appendix) as

$$\frac{\partial}{\partial t}\bar{n}E_{\mathrm{k},m,\perp} + \nabla\cdot\mathbf{\Gamma}_{E_{\mathrm{k},m,\perp}} = g\bar{\phi}\frac{\partial\bar{p}}{\partial y} - \frac{\bar{\phi}}{L_{||}}\overline{c_s n(1 - \exp(\Lambda - \frac{\phi}{T_e}))}$$

$$-\nu\bar{\phi}\overline{n\nabla_\perp^2 W} + \overline{n\mathbf{V}_E''\mathbf{V}_E''} : \nabla\tilde{\mathbf{V}}_E^T - \tilde{\mathbf{V}}_{p,0}\cdot\overline{n'\nabla\phi'}$$

$$+S_{E_{\mathrm{k},m,\perp},n} + \bar{\phi}\overline{\mathbf{V}_{p,0}\cdot\nabla n}, \qquad (4.13)$$

$$\mathbf{\Gamma}_{E_{\mathrm{k},m,\perp}} = \bar{n}E_{\mathrm{k},m,\perp}\tilde{\mathbf{V}}_E + \overline{n\mathbf{V}_E''\mathbf{V}_E''}\cdot\tilde{\mathbf{V}}_E + \bar{\phi}\tilde{\mathbf{J}}_{p,0}, \qquad (4.14)$$

$$S_{E_{\mathrm{k},m,\perp},n} = E_{\mathrm{k},m,\perp}\bar{S}_n + \tilde{\mathbf{V}}_E\cdot\overline{\mathbf{V}_E''S_n}$$

$$+D_0 E_{\mathrm{k},m,\perp}\nabla_\perp^2\bar{n} + D_0\tilde{\mathbf{V}}_E\cdot\overline{\mathbf{V}_E''\nabla_\perp^2 n}$$

$$-\frac{E_{\mathrm{k},m,\perp}}{L_{||}}\overline{c_s n\exp(\Lambda - \frac{\phi}{T_e})} - \overline{c_s n\mathbf{V}_E''\exp(\Lambda - \frac{\phi}{T_e})}\cdot\frac{\tilde{\mathbf{V}}_E}{L_{||}}. \qquad (4.15)$$

The parallel and diffusive particle fluxes are treated like volumetric particle sinks as was done before for the total kinetic energy. Note that the last four terms in $S_{E_{\mathrm{k},m,\perp},n}$ are still pure transport terms. Due to symmetry, the parallel contributions to the Reynolds stresses vanish.

The turbulent kinetic energy equation is then found (see equation B.57 in appendix) as

$$\frac{\partial}{\partial t}\bar{n}k_\perp + \nabla \cdot \mathbf{\Gamma}_{k_\perp} = \overline{g\phi'\frac{\partial p'}{\partial y}} - \frac{1}{L_{||}}\overline{\phi'(c_s n(1 - \exp(\Lambda - \frac{\phi}{T_e})))'}$$

$$-\nu\overline{\phi'(n\nabla_\perp^2 W)'} - \overline{n\mathbf{V}_E''\mathbf{V}_E''} : \nabla\tilde{\mathbf{V}}_E^T + \tilde{\mathbf{V}}_{p,0} \cdot \overline{n'\nabla\phi'}$$

$$+S_{k_\perp,n} + \overline{\phi'(\mathbf{V}_{p,0} \cdot \nabla n)'}, \qquad (4.16)$$

$$\mathbf{\Gamma}_{k_\perp} = \bar{n}k_\perp\tilde{\mathbf{V}}_E + \overline{n\mathbf{V}_E''\mathbf{V}_E''^2}/2 + \overline{\phi'\mathbf{J}_{p,0}'}, \qquad (4.17)$$

$$S_{k_\perp,n} = \frac{1}{2}\overline{\mathbf{V}_E''^2 S_n} + \frac{D_0}{2}\overline{\mathbf{V}_E''^2\nabla_\perp^2 n} - \frac{1}{2L_{||}}\overline{c_s n\mathbf{V}_E''^2 \exp(\Lambda - \frac{\phi}{T_e})}. \qquad (4.18)$$

The perpendicular transport terms (second term on LHS) and the Reynolds stress terms (fourth on RHS) in equations 4.13 and 4.16 have the same form as in hydrodynamic turbulence [37, 126]. The interchange, sheath loss and viscous term (first, second and third term on the RHS) correspond to the pressure, the sheath loss, and the viscous stress tensor term in a typical plasma momentum equation respectively. Comparing the $E_{k,m,\perp}$ and the $k_\perp$ equations, it can be seen that both the Reynolds stresses and the Favre averaging term (fifth term on RHS) exchange energy between the turbulence and the mean flow. The latter originates from the non-commutative properties of Favre averaging and the divergence operator (see equation B.38). Close inspection reveals that the Favre term has a structure similar to the turbulent transport and Reynolds energy transfer term, which is in accordance with it appearing as an energy transfer term.

Note that no assumptions have been made on the isothermal character of the plasma to derive equations 4.9, 4.13 and 4.16. As such, they are equally valid for the anisothermal case that will be studied in chapter 6. In the isothermal case considered in this chapter, the temperatures, implicitly present in $p \triangleq n(T_i + T_e)$ and in $c_s = \sqrt{T_i + T_e}$, could be brought out of the averaging operator in a straightforward way.

**Analytical interchange relation for TOKAM2D**

Section 3.2.3 derived an analytical relation for the interchange term in general, relating it to the E×B energy flux and magnetic field strength gradients. Similar physics is at play in the reduced TOKAM2D case. The equivalent derivation

for this case specifically yields following expressions for the interchange drive of the total kinetic energy $G_{E_{\mathrm{k}},\perp}$, the mean-field kinetic energy $G_{E_{\mathrm{k},m},\perp}$ and turbulent kinetic energy $G_k$:

$$G_{E_{\mathrm{k}}} \triangleq g\phi\frac{\partial p}{\partial y} = gpV_{E,x} + g\frac{\partial \phi p}{\partial y}, \tag{4.19}$$

$$G_{E_{\mathrm{k},m}} \triangleq g\bar{\phi}\frac{\partial \bar{p}}{\partial y} = 0, \tag{4.20}$$

$$G_k \triangleq \overline{g\phi'\frac{\partial p'}{\partial y}} = \overline{gp'V'_{E,x}}. \tag{4.21}$$

Note that gradients in the $y$-direction of average quantities again cancel due to symmetry. The above expressions are again valid both for the anisothermal and the isothermal case. Following the derivations in equations 3.33-3.34 for the general case in section 4.2.1, expression 4.21 can be rewritten as

$$G_k = g(\tilde{T}\overline{n'V'_{E,x}} + \overline{nT''V''_{E,x}}) = g(\tilde{T}\Gamma_{n,E,t,x} + \Gamma_{p_{\mathrm{i}},E,t,x} + \Gamma_{p_{\mathrm{e}},E,t,x}). \tag{4.22}$$

In the 1D mean-field case considered here, the relation between the interchange source of kinetic energy and the E×B energy flux $3p\mathbf{V}_E/2$ is very clear. The magnetic field gradients, shown to be the second ingredient of the interchange relation in section 3.2.3, appear here in the form of the factor $g$. Equation 4.21 shows that the interchange drive for the turbulence can hence only be positive if the radial E×B energy flux has the same sign as $g$, e.g. is outward for positive $g$, which means in the direction of decreasing magnetic field strength. Equation 4.20 illustrates that the interchange drive for the mean-field kinetic energy is zero, since there is no mean-field E×B transport of kinetic energy in 1D.

If the plasma is additionally assumed to be isothermal as it will be in this chapter, relation 4.22 simplifies to

$$G_k = gT\overline{n'V'_{E,x}} = gT\bar{\Gamma}_{n,E,t,x}. \tag{4.23}$$

This relation will be retrieved exactly when processing TOKAM2D simulations in section 4.3. Hence, it suffices to model the turbulent E×B particle flux to model the interchange term in the $k_\perp$ equation in the considered case of an isothermal 1D transport model.

## 4.2.2  Discussion of the enstrophy equations

As discussed in section 3.3, the enstrophy is normally defined as half the square of the vorticity $\zeta = \omega^2/2$. In TOKAM2D we will use the quantity $W$ instead, which is similar to the real vorticity, but not exactly equivalent, see section 2.2.3. In the TOKAM2D case which is 2D and in which a uniform magnetic field is assumed, the difference is only a constant factor $B$ though. Thus, similar to equation 3.43 we define the total, mean flow and turbulent enstrophies as

$$\zeta_{tot} \triangleq \frac{W^2}{2}, \quad \zeta_{mean} \triangleq \frac{\tilde{W}^2}{2}, \quad \bar{n}\zeta_{turb} \triangleq \frac{\overline{nW''^2}}{2}. \tag{4.24}$$

In analogy to the definition of the turbulent kinetic energy in equation 4.8, the total enstrophy is defined as a fluctuating quantity, while the mean-field and turbulent enstrophies are defined as mean-field quantities. The radial profile of $\zeta_{turb}$ for a representative TOKAM2D simulation is shown in figure 4.5.

To analytically derive transport equations for the enstrophies, a procedure similar to section 3.3.1 is followed in appendix B.3.2. The TOKAM2D enstrophy equations are found to be very similar to the general E×B-only enstrophy equations 3.51-3.53. The main difference are due to the terms that have been neglected in the general E×B-only vorticity equation 3.49 to obtain the TOKAM2D vorticity equation 4.2 (with $W = \nabla_\perp^2 \phi$). In addition, models have been filled out for the parallel and diamagnetic and viscous current divergences.

The total enstrophy equation is derived as (see equation B.66)

$$\frac{\partial n\zeta_{tot}}{\partial t} + \nabla \cdot (n\mathbf{V}_E \zeta_{tot}) = -gW\frac{\partial p}{\partial y} + \frac{c_s nW}{L_{||}}(1 - \exp(\Lambda - \frac{\phi}{T_e}))$$

$$+\nu nW\nabla_\perp^2 W + \zeta_{tot}S_n + D_0\zeta_{tot}\nabla_\perp^2 n - \frac{c_s n\zeta_{tot}}{L_{||}}\exp(\Lambda - \frac{\phi}{T_e}). \tag{4.25}$$

In this equation, terms similar to those in the original vorticity equation and in the $E_{k,\perp}$ equation derived earlier can again be identified. The first and second terms on the LHS represent time change and transport of the total enstrophy respectively. The first three terms on the RHS are interchange, sheath losses and viscous dissipation. The last three terms are due to the sources in the electron density equation. The last two terms might again be interpreted as transport terms.

The mean field and turbulent enstrophy equations are found to be (see equations B.67 and B.68)

$$\frac{\partial \bar{n}\zeta_{mean}}{\partial t} + \nabla \cdot (\bar{n}\zeta_{mean}\tilde{\mathbf{V}}_E + \overline{nW''\mathbf{V}_E''}\tilde{W}) = -g\tilde{W}\frac{\partial \bar{p}}{\partial y}$$

$$+\frac{1}{L_{||}}\tilde{W}\overline{c_s n(1 - \exp(\Lambda - \frac{\phi}{T_e}))} + \nu\tilde{W}\overline{n\nabla_\perp^2 W} + \overline{nW''\mathbf{V}_E''}\cdot\nabla\tilde{W}$$

$$+\zeta_{mean}\bar{S}_n + \tilde{W}\overline{W''S_n} + D_0\zeta_{mean}\nabla_\perp^2\bar{n} + D_0\tilde{W}\overline{W''\nabla_\perp^2 n}$$

$$-\frac{\zeta_{mean}}{L_{||}}\overline{c_s n\exp(\Lambda - \frac{\phi}{T_e})} - \frac{\tilde{W}}{L_{||}}\overline{c_s nW''\exp(\Lambda - \frac{\phi}{T_e})} \qquad (4.26)$$

and

$$\frac{\partial \bar{n}\zeta_{turb}}{\partial t} + \nabla \cdot (\bar{n}\zeta_{turb}\tilde{\mathbf{V}}_E + \frac{\overline{nW''^2\mathbf{V}_E''}}{2}) = -g\overline{W''\frac{\partial p}{\partial y}}$$

$$+\frac{1}{L_{||}}\overline{c_s nW''(1 - \exp(\Lambda - \frac{\phi}{T_e}))} + \nu\overline{nW''\nabla_\perp^2 W} - \overline{nW''\mathbf{V}_E''}\cdot\nabla\tilde{W}$$

$$+\frac{\overline{W''^2 S_n}}{2} + D_n\frac{\overline{W''^2\nabla_\perp^2 n}}{2} - \frac{1}{L_{||}}\frac{\overline{c_s nW''^2}}{2}\exp(\Lambda - \frac{\phi}{T_e}). \qquad (4.27)$$

The interpretation of most of the terms in equations 4.26 and 4.27 is very similar to that of the total enstrophy equation 4.25. A nontrivial term that appears is the fourth term in the RHS of both equations. This term exchanges enstrophy between the mean-flow and the turbulent enstrophy. The structure of this term is similar to that of the well-known RS term in the kinetic energy equations. In analogy to that, it could be assumed that this term in the enstrophy equation is indeed responsible for transferring enstrophy from the large scales to the small scales in a direct cascade. The third term in the LHS of equation 4.26 also features transport of mean-field enstrophy by the "enstrophy Reynolds stresses" in a way familiar from the kinetic energy equation. Lastly, the third term on the LHS of equation 4.27 represents the turbulent convection of turbulent enstrophy.

Note that no assumptions have been made on the isothermal character of the plasma to derive enstrophy equations 4.25-4.27. They are thus equally valid for the anisothermal case that will be studied in chapter 6. In the isothermal case considered in this chapter, the temperatures, implicitly present in $p$ and in $c_s$, can be brought outside of the averaging operator.

# 4.3  $k_\perp$ model

Having established the necessary background, this section will develop a first mean-field model for the turbulent E×B particle flux in isothermal SOL plasmas. The model presented in this section models this particle flux using a diffusion relation, and links the diffusion coefficient to the turbulent kinetic energy $k_\perp$. Section 4.3.1 evaluates the turbulent kinetic energy equation derived in the previous section using TOKAM2D data and investigates the balance of the sources and sinks of turbulent kinetic energy. Models for the dominant closure terms are proposed based on a regression analysis. The same regression analysis techniques are used to identify possible models for the average turbulent particle flux in section 4.3.2. Section 4.3.3 then compares simulation results obtained with the newly developed model to the original TOKAM2D results and to the model proposed in Ref. [34].

## 4.3.1  Characterisation of the different terms in the $k_\perp$ equation

In this section, we investigate the balance of turbulent kinetic energy described by equation 4.16. The different terms in this equation are evaluated for a set of TOKAM2D simulations to identify the dominant sources and sinks. Then, we propose closure models for the dominant terms.

**Turbulent kinetic energy balance in 2D isothermal interchange turbulence**

To assess the various terms in the $k_\perp$ equation, we performed a set of 19 TOKAM2D simulations with varying input parameters $g$, $L_{||}$, $T_i$, $\nu$ and $D_0$. The reference simulation has parameters $g = 6e - 4$, $1/L_{||} = 1e - 4$, $T_i = 1$ and $\nu = 5e - 3$ as in Ref. [109]. These parameters have then respectively been varied by factors $0.5 - 2$, $0.75 - 1.5$, $0.5 - 2$ and $0.4 - 3$ of the reference set. $D_0$ has been set equal to $\nu$ in all simulations. In order to get a clearer view of the effects at play, the figures in this section will distinguish the results for the 14 TOKAM2D simulations with viscosity $\nu = 5e - 3$ and the 5 simulations in which the viscosity is varied. The complete set of input parameters for the simulations is provided in appendix D.

Figure 4.6 shows the evaluation of the different terms in the $k_\perp$ equation 4.16 for the default case with the standard parameter settings. The left plot 4.6a shows the larger terms, while the smaller contributions are grouped as "other terms" in that figure and plotted separately in the figure 4.6b. In these figures,

(a) dominant terms

(b) other terms
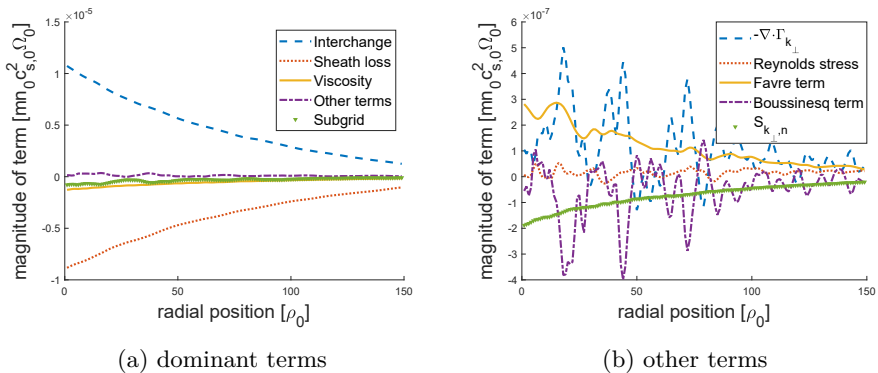
Figure 4.6: Evaluation of terms in the TOKAM2D $k_\perp$ equation 4.16.

the transport terms in the left hand side of equation 4.16 have been moved to the right hand side (i.e. a minus sign was added to those terms). Figure 4.6 clearly shows that the interchange term is the dominant source of $k_\perp$ while the sheath loss term is the dominant sink. The viscous term provides a secondary sink for $k_\perp$. The other terms are much smaller than these first three. It is particularly interesting that the perpendicular transport of $k_\perp$ is small. Thus, the turbulent kinetic energy balance almost reduces to a local balance. Note also that the Reynolds stress energy transfer between the mean flow and the turbulence is very small for the cases studied here. In our simulations, this is the result of the sheath model constraining the electrostatic potential such that no significant E×B flow can develop in the $y$-direction. We expect this term to become important to describe turbulence suppression in cases with flow shear, and it will likely be required when generalizing the model presented here towards more complex setups. The Favre term (which entered the equations because Favre averaging and the divergence operator do not commute) also exchanges energy between turbulence and mean flow and appears to be larger than the Reynolds stresses. The Boussinesq term is very noisy, but its average value appears to be small. Hence, it seems to be more of a numerical artefact than a physical term, which indicates that the Boussinesq approximation made in the TOKAM2D equation set is self-consistent, as the corresponding correction term is not important. The $S_{k_\perp,n}$ term in equation 4.16, involving the source terms on the RHS of the TOKAM2D continuity equation, is observed to be small in the considered part of the domain. It is largely dominated by the particle loss to the sheath. The "subgrid" term represents the imbalance on the evaluation of the $k_\perp$ equation. It will be shown below that it is a numerical discretisation error, that can be reduced through grid refinement.
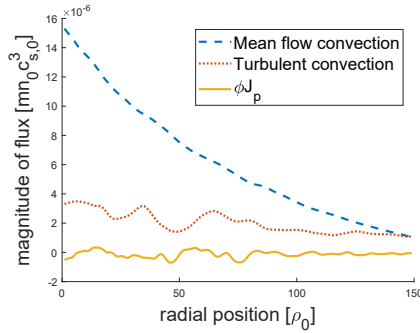
Figure 4.7: Evaluation of the different contributions to the average radial flux of turbulent kinetic energy $\mathbf{\Gamma}_{k_\perp}$ in equation 4.17.

In figure 4.6, the perpendicular transport terms have all been plotted together. Figure 4.7 shows the different fluxes that contribute to this transport separately, according to equation 4.17. It is important to note that this figure plots the fluxes of turbulent kinetic energy contributing to $\Gamma_{k_\perp}$ themselves, not their divergences that appear in equation 4.16. The divergence of the flux gives the transport term in the $k_\perp$ equation for all the perpendicular terms shown in figure 4.6. This figure shows that the perpendicular transport of turbulent kinetic energy is dominated by mean flow convection. For completeness we remind the reader that the diffusive term and the sheath loss term in the $S_{k_\perp,n}$ term in equation 4.18 can also be interpreted as transport terms of $k_\perp$.

It has to be remarked that the imbalance on the $k_\perp$ equation labelled subgrid model, is not negligible as it is actually the fourth largest term in this evaluation (see figure 4.6). Its magnitude is about 7% of the size of the interchange source in this case. A grid and time step refinement study has been conducted to verify that this error reduces with increasing refinement. It is also observed that the magnitude of $k_\perp$ increases as the grid is refined, presumably because the dissipative effect of the discretisation error is reduced. Details of this grid refinement study can be found in appendix E. The commonly used cell sizes and time steps ($\Delta x = \Delta y = \rho$, $\Delta t = 1/\Omega$)[109, 116] will be used in the remainder of this chapter, despite the error that they seem to cause, because we found no significant impact on the underlying physics interpretation or saturation behavior of the turbulence at present. However, for a detailed analysis of the forward and inverse turbulence cascades [34, 36, 71, 92], this implied subgrid model might play an important role, and requires further investigation.

**Development of a model for the $k_\perp$ equation**

In this section, we search a model to close the $k_\perp$ equation 4.16. Figure 4.6 has shown that the interchange term, the sheath loss term and the viscous term are the dominant ones in the energy balance for $k_\perp$, which is also observed in other simulations. Hence, we focus on these terms here. First the interchange source of the turbulence will be analysed by means of a regression analysis. Then, the sheath loss and viscous sinks will be discussed, as well as the saturation mechanism of the turbulence.

In this chapter, we will make use of the regression analysis methodology discussed in section 3.4.1. In order to model the output reference data $O$, power laws are suggested as the expected model form:

$$O \approx f(I,p) = p_0 \prod_{i=1}^{N_p} I_i^{p_i}. \tag{4.28}$$

In this expression, $N_p$ is the number of input quantities present in the model, which equals the number of parameters minus one (as one parameter is contained in the constant in front of the product). The exponents found in these power laws indicate whether or not a certain quantity $I_i$ in $I$ is important. This allows to trim the full set of available quantities down to those relevant for the output $O$. The data for the regression analysis is provided by 19 TOKAM2D simulations with different combinations of the model parameters $g$, $L_{||}$, $T_i$ and $\nu$ (see appendix D). The sample points $I_i$ and $O_i$ are the radial profiles of the relevant quantities of these simulations. To this end, the TOKAM2D data of each simulation are averaged both in time (where only data after convergence to a statistical steady state is used) and in the $y$-direction (which is a symmetry direction).

**Regression analysis of the interchange term**    The interchange term in the $k_\perp$ equation is crucial to the closure of this equation as it provides the main source of the turbulence. Subsection 4.2.1 has already established the analytic relation 4.23 between the interchange term and the turbulent E×B energy flux. Figures 4.8a and 4.8b confirm that this relation is indeed retrieved in TOKAM2D. Figure 4.8a shows the radial profile of the averaged interchange term for the exact TOKAM2D data and for the analytical model 4.23, evaluated using TOKAM2D data, for the reference simulation with the standard parameter settings (see appendix D). Both lines coincide. Figure 4.8b shows a scatter plot of the interchange term that is obtained by evaluating the flux model 4.23 using TOKAM2D data, versus an evaluation of the exact TOKAM2D interchange
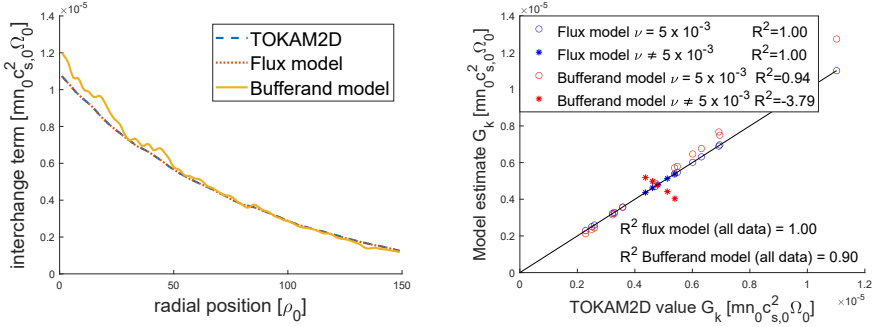
(a) radial profiles for a representative simulation

(b) scatter plot showing radially averaged values for a database of simulations

Figure 4.8: Comparison of the TOKAM2D interchange term of $k_\perp$ with models 4.23 and 4.29.

term. Each data point in the figure represents a single TOKAM2D simulation (i.e. fixed parameters $g$, $T$, $L_{||}$,...) that is not only averaged in time and in the diamagnetic direction, but also in the radial direction. These types of scatter plots give a clear image of the trends in the data across simulations. In addition, the coefficient of determination as introduced in equation 3.57 is provided (for all the data together as well as for the data set with constant viscosity and the one with varying viscosity separately). Note that $R^2$ is calculated based on the radially averaged values plotted as data points in figure 4.8b and not on the full data set of radial profiles for all simulations. The figure shows that the analytical relation 4.23 also manages to perfectly capture the trends in parameter space, as expected.

As an alternative option to model the interchange source, we analyse a model inspired by Bufferand *et al.* [34], which has been discussed in section 2.3.3. Bufferand *et al.* proposed to model the interchange term using a linear growth model $G_k = \gamma \bar{n} k_\perp$, where the growth rate of the interchange instability (in dimensional form) is given in equation 2.88. Here, we adapt this model to the isothermal TOKAM2D case and remove the threshold part of the growth rate (which allowed to match the TOKAM2D data much better) yielding

$$G_k = C_{g,Buff} c_s \sqrt{-g \frac{\partial_x \bar{n}}{\bar{n}}} \bar{n} k_\perp. \tag{4.29}$$

To determine the constant $C_{G,Buff}$, we perform a nonlinear regression on the set of TOKAM2D simulations as described in appendix D.1.2. In this case, the output quantity of interest is the interchange term $O = G_k$ and

$I = c_s\sqrt{-g\bar{n}\partial_x\bar{n}}k_\perp$ is chosen as the explanatory variable. This procedure leads to the value $C_{G,Buff} \approx 2.21$, which differs significantly from the factor $1/\sqrt{2}$ that would be obtained by filling out $g = -2\nabla B/B$ in equation 2.88.

The results of this alternative model are also shown in figures 4.8a and 4.8b. It can be seen from figure 4.8a that a somewhat different (steeper) radial profile of the interchange term is obtained with model 4.29. The magnitude of the relative error is around 10% in this case. The default TOKAM2D case used for figure 4.8a lies in the middle of the parameter range investigated in the regression analysis. As a result, the model parameters are very well matched to this case specifically. Simulations further away from the center of this TOKAM2D parameter range differ more from the TOKAM2D results. This is confirmed by figure 4.8b, which shows that model 4.29 from Ref. [34] captures the trends in parameter space rather well and has a high $R^2$ value, but some scatter, error, remains. In particular, the model does not seem to capture the trend for varying viscosities, indicated by the stars in the figure.

**Sinks of $k_\perp$ and turbulence saturation**  A regression according to section 3.4.1 is conducted for the sum of the main sinks, the sheath loss and viscous terms ($O = S_k + \varepsilon_k$). The explanatory quantities $I$ could be any set of quantities that are expected to be related to these terms. These may include mean-field quantities and gradients thereof (e.g. $k_\perp,n,\nabla n,..$), and TOKAM2D parameters (such as $g$, $T_i$, $L_{||},...$). The regression analysis optimises the exponents on these explanatory variables. Quantities with lower exponents have been dropped and exponents have been rounded to make the models more interpretable and physically plausible. This resulted in the following model:

$$S_k + \varepsilon_k \approx C_{||,k}\frac{c_s}{\sqrt{L_{||}}}\bar{n}k_\perp \quad \text{with} \quad C_{||,k} \approx -0.538. \tag{4.30}$$

It has to be noted that the sink is found to be proportional to $c_s/\sqrt{L_{||}}$, whereas it could be expected to scale as $c_s/L_{||}$, as that is the factor determining the strength of the sheath loss in the original vorticity equation 4.2. It is also worth keeping in mind that the sheath loss term $S_k$ is physically not a pure sink dissipating $k_\perp$, but is due to transport to the sheath.

The performance of this regression model is assessed in figures 4.9a and 4.9b. Figure 4.9a shows that the regression model manages to capture the radial profile of the sink terms very well, with very little error remaining. The maximum relative error is smaller than 4%. The scatter plot shown in figure 4.9b indicates that the regression model also captures trends in parameter space rather well. Note that the $R^2$ value shown in the figure is again calculated based on the
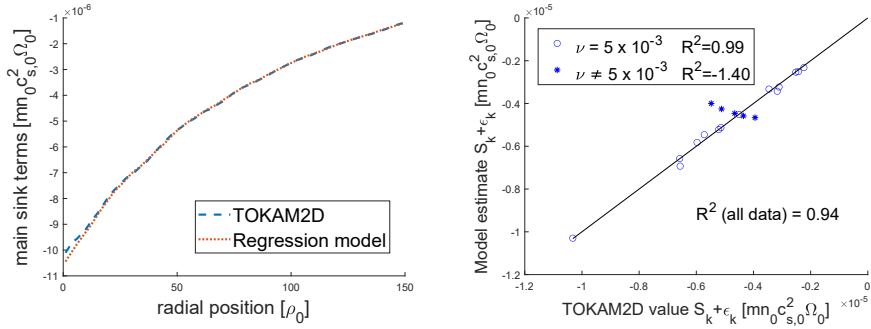
(a) radial profiles for a representative simulation

(b) scatter plot showing radially averaged values for a database of simulations

Figure 4.9: Comparison of TOKAM2D sinks terms for $k_\perp$ with model 4.30.

radially averaged data points shown in the figure and not on the underlying radial profiles. The largest errors here are found in simulations where the viscosity was significantly varied from its default value. The viscosity was not retained in regression model 4.30 because the regression analysis that was conducted showed the exponent on it to be relatively low. Another reason not to retain a scaling with the viscosity is that physically a second sink term due to viscous dissipation would be expected, rather than a factor on the sheath loss term. This is explored in Ref. [44] and will be discussed in section 4.4. There, the turbulent enstrophy equation 4.27 is also modelled and used to provide a measure for the viscous dissipation of $k_\perp$.

It is interesting to see that a purely linear sink follows from the regression analysis. This is different from the quadratic sink that was proposed in the model in Ref. [34]. In combination with the linear source growth rate model for the interchange source model, a quadratic sink then leads to the $k_\perp$ model shown in equation 2.87 discussed in section 2.3.3, and repeated below for convenience:

$$\frac{\partial \bar{n} k_\perp}{\partial t} + \nabla \cdot (\mathbf{\Gamma}_{k_\perp}) = \gamma \bar{n} k_\perp - \Delta \omega \bar{n} k_\perp^2. \tag{4.31}$$

In such a model, the linear drive of the turbulence causes the turbulent kinetic energy to increase initially. As $k_\perp$ increases, the nonlinear sink increases faster than the drive term and finally saturates the turbulence. Hence, the absence of any nonlinear sinks that is observed in TOKAM2D implies that the saturation mechanism is also different.

Combining the analytical relation 4.23 for the interchange source and regression relation 4.30 for the sink, we construct following model for the $k_\perp$ equation:

$$\frac{\partial \bar{n} k_\perp}{\partial t} + \nabla \cdot (\mathbf{\Gamma}_{k_\perp}) = g T \Gamma_{n,t,E} - C_{||,k} \frac{c_s}{\sqrt{L_{||}}} \bar{n} k_\perp. \qquad (4.32)$$

If steady state is assumed and the transport terms are neglected because of the quasi-local balance that is observed, the model reduces to an algebraic expression:

$$\bar{n} k_\perp = \frac{g \sqrt{L_{||}} T}{C_{||,k} c_s} \Gamma_{n,t,E}. \qquad (4.33)$$

The idea behind this model is the following: as soon as a turbulent E×B particle flux originates (in the direction of decreasing magnetic field strength, indicated by $g$), this leads to an increase in the turbulent kinetic energy (through the interchange source term), which in turn causes an increase of the particle flux (see section 4.3.2) and a further build-up of the turbulence. Finally, this is saturated by a sink that is proportional to the turbulent kinetic energy (effectively modelling the parallel transport of $k_\perp$ to the sheath) together with a reduction of the gradients driving the particle flux (see section 4.3.2).

Note that the presented $k_\perp$ model now features a very simple model for the sink of turbulent kinetic energy, related to the parallel sheath loss term. In this model this term effectively represents $-\overline{\phi' \nabla \cdot \mathbf{J}'_{||}}$, which can be rewritten as $-\nabla \cdot \overline{\phi' \mathbf{J}'_{||}} + \overline{\mathbf{J}'_{||} \cdot \nabla_{||} \phi'}$ (see Ref. [143] and equation 3.40 discussed in section 3.2.5). The first term can be interpreted as a transport term of $k_\perp$ in the parallel direction, while the second term is a real local source/sink of $k_\perp$ transferring energy with the parallel magnetic energy (see section 3.2.5). Because of the flute approximation made in TOKAM2D to neglect parallel gradients and fluctuations, only the transport contribution $-\nabla \cdot \overline{\phi' \mathbf{J}'_{||}}$ remains. This is also consistent with the ad-hoc model for the parallel direction in this 2D setup which aims to represent the flux out of the considered flux tube. Hence, it is the parallel transport term that constitutes the linear sink of $k_\perp$ that is found here for the simple sheath model used in equations 4.1 and 4.2. The term "sink" may not be completely appropriate here though as this sheath loss term is due to transport, redistribution, of $k_\perp$ rather than dissipation. Also, we would like to stress that the real parallel dynamics are likely to be more complicated than this simple linear sink. These parallel dynamics and the distinction between both parts of the parallel current term will be investigated in chapter 7, where 3D cases are studied.

Nonetheless does the analysis presented here indicate that the parallel direction suffices as a linear sink of the turbulence and that no nonlinear sinks (due to self-saturation) are required to saturate the turbulence in the isothermal SOL case considered here. In more complex cases different saturation mechanisms might come into play though. For example, flow shear is believed to lead to turbulence quenching and may lead to zonal flow and transport barrier formation [14, 58, 76, 93, 108, 113]. This phenomenon is not observed in this work as the electrostatic potential is very strongly constrained by the sheath potential such that no significant E×B flow in the diamagnetic $y$-direction and thus no flow shear can develop. Note that in order to incorporate more complex physical phenomena, more complex models for the sink could easily be implemented, e.g. a second sink term to model the viscous dissipation separately, or any nonlinear terms that would be found to be important could be added in the future. It might also be envisaged to include a model for the Reynolds stresses transferring energy with zonal flow in the future. Nonetheless, in section 4.3.3 it will be shown that the present model already explains the TOKAM2D results well.

## 4.3.2 Particle transport model

In this section, models for the average radial turbulent E×B particle flux $\mathbf{\Gamma}_{n,t,E} = \overline{n' \mathbf{V}'_E}$ are developed. In Section 4.2, we have already shown that this flux dominates the radial particle transport in the considered 1D case. Moreover, the radial mean-flow convection, which has been shown to be the dominant perpendicular transport term in the $k_\perp$ equation, is also determined by this particle flux.

The regression methodology discussed in section 3.4.1 is applied to find a model for $\mathbf{\Gamma}_{n,t,E}$. The input quantities $I$ of the regression analysis are chosen as any set of quantities that are expected to be related to the particle transport (including TOKAM2D parameters, mean-field properties and gradients thereof). This yields

$$\mathbf{\Gamma}_{n,t,E} = -C_D \sqrt{k_\perp} \nabla_\perp \bar{n} \quad \text{with} \quad C_D \approx 23.9. \tag{4.34}$$

It has to be noted that, also here, quantities with lower exponents have been dropped and exponents have been rounded to make the models more interpretable and physically viable.

Figures 4.10a and 4.10b compare regression model 4.34, evaluated using TOKAM2D data, to the particle flux obtained from TOKAM2D directly. Figure 4.10a shows that the model captures the radial profile of the particle flux in
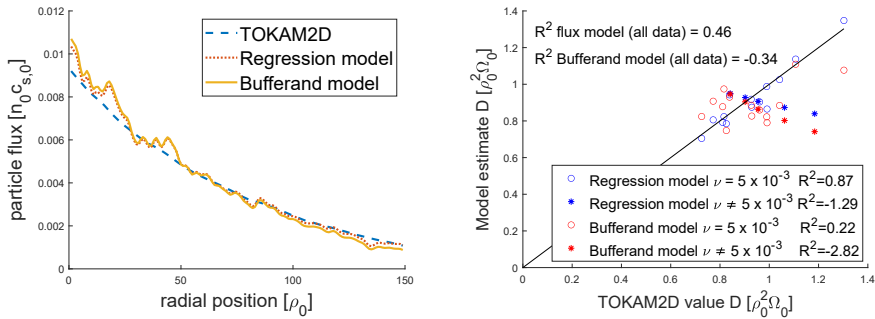
(a) radial profiles for a representative simulation

(b) scatter plot showing radially averaged values for a database of simulations

Figure 4.10: Comparison of TOKAM2D particle flux models 4.34 and 4.35.

general, however, the model profile is slightly too steep. The maximum relative error on the particle flux is 25.1%. Figure 4.10b shows that regression model 4.34 manages to capture the main trends in TOKAM2D parameter space, however, some trends seem not to be fully captured by this model. The clearest one is again the one with variations in viscosity. This time, the scaling with varying sheath loss parameter $L_{||}$ does not seem to be fully captured either though. Correction factors for this have been dropped in the regression analysis as they seemed to be of secondary importance. The introduction of the turbulent enstrophy in the diffusion coefficient has been shown to significantly reduce these errors. This will be discussed in section 4.4. Note that the $R^2$ values shown in figure 4.10b are again calculated based on the radially averaged data points shown in the figure and not on the radial profiles.

The diffusive model 4.34 for the average radial particle flux is very interesting in the sense that it proves to be rather robust, using a very limited number of parameters. This model indicates that the initial hypothesis that the turbulent kinetic energy $k_\perp$ plays an important role in the particle transport holds. In its dimensionless form $D = C_D \sqrt{k_\perp}$, the diffusion coefficient in this model only depends on characteristics of the turbulence. It could be argued that these are the only parameters the diffusion coefficient should depend on as the turbulence is the driver of the particle transport and no macroscopic, geometric parameters such as $g$ or $L_{||}$ should be involved. Recalling equation 3.5, the scaling with $\sqrt{k_\perp}$ is very natural because it provides a direct measure of the local strength of the fluctuating E×B velocity.

Also, this square-root-scaling seems quite intuitive and is also found in hydrodynamic turbulence modelling. In RANS models for hydrodynamic

turbulence, the turbulent transport of a passive scalar is often modelled using the gradient diffusion hypothesis, see section 2.1. The transport coefficient therein is commonly related to the turbulent viscosity, which is assumed to scale as $l_m\sqrt{k}$ in one-equation $k$-models, where $l_m$ is a suitable length scale, see equation 2.23. Making the diffusion coefficient in equation 4.34 dimensional by removing the TOKAM2D normalisation, it takes form, $D \sim \rho_0\sqrt{k_\perp}$, which is clearly analogous to the hydrodynamic turbulence scaling.

Furthermore, this scaling can be interpreted as a refinement of the Bohm scaling 2.81. The Bohm scaling in dimensional units may equivalently be written as $D_B \sim \rho_{Te}c_{s,Te}$, where $\rho_{Te} = c_{s,Te}/\Omega$ and $c_{s,Te} = \sqrt{T_e/m}$ are the ion gyroradius and the sound speed based on the electron temperature. Hence, the $D \sim \rho_0\sqrt{k_\perp}$ scaling basically replaces the generic electron thermal velocity in the Bohm scaling with a velocity characterising the turbulent E×B fluctuations driving the transport. Note also that the TOKAM2D normalisation of the Bohm scaling leads to $D \sim T_e$ (under the uniform magnetic field in TOKAM2D), which is exactly constant in the isothermal case where $T_e = 1$ in all simulations that are considered in this chapter. This can be seen not to be in accordance with the results shown in figure 4.10b. The Bohm model is not explicitly shown this figure, since it would just amount to all data points laying at the average value for the whole set of simulations. By construction of the $R^2$ value (see equation 3.57), this leads to a value of zero.

The gyro-Bohm scaling 2.82 can be translated to TOKAM2D units as $D \sim -T_e^{3/2}\partial_x \ln \bar{n}$ when the density decay length is taken as the perpendicular scale length. Alternatively, when the minor radius $a$ is taken as the perpendicular scale length, it could be assumed that this is proportional to the major radius, i.e. a constant aspect ratio could be assumed such that $a \sim R$. Then it could be assumed that $\rho/a \sim \rho/R \sim g$, such that $D \sim T_e^{3/2}g$. The $R^2$ values for these models have been calculated to be $-4.33$ and $0.18$ respectively. Hence, the $k_\perp$ scaling provides an improvement over both variations of the gyro-Bohm scaling for the TOKAM2D data set considered here.

The transport coefficient proposed by Bufferand *et al.* [34], shown in equation 2.86, provides another alternative model for this diffusion coefficient. This model is adapted to the 2D interchange turbulence model 4.1-4.2 by assuming a constant aspect ratio, such that the minor radius is proportional to the major radius, and thus inversely proportional to the magnetic field curvature $a \sim 1/g$. Thus,

$$\mathbf{\Gamma}_{n,t,E} = -C_{D,Buff}\frac{k_\perp}{c_s g}\nabla_\perp \bar{n}. \tag{4.35}$$

The regression methodology presented in section 3.4.1 (with $O = \mathbf{\Gamma}_{n,t,E}$ and

$I = k_\perp \nabla_\perp \bar{n}/(c_s g))$ yields $C_{D,Buff} \approx 0.507$. A one-to-one comparison of this constant with Ref. [34], who used a proportionality constant of 0.67 in equation 2.86, is somewhat difficult because of the use of $g \sim 1/R$ in equation 4.35 and the minor radius $a$ in the original model 2.86. Trying to correct for this using $R = 2.4m$ and $a = 0.72m$ for the Tore Supra tokamak from the case ran in Ref. [34], we would find $C_{D,Buff} \approx 0.67a/R = 0.201$.

Figure 4.10a shows that the error on the radial profile of the particle flux is slightly more pronounced for the model adapted from Ref. [34]. The maximum relative error is 35.7%. Figure 4.10b indicates that model 4.35 also performs less good in parameter space.

While diffusion models for the radial particle transport are routinely used in mean-field modelling and despite the merits of the diffusive model presented here, the underlying nature of the particle transport in the plasma edge is not diffusive. Radially propagating blob-filaments would rather lead to convective transport [61, 76, 78, 101, 106, 125]. As discussed in section 3.1, a well-chosen diffusion model might however give a reasonable approximation of the long time scale average particle flux caused by all the instantaneous filaments moving outward and holes moving inward in a seemingly random way. In this respect, it is worthwhile to note that the main structure and interpretation of our model still hold in the case of alternative (e.g. convective) transport assumptions: the specific closure for the particle flux enters in the continuity equation, the interchange source of $k_\perp$ and the (perpendicular) transport of $k_\perp$, leading to a self-saturating system.

## 4.3.3 Complete 1D transport model and implementation in DivOpt

The models developed above are combined to obtain a closed system of equations for the average density. This complete model is implemented in a 1D mean-field finite volume code that can simulate the average turbulent transport, whereas all the previous sections have only post-processed TOKAM2D data. In this section, the results of simulations with this model are compared to the exact TOKAM2D results, and to our interpretation of the model proposed in Ref. [34].

**Mean-field transport model for 2D isothermal interchange turbulence**

Combining $k_\perp$ model 4.32 developed in section 4.3.1 with the particle flux model 4.34 that depends on $k_\perp$ found in section 4.3.2, the radial transport in the

averaged continuity equation 4.5 can be closed. The resulting model equations proposed here are repeated below in their dimensionless form:

$$\frac{\partial \bar{n}}{\partial t} + \nabla \cdot (\bar{n}\bar{\mathbf{V}}_E + \mathbf{\Gamma}_{n,t,E} - D_0 \nabla_\perp \bar{n}) = \bar{S}_n - \frac{c_s \bar{n}}{L_{||}}, \tag{4.36}$$

$$\mathbf{\Gamma}_{n,t,E} = -C_D \sqrt{k_\perp} \nabla_\perp \bar{n} = -D \nabla_\perp \bar{n}, \tag{4.37}$$

$$\frac{\partial \bar{n} k_\perp}{\partial t} + \nabla \cdot \mathbf{\Gamma}_{k_\perp} = gT\Gamma_{n,t,E} - C_{||,k} \frac{c_s}{\sqrt{L_{||}}} \bar{n} k_\perp, \tag{4.38}$$

$$\mathbf{\Gamma}_{k_\perp} = k_\perp \mathbf{\Gamma}_{n,E} - C_{Dk} \bar{n} D \nabla k_\perp, \tag{4.39}$$

$$C_D = 23.9, \quad C_{||,k} = 0.561, \quad C_{Dk} = 0.79. \tag{4.40}$$

Some additional assumptions have been made in the model presented above. First, a detailed study of isothermal TOKAM2D data in Ref. [43] revealed that the sheath loss term in the continuity equation 4.36 can be approximately modelled as $c_s \bar{n}/L_{||}$. Moreover, an ad-hoc diffusive term has been added to the turbulent kinetic energy flux as a proxy for the (small) turbulent transport contribution in equation 4.39. The constant $C_{Dk}$ for the latter has been determined by means of a regression analysis. This last model is quite crude and might need to be improved in the future. It also has to be noted that the value of the $k_\perp$ sink parameter $C_{||,k}$ has been determined from a regression analysis for $G_k \approx C_{||,k} c_s \bar{n} k_\perp / \sqrt{L_{||}}$ and not as the value found in equation 4.30. In this way, all sinks are collected in this single sink and assumed to exactly balance the source of the turbulence locally (which is approximately observed, quasi-local balances). This allows to implicitly treat the effect of all the minor terms in the $k_\perp$ balance without having to model all of them.

In the model presented here, the turbulence level and the transport are determined by the interaction between the source of the turbulence and the mean flow gradients. The source of the turbulence depends on the particle flux (energy), which in turn depends both on $k_\perp$ and the mean flow density gradient, where the density gradient depends on the magnitude of the turbulent diffusion coefficient that is determined by $k_\perp$. Parallel sheath dynamics constitute the main sink mechanism of the turbulence.

This behaviour is compatible with the gradient removal mechanism for turbulence saturation. The idea behind this is that pressure or density gradients determine the growth rate of the turbulence (see for example equations 2.88 and 4.29). Due to the turbulence that develops, the mean flow pressure and density gradients are relaxed, leading to a reduced growth rate of the turbulence or even to its removal. This leads to intermittent behaviour, where gradients are

first built up, until the instability threshold is reached and causes a sudden, large outburst due to turbulent transport [114, 89, 133]. Arguably, the model presented here contains the averaged result of these dynamics, which lead to a shift of the equilibrium due to the interaction between the mean-flow gradients, the resulting turbulence, and the transport caused by the turbulence. Note that the sheath losses also play an important role in the model presented here. For the simple sheath model in equations 4.1 and 4.2, the corresponding sheath loss term for $k_\perp$ constitutes a linear sink of $k_\perp$. While the parallel dynamics are likely to be more complicated than the simple models used here, these findings do indicate that the parallel direction suffices as a sink of the turbulence and that no nonlinear sinks (due to self-saturation) are required to saturate the turbulence. This is in accordance with Refs. [89, 133], which also suggest that parallel losses to the wall are the main removal mechanism for the turbulence in the gradient removal regime. More analysis of the gradient removal mechanism, and its link with the model presented here is required though. It could be especially illuminating to investigate time series and transient behaviour in TOKAM2D.

It is important to emphasise that this model is only strictly valid for the isothermal, interchange-dominated, SOL case that we considered. In this case, the electrostatic potential is to a large degree set by the sheath potential. If the electrostatic potential has more freedom to develop, strong E×B flows tend to evolve in the y-direction which are sheared in the x-direction. This can lead to a large Reynolds stress sink of $k_\perp$ ($-\overline{n\mathbf{V}''_{E,x}\mathbf{V}''_{E,y}} : \nabla_x \tilde{\mathbf{V}}^T_{E,y}$ in equation 4.16), and thus to an alternative saturation mechanism for the turbulence [58, 76, 108, 93]. These interactions are not observed in the present case, but certainly not ruled out in general. Section 5.1 will provide a first step towards incorporating the effects of flow shear in the $k_\perp$ model by investigating the balance of $k_\perp$ and the effect of flow shear on the turbulent transport relation 4.34 for TOKAM2D cases with a core region added.

The new model 4.36-4.40 introduced here can be compared to the model proposed by Bufferand *et al.* [34], which has been adapted to the TOKAM2D case as summarised here:

$$\frac{\partial \bar{n}}{\partial t} + \nabla \cdot (\bar{n}\bar{\mathbf{V}}_E + \mathbf{\Gamma}_{n,t,E} - D_0 \nabla_\perp \bar{n}) = \bar{S}_n - \frac{c_s \bar{n}}{L_{||}}, \qquad (4.41)$$

$$\mathbf{\Gamma}_{n,t,E} = -C_{D,Buff}\frac{k_\perp}{mc_s g}\nabla_\perp \bar{n} = -D_{Buff}\nabla_\perp \bar{n}, \qquad (4.42)$$

$$\frac{\partial \bar{n}k_\perp}{\partial t} + \nabla \cdot \mathbf{\Gamma}_{k_\perp} = C_{g,Buff}c_s\sqrt{-g\frac{\partial_x \bar{n}}{\bar{n}}}\bar{n}k_\perp - C_{sink,Buff}\bar{n}k_\perp^2, \qquad (4.43)$$

$$\bar{\Gamma}_{k_\perp} = k_\perp \mathbf{\Gamma}_{n,E} - C_{Dk}\bar{n}D_{Buff}\nabla k_\perp, \qquad (4.44)$$

$$C_{D,Buff} = 0.507, \ C_{g,Buff} = 2.21, \ C_{sink,Buff} = 5.84. \qquad (4.45)$$

In these equations, the source term consists of the interchange term found in expression 4.29 and a sink term quadratic in $k_\perp$ that saturates the linear source is assumed to exist. As a crude approximation, this sink is assumed not to scale with any TOKAM2D parameters, i.e. $sink_k \sim \bar{n}k_\perp^2$ only. Note however that recent studies [13, 11, 12] do include a dependence on machine parameters in this sink term in the model by Bufferand *et al.*. A regression analysis has been conducted to determine the corresponding constant $C_{sink,Buff}$ such that equation $\frac{C_{G,Buff}c_s}{C_{sink,Buff}}\sqrt{-g\partial_x \ln \bar{n}}$ matches the TOKAM2D $k_\perp$ results across all simulations as good as possible. Note however that this sink term is ad-hoc as no large nonlinear sink terms have been identified in TOKAM2D in this analysis. Comparing with the value of $10^{-2}s/m^2$ reported in Ref. [34] is again not straightforward, because of the normalisation that is involved. If we assume a reference temperature of $50eV$ (temperature at the LCFS used in Ref. [34]) and a magnetic field of $2T$, we would find the coefficient $C_{sink,Buff} \approx 0.25$.

Although the saturation mechanisms of the new $k_\perp$ model and the model by Bufferand *et al.* seem very different at first sight, some remarkable similarities can be observed. While the sink of $k_\perp$ in the new model 4.36-4.40 scales linearly with $k_\perp$, this sink is still of higher order than the source of $k_\perp$. The latter scales with the particle flux which scales with $\sqrt{k_\perp}$ and the density gradient. This is not so different from the behaviour in the Bufferand model 4.41-4.45, where the scaling of the sink in $k_\perp$ is also the square of the scaling of the source in $k_\perp$. Moreover, there as well, the source is also a function of the density gradient. Nonetheless, the detailed scalings predicted by both models differ, as can be seen in the steady state local balance equivalents of both $k_\perp$ models. For the new model, combining the diffusion coefficient relation 4.37 with the

$k_\perp$ equation 4.38 in which we neglect the LHS yields

$$D = \frac{C_D^2}{C_{||,k}} \frac{g}{\sqrt{L_{||}}} \partial_x \ln \bar{n}, \quad k_\perp = \frac{C_D^2}{C_{||,k}^2} \frac{g^2}{L_{||}} (\partial_x \ln \bar{n})^2. \tag{4.46}$$

Analogously, combining the particle diffusion coefficient relation 4.42 with $k_\perp$ equation 4.43 without LHS for the Bufferand model result in

$$D = \frac{C_{D,Buff} C_{g,Buff}}{C_{sink,Buff}} \frac{1}{\sqrt{g}} \sqrt{\partial_x \ln \bar{n}}, \quad k_\perp = \frac{C_{g,Buff}}{C_{sink,Buff}} c_s \sqrt{g} \sqrt{\partial_x \ln \bar{n}}. \tag{4.47}$$

### Assessment of mean-field model performance

The mean-field transport model presented above has been implemented in DivOpt [52, 55], an in-house 2D finite volume code that is used for testing purposes. The geometry that is simulated consists of the central part of the TOKAM2D domain which has earlier been used in the post processing, see figure 4.1. Zero flux boundary conditions are applied in the diamagnetic direction for both the continuity equation and the $k_\perp$ equation to arrive at the mean-field equivalent of the fully-turbulent TOKAM2D setup with periodic boundary conditions on the diamagnetic boundaries. These boundary conditions lead to uniform profiles in the diamagnetic direction and thus to a mean-field solution which only varies in the radial direction. On the radial boundaries, flux boundary conditions that exactly match the TOKAM2D data are applied for both equations. The mean-field particle flux $\bar{n}\mathbf{V}_E$ is included in equation 4.36 for generality, but is exactly zero in the considered 1D case, as discussed earlier. Likewise, the average particle source $\bar{S}_n$ has been included in equation 4.36 for generality, but no particle source is present in the forward mean-field simulations reported in this section (since the region with a significant particle source in the TOKAM2D computational domain has been discarded in the post processing and as such also in the mean-field case). The simulations are run on an orthogonal grid with 48 cells in the radial direction and 4 cells in the diamagnetic direction (which is arbitrary due to symmetry). The global reference values used for making the TOKAM2D variables dimensional are $n_0 = 10^{19} m^{-3}$, $T_0 = 50 eV$, $B_0 = 1.725 T$ and $m$ is the mass of deuterium.

Remark that we leave the development of boundary conditions for the $k_\perp$ equation for further research. Note that the $k_\perp$ PDE model equations 4.38 and 4.43 could be simplified to algebraic $k_\perp$ equations by making a steady-state-quasi-local-balance-approximation to neglect time rate of change and

the transport of $k_\perp$ in the LHS. This removes the need to provide boundary conditions for the $k_\perp$ equation, and has been shown to provide good results for these 1D mean-field cases. However, attention is focused on the PDE versions of the $k_\perp$ equations as it is expected that transport terms will become more important in realistic geometries such that the balance of $k_\perp$ will be non-local.

Figure 4.11 shows the resulting profiles for a number of quantities of interest for two DivOpt simulations, compared to the exact TOKAM2D results (referred to as "T2D"). The two simulations that are compared are one with the transport model 4.36-4.40 derived from term by term regression of the 19 TOKAM2D simulations (referred to as "KUL"), and one with the tuned Bufferand model 4.41-4.45 (referred to as "Buff"). The results shown here are the ones for the default TOKAM2D case. Figures 4.11a and 4.11b show that both models are capable of predicting the density and the particle flux quite well. The "secondary quantities" being the diffusion coefficient and the turbulent kinetic energy are also approximated relatively well by the different models, as can be seen in figures 4.11c and 4.11d. However, the error on these quantities is significantly higher and the difference between the two models is much more pronounced.

The new model proposed in this section can be seen to capture the trend in the TOKAM2D $k_\perp$ profile very well, while the steady state Bufferand profile seems to be too flat. However, the trend in the diffusion coefficient is more similar for both models, because of the different scaling with $k_\perp$ ($D \sim \sqrt{k_\perp}$ and $D_{Buff} \sim k_\perp$ respectively). From these results we conclude that the newly developed model correctly predicts $k_\perp$, as well as its relation to the diffusion coefficient. It is hoped that including these physics will provide a good basis to further elaborate the presented model to more complex plasma flow situations. On the other hand, the model proposed by Bufferand *et al.* appears to get the trend in the diffusion coefficient right, but uses an artificial quantity to predict it, which is more likely not to work anymore in more complex flow cases.

Figures 4.11e-4.11g show the source, the sink and the flux of $k_\perp$. These results indicate that both models manage to realistically predict the profiles of the terms in the $k_\perp$ equation. Note that the TOKAM2D reference data used for the sink in figure 4.11f is that of the opposite of the interchange term, $-G_k$, as that was also the data used to fit the total sink of $k_\perp$ in equation 4.38.

It is worth remarking that the model parameters used in the above simulations are those tuned on the global TOKAM2D simulation set, not to this single TOKAM2D simulation in particular. However, the model parameters are very well matched to this default TOKAM2D case since it lies in the middle of the parameter range investigated in the regression analyses (see appendix D). Figure 4.12 on the other hand gives an idea of the kind of errors that can be expected with varying TOKAM2D parameters. It shows a scatter plot of

(a) density

(b) particle flux

(c) diffusion coefficient

(d) turbulent kinetic energy

(e) interchange source of $k_\perp$

(f) turbulent kinetic energy sink

(g) turbulent kinetic energy flux
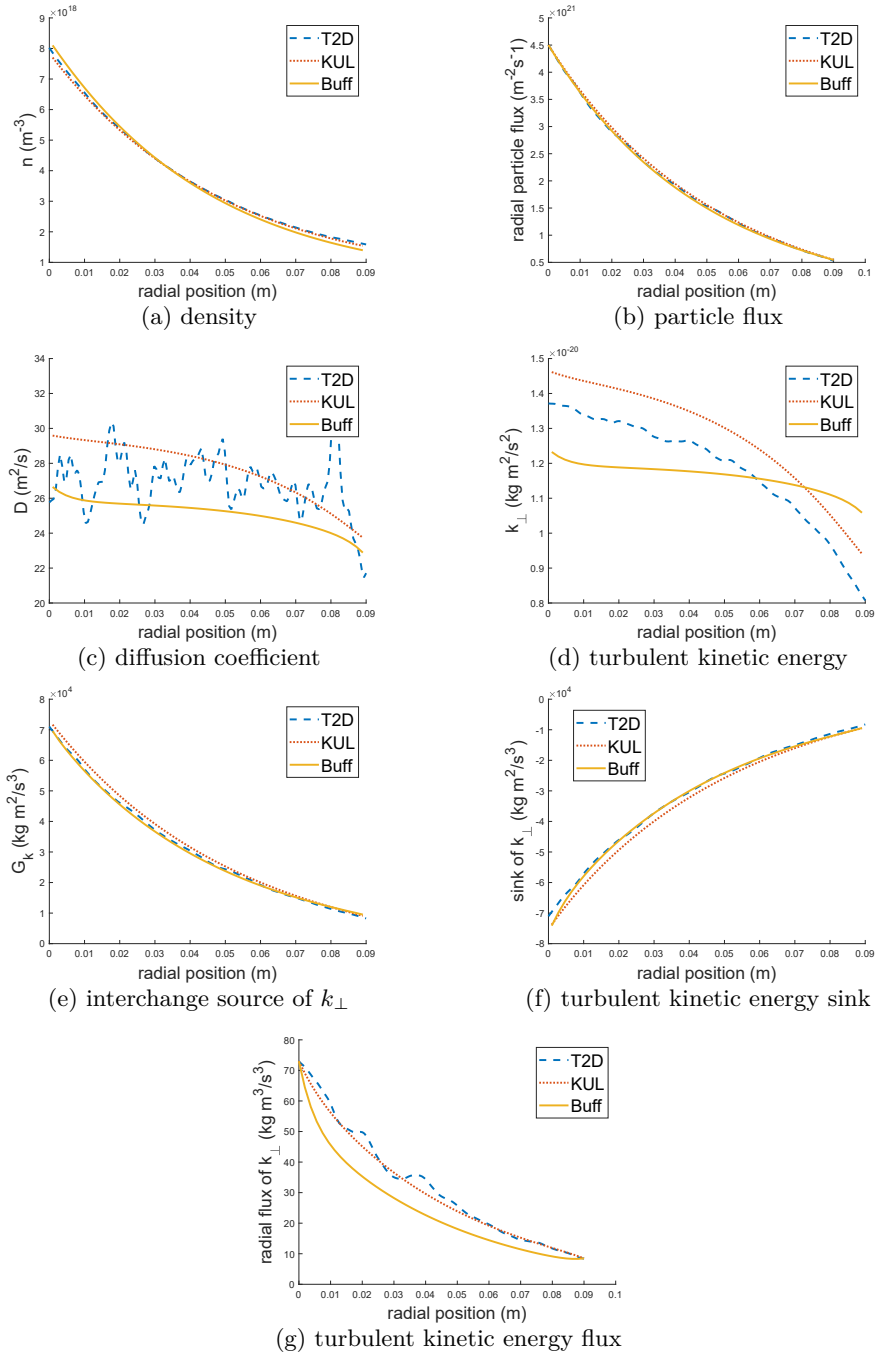
Figure 4.11: Comparison of radial profiles of a representative TOKAM2D simulation to forward mean-field DivOpt simulations with the KUL 4.36-4.40 and Bufferand 4.41-4.45 $k_\perp$ models.

the algebraic steady state local balance diffusion coefficients in equations 4.46 and 4.47. These expressions are evaluated using TOKAM2D data, and plotted versus the exact TOKAM2D diffusion coefficient. Each circle in figure 4.12 represents a single TOKAM2D simulation (i.e. fixed TOKAM2D parameters $g$, $T$, $L_{||}$,...) that is averaged in time and in the $x$ and $y$ directions. Thus, this figure is constructed by post-processing TOKAM2D data, no forward DivOpt simulations have been run to make it. The $R^2$ values shown in figure 4.12 are again calculated based on the radially averaged data points shown in the figure. Note that if they would be calculated using the radial profiles instead, the $R^2$ values would be significantly lower because the evaluation of the radial profile introduces a large amount of noise on the model data. As the radial trend in the diffusion coefficient profile is rather weak (see blue dotted line in figure 4.11c), the $R^2$ values would be dominated by this noise on the profile. Similar noise induced effects on the $R^2$ value were also observed in figure 4.10b. For the data in figures 4.8b and 4.9b which have stronger radial profiles, it may be beneficial to calculate the $R^2$ on the radial profiles, but this has not been done for the sake of comparison between the different models.

Note that figures with scatter plots of the diffusion coefficient, as figure 4.12, will be used throughout the text to assess the accuracy of the models across parameter space. The figures focus on the turbulent diffusion coefficient, since it most directly quantifies the strength of the turbulent transport which is ultimately of practical interest. If this quantity is predicted correctly, the mean-field turbulent particle flux is modelled correctly. Similarly, for the anisothermal cases that will be studied later, a correct prediction of the turbulent transport coefficients $D$, $\chi_i$ and $\chi_e$ (see equations 3.1-3.2)) implies that the mean-field turbulent particle and heat fluxes are modelled correctly. Often, the decay lengths of the density, temperature, pressure and the parallel heat flux profiles are considered as engineering quantities since they determine to a large extend the peakedness of the heat load deposited on the target plates. These decay lengths are basically determined by 1) the turbulent transport coefficients, 2) the parallel transport dynamics, and 3) mean-flow drifts. Since the parallel transport dynamics in the TOKAM2D are only modelled by artificial sink terms and mean-field drifts do not contribute to transport in TOKAM2D, it seems more sensible to stick purely to the turbulent transport coefficients.

Figure 4.12 seems to indicate that the newly proposed model manages to capture the scalings of the particle transport in TOKAM2D parameter space relatively well, although some scatter, error, does remain. Bufferand's model on the other hand appears to miss the trends in parameter space. Including a scaling with TOKAM2D parameters in the sink for $k_\perp$ in equations 4.43, as proposed in Refs. [11, 13, 12], might (partially) remedy this discrepancy. Upon running forward DivOpt simulations for a number of extreme values in figure
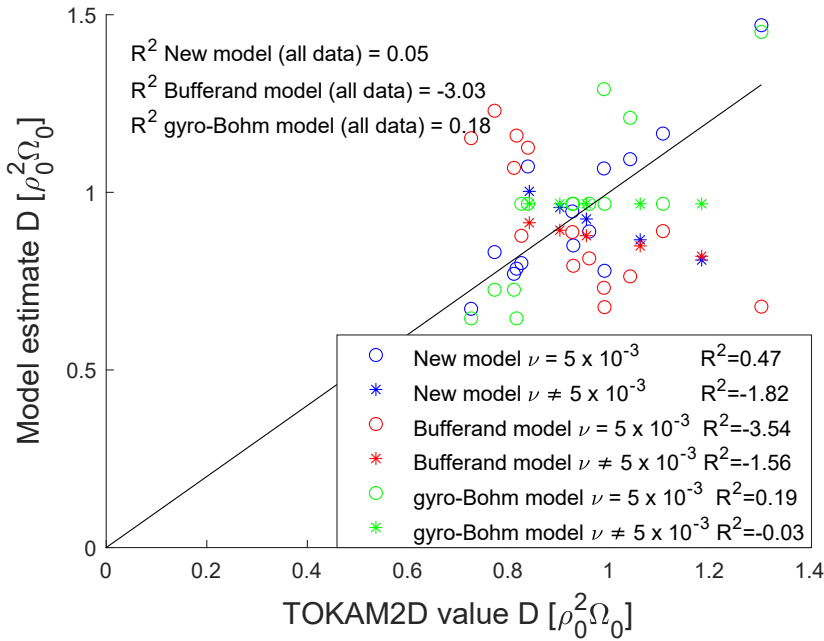
Figure 4.12: Scatter plot of the exact TOKAM2D diffusion coefficient versus model prediction for it. Newly proposed model 4.46 (blue markers), Bufferand model 4.47 (red markers) and gyro-Bohm scaling $D \sim gT_e^{3/2}$ (green markers). Each marker indicates the radial average of a single simulation in a database of TOKAM2D simulations.

4.12, the newly developed model managed to still capture the trends in the profiles, although larger errors than those in figures 4.11a-4.11g were observed as expected, confirming the results of figure 4.12.

It is also interesting to come back to the comparison between the $k_\perp$ model and the gyro-Bohm scaling 2.82. Some interesting parallels can be observed between the local-balance steady-state equivalent of the $\sqrt{k_\perp}$ model $D \sim -g\sqrt{L_{||}}c_s\partial_x \ln \bar{n}$ and the gyro-Bohm scaling which could be translated to TOKAM2D units as $D \sim -T_e^{3/2}\partial_x \ln \bar{n}$ or as $D \sim T_e^{3/2}g$. The $R^2$ depends on the assumptions of the appropriate perpendicular length scale (see section 4.3.2). Hence, the $k_\perp$ model includes adjustments with respect to either of the gyro-Bohm scalings, in terms of the temperatures, $L_{||}$ and $g$ or the perpendicular length scale. The latter form of the gyro-Bohm scaling has also been included

in figure 4.12. The general trend is captured less accurately by the gyro-Bohm model than by the $k_\perp$ model. However, it performs less badly for viscosity variations than the $k_\perp$ model. The first form of the gyro-Bohm scaling does not capture the trend at all and is not shown.

## 4.4   $k_\perp - \zeta_\perp$ model

While the $k_\perp$ model discussed in the previous section managed to fit turbulence reference data rather well over a range of TOKAM2D parameters, it was unable to capture some trends, especially those with varying viscosity. This may not be surprising as the viscous sink in the $k_\perp$ equation has been crudely aggregated in the single sink term which predominantly models the sheath loss of $k_\perp$. Indeed, the different sinks of the turbulent kinetic energy were lumped together in one contribution. In this section, based on Ref. [44], we aim to extend this model by including an equation for the turbulent enstrophy, as there are convincing physical grounds to expect the enstrophy to provide additional information about the turbulent transport in the plasma edge. Important arguments for this are that viscous dissipation of kinetic energy is closely related to the enstrophy and that enstrophy is a conserved scalar (like kinetic energy) in hydrodynamic, inviscid, 2D turbulence which has some similarities with the plasma edge turbulence considered here. Furthermore, it is concentrated on smaller length scales than the kinetic energy, hence providing additional information [4, 71, 169]. See section 3.1 for a more elaborate discussion of this. Note that in the remainder of this chapter, the symbol $\zeta_\perp$ will be used to denote the turbulent enstrophy that was denoted with $\zeta_{turb}$ before since the mean-field and total enstrophy will not be considered here.

This section is structured as follows. section 4.4.1 shows that the turbulent enstrophy ($\zeta_\perp$) can be combined with the turbulent kinetic energy to obtain an improved model for the turbulent particle diffusion coefficient. In addition, the turbulent enstrophy equation is used to evaluate the enstrophy balance using TOKAM2D reference data. Section 4.4.2 then develops a closed transport model for the combined $k_\perp - \zeta_\perp$ system and the average particle transport. Section 4.4.3 shows results obtained with the new model and compares them to the one-equation $k_\perp$ model.

### 4.4.1   Diffusion coefficient model and enstrophy balance

From the turbulent kinetic energy and the turbulent enstrophy, a characteristic time and length scale can be constructed. Using such dimensional combinations,

the turbulent diffusion coefficient is expected to scale as $D \sim k_\perp/\sqrt{\zeta_\perp}$. Note that this relation is the same in dimensional units and in dimensionless form. This is to be compared to the one-equation $k_\perp$ model that could only construct a velocity scale for the turbulence as only the turbulent kinetic energy was available. As a result, no dimensional scaling could be constructed for the diffusion coefficient with turbulent characteristics only. Instead, the scaling $D \sim \rho_0\sqrt{k_\perp}$ in dimensional units (see equation 4.34 and the explanation thereafter in section 4.3.2) is found. The global reference quantity $\rho_0$ seems somewhat odd in this expression, as a $k(-\varepsilon)$ model implies that turbulent transport can be described by local turbulent characteristics and does not depend on global reference quantities such as $\rho_0$.

Figure 4.13 compares both diffusive relations. The diffusion coefficient in this figure is calculated from the TOKAM2D data directly, while the models shown are estimates for the diffusion coefficient obtained using the new model proposed here and the $k_\perp$ only model from equation 4.34. Both diffusive models are evaluated using the exact TOKAM2D values for $k_\perp$ and $\zeta_\perp$. On the profile level (figure 4.13a), the differences between the $k_\perp$ and the $k_\perp - \zeta_\perp$ model are insignificant. Both $k_\perp$ and $\zeta_\perp$ are quantifiers of the turbulence intensity ($I$) with very similar trends in the radial profile. As a result, the radial profile of both diffusion models scales as $D \sim \sqrt{I}$.

The scatter plot in figure 4.13b illustrates trends across parameter space on the other hand. Each data point in the figure again represents a TOKAM2D simulation for a certain set of parameters of which the data are averaged in time and in the $x$- and $y$-directions. Results are shown for 18 simulations in which $g$, $L_{||}$, $\nu$ and $T_i$ are varied, see appendix D.1.3 for the exact simulation parameters. While the set of TOKAM2D simulations used in this section partly coincides with the simulations used in section 4.3, it is not identical. The horizontal axis in figure 4.13b represents the diffusion coefficient, while the vertical axis shows estimates for the diffusion coefficient obtained using the $k_\perp$ and the $k_\perp - \zeta_\perp$ models. While some scatter around the perfect fit line still remains, it is clear that the $k_\perp$-$\zeta_\perp$ estimate for the diffusion coefficient performs significantly better than the $k_\perp$ only estimate. This is confirmed by the $R^2$ values for the radially averaged data shown in table 4.1. In particular, the new model manages to capture trends with varying viscosity much better, confirming the hypothesis that the enstrophy is related to the viscous dissipation. It is to be remarked that the simulation set used in this section contains significantly more variations in the viscosity than the equation set used in section 4.3 such that this parameter becomes more important here. Note also that the parameter values used for the $k_\perp$ model are still those tuned for the initial data set of section 4.3.

Since the previous has clearly shown the turbulent enstrophy to be an interesting quantity for modelling the average particle flux, which is ultimately the term
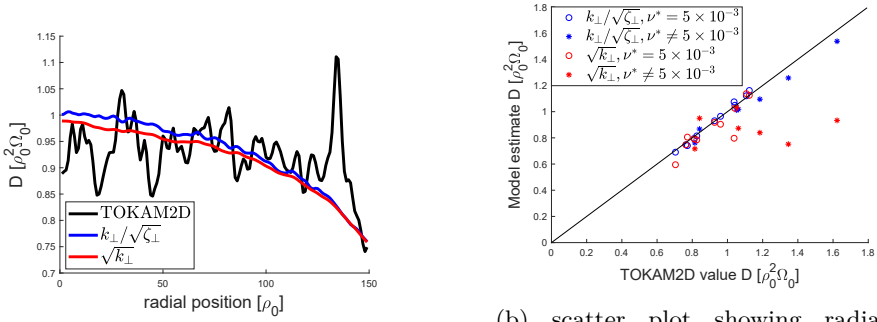
(a) radial profiles for a representative TOKAM2D simulation



(b) scatter plot showing radially averaged values for a database of TOKAM2D simulations

Figure 4.13: Comparison of $k_\perp - \zeta_\perp$ and $k_\perp$ diffusion models 4.34 and 4.49.

Table 4.1: Results of $R^2$ goodness of fit statistic of the radially averaged profiles for all terms in the $k_\perp$-only and $k_\perp - \zeta_\perp$ model. The table shows the $R^2$ values for the complete data set, for the subset with all simulations at $\nu = 5 \times 10^{-3}$ and the subset in which $\nu$ is varied.

| Model | term | $R^2$ for all cases | $R^2$ for $\nu = 5 \times 10^{-3}$ | $R^2$ for $\nu \neq 5 \times 10^{-3}$ |
|---|---|---|---|---|
| $k_\perp$ | $D = C_D \sqrt{k_\perp}$ | $-0.20$ | $0.65$ | $-1.07$ |
| | $S_k + \varepsilon_k = -C_{\|\|,k} \frac{c_S}{\sqrt{L_{\|\|}}} \bar{n} k_\perp$ | $0.74$ | $0.99$ | $0.54$ |
| $k_\perp - \zeta_\perp$ | $D = C_D \frac{k_\perp}{\sqrt{\zeta_\perp}}$ | $0.96$ | $0.98$ | $0.94$ |
| | $G_\zeta = gT\Gamma_{n,t,E} \frac{\zeta_\perp}{k_\perp}$ | $0.96$ | $0.96$ | $0.94$ |
| | $S_k = -C_{\|\|,k} \frac{c_s}{L_{\|\|} T_e^{0.75}} \frac{\bar{n} k_\perp^2}{\zeta_\perp}$ | $0.87$ | $0.95$ | $0.80$ |
| | $\varepsilon_k = -C_{\nu,k} \nu \bar{n} \zeta_\perp$ | $1.00$ | $1.00$ | $0.99$ |
| | $S_\zeta = -C_{\|\|,\zeta} \frac{c_s}{L_{\|\|} T_e} \bar{n} k_\perp$ | $0.99$ | $1.00$ | $0.97$ |
| | $\varepsilon_\zeta = -C_{\nu,\zeta} \nu \bar{n} \frac{\zeta_\perp^2}{k_\perp}$ | $0.77$ | $0.77$ | $0.67$ |

that needs to be closed, it is worthwhile to derive a model for the turbulent enstrophy. To this end, we start by evaluating the turbulent enstrophy equation 4.27 using TOKAM2D data. A balance of the different terms in this equation is shown in figure 4.14. This balance can be compared with the balance of the $k_\perp$ equation 4.16 in figure 4.6. Figure 4.14a clearly shows that the source of turbulent enstrophy, like that of turbulent kinetic energy, is dominated by the interchange term. However, sheath losses, viscosity and the subgrid dissipation seem to contribute almost equally to enstrophy losses, while the sink of the turbulent kinetic energy is dominated by the sheath losses only. Thus, these balances show that, as expected, $k_\perp$ and $\zeta_\perp$ have different characteristics. Figure 4.14b then plots separately the smaller contributions that where grouped as

(a) dominant terms
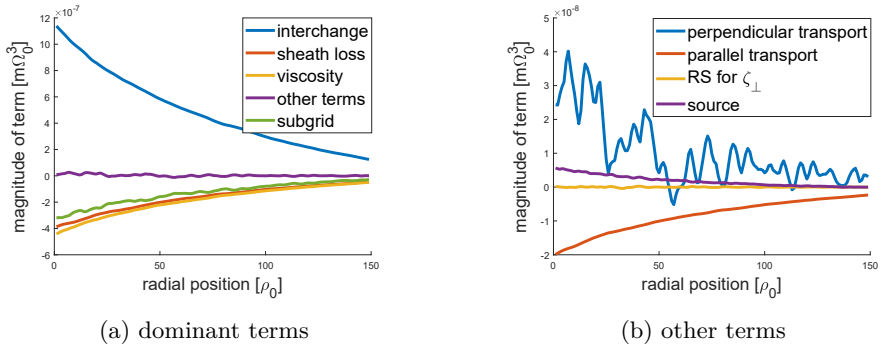
(b) other terms

Figure 4.14: Evaluation of terms in the TOKAM2D $\zeta_\perp$ equation 4.27.

"other terms" in figure 4.14a. In these figures, the transport terms in the left hand side of equation 4.27 have been moved to the right hand side (i.e. a minus sign was added to those terms).

The subgrid scale term is a numerical imbalance in the evaluation of the different terms in the corresponding equations, and is likely caused by numerical dissipation as a result of the second order WENO schemes [97, 110] that are used in TOKAM2D [46]. A grid refinement study confirmed the numerical nature of this term: relative errors on both the $k_\perp$ and $\zeta_\perp$ equations decrease as the grid and the time step are refined. Simultaneously, $k_\perp$ and $\zeta_\perp$ increase, as their respective sinks decrease in magnitude. The larger error on the $\zeta_\perp$ equation compared to the one on the $k_\perp$ equation is most likely a result of the enstrophy being concentrated on the smaller scales which suffer more from the discretization, while the kinetic energy is more strongly present on larger scales. This difference in length scale is the reason why viscous dissipation is much more important for the $\zeta_\perp$ than it is for $k_\perp$. These explanations are in accordance with the understanding of hydrodynamic 2D turbulence and its dual cascade picture [71, 169, 4]. A detailed description of the grid refinement analysis and its results can be found in appendix E.

## 4.4.2 Two-equation $k_\perp - \zeta_\perp$ model

This section proposes a model for the enstrophy equation derived in the previous section and integrates it in the mean-field transport model, together with the improved diffusive relation found in the previous section. The resulting two-equation $k_\perp$-$\zeta_\perp$ transport model proposed in this section is then

$$\frac{\partial \bar{n}}{\partial t} + \nabla \cdot (\bar{n} \bar{\mathbf{V}}_E + \mathbf{\Gamma}_{n,t,E} - D_0 \nabla_\perp \bar{n}) = \bar{S}_n - \frac{c_s \bar{n}}{L_{||}}, \quad (4.48)$$

$$\mathbf{\Gamma}_{n,t,E} = -C_D \frac{k_\perp}{\sqrt{\zeta_\perp}} \nabla_\perp \bar{n}, \quad (4.49)$$

$$\frac{\partial k_\perp}{\partial t} + \nabla \cdot \mathbf{\Gamma}_{k_\perp} = gT\Gamma_{n,t,E} - C_{||,k} \frac{c_s}{L_{||} T_e^{0.75}} \frac{\bar{n} k_\perp^2}{\zeta_\perp} - C_{\nu,k} \nu \bar{n} \zeta_\perp, \quad (4.50)$$

$$\frac{\partial \zeta_\perp}{\partial t} + \nabla \cdot \mathbf{\Gamma}_{\zeta_\perp} = C_{g,\zeta} gT\Gamma_{n,t,E} \frac{\zeta_\perp}{k_\perp} - C_{||,\zeta} \frac{c_s}{L_{||} T_e} \bar{n} k_\perp - C_{\nu,\zeta} \nu \bar{n} \frac{\zeta_\perp^2}{k_\perp}, \quad (4.51)$$

$$C_D = 7.71, \quad C_{||,k} = 4.43, \quad C_{\nu,k} = 1.85,$$

$$C_{g,\zeta} = 0.974, \quad C_{||,\zeta} = 2.02, \quad C_{\nu,\zeta} = 5.51. \quad (4.52)$$

The continuity equation 4.48 is the same as equation 4.36 from the one-equation $k_\perp$ model. The particle flux 4.49 is based on the diffusion coefficient proposed in section 4.4.1. Equation 4.50 for $k_\perp$ retains the analytically exact relation for the interchange source from the one-equation $k_\perp$ model i.e. $gT\Gamma_{n,t,E}$, while the sinks on the right hand side are now split into a sheath loss and a viscous contribution. Equation 4.51 for $\zeta_\perp$ features terms representing the same three effects: the interchange source, sheath losses and viscous dissipation. Other sources have been neglected in the $k_\perp$ and $\zeta_\perp$ equations at present as they appear to be small. The transport of $k_\perp$ and $\zeta_\perp$ on the RHS will also be neglected as this has also been observed to be small. All the model constants shown in 4.52 have been determined by means of a term-by-term regression analysis as described in 3.4.1, similar to the regression analysis performed for the $k_\perp$ model in section 4.3. The reference data used consisted of the results from the TOKAM2D simulations described in appendix D.1.3 that are averaged in time and in the diamagnetic $y$-direction. Table table 4.1 quantifies the goodness of fit of this regression analysis of the different terms and compares with the $k_\perp$-only model derived in section 4.3.

Now the rationale for the different models used in equations 4.50-4.51 is looked at in some more detail, starting with the visous dissipation terms. The visous dissipation of total enstrophy can be written as

$$\varepsilon_{Ek} \triangleq -\nu n \phi \nabla_\perp^2 W = -2\nu n \zeta_{tot} + \nu n \nabla \cdot (W \nabla_\perp \phi - \phi \nabla_\perp W). \quad (4.53)$$

Evaluating this expression using TOKAM2D data showed the first term related to the enstrophy to be the dominant, clearly establishing the relation between

viscous dissipation of kinetic energy and enstrophy. This is in line with the findings of hydrodynamic 2D turbulence [4, 71, 169]. It could also be remarked that the second term would presumably scale as $\nu n \nabla_\perp^2 E_{k,\perp}$, though it is found to be unimportant. The equivalent derivation for the viscous dissipation of the turbulent kinetic energy $\varepsilon_k \triangleq -\overline{\nu n \phi' \nabla_\perp^2 W}$ itself is significantly complicated by the fluctuations that are involved, and for that reason not used. It seems reasonable to model $\varepsilon_k$ based on a similar relation though, but using the turbulent enstrophy instead of the total enstrophy, i.e. $\varepsilon_k \approx -C_{\nu,k} \bar{n} \zeta_\perp$. This also explains that $C_{\nu,k}$ is approximately but not exactly equal to two. This model provides an excellent fit of the TOKAM2D data (see sixth row of table 4.1).

A similar derivation, again in agreement with hydrodynamic 2D turbulence [4, 71, 169], shows that the viscous dissipation of turbulent enstrophy is equal to

$$\varepsilon_\zeta \triangleq \overline{\nu n W'' \nabla_\perp^2 W''} = \nu n \overline{\frac{\nabla_\perp^2 W''^2}{2}} - 2\nu \overline{nP}, \tag{4.54}$$

where $P \triangleq (\nabla_\perp W'')^2 / 2$ is the turbulent palinstrophy. Evaluation of both contributions showed the first term to be negligible. A scaling for this turbulent palinstrophy is then constructed from $k_\perp$ and $\zeta_\perp$ based on dimensional arguments, i.e. $P \sim \zeta_\perp^2 / k_\perp$. The agreement between this model and the original TOKAM2D data is quite good, as can be seen in the last row of table 4.1.

Next we turn our attention to the enstrophy sheath loss term $S_\zeta$. Constructing a series expansion around $\bar{\phi}$ and $\tilde{T}_e$ yields

$$S_\zeta \triangleq \frac{1}{L_{||}} \overline{c_s n W'' (1 - \exp(\Lambda - \frac{\phi}{T_e}))} \tag{4.55}$$

$$\approx \frac{1}{L_{||}} (\frac{\overline{nW''\phi'}}{\tilde{T}_e} - \frac{\bar{\phi}}{\tilde{T}_e^2} \overline{nW''T_e''}) \sqrt{\tilde{T}} \exp(\Lambda - \frac{\bar{\phi}}{\tilde{T}_e}))$$

$$+ \frac{1}{L_{||}} \frac{\overline{nW''T''}}{2\sqrt{\tilde{T}}} (1 - \exp(\Lambda - \frac{\bar{\phi}}{\tilde{T}_e})), \tag{4.56}$$

where only fluctuations up to second order in $\phi$ and $T_e$ have been retained. In the isothermal case (i.e. $T_{i/e} = \tilde{T}_{i/e}$ and $T_{i/e}'' = 0$) considered here, only the first contribution to the first term is nonzero. The fluctuating part of this expression can be related to the turbulent kinetic energy. For the total term, we can write

$$nW\phi = \frac{n\nabla_\perp^2 \phi^2}{2} - 2nE_{k,\perp}. \tag{4.57}$$

Evaluating both contributions shows the second one to be dominant again. Then, assuming that the turbulent part of this term can be modelled based on the turbulent kinetic energy, and observing that $\exp\left(\Lambda - \frac{\bar{\phi}}{\tilde{T}_e}\right) \approx 1$, we obtain $S_\zeta \sim -2c_s n k_\perp/(L_{||}\tilde{T}_e)$. This model matches the TOKAM2D data extremely well (see table table 4.1), up to the factor 2 that is almost perfectly retrieved.

Thus, four of the six source terms in the $k_\perp$-$\zeta_\perp$ system are modeled based on physical and mathematical insights. The remaining terms, the sheath loss of $k_\perp$ and interchange source of $\zeta_\perp$, have been modeled purely based on regression analysis of TOKAM2D data. While the models for both terms manage to fit the data sufficiently well (see table 4.1), it is not clear if they really capture the underlying physics. Both are dominant terms in their respective equations and require further investigation. Hence, improvements in the model for these terms are expected to further enhance the performance of the transport model presented in this chapter.

We remark that both the one-equation $k_\perp$ model and the two-equation $k_\perp - \zeta_\perp$ model imply the same turbulence saturation mechanism, similar in nature to gradient removal assumptions [133, 114, 89]. The turbulent E×B particle flux (and hence density (pressure) gradient) appears directly in the source terms of the equations for $k_\perp$ and $\zeta_\perp$. Too steep gradients will lead to an increase in the turbulence intensity and resulting turbulent transport, tending to flatten out the gradients until a balance between particle flux and turbulence intensity is found. The sinks of both equations still scale linearly with the turbulence intensity $I$ assuming that both $k_\perp$ and $\zeta_\perp$ are quantifiers for this intensity, as argued before when discussing the diffusion coefficient scaling.

An interesting feature of the equation set above is that the RHS of the $k_\perp$ and $\zeta_\perp$ equations 4.50 and 4.51 differ only by a factor $\zeta_\perp/k_\perp$ and a number of constants. If the LHS is neglected (steady state and local balance assumed), this allows both equations to be written and solved together as a linear matrix system:

$$\begin{bmatrix} gT\Gamma_{n,t,E} \\ C_{g,\zeta} gT\Gamma_{n,t,E} \end{bmatrix} = \begin{bmatrix} \frac{C_{||,k}c_s}{L_{||}T_e^{0.75}} & C_{\nu,k}\nu \\ \frac{C_{||,\zeta}c_s}{L_{||}T_e} & C_{\nu,\zeta}\nu \end{bmatrix} \begin{bmatrix} \bar{n}\frac{k_\perp^2}{\zeta_\perp} \\ \bar{n}\zeta_\perp \end{bmatrix}. \tag{4.58}$$

It can be noted that the two-equation $k_\perp$-$\zeta_\perp$ approach to modelling turbulence bears a lot of similarity to $k$-$\varepsilon$ models that are commonly used to model hydrodynamic turbulence in a RANS approach [126, 34]. There as well, the combination of both quantities allows to construct a length and a time scale for the turbulence and sources and sinks of $k$ and $\epsilon$ differ by a factor $\varepsilon/k$. However, in the model presented here, both equations represent the evolution of a turbulent quantity and all of the terms in both equations have a clear physical

meaning, while in RANS modelling of hydrodynamic turbulence $\varepsilon$ is typically an ad-hoc quantity used to represent dissipation on the small scales.

### 4.4.3 Performance of the two-equation $k_\perp - \zeta_\perp$ model

This section presents results obtained with the new $k_\perp - \zeta_\perp$ model and compares them to the earlier $k_\perp$ model as well as to the original TOKAM2D data.

Figures 4.15b and 4.15d show scatter plots of the observed TOKAM2D values for $k_\perp$ and $\zeta_\perp$ versus the estimate for these quantities obtained with the two-equation $k_\perp$-$\zeta_\perp$ model and the one-equation $k_\perp$ model. The former estimate is obtained by solving system 4.58 for $k_\perp$ and $\zeta_\perp$ with all other quantities filled out using exact TOKAM2D data. Additionally, the TOKAM2D results for the subgrid model have been added to the left hand side of system 4.58 to cope with the large error on the enstrophy equation especially. The $k_\perp$ estimate for the one-equation $k_\perp$ model is likewise obtained from equation 4.33. However, no correction for the subgrid model is made in this case as this error is relatively small for the $k_\perp$ equation and because this subgrid dissipation is implicitly present in the sink constant of equation 4.33. Hence, figures 4.15b and 4.15d show that the newly developed model manages to capture the trends in the TOKAM2D parameter space very well, both for $k_\perp$ and $\zeta_\perp$. While some scatter around the perfect fit line does remain, this error is significantly smaller than that for the one equation $k_\perp$ model. In particular, the $k_\perp - \zeta_\perp$ model manages to capture variations in $\nu$ much better.

Figure 4.15f shows a similar scatter plot for the diffusion coefficient. The points indicated in this figure are obtained by filling out the model values for $k_\perp$ and $\zeta_\perp$ in particle transport relations 4.49 and 4.37 respectively. Figure 4.15f shows that the estimate of the diffusion coefficient of the two-equation $k_\perp$-$\zeta_\perp$ model is not unequivocally superior to that of the one-equation $k_\perp$ model. While the former seems to better capture the trend of the high $D$ simulations, it is still far from perfect. For the simulations at intermediate levels of $D$, the new model seems to perform slightly worse than the original one-equation model. This is rather surprising as it has clearly been shown that the diffusion relation is more reliable, that the estimate for $k_\perp$ is more accurate, and that the estimate for $\zeta_\perp$ looks very reasonable. It seems that the remaining errors on $k_\perp$ and $\zeta_\perp$ reinforce each other in the diffusive relation and cause the overall behavior to become less accurate. Section 4.5.2 will show that the diffusion relation found under steady state local balance assumptions is $D \sim g L_{||} T \Gamma_{n,t,E}/c_s$ for the $k_\perp - \zeta_\perp$ model, which is very close to the $k_\perp$ model scaling $D \sim g\sqrt{L_{||}} T \Gamma_{n,t,E}/c_s$. Hence, there is still no dependence on $\nu$ in the diffusion coefficient in the $k_\perp - \zeta_\perp$ model. The difference between both models as well as the dependence of the accuracy
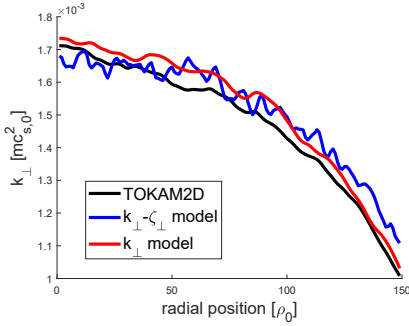
(a) radial profile of $k_\perp$
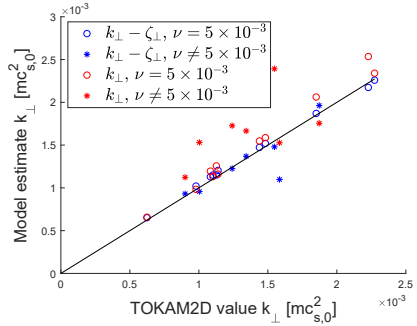
(b) scatter plot of $k_\perp$
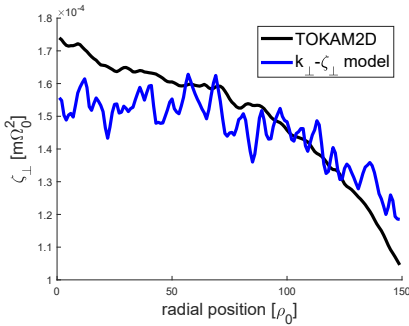
(c) radial profile of $\zeta_\perp$
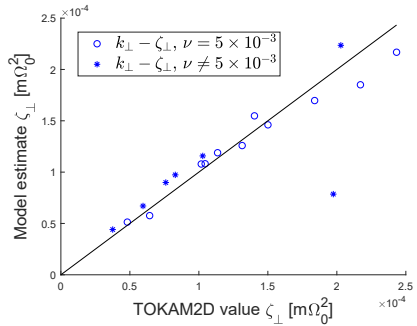
(d) scatter plot of $\zeta_\perp$
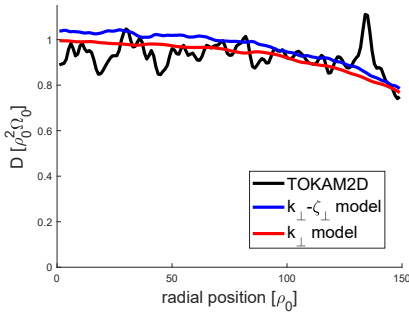
(e) radial profile of $D$
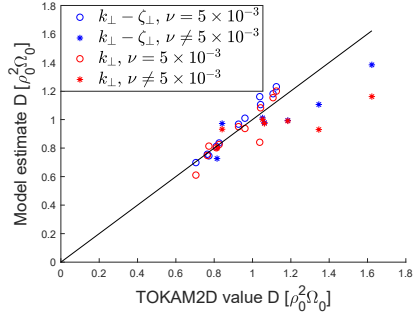
(f) scatter plot of $D$

Figure 4.15: Comparison of the performance of the $k_\perp - \zeta_\perp$ and $k_\perp$ model to the original TOKAM2D data. Radial profiles for a representative TOKAM2D simulation (left collumn) and scatter plots showing radially averaged values for a database of TOKAM2D simulations (right collumn).

on the value of the model constants will further be investigated in section 4.5. Further research is needed to determine the shortcomings of the models for the interchange source of $\zeta_\perp$ and sheath loss sink of $k_\perp$.

Figures 4.15a, 4.15c and 4.15e show the radial profiles of $k_\perp$, $\zeta_\perp$ and $D$ for the TOKAM2D simulation with the default parameter setting (see appendix D.1.1 for exact parameters). The figure shows that both models manage to capture the trends in the radial profiles rather well.

## 4.5   Bayesian model comparison

The parameters of the $k_\perp$ model in section 4.3 and the $k_\perp - \zeta_\perp$ model in section 4.4 have been determined through nonlinear least squares (LS) regression according to the methodology described in section 3.4.1. This section[5] discusses the results obtained by De Wolf *et al.* [50] who used the Bayesian inference framework outlined in section 3.4 to gain information and new insights on these plasma turbulence models, and to compare them. While Bayesian inference has already been used extensively in other fields, to our knowledge, De Wolf *et al.* use Bayesian analysis to infer about mean-field plasma turbulence models for the first time. Up till now, a framework for comparing the different models in an objective way was missing. Issues such as the amount of free parameters needed in a model and overfitting had not been considered in a systematic way, not for the empirical fitting of the diffusion coefficient discussed in section 2.3.2, nor for the RANS-like models discussed in sections 2.3.3, 4.3 and 4.4.

### 4.5.1   Bayesian inference for the submodels

De Wolf *et al.* analyse the models described earlier in this chapter in two steps. First, the models for the individual closure terms (i.e. model for the turbulent particle flux, model for the interchange source, model for the sheath loss sink,...) are inferred about individually. This is done by comparing the reference TOKAM2D output data (e.g. the $\mathbf{\Gamma}_{n,t,E}$ in equation 4.34) to the model evaluated with TOKAM2D input data (e.g. $k_\perp$ and $\bar{n}$ for equation 4.34) using a Bayesian methodology to infer about the unknown parameter (e.g. $C_D$ for equation 4.34). This allows to estimate the probability distribution of the unknown parameters as well as the Bayesian evidence for the considered

---

[5]This section discusses the results published in "De Wolf, R., Coosemans, R., Dekeyser, W., Baelmans, M. (2021). Bayesian approach to parameter estimation and model validation for nuclear fusion reactor mean-field edge turbulence modelling. *Nuclear Fusion*, 61:046048" [50].

Table 4.2: Results of the Bayesian submodels analysis. For each submodel, the table shows the parameter LS values [44, 46], the MAP of the posteriors for the constant $C$ and the error standard deviation $\sigma$ with their $2\sigma$ confidence interval, and the logevidence. Table adjusted from Ref. [50].

| Model | Submodel | LS value | $C$ | $\sigma_{rel}[\%]$ | $\ln \mathcal{L}(\mathcal{D}\vert\mathcal{M})$ |
|---|---|---|---|---|---|
| $k_\perp$ | $\mathbf{\Gamma}_{n,t,E}$ - $C_D$ | 23.9 | $25.19 \pm 0.22$ | $7.48 \pm 0.20$ | 19497 |
| | $S_k$ - $C_{\|\|,k}$ | 0.561 | $0.4854 \pm 0.0026$ | $4.79 \pm 0.13$ | 39379 |
| $k_\perp - \zeta_\perp$ | $\mathbf{\Gamma}_{n,t,E}$ - $C_D$ | 7.71 | $7.630 \pm 0.042$ | $4.84 \pm 0.13$ | 20671 |
| | $S_k$ - $C_{\|\|,k}$ | 4.43 | $4.4219 \pm 0.0020$ | $4.04 \pm 0.11$ | 39837 |
| | $\varepsilon_k$ - $C_{\nu,k}$ | 1.85 | $1.853 \pm 0.030$ | $1.47 \pm 0.04$ | 47606 |
| | $G_\zeta$ - $C_{g,\zeta}$ | 0.974 | $0.948 \pm 0.028$ | $2.62 \pm 0.07$ | 47230 |
| | $S_\zeta$ - $C_{\|\|,\zeta}$ | 2.02 | $2.0156 \pm 0.0022$ | $1.00 \pm 0.03$ | 52377 |
| | $\varepsilon_\zeta$ - $C_{\nu,\zeta}$ | 5.51 | $5.502 \pm 0.034$ | $5.51 \pm 0.15$ | 47695 |

submodels. Next, section 4.5.2 will discuss the results of the "full model" inference. The full models are the complete, self-consistent $k_\perp$ model 4.36-4.38 and $k_\perp - \zeta_\perp$ 4.48-4.51 models consisting of union of all the submodels. De Wolf *et al.* used the same 1D (radial) TOKAM2D data used for the $k_\perp - \zeta_\perp$ model as reference data. A detailed description of this data can be found in appendix D.1.3.

The results of the Bayesian analysis of the submodels is shown in table 4.2. Details on the Bayesian methodology and settings that have been used can be found in the original publication. Firstly, it can be seen that the Bayesian MAP values (listed in the fourth column) are in close correspondence to the LS values for the models reported in sections 4.3 and 4.4. The main difference is assumed to be due the correlation length that is taken into account, which effectively applies a different weighing to the data points. Also, the data set used for the least squares calibration of the $k_\perp$ submodels differs from the one used for the Bayesian inference here, see appendix D.1 for details.

Furthermore, the logevidence shown in table 4.2 allows to compare some of the submodels. Remember from section 3.4.2 that the evidence can only be compared when models explaining the same data are considered. Hence, the only comparisons that are possible is that for the particle flux $\mathbf{\Gamma}_{n,t,E}$ and for the sheath sink of the $k_\perp$ equation $S_k$. In both cases, the $k_\perp - \zeta_\perp$ submodels significantly outperform the $k_\perp$ variants. $\sigma_{rel}$ (defined in equation 3.64) denotes the standard deviation of the relative error between the model and the reference data. In general, it can be noticed to be rather low, below 10% for all models, indicating that the submodels are rather accurate.

## 4.5.2   Bayesian inference for the full models

Next, De Wolf *et al.* studied the full models, i.e. the complete $k_\perp$ model 4.36-4.38 and $k_\perp - \zeta_\perp$ 4.48-4.51 models consisting of combination of all the submodels. However, they simplified these models by neglecting the terms on the LHS of equations 4.38, 4.50 and 4.51, effectively assuming a steady-state local balance for $k_\perp$ and $\zeta_\perp$. As before, only the turbulent flux and the sheath loss sink of particles are retained in the continuity equation 4.36 or 4.48.

In addition to the previous simplification, De Wolf *et al.* set $C_{g,\zeta} = 1$ (in close correspondence with the value in table 4.2) to remove the linear dependency in the simplified form of equation 4.51, which would otherwise distort the Bayesian analysis of the $k_\perp - \zeta_\perp$ model inference. Moreover, they show that under these simplification, equations 4.50 and 4.51 of the $k_\perp - \zeta_\perp$ model can equivalently be written as

$$\bar{n} k_\perp = \sqrt{\frac{(C_{\nu,\zeta} - C_{\nu,k})(C_{||,k} - C_{||,\zeta})}{(C_{||,k} C_{\nu,\zeta} - C_{\nu,k} C_{||,\zeta})^2}} \frac{gT\Gamma_{n,t,E}}{\sqrt{\nu c_s / L_{||}}} \triangleq C_k \frac{gT\Gamma_{n,t,E}}{\sqrt{\nu c_s / L_{||}}}, \quad (4.59)$$

$$\bar{n}\zeta_\perp = \frac{C_{||,k} - C_{||,\zeta}}{C_{||,k} C_{\nu,\zeta} - C_{\nu,k} C_{||,\zeta}} \frac{gT\Gamma_{n,t,E}}{\nu} \triangleq C_\zeta \frac{gT\Gamma_{n,t,E}}{\nu}. \quad (4.60)$$

Hence, only two parameters suffice to characterise the behaviour of the reduced form of $k_\perp$-$\zeta_\perp$ system of equations 4.50-4.51 instead of four. This has strong implications for the Bayesian parameter estimation.

Since these models are self-consistent, no input reference data is required for the Bayesian analysis of these models (except for the boundary conditions), contrary to the submodel analysis. Reference output data is of course still required. De Wolf *et al.* choose a minimal set of meaningful summary quantities for this, consisting of $\Gamma_{n,t,E}$ and $k_\perp$. For the $k_\perp - \zeta_\perp$ model inference, $\zeta_\perp$ is added as well. These quantities are all combined in the likelihood function, each with their own nuisance parameter for the standard derivation for the error on them (see the original publication for a detailed description hereof). Allowing for this, the inference is 4 dimensional for the $k_\perp$ model (2 model parameters $C_D$ and $C_{||,k}$ and 2 nuisance parameters $\sigma_\Gamma$ and $\sigma_{k_\perp}$) and 8 dimensional for the $k_\perp - \zeta_\perp$ model (5 remaining model parameters $C_D$, $C_{||,k}$, $C_{\nu,k}$, $C_{||,\zeta}$ and $C_{\nu,\zeta}$ when $C_{g,\zeta} = 1$ and 3 nuisance parameters $\sigma_\Gamma$, $\sigma_{k_\perp}$ and $\sigma_{\zeta_\perp}$). Using equation 4.59 and 4.60, inferences will be run for a reduced form of the $k_\perp - \zeta_\perp$ model later.

Table 4.3: MAP values of the submodels and full models inferences. Submodels analyses have been performed twice: once with only physical submodel reference data, and once with numerical dissipation errors of the TOKAM2D data were included in the reference data. Table adapted from Ref. [50].

| Model | $k_\perp$ model | | $k_\perp - \zeta_\perp$ model | | | | | |
|---|---|---|---|---|---|---|---|---|
| | $C_D$ | $C_{||,k}$ | $C_D$ | $C_{||,k}$ | $C_{\nu,k}$ | $C_{g,\zeta}$ | $C_{||,\zeta}$ | $C_{\nu,\zeta}$ |
| Submodels, physical | 25.2 | 0.485 | 7.63 | 4.42 | 1.85 | 0.948 | 2.02 | 5.50 |
| Submodels, adjusted | 25.2 | 0.577 | 7.63 | 4.27 | 2.54 | 0.948 | 1.97 | 7.12 |
| Full model | 24.8 | 0.587 | 7.75 | 4.92 | 2.54 | / | 1.97 | 11.0* |

*values corrected for $C_{inter,\zeta} = 1$

## Full model inferences

The resulting Bayesian analysis showed that all parameters of the $k_\perp$ model are well-informed, the posteriors take a Gaussian shape with parameter correlations that can readily be explained physically. Table 4.3 then compares the MAP values between the submodels and the full model. In the second row of this table, the submodel values are adjusted to better match the intended behaviour of the full model. For the $k_\perp$ model this is done by fitting the sheath loss model in the $k_\perp$ equation not to reference data from this term exactly, but against the interchange term which it needs to compensate. Note that this was also done in section 4.3.3. These adjusted submodel MAP values can be seen to match the full model values very closely. The compatibility between the full model and submodel results indicates that the $k_\perp$ model captures the underlying dynamics well and does not exploit its larger parameter freedom to overcome model deficiencies. Furthermore, the consistent performance of the model for a set of reference data containing different quantities than the submodels testifies to the robustness of the model.

For the $k_\perp - \zeta_\perp$ model on the other hand, De Wolf *et al.* found that very strong correlations between parameters are present and that most of the parameters are poorly informed. The reason for this is that the four remaining physical parameters of the reduced form of $k_\perp$ and $\zeta_\perp$ equations 4.50-4.51 can be exactly reduced to the two parameters in equations 4.59-4.60. As a result, the inference problem is unidentifiable because any set of model parameters $C_{||,k}$, $C_{\nu,k}$, $C_{||,\zeta}$ and $C_{\nu,\zeta}$ that leads to the same value of $C_k$ and $C_\zeta$ will have the same posterior value. Hence, the 4D $C_{||,k} - C_{\nu,k} - C_{||,\zeta} - C_{\nu,\zeta}$ parameter space contains 2D manifolds that all lead to the same posterior. Note that the Bayesian techniques did correctly handle this unidentifiable problem, while the peculiar results give an indication of the dependencies in the initial model. To prove the above

reasoning, De Wolf *et al.* calculated $C_k$ and $C_\zeta$ according to equations 4.59-4.60 for each of the parameter samples, and thus constructed the posterior of the "reparameterised" samples. This posterior takes a much more regular form with quasi-Gaussian distributions and well identified parameters.

Table 4.3 compares the MAP values of the submodels and the full model. The submodel values of $C_{||,k}$ and $C_{||,\zeta}$ are adjusted by fitting the sheath loss models of both $k_\perp$ and $\zeta_\perp$ to the interchange term minus the viscous dissipation minus the subgrid term. $C_{\nu,k}$ and $C_{\nu,\zeta}$ are then adjusted by matching the viscous dissipation models for $k_\perp$ and $\zeta_\perp$ to the viscous dissipation plus the subgrid term. The subgrid term is attributed to the viscous dissipation because it is likewise assumed to behave like numerical viscous dissipation at small length scales. The results for the full model in table 4.3 are also manipulated. The effective MAP point identified by the Bayesian inference has been replaced by an equivalent point with the same $C_k$ and $C_\zeta$ and thus the same posterior value (still equal to MAP). To ease the comparison with the submodel values, this new point is chosen such that it matches the $C_{\nu,k}$ and $C_{||,\zeta}$ values of the submodel (which are assumed to be the most physically informed). Significant differences between the submodel and full model values persist, indicating that the full $k_\perp - \zeta_\perp$ model may be using the freedom its parameters provide to compensate for model deficiencies.

### $k_\perp$ vs. $k_\perp - \zeta_\perp$ model

Finally, De Wolf *et al.* compare the full $k_\perp$ and $k_\perp - \zeta_\perp$ models with each other using the Bayesian evidence. In order for the evidence to be comparable, the same reference needs to be used for both models though. However, by default the $k_\perp - \zeta_\perp$ model uses the enstrophy in the likelihood function, while the $k_\perp$ model does not. To remedy this difference, equations 4.59-4.60 are exploited to construct an equivalent, reduced $k_\perp - \zeta_\perp$ model that does not predict $\zeta_\perp$ (or need data for it) but still produces the same predictions for $\mathbf{\Gamma}_{n,t,E}$ and $k_\perp$. As discussed in section 3.4.2, the prior distribution likewise influences the model evidence. Since no (independent) information on the parameter values is available a priori, De Wolf *et al.* use uniform priors which are cut-off at a high value. While the value of this cut-off is arbitrary, it was observed that the exact value had little effect on the model evidence.

The results of the evidence and the model errors for the different models are summarised in table 4.4. While the results for the relative model error standard deviation are inconclusive, both the maximum and the logevidence indicate that the $k_\perp$ model outperforms the $k_\perp - \zeta_\perp$ model for the considered data set. Note that the evidence cannot be compared between the regular enstrophy model in

Table 4.4: Comparison of model error standard deviation and loglikelihood at MAP and logevidences of the different full models. Table adapted from Ref. [50].

| | $\sigma$ [%] | | | | |
| Model | $\bar{\Gamma}_{E,t}$ | $k_\perp$ | $\zeta_\perp$ | $\mathcal{L}_{max}$ | Logevidence |
|---|---|---|---|---|---|
| $k_\perp$ model | 8.8 | 7.3 | / | 39083 | 39060 |
| $k_\perp - \zeta_\perp$ model | 7.2 | 11.4 | 14.1 | 64159 | 64123 |
| $k_\perp - \zeta_\perp$ model, reduced | 7.2 | 11.4 | / | 38465 | 38443 |

the second row of the table and the other models because this inference includes the enstrophy in the likelihood function.

## 4.5.3 Discussion

The above analysis showed that while $k_\perp$-only submodels were outperformed by their $k_\perp - \zeta_\perp$ counterparts, the simpler full $k_\perp$ model as a whole has a higher Bayesian evidence than the full $k_\perp - \zeta_\perp$ model. These seemingly contradictory results may be due to the deficiencies in submodels in the $k_\perp - \zeta_\perp$ model that have no equivalent in the $k_\perp$ model. Also, as remarked in section 4.4 already, the full $k_\perp - \zeta_\perp$ model may combine the submodels in such a way that the submodel errors reinforce one-another and lead to less accurate predictions as a whole. Further research into this is required to overcome the deficiencies in the present model form.

Furthermore, it was observed that the posterior distribution of the full $k_\perp$ model matches the posterior of the submodel analysis rather well. This indicates that the $k_\perp$ model uses the underlying physics of the submodels as intended. The full model posterior of the $k_\perp - \zeta_\perp$ model on the other hand differs markedly from the submodel posterior, even after removing the redundancy in the specification this model. This may indicate that the $k_\perp - \zeta_\perp$ full model uses its parameter freedom to compensate for model deficiencies, and hence that it does not capture the underlying physics.

Finally, it needs to be recalled that De Wolf *et al.*, considered reduced versions of the turbulent transport models, in which the transport of turbulent kinetic energy and enstrophy themselves have been neglected. Neglecting the transport of $k_\perp$ and $\zeta_\perp$ may be a good approximation in the 1D isothermal SOL case studied here, but it is expected that these terms come into play in more general flow cases which will ultimately be of practical interest. When these transport

terms are important, the $k_\perp - \zeta_\perp$ full model can no longer be reduced to an equivalent form with less parameters.

## 4.6 Conclusion

This chapter has applied the approach and the framework presented in chapter 3 to develop a physics-based mean-field transport model for a reduced flow case as a first step towards the development of a more generally valid model. Different models for the E×B turbulent particle flux in isothermal interchange-dominated electrostatic SOL plasmas have been developed, calibrated and compared, based on data from the TOKAM2D turbulence code.

To support the model development process, the TOKAM2D turbulence code model itself has first been introduced and the main assumptions in it discussed. Mean-field equations for this code have been derived using the methodology introduced in chapter 3. In particular, analytical equations for the turbulent kinetic energy ($k_\perp$) and turbulent enstrophy ($\zeta_\perp$) have been derived. It has been shown that the main driver of the turbulent kinetic energy balance is dominated by the interchange source while a sink due to parallel current losses to the sheath provides the main sink. For the turbulent enstrophy, the interchange term likewise constitutes the main source, but now the loss to the sheath and viscous dissipation are both important. Perpendicular transport seemed to play a minor role in the balances for $k_\perp$ and $\zeta_\perp$.

Following the ansatz presented in chapter 3, transport models were developed by relating the turbulent diffusion coefficient $D$ to characteristics of the turbulence. This lead to the $k_\perp$ and the $k_\perp - \zeta_\perp$ model. In the $k_\perp$ model, the turbulent diffusion coefficient is modelled as $D \sim \sqrt{k_\perp}$, which followed from a regression analysis of averaged TOKAM2D data. This can be seen as a refinement of the Bohm scaling. The interchange source of $k_\perp$ is modelled using the analytical relation with the average particle (heat) flux, which directly leads to ballooning effects, especially in 1D geometries. A regression analysis has identified a model for the sheath loss sink that is linear in the turbulent kinetic energy. Combining the latter three elements, a closed model for the radial particle flux is obtained. The transport in this model is determined by mean-flow gradients and the turbulence level, whose source is in turn controlled by the particle transport, while parallel dissipation due to the sheath suffices to saturate the turbulence. The implementation of this model in a 1D mean-field code has been shown to be capable of reproducing the TOKAM2D results with high accuracy. Moreover, the new model provides an improvement over both the Bohm and the gyro-Bohm scalings.

The $k_\perp - \zeta_\perp$ model refined the $k_\perp$ model by relating the turbulent diffusion coefficient as $D \sim k_\perp / \sqrt{\zeta_\perp}$. This scaling performs substantially better over a range of TOKAM2D parameters, especially for varying viscosity, which was found to be a weakness of the $k_\perp$ model. Moreover, the inclusion of the enstrophy provided a quasi-analytical model for the viscous dissipation of $k_\perp$ which is now included as a separate sink. To use these improved models, the enstrophy equation was likewise modelled. Models for the dominant terms are developed through a combination of analytical derivations, dimensional scalings, and regression analysis. The results obtained by De Wolf *et al.* showed that the submodel components of the $k_\perp - \zeta_\perp$ model are indeed superior to those of the $k_\perp$ model. However, the full model as a combination of these submodels was found to do less well than the $k_\perp$ model. This is most likely due to the unfortunate alignment of errors in the submodels in the full $k_\perp - \zeta_\perp$ model. Further research into this is required to overcome the deficiencies in the present model form.

The results of these relatively simple models are promising and encourage their further development. Moreover, the models developed in this section can already be implemented in 2D mean-field codes as a first step towards a physics-based description of the turbulent transport. To this end, Carli *et al.* [39] have implemented a model based on the $k_\perp$ model in the SOLPS-ITER mean-field code. However, several effects that are expected to be important are not addressed yet. No strong shear flows developed in the considered isothermal SOL cases and their effect on the turbulence and the transport has thus not been considered. However, strong flow shear may provide an additional or alternative saturation mechanism for the turbulence (in parts of the domain) through the Reynolds stresses in more general flow cases. Furthermore, not only the interchange channel may be important to drive the turbulence, but also the drift wave channel and possibly others. To study these effects, the next chapter will add a core region to the TOKAM2D simulations by which DW-like dynamics and strong flow shear are introduced in the simulations. Another element missing in this chapter is the effect of temperature variations and fluctuations. This will be investigated in chapter 6, where the turbulent heat fluxes that result of this will also be modelled. Chapter 7 will then provide a preliminary analysis of how the results obtained for the 2D TOKAM2D case compare to turbulence simulations resolved in 3D. This allows a more profound analysis of the DW dynamics and to distinguish them from parallel transport.

# Chapter 5

# 2D isothermal E×B drift turbulence: extensions

In the previous chapter, self-consistent anomalous transport models were derived for the SOL based on the RANS approach. Two models were presented: a one-equation $k_\perp$ model and a two-equation $k_\perp - \zeta_\perp$ model. While the previous chapter strictly treated 2D isothermal interchange-dominated SOL plasmas, this chapter will slightly extend the scope to take some important additional effects into account. First, section 5.1 will investigate the influence of flow shear on the particle transport relation, which only plays a significant role in more complex cases. We will still consider the purely E×B case with $W = \nabla_\perp^2 \phi$ in this section. Section 5.2 will then consider the effect of using the total (E×B and diamagnetic drift) vorticity $W = \nabla_\perp^2 \phi + \nabla \cdot \frac{\nabla_\perp p_i}{n}$. This amounts to including the inertia of the ion diamagnetic flow in the equation set.

## 5.1   Extension to core region

While the previous chapter has only considered the SOL, also the outer core region will be studied in this section[1]. To this end, the TOKAM2D domain will

---

[1]Parts of this section have been published in "Coosemans, R., Dekeyser, W., Baelmans, M. (2021). Bayesian analysis of turbulent transport coefficients in 2D interchange dominated E×B turbulence involving flow shear. *Journal of Physics: Conference Series*, 1785:012001" [45] and in "Coosemans, R., Dekeyser, W., Baelmans, M. (2021). Turbulent kinetic energy in 2D isothermal interchange-dominated scrape-off layer E×B drift turbulence: Governing equation and relation to particle transport. *Physics of Plasmas*, 28:012302" [46].

be extended to also include a part of the core region, where a drift-wave-like model has been implemented. Around the separatrix, strong shear flows in the diamagnetic direction will result —a phenomenon that was almost absent in the previous isothermal SOL-only simulations. The focus of this section will be to study the effect of this flow shear on the particle transport relation. This will be assisted by the Bayesian framework discussed in section 3.4.

In the isothermal SOL case considered before, the electrostatic potential was to a large degree set by the sheath potential. As a result, no significant E×B flow in the diamagnetic y-direction could develop. If the electrostatic potential has more freedom to develop, strong E×B flows tend to evolve in the y-direction, especially around the separatrix, the boundary between the SOL and the core region. In the presence of radial shear of the E×B velocity in the y-direction, these flows are (partly) maintained by extracting energy from the turbulence through the Reynolds stress terms $(n\overline{\mathbf{V}''_{E,x}\mathbf{V}''_{E,y}} : (\nabla_x \tilde{\mathbf{V}}_{E,y})^T$ on the RHS of equations 4.13 and 4.16). While the turbulence saturates due to currents to the sheath in the $k_\perp$ model 4.38 developed in section 4.3, this interaction between turbulence and sheared E×B flows provides an alternative saturation mechanism for the turbulence [58, 76, 108, 93]. Hence, it is expected that shear flows, and especially a radial shear of flow in the diamagnetic direction, will reduce the turbulent transport as well as the turbulent kinetic energy [23, 88, 144, 58, 146, 56, 108, 93].

To integrate this interaction between turbulence and flow shear into the $k_\perp$ transport model, the Reynolds stress term in the exact $k_\perp$ equation 4.16 would need to be added to model the effect of flow shear in the $k_\perp$ model equation 4.38. This requires a closure model for both the Reynolds stresses $\overline{n\mathbf{V}''_E\mathbf{V}''_E}$ themselves and a model (equation) for the mean E×B flow in the diamagnetic direction $\tilde{\mathbf{V}}_{E,y}$. Manz *et al.* [108] analysed this using a mean-field versus turbulent kinetic energy approach, while Held *et al.* [93] made use of Favre averaging to further disentangle the various contributions to shear flow generation. In addition to this, the radial turbulent diffusion coefficient might also need to be adjusted for the presence of flow shear. This section will focus on the latter element, proposing new particle transport relations that explicitly account for flow shear. This analysis will furthermore demonstrate the capabilities of Bayesian techniques, and provide guidance to further improve the mean-field turbulent particle transport models.

The remainder of this section is structured as follows. In section 5.1.1, the drift-wave-like model used in the core region of the TOKAM2D turbulence code is introduced. Next, alternative mean-field models for the particle transport closure term are proposed in section 5.1.3. Then, in section 5.1.4, Bayesian inference techniques are applied to study the performance of both the existing

$k_\perp$ and $k_\perp - \zeta_\perp$ particle transport models and the newly suggested ones for the new data. Finally, section 5.1.5 provides a discussion of the results and summarises the main findings of this work.

## 5.1.1 Turbulent equations and reference data

Garcia *et al.* [76] and Nielsen *et al.* [119] have already reported the appearance of strong flows in the diamagnetic direction in 2D turbulence simulations of the complete edge region, including both the SOL and the edge region inside the separatrix. This section extends the TOKAM2D code to also contain a core region with drift wave-like dynamics. For generality, the core region extension of the TOKAM2D model will be discussed for the anisothermal case. The equations now become

$$\frac{\partial n}{\partial t} + \mathbf{V}_E \cdot \nabla n - D_0 \nabla_\perp^2 n = S_n + S_{||,ne}, \tag{5.1}$$

$$\frac{\partial W}{\partial t} + \mathbf{V}_E \cdot \nabla W - \nu_0 n \nabla_\perp^2 W = \frac{S_{||,ne} - S_{||,ni}}{n} - \frac{g}{n}\frac{\partial p}{\partial y}, \tag{5.2}$$

$$\frac{\partial p_i}{\partial t} + \mathbf{V}_E \cdot \nabla p_i - \chi_0 \nabla_\perp^2 p_i = S_{p_i} + S_{||,pi} - \frac{2m_e}{m_i}\frac{p_i - p_e}{\tau_{ei}}, \tag{5.3}$$

$$\frac{\partial p_e}{\partial t} + \mathbf{V}_E \cdot \nabla p_e - \chi_0 \nabla_\perp^2 p_e = S_{p_e} + S_{||,pe} + \frac{2m_e}{m_i}\frac{p_i - p_e}{\tau_{ei}}. \tag{5.4}$$

Remember that the direction parallel to the magnetic field is not resolved in TOKAM2D. Instead, the behaviour in the parallel direction is modelled using the artificial volumetric sources $S_{||,ni/e}$ and $S_{||,pi/e}$. In the SOL region, these sources represent the fluxes towards the plasma sheath at which the magnetic field lines end in this open field line region. They take the following form:

$$S_{||,ne} \triangleq -\frac{c_s n}{L_{||}} \exp(\Lambda - \frac{\phi}{T_e}), \qquad S_{||,ni} \triangleq -\frac{c_s n}{L_{||}},$$

$$S_{||,pi/e} \triangleq \frac{2}{3}\gamma_{i/e}T_{i/e}S_{||,ni/e}. \tag{5.5}$$

Hence, in the SOL, nothing has changed and the equations are exactly the same as B.21-B.22 presented in appendix B.1. However, a core region is now added as well, where the sources for the equations are

$$S_{||,ne} \triangleq K_{DW}[(\phi - T_e \ln n - 1.71 T_e) - \langle \phi - T_e \ln n - 1.71 T_e \rangle_y],$$

$$S_{||,ni} \triangleq 0, \qquad S_{||,pi} = 0, \qquad S_{||,pe} \triangleq \frac{2}{3} \phi S_{||,ne}. \qquad (5.6)$$

$K_{DW}$ is a new parameter determining the strength of the parallel drift wave (DW) dynamics and $\langle u \rangle_y = \int_0^{L_y} u \, dy / L_y$ denotes the diamagnetic ($y$-direction) average of $u$, with $L_y$ the diamagnetic length of the domain.

These sources in the core region have been added to give a 2D representation of DW characteristics. They are derived from the electron momentum balance $\eta_{||} n J_{||} = \nabla_{||} p_e - n \nabla_{||} \phi + 0.71 n \nabla_{||} T_e$ (see equation 2.45, with $\partial A_{||} / \partial t$ neglected in the electrostatic case). Solving for $J_{||}$ and taking the divergence, we find

$$\nabla \cdot \mathbf{J}_{||} = \nabla \cdot \frac{1}{\eta_{||}} (T_e \nabla_{||} \ln n + 1.71 \nabla_{||} Te - \nabla_{||} \phi), \qquad (5.7)$$

Replacing the parallel gradient operators in this expression with a characteristic parallel wave number $i\mathbf{K}_{||}$ and defining $K_{DW} = \mathbf{K}_{||}^2 / \eta_{||}$, we obtain $\nabla \cdot \mathbf{J}_{||} \approx K_{DW}(\phi - T_e \ln n - 1.71 T_e)$. In the final source term, the flux surface (diamagnetic) average of this term is subtracted to ensure zero net divergence of the parallel current on a flux surface. This term leads to the typical DW physics where the potential fluctuations tend to follow the density fluctuations. Note that the $S_{||,ne}$ term used here matches the parallel term in Ref. [93] in the isothermal case and is similar to the parallel term used in the core region in the HESEL code [119]. The $S_{||,pe}$ term in the core region is chosen to represent the DW coupling between kinetic energy and electron thermal energy. By the implementation chosen here, the total kinetic energy injected (or extracted) through the DW term in the vorticity equation is provided by (or to) the electron thermal energy. This is in accordance with the DW energy transfer channel discussed in section 3.2.5 (for the electrostatic case).

In the isothermal SOL case studied earlier, only equations 5.1-5.2 were solved, while the ion and electron temperature were assumed to be constant in space and time and the DW-like terms were not active. In that scenario, only the interchange instability was present to drive the turbulence. A description of the linear spectrum and the turbulence characterics for this case can be found in Ref. [116]. In this section, we will compare the results of this original case to the isothermal case with a core region where the DW-like terms come into play. It is clear that this term introduces a DW-like instability in the core region in addition to the interchange instability still at play. Note that only a subset of

the full TOKAM2D equations is solved in the isothermal case considered in this section, i.e. the thermal energy equations 5.3 and 5.4 are not solved.

Both for the regular case and for the new case with a core region, a set of simulations has been performed. Details can be found in appendix D.1.4 and D.2. We will refer to the resulting data sets as *iso* and *isoDW* respectively.

## 5.1.2  Influence of the core region on the general flow picture

In order to give an idea of the dynamics introduced by adding the core region in TOKAM2D, this section briefly discusses the general flow picture that is established as well as the balances of $k_\perp$ and $\zeta_\perp$. Firstly, the addition of the core region leads to fluctuations on very long time scales (in the order of several hundred thousands of gyro-periods $\Omega_0^{-1}$). These transients seem to be related to flow shear building up, suppressing the turbulence more and more, only to be broken up again by a sudden turbulent outburst. It needs to be remarked that (for reasons of computational time) the data analysed in this section might not suffice to fully resolve the statistics of these slow transients. Nonetheless, the averages of this data can be expected to provide a good view on the trends to be expected.

Figure 5.1 shows the averaged radial profiles of selected quantities for a typical *isoDW* simulation. Figure 5.1b illustrates that the electrostatic potential has a deep well in the core region ($x < 0$), while it is still flat in the SOL ($x > 0$). This implies strong flow shear in the core region and around the separatrix ($x = 0$), since the flow shear $S \triangleq \partial_x V_{E,y} \triangleq \partial_x^2 \phi$. Presumably as a result of this flow shear, the density gradients in the core region are much steeper than those in the SOL, see figure 5.1a. Note that the very high core density in comparison to the SOL density is artificial, not representative for real tokamaks. The magnitude of the electrostatic potential well might also be exaggerated. The mean-field components of the kinetic energy and the enstrophy are dominant in the core region because of the large mean-flow velocity and mean-flow shear, as shown in figures 5.1c and 5.1d. Moreover, the turbulent kinetic energy and enstrophy are suppressed in this region. In the SOL on the other hand, the turbulent components still dominate.

Figure 5.2 then shows the balances of $k_\perp$ and $\zeta_\perp$ for this simulation. These balances are calculated by evaluating equations 4.16 and 4.27. The only difference is that the parallel current terms (second term on the RHS of both equations) are now calculated as $\overline{\phi'(S_{||,ni} - S_{||,ne})'}$ for $k_\perp$ and $\overline{W'(S_{||,ne} - S_{||,ni})'}$ for $\zeta_\perp$. Since the parallel sources are different in the core region and the SOL, the parallel current terms change character across the

(a) density



(b) electrostatic potential



(c) kinetic energies



(d) enstrophies
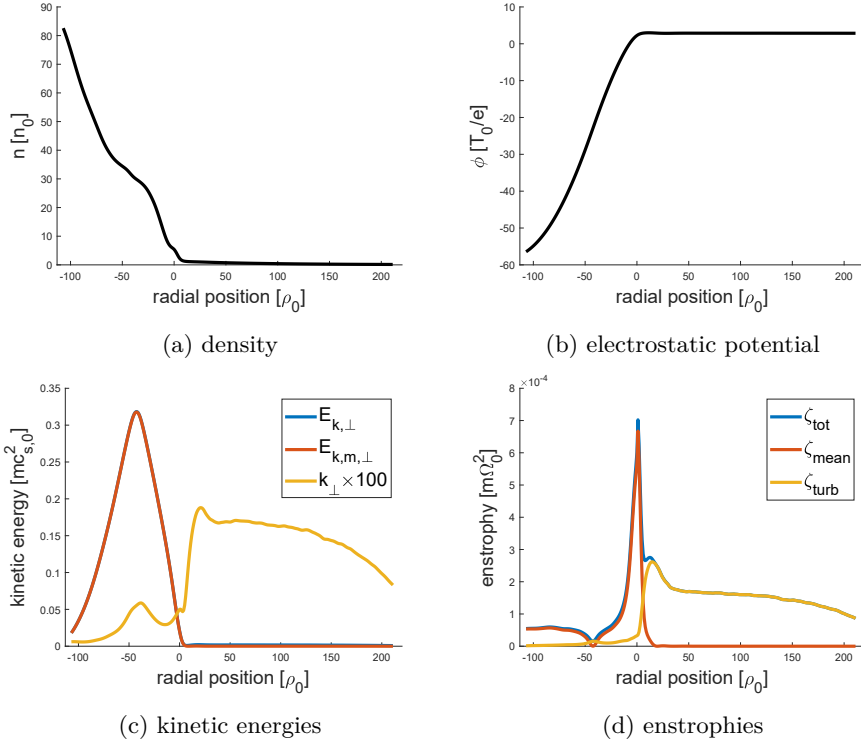
Figure 5.1: Radial profiles of characteristic quantities for a representative *isoDW* TOKAM2D simulation. The separatrix lies at $x = 0$ in these figures.

separatrix. In the core region the parallel current term of $k_\perp$ represents the DW coupling $\overline{\nabla_{||}\phi' \cdot \mathbf{J}'_{||}}$, while in the SOL it represents the parallel transport term $-\nabla \cdot \overline{\phi' \mathbf{J}'_{||}}$.

First we compare the balances in figure 5.2 to the balances of the SOL-only case in figures 4.6 and 4.14. It can be seen that the balances in the SOL are very similar whether a core region is present or not. In the core region, the balance between the different terms does become much more complex and noisy though. An interesting observation is that the DW term (red line) acts like a sink of $k_\perp$. In the simulations investigated here, the interchange drive (in blue) remains dominant, and the DW terms assumes the role of sink term. However, the DW term could act like a source as well. When the interchange term is turned off by setting $g = 0$, the DW term is indeed observed to lead to turbulence. Next to the interchange term and the parallel current term, the

(a) $k_\perp$ balance
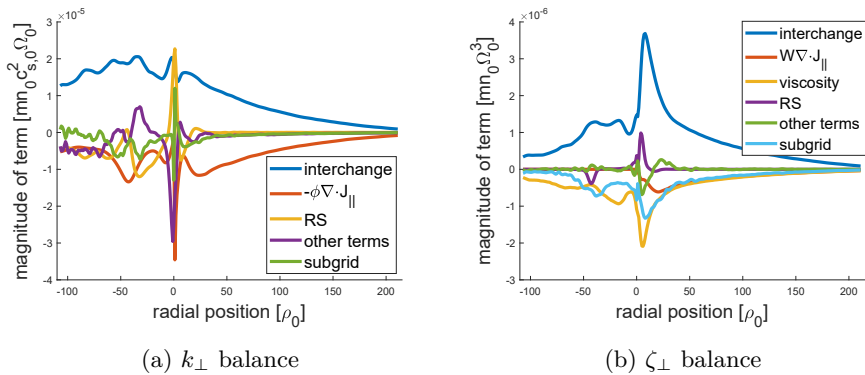
(b) $\zeta_\perp$ balance

Figure 5.2: $k_\perp$ and $\zeta_\perp$ balances for a representative *isoDW* TOKAM2D simulation. The separatrix lies at $x = 0$ in these figures.

Reynolds stress (RS) term (in yellow) becomes important in the $k_\perp$ balance in some regions due to the strong shear flows that develop. Furthermore, the "other terms" (in purple) also seem to be non-negligible in the core region. Mostly the $\nabla \cdot \overline{\phi' \mathbf{J}'_{p,0}}$ transport term and the Boussinesq correction term tend to take large values, although they generally remain very noisy. Finally, in a narrow region around the separatrix, many terms take large, peaked values. Further investigation is required to determine if this behaviour is physical, or rather the effect of numerical difficulties in resolving the sudden change in character of the (modelled) parallel dynamics.

The enstrophy balance in figure 5.2b in the core region takes a more regular, less noisy form. The interchange term (in dark blue) still acts like the main source of $\zeta_\perp$, while the DW term (in red) is negligible. The latter may be because the DW term mostly affects the larger length scales, while the enstrophy is concentrated on the small scales. As a result, practically all the dissipation in the core region is due to viscous effects (in yellow) and the numerical dissipation of the subgrid term (in light blue). All other terms (in green) as well as the equivalent to the RS term $\overline{nW'' \mathbf{V}''_E} \cdot \nabla \tilde{W}$ (in purple) remain small.

### 5.1.3 Models for mean-field particle transport

The analysis in this section focuses on the average E×B turbulent particle flux $\mathbf{\Gamma}_{n,t,E} \triangleq \overline{n' \mathbf{V}'_E}$, and on mean-field transport relations for it especially. Note that the structure of the particle fluxes and of this closure term is not changed by the new parallel model that is used in the core region, i.e. the LHS of

(a) *iso*: SOL-only



(b) *isoDW*: separatrix at $x = 0$
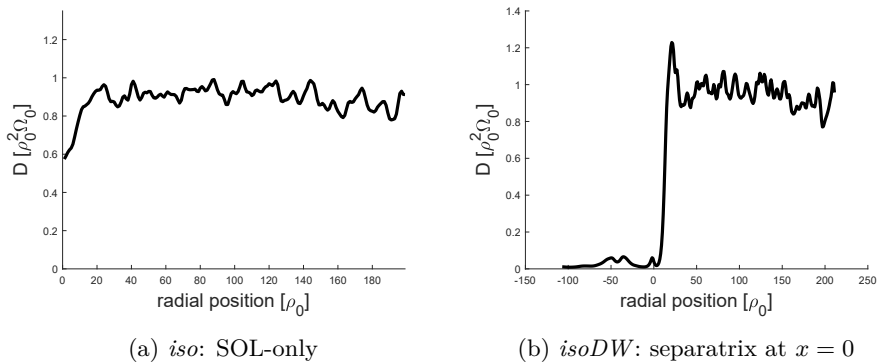
Figure 5.3: Radial profiles of the turbulent diffusion coefficients for representative TOKAM2D simulations.

equation 4.5 remains unchanged. In this work, we will investigate models for the radial component of this flux and consider the mean-field fluxes in the diamagnetic $y$-direction ($\Gamma_{n,E,y} \triangleq \overline{n\mathbf{V}_{E,y}}$), which may have both a mean-field and a turbulent component (even in the simplified 2D cases considered here), as a given. Note that this particle flux in the $y$-direction was insignificant in the isothermal SOL case considered before, but that it becomes large in the new flow cases. The generation of this flow in the diamagnetic direction is also a topic of active research. Refs. [93, 108] have analysed this in 2D systems for example. However, Refs. [144, 146] found that geodesic curvature effects in 3D toroidal geometries alter the dynamics of zonal flows significantly. Hence, in our analysis, we acknowledge that the shear in the considered 2D system may not be completely representative for realistic 3D cases, but our working hypothesis is that these 2D systems do allow to study the effect of flow shear on the transport, i.e. that the nature of the perpendicular transport in the presence of flow shear is not fundamentally changed by the dynamics of the shear generation itself.

As in the previous chapter, we will still consider diffusion models of the form $\mathbf{\Gamma}_{n,t,E} = -D\nabla_{\perp}\bar{n}$ to close the radial turbulent fluxes. Figure 5.3 shows the radial profiles of these turbulent diffusion coefficients for a representative simulation of each of the two studied flow cases. Figure 5.3a shows that the diffusion coefficient for a typical *iso* simulation has a very flat profile. In the *isoDW* case, shown in figure 5.3b, the profile in the SOL changed little, but there is a large suppression of the diffusion coefficient in the core region. Interestingly, $D$ drops much more than $k_{\perp}$ and $\zeta_{\perp}$.

Remember that section 4.3 [46] modelled the turbulent particle diffusion coefficient in the isothermal SOL case using the following $k_\perp$ model:

$$D = C_D \sqrt{k_\perp}, \tag{5.8}$$

with $C_D$ a free parameter. A value of $C_D = 23.9$ was found by means of a regression analysis for a set of TOKAM2D simulations. Still considering only the SOL under isothermal conditions, section 4.4 [44] proposed the $k_\perp - \zeta_\perp$ model as a refinement of the previous model:

$$D = C_D \frac{k_\perp}{\sqrt{\zeta_\perp}}. \tag{5.9}$$

A regression analysis for a (slightly different) set of TOKAM2D data yielded $C_D = 7.6$. A rigorous Bayesian analysis of both models in section 4.5.1 [50] showed that the $k_\perp - \zeta_\perp$ model largely outperformed the $k_\perp$ model as far as this diffusion relation is concerned.

A significant effect coming into play that was effectively absent in this *iso* flow case is flow shear. In the new flow cases, this is especially pronounced in the core region of the *isoDW* simulations. Literature indicates that mean-flow shear changes the characteristics of the turbulence and decreases the transport [23, 58, 88, 93, 108]. It is expected that both the intensity of the turbulence, thus $k_\perp$ and $\zeta_\perp$, and the magnitude of the transport for a given turbulence intensity, thus $D$ at fixed $k_\perp$ and $\zeta_\perp$, decrease. The model proposed by Miki *et al* [113], discussed in section 2.3.3, did indeed include both effects. In this work we will only investigate the latter effect.

It might be hoped that the effect of flow shear would inherently be captured by the scales used in the $k_\perp - \zeta_\perp$ model, however, it will be shown that this model no longer performs satisfactorily for the new flow cases. The ansatz followed in this contribution is that this reduced accuracy is due to the presence of radial shear of the diamagnetic component of the E×B velocity, $S \triangleq \partial_x V_{E,y}$. Another reason for discrepancies could be the DW instability coming into play next to the interchange one.

A first modification of models (5.8) and (5.9) that will be tested is to replace the total perpendicular turbulent kinetic energy $k_\perp$ by the radial turbulent kinetic energy $k_x \triangleq \overline{n\mathbf{V}''^2_{E,x}}/\bar{n}$. The idea behind this modified version is that the turbulent kinetic energy in the radial velocity component may be more strongly related to the average radial transport than the total perpendicular kinetic energy, especially in cases where there is strong shear, presumably affecting the turbulent kinetic energy in the diamagnetic velocity component $k_y \triangleq \overline{n\mathbf{V}''^2_{E,y}}/\bar{n}$.

Another adjustment proposed here is to take the effect of the flow shear explicitly into account, by adding a frequency scale accounting for the flow shear $\Omega_S$ to the regular $k_\perp - \zeta_\perp$ model:

$$D = C_D \frac{k_\perp}{\sqrt{\zeta_\perp} + C_S \Omega_S}, \tag{5.10}$$

with $C_S$ a proportionality constant to be determined. The rationale is that $\sqrt{\zeta_\perp}$ provides a characteristic frequency for the temporal decorrelation of eddies (eddy turn-over frequency), while shear provides an additional decorrelation mechanism. As shear becomes large, the latter starts dominating the former and decreases the turbulent diffusion coefficient for a given turbulence intensity as indicated by $k_\perp$ and $\zeta_\perp$.

Shear decorrelation rates indicated in literature make a natural choice for the shear frequency scale $\Omega_S$. A very basic frequency scale is $\Omega_S \sim |S|$. A slightly more complicated decorrelation rate is based on the time it takes for two fluid elements a distance $\Delta x$ away to be decorrelated by moving a diamagnetic wavelength $1/K_y$ away in the $y$-direction, resulting in $\Omega_S \sim K_y |S| \Delta x$ [23, 58]. Finally, the interplay between regular radial decorrelation and shear flow decorrelation may result in a hybrid decorrelation time $\Omega_S \sim (DK_y^2 S^2)^{1/3}$ [23, 58].

These scalings only strictly apply for transport of passive scalars in a constant shear flow. However, here we use them to model the effect of flow shear which may vary in time on the density transport. To this end, we first define the mean-flow shear $S_m \triangleq \partial_x \tilde{V}_{E,y}$, which is the shear based on the Favre average velocity in the y-direction. In order to convert the first shear time scale to a mean-field one we simply take $\Omega_S \sim |S_m|$. This will be referred to as the simple shear model in the following.

For the second time scale we have to use an approximation for $K_y$ and a relevant scale for $\Delta x$. We construct length scales for both based on the radial and diamagnetic turbulent kinetic energy, which nicely fits in the modelling framework constructed in chapter 4. This then yields $\Omega_S \sim |S_m|\sqrt{k_x/k_y}$, which will be referred to as the strong shear model.

For the hybrid decorrelation time model, a time scale is needed in addition to the $k_y$ velocity scale to construct an approximation for $K_y$. If the turbulent enstrophy is used for that, we find $K_{x/y} \sim \sqrt{\zeta_\perp/k_{x/y}}$ and then $\Omega_S \sim (DS_m^2 \zeta_\perp/k_y)^{1/3}$. Note that the diffusion coefficient is now ultimately present in the model for $D$ itself. In a mean-field code that is solved iteratively, this should not pose a problem. In case the shear frequency is dominant ($D \sim k/\Omega_S$) the diffusion coefficient can be eliminated to find $D \sim k^{3/4}/\sqrt{|S_m|K_y}$ as was done in Ref. [58]. This then yields $\Omega_S \sim \sqrt{|S_m|}(k\zeta_\perp/k_y)^{1/4}$ for the resulting

mean-field time scale.

Note that in the previous derivation for the hybrid decorrelation frequency, the "regular" turbulent enstrophy time scale of the turbulence was used. It may however be more consistent to use the shear decorrelation frequency instead. Doing so, we find $\Omega_S \sim DS_m^2/k_y$. When this is then in turn filled out in the diffusion relation for the case of dominant shear frequency, we finally obtain $D \sim \sqrt{kk_y}/|S_m|$. This can be seen to be equivalent to the regime where shear is dominant for the strong shear model (when $k = k_x$). Hence, the hybrid decorrelation time reduces to the strong shear decorrelation time in the strong shear limit in these models. The diffusion models resulting from these four mean-flow shear time scales are summarised in table 5.1.

Lastly, it will be examined whether replacing the turbulent enstrophy $\zeta_\perp = \zeta_{turb}$ by the total enstrophy $\zeta_{tot}$ (see 4.24 for definitions) improves the performance of the $k_\perp - \zeta_\perp$ model. The reasoning behind this relies on the fact that the vorticity includes the flow shear as

$$W \triangleq \nabla \cdot \nabla_\perp \phi = \nabla_x V_{E,y} - \nabla_y V_{E,x} \sim S, \tag{5.11}$$

where it is assumed that the shear of $V_{E,y}$ will be largely dominant. Hence, turbulent and mean field enstrophy are proportional to

$$\zeta_\perp = \widetilde{S''^2}, \qquad \zeta_{tot} = \widetilde{S''^2} + \tilde{S}^2. \tag{5.12}$$

As such, while the turbulent enstrophy already does include the effect of (small scale) flow shear fluctuations, the total enstrophy might add the effect of the mean-flow shear that becomes important now. Filling this out in the regular $k_\perp - \zeta_\perp$ diffusion relation yields

$$D = \frac{k_\perp}{\sqrt{\zeta_{tot}}} = \frac{k_\perp}{\sqrt{\zeta_\perp + \tilde{S}^2}}. \tag{5.13}$$

This result clearly shows similarities with the approach suggested in equation 5.10. Here as well large scale flow shear leads to a reduction of $D$ at fixed $k_\perp$ and $\zeta_\perp$, while the model reduces to the regular $k_\perp - \zeta_\perp$ model when large scale flow shear is absent. Note however that the order of operations (sum over timescales and square root operator) is different and that no free model constant $C_S$ is available or required. Furthermore, it is worth remarking that $\tilde{S} \neq S_m$, the difference being a term $\overline{n\partial_x V_y''}$.

## 5.1.4 Bayesian inference for turbulent diffusion coefficient models

In this section, the Bayesian framework for parameter estimation and model comparison discussed in section 3.4 is used to study the particle transport models in the new *isoDW* flow case and compare to results of the original *iso* cases. First, the $k_\perp$ and $k_\perp - \zeta_\perp$ models presented earlier will be assessed, and then the new models explicitly taking flow shear into account will analysed.

As data for the Bayesian analysis, we again consider the 1D profiles of the TOKAM2D reference data obtained by averaging in time (from the onset of the statistical steady state) and in the $y$-direction (which is a symmetry direction). Hence, the output data $O$ are the radial profiles of the diffusion coefficient $D$, and the input data $I$ are the radial profiles of turbulent kinetic energy $k_\perp$ and the turbulent enstrophy $\zeta_\perp$.

As discussed in section 3.4.2, describing the model error $\epsilon$ in order to construct the likelihood function is a delicate matter. Since very little is known about most of the contributions to this error, we chose to aggregate them all and assume the error at every data point has a Gaussian distribution as in equation 3.61. The standard deviation of the error is assumed to take a single value for all radial points for all simulations in each inference, i.e. $\epsilon_i \sim N(0, \sigma_{abs})$ as in expression 3.63. Hence, we chose not to scale the model error to the data point value as in expression 3.64. The reason for this is that low but noisy values of $D$ in the core region for the *isoDW* inferences led to unsatisfactory results with this scaled error. For the regular *iso* cases, a scaled error did however lead to higher evidences and thus more reliable results, but in order to maintain the parallelism between both cases, we chose to report the data without scaled error here. As this "absolute standard deviation" $\sigma_{abs}$ is not known a priori, it is an additional parameter that will be inferred. Possible spatial correlations in the model error have not been accounted for here. The total likelihood function 3.61 then reduces to the product of the likelihood functions of all individual data points.

For the priors of $C$ ($C_D$ and $C_S$) and $\sigma_{abs}$ we chose wide distributions in order not to exclude any parameter values a priori:

$$\begin{cases} \pi(C) = 2N(0, 100) & \text{if } C \geq 0 \\ \pi(C) = 0 & \text{if } C < 0 \end{cases} \qquad \begin{cases} \pi(\sigma_{abs}) = 1/\sigma_{abs} & \text{if } \sigma_{abs} \geq 0 \\ \pi(\sigma_{abs}) = 0 & \text{if } \sigma_{abs} < 0 \end{cases} \tag{5.14}$$

The results of the Bayesian analysis for this setup are summarised in table 5.1. The maximum a posteriori (MAP) value of the parameters of the models

as well as the logarithm of their evidence is shown. Both the original models and the variant in which the total perpendicular turbulent kinetic energy $k_\perp$ is replaced by the radial turbulent kinetic energy $k_x$ are studied. Results are shown for the both the *iso* and the *isoDW* data sets described in appendix D. Remember that the evidence also depends on the data, such that it can only be meaningfully compared for models which have the same output data $O$. Hence only models within (double) columns under *iso* and *isoDW* that use the same data set can be compared with each other. Also, since the (natural) logarithm of the evidence is reported, a difference of about 5 between two models can already be considered to be decisive in selecting one model over another, see table 3.1 [49, 50, 161].

### Assessment of $k_\perp$ and $k_\perp - \zeta_\perp$ models

Looking at the MAP values of the $C_D$ coefficient for the regular $k_\perp$ and $k_\perp - \zeta_\perp$ models for the *iso* case in table 5.1, it can be seen that these are rather close to the values of respectively 23.9 and 7.6 that were found by means of regression analysis in sections 4.3 and 4.4. Comparing the different models for the *iso* case, it is observed that in the data as reported here, the $k_\perp$ model does less well than the Bohm scaling ($D \sim T_e$ in the TOKAM2D case) model. However, when the model error standard deviation is scaled to the data point value ($\sigma_i = \sigma_{rel} O_i$), the evidence of the $k_\perp$ model does become higher than the Bohm model and the error lower. This testifies to the importance of the statistical model and thus on the hypotheses made in the likelihood function in a Bayesian analysis. Another reason for the relatively poor performance of the $k_\perp$ model is the rather strong variations in $\nu$ in the reference data set. This trend is captured much better by the $k_\perp - \zeta_\perp$ model, which clearly outperforms the $k_\perp$ model in this case, as was also found in chapter 4. In addition, the models where $k_x$ is used instead of $k_\perp$ perform better in almost all cases.

Visual inspection of the *iso* data, see figures 5.4a and 5.5a, shows the $k_\perp - \zeta_\perp$ model captures the data very well. Figure 5.4 compares the radial profile for the diffusion coefficient for representative simulations to the models proposed here. Figure 5.5 then gives an overview of the model's performance in parameter space. It shows a scatter plot of the model value for $D$ on the vertical axis versus the observed TOKAM2D value on the horizontal axis. Each marker in the figure represents a single TOKAM2D simulation (for a certain parameter set $g$, $L_{||}$, $\nu$,...), which is now also radially averaged. The classical coefficient of determination, defined in equation 3.57, is also reported in this figure. Note that this is calculated based on the radially averaged data here.

While a comparison of the *iso* and *isoDW* cases based on evidence and model

(a) *iso*: SOL-only

(b) *isoDW*: separatrix at $x = 0$
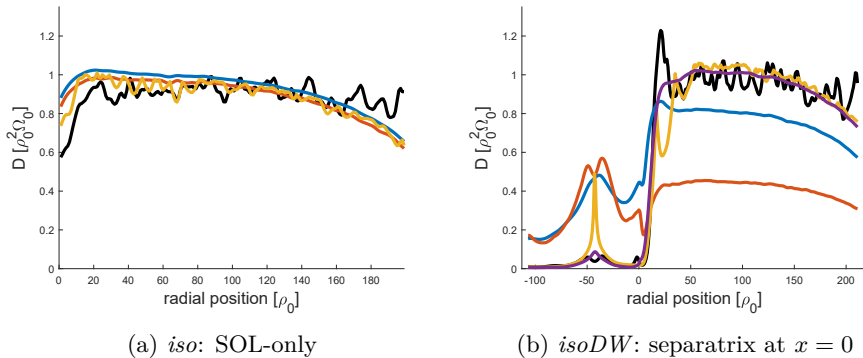
Figure 5.4: Comparison of radial profiles of the turbulent diffusion coefficient for representative cases. TOKAM2D reference data in black, $k_\perp$ model (second row in table 5.1) in blue, $k_\perp - \zeta_\perp$ model (third row in table 5.1) in red, strong shear $k_x$ model (sixth row in table 5.1) in yellow, $k_x$-DW-corrected model (last row in table 5.2, only shown for *isoDW* case) in purple.

error is not possible, the higher standard deviation of the error for the *isoDW* (for a similar order of magnitude of $D$ in the SOL) indicates that the models capture the *isoDW* case less well. Furthermore, figures 5.4b and 5.5b show that the $k_\perp$ and $k_\perp - \zeta_\perp$ models fail to adequately represent the underlying data. Figure 5.4b illustrates that the models seem to be making a trade-off between having a high enough diffusion coefficient in the SOL and capturing the suppressed value in the core region. The MAP values of the model parameters do not match between the *iso* and the *isoDW* cases because of this model inadequacy for the *isoDW* case. Judging by the Bayesian model evidence (and the standard deviation of the errors), the $k_\perp$ model performs better than the Bohm scaling, and curiously also better than the $k_\perp - \zeta_\perp$ model. No clear reason has been identified for the latter, although it could be speculated that the turbulent enstrophy does not provide the correct time scale in the core region, and that a time scale accounting for the flow shear should instead be used. Here as well, the $k_x$ variants work better than the $k_\perp$ variants.

Table 5.1: Bayesian analysis of the proposed models for the particle diffusion coefficients for the *iso* and *isoDW* datasets (part 1). Parameter values are reported at MAP.

| Model for $D$ | parameter | *iso* | | *isoDW* | |
|---|---|---|---|---|---|
| | | $k_\perp$ | $k_x$ | $k_\perp$ | $k_x$ |
| $C_D T_e$ | $C_D[-]$ | 0.925 | | 0.595 | |
| | $\sigma_{abs}[-]$ | 0.200 | | 0.517 | |
| | logevidence | 599 | | -2423 | |
| $C_D \sqrt{k}$ | $C_D[-]$ | 24.5 | 29.6 | 19.9 | 26.8 |
| | $\sigma_{abs}[-]$ | 0.216 | 0.203 | 0.379 | 0.317 |
| | logevidence | 344 | 551 | -1434 | -872 |
| $C_D \dfrac{k}{\sqrt{\zeta_\perp}}$ | $C_D[-]$ | 7.49 | 10.8 | 3.45 | 6.81 |
| | $\sigma_{abs}[-]$ | 0.134 | 0.120 | 0.578 | 0.496 |
| | logevidence | 1858 | 2225 | -2775 | -2286 |
| $C_D \dfrac{k}{\sqrt{\zeta_{tot}}}$ | $C_D[-]$ | 7.49 | 10.8 | 5.67 | 8.92 |
| | $\sigma_{abs}[-]$ | 0.134 | 0.120 | 0.407 | 0.376 |
| | logevidence | 1858 | 2226 | -1664 | -1409 |
| $C_D \dfrac{k}{\sqrt{\zeta_\perp}+\Omega_S}$ $\Omega_S = C_S\|S_m\|$ | $C_D[-]$ | 7.85 | 11.4 | 8.14 | 12 |
| | $C_S[-]$ | 10.1 | 11.2 | 5.05 | 5.11 |
| | $\sigma_{abs}[-]$ | 0.128 | 0.11 | 0.221 | 0.226 |
| | logevidence | 2013 | 2492 | 268 | 201 |
| $C_D \dfrac{k}{\sqrt{\zeta_\perp}+\Omega_S}$ $\Omega_S = C_S\|S_m\|\sqrt{\frac{k_x}{k_y}}$ | $C_D[-]$ | 7.85 | 11.3 | 8.28 | 12.1 |
| | $C_S[-]$ | 5.33 | 6.63 | 5.09 | 3.40 |
| | $\sigma_{abs}[-]$ | 0.129 | 0.110 | 0.241 | 0.212 |
| | logevidence | 1973 | 2476 | -13 | 398 |
| $C_D \dfrac{k}{\sqrt{\zeta_\perp}+\Omega_S}$ $\Omega_S = C_S\left(\frac{DS_m^2\zeta_\perp}{k_y}\right)^{1/3}$ | $C_D[-]$ | 7.79 | 11.4 | 9.81 | 13.6 |
| | $C_S[-]$ | 0.496 | 0.683 | 3.47 | 2.22 |
| | $\sigma_{abs}[-]$ | 0.135 | 0.115 | 0.343 | 0.306 |
| | logevidence | 1899 | 2339 | -1125 | -759 |
| $C_D \dfrac{k}{\sqrt{\zeta_\perp}+\Omega_S}$ $\Omega_S = C_S\left(\frac{S_m^2 k\zeta_\perp}{k_y}\right)^{1/4}$ | $C_D[-]$ | 8.00 | 11.7 | 10.2 | 14.6 |
| | $C_S[-]$ | 0.813 | 1.06 | 3.38 | 2.97 |
| | $\sigma_{abs}[-]$ | 0.131 | 0.114 | 0.270 | 0.250 |
| | logevidence | 1936 | 2383 | -371 | -122 |
| $\dfrac{C_D k}{\sqrt{\zeta_\perp}+\Omega_{S1}+\Omega_{S2}}$ $\Omega_{S1} = C_{S1}\|S_m\|\sqrt{\frac{k_x}{k_y}}$ $\Omega_{S2} = C_{S2}\left(\frac{S_m^2 k\zeta_\perp}{k_y}\right)^{1/4}$ | $C_D[-]$ | 7.78 | 11.3 | 8.29 | 12.1 |
| | $C_{S1}[-]$ | 5.35 | 6.66 | 5.10 | 3.40 |
| | $C_{S2}[-]$ | 7.21E-5 | 1.83E-4 | 5.91E-4 | 1.35E-4 |
| | $\sigma_{abs}[-]$ | 0.130 | 0.111 | 0.242 | 0.212 |
| | logevidence | 1965 | 2467 | -19 | 388 |

Table 5.2: Bayesian analysis of the proposed models for the particle diffusion coefficients for the *iso* and *isoDW* datasets (part 2). Parameter values are reported at MAP.

| Model for $D$ | parameter | iso $k_\perp$ | iso $k_x$ | isoDW $k_\perp$ | isoDW $k_x$ |
|---|---|---|---|---|---|
| $C_D$ | $C_{D,SOL}[-]$ | | | 0.894 | |
| | $C_{D,core}[-]$ | | | 0.0737 | |
| | $\sigma_{abs}[-]$ | | | 0.333 | |
| | logevidence | | | -1039 | |
| $C_{D,i}\sqrt{k_\perp}$ | $C_{D,SOL}[-]$ | | | 23.3 | 29.8 |
| | $C_{D,core}[-]$ | | | 3.54 | 5.85 |
| | $\sigma_{abs}[-]$ | | | 0.277 | 0.238 |
| | logevidence | | | -450 | 47 |
| $C_{D,i}\dfrac{k}{\sqrt{\zeta_\perp}}$ | $C_{D,SOL}[-]$ | | | 7.48 | 11.6 |
| | $C_{D,core}[-]$ | | | 0.437 | 0.904 |
| | $\sigma_{abs}[-]$ | | | 0.203 | 0.133 |
| | logevidence | | | 54 | 1880 |
| $C_{D,i}\dfrac{k}{\sqrt{\zeta_{tot}}}$ | $C_{D,SOL}[-]$ | | | 7.67 | 11.6 |
| | $C_{D,core}[-]$ | | | 0.811 | 1.25 |
| | $\sigma_{abs}[-]$ | | | 0.166 | 0.129 |
| | logevidence | | | 1180 | 1991 |
| $C_D\dfrac{G_k}{G_k+C_{||}DW_k}\dfrac{k}{\sqrt{\zeta_{tot}}}$ | $C_D[-]$ | 7.49 | 10.8 | 7.66 | 11.6 |
| | $C_{||}[-]$ | 2.65E-5 | 2.67E-5 | 12.8 | 9.99 |
| | $\sigma_{abs}[-]$ | 0.134 | 0.120 | 0.163 | 0.123 |
| | logevidence | 1848 | 2215 | 1229 | 2121 |

## Assessment of shear-adjusted particle transport models

The next six rows in table 5.1 show the shear-adjusted models suggested in section 5.1.3 and the Bayesian analysis results for them.

For the *iso* data set, the shear models only bring a modest improvement in terms of the model error standard deviation $\sigma_{abs}$ over the $k_\perp - \zeta_\perp$ models. The reason for this is that the latter already performed very well, and because the low flow shear does not play an important role in this case. Nonetheless, the increase of the logevidence largely exceeds 5 for most models, making them significantly better according to the Bayesian analysis. Surprisingly, it is the simplest shear model with $k_x$ in the numerator that has the highest evidence in this case. The model using the total enstrophy, the $k_\perp - \zeta_{tot}$ model, does not bring a significant improvement over the regular $k_\perp - \zeta_\perp$ model for this case.
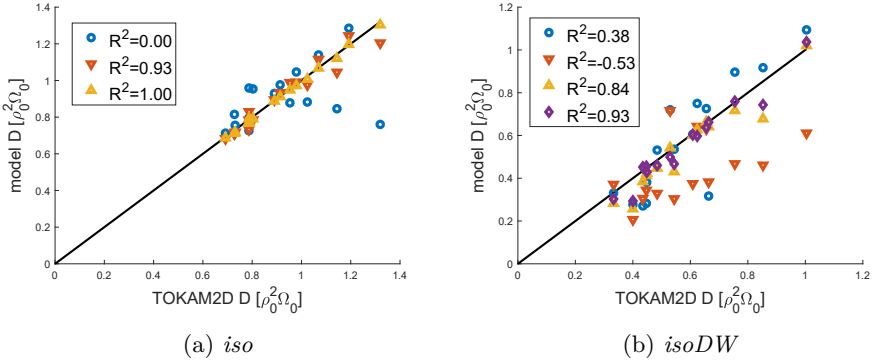
Figure 5.5: Scatter plot of the radially averaged turbulent diffusion coefficients for a database of TOKAM2D simulations. $k_\perp$ model (second row in table 5.1) in blue, $k_\perp - \zeta_\perp$ model (third row in table 5.1) in red, strong shear $k_x$ model (sixth row in table 5.1) in yellow, $k_x$-DW-corrected model (last row in table 5.2, only shown for *isoDW* case) in purple.
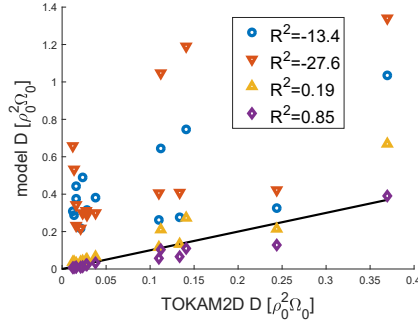


Figure 5.6: Scatter plot of the turbulent diffusion coefficient radially averaged over the core region ($x < 0$) for a database of *isoDW* simulations. $k_\perp$ model (second row in table 5.1) in blue, $k_\perp - \zeta_\perp$ model (third row in table 5.1) in red, strong shear $k_x$ model (sixth row in table 5.1) in yellow, $k_x$-DW-corrected model (last row in table 5.2) in purple.

Including the flow shear in the models for the *isoDW* data on the other hand drastically increases the evidence and decreases the model error over the regular models as expected. Here, the strong shear model with $k_x$ in the numerator has the highest evidence. The elegant $k_\perp - \zeta_{tot}$ model which does not need an additional $C_S$ parameter does yield a significant improvement over the regular $k_\perp - \zeta_\perp$ model, but performs much less well than some of the other shear-corrected models. In general, it has to be remarked that the error on the models for this *isoDW* data remains rather large.

It is also interesting to notice that both for the *iso* and *isoDW* cases the bottom model, which includes a combination of the strong shear decorrelation timescale and the hybrid decorrelation timescale to account for the possible influence of both, does not bring an improvement with respect to the model with the strong shear model time scale only. The model parameters tend to the parameters of the model with the higher evidence of both without making a compromise. In addition, the model evidence of this combined model is lower than that of the strong shear case because of its higher complexity and number of fitting parameters.

It is worth remarking that while the $k_x$ variants of the models consistently perform better than the $k_\perp$ variants, no model for $k_x$ is currently available. This would require deriving an analytical transport equation for $k_x$, which is presumably non-trivial. Furthermore, the relevant closure terms in that equation would again need to be modelled. Hence, in the near future it is foreseen to keep using the $k_\perp$ variants. Of these models, the simple shear model (fifth model in table 5.1) performs best, both for the *iso* and *isoDW* case. Moreover, the parameters are relatively similar for both cases (especially since the exact value of $C_S$ is not that important for *iso* case where flow shear is low).

In order to further investigate the significance of the shear models, we also compare with models that additionally correct for different instability mechanisms in table 5.2. The first four rows in this table represent "2-zone" models. The idea for these models is that the dynamics in the core and those in the SOL may be inherently different because of the different parallel dynamics. As such, it could be imagined that both regions actually follow the same diffusion relation, but that different model constants should be allowed in the core and the SOL. For these 2-zone models, the $k_\perp - \zeta_\perp$ model (finally) does better than the $k_\perp$ model. The $k_\perp - \zeta_{tot}$ model, including the average flow shear provides a further improvement.

The last row of table 5.2 lists another model that explicitly takes the parallel dynamics of the DW-like term into account, relative to the regular interchange term. Since the DW term is only present in the core, this effectively allows to decouple the diffusion coefficient in the core and the SOL region as well.

This model has the highest evidence of all models that were investigated. Note that this "DW correction" might also be combined with other models than the $k_\perp - \zeta_{tot}$ model. In order to keep the number of model parameters low, the combinations with other shear models has not yet been tried. For the *iso* case that is also reported for this model, the $DW_k$ parallel term has been replaced by the sheath loss term $S_k$ to see if taking parallel dynamics into account would also work here. This does not seem to be the case. Note that in the *isoDW* case, no correction for $S_k$ has been used in the SOL. These results comply with the expectation that different instabilities lead to a different structure of the turbulence leading to a different relation between turbulence intensity and transport. In particular, it is known that the DW instability leads to a much smaller phase difference between density and potential fluctuations than the interchange instability [145], which is expected to lead to lower transport at the same intensity of the fluctuations.

Comparing the results in tables 5.1 and 5.2, it can be seen that the 2-zone models and the model with the DW correction largely outperform the pure shear models. However, the $\zeta_{tot}$ variants of the former which implicitly include the flow shear do lead to improvements over the $\zeta_\perp$ ones that do not. Hence, flow shear does still seem to play a role.

Next, the parameter values are compared between the *iso* and the *isoDW* case for the models in tables 5.1 and 5.2. It can be seen that for the models that perform rather well, the parameters that influence the SOL region are rather similar for both cases. This is especially true for the important $C_D$ parameter, while the difference in the $C_S$ parameter that is less important in the SOL is larger. This indicates that the models do not only give a good match for the particular data they were developed for, but likely also capture some of the underlying physics.

For the *iso* case, figures 5.4a and 5.5a support the results from the Bayesian evidence. Figure 5.4a shows that all models manage to capture the radial profiles well and that the difference between the different models is small. Figure 5.5a then illustrates that the strong shear model still manages to improve the fit for the *iso* data set accross TOKAM2D parameter space, although the $k_\perp - \zeta_\perp$ model already did very well. Note also that part of the improvement is due to the use of $k_x$ in the denominator instead of $k_\perp$. As was discussed before already, the $k_\perp$ model misses the trend with varying $\nu$.

For the *isoDW* case then, figure 5.4b shows that both the strong shear model and the DW-correction model manage to capture both the behaviour in the SOL and the base level of the suppressed diffusion coefficient in the core region rather well. The strong shear model (like the other shear models) features significant peaks in the core region that are not present in the data though. These peaks

occur at locations where the local flow shear is very low. The DW-correction model (and the 2-zone models) do not include such peaks. Figure 5.5b seems to indicate that both models capture the trends in parameter space rather well, with the DW-correction model performing better according to the $R^2$ value as well. Hence, the $R^2$ value and the Bayesian evidence yield the same ranking for the models over the different data sets. It has to be remarked though that this plot pertains to the radial average of the entire domain, both outer core region and SOL. If a similar scatter plot is made for the core region only, the models perform less good and the $R^2$ value is reduced, see figure 5.6.

## 5.1.5 Discussion and conclusion

In this section, mean-field models for the turbulent particle diffusion coefficient for isothermal SOL cases, with and without core region, are studied. This model development process is supported by a Bayesian framework for parameter estimation and model comparison. These Bayesian techniques allowed estimating the combined posterior distribution of the proposed models, identifying terms which are irrelevant in the models and ranking the different models according to the Bayesian evidence. This Bayesian evidence is especially relevant since it automatically penalises more complex models hence guarding against over fitting.

This analysis has shown that the existing $k_\perp$ and $k_\perp - \zeta_\perp$ particle transport models proposed in chapter 4 do not capture the trends in the new simulations with a core region. The strong flow shear developing in simulations with SOL and core region was assumed to be the origin of this deficiency and the $k_\perp - \zeta_\perp$ diffusion model is adapted by incorporating shear decorrelation frequencies inspired by literature to explicitly take this effect into account.

The shear-corrected models provide a large enhancement over the earlier models, but considerable room for improvement certainly does remain for the core region. Based on this analysis, it is plausible that the discrepancies of the earlier models are indeed due to flow shear, but it cannot be ruled out that also other effects are at play.

An important consideration and possible (partial) explanation for the mediocre performance of the shear-adjusted diffusion models reported here may be in the time dependent nature of the flow shear. Assume for example that an exact expression for the relation between instantaneous transport and instantaneous flow shear would be available, $D(t) = f(S(t))$. If this relation is not linear, $\bar{D} \neq f(\bar{S})$. In our models, we use the mean flow shear as a proxy for the shear, which may impact the performance of the mean field models if fluctuations are large.

A class of models that explicitly decouples the transport relation in the core region from that in the SOL has also been examined. The idea behind these models is that the dynamics in both regions may be inherently different because of the different parallel dynamics and instabilities at play. These 2-zone models, which are still based on the ansatz that $k_\perp$ and $\zeta_\perp$ can be used to predict the turbulent transport, were shown to work very well and outperformed the models that only corrected for flow shear. This observation puts the importance of flow shear in perspective. It could be concluded that the different parallel dynamics in core and SOL region and the different instabilities and turbulence structure that result from it seem to be responsible for difference in the diffusion coefficient. Since there is strong shear in the core region and very limited shear in the SOL, the different behaviour in both regions can be emulated by incorporating the flow shear in the models, however, it seems that other models may be more appropriate for "decoupling" both regions.

Nonetheless, it has been shown that including the total enstrophy, which includes the mean-flow shear, instead of the turbulent enstrophy does consistently and significantly enhance the evidence, indicating that accounting for the mean-flow shear does bring an improvement. Hence, the mean-flow shear does seem to play a role, but may not be the dominant factor in explaining the difference in the diffusion coefficient between core and SOL for the simulations analysed here. Another adjustment that proved useful for both the *iso* and *isoDW* case for almost all models is to use the radial turbulent kinetic energy $k_x$ instead of the perpendicular kinetic energy $k_\perp$. The reason for this is most likely that the radial velocity, characterised by $k_x$, is more closely related to radial particle transport. In addition, $k_x$ is less disturbed by strong shear flows which have a larger impact on $k_y$ and thus $k_\perp$.

It has been observed that the parameters in cases with a core region and cases with only a SOL region are rather close together, especially for the models that perform well. The more complex models developed for the *isoDW* cases still do well for the simpler *iso* cases (no results shown here), indicating a good degree of consistency in these models.

When interpreting the results of the Bayesian inference, the influence of the Bayesian parameters and the statistical framework should be kept in mind. As argued in section 3.4, the results of the Bayesian analysis do not only depend on the physical model (the diffusion models that are proposed), but also on the statistical model: the form of the the prior and the likelihood function that is chosen (including the absolute or relative scaling of the model error and the correlation length). The width of the prior determines how strongly more complex models are penalised. The choice for the model error standard deviation to represent the absolute or the relative error changes the weighing of the data points. If the absolute error formulation is used, a significant relative error on

a data point with a low absolute value does not have as much importance as the same relative error would have when the relative error formulation were used. Inferences with various correlation lengths showed that the value of the parameters depends on it in a rather irregular way, especially for those models that perform less well. As such, we have chosen to use the results where no correlation length is used. The value of the correlation length did not seem to change the ranking of the different models according to their evidence though. In this context, it may be envisaged to smooth the results in the core region of the *isoDW* data since the peaks are probably due to the rather small scale specifics of the flow field which are hard to capture in a mean-field model. However, care should be taken for the interaction with the statistical model of the Bayesian framework.

In future research, forward simulations will have to prove if the models developed here effectively captured causal relations, or rather correlations without their common origin. Further research should also focus on investigating the balances of the turbulent kinetic energy and turbulent enstrophy for the new flow cases following the methodology demonstrated in chapter 4. Another research track is to further extend the physical model of the TOKAM2D simulations that are studied. Up to now, the diamagnetic drift contribution to the vorticity has been neglected, while literature indicates this may significantly influence the dynamics [105, 25, 15]. This will be investigated in the next section. Also, anisothermal cases will be investigated in chapter 6.

## 5.2   Extension to total vorticity case

All the models developed so far, i.e. chapter 4 and section 5.1, only considered the contribution from the E×B drift to the inertia and thus to the pseudo-vorticity $W$. In this section[2] the influence of including the contribution from the ion diamagnetic velocity will be investigated. This will be referred to as the "total vorticity" (TW) case, while the earlier case will be referred to as "E×B-only". Only the isothermal SOL will be considered in this section. Literature has already found that this contribution changes the dynamics of individual plasma blobs [25, 105] and that it affects the statistics of the turbulence and the resulting profiles [15].

_____

[2]Parts of this section have been presented as a poster at the Joint EU-US Transport Task Force Meeting, 6-10 September 2021, "Influence of the diamagnetic drift contribution on the turbulent kinetic energy balance in isothermal interchange-dominated ExB turbulence in the scrape-off layer", Coosemans, R., Dekeyser, W., Baelmans, M.

The subset of TOKAM2D equations B.21-B.25 considered in this section becomes

$$\frac{\partial n}{\partial t} + \mathbf{V}_E \cdot \nabla n - D_0 \nabla_\perp^2 n = -\frac{nc_s}{L_{||}} \exp(\Lambda - \frac{\phi}{T_e}) + S_n, \tag{5.15}$$

$$\frac{\partial W}{\partial t} + \mathbf{V}_E \cdot \nabla W_{TW} = -\frac{g}{n}\frac{\partial p}{\partial y} + \frac{c_s}{L_{||}}(1 - \exp(\Lambda - \frac{\phi}{T_e})) + \nu_0 n \nabla_\perp^2 W_{TW}, \tag{5.16}$$

$$W_{TW} \triangleq \nabla_\perp^2 \phi + \nabla \cdot \frac{\nabla_\perp p_i}{n}, \qquad \mathbf{V}_E \triangleq \mathbf{b} \times \nabla\phi. \tag{5.17}$$

Note that the only difference compared to the isothermal SOL equation set used in chapter 4 is the definition of the vorticity. The definition used here effectively implies that the LHS of equation 5.16 now represents

$$\frac{\partial W_{TW}}{\partial t} + \mathbf{V}_E \cdot \nabla W_{TW} = -\mathbf{b} \times \frac{D}{Dt}\nabla \cdot \mathbf{V}_0 \tag{5.18}$$

as an approximation for the divergence of the inertial contribution to the polarisation velocity $-\nabla \cdot \mathbf{V}_{p,0}$. The velocities contributing to this inertia are now assumed to be the E×B drift and the ion diamagnetic drift, i.e. $\mathbf{V}_0 = \mathbf{V}_E + \mathbf{V}_{*,i}$. However, note that the contribution from the diamagnetic velocity to convection is not taken into account, i.e. $\mathbf{V}_C = \mathbf{V}_E$.

The kinetic energy equations and enstrophy equations for this modified equation set will be presented in section 5.2.1. Then, a comparison will be made between TOKAM2D simulations with total vorticity and E×B-only simulations in section 5.2.2. Finally, 5.2.3 will test the models developed earlier for the TW simulations.

## 5.2.1 Derivation of kinetic energy and enstrophy equations

The different form of the vorticity equation has implications for the turbulent kinetic energy. As the inertia due to the diamagnetic drift is included in the model, it also needs to be included in the kinetic energy. To this end, we define the total (in the sense of including E×B and diamagnetic velocity) perpendicular kinetic energies as in equation 3.5[3]:

$$E_{E*} \triangleq \frac{\mathbf{V}_0^2}{2}, \qquad E_{m,E*} \triangleq \frac{\tilde{\mathbf{V}}_0}{2}, \qquad \bar{n}k_{E*} \triangleq \frac{\overline{n\mathbf{V}_0''^2}}{2}. \tag{5.19}$$

[3]In this section, we abolish the general subscript $\perp$ notation and use subscripts that specifically denote the velocity components that are included in order to avoid possible confusion.

**Total kinetic energy equations**

The procedure to derive transport equations for these quantities is similar to that followed for the general case in section 3.2.1. However, the specific form of the TOKAM2D equations does require some adjustments. The complete derivation of these equations is presented in appendix B.2.1.

In this appendix, the total kinetic energy equation is derived (see equation B.34) as

$$\frac{\partial n E_{E*}}{\partial t} + \nabla \cdot \mathbf{\Gamma}_{E_{E*}} = g\phi \frac{\partial p}{\partial y} - \frac{c_s n \phi}{L_{||}}(1 - \exp(\Lambda - \frac{\phi}{T_e}))$$

$$-\nu n\phi\nabla_\perp^2 W_{TW} + S_{E_{E*},n} - \nabla p_i \cdot \mathbf{V}_{p,0}$$

$$+\phi\nabla n \cdot \mathbf{V}_{p,0} - n\phi\nabla\mathbf{V}_E : \nabla\mathbf{U}_0, \tag{5.20}$$

$$\mathbf{\Gamma}_{E_{E*}} = n E_{E*}\mathbf{V}_E + \phi\mathbf{J}_{p,0}, \tag{5.21}$$

$$S_{E_{E*},n} = E_{E*}S_n + D_0 E_{E*}\nabla_\perp^2 n - \frac{E_{E*}c_s n}{L_{||}}\exp(\Lambda - \frac{\phi}{T_e}), \tag{5.22}$$

$$\mathbf{J}_{p,0} = n\mathbf{V}_{p,0} = n\mathbf{b} \times \frac{D\mathbf{V}_0}{Dt} \tag{5.23}$$

Comparing the total kinetic energy equation 5.20 for the TW case to equation 4.9 derived for the E×B-only case, we see that they are largely the same. The only differences are 1) the definition of the kinetic energy and vorticity is different, 2) $\mathbf{V}_{p,0}$ now uses both the E×B drift velocity and the diamagnetic velocity and 3) most interestingly, two new terms enter the equation. The third but last term represents the work done by the pressure gradient on the polarisation current. This term also appeared in the total perpendicular kinetic energy equation for the general case 3.10. The second new term is the last one in the equation. Just like the Boussinesq term (first term in the third line of equation 5.20), this term only appears because of the approximations made in the TOKAM2D vorticity equation, as illustrated in equations B.15 and B.30. Hence, this is also an artificial term which should not have been there. Note that this term is identically zero in the E×B-only case considered in chapters 4 and 6 since it then is proportional to $\nabla\mathbf{V}_E : \nabla\mathbf{U}_E = 0$ (at least when the magnetic field is uniform as is the case in TOKAM2D).

The $E_{m,E*}$ and $k_{E*}$ equations derived as equations B.39 and B.34 in appendix are:

$$\frac{\partial}{\partial t}\bar{n}E_{m,E*} + \nabla \cdot \Gamma_{E_{m,E*}} = g\bar{\phi}\frac{\partial \bar{p}}{\partial y} - \frac{\bar{\phi}}{L_{||}}\overline{c_s n(1 - \exp(\Lambda - \frac{\phi}{T_e}))}$$

$$-\nu\bar{\phi}\overline{n\nabla_\perp^2 W_{TW}} + \overline{n\mathbf{V}_E''\mathbf{V}_0''} : \nabla\tilde{\mathbf{V}}_0^T - \overline{n'\nabla\phi'} \cdot \tilde{\mathbf{V}}_{p,0} + S_{E_{m,E*},n}$$

$$-\nabla_\perp\bar{p}_i \cdot \tilde{\mathbf{V}}_{p,0} + \bar{\phi}\overline{\nabla n \cdot \mathbf{V}_{p,0}} - \bar{\phi}\bar{n}\nabla\mathbf{V}_E : \nabla\mathbf{U}_0, \qquad (5.24)$$

$$\Gamma_{E_{m,E*}} = \bar{n}\tilde{\mathbf{V}}_E E_{m,E*} + \overline{n\mathbf{V}_E''\mathbf{V}_0''} \cdot \tilde{\mathbf{V}}_0 + \bar{\phi}\bar{\mathbf{J}}_{p,0}, \qquad (5.25)$$

$$S_{E_{m,E*},n} = E_{m,E*}\bar{S}_n + \tilde{\mathbf{V}}_0 \cdot \overline{\mathbf{V}_0'' S_n}$$

$$+D_0 E_{m,E*}\nabla_\perp^2\bar{n} + D_0\tilde{\mathbf{V}}_0 \cdot \overline{\mathbf{V}_0''\nabla_\perp^2 n}$$

$$-\frac{E_{m,E*}}{L_{||}}\overline{c_s n \exp(\Lambda - \frac{\phi}{T_e})} - \overline{c_s n\mathbf{V}_0'' \exp(\Lambda - \frac{\phi}{T_e})} \cdot \frac{\tilde{\mathbf{V}}_0}{L_{||}}, \qquad (5.26)$$

$$\frac{\partial}{\partial t}\bar{n}k_{E*} + \nabla \cdot \Gamma_{k_{E*}} = \overline{g\phi'\frac{\partial p'}{\partial y}} - \frac{1}{L_{||}}\overline{\phi' c_s n(1 - \exp(\Lambda - \frac{\phi}{T_e}))}$$

$$-\nu\overline{\phi'(n\nabla_\perp^2 W_{TW})'} - \overline{n\mathbf{V}_E''\mathbf{V}_0''} : \nabla\tilde{\mathbf{V}}_0^T + \overline{n'\nabla\phi'} \cdot \tilde{\mathbf{V}}_{p,0} + S_{k_{E*},n}$$

$$-\overline{\nabla p_i \cdot \mathbf{V}_{p,0}''} + \overline{\phi'\nabla n \cdot \mathbf{V}_{p,0}} - \overline{n\phi'\nabla\mathbf{V}_E : \nabla\mathbf{U}_0}, \qquad (5.27)$$

$$\Gamma_{k_{E*}} = \bar{n}k_{E*}\tilde{\mathbf{V}}_E + \overline{n\mathbf{V}_E''\mathbf{V}_0''^2}/2 + \overline{\phi'\mathbf{J}_{p,0}'}, \qquad (5.28)$$

$$S_{E_{m,E*},n} = \frac{1}{2}\overline{\mathbf{V}_0''^2 S_n} + \frac{D_0}{2}\overline{\mathbf{V}_0''^2\nabla_\perp^2 n} - \frac{1}{L_{||}}\overline{c_s\frac{n\mathbf{V}_0''^2}{2}\exp(\Lambda - \frac{\phi}{T_e})}. \qquad (5.29)$$

In equations 5.24 and 5.27, the same new terms appear that appeared in the total kinetic energy equation 5.20, i.e. the first and last term in the last line of both equations. Note that the RS and turbulent transport terms now also feature the plasma velocity $\mathbf{V}_0$.

The total perpendicular kinetic energy equations 5.20, 5.24 and 5.27 for the TOKAM2D TW case are very similar to the general total perpendicular energy equations 3.10, 3.14 and 3.15. The main differences are due to approximations made in the TOKAM2D charge balance equation B.15 with respect to the

general charge balance equation 2.53. These approximations directly lead to the Boussinesq correction terms, the $n\phi\nabla\mathbf{V}_E : \nabla\mathbf{U}_0$ terms, and the different form of the particle source terms in the TOKAM2D equations.

### E×B-only kinetic energy equations

At this point, it is important to recall (from chapter 3) that the actual fluxes that we are trying to model are those due to the E×B drift, i.e. the particle flux $\mathbf{\Gamma}_{n,t,E} \triangleq \overline{n'\mathbf{V}'_E}$ in the isothermal case. It could be assumed that the E×B fluxes are more closely related to the turbulent kinetic energy in the E×B velocity fluctuations themselves than they would be to the total turbulent kinetic energy (which has contributions from the ion diamagnetic drift as well). This would indeed be more in line with the underlying hypotheses of the $k_\perp$ transport models formulated in section 3.1. As such, this section will derive equations for the kinetic energy in the E×B drift velocity only.

As in equation 3.16 in section 3.2.2 where E×B-only kinetic energy equations have been derived for the general case, we define the E×B kinetic energies as

$$E_\mathrm{E} \triangleq \frac{\mathbf{V}_E^2}{2}, \quad E_{\mathrm{E},m} \triangleq \frac{\tilde{\mathbf{V}}_E^2}{2}, \quad \bar{n}k_E \triangleq \frac{\overline{n\mathbf{V}_E''^2}}{2}. \tag{5.30}$$

Note that the sum of this and the ion diamagnetic drift's kinetic energy which could be defined as $\mathbf{V}_{*,i}^2/2$ is not equal to the total drift kinetic energy $E_{E*}$ as the $\mathbf{V}_E \cdot \mathbf{V}_{*,i}$ term would then be overlooked. Remark that definitions 5.30 are exactly the same as those for the total kinetic energy in the E×B-only case considered in chapter 4.

Analogously to the derivations in section 3.2.2, but accounting for the specifics of the TOKAM2D case, the equations for these E×B-only kinetic energies are derived in appendix B.2.2. The equations are found (see equations B.49, B.54 and B.57) as

$$\frac{\partial}{\partial t} n E_{\mathrm{E}} + \nabla \cdot \Gamma_{E_{\mathrm{E}}} = g\phi \frac{\partial p}{\partial y} - \frac{c_s n \phi}{L_{||}} (1 - \exp(\Lambda - \frac{\phi}{T_e}))$$

$$-\nu n \phi \nabla_\perp^2 W_{TW} + n\phi \frac{DW_*}{Dt} + S_{E_{\mathrm{E}},n} + \phi \mathbf{V}_{p,E} \cdot \nabla n, \tag{5.31}$$

$$\Gamma_{E_{\mathrm{E}}} = n E_{\mathrm{E}} \mathbf{V}_E + \phi \mathbf{J}_{p,E}, \tag{5.32}$$

$$S_{E_{\mathrm{E}},n} = E_{\mathrm{E}} S_n + D_0 E_{\mathrm{E}} \nabla_\perp^2 n - \frac{E_{\mathrm{E}} c_s n}{L_{||}} \exp(\Lambda - \frac{\phi}{T_e}), \tag{5.33}$$

$$\mathbf{J}_{p,E} = n\mathbf{V}_{p,E} = n\mathbf{b} \times \frac{D\mathbf{V}_E}{Dt}. \tag{5.34}$$

$$\frac{\partial}{\partial t} \bar{n} E_{\mathrm{E},m} + \nabla \cdot \bar{\Gamma}_{E_{\mathrm{E}},m} = g\bar{\phi} \frac{\partial \bar{p}}{\partial y} - \frac{\bar{\phi}}{L_{||}} \overline{c_s n(1 - \exp(\Lambda - \frac{\phi}{T_e}))}$$

$$-\nu \bar{\phi} \overline{n \nabla_\perp^2 W_{TW}} + \bar{\phi} n \overline{\frac{DW_*}{Dt}} + \overline{n\mathbf{V}_E'' \mathbf{V}_E''} : \nabla \tilde{\mathbf{V}}_E^T - \tilde{\mathbf{V}}_{p,E} \cdot \overline{n' \nabla \phi'}$$

$$+ S_{E_{\mathrm{E},m},n} + \bar{\phi} \overline{\mathbf{V}_{p,E} \cdot \nabla n}, \tag{5.35}$$

$$\bar{\Gamma}_{E_{\mathrm{E}},m} = \bar{n} E_{\mathrm{E},m} \tilde{\mathbf{V}}_E + \overline{n\mathbf{V}_E'' \mathbf{V}_E''} \cdot \tilde{\mathbf{V}}_E + \bar{\phi} \bar{\mathbf{J}}_{p,E}, \tag{5.36}$$

$$S_{E_{\mathrm{E},m},n} = E_{\mathrm{E},m} \bar{S}_n + \tilde{\mathbf{V}}_E \cdot \overline{\mathbf{V}_E'' S_n}$$

$$+ D_0 E_{\mathrm{E},m} \nabla_\perp^2 \bar{n} + D_0 \tilde{\mathbf{V}}_E \cdot \overline{\mathbf{V}_E'' \nabla_\perp^2 n}$$

$$-\frac{E_{\mathrm{E},m}}{L_{||}} \overline{c_s n \exp(\Lambda - \frac{\phi}{T_e})} - \overline{c_s n \mathbf{V}_E'' \exp(\Lambda - \frac{\phi}{T_e})} \cdot \frac{\tilde{\mathbf{V}}_E}{L_{||}}, \tag{5.37}$$

$$\frac{\partial}{\partial t}\bar{n}k_E + \nabla \cdot \bar{\Gamma}_{k_E} = g\overline{\phi'\frac{\partial p'}{\partial y}} - \frac{1}{L_{||}}\overline{\phi'c_s n(1 - \exp(\Lambda - \frac{\phi}{T_e}))}$$

$$-\nu\overline{n\phi'\nabla_\perp^2 W_{TW}} + \overline{n\phi'\frac{DW_*}{Dt}} - \overline{n\mathbf{V}_E''\mathbf{V}_E''} : \nabla\tilde{\mathbf{V}}_E^T + \tilde{\mathbf{V}}_{p,E} \cdot \overline{n'\nabla\phi'}$$

$$+ S_{k_E,n} + \overline{\phi'(\mathbf{V}_{p,E} \cdot \nabla n)'}, \qquad (5.38)$$

$$\bar{\Gamma}_{k_E} = \bar{n}k_E\tilde{\mathbf{V}}_E + \overline{n\mathbf{V}_E''\mathbf{V}_E''^2}/2 + \overline{\phi'\mathbf{J}_{p,E}'}, \qquad (5.39)$$

$$S_{k_E,n} = \frac{1}{2}\overline{\mathbf{V}_E''^2 S_n} + \frac{D_0}{2}\overline{\mathbf{V}_E''^2\nabla_\perp^2 n} - \frac{1}{L_{||}}c_s\overline{\frac{n\mathbf{V}_E''^2}{2}\exp(\Lambda - \frac{\phi}{T_e})}. \qquad (5.40)$$

Hence, comparing this E×B-only kinetic energy equations for the TW case to the original E×B-only kinetic energy equations 4.9, 4.16 and 4.13 for the E×B-only case, the only differences are the second term on the second line and the viscous term which is now calculated for the total vorticity instead of the E×B-only one. The new $n\phi DW_*/Dt$ terms can be seen as a correction term to account for the fact that the total vorticity needs to be used instead of the E×B-only one in the charge balance equation. Alternatively, this term can be identified with the contribution of the diamagnetic drift to the divergence of the polarisation drift $\nabla \cdot \mathbf{J}_{p,*}$.

### Enstrophy equations

As for the kinetic energy, equations for the enstrophy can also be derived for the TW case, both for the total and for the E×B-only part. Hence, we define the total enstrophy (with contributions from the E×B and the ion diamagnetic drift) as

$$\zeta_{tot,E*} \triangleq \frac{W_{TW}^2}{2}, \quad \zeta_{mean,E*} \triangleq \frac{\tilde{W}_{TW}^2}{2}, \quad \bar{n}\zeta_{,E*} \triangleq \frac{\overline{nW_{TW}''^2}}{2}, \qquad (5.41)$$

and the E×B-only enstrophy as

$$\zeta_{tot,E} \triangleq \frac{W_E^2}{2}, \quad \zeta_{mean,E} \triangleq \frac{\tilde{W}_E^2}{2}, \quad \bar{n}\zeta_E \triangleq \frac{\overline{nW_E''^2}}{2}. \qquad (5.42)$$

Note that the E×B-only enstrophy as defined here is exactly the same as the enstrophy considered in the E×B-only case in chapter 4. The detailed derivation of the transport equations for these quantities can be found in appendix B.3.

The total enstrophy equations B.62-B.64 derived in the appendix take exactly the same form as those for the E×B-only case discussed in section 4.2.2. However, the vorticity $W$ used there (which is implicitly assumed to be the E×B-only vorticity $W_E$) needs to be replaced by the total vorticity $W_{TW}$. As exactly the same form of the enstrophy equations 4.25, 4.26 and 4.27 of the equations is retrieved, they are not repeated here. Note that contrary to the total energy equation, no new terms (e.g. due to approximations in the vorticity equation) appear in these total enstrophy equations.

The E×B-only enstrophy equations are then shown to take the following form in appendix (see equations B.66-B.68):

$$\frac{\partial n\zeta_{tot,E}}{\partial} + \nabla \cdot (n\mathbf{V}_E \zeta_{tot,E}) = -gW_E \frac{\partial p}{\partial y}$$

$$+\frac{c_s n W_E}{L_{||}}(1 - \exp(\Lambda - \frac{\phi}{T_e})) + \nu n W_E \nabla_\perp^2 W - nW_E \frac{DW_*}{Dt}$$

$$+\zeta_{tot,E} S_n + D_0 \zeta_{tot,E} \nabla_\perp^2 n - \frac{c_s n \zeta_{tot,E}}{L_{||}} \exp(\Lambda - \frac{\phi}{T_e}), \qquad (5.43)$$

$$\frac{\partial \bar{n}\zeta_{mean,E}}{\partial t} + \nabla \cdot (\bar{n}\zeta_{mean,E}\tilde{\mathbf{V}}_E + \overline{nW_E''\mathbf{V}_E''}\tilde{W}_E) = -g\tilde{W}_E \frac{\partial \bar{p}}{\partial y}$$

$$+\frac{\tilde{W}_E}{L_{||}}\overline{c_s n(1 - \exp(\Lambda - \frac{\phi}{T_e}))} + \nu \tilde{W}_E \overline{n\nabla_\perp^2 W_{TW}} - \tilde{W}_E \overline{n\frac{DW_*}{Dt}}$$

$$+\overline{nW_E''\mathbf{V}_E''} \cdot \nabla \tilde{W}_E + \zeta_{mean,E}\bar{S}_n + \tilde{W}_E \overline{W_E'' S_n} + D_0 \zeta_{mean,E} \nabla_\perp^2 \bar{n}$$

$$+D_0 \tilde{W}_E \overline{W_E'' \nabla_\perp^2 n} - \frac{\zeta_{mean,E}}{L_{||}}\overline{c_s n \exp(\Lambda - \frac{\phi}{T_e})}$$

$$-\frac{\tilde{W}_E}{L_{||}}\overline{c_s n W_E'' \exp(\Lambda - \frac{\phi}{T_e})}, \qquad (5.44)$$

$$\frac{\partial \bar{n}\zeta_E}{\partial t} + \nabla \cdot (\bar{n}\zeta_E \tilde{\mathbf{V}}_E + \overline{\frac{nW_E''^2 \mathbf{V}_E''}{2}}) = -g\overline{W_E'' \frac{\partial p}{\partial y}}$$

$$+\frac{1}{L_{||}} \overline{c_s n W_E''(1 - \exp(\Lambda - \frac{\phi}{T_e}))} + \nu \overline{nW_E'' \nabla_\perp^2 W_{TW}} - \overline{nW_E'' \frac{DW_*}{Dt}}$$

$$-\overline{nW_E'' \mathbf{V}_E''} \cdot \nabla \tilde{W}_E + \overline{\frac{W_E''^2 S_n}{2}} + D_n \overline{\frac{W_E''^2 \nabla_\perp^2 n}{2}}$$

$$-\frac{1}{L_{||}} \overline{\frac{c_s n W_E''^2}{2} \exp(\Lambda - \frac{\phi}{T_e})}. \qquad (5.45)$$

These E×B-only vorticity equation for the TW case are again very similar to those for the E×B-only case. The only differences are the total vorticity in the viscous term and the appearance of the fourth term on the RHS. The latter could be interpreted as a correction term for the fact that not all vorticity is due to the E×B drift anymore.

The TOKAM2D total and E×B-only enstrophy equations derived here can be seen to be very similar to the total (3.44-3.46) and E×B-only (3.51-3.53) enstrophy equations for the general case. The main difference is due to the terms that have been neglected in the general vorticity equation 3.49 to obtain the TOKAM2D vorticity equation 4.2. In addition, models have been filled out for the parallel and diamagnetic and viscous current divergences.

### 5.2.2 $k_\perp$ balances and influence of total vorticity on transport

In this section we will compare some mean-field observables of the turbulence and the resulting transport between the E×B-only case considered in chapter 4 and the TW case studied here. To this end, two sets of TOKAM2D simulations have been run: one with the regular E×B-only vorticity and another set with all the same simulation parameters but with the contribution from the diamagnetic drift to the vorticity included. A detailed description of these simulations can be found in appendix D.1.4. Note that the (former) set of simulations is not exactly the same set of simulations used in chapter 4.

Figure 5.7 evaluates the different variants of the $k_\perp$ equation. Figure 5.7d shows the balance of $k_\perp = k_E$ for the E×B-only case discussed in chapter 4 as a reference. As the figure recalls, the interchange term acts as the dominant source, while the sheath losses are the dominant sink. "Other terms" denotes the sum of all terms in the $k_\perp$ equations that are not explicitly mentioned in the legend 5.7b, while the "subgrid" term again represents the unbalance left in

(a) $k_{E*}$ balance for TW case, equation 5.27

(b) color legend



(c) $k_E$ balance for TW case, equation 5.38

(d) $k_E$ balance for E×B-only case, equation 4.16
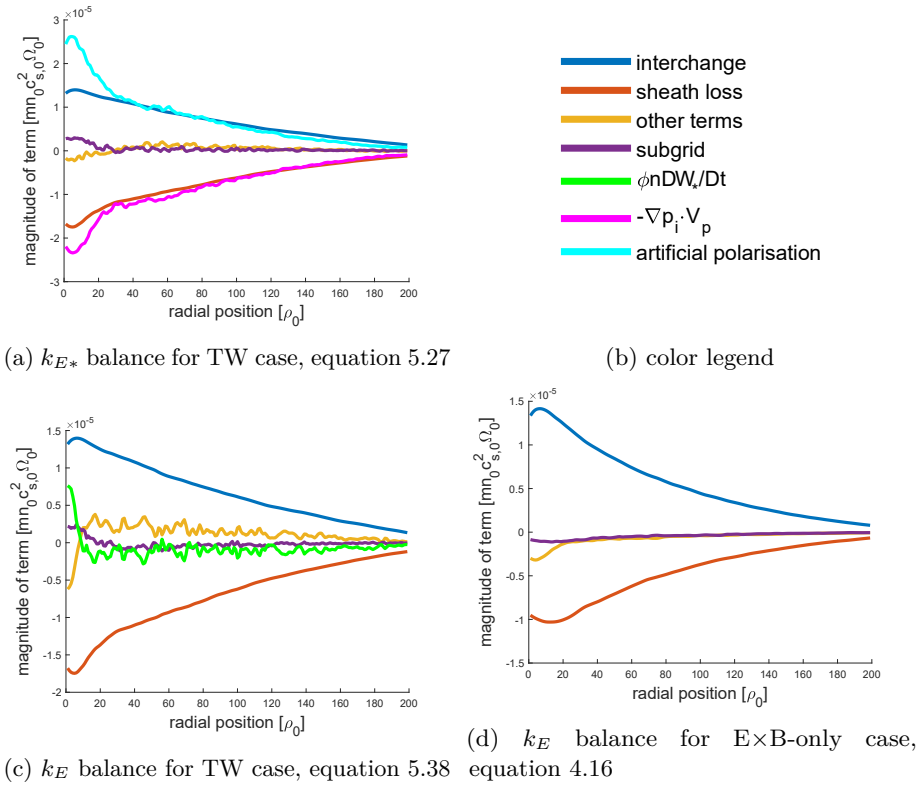
Figure 5.7: Evaluation of terms in the TOKAM2D $k_\perp$ equation for different cases.

the evaluation of the equation. Both can be seen to only play a secondary role in all subplots. Note that figure 5.7d basically plots the same data as figure 4.6. The only differences are that a larger part of the computational domain is shown, and that the viscous term is included in "other terms" instead of having been plotted separately.

Figure 5.7a shows the balance of $k_{E*}$ according to equation 5.27 for the total vorticity case. While the interchange source and the sheath loss sink are still important in the balance, the two new terms are clearly of the same order of magnitude. The "artificial polarisation" term, indicating the $-n\phi'\nabla\mathbf{V}_E : \nabla\mathbf{U}_0$ term resulting from approximations in the charge balance equation, becomes a major source. The pressure work against the polarisation velocity plays the role of a dominant sink, which almost perfectly cancels the new source.

Figure 5.7c then shows the evaluation of the E×B-only turbulent kinetic energy $k_E$ for this TW case. In line with the cancellation observed in the previous figure, the balance basically reduces to one between interchange and sheath losses again. The only direct influence of the total vorticity in this evaluation of the equation is the correction for the diamagnetic vorticity, which appears to play a minor role.

Some remarks are in place on these results. Firstly, the fact that an artificial term becomes a dominant source of the turbulence (at least for $k_{E*}$) is worrying, and it could be argued that the whole of the simulation becomes physically irrelevant. The fact that the term does not explicitly appear in the balance of $k_E$ does not mean that it could not implicitly influence the dynamics of this quantity either. On the other hand, the diamagnetic drift velocity and the kinetic energy it brings may not be of physical relevance. The origin of the diamagnetic drift is the gyration of particles around their respective magnetic field line and the mere existence or presence of this velocity does not in itself imply any net transport. In fact, only the divergence of the diamagnetic fluxes are relevant [82]. As such, it could be speculated that the diamagnetic kinetic energy and its contribution to the total energy is irrelevant, and that the artificial drive of this total energy is not so much of a problem. The almost pure cancellation of terms might be interpreted as an indication that the dynamics of interest are not so much influenced by these diamagnetic drift contributions.

Figure 5.8 then shows a comparison between turbulent kinetic energy and turbulent diffusion coefficient for the case with and without contributions from the diamagnetic velocity to the inertia. It can be seen from figure 5.8a that both the total turbulent kinetic energy $k_{E*}$ and the E×B-only kinetic energy $k_E$ in the TW case are significantly larger than the (E×B-only) kinetic energy from the E×B-only case. Hence, the diamagnetic contribution to the kinetic energy does not simply add up to the E×B-only part. Moreover, there is no clear relation between the kinetic energy in the TW case and in the E×B-only case. The same conclusions hold for the turbulent diffusion coefficient in both cases, shown in figure 5.8b. The diffusion coefficient is significantly higher in the TW case, and there is no obvious relation to the diffusion coefficient observed in the E×B-only case. From these results, it can be concluded that the inclusion of the diamagnetic contribution to the inertia does inherently influence the dynamics of the turbulence and the resulting transport.

## 5.2.3 $k_\perp$ model for total vorticity case

In this section, we will investigate whether the models for the E×B-only isothermal SOL developed in section 4 can be applied to the TW case as well.

(a) comparison for $k_\perp$

(b) comparison for $D$
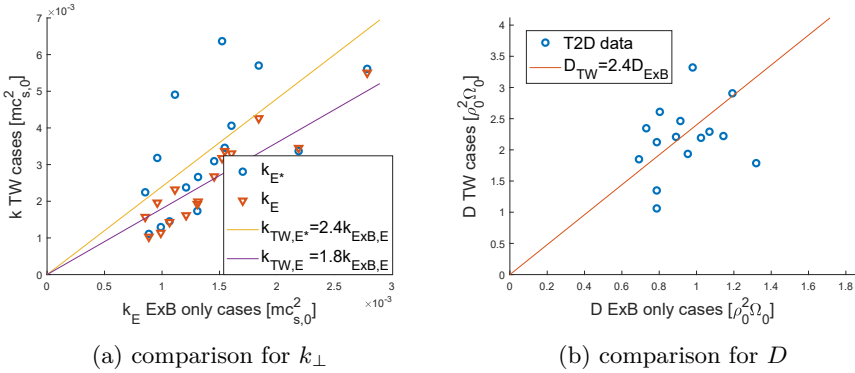
Figure 5.8: Comparison of the TW and E×B-only cases. Each marker in the scatter plots represents the radial average of a single simulation in a database of TOKAM2D simulations.

Because of the dubious physical relevance of the treatment of the diamagnetic inertia in the TOKAM2D as identified in the previous section, we prefer to keep this analysis rather brief. Nonetheless, testing the models developed earlier in this new case can be an interesting check on their robustness.

### Models for the diffusion coefficient

First, we will consider the diffusion model itself. Bayesian analyses for the E×B-only and the TW cases have been run to compare the performance of different diffusion models. The Bayesian inference was run analogously to that of the submodels in sections 4.5 and 5.1. The same wide, uninformative priors were used as in equation 5.14. The likelihood function is constructed in exactly the same way as in 5.1.4. Hence, a Gaussian distribution is assumed for the error without (spatial) correlation between different data points and the standard deviation of the error $\sigma_i$ has been taken as in expression 3.63. The reason for not scaling $\sigma_i$ to the data point value is that the large fluctuations on the TW data made these results unreliable.

Table 5.3[4] shows the results of these inferences. Considering the TW case first, it can be seen that the models based on total (E×B and diamagnetic) quantities do better than the E×B-only variables. This disproves our hypothesis made in

---

[4]Note that the results for the E×B-only case in this table have been obtained for the same models, the same Bayesian parameters and for the same data set as the first three models of the *iso-*$k_\perp$ case in table 5.1. The minor differences in the results are due to a slight difference in the part of the domain that is used, see appendix D.1.4.

section 5.2.1 that the E×B-only quantities would be better predictors for the turbulent E×B transport than the total quantities. It might be argued that this is a chance result that would not be observed in more accurate models though. More complex models involving flow shear and the phase between density and potential fluctuations (see section 5.1 and chapter 6) have been tried as well, but were found not to yield an improvement over the simpler models shown in table 5.3.

Table 5.3: Bayesian analysis of the proposed models for the particle diffusion coefficients for the E×B-only and the TW cases. Parameter values are reported at MAP.

| model for $D$ | parameter | E×B-only $k_E/\zeta_E$ | TW $k_E/\zeta_E$ | TW $k_{E*}/\zeta_{,E*}$ |
|---|---|---|---|---|
| $C_D T_e$ | $C_D[-]$ | 0.925 | 2.17 | |
| | $\sigma_{abs}[-]$ | 0.197 | 0.801 | |
| | logevidence | 616 | -3651 | |
| $C_D\sqrt{k}$ | $C_D[-]$ | 24.3 | 42.8 | 37.8 |
| | $\sigma_{abs}[-]$ | 0.203 | 0.738 | 0.714 |
| | logevidence | 522 | -3399 | -3300 |
| $C_D\frac{k}{\sqrt{\zeta}}$ | $C_D[-]$ | 7.42 | 18.0 | 7.93 |
| | $\sigma_{abs}[-]$ | 0.116 | 0.770 | 0.744 |
| | logevidence | 2214 | -3531 | -3423 |

Next, the results from the TW case are compared to those of the E×B-only case. While the evidence cannot be compared between the E×B-only case and the TW case because the output data is different for both, it can be seen that the error of the diffusion models is higher in the TW case. Note that this may not solely be due to the models working less well, but could also be due to increased noise on the data itself (that is not recovered by the models). Another notable observation is that the values for the model parameters shift significantly for almost all models. Only for the total $k_\perp - \zeta_\perp$ model are the parameter values at MAP similar to one another in both cases. This testifies of changes in the dynamics of the simulations, as was already illustrated in figures 5.8. The new source and sink terms that come into play (artificial or not) presumably change the structure of the turbulence, and through that the relation between the intensity of the turbulence (as indicated by $k_\perp$ and $\zeta_\perp$) and the resulting transport. Preliminary results seem to indicate that the spectral structure of the phase difference between density and potential fluctuations in particular changes significantly. A single model valid for both cases with the same parameters, if it exists, would hence need to include additional physical elements.

Comparing the different models with one another then, the $k_\perp$ and $k_\perp - \zeta_\perp$ model are observed to do better than the simple Bohm scaling model in the TW case. Contrary to the E×B-only case, the $k_\perp - \zeta_\perp$ model has a lower evidence and higher model error than the $k_\perp$ model. No reason for this has yet been found. Note also that in the data as reported here, the $k_\perp$ model does less well than the Bohm scaling model for the E×B-only case. However, when the model error $\sigma_i$ is scaled to the data point value ($\sigma_i = \sigma_{rel} O_i$), which does work well for this case, the evidence increases for all models, indicating that this is a better statistical model for this case. The evidence of the $k_\perp$ model does become higher than the Bohm model and the error lower. This again testifies to the importance of the statistical model and thus on the hypotheses made in the likelihood function in a Bayesian analysis.

Based on the results of table 5.3, we decide to only investigate the $k_E$ variant of the $k_\perp$ model. The $k_\perp - \zeta_\perp$ model was shown not to lead to improvement, while it would need an additional model for the enstrophy equation. This is also the reason why we have not considered the enstrophy balances in section 5.2.2. While $k_{E*}$ was shown to be a better predictor for $D$, $k_E$ is also deemed to be adequate. Moreover, constructing a model equation for $k_{E*}$ would be considerably more difficult because new terms due to the pressure work on the polarisation velocity and the artificial polarisation would need to be modelled (see section 5.2.2 and figure 5.7 in particular).

**Model for the $k_E$ equation**

In section 5.2.2 it has been shown that the balance of $k_E$ is dominated by the interchange source and the sheath loss sink, exactly like it was in the E×B-only case. In addition, the interchange term in the $k_E$ balance is the same in both cases, such that the analytical interchange relation 4.23 derived in section 4.2.1 still holds. Hence, the only term that still requires modelling is the sheath loss term. A Bayesian inference is run for this term with a very similar setup as that for the diffusion coefficient in the previous section. The main difference is that now the likelihood function is based on the relative error, i.e. the model error for each data point is assumed to scale with the value of the data point $\sigma_i = \sigma_{rel} O_i$ as in expression 3.64. The noise on the data for the TW case was smaller here, such that this statistical model could be used.

The sheath loss term was found to still largely follow the scalings identified for the E×B-only case in chapter 4. This is illustrated in table 5.4, which compares the sheath models for the E×B-only and the TW case. Here as well, the error of the sheath models is higher in the TW case. Recall that this may not only be a result of the performance of the physical model but may also be due to

the data. Also, remember that the evidence cannot be compared between both cases, because of the difference in output data. While there is a notable shift in the model coefficients between both cases, it is less significant than it was for the diffusion models in table 5.3, at least for the E×B-only evaluation of the models. This E×B-only evaluation is observed to be a better predictor than the evaluation including the diamagnetic kinetic energy, both in terms of error and in terms of evidence. This is rather logical since the sheath term itself only contains the electrostatic potential and does not include a direct link with the pressure and thus the diamagnetic drift. Lastly, it is remarkable that the $k_\perp - \zeta_\perp$ model for the $S_k$ (see expression 4.50) does less well than the simpler $k_\perp$ model for it (see expression 4.30) for the TW data, while it is the other way around for the E×B-only case. No explanation for this has yet been found.

Table 5.4: Bayesian analysis of the proposed models for the sheath loss term in the $k_\perp$ equation for the E×B-only and the TW cases. Parameter values are reported at MAP.

| model for $S_k$ | parameter | E×B-only $k_E/\zeta_E$ | TW $k_E/\zeta_E$ | TW $k_{E*}/\zeta_{,E*}$ |
|---|---|---|---|---|
| $C_{\|,k} \frac{c_s}{\sqrt{L_{\|}}} \bar{n} k$ | $C_{\|,k}[-]$ | 0.475 | 0.423 | 0.312 |
| | $\sigma_{rel}[\%]$ | 11.9 | 17.6 | 27.2 |
| | logevidence | 40342 | 37711 | 36384 |
| $C_{\|,k} \frac{c_s}{L_{\|}} \frac{\bar{n} k^2}{\zeta}$ | $C_{\|,k}[-]$ | 4.39 | 6.19 | 1.17 |
| | $\sigma_{rel}[\%]$ | 10.4 | 22.2 | 45.2 |
| | logevidence | 40751 | 37011 | 34840 |

## $k_E$ transport model for the TW case

The previous section showed that the submodels from the $k_\perp$ developed for the E×B-only case in section 4.3 still hold to some extent in the TW case. In this section, it will be investigated if the full model, combining the various submodels, can self-consistently reproduce the TOKAM2D reference data. The full model that will be used is that shown in equations 4.36-4.39, repeated below for convenience:

$$\frac{\partial \bar{n}}{\partial t} + \nabla \cdot \mathbf{\Gamma}_{n,t,E} = \bar{S}_n - C_{||,n} \frac{c_s \bar{n}}{L_{||}}, \tag{5.46}$$

$$\mathbf{\Gamma}_{n,t,E} = -C_D \sqrt{k_E} \nabla_\perp \bar{n} = -D \nabla_\perp \bar{n}, \tag{5.47}$$

$$\frac{\partial \bar{n} k_E}{\partial t} + \nabla \cdot \mathbf{\Gamma}_{k_E} = gT \Gamma_{n,t,E} - C_{||,k} \frac{c_s}{\sqrt{L_{||}}} \bar{n} k_E, \tag{5.48}$$

$$\mathbf{\Gamma}_{k_E} = k_E \mathbf{\Gamma}_{n,E} - C_{Dk} \bar{n} D \nabla k_E. \tag{5.49}$$

Note that we have already dropped the mean-field and classical transport terms in the continuity equation since these are negligible in the case under consideration. In addition, a small correction factor has been used for the sheath loss sink of particles in equation 5.46.

The model coefficients used for both cases are summarised in table 5.5. Note that the $C_{||,k}$ parameters differ slightly from those shown in 5.4. The reason for that is that in the full models, the sink coefficient has been tuned such that it compensates the interchange source instead of really representing the sheath loss sink. This way, secondary sink terms are also implicitly modelled. Secondly, the value of the $C_D$ coefficient for the E×B-only case has been chosen to be the one obtained with scaled errors in the Bayesian inference (with higher evidence) instead of the value shown in table 5.3.

Table 5.5: Model parameters used in DOL simulations simulations.

|  | $\mathbf{C_D}$ | $\mathbf{C_{||,k}}$ | $\mathbf{C_{D,k}}$ | $\mathbf{C_{||,n}}$ |
|---|---|---|---|---|
| **E×B-only** | 23.3 | 0.575 | 0.79 | 0.997 |
| **TW** | 42.8 | 0.407 | 0.79 | 0.997 |

Next, equations 5.46-5.49 with the parameters shown in table 5.5 are solved using the DivOptLight (DOL) finite volumes mean-field transport code. As the name suggests, DOL is a simplified version of the DivOpt code [52, 55] used in section 4.3.3. In DOL, all contributions in the poloidal direction are neglected and sheath conditions are added as sinks in the resulting 1D equations. This code allows to self-consistently simulate the transport, without needing input from TOKAM2D data. In order to properly compare, the geometry of DOL replicates the 1D equivalent of the TOKAM2D geometry and the particle and turbulent kinetic energy fluxes obtained from the TOKAM2D reference data are

applied as boundary conditions. As such, the DOL setup is equivalent with the original TOKAM2D setup averaged over the $y$-direction. Note that again only the central part of the TOKAM2D domain is considered where the influence of the fringe regions and the particle sources is negligible.

Figure 5.9 shows the results of the default simulation for both the E×B-only and the TW case. As can be seen from figure 5.9a, the density profile is captured rather well for both cases. Furthermore, the TW density profile is much flatter, which is the result of the higher turbulent diffusion coefficient shown in figure 5.9b. While the data for these transport coefficients is rather noisy, they seem to be reproduced rather well by the DOL simulations in both cases. Lastly, also the E×B-only turbulent kinetic energy is much higher for the TW case as shown in figure 5.9c. This quantity as well is captured to an acceptable accuracy by both cases. However, their seems to be a mismatch around the boundaries for the TW case, which is presumably because of the lacking models for the transport of $k_E$. The trend in the center of the domain seems to be accurately represented though.

DOL simulations have likewise been conducted for the other TOKAM2D reference simulations. The parameters and setup of the simulations was exactly the same for all DOL simulations, except for the boundary conditions which represent the incoming and outgoing fluxes for each individual simulation. Figure 5.10 summarises the results of all these simulations in a scatter plot. Each marker in these plots indicates the results of a single DOL-TOKAM2D simulation that has been averaged over the radial direction. These figures tend to give a good idea of the model performance in TOKAM2D parameter space. Figure 5.10a shows that the main trend in the diffusion coefficient seems to be captured for both cases, despite significant remaining scatter. Surprisingly, the $R^2$ value is even higher for the TW case than for the original E×B-only case. This is due to the strong variations in viscosity $\nu$ present in the data set, for which the $k_\perp$ model has already been shown to work poorly in chapter 4. Even though the reason for this remains obscure, the viscosity variations seem to have less effect on the TW case. This might be related to the change in the definition of $W$ from $W_E$ to $W_{TW}$ in the viscous term of the charge balance equation 5.16. Figure 5.10b then shows the underlying results for $k_E$. Here as well the DOL simulations are rather accurate. For $k_E$, the $R^2$ value is higher for the E×B-only case. Note that a Bayesian inference for the combined posterior of all parameters of the full model (as conducted in section 4.5) is not attempted for the TW case.

The conclusion from figures 5.9 and 5.10 is that the $k_E$ model captures the dominant dynamics of the turbulent transport since it can predict profiles of relevant quantities with good accuracy. This is true for both the E×B-only case studied in detail in section 4.3 and for the TW case. In addition the model also

(a) density



(b) Diffusion coefficient



(c) E×B-only turbulent kinetic energy
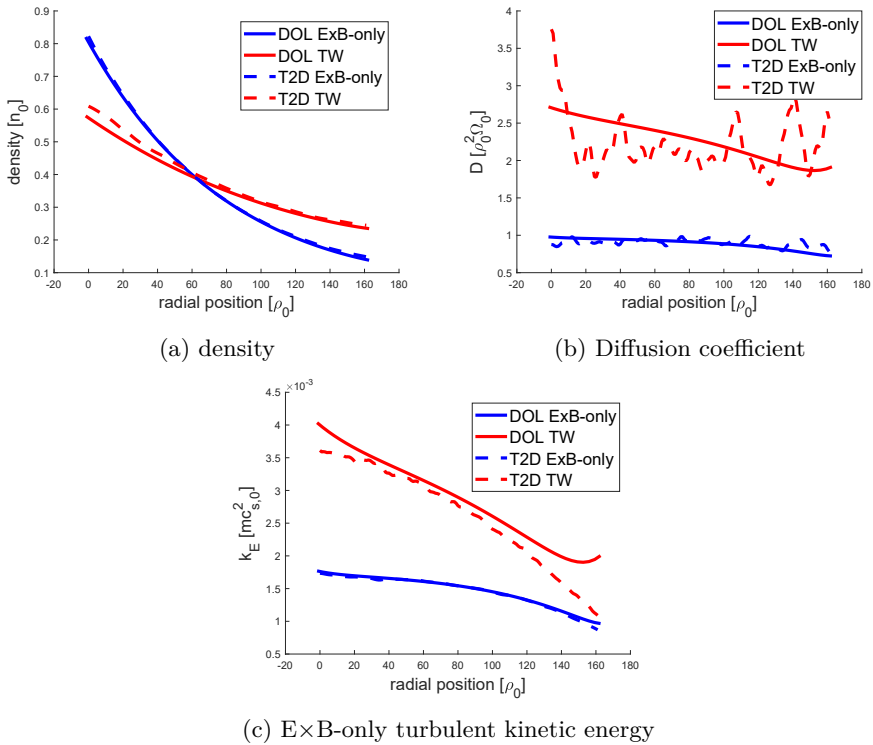
Figure 5.9: Comparison of radial profiles of forward mean-field DOL simulations to representative TOKAM2D reference data for the TW and E×B-only cases.

gives a reasonably good idea of the behaviour in parameter space for both cases, even though there clearly is room for improvement in that aspect. However, it has to be noted that different model parameters are needed for both cases.

## 5.2.4 Conclusion

This section has clearly proven that incorporating the effect of the diamagnetic drift in the plasma vorticity has a significant effect on plasma edge turbulence and the resulting transport. Analytical derivations showed a nonphysical "artificial polarisation" term to appear in the total turbulent kinetic energy equation. Evaluating the energy balance showed it to become an important source term. This poses questions on the physical validity of the reference data.
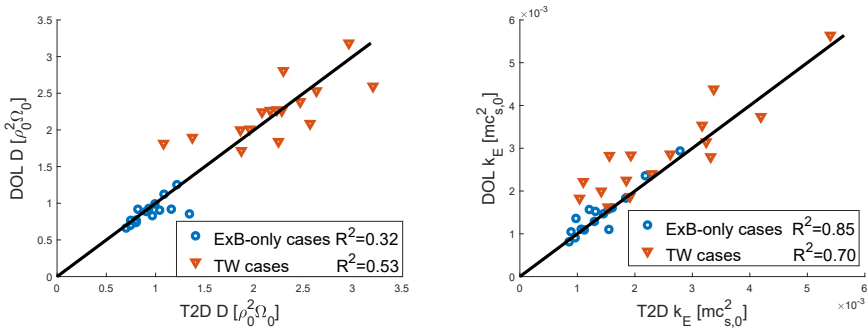
(a) effective turbulent diffusion coefficient     (b) E×B-only turbulent kinetic energy

Figure 5.10: Scatter plots comparing forward mean-field DOL simulations with TOKAM2D reference data for the TW and E×B-only cases. Each marker in the plots represents the radial average of a single simulation in a database of simulations.

Equations have likewise been derived for the E×B component of the turbulent kinetic energy only. The balance of this equation approximately reduced to a balance between the interchange term and the sheath loss term, as was the case in the E×B-only case in section 4.3. The closure models developed for that case still hold approximately in the TW case considered here, even though the model parameters changed significantly. This may be due to the changes in the structure of the turbulence caused by the new source and sink terms that come into play. Preliminary results seem to indicate that the spectral structure of the phase difference between density and potential fluctuation driving the transport in particular changes significantly.

Comparing simulations with the contribution from the diamagnetic drift to the vorticity to equivalent simulations without this contribution showed both the turbulent kinetic energy (E×B-only and total) and the effective turbulent diffusion coefficient to be much larger in the TW case. This trend is reproduced by the mean-field model, because of the adjusted model parameters. Nonetheless, this seems to testify to the robustness of the physics in the $k_\perp$ transport model.

It remains unclear why exactly the turbulence intensity and the turbulent transport increase and why the model parameters shift. The physical mechanisms for this and thus the physical reason for the influence of the diamagnetic contribution remain obscure. However, the implicit presence of the artificial polarisation term in the equation set limits the relevance of further studies of these phenomena with (the current version of) the TOKAM2D code. It seems necessary to further investigate this in a different turbulence code

(or in an improved version of TOKAM2D) where the diamagnetic current's contribution to the divergence of the polarisation current is more carefully treated.

## 5.3   Conclusion

This chapter extended the analysis of the E×B-only 2D isothermal SOL case studied in chapter 4 by adding a core region to it in section 5.1 and by adding the inertia of the ion diamagnetic drift in the polarisation current in section 5.2. Either of the effects that were added introduces new dynamics in the simulations. The core region most notably featured strong shear flows and DW-like dynamics instead of a sheath connection, while the inclusion of the diamagnetic drift's inertia led to new terms becoming significant in the kinetic energy balance. As a result, changes in the structure of the turbulence occurred with respect to the standard case investigated in the previous chapter. Even though the mean-field turbulent transport models developed for the standard case still capture some of the basic elements for the new cases, adjustments are required to reflect these changes in the character of the turbulence.

While several modifications have been explored to improve the performance of the models, further research is still needed to elucidate the precise role of the new dynamics and instabilities. In particular, a model with fixed parameters that holds irrespective of the exact case that is investigated remains elusive. In order to achieve such model, it might be interesting to investigate still different characteristic quantities of the turbulence, such as the phase shift between density and potential fluctuations for example. For investigating the core region in particular, it seems preferable to continue this research for 3D reference data though, since the DWs are effectively a 3D phenomenon such that only an approximate description of them was possible in 2D. For the TW case, reference data should be used in which the artificial terms identified in this chapter do not occur.

# Chapter 6

# 2D anisothermal E$\times$B drift turbulence in the SOL

While chapters 4 and 5 have only considered edge plasmas in which the ion and electron temperatures were constant in time and in space, this chapter[1] investigates the SOL under fully anisothermal conditions. Hence, the temperatures are allowed to evolve self-consistently, introducing not only mean-field temperature profiles, but also spatio-temporal fluctuations of $T_i$ and $T_e$. The 2D electrostatic conditions without neutrals are maintained here. In addition, only the E$\times$B drift will be considered in the inertia again (contrary to the generalisation allowed in section 5.2).

Because temperature fluctuations are included, part of the mean-field radial heat flux is now due to turbulent convection. This constitutes a new closure term which needs to be modelled in addition to the average turbulent particle flux. Furthermore, it is investigated whether the temperature fluctuations themselves introduce changes to the turbulent plasma dynamics. In particular, the sheath-driven conducting-wall (SCW) instability [15, 17, 20, 21] is found to appear as an additional source of the turbulence. The $k_\perp$ model developed for the isothermal case in section 4.3 will be extended to self-consistently include these new effects.

The remainder of this chapter is structured as follows. Section 6.1 will briefly

---

[1]Parts of this chapter have been published in "Coosemans, R., Dekeyser, W., Baelmans, M. (2022). A self-consistent mean-field model for turbulent particle and heat transport in 2D interchange-dominated electrostatic ExB turbulence in a sheath-limited scrape-off layer. *Contributions to Plasma Physics*, e202100193" [47].

introduce the anisothermal TOKAM2D model and derive the corresponding mean-field equations. The SCW instability will be identified in this section and a case will be set up where this instability is artificially removed. Comparison with the original case allows to single out the influence of the SCW instability. Section 6.2 then investigates models for the turbulent transport coefficient for particle and heat transport, the interchange source of $k_\perp$ and the sheath contribution to $k_\perp$ separately. Next, section 6.3 combines these individual "submodels" into a self-consistent model for the mean-field transport. Forward simulations with this model are compared to the TOKAM2D reference data. Section 6.4 then comes back to the SCW instability analysing the effects resulting from it in more detail. Finally, section 6.5 summarises the main findings of this chapter.

## 6.1   Anisothermal TOKAM2D setup and equations

The isothermal TOKAM2D code and the simulation setup are discussed in detail in section 4.1. In this chapter, thermal energy equations are added to describe the evolution of the ion and electron temperatures, as described in appendix B.1. The subset of the full TOKAM2D equations B.21-B.25 that describes the anisothermal SOL which will be considered in this chapter is the following [141, 109, 116]:

$$\frac{\partial n}{\partial t} + \mathbf{V}_E \cdot \nabla n - D_0 \nabla_\perp^2 n = S_n - \frac{n c_s}{L_{||}} \exp(\Lambda - \frac{\phi}{T_e}), \qquad (6.1)$$

$$\frac{\partial W}{\partial t} + \mathbf{V}_E \cdot \nabla W - \nu_0 \nabla_\perp^2 W = -\frac{g}{n}\frac{\partial p}{\partial y} + \frac{c_s}{L_{||}}(1 - \exp(\Lambda - \frac{\phi}{T_e})), \qquad (6.2)$$

$$\frac{\partial p_i}{\partial t} + \mathbf{V}_E \cdot \nabla p_i - \chi_0 \nabla_\perp^2 p_i = S_{p_i} - \frac{2}{3}\frac{\gamma_i p_i c_s}{L_{||}} - \frac{2m_e}{m_i}\frac{p_i - p_e}{\tau_{ei}}, \qquad (6.3)$$

$$\frac{\partial p_e}{\partial t} + \mathbf{V}_E \cdot \nabla p_e - \chi_0 \nabla_\perp^2 p_e$$

$$= S_{p_e} - \frac{2}{3}\frac{\gamma_e p_e c_s}{L_{||}} \exp(\Lambda - \frac{\phi}{T_e}) + \frac{2m_e}{m_i}\frac{p_i - p_e}{\tau_{ei}}, \qquad (6.4)$$

$$W \triangleq \nabla_\perp^2 \phi, \qquad \mathbf{V}_E \triangleq \mathbf{b} \times \nabla \phi. \qquad (6.5)$$

Note that we reintroduce the assumption that the only contribution to the voriticity $W$ and thus to the inertia is due to the E×B drift. It can also be remarked that the energetic coupling between the kinetic energy and the

thermal energy is not self-consistently included in these equations. Following the energetic interactions outlined in section 3.2.5, the total kinetic energy interchange and viscous stress terms (first and third term on the RHS of equation 4.9) should exchange energy with the thermal energy equations.[2]

In this thesis, we are interested in modelling the average behaviour of this system. Time- (or ensemble-) averaging equations 6.1, 6.3 and 6.4 yields the following mean-field equations.

$$\frac{\partial \bar{n}}{\partial t} + \nabla \cdot \boldsymbol{\Gamma}_{n,E} = \bar{S}_n - \frac{1}{L_{||}} \overline{c_s n \exp(\Lambda - \frac{\phi}{T_e})} + D_0 \nabla_\perp^2 \bar{n}, \quad (6.6)$$

$$\frac{\partial \bar{p}_i}{\partial t} + \nabla \cdot \boldsymbol{\Gamma}_{p_i,E} = \bar{S}_{p_i} - \frac{2}{3}\frac{\gamma_i}{L_{||}} \overline{c_s p_i} + \chi_0 \nabla_\perp^2 \bar{p}_i - \frac{2m_e}{m_i}\frac{\bar{p}_i - \bar{p}_e}{\tau_{ei}}, \quad (6.7)$$

$$\frac{\partial \bar{p}_e}{\partial t} + \nabla \cdot \boldsymbol{\Gamma}_{p_e,E}$$

$$= \bar{S}_{p_e} - \frac{2}{3}\frac{\gamma_e}{L_{||}} \overline{c_s p_e \exp(\Lambda - \frac{\phi}{T_e})} + \chi_0 \nabla_\perp^2 \bar{p}_e + \frac{2m_e}{m_i}\frac{\bar{p}_i - \bar{p}_e}{\tau_{ei}}, \quad (6.8)$$

$$\boldsymbol{\Gamma}_{n,E} \triangleq \overline{n\mathbf{V}_E} = \bar{n}\bar{\mathbf{V}}_E + \overline{n'\mathbf{V}'_E} \triangleq \boldsymbol{\Gamma}_{n,m,E} + \boldsymbol{\Gamma}_{n,t,E}, \quad (6.9)$$

$$\boldsymbol{\Gamma}_{p,i/e} \triangleq \overline{nT_{i/e}\mathbf{V}_E} = \tilde{T}_{i/e}\boldsymbol{\Gamma}_{n,E} + \overline{nT''_{i/e}\mathbf{V}''_E} \triangleq \boldsymbol{\Gamma}_{pi/e,m,E} + \boldsymbol{\Gamma}_{pi/e,t,E}. \quad (6.10)$$

Note that the mean-field continuity equation had already been derived as equation 4.5 when treating the isothermal case. Furthermore, the definitions of the mean-field E×B fluxes correspond to those used for the general case in equations 2.65 and 2.70. Remark also that the convective terms $\mathbf{V}_E \cdot \nabla u$ on the LHS of equations 6.1, 6.3 and 6.4 are written as $\nabla \cdot (u\mathbf{V}_E)$ in equations 6.6-6.8 for generality. In the TOKAM2D case where $\nabla \cdot \mathbf{V}_E = 0$, this is analytically exact.

Remember also that as in the isothermal TOKAM2D case, the radial component of particle flux due to convection with the mean-field E×B velocity, $\boldsymbol{\Gamma}_{n,m,E}$, is zero, since $\bar{\mathbf{V}}_{E,x} = 0$ due to symmetry. For the heat flux, both convection with the mean-field particle flux, $\boldsymbol{\Gamma}_{pi/e,m,E}$[3] and the turbulent part $\boldsymbol{\Gamma}_{pi/e,t,E}$ are relevant, both for ions and electrons. This is illustrated in figure 6.1, where

---

[2]The sheath loss term (second term on the RHS of equation 4.9) on the other hand is interpreted as the $-\nabla \cdot \phi \mathbf{J}_{||}$ parallel transport term which does not interact with other energy equations.

[3]Note that in this terminology, the mean-field pressure flux $\boldsymbol{\Gamma}_{pi/e,m,E}$ includes a contribution due to convection with the mean-field turublent particle flux $\tilde{T}_{i/e}\boldsymbol{\Gamma}_{n,t,E}$.

(a) particle flux
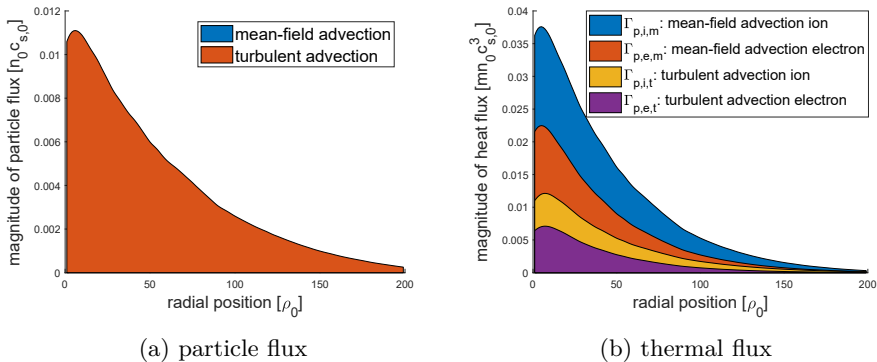
(b) thermal flux

Figure 6.1: Decomposition of particle and thermal flux for the anisothermal TOKAM2D case.

these terms are evaluated for a representative TOKAM2D case. As in the previous chapter, the radial profiles in this figure are obtained by averaging the TOKAM2D data in time and over the (periodic) y-direction.

Inspection of equations 6.6-6.10 shows that only the turbulent particle and thermal fluxes, $\mathbf{\Gamma}_{n,t,E}$ and $\mathbf{\Gamma}_{pi/e,t,E}$ respectively, and the sheath losses on the RHS of equations 6.6-6.8 require closure. We will mostly focus on the closures of these turbulent fluxes. As in equations 3.1 and 3.2, a diffusive model is proposed:

$$\mathbf{\Gamma}_{n,t,E} \approx -D\nabla\bar{n}, \tag{6.11}$$

$$\mathbf{\Gamma}_{pi/e,t,E} \approx -\chi_{i/e}\bar{n}\nabla\tilde{T}_{i/e}. \tag{6.12}$$

Note that the latter expression represents the flux of pressure, which still needs to be multiplied by a factor 3/2 to obtain the turbulent E×B thermal energy flux.

Following chapters 4 and 5, the transport coefficients in these expressions will be related to the turbulent kinetic energy $k_\perp$ in section 6.2.1. With this in mind and to get more information on the underlying dynamics of the turbulence, the balance of the turbulent kinetic energy is studied. Since only the E×B velocity is considered in the inertia, we consider the E×B-only kinetic energy $k_\perp = \overline{n\mathbf{V}_E''^2/2}$ in this chapter.[4] The transport equation for this quantity has

_____

[4]As there is again no cause for confusion in this chapter, we choose to use the symbol $k_\perp$ for generality again.

(a) SCW1 case

(b) SCW0 case
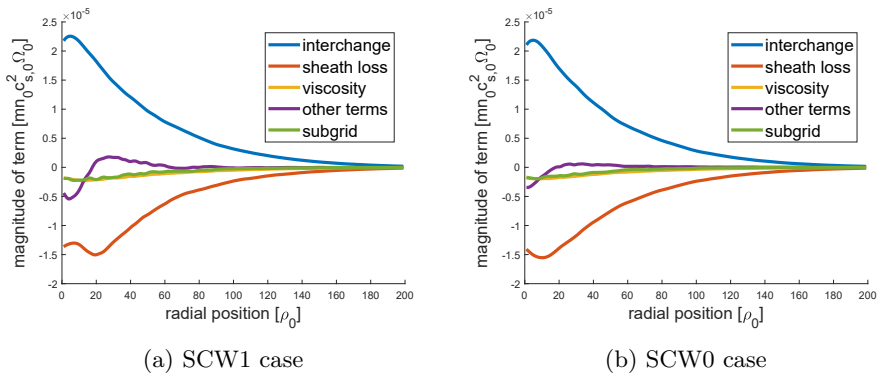
Figure 6.2: Turbulent kinetic energy balance according to equation 4.16 for a representative anisothermal TOKAM2D simulation.

been derived analytically in section 4.2.1 as equation 4.16. Note that this equation is equally valid in the anisothermal case.

Figure 6.2a shows an evaluation of the terms in this equation for a representative TOKAM2D simulation. The label SCW1 in this figure indicates that the full set of anisothermal equations is used, which includes a new sheath conducting wall instability compared to the isothermal case. It is clear from this figure that the interchange term $G_k$ (first term on the RHS of equation 4.16) is the dominant source, while the sheath term $S_k$ (second term on the RHS of equation 4.16) provides the dominant sink of the turbulence. The viscous sink (third term on the RHS of equation 4.16) and the subgrid term, which is the unbalance on the numerical evaluation of equation 4.16, act as secondary sinks. The other terms in the equation do not seem to play an important role. This picture is qualitatively very similar to that painted in section 4.3 for the isothermal case.

Closer evaluation of the sheath term shows that its behaviour is much more complex in the anisothermal case than it was in the isothermal case though. A series expansion in $n$, $\phi$ and $T_e$ around $\bar{n}$, $\bar{\phi}$ and $\tilde{T}_e$ respectively up to fluctuations of second order yields

$$S_k \triangleq -\frac{1}{L_{||}} \overline{c_s n \phi'(1 - \exp(\Lambda - \frac{\phi}{T_e}))} \approx S_{\phi^2} + S_{\phi T_e} + S_{n\phi} + S_{\phi T}$$

$$\triangleq \frac{\bar{n}\sqrt{\tilde{T}_i + \tilde{T}_e}}{L_{||}} \exp(\Lambda - \frac{\bar{\phi}}{\tilde{T}_e})(-\frac{\overline{\phi'^2}}{\tilde{T}_e} + \frac{\bar{\phi}}{\tilde{T}_e^2}\overline{\phi'T_e''})$$

$$-\frac{1}{L_{||}}(1 - \exp(\Lambda - \frac{\bar{\phi}}{\tilde{T}_e}))(\sqrt{\tilde{T}_i + \tilde{T}_e}\overline{n'\phi'} + \frac{\bar{n}}{2\sqrt{\tilde{T}}}\overline{\phi'(T_i'' + T_e'')}). \qquad (6.13)$$

As is shown in figure 6.3a, the first term in this expansion provides a sink indeed, but the second contribution acts like a large source of $k_\perp$. The last two terms in the series expansion are small because $(1 - \exp(\Lambda - \bar{\phi}/\tilde{T}_e)) \approx 0$. The series expansion is a reasonable approximation since the sum of the four contributions is close to the original, total term, as indicated in the figure with the dashed red line. While in the isothermal case only the first (and third) terms were present, the second (and fourth) source term comes into play now that electron temperature fluctuations are present in equations 6.1-6.4. Physically, this new source term can be identified with the sheath conducting wall (SCW) mode described for TOKAM2D specifically in Refs. [17, 15] and in general in Refs. [21, 20]. It will be shown to significantly influence the results.



(a) SCW1 case          (b) SCW0 case
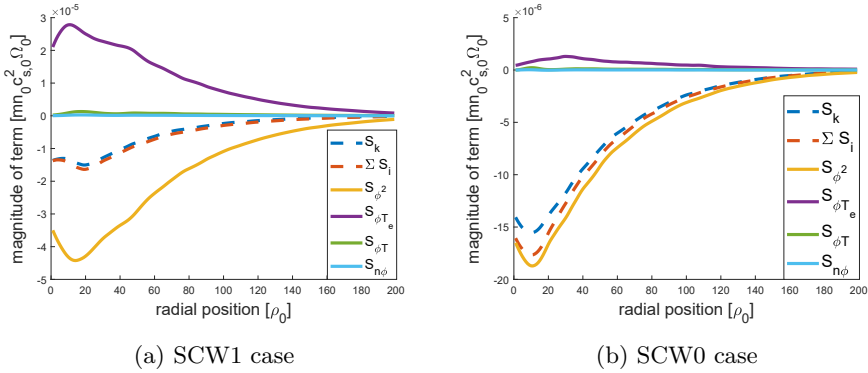
Figure 6.3: Decomposition of the sheath term $S_k$ in the turbulent kinetic energy equation according to series expansion 6.13.

As described by Baudoin [15], the basic mechanism of the SCW instability is the following. When an electron temperature perturbation in the diamagnetic

direction is present, this will cause the electrostatic potential to follow this perturbation such that the factor $\exp(\Lambda - \phi/T_e)$ in the RHS of equations 6.6-6.8 remains limited. The resulting electric field in the diamagnetic direction will then lead to a radial E×B drift. If a radial gradient in the electron temperature is present, it will be convected by this E×B drift which develops and amplifies the initial perturbation. Hence, this instability will grow and provide a drive for turbulence. Dedicated TOKAM2D simulations where the interchange term was set to zero ($g = 0$) have shown that this SCW mode suffices to develop a turbulent flow field.

In order to distinguish between the effect of this SCW mode that appears in the anisothermal case, and other possible effects inherent to the inclusion of temperature variations, a case is set up in which the SCW mode is removed. This will be called the SCW0 case, while the original case is referred to as SCW1. The SCW0 case is constructed by replacing the local, instantaneous $T_e$ by the diamagnetic average $\langle T_e \rangle_y$ in all the exponential terms in equations 6.6-6.8, as was suggested in Ref. [15]. In the SCW instability mechanism described above, this means that the electrostatic potential no longer needs to follow diamagnetic fluctuations of $T_e$, such that no radial E×B drifts originate to compensate these diamagnetic fluctuations and the instability mechanism is broken. In equation 6.13 as well, this reduces the factor $\overline{\phi' T_e''}$ in the SCW drive to $\overline{\langle \phi \rangle_y' \langle T_e \rangle_y''}$. Since the remaining fluctuations in the latter expression are already averaged over the diamagnetic direction, it is expected to be much smaller than the former. Note that it need not be exactly zero since fluctuations in time of diamagnetically averaged profiles may still persist.

Figure 6.3b shows that the SCW contribution $S_{\phi T_e}$ to $S_k$ is indeed largely suppressed in the SCW0 case as intended. However, comparing the $k_\perp$ balance shown in 6.2b of this case to that of the original SCW1 case in figure 6.2a, it is observed that they differ very little, i.e. the sum of all sheath terms remains largely unchanged. Nonetheless, it will be shown that the resulting value of $k_\perp$ does significantly differ, as well as the model coefficients that will be required for both cases.

Another difference with the isothermal SOL case is that stronger shear flows tend to develop. As in the isothermal case, the electrostatic potential $\phi$ tends to follow the electron temperature $T_e$ to limit the magnitude of the sheath loss terms $\sim \exp(\Lambda - \phi/T_e)$ in equations 6.1, 6.2 and 6.4 (both in the SCW1 and SCW0 case). Since $T_e$ is now allowed to evolve self-consistently, both $T_e$ and $\phi$ now develop a radial profile, resulting in a radial shear of the diamagnetic E×B velocity $\partial_x V_{E,y} = \partial_x^2 \phi$. As far as the author has been able to uncover, this flow shear does not seem to play a large role. The Reynolds stress contribution to the $k_\perp$ balance ($-\overline{n \mathbf{V}_{E,x}'' \mathbf{V}_{E,y}''} : \partial_x \tilde{\mathbf{V}}_{E,y}^T$) seems to remain small. Flow shear was

not identified to be of major importance for the turbulent transport relation either.

## 6.2 $k_\perp$ model for radial turbulent transport

In this section, a mean-field model for the turbulent transport coefficients $D$, $\chi_i$ and $\chi_e$ in equations 6.11 and 6.12 is constructed. This is done by relating these coefficients to the turbulent kinetic energy, and constructing a model equation for the latter. The closure models required for this are constructed based on an analysis of a set of TOKAM2D simulations. In these simulations, the TOKAM2D parameters have been varied in the following range: $g = 3-12\times10^{-4}$, $1/L_{||} = 0.2 - 2 \times 10^{-4}$, $D_0 = \nu_0 = 2.5 - 10 \times 10^{-3}$, $T_{inj,i/e} = 2 - 8$. This set of simulations has been run twice: once with the SCW instability (SCW1 case) and once with the SCW instability suppressed (SCW0 case). See appendix D.3 for a more detailed description of this set of TOKAM2D simulations.

### 6.2.1 Diffusion model for heat and particle transport

A first interesting observation to make is that the turbulent particle transport coefficient is very similar to that for the ion and electron heat transport, i.e. $D \sim \chi_i \sim \chi_e$ as was already remarked in Ref. [45]. The transport coefficients only seem to differ by a factor of order unity, as is illustrated in figure 6.4. Each marker in this plot represents the transport coefficients of a single TOKAM2D simulation which have been averaged over time, $x$- and $y$-directions. Even though the $x$-direction is not a symmetry direction and strong profiles are present along it, such plots tend to give a good overview of the trends in parameter space. It can be seen that the proportionality constants between $D$, $\chi_i$ and $\chi_e$ slightly differ between the SCW1 and the SCW0 case. In the SCW1 case, $\chi_i$ becomes noticeably larger than $D$ and $\chi_e$, while the differences between the three are smaller in the SCW0 case.

As a first model, it is proposed that all three transport coefficients follow a scaling with $\sqrt{k_\perp}$ as was found to hold approximately for the isothermal case in chapters 4 and 5. To estimate the closure constants from the set of TOKAM2D reference simulations, the Bayesian inference framework presented in section 3.4 is used. The absolute formulation for the standard deviation of the model error (see equation 3.63) is used since using the relative error formulation (see equation 3.64) led to unsatisfactory results because of the reference data having very low values towards the other side of the TOKAM2D computational domain.

(a) SCW1 case            (b) SCW0 case
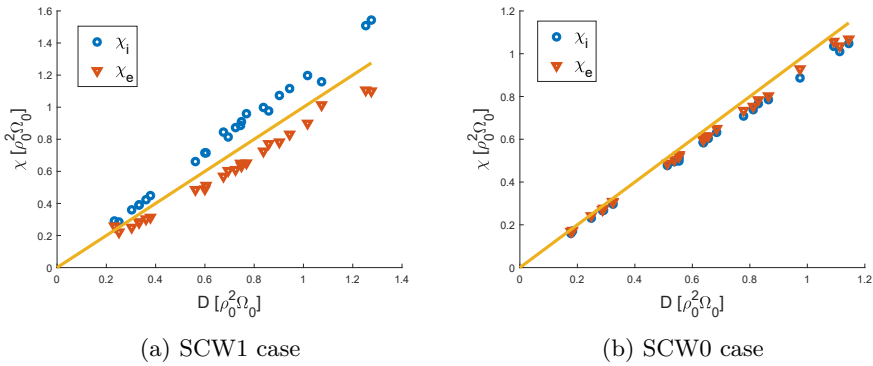
Figure 6.4: Scatter plot of ion and electron heat transport coefficients against the particle transport coefficient. Each marker represents the radial average of a single simulation in a database of TOKAM2D simulations.

The priors for the model constants and the standard deviation of the model errors are taken as in equation 5.14 in chapter 5:

$$
\begin{cases} \pi(C) = 2N(0, 100) & \text{if } C \geq 0 \\ \pi(C) = 0 & \text{if } C < 0 \end{cases} \qquad \begin{cases} \pi(\sigma_{abs}) = 1/\sigma_{abs} & \text{if } \sigma_{abs} \geq 0 \\ \pi(\sigma_{abs}) = 0 & \text{if } \sigma_{abs} < 0 \end{cases} \qquad (6.14)
$$

The resulting MAP values for the transport coefficients and model error standard deviation as well as the model evidence are shown on the fourth row in table 6.1. The first three rows in the table show the results for various (gyro-)Bohm-like scalings. Furthermore, figures 6.5 and 6.6 show the radial profile for a typical simulation and a scatter plot across the set of simulations for the particle diffusion coefficient for the MAP values. From figure 6.5 it is clear that the $k_\perp$ model captures the profile of the diffusion coefficient very well, both for the SCW1 and the SCW0 case. It can be noted that the match at the left side of the domain is less convincing, which is presumed to be due to the non-negligible influence of the particle and energy sources that are present there. In addition, flow shear is also strongest in this region, which might also influence the transport. Figure 6.6 indicates that the basic scaling in parameter space is also captured by the $k_\perp$ model for both cases. However, some discrepancy remains in the finer trends. This discrepancy as well as the scatter on the results is markedly higher for the SCW1 case than for the SCW0 case.

Even though the results cannot strictly be compared between the different cases because the output data is different, it seems the $k_\perp$ model works better for the SCW0 case judging by the results in figure 6.5 as well as by the $\sigma_{abs}$ values in table 6.1. Furthermore, the agreement of the $C_D$ parameter of the isothermal case ($\sim 23 - 25$, see tables 4.2, 5.1 and 5.3 ) is better with the SCW0 case than with the SCW1 case.

Table 6.1: Bayesian analysis of the proposed models for the particle and heat transport coefficients for the anisothermal SCW1 and SCW0 datasets. Parameter values are reported at MAP.

| Model | parameter | SCW1 | | | SCW0 | | |
|---|---|---|---|---|---|---|---|
| | | $D$ | $\chi_i$ | $\chi_e$ | $D$ | $\chi_i$ | $\chi_e$ |
| $CT_e$ | $C[-]$ | 1.21 | 1.43 | 1.04 | 1.05 | 0.953 | 0.958 |
| | $\sigma_{abs}[-]$ | 0.266 | 0.321 | 0.246 | 0.227 | 0.217 | 0.245 |
| | logevidence | -470 | -1368 | -101 | 290 | 503 | -76 |
| $CgT_e^{3/2}$ | $C[-]$ | 1685 | 1988 | 1458 | 1461 | 1320 | 1315 |
| | $\sigma_{abs}[-]$ | 0.388 | 0.460 | 0.348 | 0.339 | 0.319 | 0.348 |
| | logevidence | -2397 | -3272 | -1846 | -1725 | -1412 | -1823 |
| $CT_e^{3/2}\nabla\ln\bar{p}$ | $C[-]$ | 55.3 | 66.1 | 47.6 | 49.5 | 44.7 | 44.0 |
| | $\sigma_{abs}[-]$ | 0.533 | 0.629 | 0.471 | 0.444 | 0.442 | 0.433 |
| | logevidence | -3784 | -4568 | -3194 | -2912 | -2539 | -2884 |
| $C\sqrt{k_\perp}$ | $C[-]$ | 16.8 | 19.9 | 14.5 | 20.8 | 18.9 | 19.2 |
| | $\sigma_{abs}[-]$ | 0.189 | 0.229 | 0.189 | 0.121 | 0.120 | 0.139 |
| | logevidence | 1181 | 257 | 1168 | 3283 | 3321 | 2627 |
| $C\frac{k_\perp}{\sqrt{\zeta_\perp}}$ | $C[-]$ | 4.33 | 5.14 | 3.74 | 6.50 | 5.90 | 5.97 |
| | $\sigma_{abs}[-]$ | 0.194 | 0.237 | 0.190 | 0.0977 | 0.104 | 0.136 |
| | logevidence | 1039 | 81 | 1134 | 4318 | 4021 | 2756 |
| $C\sqrt{k_\perp}\sin\Psi$ | $C[-]$ | 25.0 | 29.2 | 21.6 | 22.1 | 20.1 | 20.4 |
| | $\sigma_{abs}[-]$ | 0.163 | 0.205 | 0.170 | 0.123 | 0.124 | 0.138 |
| | logevidence | 1504 | 783 | 1681 | 3123 | 3183 | 2665 |
| $C\frac{k_\perp}{\sqrt{\zeta_\perp}}\sin\Psi$ | $C[-]$ | 6.59 | 7.81 | 5.70 | 6.96 | 6.31 | 6.40 |
| | $\sigma_{abs}[-]$ | 0.143 | 0.188 | 0.152 | 0.0924 | 0.103 | 0.130 |
| | logevidence | 2505 | 1199 | 2211 | 4588 | 4078 | 2964 |
| $C\frac{G_k}{G_k+C_{SCW}S_{\phi Te}}\sqrt{k_\perp}$ | $C[-]$ | 21.3 | 24.8 | 18.4 | 21.4 | 19.2 | 19.2 |
| | $C_{SCW}[-]$ | 0.143 | 0.128 | 0.146 | 0.257 | 0.156 | 8.62E-3 |
| | $\sigma_{abs}[-]$ | 0.154 | 0.192 | 0.164 | 0.119 | 0.119 | 0.139 |
| | logevidence | 2142 | 1078 | 1832 | 3375 | 3349 | 2619 |
| $C\frac{G_k}{G_k+C_{SCW}S_{\phi Te}}\frac{k_\perp}{\sqrt{\zeta_\perp}}$ | $C[-]$ | 5.76 | 6.61 | 5.02 | 6.50 | 5.90 | 5.97 |
| | $C_{SCW}[-]$ | 0.176 | 0.151 | 0.184 | 1.23E-3 | 2.98E-5 | 3.55E-5 |
| | $\sigma_{abs}[-]$ | 0.155 | 0.199 | 0.161 | 0.0977 | 0.104 | 0.136 |
| | logevidence | 2101 | 921 | 1930 | 4308 | 4011 | 2745 |

In addition, table 6.1 and figures 6.5 and 6.6 also show the results for the Bohm and gyro-Bohm scalings 2.81 and 2.82. The Bohm scaling in normalised TOKAM2D units and with the magnetic field assumed to be constant becomes $D \sim T_e$. Under the same assumptions and using the pressure decay length as the

(a) SCW1 case  (b) SCW0 case
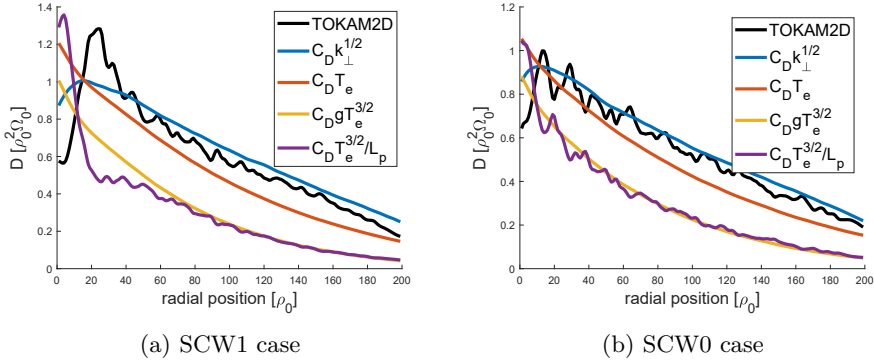
Figure 6.5: Comparison of radial diffusion coefficient profiles for different models for a representative anisothermal TOKAM2D simulation for the SOL.

perpendicular length scale leads to $D \sim T_e^{3/2} \nabla \ln \bar{p}$ for the gyro-Bohm scaling. Alternatively, when the tokamak minor radius is used as the characteristic perpendicular length scale, and a constant aspect ratio is assumed such that $L_\perp \sim a \sim R \sim 1/g$, the gyro-Bohm scaling becomes $D \sim g T_e^{3/2}$. (See also table 6.4 for a summary.)

The evidence of these Bohm and gyro-Bohm scalings can be seen to be much lower than that of the $k_\perp$ model for all transport coefficients, both in the SCW1 and the SCW0 case. Figure 6.5 shows that the Bohm scaling manages to capture the trend in the profile sufficiently well, while the profiles of the gyro-Bohm scaling are too steep due to the $T_e^{3/2}$ scaling. Also, oddly, the coefficients for the gyro-Bohm scaling seem to be poorly tuned for this reference case. Considering the behaviour in TOKAM2D parameter space then, the $k_\perp$ model again outperforms the Bohm and gyro-Bohm models. This confirms the results of the comparison for the isothermal case presented in section 4.3.

radially averaged values for a database of TOKAM2D simulations

Sections 4.4 and 5.1 have tried to improve the accuracy of the $k_\perp$ model by taking the effect of enstrophy and flow shear into account in the diffusion relation. The results in table 6.1 indicate that the enstrophy does not allow to remove the remaining model discrepancies in the SCW1 case, since the evidence for the $k_\perp - \zeta_\perp$ model is lower than that of the $k_\perp$ model. For the SCW0 case, the inclusion of the enstrophy does allow a large improvement of the results. Including the flow shear can improve the results, although this seems to play a secondary role.

(a) SCW1 case

(b) SCW0 case
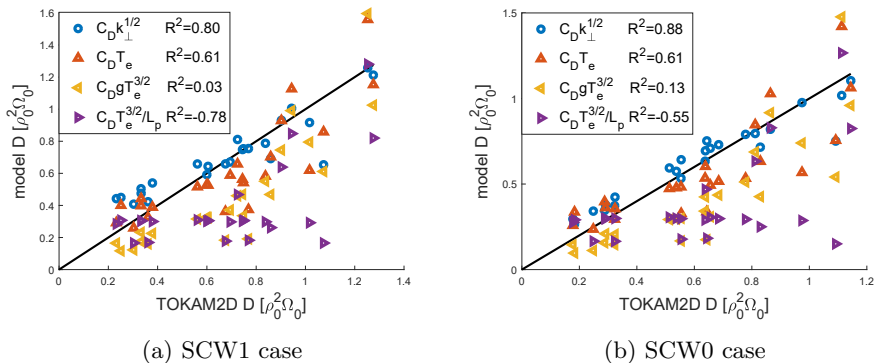
Figure 6.6: Scatter plot showing radially averaged values of different models for the diffusion coefficient for a database of TOKAM2D simulations.

Hence, in the SCW1 anisothermal case the main reason for the remaining model discrepancy is due to the SCW drive coming into play next to the interchange drive. Each instability mechanism individually would lead to a different structure of the turbulence. Because of this, the relation between the fluctuation level, and thus $k_\perp$, and the resulting transport is different in both regimes. As a result, the diffusion relation changes as the relative magnitude of both driving mechanisms of the turbulence varies. The strong influence of the SCW term on the accuracy of the $k_\perp$ model is illustrated in figure 6.7. When the SCW term $S_{\phi Te}$ is large compared to the interchange term $G_k$, the turbulence largely follows the SCW turbulence structure. The small phase difference between density and potential fluctuations for this kind of turbulence leads to lower transport for the same level of $k_\perp$, resulting in an overestimation of $D$ as seen in the figure. Note that this explanation is in line with the lower $C_D$ coefficient found here than in the isothermal case where only interchange was present.

The influence of the SCW term on the diffusion models will be further analysed in section 6.4. It will be found that correcting the diffusion relation for the phase difference between density and potential fluctuations ($\psi$) can significantly improve the accuracy of the models. This leads to the last four models shown in table 6.1 which will further be discussed there. Given the acceptable fit of the transport coefficients illustrated above we keep the basic $D \sim \sqrt{k_\perp}$ scaling in the remainder of this section and in section 6.3, where we propose a closed mean-field model for the anisothermal case.
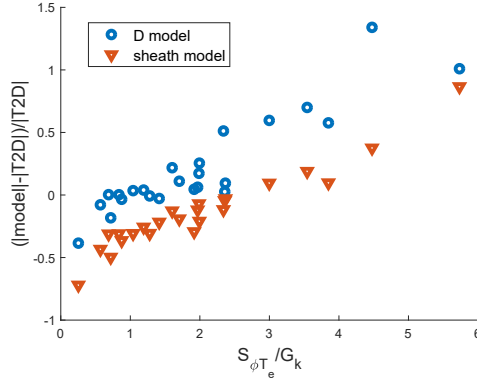
Figure 6.7: Scatter plot of the relative error on the model $D = C_D\sqrt{k_\perp}$ and on model 6.16 for $S_k$ against the relative importance of the SCW term in the $k_\perp$ balance. Each marker represents the radial average of a single simulation in a database of TOKAM2D SCW1 simulations.

## 6.2.2 Modelling the $k_\perp$ equation

Having established that $k_\perp$ can be used as a predictor for the turbulent transport, we need to derive a model for $k_\perp$. To this end we propose suitable closures for the dominant interchange source and sheath sink terms in the transport equation 4.16 of $k_\perp$, neglecting other terms in the balance.

Section 4.2.1 has already derived an exact, analytical relation for the interchange term in the TOKAM2D $k_\perp$ equation. Equation 4.22 is repeated here for convenience:

$$G_k = g(\tilde{T}\overline{n'V'_{E,x}} + \overline{nT''V''_{E,x}}) = g(\tilde{T}\Gamma_{n,E,t,x} + \Gamma_{p_i,E,t,x} + \Gamma_{p_e,E,t,x}), \quad (6.15)$$

where $T$ is defined as $T = T_i + T_e$. Hence, with the closures for the turbulent particle and heat fluxes available from the previous section, no additional closures are required for the interchange term. It can again be observed that this expression directly relates the interchange drive of the turbulence with the turbulent E×B heat flux and with the magnetic field strength gradient through the factor $g$. Note also that if the diffusive relations 6.11-6.12 are filled out in the interchange relation 6.15, the drive of the turbulence occurs through the mean-field gradients (in combination with the magnetic geometry).

The sheath term $S_k$ in $k_\perp$ equation 4.16 is the dominant sink, as was concluded from figure 6.2. Closer analysis in equation 6.13 revealed it to be composed of

multiple contributions. In the SCW1 case, one contribution acts as a large sink and another as a large source (see figure 6.3a). So far we have neglected this detailed behaviour in our model development effort though. One reason for this is that the real underlying parallel dynamics can only be crudely modelled in 2D turbulence codes like TOKAM2D. A dedicated analysis of 3D turbulence code data would probably be required to properly disentangle these effects. Hence, we only use a model for the total sheath term for now:

$$S_k = -C_{||,k} \frac{c_{s,m}}{\sqrt{L_{||} \tilde{T}_e}} \bar{n} k_\perp, \tag{6.16}$$

where we defined $c_{s,m} = \sqrt{\tilde{T}}$ as a proxy for the average sound speed. This model is inspired by the isothermal model 4.30 for the sheath term used in section 4.3. Table 6.2 shows the results of a Bayesian analysis for the SCW1 and SCW0 data sets. This analysis was carried out analogously to that for the transport coefficients in section 6.2.1. However, here the relative formulation for the model error standard deviation has been used, which was found to yield a higher evidence than that of the absolute error formulation. The prior in equation 6.14 is again used (but with $\sigma_{rel}$ instead of $\sigma_{abs}$). From table 6.2 it is clear that the relative error of the model is much lower for the SCW0 case.

Table 6.2: Bayesian analysis of the proposed model for the sheath term in the $k_\perp$ equation for the anisothermal SCW1 and SCW0 datasets. Parameter values are reported at MAP.

| Model for $S_k$ | parameter | SCW1 | SCW0 |
|---|---|---|---|
| $-C_{||,k} \frac{c_{s,m}}{\sqrt{L_{||}\tilde{T}_e}} \bar{n} k_\perp$ | $C_{||,k}[-]$ | 27.4 | 46.9 |
| | $\sigma_{rel}[\%]$ | 0.585 | 0.18 |
| | logevidence | 57745 | 64166 |

Figure 6.8 illustrates the performance of sheath model 6.16 when the MAP value of the model parameter is used for both the SCW1 and the SCW0 case. The model predicts the radial profile for single simulations very well, especially for the SCW0 case. However, in the SCW1 case it fails to predict more detailed trends with varying TOKAM2D parameters. The main reason for this is presumably the varying ratio between both contributions of the sheath loss term. This hypothesis is supported by the much better performance for the SCW0 case. Figure 6.7 also shows the model error to be an increasing function of the relative strength of the SCW term. This further supports the idea that a strong SCW contribution leads to a less negative total sheath term and through that to an overestimation of the magnitude of this term in model 6.16.
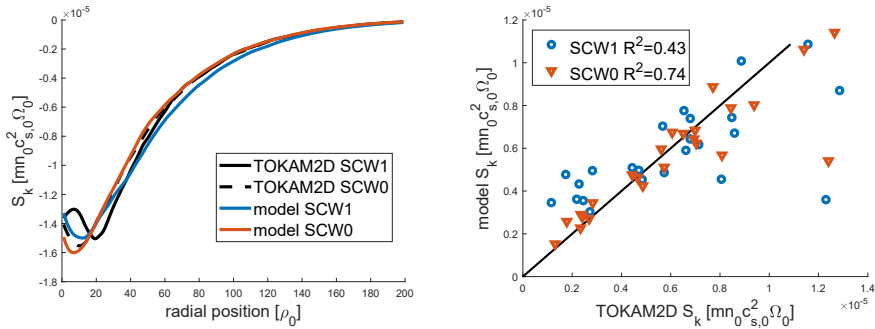
(a) radial profiles for a representative simulations

(b) scatter plot showing radially averaged values for a database of simulations

Figure 6.8: Comparison of the TOKAM2D sheath term for $k_\perp$ with model 6.16 for the SCW1 and SCW0 cases.

## 6.3 Mean-field transport model results

Filling out the models found in section 6.2 in the mean-field equations 6.6-6.8 and 4.16, the following self-consistent model is obtained:

$$\frac{\partial \bar{n}}{\partial t} + \nabla \cdot (\mathbf{\Gamma}_{n,m,E} + \mathbf{\Gamma}_{n,t,E}) = \bar{S}_n - C_{||,n} \frac{c_{s,m}\bar{n}}{L_{||}}, \tag{6.17}$$

$$\frac{\partial \bar{p}_i}{\partial t} + \nabla \cdot (\tilde{T}_i \mathbf{\Gamma}_{n,m,E} + \tilde{T}_i \mathbf{\Gamma}_{n,t,E} + \mathbf{\Gamma}_{p_i,t,E})$$

$$= \bar{S}_{p_i} - \frac{2}{3} \frac{C_{||,p_i} \gamma_i c_{s,m} \bar{p}_i}{L_{||}} - \frac{2m_e}{m_i} \frac{\bar{p}_i - \bar{p}_e}{\tau_{ei}}, \tag{6.18}$$

$$\frac{\partial \bar{p}_e}{\partial t} + \nabla \cdot (\tilde{T}_e \mathbf{\Gamma}_{n,m,E} + \tilde{T}_e \mathbf{\Gamma}_{n,t,E} + \mathbf{\Gamma}_{p_e,t,E})$$

$$= \bar{S}_{p_e} - \frac{2}{3} \frac{C_{||,p_e} \gamma_e c_{s,m} \bar{p}_e}{L_{||}} + \frac{2m_e}{m_i} \frac{\bar{p}_i - \bar{p}_e}{\tau_{ei}}, \tag{6.19}$$

$$\frac{\partial \bar{n} k_\perp}{\partial t} + \nabla \cdot (k_\perp \mathbf{\Gamma}_{n,m,E} + k_\perp \mathbf{\Gamma}_{n,t,E} + \mathbf{\Gamma}_{k_\perp,t})$$

$$= g(\tilde{T}\Gamma_{n,t,E} + \Gamma_{p_i,t,E} + \Gamma_{p_e,t,E}) - C_{||,k} \frac{c_{s,m}}{L_{||}\sqrt{\tilde{T}_e}} \bar{n} k_\perp, \tag{6.20}$$

$$\mathbf{\Gamma}_{n,m,E} \triangleq \bar{n}\bar{\mathbf{V}}_E, \qquad \mathbf{\Gamma}_{n,t,E} = -C_D\sqrt{k_\perp}\nabla\bar{n},$$

$$\mathbf{\Gamma}_{p_\mathrm{i},t,E} = -C_i\sqrt{k_\perp}\bar{n}\nabla\tilde{T}_i, \qquad \mathbf{\Gamma}_{p_\mathrm{e},t,E} = -C_e\sqrt{k_\perp}\bar{n}\nabla\tilde{T}_e,$$

$$\mathbf{\Gamma}_{k_\perp,t} = -C_{D,k}\sqrt{k_\perp}\bar{n}\nabla k_\perp. \tag{6.21}$$

Note that some additional closures have also been filled out. The sheath sink terms on the RHS of equations 6.6-6.8 have been replaced by a straightforward mean-field equivalent and a correction factor. This approximation is very accurate. The classical diffusion terms have been neglected, since these are much smaller than the turbulent transport, but could simply be reintroduced. In equation 6.21, a simple diffusive model is proposed to close the remaining transport terms $\mathbf{\Gamma}_{k_\perp,t}$ on the LHS of equation 4.16. The mean-field E×B particle transport $\mathbf{\Gamma}_{n,m,E}$ has been retained for generality, but will vanish in the 1D simulations performed hereafter.

The basic physics of this model is that mean-field density and temperature gradients lead to a turbulent E×B energy flux (if a nonzero $k_\perp$ is present). If these fluxes are oriented in the direction of decreasing magnetic field strength (as indicated by $g$), these fluxes drive the interchange source of $k_\perp$. This system saturates when the mean-field gradients and $k_\perp$ have reached a level that is sufficient to carry the power and particles across the field lines, and at which the sheath sink can balance the interchange drive of $k_\perp$. Note that these physics are very similar to that of the $k_\perp$ model for the isothermal case developed in section 4.3. The main difference is that the E×B turbulent heat flux driving the turbulent kinetic energy now has multiple contributions. Next to the convection with mean-field turbulent particle flux, ion and electron temperature turbulent convection now also contribute. The interpretation of this model as a steady state manifestation of the gradient removal mechanism [89, 114, 133] still holds as well. As the mean-field gradients are reduced by the turbulent transport, the turbulence itself is also reduced.

The above model 6.17-6.21 is used to simulate a 1D radial geometry with the DivOptLight (DOL) code (see section 5.2.3). The model coefficients that are used are summarised in table 6.3. It can be noted that the important parameter $C_{||,k}$ is corrected with respect to the value shown in table 6.2 in order to compensate for the effect of the minor terms that are not modelled explicitly. As in the isothermal case, this has been done by redoing the Bayesian analysis for the $S_k$ term (with the same model 6.13), but using the $G_k$ as reference data. The $C_{D,k}$ parameter has been taken equal to that used in the isothermal case in section 4.3.

The parameters and boundary conditions of the DOL simulations are set as in the corresponding TOKAM2D simulations such that both can be readily

compared. To this end, the same TOKAM2D parameters $g$, $L_{||}$, $\gamma_i$, $\gamma_e$, $\tau_{ei}$ are used and the boundary conditions impose the TOKAM2D flux of particles, thermal ion and electron energy and $k_\perp$ at the boundaries. The fixed particle and thermal energy sources $\bar{S}_n$, $\bar{S}_{p_i}$ and $\bar{S}_{p_e}$ have not been included since only the region where these are negligible is simulated (these sources are implicitly present in the imposed boundary condition fluxes). An equidistant 1D grid of 48 cells is used in all simulations.

Table 6.3: Model parameters used in 1D mean-field DOL simulations.

| | $\mathbf{C_D}$ | $\mathbf{C_i}$ | $\mathbf{C_e}$ | $\mathbf{C_{D,k}}$ | $\mathbf{C_{||,n}}$ | $\mathbf{C_{||,p_i}}$ | $\mathbf{C_{||,p_e}}$ | $\mathbf{C_{||,k}}$ |
|---|---|---|---|---|---|---|---|---|
| **SCW1** | 16.8 | 19.9 | 14.5 | 0.790 | 1.03 | 1.01 | 1.08 | 37.4 |
| **SCW0** | 20.8 | 18.9 | 19.1 | 0.790 | 0.992 | 1.01 | 0.998 | 54.9 |

Figure 6.9 shows the profiles of some key quantities of the DOL simulation of the reference SCW1 case, and compares them to the original TOKAM2D profiles. The figure illustrates that the mean-field $k_\perp$ model manages to capture the density and temperature profiles very accurately. In addition, the profile of the turbulent kinetic energy is closely matched (although a minor offset remains), leading to a very good estimation of the turbulent transport coefficients. One level deeper, the interchange source and sheath loss sink of $k_\perp$ are also very well matched to the reference data. The transport of $k_\perp$, which has only been modelled very crudely, does not capture the reference data very well. Since the transport represents only a minor term in the balance of $k_\perp$ in the considered cases, this does not lead to major errors. Nonetheless, this may explain the minor differences with respect to the TOKAM2D reference data near the boundaries, which is most pronounced for $k_\perp$. Similar results have been obtained for the SCW0 case, but these are not explicitly shown in the interest of space. Hence, the model not only captures the relevant macroscopic quantities, but manages to do so based on an accurate estimate of the underlying turbulent kinetic energy driving the transport.

The model parameters shown in table 6.3 were well matched to the previous simulation of the reference case since it lies in the middle of the scanned operational range. Figure 6.10 now shows a scatter plot of the particle diffusion coefficient and $k_\perp$ for all the TOKAM2D simulations in the database against the equivalent DOL simulations for both the SCW1 and the SCW0 case (all with the same parameters shown in table 6.3). While the main trend in $k_\perp$ across parameter space is captured, significant scatter clearly remains on the estimate. Surprisingly, the $R^2$ value is higher for the SCW1 case than for the SCW0 case. Furthermore, figure 6.10 clearly shows that the $k_\perp$ value is

(a) density



(b) temperatures



(c) diffusion coefficient



(d) turbulent kinetic energy



(e) interchange term



(f) turbulent kinetic energy sink



(g) turbulent kinetic energy flux
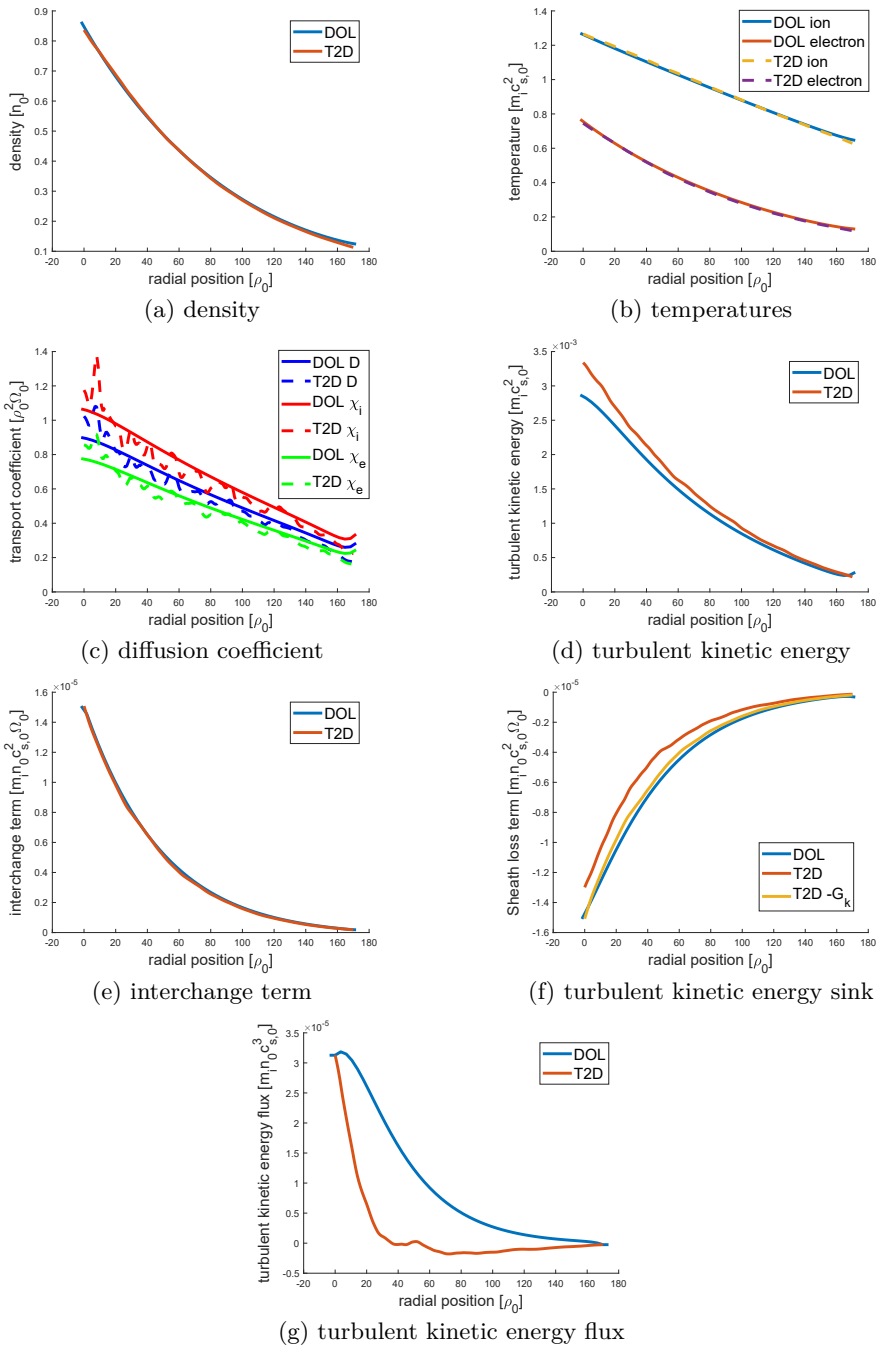
Figure 6.9: Comparison of radial profiles of a representative TOKAM2D SCW1 simulation to a forward mean-field DOL simulations with $k_\perp$ model 6.17-6.21.

(a) diffusion coefficient          (b) turbulent kinetic energy
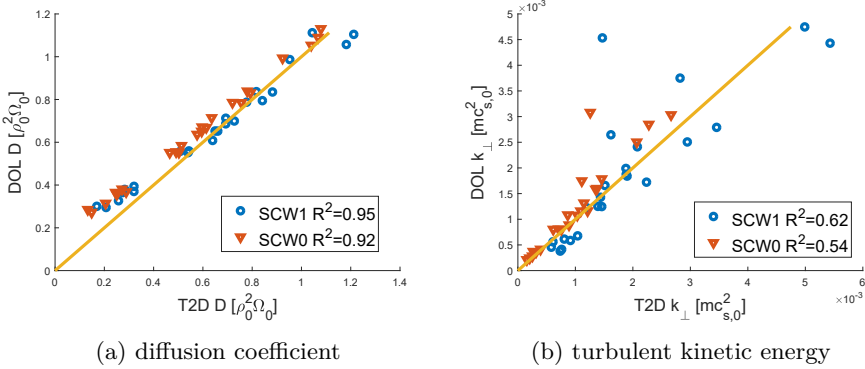
Figure 6.10: Scatter plots comparing forward mean-field DOL simulations against the original TOKAM2D reference data for the SCW1 and SCW0 cases. Each marker in the plots represents the radial average of a single simulation in a database of simulations.

significantly higher in the SCW1 case due to the contribution of $S_{\phi Te}$ to the turbulent kinetic energy. Remarkably, the particle diffusion coefficient shows much less discrepancies. This behaviour can be explained by the compensation of the error caused by the SCW term on the estimate of $k_\perp$ by the error on the diffusion relation $D \sim \sqrt{k_\perp}$ itself. As shown in figure 6.7, the SCW term leads to an overestimation of $D$ on the one hand. On the other hand, it likewise leads to an overestimation of the magnitude of the sheath sink, leading in turn to an underestimation of $k_\perp$, compensating the overestimation of $D$ to a large extent. Physically, this can be explained as the SCW drive leading to more $k_\perp$, but this does not significantly increase the transport since this "SCW turbulence" contribution leads to a limited amount of transport due to the modified phase shift between density and potential fluctuations (see section 6.4).

Now it is also interesting to investigate the scaling for the transport coefficient that is implied by the $k_\perp$ model and to compare it to the Bohm and gyro-Bohm scalings again. This is summarised in table 6.4. As already mentioned in section 4.3 for the isothermal case, the $k_\perp$ scaling 6.21 for the transport coefficients can be seen as a refinement of the Bohm scaling. It effectively replaces the generic electron thermal velocity scale with $\sqrt{k_\perp/m}$, which is a characteristic velocity specifically for the E×B turbulent fluctuations driving the transport. However, also in the anisothermal case, the reference gyro-radius $\rho_0$ remains in this expression as a global length scale. Remember that the $k_\perp - \zeta_\perp$ scaling allowed to overcome this. No self-consistent $k_\perp - \zeta_\perp$ model is elaborated for the anisothermal case though.

Table 6.4: Comparison of the scaling for the transport coefficients implied by $k_\perp$ model to Bohm and gyro-Bohm scalings.

| scaling | variant | TOKAM2D units $[\rho_0 c_{s,0}]$ | dimensional $[m^2/s]$ |
|---------|---------|----------------------------------|------------------------|
| **k$_\perp$** | submodel | $\sqrt{k_\perp}$ | $\rho_0\sqrt{\frac{k_\perp}{m}}$ |
| | full model | $gL_{\|\|}\frac{\sqrt{\tilde{T}_e\tilde{T}}}{L_p}$ | $\frac{L_{\|\|}}{R}\frac{\rho_0}{L_p}\frac{\sqrt{\tilde{T}_e\tilde{T}}}{eB}$ |
| **Bohm** | | $\tilde{T}_e$ | $\frac{\tilde{T}_e}{eB}=\rho_{T_e}\sqrt{\frac{\tilde{T}_e}{m}}$ |
| **gyro-Bohm** | $L_\perp \sim L_p$ | $\frac{\tilde{T}_e^{3/2}}{L_p}$ | $\frac{\rho_{T_e}}{L_p}\frac{\tilde{T}_e}{eB}$ |
| | $L_\perp \sim R$ | $g\tilde{T}_e^{3/2}$ | $\frac{\rho_{T_e}}{R}\frac{\tilde{T}_e}{eB}$ |

To compare with the gyro-Bohm scaling, the $k_\perp$ model predictions are further reworked. Filling out the turbulent fluxes using equation 6.21 in the $k_\perp$ equation 6.20 and neglecting the LHS (hence assuming steady state and a local balance), it can be solved as follows:

$$\sqrt{k_\perp} = -\frac{gL_{\|\|}\sqrt{\tilde{T}_e\tilde{T}}}{C_{\|\|,k}}(C_D\frac{\partial_x\bar{n}}{\bar{n}} + C_i\frac{\partial_x\tilde{T}_i}{\tilde{T}} + C_e\frac{\partial_x\tilde{T}_e}{\tilde{T}}). \tag{6.22}$$

Multiplying this with the appropriate constants readily yields the turbulent transport coefficients $D$, $\chi_i$ and $\chi_e$. If it is now additionally assumed that $C_D = C_i = C_e$ and thus $D = \chi_i = \chi_e$, this can further be rewritten as

$$D = -\frac{C_D^2}{C_{\|\|,k}}gL_{\|\|}\sqrt{\tilde{T}_e\tilde{T}}\partial_x\ln\bar{p} \tag{6.23}$$

The dimensional form in table 6.4 is then obtained by filling out $g \sim \rho_0/R$.

This scaling now shows some similarity to the gyro-Bohm scaling. Compared to the $L_p$ variant of the latter though, a factor $L_{\|\|}/R$ is added. Furthermore, the gyro-radius does not appear as a local quantity, but rather as the global reference value $\rho_0$. Finally, the scaling with $T_e$ is replaced by a scaling with $\tilde{T}_e\tilde{T}$. As discussed in section 2.3.3, the Bohm and gyro-Bohm scalings are usually only used as global machine scaling laws. The dimensional full model form of the $k_\perp$ model could presumably also be used as such a scaling for the OMP in interchange-dominated turbulence in a sheath connected SOL. However, the $k_\perp$ model discussed in this chapter (and in this thesis in general) has much wider

applications. Firstly, the model allows to calculate local values of the turbulent transport coefficients. In particular, (with some generalisations) it can be used in 2D mean-field codes to provide a physics-based 2D profile of the transport coefficients. This has been demonstrated by the implementations of models based on the $k_\perp$ model in SOLPS-ITER by Carli *et al.* [39, 38] and Dekeyser *et al.* [54]. Secondly, the methodology of the model and the $D \sim \sqrt{k_\perp}$ submodel in particular is expected to hold more generally such that the model could be extended to more general cases as well (e.g. cases with flow shear, with strong DW drive, non-sheath-limited cases,...).

While the results of the $k_\perp$ model presented up to here are encouraging already, the next section will further study its remaining deficiencies and highlight the role of the SCW instability in these.

## 6.4 Detailed look at the sheath term: influence of SCW term

Figure 6.7 has clearly illustrated the link between the sheath-conducting wall instability acting as a source of the turbulence and the error on both the diffusion relation 6.21 and the sheath sink model 6.16. This section will highlight the role of the phase shift between density and potential fluctuations in the error on the diffusion relation and the role the SCW term plays in establishing this phase shift.

Drawing inspiration from Fedorczak *et al.* [68] and Peret *et al.* [122], we start by taking the Fourier decomposition of the instantaneous density and the electrostatic potential along the diamagnetic $y$-direction (which is symmetric in TOKAM2D) at every radial position:

$$n = \int_{-\infty}^{\infty} \hat{n}_{K_y} \sin{(K_y y + \psi_{n,K_y})} dK_y,$$

$$\phi = \int_{\infty}^{\infty} \hat{\phi}_{K_y} \sin{(K_y y + \psi_{\phi,K_y})} dK_y, \tag{6.24}$$

where $K_y$ is the diamagnetic wave number, $\hat{n}_{K_y}$ and $\hat{\phi}_{K_y}$ are the amplitudes corresponding to the spectral component with wave-number $K_y$ and $\psi_{n,K_y}$ and $\psi_{\phi,K_y}$ are the phase of the density and the potential fluctuations for wave number $K_y$. Note that the quantities $n$, $\phi$, $\hat{n}_{K_y}$, $\hat{\phi}_{K_y}$, $\psi_{n,K_y}$ and and $\psi_{\phi,K_y}$ are functions of the radial $x$-coordinate and fluctuate in time. By integration

over the periodic $y$-direction, the local, instantaneous E×B particle flux can be calculated as [68, 122]

$$\Gamma_{n,E,x} = nV_{E,x} = -n\frac{\partial \phi}{\partial y} = 8\pi \int_0^\infty K_y \hat{n}_{K_y} \hat{\phi}_{K_y} \sin \psi_{K_y} dK_y, \qquad (6.25)$$

where $\psi_{K_y} = \psi_{n,K_y} - \psi_{\phi,K_y}$. Hence, the phase difference between density and potential differences directly influences the particle flux. We will now show the SCW term changes this phase structure. To calculate the averaged particle flux of interest, this expression should still be averaged in time as

$$\Gamma_{n,E,x} = 8\pi \int_0^\infty K_y \overline{\hat{n}_{K_y} \hat{\phi}_{K_y} \sin \psi_{K_y}} dK_y. \qquad (6.26)$$

Note that Fedorczak *et al.* [68] and Peret *et al.* [122] found that the correlation between spectral component fluctuations is negligible for the isothermal SOL TOKAM2D case.

For the TOKAM2D cases available, the instantaneous spectra were approximated using the default Matlab fast Fourier transform algorithm. The resulting complex numbers were then used to calculate the amplitudes ($\hat{n}_{K_y}$ and $\hat{\phi}_{K_y}$) and phases ($\psi_{n,K_y}$ and $\psi_{\phi,K_y}$) at every point in time at every radial position. Histograms of the phase difference $\psi_{K_y} = \psi_{n,K_y} - \psi_{\phi,K_y}$ are constructed by binning all the time points for a selected radial position. The phase structure does not seem to change significantly in the radial direction for the considered cases.

The resulting histograms for a number of cases are shown in figure 6.11. Figure 6.11d shows the isothermal SOL case studied in chapter 4. For this case, the phase difference is close to $\pi/2$ for all wave numbers. This is indeed the expected phase difference for pure interchange turbulence [15, 17, 145] and matches the results obtained by Fedorczak *et al.* [68] and Peret *et al.* [122]. Note also that this phase difference of $\psi = \pi/2$ leads to maximum transport in equation 6.25 for given amplitudes. For the SCW0 case shown in figure 6.11b, the phase structure is very similar. This makes sense, since in this case as well, only the interchange drive of the turbulence is present. In the SCW1 case of figure 6.11a on the other hand, the results are quite different. While at high $K_y$ the phase still goes to $\psi \approx \pi/2$, at low $K_y$ where the spectrum is now most intense, the phase is instead close to zero. Remark that $\psi = 0$ does not lead to any transport. This low phase in part of the spectrum of the SCW1 case is clearly the influence of the SCW mode, which in itself is shown to lead to a very low phase difference in figure 6.11c. This complies with the linear analysis performed by Baudoin *et al.* [15, 17] predicting a phase difference between zero and $\pi/4$ for the pure SCW mode.

(a) SCW1 case

(b) SCW0 case

(c) SCW1 $g = 0$ case

(d) E×B-only isothermal case
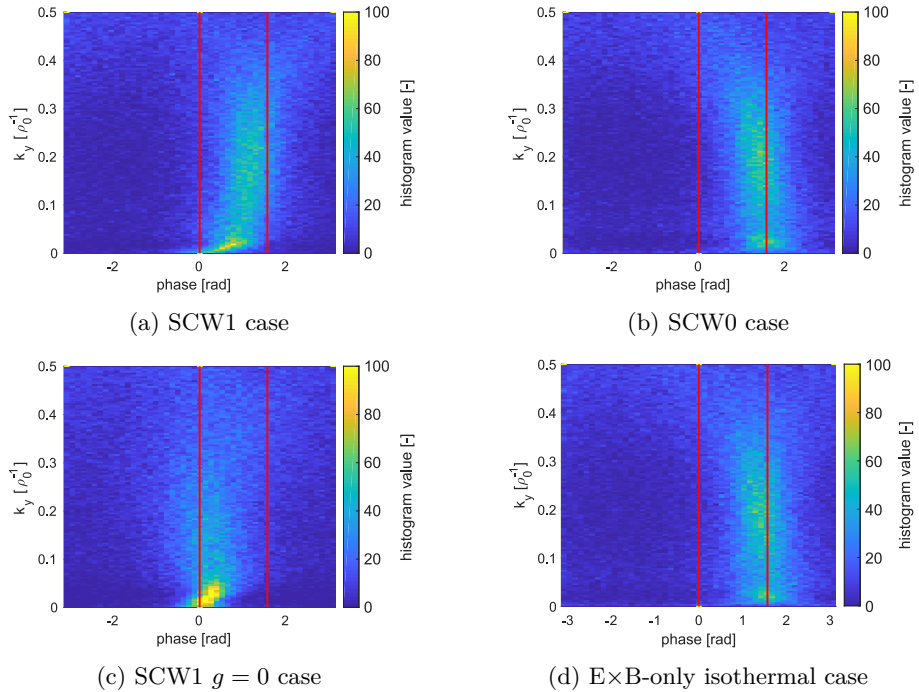
Figure 6.11: Histograms of the phase difference between density and potential fluctuations against wave number in the diamagnetic direction for different TOKAM2D cases at a selected radial location. Red lines indicate $\psi = 0$ and $\psi = \pi/2$.

Now the question is how these insights on the phase difference can be integrated in the $k_\perp$ model to obtain improved transport models. As a first step, we here assume that the relation $\mathbf{\Gamma}_{n,t,E} \sim -\sqrt{k_\perp}\nabla\bar{n}$ gives a good estimate of the (wave number integrated) amplitude of 6.26, but that the information on the phase difference $\psi$ is not incorporated in the model. Under this assumption, a correction for the phase difference is required in the transport relation. To this end, we define an effective phase difference by weighing the instantaneous spectra of the phase difference with the instantaneous spectrum of the radial E×B particle flux and averaging this in time:

$$\Psi \triangleq \frac{\int_{-\infty}^{\infty} \overline{\hat{\Gamma}_{K_y}\psi_{K_y}}dK_y}{\int_{-\infty}^{\infty} \overline{\hat{\Gamma}_{K_y}}dK_y}. \tag{6.27}$$

(a) SCW1 case

(b) SCW0 case
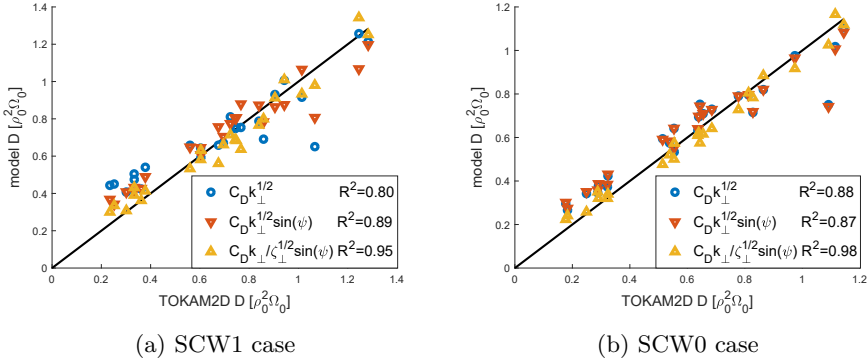
Figure 6.12: Scatter plot of the turbulent diffusion coefficient between TOKAM2D reference data and different models. Each marker indicates the radial average of a single simulation in a database of simulations.

In this expression, $\hat{\Gamma}_{K_y} = 8\pi K_y \hat{n}_{K_y} \hat{\phi}_{K_y}$ is understood to mean the magnitude of the spectrum of the radial E×B particle flux from equation 6.25. The effective phase difference $\Psi$ is only a relation of the radial position since the dependencies of $\psi_{K_y}$ on time and wave number have been integrated out.

Next, we use this phase difference to correct the diffusion relation as

$$\boldsymbol{\Gamma}_{n,t,E} \sim \sqrt{k_\perp} \sin \Psi. \tag{6.28}$$

This then yields the sixth and seventh rows in table 6.1, where the same correction has also been applied to the $k_\perp - \zeta_\perp$ transport relation. From these results, it is clear that including this correction for the phase difference improves both models for the SCW1 case. Moreover, after having made this correction, the $k_\perp - \zeta_\perp$ model does become better than the $k_\perp$ model, as had been expected a priori. On the other hand, this correction does not bring an improvement for all models and all quantities in the SCW0 case. This is presumably because the noise on the evaluation of the phase difference overshadows the small deviations away from $\pi/2$ of the real phase difference for some cases. The improved performance of the phase-corrected models is further illustrated in the scatter plots in figure 6.12. No figures of the radial profiles are shown because they do not change significantly due to the limited variations of the characteristic phase in the radial direction.

It has also been tried to correct the $k_\perp$ and $k_\perp - \zeta_\perp$ models with a factor accounting for the SCW mode itself in the last two rows of table 6.1. This provides an alternative way to correct for the change in the structure of the
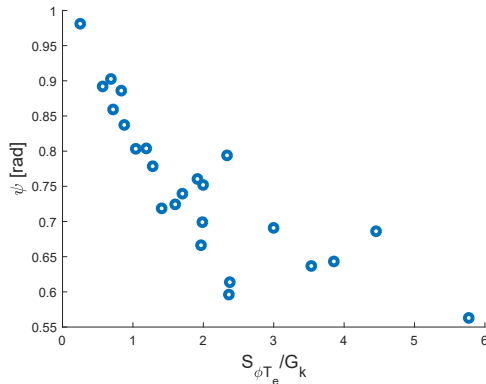
Figure 6.13: Scatter plot of the characteristic phase difference between density and potential fluctuations against the relative importance of the SCW term in the $k_\perp$ balance for the SCW1 case. Each marker indicates the radial average of a single simulation in a database of TOKAM2D simulations.

turbulence when the SCW drive is important, of which the phase difference seems to present an important element. Note that this model form is similar to that used for the DW term in the last row of table 5.2 in section 5.1. For the SCW1 case, these SCW-corrected models likewise provide a large improvement over the standard models. The $k_\perp$-only variant performs better than the phase-corrected model. The $k_\perp - \zeta_\perp$-variant has a lower evidence than the former and also a lower evidence than the $k_\perp - \zeta_\perp$ phase-corrected model.

With this we have further clarified some of the physics involved in the transport and suggested an improved form of the transport model. However, in order to get a self-consistent estimate of the transport coefficients, a model for the characteristic phase difference $\Psi$ or for the SCW term $S_{\phi Te}$ is needed. The SCW term would need to be modelled separately from the sink term $S_{\phi^2}$ in the $k_\perp$ equation as well (see equation 6.13). Figure 6.13 shows there is a clear correlation between $\Psi$ and $G_k/S_{\phi Te}$. Hence, it would probably be possible to close the model if a model for the SCW term were available. This is left for future work. Furthermore, it might also be worthwhile to further investigate the influence of the wave number scale $K_y$, which also appeared in equation 6.26, on the transport. It may be investigated how this changes between the various cases in the TOKAM2D data sets. It could be speculated that the influence hereof is (partially) accounted for by including the enstrophy in the transport relations. The reasoning for this is that $\zeta_\perp$ tends to concentrate on smaller length scales than $k_\perp$, such that the inclusion of both quantities may

better represent the characteristic length scale of the transport. This is also left for future research.

## 6.5 Conclusion

This chapter has generalised the $k_\perp$ mean-field turbulent transport model that was originally developed for 2D isothermal interchange-dominated electrostatic E×B drift turbulence in a sheath-limited SOL in section 4.3 to the anisothermal case. In this model, the turbulent transport of particles and heat is related to the turbulent kinetic energy and an additional equation for the latter is added to the mean-field equation set.

While an analytical relation for the dominant interchange source of $k_\perp$ is still available, the behaviour of the sheath term that mimics parallel transport to the sheath is significantly complicated. It is shown to consist of a source and a sink contribution. These new dynamics are shown to influence the transport behaviour, but are not yet self-consistently modelled in this work. Nonetheless, the results of the anisothermal model are very promising and a good match of the original TOKAM2D turbulence code results can be obtained. Hence, the anisothermal model, and the self-saturation behaviour between turbulence and mean-field gradients contained within it, seems to capture some of the basic physics of SOL plasma transport very well.

The new dynamics introduced by the sheath source are identified with the sheath-conduction wall (SCW) instability. It is shown that this new source term changes the characteristic phase difference between density and potential fluctuations. As a result, the turbulent fluxes at fixed $k_\perp$ vary as the relative importance of the interchange and SCW drive varies. Including the characteristic phase difference in the transport relation is shown to lead to an improved performance on the submodel level.

However, the TOKAM2D code used as a reference in this work does not contain all the necessary physics to describe the SOL of future fusion reactors, such that the model developed in this chapter should still be seen as a stepping stone in the ongoing research to develop more complete mean-field models for the turbulent transport. Detailed modelling of the phenomena introduced by the sheath term in the $k_\perp$ equation seems more appropriate in a 3D setting where the parallel direction is explicitly resolved. Analysing 3D reference data will also allow to study drift wave dynamics in more detail and to distinguish those from parallel transport effects. The next chapter will provide a preliminary discussion of such 3D cases.

# Chapter 7

# A look ahead: preliminary analysis of 3D cases

The general framework of mean-field equations and the strategy to be followed for their closure presented in chapters 2 and 3 made no assumptions on the dimensionality of the turbulence. However, chapters 4-6 have been limited to a discussion of purely 2D plasma edge turbulence, accounting for the parallel direction through approximate volumetric sinks. While this allowed to gain valuable insights on the basic dynamics of the perpendicular turbulent transport, the considered cases were still rather far-off from a reactor relevant case. Nonetheless, it is expected that the basic physics modelled for the reduced cases can be extrapolated to more complex cases as well. This chapter will couple back to the general case considered in chapter 3. It will look ahead considering the implications of the developed model for mean-field transport in general and discuss the elements of the model that require further refinement. This discussion will be supported by a preliminary analysis of 3D turbulence code simulations with the TOKAM3X code [157].

First, section 7.1 provides a preliminary analysis of 3D isothermal slab cases for which reference data is obtained from TOKAM3X simulation results. Then, section 7.2 discusses the implications of the models developed in this thesis for the mean-field transport in realistic geometries, as well as the effects which are still missing. Finally, section 7.3 presents the main conclusions of this chapter.

# 7.1 Analysis of 3D slab cases

This section elaborates how the models developed earlier for purely 2D cases need to be generalised to be used in 3D (2D mean-field). To this end, isothermal TOKAM3X slab cases will be studied, where the focus lies on the SOL. Section 7.1.1 first presents the TOKAM3X code and the setup of the studied cases. Next section 7.1.2 derives the corresponding mean-field equations. Section 7.1.3 then provides a preliminary discussion the turbulent kinetic energy balance and the transport relations, focusing on the differences with respect to the 2D cases investigated before.

## 7.1.1 TOKAM3X setup and equations

TOKAM3X is a versatile 3D turbulence code capable of modelling anisothermal edge plasma turbulence in complex geometries [16, 15, 72, 157]. Furthermore, it has been coupled to the EIRENE code to self-consistently study the effect of neutrals [64]. However, in line with the stepwise approach followed in this thesis, reference data from a reduced version will be used for simplicity and to facilitate comparison with results from earlier chapters in this preliminary study. Hence, the plasma edge will be assumed to be isothermal, a slab geometry is considered and no neutrals are simulated.

This slab geometry is shown in figure 7.1. A straight time-constant magnetic field is assumed which only has a toroidal ($\varphi$) component. As a result, the toroidal direction coincides with the parallel direction and the poloidal direction ($\theta$) coincides with the diamagnetic direction in this simplified geometry. The magnetic field strength decays in the radial direction ($r$) though. The slab domain has two regions: a closed field line region and a SOL region. In the closed field line region, periodic boundary conditions are applied in the toroidal direction (black surface), representing the toroidal periodicity in a tokamak. In the SOL, the magnetic field lines are assumed to end on material surfaces (indicated with red), which are represented by Bohm boundary conditions. On the poloidal boundaries (top and bottom), periodic boundary conditions are applied while Neumann conditions are applied on radial boundaries [83]. Note that in this geometry the toroidal direction coincides with the parallel direction, and the polodidal direction with the diamagnetic direction. Hence, geometrically, the case considered here is identical to the TOKAM2D case investigated in chapters 4-6, the only difference being that the parallel direction is now effectively resolved instead of being modelled using volumetric sinks intended to replicate its behaviour.
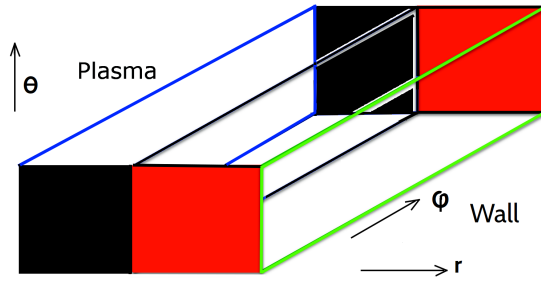
Figure 7.1: Visualisation of the TOKAM3X slab geometry. Reproduced from Ref. [83].

For this isothermal slab case, the TOKAM3X equations simplify to [83, 157]

$$\frac{\partial n}{\partial t} + \nabla \cdot n\mathbf{V}_C - D_N\nabla_\perp^2 n = S_n, \tag{7.1}$$

$$\frac{\partial W}{\partial t} + \nabla \cdot W\mathbf{V}_C - D_W\nabla_\perp^2 W = \nabla \cdot \mathbf{J}_{\nabla B} + \nabla \cdot \mathbf{J}_{||}, \tag{7.2}$$

$$\frac{\partial nV_{||}}{\partial t} + \nabla \cdot n\mathbf{V}_C V_{||} - D_{||}\nabla_\perp^2 nV_{||} = -\nabla_{||}p, \tag{7.3}$$

$$\eta_{||}nJ_{||} = \nabla_{||}p_e - n\nabla_{||}\phi, \tag{7.4}$$

$$W = \nabla \cdot \left(\frac{\nabla_\perp\phi}{B^2} + \frac{\nabla_\perp p_\mathrm{i}}{nB^2}\right), \tag{7.5}$$

$$\mathbf{V}_C \triangleq \mathbf{V}_{||} + \mathbf{V}_E + \mathbf{V}_{\nabla B,i}, \qquad \mathbf{J}_{\nabla B} \triangleq n\mathbf{V}_{\nabla B,i} - n\mathbf{V}_{\nabla B,e}, \tag{7.6}$$

$$\mathbf{V}_E \triangleq \frac{\mathbf{b} \times \nabla\phi}{B}, \qquad \mathbf{V}_{\nabla B,i/e} \triangleq \pm\frac{2T_{i/e}}{B}\frac{\mathbf{b} \times \nabla B}{B}, . \tag{7.7}$$

Like the TOKAM2D equations 4.1-4.3, these equations are normalised with the ion mass $m$, the reference ion gyro-frequency $\Omega_0 = eB_0/m$ and radius $\rho_0 = c_{s,0}\Omega_0$, with $B_0$ the reference magnetic field strength, $c_{s,0} = \sqrt{T_0/m_i}$ the reference sound speed and $T_0$ the reference temperature. Note that the magnetic field strength $B$ is no longer uniform though. The magnetic field direction $\mathbf{b}$ is constant though, such that the $D\mathbf{b}/Dt$ terms in the parallel momentum and charge balance equations drop. Unless specifically mentioned otherwise, the equations and plots in this section make use of normalised units.

In these equations, the diamagnetic current $\mathbf{J}_*$ and diamagnetic velocities $\mathbf{V}_*$ are

replaced by the magnetic drifts $\mathbf{J}_{\nabla B}$ and $\mathbf{V}_{\nabla B}$, except in the (pseudo-)vorticty $W$. For the divergence of particle fluxes and currents, they are exactly the same under a low $\beta$ approximation [15, 82]. For the convection of $W$ and $V_{||}$ this is motivated by the gyro-viscous cancellation. The details of this cancellation remain a topic of study in the community though [127, 136, 138]. Note that the velocity $\mathbf{V}_C$ used in the convection operator is not the same as the plasma velocity $\mathbf{V}_0$ used for calculating the inertia since $\mathbf{V}_{*,i} \neq \mathbf{V}_{\nabla B,i}$.

The continuity equation 7.1 and parallel momentum equation 7.3 readily follow from the general equations 2.25 and 2.44 respectively, with the convective velocity given by equation 7.6 and a diffusion term for the classical transport. Note that the parallel momentum sources are absent because no neutrals are simulated. The electron momentum equation 7.4 is equal to the general one in equation 2.45, where the electromagnetic term is dropped in the considered electrostatic case, as well as the $n\nabla_{||}T_e$ term because of the isothermal assumptions.

Vorticity definition 7.5 in TOKAM3X is the same as that used in equation 2.46. Hence, the vorticity equation-like form of the general charge balance equation 2.53 can be compared to the TOKAM3X charge balance equation 7.2. Comparing both equations, the parallel current divergences can be seen to be the same ($\nabla \cdot \mathbf{J}_* = \nabla \cdot \mathbf{J}_{\nabla B}$ for a low $\beta$ plasma). As in TOKAM2D, $\mathbf{J}_{p,\Pi}$ is modelled by a diffusion-like term (equivalent to Newtonian viscosity) and momentum sources are neglected (in the absence of neutrals). Hence, the remaining terms approximate the polarisation current divergence:

$$\frac{\partial W}{\partial t} + \nabla \cdot \mathbf{V}_C W \approx -\nabla \cdot \mathbf{J}_{p,0}. \tag{7.8}$$

This means that $S_{W,cor}$ (defined in equation 2.54) is neglected. Furthermore, a strong Boussinesq approximation is made assuming that the density in the polarisation current can be neglected, i.e. replaced by the constant reference density in non-normalised units.

Data from two TOKAM3X simulations has been provided by W. Gracias and P. Tamain. One simulation considers the total vorticity case with $W$ exactly as in equation 7.5, while the other is an E×B-only case in which the diamagnetic current contribution to the inertia (second term in equation 7.5) has been neglected. The other parameters are identical between both cases, and can be found in appendix F.3.

(a) density



(b) electrostatic potential



(c) turbulent diffusion coefficient



(d) turbulent kinetic energy
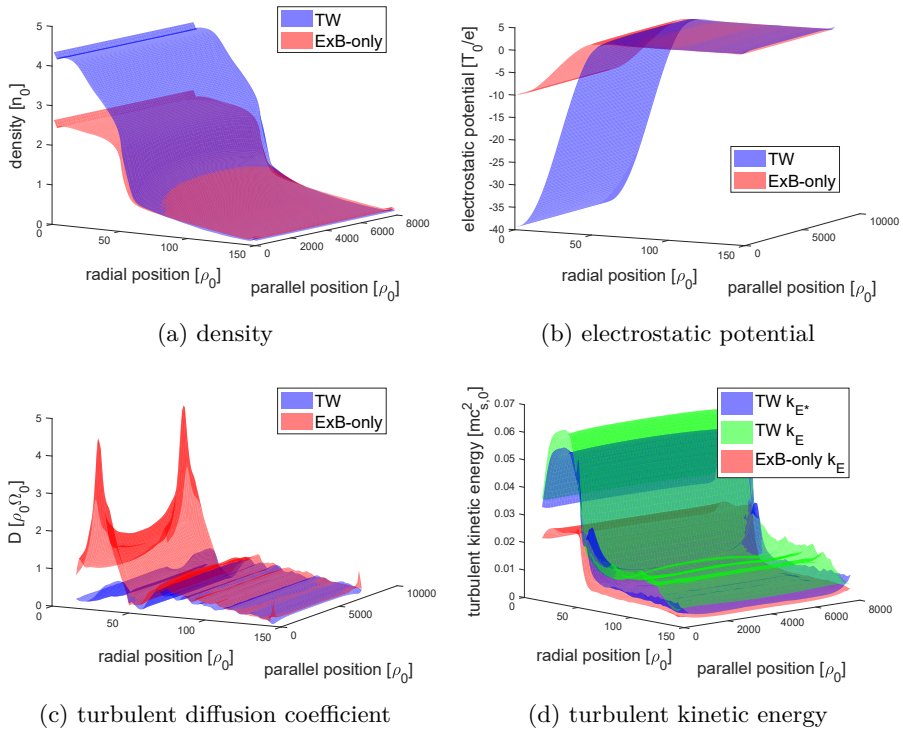
Figure 7.2: Averaged radial-parallel profiles for selected TOKAM3X quantities for TW and E×B-only cases.

## 7.1.2 Mean-field equations

As before, we are interested in mean-field quantities in this thesis. These can now be obtained from the TOKAM3X equations by time averaging (as before) and by averaging over the poloidal/diamagnetic direction which is still periodic. Thus, the obtained mean-field data is now two-dimensional along the radial and parallel directions. Away from the target plates, most of the profiles are relatively uniform in the parallel direction though, see figure 7.2. This behaviour was indeed anticipated because of the fast transport in the parallel direction.

As in the previous chapters, the main interest in this thesis is to self-consistently calculate mean-field quantities. The main closure problem to be addressed here is that of the continuity equation. Similar to equation 2.62 for the general case, we here have

$$\frac{\partial \bar{n}}{\partial t} + \nabla \cdot (\bar{n}\tilde{\mathbf{V}}_{||} + \bar{n}\bar{\mathbf{V}}_E + \overline{n'\mathbf{V}'_E} + \bar{n}\tilde{\mathbf{V}}_{\nabla B,i}) = \bar{S}_n. \tag{7.9}$$

Again, the only closure in this equation is the turbulent E×B particle flux $\mathbf{\Gamma}_{n,t,E} \triangleq \overline{n'\mathbf{V}'_E}$. Like the diamagnetic drift flux, the $\nabla B$ drift flux can be closed from the average pressure $(\overline{n\mathbf{V}_{\nabla B,i}} \sim \overline{nT_i} = \bar{p}_i)$. The basic idea is still to use a diffusion relation for $\mathbf{\Gamma}_{n,t,E}$ and to relate the effective turbulent diffusion coefficient to quantifiers of the turbulence, and to the turbulent kinetic energy in particular.

Since there is no density weighing of the inertia in the LHS of the charge balance equation 7.2, we will also not use density weighing in the definition of the perpendicular kinetic energy and work with the regular Reynolds decomposition (see equation 2.7) instead of the Favre decomposition we used before. Thus, the total perpendicular kinetic energies are now defined as

$$E_{E*} \triangleq \frac{\mathbf{V}^2_{0,\perp}}{2}, \quad E_{m,E*} \triangleq \frac{\bar{\mathbf{V}}^2_{0,\perp}}{2}, \quad k_{E*} \triangleq \frac{\overline{\mathbf{V}'^2_{0,\perp}}}{2}, \tag{7.10}$$

where the perpendicular velocities in the kinetic energy are those considered for the inertia, i.e. $\mathbf{V}_{0,\perp} = \mathbf{V}_E + \mathbf{V}_{*,i}$. Note that in this case the sum of the mean-field and turbulent kinetic energies equals the average total kinetic energy (without weighing with the density):

$$\overline{E_{E*}} = E_{m,E*} + k_{E*}. \tag{7.11}$$

Likewise, we define the E×B-only kinetic energies for TOKAM3X as

$$E_{\mathrm{E}} \triangleq \frac{\mathbf{V}^2_E}{2}, \qquad E_{\mathrm{E},m} \triangleq \frac{\bar{\mathbf{V}}^2_E}{2}, \qquad k_E \triangleq \frac{\overline{\mathbf{V}'^2_E}}{2}. \tag{7.12}$$

The transport equations for the total perpendicular and E×B-only turbulent kinetic energies are derived in appendix F as equations F.10 and F.17:

$$
\frac{\partial k_\perp}{\partial t} + \nabla \cdot (k_\perp \mathbf{V}_C + \frac{\overline{\mathbf{V}_{0,\perp}'^2 \mathbf{V}_C'}}{2} + \overline{\phi' \mathbf{J}_{||}'} + \overline{\phi' \mathbf{V}_{p,0}'})
$$

$$
= \overline{\nabla_{||}\phi' \cdot \mathbf{J}_{||}'} - \overline{\phi' \nabla \cdot \mathbf{J}_{\nabla B}} - D_W \overline{\phi' \nabla_\perp^2 W'} - \overline{\mathbf{V}_C' \mathbf{V}_{0,\perp}'} : \nabla \bar{\mathbf{V}}_{0,\perp}^T
$$

$$
- \overline{\frac{\nabla p_{\mathrm{i}}}{n} \cdot \mathbf{V}_{p,0}'} - \overline{\phi' \nabla \cdot (\frac{\mathbf{U}_0}{B} \frac{D \ln B}{Dt})} - \overline{\phi' \nabla \cdot (\frac{\mathbf{U}_0}{B} \cdot \nabla \mathbf{V}_C)}
$$

$$
- k_\perp \nabla \cdot \bar{\mathbf{V}}_C - \frac{\overline{\mathbf{V}_{0,\perp}'^2 \nabla \cdot \mathbf{V}_C'}}{2} - \bar{\mathbf{V}}_{0,\perp} \cdot \overline{\mathbf{V}_{0,\perp}' \nabla \cdot \mathbf{V}_C'}, \qquad (7.13)
$$

$$
\frac{\partial k_E}{\partial t} + \nabla \cdot (k_E \mathbf{V}_C + \frac{\overline{\mathbf{V}_E'^2 \mathbf{V}_C'}}{2} + \overline{\phi' \mathbf{J}_{||}'} + \overline{\phi' \mathbf{V}_{p,E}'})
$$

$$
= \overline{\nabla_{||}\phi' \cdot \mathbf{J}_{||}'} - \overline{\phi' \nabla \cdot \mathbf{J}_{\nabla B}} - D_W \overline{\phi' \nabla_\perp^2 W'} - \overline{\mathbf{V}_C' \mathbf{V}_E'} : \nabla \bar{\mathbf{V}}_E^T
$$

$$
+ \overline{\phi' (\frac{\partial W_*}{\partial t} + \nabla \cdot W_* \mathbf{V}_C)} - \overline{\phi' \nabla \cdot (\frac{\mathbf{U}_E}{B} \frac{D \ln B}{Dt})} - \overline{\phi' \nabla \cdot (\frac{\mathbf{U}_E}{B} \cdot \nabla \mathbf{V}_C)}
$$

$$
- k_E \nabla \cdot \bar{\mathbf{V}}_C - \frac{\overline{\mathbf{V}_E'^2 \nabla \cdot \mathbf{V}_C'}}{2} - \bar{\mathbf{V}}_E \cdot \overline{\mathbf{V}_E' \nabla \cdot \mathbf{V}_C'}, (7.14)
$$

with

$$
\mathbf{V}_{p,0} \triangleq -\frac{1}{B}(\frac{\partial \mathbf{U}_0}{\partial t} + \nabla \cdot \mathbf{V}_C \mathbf{U}_0), \qquad \mathbf{U}_0 \triangleq \mathbf{V}_0 \times \mathbf{b}, \qquad (7.15)
$$

$$
\mathbf{V}_{p,E} \triangleq -\frac{1}{B}(\frac{\partial \mathbf{U}_E}{\partial t} + \nabla \cdot \mathbf{V}_C \mathbf{U}_E), \qquad \mathbf{U}_E \triangleq \mathbf{V}_E \times \mathbf{b}. \qquad (7.16)
$$

Hence, these turbulent kinetic energy equations are similar to those for the general case shown in equations 3.15 and 3.24. The differences are due to the simplifications in the TOKAM3X charge balance equation 7.2 w.r.t. the general charge balance equation 2.53. The most noticeable differences are the last five terms, which stem from simplification in the TOKAM3X charge balance equation with respect to the general form of the charge balance equation 2.53, and are thus non-physical. Furthermore, there is a factor $n$ difference in all terms related to the inertia which are now written using Reynolds averages.

This is the result of the strong Boussinesq approximation by which the density in the LHS of equation 7.2 has been neglected. Also because of this, the Favre term that was identified before does not appear now.

It is interesting to note that the parallel current transport term $\nabla \cdot \overline{\phi' \mathbf{J}'_{||}}$ can now be distinguished from the drift wave (DW) term $\overline{\nabla_{||} \phi' \cdot \mathbf{J}'_{||}}$ and that both can be present at the same time. Remember that in the TOKAM2D case studied in chapters 4-6, either the one or the other was present. The TOKAM2D sheath loss term in the SOL has been identified with the transport contribution, since this term indeed represents the flux out of the flux tube in the parallel direction. The parallel current term in the core region introduced in section 5.1 was intended to mimic DW behaviour and has been identified with the $\overline{\nabla_{||} \phi' \cdot \mathbf{J}'_{||}}$ term.

### 7.1.3 Preliminary modelling results

At this point, it needs to be mentioned that only a very limited set of TOKAM3X data is available. Just two cases at a particular set of parameters are at hand. Based on such a limited sample, no compelling conclusions can be drawn and no reliable model development can be performed. Furthermore, the above $k_\perp$ equations have been illustrated to contain a number of nonphysical terms due to approximations made in the TOKAM3X model equations. Some of these seem to provide a considerable contribution to the energy balance. Moreover, the unbalance left on the evaluation of the turbulent kinetic energy equations is substantial (see later). At present, it is unclear what the cause of this unbalance is. For the above reasons, some doubt remains of the fidelity of the results of the TOKAM3X analysis. Because of this, the results presented next should be treated with some apprehension and should rather be considered to be a first preliminary look into 3D dynamics.

#### $k_\perp$ balances

Even when only considering the SOL, the evaluation of turbulent kinetic energy equations 7.13 and 7.14 for the TOKAM3X slab cases shows that more terms become important than before, as can be seen in figure 7.3. The plots in this figure are obtained by averaging the central part of the 2D radial-parallel mean-field profiles over the parallel direction, hence obtaining purely radial profiles. While the parallel direction is not symmetric, the profiles were observed to be rather uniform in this direction (as long as the parallel boundary is not approached too closely).
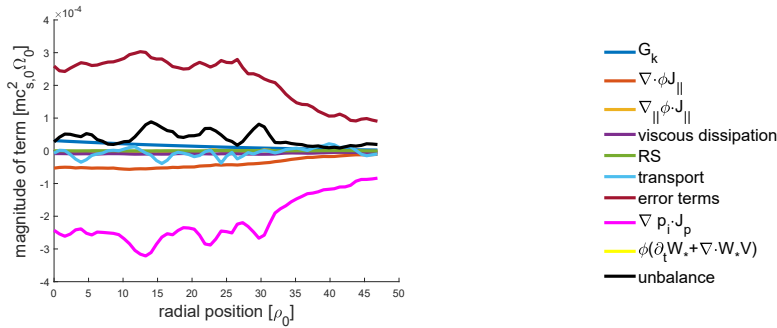
(a) $k_{E*}$ balance for TW case, equation 7.13

(b) color legend
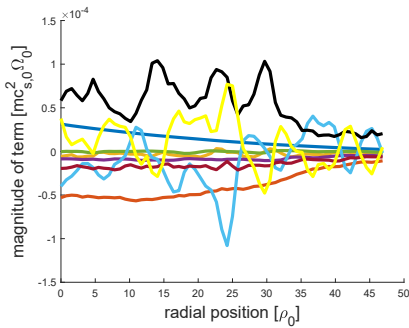


(c) $k_E$ balance for TW case, equation 7.14
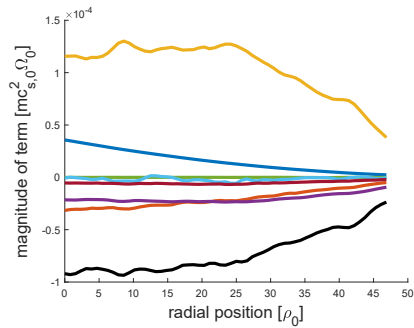
(d) $k_E$ balance for E×B-only case, equation 7.14

Figure 7.3: Evaluation of terms in the TOKAM3X $k_\perp$ equation for different cases. Mean-field data averaged over the parallel direction as well to obtain radial profiles.

For the E×B-only case in figure 7.3d), the DW term $\overline{\nabla_{||}\phi' \cdot \mathbf{J}'_{||}}$ becomes a very large source, while the interchange source only plays a minor role. Note that this behaviour is different from the DW-like term in the core region for the (E×B-only) TOKAM2D case presented in section 5.1. The parallel current transport term $\nabla \cdot \overline{\phi'\mathbf{J}'_{||}}$ together with the viscous dissipation present the main sinks. However, they seem to be too small to compensate the DW term, such that a large unbalance remains on the evaluation of this energy balance. It still needs to be mentioned that the time change term in the polarisation velocity (first term in expressions 7.15 and 7.16) could not be evaluated with the available data. This might still change the balances, however, this contribution was found to be small in the TOKAM2D cases presented earlier.

In the E×B kinetic energy balance for the TW case in figure 7.3c, the interchange term and the parallel current terms remain important. However, in addition to these terms, also the perpendicular turbulent transport terms (including the $\nabla \cdot \overline{\phi' \mathbf{J}'_{p,E}}$ contribution) and the correction term for the total vorticity (fifth term on the RHS of equation 7.14) become large, although significant noise is present on these terms. Furthermore, the total kinetic energy balance for this case (figure 7.3a) is dominated by the $\overline{\mathbf{V}'_{p,0} \cdot \nabla p_i/n}$ and $\overline{\phi' \nabla \cdot (\mathbf{U}_{*,i}/B \cdot \nabla \mathbf{V}_C)}$ terms which appear in this balance. The latter term is purely due to simplifications in the TOKAM3X charge balance equation and is thus nonphysical. This puts doubts on the physical validity of these results. Note that this behaviour is similar to the TOKAM2D TW case described in section 5.2, and that also the nonphysical term in both equations is similar. For the TW case as well, the error remaining on the evaluation of the $k_\perp$ equations is non-negligible.

**Modelling the $k_\perp$ equation**

Despite other (source) terms coming into play as well, the interchange term is expected to remain an important source term in more realistic 3D cases as well. For this term, the analytical relation 3.34 becomes

$$G_k = -\tilde{T}\mathbf{\Gamma}_{n,t,E} \cdot \nabla \ln(B^2), \tag{7.17}$$

for the isothermal TOKAM3X slab case, assuming a low $\beta$ plasma. This is indeed found to be an excellent model for both slab cases.

The sheath sink term 4.30 that was used before seems to be most closely related to the transport part of the parallel current contribution. Indeed, in the TOKAM3X data available it is found that $\nabla \cdot \overline{\phi' \mathbf{J}'_{||}} \sim c_s n_0 k_\perp / \sqrt{L_{||}}$ still holds approximately in the SOL region. However, calculating $k_\perp$ from the balance between the interchange term and this sheath loss model as was done for the TOKAM2D cases now is inaccurate, as illustrated in figure 7.4. This was to be expected based on the kinetic energy balances shown earlier. Moreover, the validity of this model for $\nabla \cdot \overline{\phi' \mathbf{J}'_{||}}$ is expected to be very limited. In the core region for example, it is clearly inadequate. Instead, it seems preferable to find a model for the local flux $\overline{\phi' \mathbf{J}'_{||}}$. In the SOL region of the TOKAM3X slab cases, this flux has a profile which is roughly proportional to the parallel convection of $k_\perp$, i.e. $\overline{\phi' \mathbf{J}'_{||}} \sim \bar{n} k_\perp \tilde{\mathbf{V}}_{||}$. While this model is most likely too crude, it does clearly indicate that this "anomalous" contribution to the parallel transport of $k_\perp$ is an important effect since the proportionality factor was found to be in the order of $20-50$. Hence, parallel transport of $k_\perp$ is found to be much faster than would be expected based on parallel convection only. Physically, Scott
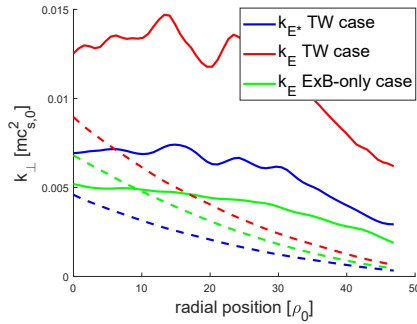
Figure 7.4: Assesment of interchange-parallel sheath loss $k_\perp$ model in TOKAM3X. TOKAM3X $k_\perp$ value in solid line, corresponding model value in dashed line. Mean-field data averaged over the parallel direction as well to obtain radial profiles.



(a) E×B-only case

(b) TW case
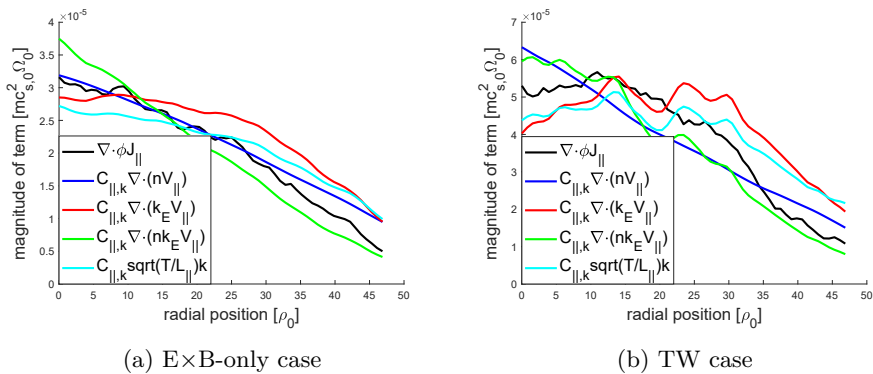
Figure 7.5: TOKAM3X models for the $\nabla \cdot \overline{\phi' \mathbf{J}'_{||}}$ term in the $k_\perp$ equation. Mean-field data averaged over the parallel direction as well to obtain radial profiles.

relates the flux $\phi \mathbf{J}_{||}$ to the parallel part the Poynting energy flux, and more specifically to the energy transport by shear Alfvén waves along $\mathbf{B}$ [143].

This qualitative discussion is supported by the the Bayesian inference results presented in table 7.1 and the profiles in figure 7.5. The Bayesian inferences in this section have been run with the same framework discussed in section 3.4. As in chapters 5 and 6, the likelihood function is takes the form of equation 3.61 without correlation distance, with the absolute model error formulation

of equation 3.63. The priors are chosen as in equation 5.14. The reference data consists of the 2D radial-parallel mean-field data. (Hence, not on the parallelly averaged data.) Note that investigating the scaling of the $\nabla \cdot \overline{\phi' \mathbf{J}'_{||}}$ with density is questionable with the current data. Due to the strong Boussinesq approximation used in TOKAM3X, this term might now be interpreted as a sink that needs to compensate not $\bar{n}k_\perp$, but just $k_\perp$. Remark also that the parameter scaling of the first two models in table 7.1 ($c_s/\sqrt{L_{||}}$) cannot be confirmed with the current data, since only a cases at a single parameter value is available. Given the limitations of the available data and the contrasting results for the E×B-only and TW case, it seems misleading to select a best model based on this analysis.

Table 7.1: Bayesian analysis of the models proposed for the $\nabla \cdot \overline{\phi' \mathbf{J}'_{||}}$ parallel transport of $k_\perp$ for the TOKAM3X E×B-only and TW cases. Parameter values are reported at MAP.

| model for $\nabla \cdot \overline{\phi' \mathbf{J}'_{||}}$ | parameter | E×B-only $k_E$ | TW $k_E$ | TW $k_{E*}$ |
|---|---|---|---|---|
| $C_{||,k}\frac{c_s}{\sqrt{L_{||}}}k$ | $C_{||,k}[-]$ | 0.332 | 0.221 | 0.432 |
| | $\sigma_{abs}[-]$ | 6.95E-6 | 1.90E-5 | 1.81E-5 |
| | logevidence | 29332 | 26514 | 26642 |
| $C_{||,k}\frac{c_s}{\sqrt{L_{||}}}\bar{n}k$ | $C_{||,k}[-]$ | 0.602 | 0.476 | 0.909 |
| | $\sigma_{abs}[-]$ | 6.73E-6 | 1.99E-5 | 1.98E-5 |
| | logevidence | 29421 | 26376 | 26391 |
| $\nabla \cdot C_{||,k}k\bar{\mathbf{V}}_{||}$ | $C_{||,k}[-]$ | 18.6 | 12.0 | 24.4 |
| | $\sigma_{abs}[-]$ | 8.56E-6 | 2.09E-5 | 1.89E-5 |
| | logevidence | 28749 | 26246 | 26530 |
| $\nabla \cdot C_{||,k}\bar{n}k\bar{\mathbf{V}}_{||}$ | $C_{||,k}[-]$ | 43.9 | 34.4 | 64.3 |
| | $\sigma_{abs}[-]$ | 5.87E-6 | 1.81E-5 | 1.90E-5 |
| | logevidence | 29811 | 26653 | 26516 |
| $\nabla \cdot C_{||,k}\bar{n}\bar{\mathbf{V}}_{||}$ | $C_{||,k}[-]$ | 0.200 | 0.440 | |
| | $\sigma_{abs}[-]$ | 5.88E-6 | 1.79E-5 | |
| | logevidence | 29800 | 26677 | |

The parallel current term $\overline{\nabla_{||}\phi' \cdot \mathbf{J}'_{||}}$ associated with the DW energy transfer channel (see section 3.2.5) has not yet been duly modelled. Based on the available data, it is hard to draw clear conclusions on the behaviour of this term. In the E×B-only TOKAM3X slab case, it acts like the dominant source of $k_\perp$ in the SOL (see figure 7.3d). The fact that the profile of $k_\perp$ shows a keen resemblance with the profile of this term (see figure 7.6) seems to testify to its importance for this case. Table 7.2 provides a tentative quantification hereof, the numerical value of $C_{||,k}$ clearly showing it to be much larger then the $\nabla \cdot \overline{\phi' \mathbf{J}'_{||}}$
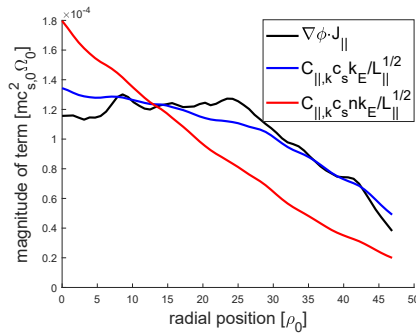
Figure 7.6: TOKAM3X models for the $\overline{\nabla_{||}\phi' \cdot \bar{\mathbf{J}}'_{||}}$ term in the $k_\perp$ equation. Mean-field data averaged over the parallel direction as well to obtain radial profiles.

parallel transport term. Note that the parameter scaling $c_s/\sqrt{L_{||}}$ is arbitrary and only chosen to facilitate the comparison with this parallel transport term. On the other hand, the $\overline{\nabla_{||}\phi' \cdot \mathbf{J}'_{||}}$ DW term does not seem to play a role in the energy balance for the equivalent TW case (see figures 7.3a and 7.3c).

Table 7.2: Bayesian analysis of the proposed models for the DW term $\overline{\nabla_{||}\phi' \cdot \mathbf{J}'_{||}}$ in the $k_E$ equation for the TOKAM3X E×B-only case. Parameter values are reported at MAP.

| model for $\overline{\nabla_{||}\phi' \cdot \mathbf{J}'_{||}}$ | parameter | |
|---|---|---|
| $C_{||,k}\dfrac{c_s}{\sqrt{L_{||}}}k_E$ | $C_D[-]$ | 1.64 |
| | $\sigma_{abs}[-]$ | 1.31E-5 |
| | logevidence | 27980 |
| $C_{||,k}\dfrac{c_s}{\sqrt{L_{||}}}\bar{n}k_E$ | $C_D[-]$ | 2.80 |
| | $\sigma_{abs}[-]$ | 3.62E-5 |
| | logevidence | 24704 |

**Particle transport relation**

Table 7.3 and figure 7.7 show the results for the Bohm, $k_\perp$ and $k_\perp - \zeta_\perp$ diffusion models for the average E×B turbulent particle flux $\mathbf{\Gamma}_{n,t,E}$. In this isothermal TOKAM3X case, the Bohm relation is normalised as $D \sim T_e/B$, where $B$ is the normalised field strength. Since $B$ only slightly decays in the radial direction, and $T_e$ is uniform, this predicts an almost uniform profile. Here it needs to be

(a) E×B-only case

(b) TW case
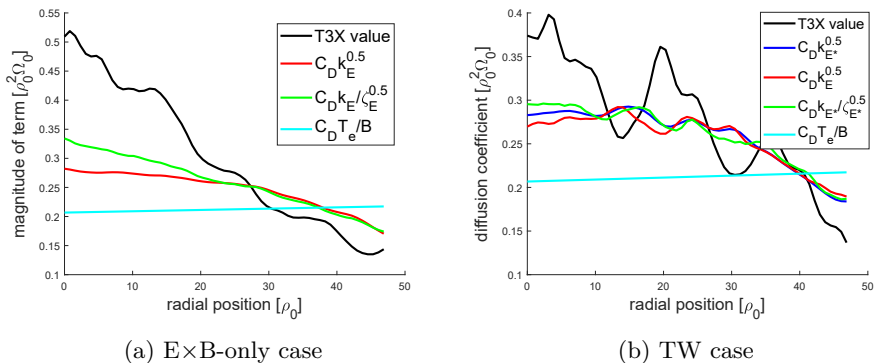
Figure 7.7: Comparison of TOKAM3X reference data for the turbulent diffusion coefficient to the $k_\perp$ and $k_\perp - \zeta_\perp$ models. Mean-field data averaged over the parallel direction as well to obtain radial profiles.

remarked that the Bayesian inference is run as before, but using the relative standard deviation formulation in equation 3.64.

Table 7.3: Bayesian analysis of the models proposed for the turbulent particle diffusion coefficients for the TOKAM3X E×B-only and the TW cases. Parameter values are reported at MAP.

| model for $D$ | parameter | E×B-only $k_E/\zeta_E$ | TW $k_E/\zeta_E$ | $k_{E*}/\zeta_{,E*}$ |
|---|---|---|---|---|
| $C_D \frac{T_e}{B}$ | $C_D[-]$ | 0.197 | 0.219 | |
| | $\sigma_{rel}[\%]$ | 40.0 | 28.9 | |
| | logevidence | 2173 | 3188 | |
| $C_D\sqrt{k}$ | $C_D[-]$ | 3.92 | 2.41 | 3.40 |
| | $\sigma_{rel}[\%]$ | 27.8 | 17.9 | 16.2 |
| | logevidence | 3193 | 4540 | 4810 |
| $C_D \frac{k}{\sqrt{\zeta_{turb}}}$ | $C_D[-]$ | 5.10 | | 3.54 |
| | $\sigma_{rel}[\%]$ | 23.4 | | 15.3 |
| | logevidence | 3684 | | 4982 |
| $C_D \frac{k}{\sqrt{\zeta_{tot}}}$ | $C_D[-]$ | 5.10 | | 3.54 |
| | $\sigma_{rel}[\%]$ | 23.3 | | 15.3 |
| | logevidence | 3689 | | 4984 |

These result indicate that the $k_\perp$ and $k_\perp - \zeta_\perp$ models show a good correlation with the diffusion coefficient profile for the TW case, while the fit for the E×B-only case is much less convincing. While the profiles of both models are

very similar, the evidence indicates that the $k_\perp - \zeta_\perp$ model is to be preferred. Against the expectations formulated earlier, using the E×B-only kinetic energy $k_E$ instead of the total perpendicular turbulent kinetic energy $k_{E*}$ does not bring an improvement. (Note that we have not yet reconstructed the E×B-only enstrophy in the postprocessing for the TW case, which is why no data of these models is shown.) Using the total enstrophy instead of the turbulent enstrophy to account for the mean-flow shear still seems to bring a slight improvement. The Bohm scaling clearly performs less good. Comparing the model parameters with those of the isothermal SOL results for TOKAM2D in table 5.3, it can be seen that for most of the models, the model parameters change strongly.

In conclusion, the limited data available does seem to indicate some correlation between $D$ and $\sqrt{k_\perp}$, although the correspondence is less convincing than for the TOKAM2D cases and the proportionality coefficient takes a different value. These differences might be due to changes in the structure of the turbulence induced by the different terms which are now important in the turbulent kinetic energy balances. However, too little data is available and too much questions remain on the available data to draw pertinent conclusions.

## 7.2 The impact of realistic 3D geometries: a first exploration

The previous section presented a preliminary analysis of 3D slab cases based on a limited set of available TOKAM3X reference data. This section comments on the extension of the findings of the previous section and chapters to realistic 3D geometries. This will amount to a discussion of the implications of the $k_\perp$ model which has been developed for the transport in mean-field code simulations. Attention will also be paid to the remaining shortcomings of the model.

### 7.2.1 Mean-field closure terms

Section 2.3.1 established that the mean-field E×B particle flux $\mathbf{\Gamma}_{n,t,E}$ in the average continuity equation 2.62 or 2.63 and the E×B turbulent heat fluxes $\mathbf{\Gamma}_{p_\mathrm{i},t,E}$ and $\mathbf{\Gamma}_{p_\mathrm{e},t,E}$ in the thermal energy equations 2.68 and 2.69 are vital closure terms to be modelled. Section 3.1 suggested to model these fluxes through diffusion relations 3.1 and 3.2 (repeated here for convenience)

$$\mathbf{\Gamma}_{n,t,E} \approx -D\nabla_\perp \bar{n}, \quad \mathbf{\Gamma}_{p_\mathrm{i},t,E} \approx -\chi_i \bar{n}\nabla_\perp \tilde{T}_i, \quad \mathbf{\Gamma}_{p_\mathrm{e},t,E} \approx -\chi_e \bar{n}\nabla_\perp \tilde{T}_e \quad (7.18)$$

and to relate the effective turbulent transport coefficients $D$, $\chi_i$ and $\chi_e$ to characteristic quantities for the turbulence. Chapter 6 showed that the three transport coefficient are proportional to one-another up to a constant of order unity for the investigated 2D electrostatic sheath connected SOL cases. It remains to be confirmed if this scaling holds more generally. For now it is assumed that this results holds to a certain extent in more complex cases as well.

Under that assumption, it suffices to model only one of the transport coefficients to obtain a model for the three. Combining the best performing models suggested in chapters 5 and 6, an elaborate scaling of the form

$$D = C_D \frac{k_E}{\sqrt{m\zeta_\perp} + C_S m S_m} sin(\Psi) \tag{7.19}$$

may be suggested, where it might still be necessary to adjust the coefficients $C_D$ and/or $C_S$ depending on the turbulence regime (core or SOL, interchange or DW dominated case, sheath connected or not). This transport coefficient model, how general it is, and in how far case specific parameter tuning is needed, certainly requires further investigation in realistic 3D cases. However, given its rather robust performance in chapters 4-6, it seems reasonable to assume that the basic scaling

$$D \sim \rho \sqrt{k_E/m} \tag{7.20}$$

will hold to some extent, even though the proportionality factor may not take a strictly fixed value that works for all cases. Assuming that this scaling holds, the next section will summarise the progress that has been made in modelling the transport equation of $k_E$, and which terms and effects require further attention. Besides the relevance for the transport coefficients themselves, this also led to insights on the dynamics and drives of the turbulence itself.

## 7.2.2 Modelling the turbulent kinetic energy equation

The general kinetic energy equation for a low $\beta$ edge plasma has been derived in section 3.2 as equation 3.24. Rewriting yields

$$\frac{\partial \bar{n} k_E}{\partial t} + \nabla \cdot (\bar{n} k_E \tilde{\mathbf{V}}_C + \frac{\overline{mn\mathbf{V}_E''^2 \mathbf{V}_C''}}{2} + \overline{\Pi \cdot \mathbf{V}_E''} + \overline{\phi' \mathbf{J}_{||}'} + \overline{\phi' \mathbf{J}_p'})$$

$$\approx \overline{\nabla_{||}\phi' \cdot \mathbf{J}_{||}'} + \overline{p'\nabla \cdot \mathbf{V}_E'} + \overline{\nabla\phi' \cdot \mathbf{J}_{p,*}'} - m\overline{n\mathbf{V}_C''\mathbf{V}_E''} : \nabla\tilde{\mathbf{V}}_E^T + \overline{\Pi : \nabla\mathbf{V}_E''^T}$$

$$-mnV_{||}\frac{\overline{D\mathbf{b}}}{Dt} \cdot \mathbf{V}_E'' - \frac{m\overline{S_{n,i}\mathbf{V}_E''^2}}{2} - m\mathbf{V}_E \cdot \overline{\mathbf{V}_E'' \cdot S_{n,i}} + \overline{S_{nV} \cdot \mathbf{V}_E''}.(7.21)$$

Some terms which are expected to be small are neglected here. It is assumed that $\nabla \cdot (p\mathbf{V}_E + \phi\mathbf{J}_*) \approx 0$ due to the smallness of magnetic field gradients w.r.t. length scales of the turbulent quantities. The Favre term has likewise been left away since all TOKAM2D results showed it to be small.

This thesis has confirmed that the interchange term can act like the major drive of the turbulence in the SOL on the low field side (LFS). A general analytical equation has been derived for this term in equation 3.34:

$$G_k = \overline{p'\nabla \cdot \mathbf{V}_E'} = -(\tilde{T}\mathbf{\Gamma}_{n,t,E} + \mathbf{\Gamma}_{p_i,t,E} + \mathbf{\Gamma}_{p_e,t,E}) \cdot \nabla\ln(B^2), \qquad (7.22)$$

which assumes a low $\beta$ electrostatic plasma. As mentioned before, this term has a ballooned character, since heat fluxes are normally outward everywhere in the reactor, while the magnetic field gradient is only opposed to this flux on the LFS. As a result, the interchange term tends to act like a source on the LFS, while it acts like a sink on the high field side (HFS). This is illustrated in figure 7.8a, showing the interchange term in the poloidal plane of a SOLPS-ITER mean-field code simulation in which a model based on the $k_\perp$ model developed in this thesis has been implemented [55]. Note that this interchange model holds in general and is thus not only relevant in interchange dominated turbulence regimes. It is interesting to remark that even when another term would provide a poloidally uniform drive of $k_\perp$, the turbulence on the HFS would be decreased and that on the LFS increased due to the resulting turbulent E×B heat fluxes.

The term that was found to balance the interchange on the LFS SOL in the TOKAM2D cases is the parallel loss to the sheath. This term is the equivalent of the transport part of the parallel current contribution (fifth term on the LHS of equation 7.21). This was confirmed to some extend by the available TOKAM3X cases. For these TOKAM3X cases, it was also found that the

(a) interchange term $G_k$

(b) Turbulent kinetic energy $k_\perp$
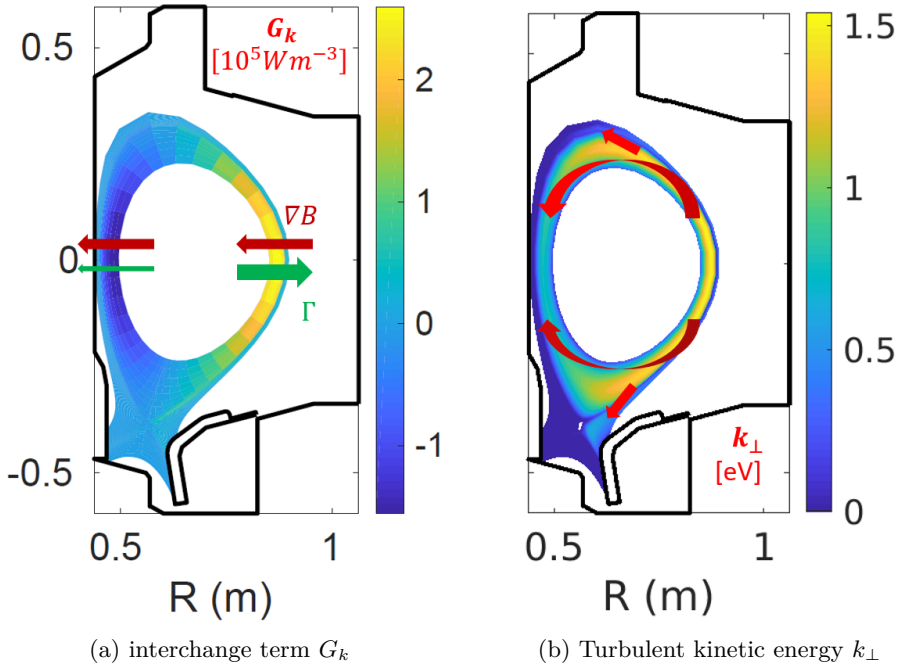
Figure 7.8: Profiles in the poloidal plane of the C-Mod tokamak as obtained from a self-consistent SOLPS-ITER mean-field transport simulation. Figures reproduced from Ref. [54].

underlying "anomalous" parallel flux $\overline{\phi' \mathbf{J}_{||}'}$ largely exceeded both the mean-field and the turbulent parallel convection.

This has interesting implications for the distribution of $k_\perp$ in tokamaks. The exploratory SOLPS-ITER case set up by Dekeyser *et al.* [54] had the interchange term as the dominant source of $k_\perp$ with this fast transport acting like the main compensation mechanism. The resulting balance showed strong production of turbulence around the OMP (as shown in figure 7.8a), which is quickly removed by the fast parallel transport. In the SOL, this allows saturation of the turbulence by removal of $k_\perp$ to the divertor targets, which is reminiscent of the physics of the TOKAM2D cases. In the core region on the other hand, $k_\perp$ can be transported away from the OMP to the HFS, where it may be dissipated by the interchange term acting like a sink in that region. These mechanisms are illustrated in figure 7.8b showing the resulting mean-field solution for $k_\perp$. Hence, this term adds a strongly non-local element to the balance of $k_\perp$ and thus to the turbulent transport of particles and heat. Furthermore, this increased

parallel spreading of $k_\perp$ also means that the resulting turbulent transport is less ballooned than would have been the case had the interchange source (on the LFS) been balanced by a local sink.

It is not claimed in this text that this flow picture or the corresponding saturation mechanism is generally valid in any tokamak operating regime. Nonetheless, the insights provided by them and the role of the $\overline{\phi' \mathbf{J}'_{||}}$ flux in enhancing the parallel spreading of the turbulence are believed to be novel and may in general be considered in the overall flow picture in tokamaks. Many other effects which were not yet taken into account may modify these dynamics though.

### 7.2.3 Limitations of the $k_\perp$ model

In the current stage of its development, the validity of the $k_\perp$ model is limited since it has mostly been developed and tested for interchange-dominated, sheath-connected, electrostatic SOL cases. A number of terms which are expected to be important in the $k_\perp$ transport equation 7.21 in different cases is neglected.

The $\overline{\nabla_{||}\phi' \cdot \mathbf{J}'_{||}}$ term associated with the DW energy transfer channel (see section 3.2.5) has for example not yet been duly modelled.[1] It is observed that the role of this term varies depending on the turbulence regime. This term has been observed to be the dominant source of $k_\perp$ in the E×B-only TOKAM3X slab case, but was negligible in the corresponding TW case. Moreover, the term intended to mimic DW dynamics in the core region of TOKAM2D acted like a sink (see section 5.1.2). Hence, it seems that the behaviour of this term can change significantly depending on the regime the turbulence is in and how exactly the competition with other terms occurs. Much more analysis is thus required to model this term.

Another term in the $k_\perp$ equation which requires further modelling attention is the Reynolds stress term term $-mn\overline{\mathbf{V}''_C \mathbf{V}''_E} : \nabla \tilde{\mathbf{V}}^T_E$. In the SOL, the flow shear is limited because the electrostatic potential is tied to the sheath potential at the end of the field lines. However, around the separatrix and in the core region, strong poloidal flows which are sheared in the radial direction may develop, such that the $mn\overline{\mathbf{V}''_{C,r} \mathbf{V}''_{E,\theta}}\partial_r \tilde{\mathbf{V}}_{E,\theta}$ contribution in particular may become important (see for example section 5.1.2). Primarily, this term is expected to break up the turbulent eddies and as such act like a sink of $k_\perp$ (in line with the inverse energy cascade). However, when the turbulence is sufficiently damped and when the flow shear is sufficiently strong, the Kelvin-Helmholtz (KH) instability may come into play. This secondary instability might then lead to the RS term to

---

[1]Note that Dekeyser *et al.* modelled this term as a small linear sink of $k_\perp$, reminiscent of its behaviour in the investigated TOKAM3X TW slab case.

act like a source of $k_\perp$ [79, 115, 135]. Furthermore, as indicated in equation 7.19, strong flow shear could also influence the diffusion relation itself. Hence, flow shear is expected to lead to both a reduction of $k_\perp$ and a reduction of the transport coefficients at the same $k_\perp$. In addition, since both effects depend on the flow shear, a model for $\partial_r \tilde{\mathbf{V}}_{E,\theta}$ itself is required. While the mean-field E×B velocity can be calculated from the mean-field charge balance equation for the electrostatic potential, the closure terms in this equation need further attention.

Dekeyser *et al.* implemented a negative turbulent viscosity model in SOLPS-ITER to model the RS as a first approximation. Note that such model does not allow the RS to act like a source of $k_\perp$ as would be implied in the KH-regime. The RS were then also used in the polarisation current such that they contribute to the formation of the shear flow itself as they should. Furthermore, Dekeyser *et al.* used a shear dependent diffusion coefficient ($D \sim k_\perp/(\sqrt{k_\perp} + C_S|\nabla\mathbf{V}_E|)$). These elements caused a clear suppression of the turbulent transport coefficients around the separatrix as physically expected. While this behaviour is promising, further investigation of models for both the RS and the influence of shear on the transport coefficient based on an analysis of reliable and sufficiently complex reference data is certainly required.

Furthermore, the effects of perpendicular turbulent transport of $k_\perp$ might also require further attention. In the TOKAM2D cases studied earlier, its contribution to the balance of $k_\perp$ was found to be small. However, this may not be the case in general. In TOKAM3X TW case for example, the perpendicular turbulent transport terms (both $\overline{\phi'\mathbf{J}'_{p,0}}$ and $mn\overline{\mathbf{V}''_C\mathbf{V}''^2_E}/2$) seemed to become large but noisy. In regions where the perpendicular gradients of $k_\perp$ are steeper, such as presumably around the separatrix due to flow shear, more radial transport of it would likewise be expected [151]. Another element that may need to be taken into account is the influence of the diamagnetic contribution to the polarisation current $\mathbf{J}_{p,*}$ and its effect on the balance of $k_E$ or $k_{E*}$. However, both in TOKAM2D and in TOKAM3X, the implementation of this contribution is questionable, such that no firm conclusions on the importance of these effects can be formulated and certainly no models proposed.

The viscous dissipation of $k_\perp$ has been shown to be of secondary importance in all investigated cases. It could be modelled by including the enstrophy into the model. As illustrated by De Wolf *et al.*, the $k_\perp$ and $\zeta_\perp$ equations still require to be properly decoupled for this to bring an improvement. If the additional complexity of an enstrophy equation is not desired, it may be possible to model the viscous dissipation of $k_\perp$ with a dimensional scaling and using $I \sim k_\perp \sim \zeta_\perp$ as has been observed in the TOKAM2D data (with $I$ a measure of the turbulence intensity).

Finally, there are still the source terms of $k_E$ due to particle and momentum

sources (which are mainly due to neutrals), and due to changes of the magnetic field direction. Since only slab cases without neutrals have been studied in this thesis, no comment on the importance of either of these can be made. However, it cannot be excluded that these effects would play a role in tokamaks (in particular regions are regimes).

Depending on which of the terms in the $k_\perp$ equation are dominant in a certain case, i.e. which regime the turbulence is in, it can be expected that the structure of the turbulence is different. As a result, it is likely that the exact relation between the intensity of the turbulence (e.g. $k_\perp$) and the transport resulting from it (i.e. the turbulent transport coefficients) will be different. Hence, it is possible that depending on the regime, different model constants might be needed in equation 7.20 or even a different form of the transport relation itself. The occurrence of different turbulence regimes and the threshold values for the transition between them have not explicitly been investigated in this thesis. This topic has however been studied in literature, see for example Refs.[63, 79, 114, 145]. Nonetheless, it is expected that a basic scaling between the transport coefficients and well-chosen quantifiers of the turbulence can be used to get an idea of the characteristics of the transport. Furthermore, as has been proven here, for particular regimes such as electrostatic interchange-dominated E×B turbulence in a sheath-connected SOL, these models can provide very accurate predictions.

## 7.3  Conclusion

This section has provided a first step to the generalisation of the $k_\perp$ model to 3D cases, and the implications of the model for the perpendicular turbulent transport in the plasma edge of nuclear fusion reactors.

A preliminary analysis of isothermal TOKAM3X slab cases showed that the turbulent kinetic energy balance becomes more complex with more terms playing a role, as was anticipated. While the interchange term does seem to remain an appreciable source, also other terms come into play, most notably the DW source. Furthermore, the "anomalous" parallel flux of $k_\perp$ due to parallel current fluctuations is found to largely dominate the parallel transport of $k_\perp$. It is argued that the large sheath loss sink of $k_\perp$ observed (and modelled) in the 2D case studied in earlier chapters is to be related to this parallel flux. Only a very limited TOKAM3X data set was available and some doubt remains on the simulation results and the analysis though, requiring the results to be treated with some apprehension.

Extrapolating the $k_\perp$ model mainly developed for the 2D interchange-dominated, sheath-limited SOL to realistic 3D geometries, it is found that poloidally ballooned profiles are inherently predicted, including dissipation of $k_\perp$ on the HFS. Furthermore, fast parallel transport of $k_\perp$ leads to spreading of the turbulence over a wider poloidal angle and the removal of $k_\perp$ towards the targets in the SOL. The physics-based, self-consistent inclusion of these phenomena is novel in 2D mean-field simulations. However, further development of the model is required to comprehensively include additional physical effects (parallel transport, DWs, effect of flow shear, neutrals, perpendicular transport,...). Furthermore, it should be checked if the transport in the core region can be modelled with the same models, i.e. if the same transport as in the SOL results when the same level of $k_\perp$ and the same balance is present, as was implicitly presumed. Moreover, the model needs to be extensively tested in order to assess how universal its parameters are and thus to establish its predictive capabilities.

# Chapter 8

# Conclusion and suggestions for further research

## 8.1 Conclusions

The absence of greenhouse gas emissions, the widely available fuel, the inherent safety and the limited nuclear waste make nuclear fusion an attractive option for electricity generation in the future. However, a number of technological challenges still stand, one of which is the high heat and particle load on the divertor. Turbulent transport processes largely determine the outward power and particle fluxes and thus the efficiency of the plasma confinement. Taking the turbulent transport in the plasma edge into account is of crucial importance to predict the load on the divertor.

As experimental tokamaks are extremely expensive, numerical simulations of the plasma edge are crucial to predict the performance of future reactors and to obtain improved designs. In particular, mean-field transport codes, which only calculate the average characteristics of the plasma in every point, are the main tools used for designing the plasma facing components and the divertor. However, the description of turbulent transport in these codes is lacking. Typically, the turbulent fluxes are described via an ad hoc diffusive approximation, in which the diffusion coefficients are determined for a particular experiment. Since these diffusion coefficients vary from one location to another, from one regime to another and from one device to another, this poses severe limitations on the predictive capabilities of these mean-field codes. On the other hand, the routine use of turbulence code simulations resolving the detailed

turbulent flow field including all the fine scale fluctuations remains inhibitive for reactor design due to their high computational cost.

This thesis has proposed an approach for modelling the turbulent fluxes inspired by Reynolds-averaged Navier-Stokes (RANS) methods commonly used in hydrodynamic turbulence. In this approach, only the average of the turbulent flow field is resolved, as in the mean-field approach for plasma edge simulations, but the closure terms are modelled by relating them to quantities characteristic of the turbulence.

## General framework

The approach followed in this thesis starts by rigorously averaging the Braginskii-like fluid equations. This procedure allows to identify the closure terms, which cannot be calculated from mean-field quantities directly. It is illustrated that the average E×B turbulent fluxes of particles and heat are the main closure terms to be modelled for the transport across magnetic flux surfaces. The exact form of these fluxes in terms of correlations between regular and density weighed fluctuations is presented.

It is proposed to retain the diffusive description for the E×B turbulent fluxes as commonly used in mean-field transport codes, but to relate the transport coefficients to characteristics of the turbulence as in the RANS approach. In particular, they are related to the turbulent kinetic energy $k_\perp$ and the enstrophy $\zeta_\perp$ of the E×B drift causing the fluxes of interest. Hence, these quantities do not only quantify the intensity of the turbulence, but also provide characteristic time and length scales for the fluctuations causing the transport.

Following Scott [143] but treating the density in averaging more systematically, mean-field transport equations are derived analytically for $k_\perp$ and $\zeta_\perp$ based on the Braginskii equations. Another extension of the work by Scott is that equations are not only derived for the total perpendicular kinetic energy, but also for its E×B contribution separately. These analytical equations show the exact form of the different source, sink and transport terms of $k_\perp$, and the corresponding interactions with the different energy forms present in the plasma. In the turbulent kinetic energy equation, it is expected that the interchange, drift wave (DW) and Reynolds stress (RS) energy transfer channels will provide the dominant sources and sinks. Most of the terms in these $k_\perp$ and $\zeta_\perp$ equations in turn also constitute closure terms to be modelled (if they are relevant).

From this general framework, the question naturally follows which form the diffusion relation needs to take exactly, which terms in the $k_\perp$ and $\zeta_\perp$ equations are dominant (under which conditions) and how these dominant terms can

in turn be modelled. These questions are answered by applying the above framework to reference data obtained from detailed turbulence code simulations. By comparing this reference data to the models that are developed, the free parameters in the models can be estimated and the adequacy of the models tested. To support this, a Bayesian framework for parameter estimation and model comparison is employed. This statistical methodology allows to extract plenty of information on the parameters. In particular, a probability distribution for the model parameters, including their mutual correlation is obtained. Furthermore, the Bayesian evidence allows to compare different models with each other, while inherently taking differences in model complexity into account, thus guarding against overfitting of the reference data.

**Turbulent transport model development**

In order to start with an intelligible case and to build up the model from the basics of plasma edge turbulence, the simplified conditions of isothermal interchange-dominated electrostatic turbulence in a sheath-connected SOL are considered first. The TOKAM2D turbulence code [141, 109, 116] is used to provide reference data for this case. In analogy to the earlier work on the general case, mean-field equations, including those for $k_\perp$ and $\zeta_\perp$, are derived for this case specifically.

The analysis conducted for this case has shown that the effective turbulent particle diffusion coefficient can indeed be linked to $k_\perp$ and $\zeta_\perp$ as anticipated. Both the averaged profile of individual simulations and the scaling across simulations with different physical parameters can be approximated as $D \sim \sqrt{k_\perp}$. $\sqrt{k_\perp}$ acts like a characteristic velocity scale for the turbulence such that this relation can be interpreted as a refinement of the Bohm scaling [71, 94, 95] where the electron thermal velocity is used for that. Additionally including the turbulent enstrophy, the alternative scaling $D \sim k_\perp/\sqrt{\zeta_\perp}$ is found. In this scaling, both a length and a time scale are now constructed based on turbulent quantities. This allows to further improve the accuracy of the model in TOKAM2D parameter space, especially for varying viscosity.

For these relations to be used in a self-consistent way, a model for $k_\perp$ and $\zeta_\perp$ is required. First, the balance of $k_\perp$ is studied for the isothermal SOL case. It is shown that the interchange term provides the dominant source, while the losses to the sheath (as a model for the unresolved parallel direction in TOKAM2D) act like the main sink. Viscous dissipation plays a secondary role, while all other terms are smaller in magnitude. It is thus found that the $k_\perp$ equation can approximately be modelled as a balance between interchange and sheath

losses. The turbulent enstrophy balance is found to be similar, however, the viscous dissipation of $\zeta_\perp$ is roughly as important as the sheath losses.

The interchange term for $k_\perp$ is modelled using an analytical relation which was already derived for the general case (exact under low $\beta$ assumptions). This relation shows that the interchange term is proportional to the opposite of the scalar product of the E×B turbulent energy flux and the magnetic field strength gradient. A prominent feature of this relation is that it explains the ballooned character of plasma edge transport. On the outboard side of the tokamak, the energy flux and the magnetic field strength gradient have opposite directions, leading to a source of $k_\perp$ and thus to strong transport. On the inboard side though, the energy flux and the magnetic field strength gradient are aligned leading to a sink of $k_\perp$ and thus to reduced transport. If the turbulent fluxes are known (from the diffusion relation), the interchange term can be calculated without further closure model. Moreover, this clearly links the drive of the turbulence with the mean-field thermal gradients which are expected to drive the turbulence. The sheath loss term is modelled using a simple regression relation, scaling linearly with $k_\perp$.

The combination of the particle diffusion, interchange source, and sheath loss relations then leads to the $k_\perp$ model which can self-consistently predict the turbulent E×B particle flux. The physics of this model can be interpreted as a mean-field equivalent to the gradient removal mechanism [133, 114, 89]. When a mean-field density gradient is present (and $k_\perp \neq 0$), this leads to a turbulent particle flux down the gradient. If this flux is in the direction opposite to the magnetic field gradient, this leads to a source of $k_\perp$, which in turn leads to increased transport, etc. This system saturates when the mean-field gradient is reduced and $k_\perp$ is increased to such levels that the particle flux can still be carried across the flux surfaces but that the sheath loss sink of $k_\perp$ suffices to compensate the source. Forward 1D mean-field simulations with this $k_\perp$ model are capable of reproducing the profiles of the averaged TOKAM2D reference data very well.

This $k_\perp$ model is further extended to a self-consistent $k_\perp - \zeta_\perp$ model by adding a model equation for the turbulent enstrophy. The interchange, sheath loss and viscous terms in this equation are modelled using series decomposition, dimensional scalings and regression analyses. Furthermore, the enstrophy allows to use an analytical relation to include the viscous dissipation of $k_\perp$ separately from the sheath loss sink of $k_\perp$ and to improve the regression relation for the sheath loss sink. While these "submodels" for the individual terms all seem to work adequately, they do significantly increase the complexity of the complete $k_\perp - \zeta_\perp$ model w.r.t. the $k_\perp$ model. The Bayesian analysis performed by De Wolf *et al.* has shown that this more complex "full model" is outperformed by the simpler $k_\perp$ model. The reason for this is probably that the limited errors

on the submodels align, leading to more significant errors overall.

Next, the scalings for the diffusion coefficient are further investigated in more complex flow cases. To that end, the TOKAM2D domain is extended with a core region, that intends to mimic DW dynamics. This leads to the development of strong flow shear around the separatrix and the reduction of the effective turbulent diffusion coefficient, in line with the behaviour in more complete turbulence codes and experiments. The $k_\perp$ and $k_\perp - \zeta_\perp$ scalings are found not to be adequate to predict the diffusion coefficient in the outer edge region and the SOL at the same time with just a single coefficient. It is suggested to extend the $k_\perp - \zeta_\perp$ model by explicitly including shear decorrelation rates for the turbulence in addition to the $\sqrt{\zeta_\perp}$ rate already included. This allows to largely improve the Bayesian evidence. However, it is found that using the default $k_\perp - \zeta_\perp$ scaling while allowing a different coefficient in the core and the edge region performs even better. This may imply that $k_\perp$ and $\zeta_\perp$ can effectively be used to predict the turbulent transport, but that the model coefficient needs to be adjusted for the specific regime and structure of the turbulence (e.g. interchange or DW regime). Alternatively, it could be argued that the model form should be changed or extended with further quantifiers of the turbulence to be able to use it more generally. Note that the influence of the flow shear on $k_\perp$ and $\zeta_\perp$, a second mechanism by which shear could reduce transport, is not studied here.

Another extension of the TOKAM2D model that has been investigated is the total vorticity (TW) case in which the contribution of the diamagnetic ion drift to the inertia is incorporated (next to the E×B drift contribution). The E×B-only kinetic energy ($k_E$) balance is demonstrated to change little, it is still dominated by the interchange source and the sheath loss sink. Forward simulations with the $k_\perp = k_E$ model developed earlier still provide acceptable results with respect to the reference data, although the model coefficients had to be significantly adjusted. However, the total (E×B and ion diamagnetic) turbulent kinetic energy balance feature two dominant new terms which largely balance each other. The new source term enters purely due to the approximations made in the TOKAM2D charge balance equation, and is thus nonphysical. Hence, the physical relevance of the results obtained related to this TW case is questionable. It could be argued that the decent performance of the $k_\perp$ model even in this case testifies to its robustness.

Next, the generalisation towards the anisothermal (E×B-only) SOL case in TOKAM2D has been considered. Since electron and ion temperature fluctuations are now allowed, the turbulent E×B heat fluxes require modelling next to the E×B turbulent particle flux. A first result that is obtained is that the effective turbulent transport coefficients for all three are proportional $D \sim \chi_i \sim \chi_e$ up to a constant of order unity. Furthermore, the scaling $D \sim \sqrt{k_\perp}$

identified for the isothermal case is observed to still predict the profiles very well and to capture the main trend in parameter space. The change in the model coefficient with respect to the isothermal case is limited. The balance of $k_\perp$ in this case is largely similar to that in the isothermal case, with the interchange term still acting like the main source, the sheath term acting like the main sink and the other terms being significantly smaller. However, upon closer evaluation, the sheath term now has a large sink contribution as before, and a large source contribution related to the correlation between potential and electron temperature fluctuations which was absent in the isothermal case. The source term is associated with the sheath-conducting wall instability (SCW) and thus provides a second drive term for the turbulence next to the interchange term.

The analytical model for the interchange term discussed before remains valid in the anisothermal case, however, both the heat flux due to convection with the mean turbulent particle flux and due to turbulent conduction come into play. For the sheath term as well, the model form is changed little. Even though the SCW contribution is inherently present in it, only the total sheath term (which always remained negative) is modelled, for which a regression model that is linear in $k_\perp$ is still used. Hence, the SCW term is not modelled explicitly in any of the submodels. It is shown that this does lead to an increased error on the submodel level, both for the sheath loss model and for the transport coefficients. For the sheath loss term, the magnitude of the sheath loss is overestimated in cases where the SCW contribution is large (hence lowering the magnitude of the overall negative term). For the transport coefficients, it is shown that when the SCW drive is large compared to the interchange drive, the turbulence is closer to the SCW structure of the turbulence. This structure is characterised by a low phase shift between density and potential fluctuations, leading to low transport for a given value of $k_\perp$. Correcting the transport coefficients for this phase shift does indeed improve their performance.

While neither the phase shift nor the SCW term from which it results is self-consistently modelled at the moment, the transport coefficients resulting from the forward simulations with the full model compare well to the averaged TOKAM2D reference data nonetheless. The reason for this is that the unmodelled SCW drive tends to increase $k_\perp$, but at the same time decrease the characteristic phase shift between density and potential fluctuations, lowering the transport. The net result of both is that the SCW term has little effect on the value of the transport coefficients. Note that the basic physics of the resulting anisothermal $k_\perp$ transport model are very similar to the self-saturation picture drawn for the isothermal case before. Both density and temperature gradients now lead to heat fluxes, which drive the interchange source of the turbulence, and the turbulence now saturates when both kinds of gradients are such that a balance is established

between this interchange term and the sheath losses of $k_\perp$. Furthermore, when steady state is assumed and the perpendicular transport of $k_\perp$ neglected, the resulting scaling of the transport coefficient can be interpreted as a modification of the gyro-Bohm scaling [71, 73, 94, 95].

Finally, a preliminary analysis of TOKAM3X [157] turbulence code data for an isothermal 3D slab SOL has shown that the turbulent kinetic energy balance may take a more complex form in 3D. The parallel current term in the $k_\perp$ equation now has a transport and a DW contribution, which might both play an important role. In particular, this transport term is the 3D equivalent of the sheath losses in TOKAM2D. This transport term is expected to lead to a parallel spreading of the turbulence and introduces a strongly non-local element into the balance of $k_\perp$ and thus into the turbulent particle and heat fluxes. Furthermore, the perpendicular transport of $k_\perp$ and the correction term for the diamagnetic contribution to the polarisation current may also become more important. On the other hand, the relation between $k_\perp$ and the turbulent transport coefficient is less clear for the very limited data set that was available. Also, the model coefficients in this relation shift significantly.

In summary, this work has shown that a model based on $k_\perp$ is very well capable of reproducing the average E×B perpendicular transport for specific cases. Moreover, this model can be implemented in mean-field codes such as SOLPS-ITER [29] in order to obtain a physics based profile of the turbulent transport coefficient in the poloidal plane. The resulting profile automatically shows some experimentally observed features such as ballooning of the transport, transport reduction around the separatrix and parallel spreading of the turbulence. Moreover, this profile can be established by specifying a limited number of coefficients with a clear physical meaning. Hence, it is expected that these coefficients will remain accurate, at least in a certain turbulence regime, such that this model and its further developments can be used for predictive purposes. Nonetheless, many effects are not yet accounted for and require further research

## 8.2 Suggestions for future research

Firstly, even though the model predictions for the investigated 2D cases worked very well in general, some parameter scalings are not recovered. This requires further investigation. In particular, section 4.5 showed that a proper decoupling of the equations in the $k_\perp - \zeta_\perp$ model should be further studied. Also, the influence of flow shear, the diamagnetic contribution to the polarisation drift and different drivers of the turbulence require further analysis. It should be further studied how the diffusive transport relations need to be adjusted to

account for these different effects with a minimum of physics based parameters. The relation with the characteristic phase difference and the length scale of the turbulence seem to be promising research tracks to further pursue. Since the DW channel and the SCW mode are inherently phenomena related to parallel dynamics, it seems preferable to study these in a 3D setting directly though. For studying the diamagnetic contribution to the inertia, reference data is required in which this is resolved without major nonphysical assumptions hindering the analysis.

However, more generally and away from the 2D cases, the diffusion relation linking the transport coefficients and $k_\perp$ in general should be tested in more complex cases. Especially in 3D cases with a realistic geometry it should be checked how the relation between $k_\perp$ and the turbulent transport behaves. Since large differences in the transport in different regions of the reactor are expected, it would be interesting to check if the link between $k_\perp$ and the transport holds in all regions. Validating this relation for the core region would be particularly relevant since this work has mainly studied the SOL. In line with this, it should be investigated how the diffusion relation evolves when different terms dominate the turbulence, i.e. interchange or DW dominated, strong flow shear or not, sheath modes or not,... If the link between $k_\perp$ and the transport is found to hold, the sources and sinks of the turbulence in these general 3D cases should be studied. Accurate models for the parallel dynamics, both in the form of the DW channel and the parallel flux $\overline{\phi' \mathbf{J}'_\parallel}$ and the effect of flow shear are expected to be especially important.

Another interesting research track might be to elaborate an alternative non-diffusive particle transport relation to better take the underlying nature of the blob-filaments into account. It may be attempted to combine the characteristic blob velocities identified for example in Refs. [61, 101, 106] to the statistical distribution of the fluctuations described in Refs. [75, 76].

Another element that still needs to be integrated in the $k_\perp$ model framework is the interaction between the turbulent transport and neutrals. On the one hand the neutrals influence the dynamics of the turbulence and the transport through friction and ionisation sources. The other way around, the turbulent fluctuations may induce closure terms into the mean-field sources and sinks of the neutrals. Furthermore, the influence of electromagnetic fluctuations and $\mathbf{A}'_\parallel$ in particular on the dynamics of the turbulence and the transport may be investigated.

Another standing problem is how the boundary conditions for the turbulent quantities $k_\perp$ and $\zeta_\perp$ are to be chosen in predictive mean-field simulations. In this work, boundary conditions could always be taken from data of the turbulence code simulations, but these will no longer be available for predictive

mean-field simulations. It may be an option to use the local-balance equivalent of the $k_\perp$ and $\zeta_\perp$ equations as boundary conditions to get a self-consistent estimate.

Once a sufficiently comprehensive model is obtained and implemented in a mean-field code, a logical next step is to compare it to experimental discharges in different machines and operating regimes. This will allow to check how universal the model and the model parameters really are, and thus to effectively assess its predictive performance. Note that comparison to experiments can be started before the model is "completed" for discharges which are known to be governed by dynamics that are already in the model. In effect, this process has already started through the work of Carli *et al.* [39, 38] and Dekeyser *et al.* [54].

Finally, some methodological extensions could be envisaged as well. It could be of interest to extend the analysis to also include slow transient effects. This would allow to use more information from the turbulence code data and may allow to go deeper into the dynamics at play. The capability of the model to capture slow transients would widen the range of applications and scenarios for its use. It would for example enable simulations of the transient effects when changing operating regimes in the reactor. Secondly, also the Bayesian framework could be further elaborated. A particular feature of interest would be to include the uncertainty on the input data that is used. Also, a further study into the best way to combine data from the different quantities in the reference data when analysing the full models might provide new insights. Lastly, it may be interesting to look into machine learning techniques and to investigate how these could improve or complement the physics based approach suggested here.

# Appendix A

# Charge balance equation and energetic couplings between kinetic energies

First, this appendix discusses the similarities and differences between the charge balance equation and the vorticity equation in section A.1. Then, kinetic energy equations for the diamagnetic ion drift and the mixed kinetic energy (kinetic energy in the product $\mathbf{V}_E \cdot \mathbf{V}_{*,i}$) are derived in sections A.2 and A.3. Finally, the energetic interactions of these kinetic energies are discussed in section A.4.

## A.1 Link between vorticity equation and charge balance equation

In plasma edge turbulence modelling, the charge balance equation 2.41 is commonly formulated as a transport equation for a quantity that approximates the (parallel component of the) vorticity. For this reason, the charge balance equation is often called the vorticity equation, even though strictly speaking this is somewhat of a misnomer. With this in mind, it is interesting to compare the charge balance equation 2.41 to the vorticity equation 2.24. This appendix will semi-quantitatively show that the charge balance equation is equivalent to the projection of the vorticity equation onto the parallel direction.

Using equation 2.42 the LHS of the charge balance equation 2.41 can be written as

$$-\nabla \cdot \mathbf{J}_{p,0} = \nabla \cdot \frac{mn}{B} \frac{D}{Dt} \left( \frac{\nabla_\perp \phi}{B} + \frac{\nabla_\perp p_i}{enB} \right)$$

$$+ \nabla \cdot \frac{mS_{n_i}}{B} \left( \frac{\nabla_\perp \phi}{B} + \frac{\nabla_\perp p_i}{enB} \right) + \nabla \cdot \left( \frac{D\mathbf{b}}{Dt} \times \frac{mn\mathbf{V}_0}{B} \right). \tag{A.1}$$

This resembles the LHS of the vorticity equation 2.24 projected onto the parallel direction $\mathbf{b}$ divided by the magnetic field strength $B$:

$$nm \frac{D\boldsymbol{\omega}}{Dt} \cdot \frac{\mathbf{b}}{B} = \frac{mn}{B} \frac{D}{Dt} (\boldsymbol{\omega} \cdot \mathbf{b}) - \frac{nm\boldsymbol{\omega}}{B} \cdot \frac{D\mathbf{b}}{Dt}$$

$$= \frac{mn}{B} \frac{D}{Dt} \left( \frac{1}{B} \nabla \cdot (\nabla_\perp \phi + \frac{\nabla_\perp p_i}{en}) \right) - \frac{nm\boldsymbol{\omega}}{B} \cdot \frac{D\mathbf{b}}{Dt}. \tag{A.2}$$

In this expression, the definition of the vorticity has been applied to the dominant plasma velocity, $\boldsymbol{\omega} = \nabla \times \mathbf{V} = \nabla \times \mathbf{V}_0$. Note that a term proportional to $\nabla \times \mathbf{B}$ has been dropped by the low-$\beta$ approximation in the product $\boldsymbol{\omega} \cdot \mathbf{b}$. While expressions A.1 and A.2 are not exactly equal to each other, they are clearly similar, showing qualitatively the link between both equations.

The right hand sides of the parallel vorticity equation and the charge balance equations can be illustrated to strongly resemble each other as well. It is particularly interesting to look at the pressure and the Lorentz force term in the vorticity equation. Manipulating the pressure term (third term on the RHS of equation 2.24) in a fashion similar to the time change term, the following expression is found:

$$mn(\frac{\nabla \rho \times \nabla p}{\rho^2}) \cdot \frac{\mathbf{b}}{B} = \nabla \cdot \mathbf{J}_* - \frac{\nabla \cdot (n\mathbf{J}_*)}{n}. \tag{A.3}$$

The first term in this expression clearly is the same as in the charge balance equation 2.41. Effecting the same manipulations on the Lorentz force term in the vorticity equation yields

$$mn(\nabla \times (\frac{\mathbf{J} \times \mathbf{B}}{mn})) \cdot \frac{\mathbf{B}}{B^2} \approx \nabla \cdot \mathbf{J}_{||} - \frac{\nabla_\perp n \cdot \mathbf{J}_\perp}{n}. \tag{A.4}$$

In this derivation, the low $\beta$ approximation has again been made to neglect a term involving $\nabla \times \mathbf{B}$. In addition, the charge balance equation itself has been

used to rewrite $-\nabla \cdot \mathbf{J}_{||} = \nabla \cdot \mathbf{J}_{\perp}$. The first term in expression A.4 appears in charge balance equation 2.41 as well. Hence, somewhat surprisingly, it is the Lorentz force term in the vorticity equation that corresponds to the parallel current divergence in the charge balance equation.

## A.2  Diamagnetic kinetic energy equations

The total, mean-field and turbulent diamagnetic kinetic energies are defined as

$$E_* \triangleq \frac{m\mathbf{V}_{*,i}^2}{2}, \quad E_{*,m} \triangleq \frac{m\tilde{\mathbf{V}}_{*,i}^2}{2}, \quad \bar{n}k_* \triangleq \frac{m\overline{n\mathbf{V}_{*,i}''^2}}{2}. \tag{A.5}$$

In analogy to equations 3.8 and 3.19, a transport relation for the total kinetic energy in the diamagnetic drift velocity can be obtained as

$$-\frac{\nabla_{\perp}p_{\mathrm{i}}}{en} \cdot (\mathbf{J}_{p,*} + \mathbf{J}_{p,\Pi} + \mathbf{J}_{p,||}) = \mathbf{U}_{*,i} \cdot \left( \frac{\partial}{\partial t}mn\mathbf{U}_{*,i} + \nabla \cdot mn\mathbf{V}_C\mathbf{U}_{*,i} \right)$$

$$+\mathbf{U}_{*,i} \cdot \left( \frac{D\mathbf{b}}{Dt} \times mn\mathbf{V}_{||} + \nabla \cdot \Pi \times \mathbf{b} - \mathbf{S}_m \times \mathbf{b} \right)$$

$$= \frac{\partial nE_*}{\partial t} + \nabla \cdot (nE_*\mathbf{V}_C + \Pi \cdot \mathbf{V}_{*,i}) - \Pi : \nabla \mathbf{V}_{*,i}^T$$

$$+mnV_{||}\frac{D\mathbf{b}}{Dt} \cdot \mathbf{V}_{*,i} + E_*S_{n,i} - \mathbf{S}_m \cdot \mathbf{V}_{*,i}. \tag{A.6}$$

The LHS of this expression can be written as

$$-\frac{\nabla_{\perp}p_{\mathrm{i}}}{en} \cdot (\mathbf{J}_{p,*} + \mathbf{J}_{p,\Pi} + \mathbf{J}_{p,||}) = -\nabla_{\perp}p_{\mathrm{i}} \cdot (\mathbf{V}_{p,*} + \mathbf{V}_{p,\Pi} + \mathbf{V}_{p,||}). \tag{A.7}$$

Combining the previous two equations readily yields the total diamagnetic kinetic energy equation as

$$\frac{\partial nE_*}{\partial t} + \nabla \cdot (nE_*\mathbf{V}_C + \Pi \cdot \mathbf{V}_{*,i}) = -\nabla_{\perp}p_{\mathrm{i}} \cdot (\mathbf{V}_{p,*} + \mathbf{V}_{p,\Pi} + \mathbf{V}_{p,||})$$

$$+\Pi : \nabla \mathbf{V}_{*,i}^T - mnV_{||}\frac{D\mathbf{b}}{Dt} \cdot \mathbf{V}_{*,i} - E_*S_{n,i} + \mathbf{S}_m \cdot \mathbf{V}_{*,i}. \tag{A.8}$$

In analogy to equations 3.12 and A.6, an equation for the mean-field kinetic energy in the diamagnetic drift velocity can be written as

$$\frac{\partial \bar{n} E_{*,m}}{\partial t} + \nabla \cdot (\bar{n} E_{*,m} \tilde{\mathbf{V}}_C + m \overline{n \mathbf{V}''_C \mathbf{V}''_{*,i}} \cdot \tilde{\mathbf{V}}_{*,i} + \bar{\Pi} \cdot \tilde{\mathbf{V}}_{*,i})$$

$$= -\nabla_\perp \bar{p}_i \cdot (\tilde{\mathbf{V}}_{p,*} + \tilde{\mathbf{V}}_{p,\Pi} + \tilde{\mathbf{V}}_{p,||}) + m \overline{n \mathbf{V}''_C \mathbf{V}''_{*,i}} : \nabla \tilde{\mathbf{V}}^T_{*,i}$$

$$+ \bar{\Pi} : \nabla \tilde{\mathbf{V}}^T_{*,i} - \overline{mnV_{||} \frac{D\mathbf{b}}{Dt}} \cdot \tilde{\mathbf{V}}_{*,i} - E_{*,m} \bar{S}_{n_i} + \bar{\mathbf{S}}_m \cdot \tilde{\mathbf{V}}_{*,i} \qquad (A.9)$$

Taking the difference between the average of equation A.13 and equation A.14, an equation for the turbulent diamagnetic kinetic energy is obtained:

$$\frac{\partial \bar{n} k_*}{\partial t} + \nabla \cdot (\bar{n} k_* \tilde{\mathbf{V}}_C + \frac{\overline{m n \mathbf{V}''^2_{*,i} \mathbf{V}''_C}}{2} + \overline{\Pi \cdot \mathbf{V}''_{*,i}})$$

$$= -\overline{\nabla_\perp p_i \cdot (\mathbf{V}''_{p,*} + \mathbf{V}''_{p,\Pi} + \mathbf{V}''_{p,||})} - \overline{m n \mathbf{V}''_C \mathbf{V}''_{*,i}} : \nabla \tilde{\mathbf{V}}^T_{*,i} + \overline{\Pi : \nabla \mathbf{V}''^T_{*,i}}$$

$$- \frac{\overline{m S_{n_i} \mathbf{V}''^2_{*,i}}}{2} - \overline{mnV_{||} \frac{D\mathbf{b}}{Dt} \cdot \mathbf{V}''_{*,i}} - m \tilde{\mathbf{V}}_{*,i} \cdot \overline{\mathbf{V}''_{*,i} S_{n_i}} + \overline{\mathbf{S}_m \cdot \mathbf{V}''_{*,i}} (A.10)$$

## A.3  Mixed kinetic energy equations

Decomposing the total perpendicular kinetic energy as

$$E_{k,\perp} \triangleq \frac{m \mathbf{V}^2_{0,\perp}}{2} = \frac{m(\mathbf{V}_E + \mathbf{V}_{*,i})^2}{2}$$

$$= \frac{m \mathbf{V}^2_E}{2} + \frac{m \mathbf{V}^2_{*,i}}{2} + m \mathbf{V}_E \cdot \mathbf{V}_{*,i} \triangleq E_E + E_* + E_{\text{mix}}, \qquad (A.11)$$

it is noted that there is a kinetic energy contribution from the "mixed" ExB-ion diamagnetic kinetic energy. We define this mixed kinetic energy as

$$E_{\text{mix}} \triangleq m \mathbf{V}_E \cdot \mathbf{V}_{*,i}, \quad E_{\text{mix},m} \triangleq m \tilde{\mathbf{V}}_E \cdot \tilde{\mathbf{V}}_{*,i}, \quad \bar{n} k_{\text{mix}} \triangleq m \overline{n \mathbf{V}''_E \cdot \mathbf{V}''_{*,i}}. (A.12)$$

Note that these mixed kinetic energies can be negative when $\mathbf{V}_E$ and $\mathbf{V}_{*,i}$ are counter-aligned. According to equation A.11, an equation for the total mixed kinetic energy can be calculated as the difference between equation 3.10 and

equations 3.22 and A.8. Likewise, an equation for the mean-field mixed kinetic energy is obtained from the difference between 3.14 and equations 3.23 and A.9, and for the turbulent mixed kinetic energy from the difference between 3.15 and equations 3.24 and A.10. This then yields

$$\frac{\partial n E_{\text{mix}}}{\partial t} + \nabla \cdot n E_{\text{mix}} \mathbf{V}_C = -\nabla_\perp p_{\text{i}} \cdot \mathbf{V}_{p,E} - \nabla \phi \cdot \mathbf{J}_{p,*} - E_{\text{mix}} S_{n_{\text{i}}}. \quad \text{(A.13)}$$

$$\frac{\partial \bar{n} E_{\text{mix},m}}{\partial t} + \nabla \cdot (\bar{n} E_{\text{mix},m} \mathbf{V}_C + m \overline{\mathbf{V}_C'' \mathbf{V}_E''} \cdot \tilde{\mathbf{V}}_{*,i}$$

$$+ m \overline{\mathbf{V}_C'' \mathbf{V}_{*,i}''} \cdot \tilde{\mathbf{V}}_E) = -\nabla_\perp \bar{p}_i \cdot \tilde{\mathbf{V}}_{p,E} - \nabla \bar{\phi} \cdot \bar{\mathbf{J}}_{p,*} - E_{\text{mix},m} \bar{S}_{n_{\text{i}}}$$

$$+ m \overline{\bar{n} \mathbf{V}_C'' \mathbf{V}_E''} : \nabla \tilde{\mathbf{V}}_{*,i}^T + m \overline{\bar{n} \mathbf{V}_C'' \mathbf{V}_{*,i}''} : \nabla \tilde{\mathbf{V}}_E^T - e \tilde{\mathbf{V}}_{p,*} \cdot \overline{n' \nabla \phi'}. \quad \text{(A.14)}$$

$$\frac{\partial \bar{n} k_{\text{mix}}}{\partial t} + \nabla \cdot (\bar{n} k_{\text{mix}} \tilde{\mathbf{V}}_C + m \overline{\bar{n} \mathbf{V}_E'' \cdot \mathbf{V}_{*,i}'' \mathbf{V}_C''}) = -\overline{\nabla_\perp p_{\text{i}} \cdot \mathbf{V}_{p,E}''}$$

$$- \overline{\nabla \phi' \cdot \mathbf{J}_{p,*}'} - m \overline{S_{n_{\text{i}}} \mathbf{V}_E'' \cdot \mathbf{V}_{*,i}''} - m \tilde{\mathbf{V}}_E \cdot \overline{\mathbf{V}_{*,i}'' S_{n_{\text{i}}}} - m \tilde{\mathbf{V}}_{*,i} \cdot \overline{\mathbf{V}_E'' S_{n_{\text{i}}}}$$

$$- m \overline{\bar{n} \mathbf{V}_C'' \mathbf{V}_E''} : \nabla \tilde{\mathbf{V}}_{*,i}^T - m \overline{\bar{n} \mathbf{V}_C'' \mathbf{V}_{*,i}''} : \nabla \tilde{\mathbf{V}}_E^T + e \tilde{\mathbf{V}}_{p,*} \cdot \overline{n' \nabla \phi'}. \quad \text{(A.15)}$$

## A.4   Energetic couplings

The sources and sinks in the RHS of equations to 3.22-3.24, A.8-A.10 and A.13-A.15 again represent the energetic couplings between the different energy equations. Firstly, this shows that the interchange and DW terms really transfer energy with the ExB kinetic energy only, and not with the other perpendicular kinetic energy contributions. The viscous stresses on the other hand, transfer energy between the ion thermal energy (equation 2.68) and the ExB-only and diamagnetic kinetic energy individually, acting on the respective velocities of the latter. The kinetic energy source due to momentum sources and the $D\mathbf{b}/Dt$ terms are likewise split between both forms of kinetic energy. The kinetic energy source due to the particle source acts independently on all three kinds of kinetic energy.

In addition, the pressure work on the polarisation velocity exchanges energy between the ion thermal energy and $E_*$ and $E_{\text{mix}}$ separately. Thus, it can be

seen that, somewhat surprisingly, the diamagnetic kinetic energy equation is not directly coupled to the other perpendicular kinetic energy equations at all. Then, the $\nabla\phi \cdot \mathbf{J}_{p,*}$ term exchanges energy between $E_{\mathrm{E}}$ and $E_{\mathrm{mix}}$. Thus, the latter "mixed" form of kinetic energy exchanges energy with the ion thermal energy and the ExB kinetic energy.

Lastly, the various forms of the Reynolds stress and Favre terms exchange energy between the mean-field kinetic energy equation and the corresponding turbulent kinetic energy equation.

# Appendix B

# Derivation of TOKAM2D equations and equations for the kinetic energy and enstrophy

This appendix[1] first derives the equations solved by the TOKAM2D code, and discusses the setup of simulations with this code. Then, the kinetic energy and enstrophy equations for the TOKAM2D code are derived. Equations will be derived both for the total quantities containing contributions from both the E×B drift and the ion diamagnetic drift, and for the E×B only quantities. The methodology to derive these equations for TOKAM2D is broadly similar to that used for the general case in chapter 3.

Section B.1 first derives the equations of the TOKAM2D code and discusses the TOKAM2D setup. Then, section B.2 derives kinetic energy equations for TOKAM2D, after which section B.3 derives the enstrophy equations.

---

[1]Parts of this appendix have been published in "Coosemans, R., Dekeyser, W., Baelmans, M. (2021). Turbulent kinetic energy in 2D isothermal interchange-dominated scrape-off layer E×B drift turbulence: Governing equation and relation to particle transport. *Physics of Plasmas*, 28:012302" [46] and in "Coosemans, R., Dekeyser, W., Baelmans, M. (2020). A new mean-field plasma edge transport model based on turbulent kinetic energy and enstrophy. *Contributions to Plasma Physics*, 60:e201900156" [44].

# B.1   TOKAM2D setup and equations

Section 2.2 has presented the equations commonly used to describe the instantaneous dynamics of plasma edge turbulence. These equations will be simplified to the case of 2D interchange-dominated electrostatic E×B drift turbulence in a sheath-limited SOL. This yields the equation set that is solved in the TOKAM2D turbulence code described in detail in Refs. [109, 116, 141]. TOKAM2D will be used to obtain detailed reference data for the turbulence in chapters 4-6.

TOKAM2D considers a collection of flux tubes in the SOL connecting two plasma sheaths. A flute approximation is made to neglect fluctuations along the parallel direction and an infinite conductivity is assumed such that plasma quantities are constant in this direction. Under these assumptions, the geometry reduces from 3D to 2D. Formally, the TOKAM2D equations are derived by averaging over the uniform parallel direction of these flux tubes. The fluxes out of this flux tube in the parallel direction are incorporated as artificial volumetric sinks on the right-hand side of the equations. The form of these sinks is inspired by Bohm-like sheath conditions. The above assumptions effectively imply a sheath-limited regime. The TOKAM2D equations are expected to be representative for dynamics around the outer midplane (OMP) region under such a sheath-limited regime.

We briefly derive the equation set used by the TOKAM2D turbulence code to describe this case. TOKAM2D considers a rectangular 2D domain, which is shown in figure 4.1. $x$ is the radial direction and $y$ is the diamagnetic direction perpendicular to $x$ and to the magnetic field direction $\mathbf{b}$, such that the three form a right handed coordinate system. Hence, $y$ points in the electron diamagnetic direction. The direction along $\mathbf{b}$ is assumed to be uniform and is not resolved. In TOKAM2D, the magnetic field is assumed to be constant in time and uniform in space (except for magnetic field gradients in the $\nabla \cdot \mathbf{J}_*$ term in the charge balance equation which act as effective gravity). In order to ease notation, we change the definitions of $\mathbf{V}_E$, $\mathbf{V}_{*,i}$, $\mathbf{U}$, $\mathbf{U}_0$ and $W$ as follows

$$\mathbf{V}_E \triangleq \mathbf{b} \times \nabla \phi, \qquad \mathbf{V}_{*,i} \triangleq \mathbf{b} \times \frac{\nabla p_{\mathrm{i}}}{n}, \qquad \mathbf{U} \triangleq -\mathbf{b} \times \mathbf{V}, \tag{B.1}$$

$$\mathbf{U}_0 = \nabla_\perp \phi + \frac{\nabla_\perp p_{\mathrm{i}}}{n}, \quad W \triangleq \nabla \cdot \mathbf{U}_0 = \nabla_\perp^2 \phi + \nabla \cdot \left( \frac{\nabla_\perp p_i}{n} \right), \tag{B.2}$$

hence excluding the magnetic field from these definitions. Note that in this 2D case with a constant magnetic field, the pseudo-vorticty $W$ and (the parallel component of) the real vorticity are equivalent, see equation 2.48.

The electron continuity equation 2.26, ion thermal energy equation 2.31 and electron thermal energy equation 2.32 can be rewritten as

$$\frac{\partial n}{\partial t} + \frac{\mathbf{V}_E}{B} \cdot \nabla n - D_0 \nabla_\perp^2 n = S_n - \nabla \cdot (n\mathbf{V}_{e,||}), \text{ (B.3)}$$

$$\frac{3}{2}\frac{\partial p_i}{\partial t} + \frac{3}{2}\frac{\mathbf{V}_E}{B} \cdot \nabla p_i - \frac{3}{2}\chi_0 \nabla_\perp^2 p_i = \frac{3}{2}S_{p_i} - \nabla \cdot (\frac{5}{2}p_i \mathbf{V}_{||} + \mathbf{q}_{i,||}) - Q_{ei}, \text{ (B.4)}$$

$$\frac{3}{2}\frac{\partial p_e}{\partial t} + \frac{3}{2}\frac{\mathbf{V}_E}{B} \cdot \nabla p_e - \frac{3}{2}\chi_0 \nabla_\perp^2 p_e = \frac{3}{2}S_{p_e} - \nabla \cdot (\frac{3}{2}p_e \mathbf{V}_{e,||} + \mathbf{q}_{e,||}) + Q_{ei}. \text{(B.5)}$$

Here, it has been assumed that only the E×B velocity and the parallel velocities are relevant for the density and thermal energy convection, i.e. $\mathbf{V}_C \triangleq \mathbf{V}_{||} + \mathbf{V}_E$ and that the perpendicular classical particle and heat fluxes can be modelled using simple diffusion models with $D_0$ and $\chi_0$ as constant transport coefficients. These diffusion terms are required for numerical stability as they stop the direct cascade to length scales smaller than the gyro-radius, which would be unphysical in a drift-reduced fluid approach. The divergence of the E×B drift $\nabla \cdot \mathbf{V}_E$ vanishes exactly (see equation 3.29) in the TOKAM2D code since the magnetic field strength is assumed to be uniform over the whole domain. Furthermore, since a flux tube with no gradients along the parallel direction is considered, the pressure work on the parallel velocity $\nabla p \cdot \mathbf{V}_{||}$ vanishes. Viscous heating of the ions and the resistive heating of the electrons is neglected.

Note that the divergences of the parallel heat and particle fluxes are retained. These terms represent the flow of particles and thermal energy out of the flux tube at the parallel ends of it. In the SOL, the flux tube ends at a material surface where a very thin plasma sheath forms. Such plasma-wall interactions are described in detail in Ref. [153] for example. The behaviour of the sheath can be described by Bohm conditions. The flux of ions and electrons, ion and electron heat and the current at the entrance of the plasma sheath are the following:

$$\Gamma_{sheath,i} = nc_s, \tag{B.6}$$

$$\Gamma_{sheath,e} = nc_s \exp(\Lambda - \phi/T_e), \tag{B.7}$$

$$q_{sheath,i} = \gamma_i p_i c_s, \tag{B.8}$$

$$\mathbf{q}_{sheath,e} = \gamma_e p_e c_s \exp(\Lambda - \phi/T_e), \tag{B.9}$$

$$J_{sheath} = en c_s(1 - \exp(\Lambda - \phi/T_e)). \tag{B.10}$$

In these expressions $\Lambda = \frac{1}{2}\ln(\frac{m_i}{2\pi m_e})$ [116] is the sheath potential drop and $\gamma_i$ and $\gamma_e$ are sheath heat transmission coefficients that can further be calculated, see for example Refs. [116, 153]. These relations are used to model the parallel flux divergences as

$$\nabla \cdot n\mathbf{V}_{||} \approx \frac{\Gamma_{sheath}}{L_{||}}, \quad \nabla \cdot \mathbf{J}_{||} \approx \frac{J_{sheath}}{L_{||}}, \quad \nabla \cdot (\frac{5}{2}p\mathbf{V}_{||}+\mathbf{q}_{||}) \approx \frac{q_{sheath}}{L_{||}}. \quad \text{(B.11)}$$

In these relations, $L_{||}$ is half the connection length, the distance along the field line between the intersections with the solid surface, i.e. the parallel length of the flux tube considered here. Then, the ion-electron heat transfer is modelled as $Q_{ei} = \frac{3m_e}{m_i}\frac{p_i - p_e}{\tau_{ei}}$, with $\tau_{ei}$ the ion-electron collision time. Filling out these models, the equations become

$$\frac{\partial n}{\partial t} + \frac{\mathbf{V}_E}{B} \cdot \nabla n - D_0 \nabla_\perp^2 n = S_n - \frac{nc_s}{L_{||}} \exp(\Lambda - \frac{\phi}{T_e}), \quad \text{(B.12)}$$

$$\frac{\partial p_i}{\partial t} + \frac{\mathbf{V}_E}{B} \cdot \nabla p_i - \chi_0 \nabla_\perp^2 p_i = S_{p_i} - \frac{2\gamma_i p_i c_s}{3L_{||}} - \frac{2m_e}{m_i}\frac{p_i - p_e}{\tau_{ei}}, \quad \text{(B.13)}$$

$$\frac{\partial p_e}{\partial t} + \frac{\mathbf{V}_E}{B} \cdot \nabla p_e - \chi_0 \nabla_\perp^2 p_e$$

$$= S_{p_e} - \frac{2\gamma_e p_e c_s}{3L_{||}} \exp(\Lambda - \frac{\phi}{T_e}) + \frac{2m_e}{m_i}\frac{p_i - p_e}{\tau_{ei}}. \quad \text{(B.14)}$$

Next, we consider the charge balance equation which provides an equation for the electrostatic potential $\phi$. The vorticity equation 2.53, is reduced to

$$\frac{mn}{B^2}\frac{\partial W}{\partial t} + \frac{mn}{B^2}\mathbf{V}_E \cdot \nabla W = \nabla \cdot \mathbf{J}_{||} + \nabla \cdot \mathbf{J}_* + \nabla \cdot \mathbf{J}_{p,\Pi} + S_{W,cor}, \quad \text{(B.15)}$$

$$S_{W,cor} = e\nabla n \cdot \mathbf{V}_{p,0} - \frac{mn}{B^2}\nabla \mathbf{V}_E : \nabla \mathbf{U}_0 - \frac{mn}{B^2}\mathbf{U}_0 \cdot \nabla \frac{S_{n_i}}{n} - \frac{m}{B^2}S_{n_i}W. \quad \text{(B.16)}$$

As in the continuity and thermal energy equations, the velocity important for convection is assumed to be $\mathbf{V}_C \triangleq \mathbf{V}_E + \mathbf{V}_{||}$. Note that the perpendicular component of this velocity is now different from the velocity used for the inertia, i.e. $\mathbf{V}_C \neq \mathbf{V}_{0,\perp}$. Parallel gradients have again been dropped in this equation. Since the magnetic field is assumed to be constant in time and uniform in space, all derivatives of the magnetic field also vanish.

In TOKAM2D, $S_{W,cor}$ is also neglected. The first one of these terms is dropped by the commonly made Boussinesq approximation [74, 132, 141, 170]. The

second term can be shown to be zero when the diamagnetic drift contribution to $\mathbf{U}_0$ is neglected, as will be the case in the next sections of this chapter. Since neutrals are not treated in TOKAM2D, the only particle source is an imposed source close the domain boundary, a region which will be excluded from the analysis in this thesis. Hence, neglecting the particle source terms can be justified.

Next, we will discuss the treatment of the different current divergence terms on the RHS of equation B.15 separately. The divergence of the parallel current is treated like the divergence of the parallel heat and particle fluxes. Using expression B.11, it is modelled as

$$\nabla \cdot \mathbf{J}_{||} \approx \frac{enc_s}{L_{||}}(1 - \exp(\Lambda - \frac{\phi}{T_e})) \tag{B.17}$$

Then, with the help of some vector algebra the diamagnetic current divergence in equation B.15 is written as

$$\nabla \cdot \mathbf{J}_* \triangleq \nabla \cdot (\mathbf{B} \times \frac{\nabla p}{B^2}) \approx \frac{\mathbf{b}}{B} \cdot (\nabla \ln(B^2) \times \nabla p) = -\frac{g}{B}\frac{\partial p}{\partial y}. \tag{B.18}$$

In this derivation, a term $(\nabla \times \mathbf{B}) \cdot \nabla p/B^2$ is neglected through the low $\beta$ approximation (see section 2.2.2). In the last step, the magnetic field strength is assumed to vary in the radial $x$-direction only, and the magnetic field gradient is written as $g = -\partial \ln(B^2)/\partial x$. Note that spatial variations of the magnetic field are retained in this term specifically in TOKAM2D in order to be able to represent the important interchange drive for the turbulence. Moreover, the parameter $g$ is to be interpreted as the average magnetic field curvature along the parallel extent of the flux tube.

Finally, the contribution of viscous stresses and momentum sources to the polarisation current $\mathbf{J}_{p,\Pi} \triangleq (-\nabla \cdot \Pi + \mathbf{S}_m) \times \mathbf{b}/B$ is approximated as

$$\nabla \cdot \mathbf{J}_{p,\Pi} = -\nabla \cdot (\frac{\nabla \cdot \Pi}{B} \times \mathbf{b}) = \frac{m\nu_0}{B^2}n\nabla_\perp^2 W. \tag{B.19}$$

Next to its physical meaning of viscous dissipation, this term is likewise required for numerical stability of the TOKAM2D code.

Filling out expressions B.17, B.18 and B.19 in equation B.15 and neglecting $S_{W,cor}$ as is done in TOKAM2D, we obtain

$$\frac{mn}{B^2}\left(\frac{\partial W}{\partial t} + \mathbf{V}_E \cdot \nabla W\right) - \frac{m}{B^2}\nu_0 n \nabla_\perp^2 W$$

$$= -\frac{g}{B}\frac{\partial p}{\partial y} + \frac{enc_s}{L_{||}}\left(1 - \exp(\Lambda - \frac{\phi}{T_e})\right). \tag{B.20}$$

Finally, equations B.12, B.13, B.14 and B.20 are normalised with the ion mass $m$, reference ion gyro-frequency $\Omega_0 = eB_0/m$ and reference gyro-radius $\rho_0 = c_{s,0}\Omega_0$, with $B_0$ the reference magnetic field strength, $c_{s,0} = \sqrt{T_0/m_i}$ the reference sound speed and $T_0$ the reference temperature. The density is normalised to the reference density $n_0$. Note that the reference temperatures are defined in energy units of [J] or equivalently [eV]. This normalisation procedure is illustrated for typical tokamak SOL conditions in appendix C. Note that for clarity of notation, we choose to keep using the same symbols after the normalisation. In the remainder of this appendix and in chapters 4-6, the plasma quantities are all normalised, unless explicitly stated otherwise. This yields the full equation set as

$$\frac{\partial n}{\partial t} + \mathbf{V}_E \cdot \nabla n - D_0 \nabla_\perp^2 n = S_n - \frac{nc_s}{L_{||}}\exp(\Lambda - \frac{\phi}{T_e})$$

$$+ K_{DW}[(\phi - T_e \ln n - 1.71T_e) - \langle \phi - T_e \ln n - 1.71T_e \rangle_y], \tag{B.21}$$

$$\frac{\partial W}{\partial t} + \mathbf{V}_E \cdot \nabla W - \nu_0 \nabla_\perp^2 W = -\frac{g}{n}\frac{\partial p}{\partial y} + \frac{c_s}{L_{||}}\left(1 - \exp(\Lambda - \frac{\phi}{T_e})\right)$$

$$+ K_{DW}[(\phi - T_e \ln n - 1.71T_e) - \langle \phi - T_e \ln n - 1.71T_e \rangle_y], \tag{B.22}$$

$$\frac{\partial p_i}{\partial t} + \mathbf{V}_E \cdot \nabla p_i - \chi_0 \nabla_\perp^2 p_i = S_{p_i} - \frac{2m_e}{m_i}\frac{p_i - p_e}{\tau_{ei}} - \frac{2}{3}\frac{\gamma_i p_i c_s}{L_{||}}, \tag{B.23}$$

$$\frac{\partial p_e}{\partial t} + \mathbf{V}_E \cdot \nabla p_e - \chi_0 \nabla_\perp^2 p_e$$

$$= S_{p_e} + \frac{2m_e}{m_i}\frac{p_i - p_e}{\tau_{ei}} - \frac{2}{3}\frac{\gamma_e p_e c_s}{L_{||}}\exp(\Lambda - \frac{\phi}{T_e})$$

$$+ \frac{2}{3}K_{DW}\phi[(\phi - T_e \ln n - 1.71T_e) - \langle \phi - T_e \ln n - 1.71T_e \rangle_y], \tag{B.24}$$

$$W \triangleq \nabla_\perp^2 \phi + \nabla \cdot \frac{\nabla_\perp p_i}{n}, \qquad \mathbf{V}_E \triangleq \mathbf{b} \times \nabla \phi. \tag{B.25}$$

Note that charge balance equation B.20 is divided by the density $n$ to obtain equation B.22. In addition, the last terms in equations B.21, B.22 and B.24 were added to to the equations. These terms induce DW-like dynamics in the simulations and are only active in the core region where they replace the penultimate terms in equations B.21, B.22 and B.24 representing the losses to the sheath in the SOL. The physics and the derivation of these DW-like terms are discussed in section 5.1.1. This is then the set of equations that is solved by the TOKAM2D turbulence code.

Various options are implemented for turning on or off certain physical effects in equations B.21-B.25 if desired. The terms in black are always active in the SOL. The basic isothermal SOL-only case studied in chapter 4 considers just this minimal set. In section 5.1, a core region is added in which the terms in blue replace the penultimate terms in equations B.22, B.22 and B.22 which are used in the SOL. Section 5.2 then considers the effect of the total vorticity by adding the diamagnetic contribution to the pseudo-vorticity in green to the basic model in black (DW-like terms in blue are no longer active). The anisothermal SOL only case is studied in chapter 6, for which the thermal energy equations in red are added to the basic equations in black. (The terms in blue and green are not actived in this case.) Finally, the term in purple is only active in the core region in the anisothermal case. This situation is not studied in this thesis.

TOKAM2D solves (a subset of) equations B.21-B.25 for a Cartesian $x, y$-coordinate system representing the plane perpendicular to the magnetic field. In this thesis the finite volume version of the TOKAM2D code [109, 116] is used. Periodic boundary conditions are used on diamagnetic ($y$) boundaries, while Neumann boundary conditions are applied on radial ($x$) boundaries such that there is no radial flux of any quantity at the radial boundaries of the domain.[2] In addition, fringe regions are applied near the radial boundaries of the domain to drive fluctuations in the $y$-direction to zero in those regions. The particle source $S_n$ has a Gaussian profile in the $x$-direction and is constant both in the $y$-direction and in time. Ion and electron thermal energy sources $S_{p_i}$ and $S_{p_e}$ are applied that have the same shape as the particle source, they are determined as $S_{p,i/e} = T_{inj,i/e} S_n$, with $T_{inj,i}$ and $T_{inj,e}$ user defined simulation parameters determining the thermal energy of the injected ion and electrons. In the simulations performed for this thesis, the particle source is situated towards the inner boundary of the domain. More details regarding the TOKAM2D simulation parameters used in the various sets of simulations reported here can be found in appendix D. Figure 4.1 shows a sketch of the different regions in the TOKAM2D computational domain.

_____

[2]Particles and thermal energy enter the domain through the sources instead.

## B.2   TOKAM2D kinetic energy equations

The TOKAM2D vorticity equation 4.2 together with the definition for the
TOKAM2D vorticity 4.3 effectively implies that the LHS of the charge balance
equation represents

$$\frac{\partial W}{\partial t} + \mathbf{V}_E \cdot \nabla W = \frac{D}{Dt} \nabla \cdot \mathbf{U}_0 \tag{B.26}$$

as an approximation for the divergence of the inertial contribution to the
polarisation velocity $-\nabla \cdot \mathbf{V}_{p,0}$. The velocities contributing to this inertia are
now assumed to be the E×B drift and the ion diamagnetic drift, i.e.

$$\mathbf{U}_0 = \mathbf{V}_0 \times \mathbf{b} = (\mathbf{V}_E + \mathbf{V}_{*,i}) \times \mathbf{b} = \nabla_\perp \phi + \nabla_\perp p_i / n. \tag{B.27}$$

However, note that the contribution from the diamagnetic velocity to convection
is not taken into account, i.e. $\mathbf{V}_C = \mathbf{V}_E$.

Given these contributions to the inertia, the total (in the sense of including
E×B and diamagnetic velocity) perpendicular kinetic energies have been defined
in equations 5.19-5.19 as:

$$E_{E*} = \frac{\mathbf{V}_0^2}{2}, \qquad E_{m,E*} = \frac{\tilde{\mathbf{V}}_0}{2}, \qquad \bar{n}k_{E*} \overline{\frac{n\mathbf{V}_0''^2}{2}}. \tag{B.28}$$

Since these may be expected to be more directly related to the E×B turbulent
fluxes that need to be modelled, the TOKAM2D E×B-only kinetic energies
have been defined in equation 5.30 as:

$$E_{\mathrm{E}} = \frac{\mathbf{V}_E^2}{2}, \quad E_{\mathrm{E},m} = \frac{\tilde{\mathbf{V}}_E^2}{2}, \quad \bar{n}k_E = \overline{\frac{n\mathbf{V}_E''^2}{2}}. \tag{B.29}$$

Section B.2.1 will first derive equations for the total perpendicular kinetic
energies, after which section B.2.2 will derive equations for the E×B-only
kinetic energies.

## B.2.1   TOKAM2D total kinetic energy equations

### Derivation of $E_{E*}$ equation

The procedure to derive transport equations for the total perpendicular kinetic energy is similar to that followed for the general case in section 3.2.1.

To derive transport equations for these quantities, we again start from the TOKAM2D vorticity equation 4.2. The LHS of this equation 4.2 is now equal to

$$\frac{DW}{Dt} = \frac{D}{Dt}\nabla \cdot \mathbf{U}_0 = -\nabla \cdot \mathbf{V}_{p,0} - \nabla\mathbf{V}_E : \nabla\mathbf{U}_0, \tag{B.30}$$

where we defined the inertial contribution to the TOKAM2D polarisation current as

$$\mathbf{V}_{p,0} = \frac{\mathbf{J}_{p,0}}{n} = -\frac{D\mathbf{U}_0}{Dt}. \tag{B.31}$$

Note that the second term in expression B.30 has been neglected in the derivation of the TOKAM2D vorticity equation in equation B.15 in section 4.1. Multiplying the expression by $n\phi$ and rewriting, we get

$$n\phi\frac{DW}{Dt} = -\nabla \cdot \phi\mathbf{J}_{p,0} + \nabla\phi \cdot \mathbf{J}_{p,0} + \phi\nabla n \cdot \mathbf{V}_{p,0} - n\phi\nabla\mathbf{V}_E : \nabla\mathbf{U}_0. \tag{B.32}$$

In this expression, the second term in the RHS is to be associated with the kinetic energy. However, the diamagnetic contribution is not yet fully included. To this end, $\nabla p_{\mathrm{i}} \cdot \mathbf{V}_{p,0}$ is added to both sides, to obtain

$$n\phi\frac{DW}{Dt} + \nabla p_i \cdot \mathbf{V}_{p,0}$$

$$= -\nabla \cdot \phi\mathbf{J}_{p,0} - n\frac{DE_{E*}}{Dt} + \phi\nabla n \cdot \mathbf{V}_{p,0} - n\phi\nabla\mathbf{V}_E : \nabla\mathbf{U}_0. \tag{B.33}$$

Rewriting the kinetic energy term in the conservative form (using continuity equation B.21) and filling out the RHS of TOKAM2D vorticty equation 4.2 in the first term on the LHS, the total kinetic energy equation is obtained:

$$\frac{\partial n E_{E*}}{\partial t} + \nabla \cdot \Gamma_{E_{E*}}$$

$$= g\phi \frac{\partial p}{\partial y} - \frac{c_s n \phi}{L_{||}} (1 - \exp(\Lambda - \frac{\phi}{T_e})) - \nu n \phi \nabla_\perp^2 W + S_{E_{E*},n}$$

$$- \nabla p_i \cdot \mathbf{V}_{p,0} + \phi \nabla n \cdot \mathbf{V}_{p,0} - n \phi \nabla \mathbf{V}_E : \nabla \mathbf{U}_0, \qquad \text{(B.34)}$$

$$\Gamma_{E_{E*}} = n E_{k,\perp} \mathbf{V}_E + \phi \mathbf{J}_{p,0}, \qquad \text{(B.35)}$$

$$S_{E_{E*},n} = E_{E*} S_n + D_0 E_{E*} \nabla_\perp^2 n - \frac{E_{E*} c_s n}{L_{||}} \exp(\Lambda - \frac{\phi}{T_e}). \qquad \text{(B.36)}$$

### Derivation of $E_{m,E*}$ and $k_{E*}$ equations

In order to arrive at equations for $E_{m,E*}$ and $k_{E*}$, the $E_{E*}$ equation B.34 should be split in a contribution due to mean flows and a contribution due to fluctuations.

We obtain an expression for the time rate of change of $E_{m,E*}$ by taking the scalar product of the inertial part of the average polarisation current $\bar{\mathbf{J}}_{p,0}$ with $\widetilde{\nabla}\phi + \nabla \bar{p}_i / \bar{n}$ and then using the averaged continuity equation 4.5 to rewrite:

$$\frac{\partial}{\partial t} \bar{n} E_{m,E*} + \nabla \cdot (\bar{n} E_{m,E*} \tilde{\mathbf{V}}_E + \overline{n \mathbf{V}_E'' \mathbf{V}_0''} \cdot \tilde{\mathbf{V}}_0)$$

$$= -\left( \widetilde{\nabla}\phi + \frac{\nabla \bar{p}_i}{\bar{n}} \right) \cdot \bar{\mathbf{J}}_{p,0} + \overline{n \mathbf{V}_E'' \mathbf{V}_0''} : \nabla \tilde{\mathbf{V}}_0^T + \tilde{\mathbf{V}}_0 \cdot \overline{\mathbf{V}_0'' S_n} + E_{m,E*} \bar{S}_n. \text{ (B.37)}$$

In order to use this expression starting from an averaged charge balance equation $(\nabla \cdot \bar{\mathbf{J}} = 0)$, $\widetilde{\nabla}\phi \cdot \bar{\mathbf{J}}_{p,0}$ is rewritten to include $\overline{nDW/Dt}$:

$$-\widetilde{\nabla}\phi \cdot \bar{\mathbf{J}}_{p,0} = \bar{\phi}\nabla \cdot \bar{\mathbf{J}}_{p,0} - \nabla \cdot (\bar{\phi}\bar{\mathbf{J}}_{p,0}) - \frac{\bar{\mathbf{J}}_{p,0}}{\bar{n}} \cdot \overline{n'\nabla\phi'}$$

$$= -\bar{\phi}n\frac{\overline{DW}}{Dt} - \overline{\bar{\phi}n\nabla\mathbf{V}_E : \nabla\mathbf{U}_0} + \bar{\phi}\overline{\nabla n \cdot \mathbf{V}_{p,0}}$$

$$- \nabla \cdot (\bar{\phi}\bar{\mathbf{J}}_{p,0}) - \tilde{\mathbf{V}}_{p,0} \cdot \overline{n'\nabla\phi'}. \qquad \text{(B.38)}$$

Note that this is more complicated than for the total kinetic energy case in equation B.32 because Favre averages and gradients do not commute. As a

result, an additional "Favre averaging term", which is the last term in B.38, originates.

Filling out equation B.38 in equation B.37, and then filling out the RHS of the vorticity equation 4.2 for $DW/Dt$ leads to the $E_{m,E*}$ equation

$$\frac{\partial}{\partial t}\bar{n}E_{m,E*} + \nabla \cdot \Gamma_{E_{m,E*}} = g\bar{\phi}\frac{\partial \bar{p}}{\partial y} - \frac{\bar{\phi}}{L_{||}}\overline{c_s n(1 - \exp(\Lambda - \frac{\phi}{T_e}))}$$

$$-\nu\bar{\phi}\overline{n\nabla_\perp^2 W} + \overline{n\mathbf{V}_E''\mathbf{V}_0''} : \nabla\tilde{\mathbf{V}}_0^T - \overline{n'\nabla\phi'} \cdot \tilde{\mathbf{V}}_{p,0} + S_{E_{m,E*},n}$$

$$-\nabla_\perp \bar{p}_i \cdot \tilde{\mathbf{V}}_{p,0} + \bar{\phi}\overline{\nabla n \cdot \mathbf{V}_{p,0}} - \bar{\phi}\bar{n}\nabla\mathbf{V}_E : \nabla\mathbf{U}_0, \qquad \text{(B.39)}$$

$$\Gamma_{E_{m,E*}} = \bar{n}\tilde{\mathbf{V}}_E E_{m,E*} + \overline{n\mathbf{V}_E''\mathbf{V}_0''} \cdot \tilde{\mathbf{V}}_0 + \bar{\phi}\bar{\mathbf{J}}_{p,0}, \qquad \text{(B.40)}$$

$$S_{E_{m,E*},n} = E_{m,E*}\bar{S}_n + \tilde{\mathbf{V}}_0 \cdot \overline{\mathbf{V}_0''S_n}$$

$$+D_0 E_{m,E*}\nabla_\perp^2 \bar{n} + D_0 \tilde{\mathbf{V}}_0 \cdot \overline{\mathbf{V}_0''\nabla_\perp^2 n}$$

$$-\frac{E_{m,E*}}{L_{||}}\overline{c_s n \exp(\Lambda - \frac{\phi}{T_e})} - \overline{c_s n\mathbf{V}_0'' \exp(\Lambda - \frac{\phi}{T_e})} \cdot \frac{\tilde{\mathbf{V}}_0}{L_{||}}. \qquad \text{(B.41)}$$

Taking the difference between the average of the total kinetic energy equation B.34 and the mean-flow kinetic energy equation B.39 yields the turbulent kinetic energy equation:

$$\frac{\partial}{\partial t}\bar{n}k_{E*} + \nabla \cdot \Gamma_{k_{E*}} = g\overline{\phi'\frac{\partial p'}{\partial y}} - \frac{1}{L_{||}}\overline{\phi'c_s n(1 - \exp(\Lambda - \frac{\phi}{T_e}))}$$

$$-\nu\overline{\phi'(n\nabla_\perp^2 W_{TW})'} - \overline{n\mathbf{V}_E''\mathbf{V}_0''} : \nabla\tilde{\mathbf{V}}_0^T + \overline{n'\nabla\phi'} \cdot \tilde{\mathbf{V}}_{p,0} + S_{k_{E*},n}$$

$$-\overline{\nabla p_i \cdot \mathbf{V}_{p,0}''} + \overline{\phi'\nabla n \cdot \mathbf{V}_{p,0}} - \overline{n\phi'\nabla\mathbf{V}_E : \nabla\mathbf{U}_0}, \qquad \text{(B.42)}$$

$$\Gamma_{k_{E*}} = \bar{n}k_{E*}\tilde{\mathbf{V}}_E + \overline{n\mathbf{V}_E''\mathbf{V}_0''^2}/2 + \overline{\phi'\mathbf{J}_{p,0}'}, \qquad \text{(B.43)}$$

$$S_{E_{m,E*},n} = \frac{1}{2}\overline{\mathbf{V}_0''^2 S_n} + \frac{D_0}{2}\overline{\mathbf{V}_0''^2\nabla_\perp^2 n} - \frac{1}{L_{||}}\overline{\frac{n\mathbf{V}_0''^2}{2} \exp(\Lambda - \frac{\phi}{T_e})}. \qquad \text{(B.44)}$$

## B.2.2 TOKAM2D E×B-only kinetic energy equations

### Derivation of $E_{\mathrm{E}}$ equation

The derivation of the E×B-only kinetic energy equations are analogous to those for the total case. However the derivation now proceeds based on the E×B contribution to the polarisation current only instead of the total inertial contribution (which also contains a contribution from the ion diamagnetic drift). We define this E×B-only polarisation current for TOKAM2D as

$$\mathbf{J}_{p,E} = n\mathbf{V}_{p,E} = n\mathbf{b} \times \frac{D\mathbf{V}_E}{Dt} = -n\frac{D\mathbf{U}_E}{Dt}, \tag{B.45}$$

with $\mathbf{U}_E = \mathbf{V}_E \times \mathbf{b} = \nabla_\perp \phi$. To relate this to the TOKAM2D charge balance equation 4.2, we split the total TOKAM2D vorticity into an E×B and a diamagnetic contribution as well (in analogy to equation 3.47):

$$W = W_E + W_* = \nabla_\perp^2 \phi + \nabla \cdot \left( \frac{\nabla_\perp p_{\mathrm{i}}}{n} \right) = \nabla \cdot \mathbf{U}_E + \nabla \cdot \mathbf{U}_{*,i}. \tag{B.46}$$

Thus, we can write that

$$\frac{DW}{Dt} = \frac{D}{Dt}\nabla \cdot \mathbf{U}_E + \frac{DW_*}{Dt} = -\nabla \cdot \mathbf{V}_{p,E} - \nabla\mathbf{V}_E : \nabla\mathbf{U}_E + \frac{DW_*}{Dt}, \tag{B.47}$$

Note that the $\nabla\mathbf{V}_E : \nabla\mathbf{U}_E$ can be shown to be identically zero in the TOKAM2D case. Multiplying the E×B-contribution only with $n\phi$, we now find

$$n\phi\frac{DW_E}{Dt} = -\nabla \cdot \phi\mathbf{J}_{p,E} + \nabla\phi \cdot \mathbf{J}_{p,E} + \phi\nabla n \cdot \mathbf{V}_{p,E}. \tag{B.48}$$

The second term on the RHS of this expression is now exactly the time rate of change of the E×B kinetic energy $nDE_{\mathrm{E}}/Dt$, i.e. no additional term similar to $\nabla p \cdot \mathbf{V}_p$ is required in this case. Hence, the previous equation can be reworked into an E×B-only kinetic energy equation by filling out $DW_E/Dt = DW/Dt - DW_*/Dt$ and filling out the TOKAM2D charge balance equation 4.2

for $DW/Dt$:

$$\frac{\partial}{\partial t} n E_{\mathrm{E}} + \nabla \cdot \Gamma_{E_{\mathrm{E}}} = g\phi \frac{\partial p}{\partial y} - \frac{c_s n \phi}{L_{||}} (1 - \exp(\Lambda - \frac{\phi}{T_e}))$$

$$-\nu n\phi \nabla_\perp^2 W + n\phi \frac{DW_*}{Dt} + S_{E_{\mathrm{E}},n} + \phi \mathbf{V}_{p,E} \cdot \nabla n, \tag{B.49}$$

$$\Gamma_{E_{\mathrm{E}}} = n E_{\mathrm{E}} \mathbf{V}_E + \phi \mathbf{J}_{p,E}, \tag{B.50}$$

$$S_{E_{\mathrm{E}},n} = E_{\mathrm{E}} S_n + E_{\mathrm{E}} D_0 \nabla_\perp^2 n - \frac{E_{\mathrm{E}} c_s n}{L_{||}} \exp(\Lambda - \frac{\phi}{T_e}), \tag{B.51}$$

Note that the continuity equation B.21 was used to get from the advective form to the conservative form of this equation. Remark also that equation B.49 can also be derived by algebraic manipulation of equation B.34, but this derivation is much more tedious.

### Derivation of $E_{\mathrm{E},m}$ and $k_E$ equations

An expression for the time rate of change of $E_{\mathrm{E},m}$ is obtained by taking the scalar product of $\bar{\mathbf{J}}_{p,E}$ with $\widetilde{\nabla}\phi$ and then using the averaged continuity equation 4.5 to rewrite:

$$\frac{\partial}{\partial t} \bar{n} E_{\mathrm{E},m} + \nabla \cdot (\bar{n} E_{\mathrm{E},m} \tilde{\mathbf{V}}_E + \overline{n \mathbf{V}_E'' \mathbf{V}_E''} \cdot \tilde{\mathbf{V}}_E)$$

$$= -\widetilde{\nabla}\phi \cdot \bar{\mathbf{J}}_{p,E} + \overline{n \mathbf{V}_E'' \mathbf{V}_E''} : \nabla \tilde{\mathbf{V}}_E^T + \tilde{\mathbf{V}}_E \cdot \overline{\mathbf{V}_E'' S_n} + E_{\mathrm{E},m} \bar{S}_n. \tag{B.52}$$

A expression equivalent to B.38 can be written to relate $\widetilde{\nabla}\phi \cdot \bar{\mathbf{J}}_{p,E}$ to include $\overline{n DW/Dt}$:

$$-\widetilde{\nabla}\phi \cdot \bar{\mathbf{J}}_{p,E} = -\bar{\phi}\overline{n\frac{DW}{Dt}} + \bar{\phi}\overline{n\frac{DW_*}{Dt}} + \bar{\phi}\overline{\nabla n \cdot \mathbf{V}_{p,E}}$$

$$- \nabla \cdot (\bar{\phi}\bar{\mathbf{J}}_{p,0}) - \tilde{\mathbf{V}}_{p,0} \cdot \overline{n'\nabla\phi'}. \tag{B.53}$$

Filling out equation B.53 in equation B.52, and then filling out the charge balance equation 4.2 for $DW/Dt$, the mean-field E×B-only kinetic energy

equation for TOKAM2D can be written as

$$\frac{\partial}{\partial t}\bar{n}E_{\mathrm{E},m} + \nabla \cdot \boldsymbol{\Gamma}_{E_{\mathrm{E},m}} = g\bar{\phi}\frac{\partial \bar{p}}{\partial y} - \frac{\bar{\phi}}{L_{||}}\overline{c_s n(1 - \exp(\Lambda - \frac{\phi}{T_e}))}$$

$$-\nu\bar{\phi}\overline{n\nabla_\perp^2 W} + \bar{\phi}\overline{n\frac{DW_*}{Dt}} + \overline{n\mathbf{V}_E''\mathbf{V}_E''} : \nabla\tilde{\mathbf{V}}_E^T - \tilde{\mathbf{V}}_{p,E} \cdot \overline{n'\nabla\phi'}$$

$$+S_{E_{\mathrm{E},m},n} + \bar{\phi}\overline{\mathbf{V}_{p,E} \cdot \nabla n}, \tag{B.54}$$

$$\bar{\boldsymbol{\Gamma}}_{E_{\mathrm{E},m}} = \bar{n}E_{\mathrm{E},m}\tilde{\mathbf{V}}_E + \overline{n\mathbf{V}_E''\mathbf{V}_E''} \cdot \tilde{\mathbf{V}}_E + \bar{\phi}\bar{\mathbf{J}}_{p,E}, \tag{B.55}$$

$$S_{E_{\mathrm{E},m},n} = E_{\mathrm{E},m}\bar{S}_n + \tilde{\mathbf{V}}_E \cdot \overline{\mathbf{V}_E''S_n}$$

$$+D_0 E_{\mathrm{E},m}\nabla_\perp^2\bar{n} + D_0\tilde{\mathbf{V}}_E \cdot \overline{\mathbf{V}_E''\nabla_\perp^2 n}$$

$$-\frac{E_{\mathrm{E},m}}{L_{||}}\overline{c_s n\exp(\Lambda - \phi/T_e)} - \overline{c_s n\mathbf{V}_E''\exp(\Lambda - \phi/T_e)} \cdot \frac{\tilde{\mathbf{V}}_E}{L_{||}}. \tag{B.56}$$

Taking the difference between the average of equation B.49 and equation B.54, the E×B-only turbulent kinetic energy equation is obtained as

$$\frac{\partial}{\partial t}\bar{n}k_E + \nabla \cdot \boldsymbol{\Gamma}_{k_E} = \overline{g\phi'\frac{\partial p'}{\partial y}} - \frac{1}{L_{||}}\overline{\phi'c_s n(1 - \exp(\Lambda - \frac{\phi}{T_e}))}$$

$$-\nu\overline{n\phi'\nabla_\perp^2 W} + \overline{n\phi'\frac{DW_*}{Dt}} - \overline{n\mathbf{V}_E''\mathbf{V}_E''} : \nabla\tilde{\mathbf{V}}_E^T + \tilde{\mathbf{V}}_{p,E} \cdot \overline{n'\nabla\phi'}$$

$$+S_{k_E,n} + \overline{\phi'(\mathbf{V}_{p,E} \cdot \nabla n)'}, \tag{B.57}$$

$$\bar{\boldsymbol{\Gamma}}_{k_E} = \bar{n}k_E\tilde{\mathbf{V}}_E + \overline{n\mathbf{V}_E''\mathbf{V}_E''^2}/2 + \overline{\phi'\mathbf{J}_{p,E}'}, \tag{B.58}$$

$$S_{k_E,n} = \frac{1}{2}\overline{\mathbf{V}_E''^2 S_n} + \frac{D_0}{2}\overline{\mathbf{V}_E''^2\nabla_\perp^2 n} - \frac{1}{L_{||}}c_s\overline{\frac{n\mathbf{V}_E''^2}{2}\exp(\Lambda - \frac{\phi}{T_e})}. \tag{B.59}$$

A comment on the TOKAM2D E×B-only case that is mostly studied in chapters 4-6 is still in place here. In this E×B-only case, only the E×B contribution to the inertia in the polarisation current is considered, while the diamagnetic contribution is neglected. Hence, also in the vorticity the diamagnetic contribution is neglected $W_* = 0$, such that $W \equiv W_E$. In this E×B-only case the E×B-only kinetic energy equations B.49, B.54 and B.57

remain valid, but slightly simplify as the $n\phi DW_*/Dt$ terms on the RHS vanish. Also note that the viscous term becomes $\nu n\phi\nabla_\perp^2 W_E$.

# B.3 TOKAM2D enstrophy equations kinetic energy equations

## B.3.1 Derivation of total enstrophy equations

As for the kinetic energy, equation for the enstrophy can also be derived both for the total and for the E×B-only part. Hence, we define the total enstrophy (with contributions from the E×B and the ion diamagnetic drift) as

$$\zeta_{tot,E*} = \frac{W^2}{2}, \quad \zeta_{mean,E*} = \frac{\tilde{W}^2}{2}, \quad \bar{n}\zeta_{,E*} = \frac{\overline{nW''^2}}{2}, \tag{B.60}$$

and the E×B-only enstrophy as

$$\zeta_{tot,E} = \frac{W_E^2}{2}, \quad \zeta_{mean,E} = \frac{\tilde{W}_E^2}{2}, \quad \bar{n}\zeta_E = \frac{\overline{nW_E''^2}}{2}. \tag{B.61}$$

Note that the sum of this E×B-only enstrophies and a diamagnetic enstrophy which could be defined as $W_*^2/$ is not equal to the total enstrophy, since $W_EW_*$ terms would then be ignored.

To analytically derive transport equations for the enstrophy, we follow a procedure similar to section 3.3.1. An equation for the total enstrophy can readily be derived by multiplying the TOKAM2D charge balance equation 4.2 by $nW$:

$$\frac{\partial n\zeta_{tot}}{\partial t} + \nabla\cdot(n\mathbf{V}_E\zeta_{tot}) = -gW\frac{\partial p}{\partial y} + \frac{c_snW}{L_{||}}(1 - \exp(\Lambda - \frac{\phi}{T_e}))$$

$$+\nu nW\nabla_\perp^2 W + \zeta_{tot}S_n + D_0\zeta_{tot}\nabla_\perp^2 n - \frac{c_sn\zeta_{tot}}{L_{||}}\exp(\Lambda - \frac{\phi}{T_e}). \tag{B.62}$$

Note that the continuity equation B.21 was used to get from the advective form to the conservative form of this equation.

The mean field enstrophy equation is obtained by first averaging the charge balance equation 4.2 multiplied by $n$, effectively yielding an equation for $\bar{n}\tilde{W}$. Then, this equation is multiplied by $\tilde{W}$ to obtain

$$\frac{\partial \bar{n}\zeta_{mean}}{\partial t} + \nabla \cdot (\bar{n}\zeta_{mean}\tilde{\mathbf{V}}_E + \overline{nW''\mathbf{V}_E''}\tilde{W}) = -g\tilde{W}\frac{\partial \bar{p}}{\partial y}$$

$$+\frac{\tilde{W}}{L_{||}}\overline{c_s n(1 - \exp(\Lambda - \frac{\phi}{T_e}))} + \nu\tilde{W}\overline{n\nabla_\perp^2 W} + \overline{nW''\mathbf{V}_E''}\cdot \nabla\tilde{W}$$

$$+\zeta_{mean}\bar{S}_n + \tilde{W}\overline{W''S_n} + D_0\zeta_{mean}\nabla_\perp^2\bar{n} + D_0\tilde{W}\overline{W''\nabla_\perp^2 n}$$

$$-\frac{\zeta_{mean}}{L_{||}}\overline{c_s n \exp(\Lambda - \frac{\phi}{T_e})} - \frac{\tilde{W}}{L_{||}}\overline{c_s n W'' \exp(\Lambda - \frac{\phi}{T_e})}. \qquad \text{(B.63)}$$

The difference between the averaged total enstrophy equation B.62 and the mean flow enstrophy equation B.63 then yields the turbulent enstrophy equation:

$$\frac{\partial \bar{n}\zeta_{turb}}{\partial t} + \nabla \cdot (\bar{n}\zeta_{turb}\tilde{\mathbf{V}}_E + \frac{\overline{nW''^2\mathbf{V}_E''}}{2}) = -g\overline{W''\frac{\partial p}{\partial y}}$$

$$+\frac{1}{L_{||}}\overline{c_s n W''(1 - \exp(\Lambda - \frac{\phi}{T_e}))} + \nu\overline{nW''\nabla_\perp^2 W} - \overline{nW''\mathbf{V}_E''}\cdot\nabla\tilde{W}$$

$$+\frac{\overline{W''^2 S_n}}{2} + D_n\frac{\overline{W''^2\nabla_\perp^2 n}}{2} - \frac{1}{L_{||}}\frac{\overline{c_s n W''^2}}{2}\exp(\Lambda - \frac{\phi}{T_e}). \qquad \text{(B.64)}$$

## B.3.2  Derivation of E×B-only enstrophy equations

To derive the E×B-only enstrophy equations we again make use of the decomposition of the vorticity in an E×B and a diamagetic contribution shown in equation B.46. Following this decomposition, we write the LHS of the TOKAM2D charge balance equation 4.2 as

$$\frac{DW}{Dt} = \frac{DW_E}{Dt} + \frac{DW_*}{Dt} \qquad \text{(B.65)}$$

Multiplying this charge balance equation with $W_E$ and using the continuity equation B.21 to get to the conservative form readily yields the total E×B-only

enstrophy equation as

$$\frac{\partial n\zeta_{tot,E}}{\partial} + \nabla \cdot (n\mathbf{V}_E\zeta_{tot,E}) = -gW_E\frac{\partial p}{\partial y}$$

$$+\frac{c_s n W_E}{L_{||}}(1 - \exp(\Lambda - \frac{\phi}{T_e})) + \nu n W_E \nabla_\perp^2 W - n W_E \frac{DW_*}{Dt}$$

$$+\zeta_{tot,E}S_n + D_0\zeta_{tot,E}\nabla_\perp^2 n - \frac{c_s n \zeta_{tot,E}}{L_{||}}\exp(\Lambda - \frac{\phi}{T_e}). \qquad \text{(B.66)}$$

Similarly, multiplying the average of the product between the density and the TOKAM2D vorticity equation 4.2 with $\tilde{W}_E$ yields

$$\frac{\partial \bar{n}\zeta_{mean,E}}{\partial t} + \nabla \cdot (\bar{n}\zeta_{mean,E}\tilde{\mathbf{V}}_E + \overline{nW_E''\mathbf{V}_E''}\tilde{W}_E) = -g\tilde{W}_E\frac{\partial \bar{p}}{\partial y}$$

$$+\frac{\tilde{W}_E}{L_{||}}\overline{c_s n(1 - \exp(\Lambda - \frac{\phi}{T_e}))} + \nu\tilde{W}_E\overline{n\nabla_\perp^2 W} - \tilde{W}_E n\overline{\frac{DW_*}{Dt}}$$

$$+\overline{nW_E''\mathbf{V}_E''} \cdot \nabla\tilde{W}_E + \zeta_{mean,E}\bar{S}_n + \tilde{W}_E\overline{W_E''S_n} + D_0\zeta_{mean,E}\nabla_\perp^2 \bar{n}$$

$$+D_0\tilde{W}_E\overline{W_E''\nabla_\perp^2 n} - \frac{\zeta_{mean,E}}{L_{||}}\overline{c_s n \exp(\Lambda - \frac{\phi}{T_e})}$$

$$-\frac{\tilde{W}_E}{L_{||}}\overline{c_s n W_E'' \exp(\Lambda - \frac{\phi}{T_e})}. \qquad \text{(B.67)}$$

Then, the E×B-only turbulent enstrophy equation for TOKAM2D is obtained by taking the difference between the average of equation B.66 and B.67:

$$\frac{\partial \bar{n}\zeta_E}{\partial t} + \nabla \cdot (\bar{n}\zeta_E\tilde{\mathbf{V}}_E + \frac{\overline{nW_E''^2\mathbf{V}_E''}}{2}) = -g\overline{W_E''\frac{\partial p}{\partial y}}$$

$$+\frac{c_s}{L_{||}}\overline{nW_E''(1 - \exp(\Lambda - \frac{\phi}{T_e}))} + \nu\overline{nW_E''\nabla_\perp^2 W} - \overline{nW_E''\frac{DW_*}{Dt}}$$

$$-\overline{nW_E''\mathbf{V}_E''} \cdot \nabla\tilde{W}_E + \frac{\overline{W_E''^2 S_n}}{2} + D_n\frac{\overline{W_E''^2\nabla_\perp^2 n}}{2}$$

$$-\frac{1}{L_{||}}\frac{\overline{c_s n W_E''^2}}{2}\exp(\Lambda - \frac{\phi}{T_e}). \qquad \text{(B.68)}$$

If desired, the first four terms in the RHS of equations B.66-B.68 could be rewritten using the charge balance equation 4.2 as follows

$$-gW_E\frac{\partial p}{\partial y} + \frac{c_s n W_E}{L_{||}}(1 - \exp(\Lambda - \frac{\phi}{T_e})) - \nu n W_E \nabla_\perp^2 W + n W_E \frac{DW_*}{Dt}$$

$$= -gW\frac{\partial p}{\partial y} + \frac{c_s n W}{L_{||}}(1 - \exp(\Lambda - \frac{\phi}{T_e})) - \nu n W \nabla_\perp^2 W$$

$$+ nW\frac{DW_*}{Dt} + nW_*\frac{DW_E}{Dt}. \quad (B.69)$$

Hence these terms can be written with the total vorticity $W$ instead of the E×B-only vorticity $W_E$ to obtain the same closures in the RHS as in the total enstrophy equations B.62-B.64. However, a correction term of the form $nW_* DW_E/Dt$ then needs to be added (in addition to the $DW_*/Dt$ term which was already there as correction w.r.t. the total enstrophy case).

In the TOKAM2D E×B-only case (where $W_* = 0$ and $W \equiv W_E$ are assumed) that is mostly studied in chapters 4-6, the E×B-only enstrophy equations B.66-B.68 remain valid. Moreover, the equations slightly simplify as the fourth term on the RHS can be dropped.

# Appendix C

# Representative dimensional values for plasma quantities in TOKAM2D

By way of example to interpret the normalised quantities used in the main text, this appendix[1] considers a tokamak operating with a pure deuterium plasma. Typical values around the separatrix of such a machine could be $B_0 = 5T$, $n_0 = 5 \times 10^{19}/m^3$ and $T_0 = 50eV$. For these reference values, the reference quantities used in the normalisation become

$$\Omega_0 = eB_0/m_i = 2.4 \times 10^8 Hz, \tag{C.1}$$

$$c_{s,0} = \sqrt{T_0/m_i} = 4.9 \times 10^4 m/s, \tag{C.2}$$

$$\rho_0 = c_{s,0}/\Omega_0 = 2.0 \times 10^{-4} m. \tag{C.3}$$

These reference quantities are then used in table C.1 to calculate typical dimensional values from the typical values of (anisothermal SOL) TOKAM2D simulation results for a number of key quantities. The particle diffusion coefficient can be seen to be rather high, characteristic of a highly turbulent SOL.

---

[1]This appendix has been published in the appendix of "Coosemans, R., Dekeyser, W., Baelmans, M. (2022). A self-consistent mean-field model for turbulent particle and heat transport in 2D interchange-dominated electrostatic E×B turbulence in a sheath-limited scrape-off layer. *Contributions to Plasma Physics*, e202100193" [47].

Table C.1: Typical dimensional and normalised values for turbulent quantities as obtained from the default TOKAM2D simulation.

| | normalisation | T2D value [-] | dimensional value |
|---|---|---|---|
| $\mathbf{D}$ | $\rho_0^2 \Omega_0$ | $0.2 - 1.2$ | $2 - 12 m^2/s$ |
| $\mathbf{n}$ | $n_0$ | $1$ | $5 \times 10^{19} m^{-3}$ |
| $\mathbf{T_{i/e}}$ | $T_0 = mc_{s,0}^2$ | $1$ | $50 eV$ |
| $\mathbf{\Gamma_n}$ | $n_0 c_{s,0}$ | $10^{-2}$ | $2.4 \times 10^{22} m^{-2} s^{-1}$ |
| $\mathbf{\Gamma_{p_i}} + \mathbf{\Gamma_{p_e}}$ | $n_0 T_0 c_{s,0}$ | $3 \times 10^{-2}$ | $5.9 \times 10^5 J m^{-2} s^{-1}$ |
| $\mathbf{k_\perp}$ | $T_0 = mc_{s,0}^2$ | $3 \times 10^{-3}$ | $0.15 eV$ |

# Appendix D

# TOKAM2D simulation parameters

This appendix[1] details the simulation parameters used in the TOKAM2D simulations presented in chapters 4-6. All reported simulations were run for the finite volume version of the code with a non-periodic x-direction and using the strong Boussinesq assumption. Fringe regions are applied on the radial edges of the domain to smoothly enforce diamagnetically uniform profiles in these zones. The width of the fringe region near the inner and outer radial boundary is set to 10 gyro-radii on both sides in all simulations. Note that the data used in the post processing only considers the physical middle part of the computational domain where there is no fringe region and the influence of the particle and thermal energy sources is negligible.

In all simulations a particle source $S_n$ with Gaussian profile in the $x$ direction that is uniform in the diamagnetic $y$ direction and in time is applied. This source

---

[1]Parts of this appendix have been published in the appendices of "Coosemans, R., Dekeyser, W., Baelmans, M. (2021). Turbulent kinetic energy in 2D isothermal interchange-dominated scrape-off layer E×B drift turbulence: Governing equation and relation to particle transport. *Physics of Plasmas*, 28:012302" [46], of "Coosemans, R., Dekeyser, W., Baelmans, M. (2020). A new mean-field plasma edge transport model based on turbulent kinetic energy and enstrophy. *Contributions to Plasma Physics*, 60:e201900156" [44], of "Coosemans, R., Dekeyser, W., Baelmans, M. (2021). Bayesian analysis of turbulent transport coefficients in 2D interchange dominated E×B turbulence involving flow shear. *Journal of Physics: Conference Series*, 1785:012001" [45], and of "Coosemans, R., Dekeyser, W., Baelmans, M. (2022). A self-consistent mean-field model for turbulent particle and heat transport in 2D interchange-dominated electrostatic ExB turbulence in a sheath-limited scrape-off layer. *Contributions to Plasma Physics*, e202100193" [47].

is centered 10 gyro-radii from the inner boundary and has a standard deviation of 8 gyro-radii in the radial direction. The cell size is set to $\Delta x = \Delta y = 1[\rho_0]$ for all simulations. The parameters were chosen such that $D_0 = \nu_0$ and $\Lambda = 2.8388$ in all the reported simulations.

# D.1 Isothermal TOKAM2D simulations for the SOL

In the isothermal case, the ion and electron temperatures take spatio-temporally constant values equal to $T_i = Ti0$ and $T_e = Te0$. In particular, $Te0 = 1$ has been set in all simulations, since the dimensional electron temperature could then still be set to any desired value through the choice of the reference temperature $T_0$. All these isothermal SOL simulations were run with a time step $\Delta t = 1[\Omega_0^{-1}]$.

## D.1.1 Default simulation

The default settings for the simulations are shown in table D.1. The last four columns are not classical TOKAM2D parameters, but are parameters used in the post-processing. $x_{start}$ and $x_{end}$ denote the first and the last cell that are considered in the post-processing. They serve to remove the nonphysical fringe region and the zone where the particle source is large. $t_{start}$ and $t_{end}$ denote the first and the last time steps used for the averaging, they serve to remove the non-converged first part of the simulation and to show the length of the simulation.

Table D.1: Default parameters used in TOKAM2D simulations and their post processing.

| Nr. | Lx | Ly | $g$ | $Ti0$ | $L_{\parallel}^{-1}$ | $\nu_0$ | $x_{start}$ | $x_{end}$ | $t_{start}$ | $t_{end}$ |
|-----|-----|-----|------|-------|------------|---------|-------------|-----------|-------------|-----------|
| 1 | 256 | 256 | 6e-4 | 1 | 1e-4 | 5e-3 | 51 | 199 | 2e5 | 8e5 |

## D.1.2 TOKAM2D parameters used in section 4.3

Table D.2 shows the parameters of the simulations used for the regression analysis in section 4.3 on the development of the $k_{\perp}$ model. Only the parameters that differ from the default simulation (for which the parameters are listed in table D.1) are shown, except for the first simulation which is the default simulation.

Table D.2: TOKAM2D and post-processing parameters of the simulations used in the regression analysis in section 4.3

| Nr. | $g$ | $Ti0$ | $L_{||}^{-1}$ | $\nu_0$ | $t_{start}$ | $t_{end}$ |
|---|---|---|---|---|---|---|
| 1 | 6e-4 | 1 | 1e-4 | 5e-3 | 2e5 | 8e5 |
| 2 | 4.5e-4 | | | | | |
| 3 | 7.5e-4 | | | | | |
| 4 | | | 5e-5 | | | |
| 5 | | | 8e-5 | | | |
| 6 | | | 2e-4 | | | |
| 7 | | 0.5 | | | | |
| 8 | | 2 | | | | |
| 9 | | | | 2e-3 | | |
| 10 | | | | 4e-3 | | |
| 11 | | | | 6e-3 | | |
| 12 | | | | 1e-2 | | |
| 13 | | | | 1.5e-2 | | |
| 14 | 4e-4 | 0.8 | | | | |
| 15 | 4e-4 | 1.4 | | | | |
| 16 | 9e-4 | 1.8 | | | | |
| 17 | 8e-4 | 0.75 | | | | |
| 18 | | 0.9 | 0.75e-4 | | | |
| 19 | 4.5e-4 | | 1.5e-4 | | | |

## D.1.3   TOKAM2D parameters used in sections 4.4 and 4.5

Table D.3 shows the parameters of the simulations used for the regression analysis in section 4.4 on the development of the $k_\perp - \zeta_\perp$ model and in section 4.5 compare the $k_\perp$ and $k_\perp - \zeta_\perp$ models. Only the parameters that differ from the default simulation (for which the parameters are listed in table D.1) are shown, except for the third simulation which is the default simulation.

Table D.3: TOKAM2D and post-processing parameters of the simulations used in the regression analysis in section 4.4.

| Nr. | $g$ | $Ti0$ | $L_{\parallel}^{-1}$ | $\nu_0$ | $t_{start}$ | $t_{end}$ |
|---|---|---|---|---|---|---|
| 1 | 4e-4 | | | | | |
| 2 | 4.5e-4 | | | | | |
| 3 | 6e-4 | 1 | 1e-4 | 5e-3 | 2e5 | 8e5 |
| 4 | 7.5e-4 | | | | | |
| 5 | 9e-4 | | | | | |
| 6 | | | | 2e-3 | | |
| 7 | | | | 1e-2 | | |
| 8 | | | | 1.5e-2 | | |
| 9 | | | 5e-5 | 2e-2 | | |
| 10 | 9e-4 | | 5e-5 | 2e-2 | | |
| 11 | | | 8e-5 | | | |
| 12 | 4.5e-4 | | 1.5e-4 | | | |
| 13 | | 0.5 | | | | |
| 14 | | 2 | | | | |
| 15 | 3e-4 | 4 | | 7e-3 | | |
| 16 | 7e-4 | 0.7 | 3e-5 | | | |
| 17 | | 0.3 | 1.5e-4 | 8e-3 | | |
| 18 | 4e-4 | 0.4 | 6e-5 | | | |

## D.1.4 TOKAM2D parameters used in chapter 5

Table D.4 shows the parameters of the simulations used for the regression analysis for the SOL in chapter 5. Only the parameters that differ from the default simulation (for which the parameters are listed in table D.1) are shown, except for the first simulation which is the default simulation. Each of the simulations listed in the table are run twice: once with the E×B-only vorticity $W = \nabla_{\perp}^2 \phi$ and once with the total vorticity $W = \nabla_{\perp}^2 \phi + \nabla \cdot \left( \frac{\nabla p_i}{n} \right)$. Both sets of simulations are compared in section 5.2. In section 5.1 on the other hand, only the E×B-only simulations are considered, which are there compared with simulations that also feature a core region. These are described in appendix D.2.

In the regression analysis of section 5.1, the data from the radial positions $21 \leq x \leq 219$ from these simulations has been used.

In the regression analysis of section 5.2, the data from the radial positions $21 \leq x \leq 209$ from these simulations has been used, while for the 1D mean-field

DivOptLight (DOL) simulations, the domain $49 \leq x \leq 210$ has been simulated.

Table D.4: TOKAM2D and post-processing parameters of the simulations used in the regression analysis in section 5.2.

| Nr. | $g$ | $Ti0$ | $L_{\parallel}^{-1}$ | $\nu_0$ | $t_{start}$ | $t_{end}$ |
|-----|--------|------|--------|--------|-------|------|
| 1 | 6e-4 | 1 | 1e-4 | 5e-3 | 2e5 | 8e5 |
| 2 | 4e-4 | | | | | |
| 3 | 9e-4 | | | | | |
| 4 | | 0.5 | | | | |
| 5 | | 1.2 | | | | |
| 6 | | 1.5 | | | | |
| 7 | | | 5.e-5 | | | |
| 8 | | | 2.e-4 | | | |
| 9 | | | | 2e-3 | | |
| 10 | | | | 1e-2 | | |
| 11 | | | | 1.5e-2 | | |
| 12 | 4e-4 | 0.8 | | | | |
| 13 | 9e-4 | 1.5 | | | | |
| 14 | 4.5e-4 | | 1.5e-4 | | | |
| 15 | | | 5e-5 | 2e-2 | | |
| 16 | | 0.3 | 1.5e-4 | 8e-3 | | |

# D.2 Isothermal TOKAM2D simulations for the SOL and core region

Table D.5 shows the parameters of the simulations with SOL and outer core region used in section 5.1. $Lx$ and $Ly$ denote the radial and diamagnetic domain length and $x_{sep}$ the location of the separatrix. The radial range $x_{start} \leq x \leq x_{end}$ used for the analysis in section 5.1 is also shown. In these simulations, neither the ion nor the electron temperature has been varied and both were chosen $Ti0 = Te0 = 1$. A time step of $\Delta t = 0.1$ gyro-periods is used in all these simulations. Data from simulation 15 is used in figures 5.3b and 5.4b.

Table D.5: TOKAM2D and post-processing parameters of the simulations of the *isoDW* data set.

| Nr. | $g$ | $L_{\parallel}^{-1}$ | $K_{DW}$ | $\nu_0$ | $Lx$ | $Ly$ | $x_{sep}$ | $x_{start}$ | $x_{end}$ |
|---|---|---|---|---|---|---|---|---|---|
| 1 | 2e-3 | 1.25e-4 | 5.9e-4 | 2.7e-3 | 170 | 200 | 61 | 21 | 149 |
| 2 | 2.3e-4 | 2.5e-5 | 2.74e-4 | 5e-3 | 170 | 200 | 61 | 21 | 149 |
| 3 | 6e-4 | 1e-4 | 1e-4 | 5e-3 | 170 | 200 | 61 | 21 | 149 |
| 4 | 2.3e-4 | 2.5e-5 | 3.6e-5 | 2e-2 | 170 | 200 | 61 | 21 | 149 |
| 5 | 6e-4 | 1e-4 | 1e-5 | 5e-3 | 170 | 200 | 61 | 21 | 149 |
| 6 | 2e-3 | 1.25e-4 | 5.9e-4 | 2.7e-3 | 256 | 256 | 105 | 21 | 219 |
| 7 | 2.3e-4 | 2.5e-5 | 2.74e-4 | 5e-3 | 256 | 256 | 105 | 21 | 219 |
| 8 | 6e-4 | 1e-4 | 1e-4 | 5e-3 | 256 | 256 | 105 | 21 | 219 |
| 9 | 2.3e-4 | 2.5e-5 | 3.6e-5 | 2e-2 | 256 | 256 | 105 | 21 | 219 |
| 10 | 6e-4 | 1e-4 | 1e-5 | 5e-3 | 256 | 256 | 105 | 21 | 219 |
| 11 | 2e-3 | 1.25e-4 | 5.9e-4 | 2.7e-3 | 384 | 256 | 129 | 21 | 339 |
| 12 | 2.3e-4 | 2.5e-5 | 2.74e-4 | 5e-3 | 384 | 256 | 129 | 21 | 339 |
| 13 | 6e-4 | 1e-4 | 1e-4 | 5e-3 | 384 | 256 | 129 | 21 | 339 |
| 14 | 2.3e-4 | 2.5e-5 | 3.6e-5 | 2e-2 | 384 | 256 | 129 | 21 | 339 |
| 15 | 6e-4 | 1e-4 | 1e-5 | 5e-3 | 384 | 256 | 129 | 21 | 339 |

# D.3 Anisothermal TOKAM2D simulations for the SOL

This appendix summarises the TOKAM2D simulation parameters used for the analysis of the anisothermal TOKAM2D case in chapter 6.

A particle source $S_n$ that is uniform in time and in the diamagnetic $y$ direction with Gaussian profile in the $x$ direction is applied. This source has its maximum 10 cells from the core boundary and has a standard deviation of 8 cells. Electron and ion thermal energy sources $S_{p_e}$ and $S_{p_i}$ are applied that have the same shape as the particle source, they are determined as $S_{p,i/e} = 2/3 E_{inj,i/e} S_n$.

All simulations are all conducted on a grid of 256x256 cells with a cell size $\Delta x = \Delta y = 1$ gyro-radius and a time step of $\Delta t = 0.1$ gyro-period. In the radial direction, only the data points in the range $21 \leq x \leq 219$ are retained for the analysis in order to exclude the fringe region. All diamagnetic data points are used. In the 1D mean-field DivOptLight (DOL) simulations, the radial domain is further trimmed to $50 \leq x \leq 219$ in order to also exclude the region where the particle and thermal energy sources are active.

The physical TOKAM2D parameters which are varied in the simulations are shown in table D.6. The first simulation is the reference one, only parameters that differ from this default simulation are shown for other simulations. This first simulation is also the one of used in all figures showing radial profiles in chapter 6 and in figure 6.11. Apart from the parameters shown in table D.6, the settings $\gamma_i = 2.5$ and $\gamma_e = 4$ are used in all simulations.

Table D.6: Simulation parameters of the anisothermal TOKAM2D data set.

| Nr. | $g$ | $E_{inj,i}$ | $E_{inj,e}$ | $L_{\parallel}^{-1}$ | $\nu_0$ |
|---|---|---|---|---|---|
| 1 | 6e-4 | 3 | 3 | 1e-4 | 5e-3 |
| 2 | | | | 2e-5 | |
| 3 | | | | 5e-5 | |
| 4 | | | | 8e-5 | |
| 5 | | | | 1.5e-4 | |
| 6 | | | | 2e-4 | |
| 7 | | 2 | | 1.4e-4 | |
| 8 | | | 2 | 1.4e-4 | |
| 9 | | 5 | | | |
| 10 | | | 5 | | |
| 11 | | 6 | 2 | | |
| 12 | | 2 | 6 | | |
| 13 | | 8 | 2 | | |
| 14 | | 2 | 8 | | |
| 15 | | 2 | 2 | | |
| 16 | | 6 | 6 | | |
| 17 | 3e-4 | | | | |
| 18 | 9e-4 | | | | |
| 19 | 1.2e-3 | | | | |
| 20 | | | | | 2.5e-3 |
| 21 | | | | | 1e-2 |
| 22 | 4e-4 | | | | 8e-3 |
| 23 | 8e-4 | | | | 4e-3 |
| 24 | | 4 | 4 | 1.2e-4 | |

The simulations in table D.6 have all been run twice: once with the SCW mode on (SCW1 case) and once with the SCW mode suppressed (SCW0 case). Furthermore, the default simulation 1 has been run once more for the SCW1 case, but with $g = 0$ to supply the data for figure 6.11c.

# Appendix E

# TOKAM2D grid refinement

This appendix[1] conducts a grid and time step refinement study to verify for the isothermal TOKAM2D case discussed in chapter 4. It is verified that the error on the turbulent kinetic energy balance and on the turbulent enstrophy balance, shown in figures 4.6 and 4.14 respectively, reduces with increasing refinement. Given the first order time integration and second order WENO spatial discretization schemes [97, 110] used by the finite volumes version of the TOKAM2D code used in this contribution [109, 116], the error is expected to scale like $O(\Delta x^2) + O(\Delta y^2) + O(\Delta t)$. During the refinement we systematically reduced the cell size with a factor 2 in both directions, and the time step with a factor 4 such that we would theoretically obtain second order convergence.

The exact parameters used in the TOKAM2D grid refinement simulations are shown in table E.1. Only the parameters that differ from the default simulation (for which the parameters are listed in table D.1) are shown. For all these simulations, the particle source $S_n$ is centered 5 gyro-radii from the inner boundary and has a standard deviation of 4 gyro-radii in the radial direction. Note that the start and end points of the considered domain in space and in time are expressed in cell numbers and in time steps, rather than gyro-radii and gyro-periods.

Figure E.1 shows the results for the radially averaged value of the relative error on the $k_\perp$ and $\zeta_\perp$ equations as a function of the refinement step. The figure shows that the relative error and the subgrid model decrease as the grid and

---

[1]Parts of this appendix have been published in the appendix of "Coosemans, R., Dekeyser, W., Baelmans, M. (2021). Turbulent kinetic energy in 2D isothermal interchange-dominated scrape-off layer E×B drift turbulence: Governing equation and relation to particle transport. *Physics of Plasmas*, 28:012302" [46].

Table E.1: TOKAM2D and post-processing parameters of the simulations used in the grid refinement analysis.

| Nr. | Lx | Ly | $\Delta x$ | $\Delta y$ | $\Delta t$ | $x_{start}$ | $x_{end}$ | $t_{start}$ | $t_{end}$ |
|-----|-----|-----|------|------|------|------|------|------|-------|
| a | 64 | 64 | 2 | 2 | 4 | 13 | 49 | 8e5 | 1.04e7 |
| b | 128 | 128 | 1 | 1 | 1 | 26 | 99 | 2e5 | 2.6e6 |
| c | 256 | 256 | 0.5 | 0.5 | 0.25 | 51 | 199 | 8e5 | 3.2e6 |
| d | 512 | 512 | 0.25 | 0.25 | 1/16 | 101 | 399 | 1.6e6 | 8e6 |

time step are refined. The figure also shows that the expected second order convergence has not been reached yet for the $k_\perp$ equation, while it might be reached in the last refinement step for the $\zeta_\perp$ equation. Hence, the grid would have to be refined even further to complete the grid convergence study. This has not been done yet for reasons of computational cost. An alternative explanation may be that the discretization scheme we used may not be second order for one of the terms in the $k_\perp$ equation.

Figure E.2 shows the difference between $k_\perp$ and $\zeta_\perp$ on the finest grid and $k_\perp$ and $\zeta_\perp$ on the coarser grids. The theoretically expected second order convergence does seem to be recovered here. This figure clearly shows that both quantities increase as the grid is refined. Indeed, as the grid is refined, the dissipative effect of the discretisation error is reduced, which leads to an increase of $k_\perp$ and $\zeta_\perp$. This numerical dissipation thus acts as an additional subgrid model that is not present in the governing equations 4.1-4.2. Alternatively, it could be argued that refining the grid allows smaller scale structure to be resolved and to contribute to $k_\perp$ and $\zeta_\perp$, leading to an increase of these quantities. This as well is an undesirable effect though since it is unphysical to have fluctuations at scales smaller than a gyro-radius in the drift-reduced fluid approach followed in TOKAM2D. The viscous dissipation in the model equations should inhibit the direct cascade to these scales. The commonly used cell sizes and time steps ($\Delta x = \Delta y = \rho_0$, $\Delta t = 1/\Omega_0$)[109, 116] will be used in the remainder of chapter 4, despite the error that they seem to cause, because we found no significant impact on the underlying physics interpretation or saturation behavior of the turbulence at present. However, for a detailed analysis of the forward and inverse turbulence cascades[92, 36, 71, 34], this implied subgrid model might play an important role, and requires further investigation.

It is also interesting to compare the slightly different behaviour of $k_\perp$ and $\zeta_\perp$ during the refinement. Clearly, the error on the turbulent enstrophy equation is much larger than that on the turbulent kinetic energy equation. The turbulent enstrophy also increases more strongly as the grid is refined. This is most likely a result of the enstrophy being concentrated on the smaller scales which suffer more from the discretization, while the kinetic energy is more strongly present
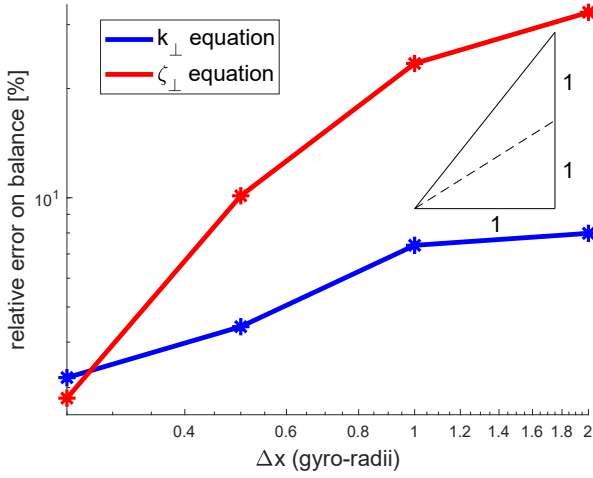
Figure E.1: Relative error on the turbulent kinetic energy 4.16 and enstrophy 4.27 equations as a function of the number of grid cells. Time step is refined during grid refinement as well
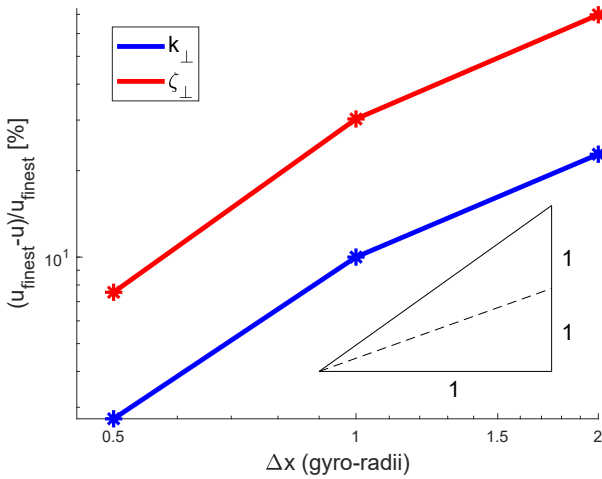.



Figure E.2: Turbulent kinetic energy and enstrophy as a function of the number of grid cells. Time step is refined during grid refinement as well
.

on larger scales. Alternatively, it could be argued that since more enstrophy is present on the small scales, resolving the turbulence on finer grids affects this quantity more. The difference in length scale is probably the reason why viscous dissipation is much more important for the $\zeta_\perp$ than it is for $k_\perp$. These explanations are in accordance with the understanding of hydrodynamic 2D turbulence and its dual cascade picture. [4, 71, 169].

Lastly, it is worth mentioning that isothermal SOL TOKAM2D simulations at the regular grid size ($\Delta x = \Delta y = 1[\rho_0]$ and $\Delta t = 1[\Omega_0^{-1}]$) with the viscosity set to zero ($\nu_0 = D_0 = 0$) were also run to further check this subgrid behaviour. These simulations ran without issues and the results seem comparable to those of the simulations with $\nu_0 \neq 0$. While the exact numerical values differed of course, the general trends in the profiles and behaviour of the simulation seem unchanged. This does indeed seem to imply that some form of subgrid model is present, stabilising the simulations and limiting the direct cascades to length scales smaller than the grid size as the physical viscosity is intended to do.

# Appendix F

# Supplementary information and derivations for the TOKAM3X slab cases

This appendix provides detailed information and derivations regarding the isothermal TOKAM3X slab cases to support the discussion in section 7.1. Sections F.1 and F.2 derive the kinetic energy and enstrophy equations for the TOKAM3X code specifically. Next, section F.3 presents the detailed simulation parameters of the available TOKAM3X slab cases.

## F.1   Derivation of the kinetic energy equations

In this section, the kinetic energy equations for TOKAM3X equation set 7.1-7.7 specifically are derived. Section F.1.1 derives the equations for the total perpendicular kinetic energies defined as

$$E_{E*} = \frac{\mathbf{V}_{0,\perp}^2}{2}, \quad E_{m,E*} = \frac{\bar{\mathbf{V}}_{0,\perp}^2}{2}, \quad k_{E*} = \frac{\overline{\mathbf{V}_{0,\perp}'^2}}{2}, \tag{F.1}$$

where the perpendicular velocities in the kinetic energy are those considered for the inertia, i.e. $\mathbf{V}_{0,\perp} = \mathbf{V}_E + \mathbf{V}_{*,i}$. Then, section F.1.2 derives the equations for the E×B-only kinetic energies defined as

$$E_{\mathrm{E}} = \frac{\mathbf{V}_E^2}{2}, \qquad E_{\mathrm{E},m} = \frac{\bar{\mathbf{V}}_E^2}{2}, \qquad k_E = \frac{\overline{\mathbf{V}_E'^2}}{2}. \tag{F.2}$$

Note that we do not use density weighing in the definition of these kinetic energies and work with the regular Reynolds decomposition (see equation 2.7) instead of the Favre decomposition we used before. The reason for this is that there is no no density weighing of the inertia in the LHS of the charge balance equation 7.2. If we would want to construct equations for the density weighed equations, the RHS of the charge balance equation would have to be multiplied with the (normalised) density, and this is deemed to be nonphysical. Moreover, this would hinder the comparison of terms with the general case. Remark also that all equations in this appendix are written in normalised TOKAM3X units (see section 7.1).

Next, section F.1.1 derives the equations for the parallel kinetic energies defined as

$$E_{\mathrm{k},||} = \frac{\mathbf{V}_{||}^2}{2}, \qquad E_{\mathrm{k},m,||} = \frac{\tilde{\mathbf{V}}_{||}^2}{2}, \qquad \bar{n}k_{||} = \frac{\overline{n\mathbf{V}_{||}''^2}}{2}. \tag{F.3}$$

Note that since the density is taken into account in the TOKAM3X parallel momentum equation 7.3, density weighing and Favre averages are used for the parallel kinetic energy as in chapter 3 for the general case.

## F.1.1  Total perpendicular kinetic energy equations

Perpendicular kinetic energy equations can be derived in a way similar to section 3.2.1, although the density weighing can now be left out of the derivations.

The LHS of the charge balance 7.2 equation can be rewritten as

$$\frac{\partial W}{\partial t} + \nabla \cdot \mathbf{V}_C W$$

$$= -\nabla \cdot \mathbf{V}_{p,0} - \nabla \cdot (\frac{\mathbf{U}_0}{B} \cdot \nabla \mathbf{V}_C) - \nabla \cdot (\frac{\mathbf{U}_0}{B} \frac{D \ln B}{Dt}) \tag{F.4}$$

where we defined the inertial part of the TOKAM3X polarisation current as

$$\mathbf{V}_{p,0} = -\frac{1}{B}(\frac{\partial \mathbf{U}_0}{\partial t} + \nabla \cdot \mathbf{V}_C \mathbf{U}_0). \tag{F.5}$$

Note that the term $\nabla \cdot (\frac{\mathbf{U}_0}{B} \cdot \nabla \mathbf{V}_C) = \nabla \mathbf{V}_C : \nabla \mathbf{U}_0 + \mathbf{U}_0 \cdot \nabla (\nabla \cdot \mathbf{V}_C)$, which is effectively neglected in TOKAM3X, is similar to the term neglected in TOKAM2D in equation B.30.

The inertia in the polarisation velocity can again be related to the kinetic energy:

$$-(\nabla_\perp \phi + \frac{\nabla_\perp p_\mathrm{i}}{n}) \cdot \mathbf{V}_{p,0} = \frac{\partial E_{E*}}{\partial t} + \nabla \cdot E_{E*} \mathbf{V}_C + E_{E*} \nabla \cdot \mathbf{V}_C. \qquad \text{(F.6)}$$

Multiplying equation F.4 with $\phi$, adding $\nabla p_\mathrm{i} \cdot \mathbf{V}_{p,0}$ to both sides, and then rewriting yields

$$\frac{\partial E_{E*}}{\partial t} + \nabla \cdot (E_{E*} \mathbf{V}_C + \phi \mathbf{V}_{p,0}) = -\phi (\frac{\partial W}{\partial t} - \nabla \cdot \mathbf{V}_C W) - \frac{\nabla p_\mathrm{i}}{n} \cdot \mathbf{V}_{p,0}$$

$$-\phi \nabla \cdot (\frac{\mathbf{U}_0}{B} \frac{D \ln B}{Dt}) - \phi \nabla \cdot (\frac{\mathbf{U}_0}{B} \cdot \nabla \mathbf{V}_C) - E_{E*} \nabla \cdot \mathbf{V}_C \text{(F.7)}$$

Finally, the RHS of equation 7.2 is filled out for the first on the RHS of equation F.7, yielding

$$\frac{\partial E_{E*}}{\partial t} + \nabla \cdot (E_{E*} \mathbf{V}_C + \phi \mathbf{J}_{||} + \phi \mathbf{V}_{p,0})$$

$$= \nabla_{||} \phi \cdot \mathbf{J}_{||} - \phi \nabla \cdot \mathbf{J}_{\nabla B} - D_W \phi \nabla_\perp^2 W - \frac{\nabla p_\mathrm{i}}{n} \cdot \mathbf{V}_{p,0}$$

$$-\phi \nabla \cdot (\frac{\mathbf{U}_0}{B} \frac{D \ln B}{Dt}) - \phi \nabla \cdot (\frac{\mathbf{U}_0}{B} \cdot \nabla \mathbf{V}_C) - E_{E*} \nabla \cdot \mathbf{V}_C, \qquad \text{(F.8)}$$

Comparing to the original $E_{\mathrm{k},\perp}$ equation 3.10, it can be seen that in all terms related to the polarisation current or the inertia, the (normalised) density has dropped. This is a logical consequence of the Boussinesq approximation by which the (normalised) density had been neglected in the TOKAM3X charge balance equation 7.2. Furthermore, the definition of $\mathbf{V}_{p,0}$ is slightly different in both cases. In addition, the terms on the third line of equation F.8 appear because of the approximations made in the TOKAM3X charge balance equation. This is evident from the last two terms in equation F.4. These terms can also be linked to the terms not accounted for in the general charge balance equation 2.53. The last term in that equation is effectively included in the definition of the TOKAM3X polarisation velocity, and the Boussinesq term does not appear because the density is ignored altogether by

a stronger Boussinesq approximation in TOKAM3X. Furthermore, realising that $\nabla \cdot (\frac{\mathbf{U}_0}{B} \cdot \nabla \mathbf{V}_C) = \nabla \mathbf{V}_C : \nabla \frac{\mathbf{U}_0}{B} + \frac{\mathbf{U}_0}{B} \cdot \nabla(\nabla \cdot \mathbf{V}_C)$, the other terms can also be traced back. Lastly, it can be noted that due to the assumption made by leaving out the density, $\nabla \cdot \mathbf{V}_C$ replaces the particle source in the equations.

A mean-field perpendicular kinetic energy equation can be derived following an analogous derivation using mean-field quantities instead. In particular, the equivalent to equation F.6 is obtained by multiplying $\bar{\mathbf{V}}_{p,0}$ with $\nabla_\perp \bar{\phi} + \overline{\nabla p_{\mathrm{i}}/n}$. This yields

$$\frac{\partial E_{m,E*}}{\partial t} + \nabla \cdot (E_{m,E*} \bar{\mathbf{V}}_C + \overline{\mathbf{V}'_C \mathbf{V}'_0} \cdot \bar{\mathbf{V}}_{0,\perp} + \bar{\phi}\bar{\mathbf{J}}_{||} + \bar{\phi}\bar{\mathbf{V}}_{p,0})$$

$$= \nabla_{||}\bar{\phi} \cdot \bar{\mathbf{J}}_{||} - \bar{\phi}\nabla \cdot \bar{\mathbf{J}}_{\nabla B} - D_W \bar{\phi}\nabla_\perp^2 \bar{W} - \overline{\frac{\nabla p_{\mathrm{i}}}{n}} \cdot \bar{\mathbf{V}}_{p,0}$$

$$+ \overline{\mathbf{V}'_C \mathbf{V}'_{0,\perp}} : \nabla \bar{\mathbf{V}}_{0,\perp}^T - \bar{\phi}\overline{\nabla \cdot (\frac{\mathbf{U}_0}{B} \frac{D \ln B}{Dt})}$$

$$- \bar{\phi}\nabla \cdot (\overline{\frac{\mathbf{U}_0}{B} \cdot \nabla \mathbf{V}_C}) - E_{m,E*}\nabla \cdot \bar{\mathbf{V}}_C, \tag{F.9}$$

The difference between the average equation F.8 and equation F.9 then provides an equation for $k_\perp$:

$$\frac{\partial k_{E*}}{\partial t} + \nabla \cdot (k_{E*}\mathbf{V}_C + \overline{\frac{\mathbf{V}'^2_{0,\perp}\mathbf{V}'_C}{2}} + \overline{\phi'\mathbf{J}'_{||}} + \overline{\phi'\mathbf{V}'_{p,0}})$$

$$= \overline{\nabla_{||}\phi' \cdot \mathbf{J}'_{||}} - \overline{\phi'\nabla \cdot \mathbf{J}_{\nabla B}} - D_W \overline{\phi'\nabla_\perp^2 W'} - \overline{\frac{\nabla p_{\mathrm{i}}}{n}} \cdot \mathbf{V}'_{p,0}$$

$$- \overline{\mathbf{V}'_C \mathbf{V}'_{0,\perp}} : \nabla \bar{\mathbf{V}}_{0,\perp}^T - \overline{\phi'\nabla \cdot (\frac{\mathbf{U}_0}{B} \frac{D \ln B}{Dt})} - \overline{\phi'\nabla \cdot (\frac{\mathbf{U}_0}{B} \cdot \nabla \mathbf{V}_C)}$$

$$- k_{E*}\nabla \cdot \bar{\mathbf{V}}_C - \overline{\frac{\mathbf{V}'^2_{0,\perp}\nabla \cdot \mathbf{V}'_C}{2}} - \bar{\mathbf{V}}_{0,\perp} \cdot \overline{\mathbf{V}'_{0,\perp}\nabla \cdot \mathbf{V}'_C}, \tag{F.10}$$

## F.1.2 E×B-only kinetic energy equations

E×B-only kinetic energy equations can be derived from the E×B contribution to the polarisation current as in section 3.2.2. Following the definition of E×B and ion diamagnetic vorticity in equation 3.47, we split the LHS of the charge balance equation in an E×B part and an ion diamagnetic contribution:

$$\frac{\partial W}{\partial t} + \nabla \cdot W\mathbf{V}_C = \left(\frac{\partial W_E}{\partial t} + \nabla \cdot W_E\mathbf{V}_C\right) + \left(\frac{\partial W_*}{\partial t} + \nabla \cdot W_*\mathbf{V}_C\right) \text{(F.11)}$$

In analogy with equation F.4, the E×B-only contribution can can be rewritten as

$$\frac{\partial W_E}{\partial t} + \nabla \cdot \mathbf{V}_C W_E = -\nabla \cdot \mathbf{V}_{p,E} - \nabla \cdot (\frac{\mathbf{U}_E}{B} \cdot \nabla \mathbf{V}_C) - \nabla \cdot (\frac{\mathbf{U}_E}{B}\frac{D \ln B}{Dt}) \text{(F.12)}$$

where we defined the E×B part of the TOKAM3X polarisation current as

$$\mathbf{V}_{p,E} = -\frac{1}{B}(\frac{\partial \mathbf{U}_E}{\partial t} + \nabla \cdot \mathbf{V}_C \mathbf{U}_E). \tag{F.13}$$

The product $\phi\nabla \cdot \mathbf{V}_{p,E}$ can now be associated with the E×B-only kinetic energy as

$$\phi\nabla \cdot \mathbf{V}_{p,E} = -\nabla_\perp\phi \cdot \mathbf{V}_{p,E} + \nabla \cdot \phi\mathbf{V}_{p,E}$$

$$= \frac{\partial E_E}{\partial t} + \nabla \cdot (E_E\mathbf{V}_C + \phi\mathbf{V}_{p,E}) + E_E\nabla \cdot \mathbf{V}_C. \tag{F.14}$$

Combining expressions F.11, F.12, and F.14 and filling out charge balance equation 7.2 then provides an equation for the TOKAM3X E×B-only kinetic energy as

$$\frac{\partial E_E}{\partial t} + \nabla \cdot (E_E\mathbf{V}_C + \phi\mathbf{J}_{||} + \phi\mathbf{V}_{p,E})$$

$$= \nabla_{||}\phi \cdot \mathbf{J}_{||} - \phi\nabla \cdot \mathbf{J}_{\nabla B} - D_W\phi\nabla_\perp^2 W + (\frac{\partial W_*}{\partial t} + \nabla \cdot W_*\mathbf{V}_C)$$

$$-\phi\nabla \cdot (\frac{\mathbf{U}_E}{B}\frac{D \ln B}{Dt}) - \phi\nabla \cdot (\frac{\mathbf{U}_E}{B} \cdot \nabla \mathbf{V}_C) - E_E\nabla \cdot \mathbf{V}_C, \tag{F.15}$$

The mean-field E×B-only kinetic energy equation can be derived following the same methodology. In this case, the average of $\frac{\partial \bar{W}_E}{\partial t} + \nabla \cdot \overline{W_E\mathbf{V}_C}$ is multiplied by $\bar{\phi}$. This then leads to

$$\frac{\partial E_{\mathrm{E},m}}{\partial t} + \nabla \cdot (E_{\mathrm{E},m}\bar{\mathbf{V}}_C + \overline{\mathbf{V}'_C\mathbf{V}'_E} \cdot \bar{\mathbf{V}}_E + \bar{\phi}\bar{\mathbf{J}}_{||} + \bar{\phi}\bar{\mathbf{V}}_{p,E}) = \nabla_{||}\bar{\phi} \cdot \bar{\mathbf{J}}_{||}$$

$$-\bar{\phi}\nabla \cdot \bar{\mathbf{J}}_{\nabla B} - D_W\bar{\phi}\nabla_\perp^2\bar{W} + \overline{\mathbf{V}'_C\mathbf{V}'_E} : \nabla\bar{\mathbf{V}}_E^T + \bar{\phi}(\frac{\partial \bar{W}_*}{\partial t} + \nabla \cdot \overline{W_*\mathbf{V}_C})$$

$$-\bar{\phi}\overline{\nabla \cdot (\frac{\mathbf{U}_E}{B}\frac{D\ln B}{Dt})} - \bar{\phi}\nabla \cdot (\overline{\frac{\mathbf{U}_E}{B} \cdot \nabla\mathbf{V}_C}) - E_{\mathrm{E},m}\nabla \cdot \bar{\mathbf{V}}_C. \quad \text{(F.16)}$$

The difference between the average equation F.15 and equation F.16 again provides an equation for $k_E$:

$$\frac{\partial k_E}{\partial t} + \nabla \cdot (k_E\mathbf{V}_C + \frac{\overline{\mathbf{V}'^2_E\mathbf{V}'_C}}{2} + \overline{\phi'\mathbf{J}'_{||}} + \overline{\phi'\mathbf{V}'_{p,E}}) = \overline{\nabla_{||}\phi' \cdot \mathbf{J}'_{||}}$$

$$-\overline{\phi'\nabla \cdot \mathbf{J}_{\nabla B}} - D_W\overline{\phi'\nabla_\perp^2 W'} - \overline{\mathbf{V}'_C\mathbf{V}'_E} : \nabla\bar{\mathbf{V}}_E^T$$

$$+\overline{\phi'(\frac{\partial W_*}{\partial t} + \nabla \cdot W_*\mathbf{V}_C)} - \overline{\phi'\nabla \cdot (\frac{\mathbf{U}_E}{B}\frac{D\ln B}{Dt})} - \overline{\phi'\nabla \cdot (\frac{\mathbf{U}_E}{B} \cdot \nabla\mathbf{V}_C)}$$

$$-k_E\nabla \cdot \bar{\mathbf{V}}_C - \frac{\overline{\mathbf{V}'^2_E\nabla \cdot \mathbf{V}'_C}}{2} - \bar{\mathbf{V}}_E \cdot \overline{\mathbf{V}'_E\nabla \cdot \mathbf{V}'_C}, \quad \text{(F.17)}$$

### F.1.3   Parallel kinetic energy equations

Parallel kinetic energy equation for TOKAM3X can readily be derived following the methodology applied for the general case in section 3.2.4. This yields the following equations:

$$\frac{\partial nE_{\mathrm{k},||}}{\partial t} + \nabla \cdot (nE_{\mathrm{k},||}\mathbf{V}_C) = -\mathbf{V}_{||} \cdot \nabla_{||}p + D_{||}V_{||}\nabla_\perp^2 nV_{||} - E_{\mathrm{k},||}S_{n_\mathrm{i}}, \quad \text{(F.18)}$$

$$\frac{\partial \bar{n}E_{\mathrm{k},m,||}}{\partial t} + \nabla \cdot (\bar{n}E_{\mathrm{k},m,||}\tilde{\mathbf{V}}_C + \overline{n\mathbf{V}''_C\mathbf{V}''_{||}} \cdot \tilde{\mathbf{V}}_{||})$$

$$= \overline{n\mathbf{V}''_C\mathbf{V}''_{||}} : \nabla\tilde{\mathbf{V}}_{||}^T - \tilde{\mathbf{V}}_{||} \cdot \nabla_{||}\bar{p} + D_{||}\tilde{V}_{||}\nabla_\perp^2 \bar{n}\tilde{V}_{||} - E_{\mathrm{k},m,||}\bar{S}_{n_\mathrm{i}}, \quad \text{(F.19)}$$

$$\frac{\partial \bar{n} k_{||}}{\partial t} + \nabla \cdot (\bar{n} k_{||} \tilde{\mathbf{V}}_C + \frac{1}{2} \overline{n \mathbf{V}_{||}''^2 \mathbf{V}_C''}) = -\overline{n \mathbf{V}_C'' \mathbf{V}_{||}''} : \nabla \tilde{\mathbf{V}}_{||}{}^T$$

$$-\overline{\mathbf{V}_{||}'' \cdot \nabla_{||} p} + D_{||} \overline{V_{||}'' \nabla_\perp^2 n V_{||}} - (\overline{E_{k,||} S_n} - E_{k,m,||} \bar{S}_n). \tag{F.20}$$

These equations are not be investigated in more detail in this thesis though.

## F.2   Derivation of enstrophy equations

Enstrophy equation (both total and E×B-only) can be derived following a methodology analogous to that applied for the general case in section 3.3. For TOKAM3X, we define the total enstrophies as

$$\zeta_{tot} \triangleq \frac{W^2}{2}, \quad \zeta_{mean} \triangleq \frac{\bar{W}^2}{2}, \quad \zeta_{turb} \triangleq \frac{\overline{W'^2}}{2}, \tag{F.21}$$

and the ExB-only enstrophies as

$$\zeta_{tot,E} \triangleq \frac{W_E^2}{2}, \quad \zeta_{mean,E} \triangleq \frac{\bar{W}_E^2}{2}, \quad \zeta_{turb,E} \triangleq \frac{\overline{W_E'^2}}{2}. \tag{F.22}$$

Note that again, it seems most sensible to leave away the density weighing here and use simple Reynolds averages in the derivations because the density scaling has been neglected in the LHS of the TOKAM3X charge balance equation.

### F.2.1   Total enstrophy equations

Multiplying the TOKAM3X charge balance equation 7.2 with $W$ and rewriting yields an equation for the total enstrophy as

$$\frac{\partial \zeta_{tot}}{\partial t} + \nabla \cdot \zeta_{tot} \mathbf{V}_C = W \nabla \cdot \mathbf{J}_{\nabla B} + W \nabla \cdot \mathbf{J}_{||} + D_W W \nabla_\perp^2 W - \zeta_{tot} \nabla \cdot \mathbf{V}_C \tag{F.23}$$

Multiplying the average charge balance equation with the average vorticity provides an equation for the mean-field enstrophy as

$$\frac{\partial \zeta_{mean}}{\partial t} + \nabla \cdot (\zeta_{mean} \bar{\mathbf{V}}_C + \overline{W' \mathbf{V}_C'} \bar{W}) = \bar{W} \nabla \cdot \bar{\mathbf{J}}_{\nabla B} + \bar{W} \nabla \cdot \bar{\mathbf{J}}_{||}$$

$$+ D_W \bar{W} \nabla_\perp^2 \bar{W} + \overline{W' \mathbf{V}_C'} \cdot \nabla \bar{W} - \zeta_{mean} \nabla \cdot \bar{\mathbf{V}}_C. \tag{F.24}$$

The difference of the these two equations yields an equation for the turbulent enstrophy:

$$\frac{\partial \zeta_{turb}}{\partial t} + \nabla \cdot (\zeta_{turb} \bar{\mathbf{V}}_C + \frac{\overline{W'^2 \mathbf{V}'_C}}{2}) = \overline{W' \nabla \cdot \mathbf{J}'_{\nabla B}} + \overline{W' \nabla \cdot \mathbf{J}'_{||}}$$

$$+ D_W \overline{W' \nabla_\perp^2 W'} - \overline{W' \mathbf{V}'_C} \cdot \nabla \bar{W} - (\overline{\zeta_{tot} \nabla \cdot \mathbf{V}_C} - \zeta_{mean} \nabla \cdot \bar{\mathbf{V}}_C). \quad \text{(F.25)}$$

## F.2.2   E×B-only enstrophy equations

To derive E×B-only enstrophy equations for TOKAM3X, we again make use of the decomposition of the LHS of the TOKAM3X charge balance equation F.11. Applying the exact same manipulations as in the previous section, but only multiplying with $W_E$ leads to the following equations:

$$\frac{\partial \zeta_{tot,E}}{\partial t} + \nabla \cdot \zeta_{tot,E} \mathbf{V}_C = W_E \nabla \cdot \mathbf{J}_{\nabla B} + W_E \nabla \cdot \mathbf{J}_{||}$$

$$+ D_W W_E \nabla_\perp^2 W - \zeta_{tot,E} \nabla \cdot \mathbf{V}_C - W_E \left( \frac{\partial W_*}{\partial t} + \nabla \cdot W_* \mathbf{V}_C \right), \quad \text{(F.26)}$$

$$\frac{\partial \zeta_{mean,E}}{\partial t} + \nabla \cdot (\zeta_{mean,E} \bar{\mathbf{V}}_C + \overline{W'_E \mathbf{V}'_C} \bar{W}_E)$$

$$= \bar{W}_E \nabla \cdot \bar{\mathbf{J}}_{\nabla B} + \bar{W}_E \nabla \cdot \bar{\mathbf{J}}_{||} + D_W \bar{W}_E \nabla_\perp^2 \bar{W} + \overline{W'_E \mathbf{V}'_C} \cdot \nabla \bar{W}_E$$

$$- \zeta_{mean,E} \nabla \cdot \bar{\mathbf{V}}_C - \bar{W}_E \left( \frac{\partial \bar{W}_*}{\partial t} + \nabla \cdot \overline{W_* \mathbf{V}_C} \right), \quad \text{(F.27)}$$

$$\frac{\partial \zeta_{turb,E}}{\partial t} + \nabla \cdot (\zeta_{turb,E} \bar{\mathbf{V}}_C + \frac{\overline{W'^2_E \mathbf{V}'_C}}{2})$$

$$= \overline{W'_E \nabla \cdot \mathbf{J}'_{\nabla B}} + \overline{W'_E \nabla \cdot \mathbf{J}'_{||}} + D_W \overline{W'_E \nabla_\perp^2 W'} - \overline{W'_E \mathbf{V}'_C} \cdot \nabla \bar{W}_E$$

$$- (\overline{\zeta_{tot,E} \nabla \cdot \mathbf{V}_C} - \zeta_{mean,E} \nabla \cdot \bar{\mathbf{V}}_C) - \overline{W'_E \left( \frac{\partial W_*}{\partial t} + \nabla \cdot W_* \mathbf{V}_C \right)}. \quad \text{(F.28)}$$

The enstrophy equations derived in this appendix will not be investigated in more detail in this thesis though.

# F.3   TOKAM3X simulation parameters

The data available TOKAM3X data solved equation set 7.1-7.7 in a slab geometry. This geometry has radial, poloidal and toroidal dimensions $L_x = 150\rho_0$, $L_y = 100\rho_0$, $L_z = 8000\rho_0$, with $\rho_0$ the reference gyro-radius. A uniformly distributed, Cartesian grid is used with $N_x = 192$, $N_y = 128$ and $N_z = 64$ cells in the radial, poloidal and toroidal directions. A time step of $\Delta t = 0.1\Omega_0^{-1}$ is used, with $\Omega_0$ the reference ion gyro-frequency.

The magnetic field is purely toroidal and decays in the radial direction from $B_z = 1.06$ to $B_z = 0.90$. This magnetic field is uniform in the toroidal and poloidal directions. A particle source is applied which is also uniform in the poloidal and toroidal directions, with a (half) Gaussian profile in the radial direction. This particle source has an amplitude $0.4449 \times 10^{-3}$ and a standard deviation of 4 gyro-radii. A pure deuterium plasma is simulated with uniform ion and electron temperatures $Te = Ti = 1$. Furhtermore, a uniform parallel resisitivity $\eta_{||} = 2.6580 \times 10^{-5}$ and uniform classical transport coefficients $D_N = D_{||} = D_W = 0.0027$ are used.

In Bayesian inference results and in the figures of section 7.1.3, only the part of the domain in the centre of the SOL is used. This data corresponds to cells $120 \leq i_x \leq 180$ in the radial $x$ direction and cells $10 \leq i_z \leq 55$ in the toroidal $z$ direction. In this region, the immediate influence of the target plates, the core region and the flow shear around the separatrix is presumably very small.

# Bibliography

[1] SOLPS 5.0. code manual. 27 February 2013.

[2] AHLERS, G., GROSSMANN, S., AND LOHSE, D. Heat transfer and large scale dynamics in turbulent Rayleigh-Bénard convection. *Rev. Mod. Phys. 81*, 2 (2009), 503.

[3] AHO-MANTILA, L., WISCHMEIER, M., MÜLLER, H., POTZEL, S., COSTER, D., BONNIN, X., CONWAY, G., AND THE ASDEX UPGRADE TEAM. Outer divertor of ASDEX Upgrade in low-density L-mode discharges in forward and reversed magnetic field: I. comparison between measured plasma conditions and SOLPS5.0 code calculations. *Nucl. Fusion 52*, 10 (2012), 103006.

[4] ALEXAKIS, A., AND DOERING, C. Energy and enstrophy dissipation in steady state 2D turbulence. *Phys. Lett. 359*, 6 (2006), 652–657.

[5] ARIEW, R. *Ockham's Razor: A Historical and Philosophical Analysis of Ockham's Principle of Parsimony.* PhD thesis, University of Illinois at Urbana-Champaign, 1976.

[6] ARLOT, S., AND CELISSE, A. A survey of cross-validation procedures for model selection. *Statist. Surv. 4* (2010), 40–79.

[7] BAELMANS, M. *Code improvements and applications of a two-dimensional edge plasma model for toroidal fusion devices.* PhD thesis, KU Leuven, 1993. available at https://limo.libis.be/permalink/f/t5q1v2/LIRIAS1744657.

[8] BAELMANS, M., BLOMMAERT, M., DESCHUTTER, J., DEKEYSER, W., AND REITER, D. Efficient parameter estimation in 2D transport models based on an adjoint formalism. *Plasma Phys. Controlled Fusion 56*, 11 (2014), 114009.

[9] BAILLY, C., AND COMTE-BELLOT, G. *Turbulence*. Springer International Publishing, Switzerland, 2015.

[10] BALESCU, R., VLAD, M., SPINEANU, F., AND MISGUICH, J. Anomalous transport in plasmas. *Int. J. Quantum Chem. 98*, 2 (2004), 125–130.

[11] BASCHETTI, S., BUFFERAND, H., CIRAOLO, G., FEDORCZAK, N., GHENDRIH, P., SERRE, E., AND TAMAIN, P. Optimization of turbulence reduced model free parameters based on L-mode experiments and 2D transport simulations. *Contrib. Plasma Phys. 58* (2018), 511–517.

[12] BASCHETTI, S., BUFFERAND, H., CIRAOLO, G., FEDORCZAK, N., GHENDRIH, P., TAMAIN, P., SERRE, E., THE EUROfusion MST1 TEAM, AND THE TCV TEAM. A $k$-$\epsilon$ model for plasma anomalous transport in tokamaks: closure via the scaling of the global confinement. *Nucl. Mater. Energy 19* (2019), 200–204.

[13] BASCHETTI, S., BUFFERAND, H., CIRAOLO, G., AND GHENDRIH, P. Study of the role of the magnetic configuration in a $k$-$\epsilon$ model for anomalous transport in tokamaks. *J. Phys.: Conf. Ser. 1125* (2018), 012001.

[14] BASCHETTI, S., BUFFERAND, H., CIRAOLO, G., GHENDRIH, P., SERRE, E., TAMAIN, P., AND THE WEST TEAM. Self-consistent cross-field transport model for core and edge plasma transport. *Nucl. Fusion 61*, 10 (2021), 106020.

[15] BAUDOIN, C. *Numerical evaluations of mechanisms governing the heat transport in the edge plasma of tokamaks*. PhD thesis, Aix-Marseille University, 2018. available at http://www.theses.fr/2018AIXM0053.

[16] BAUDOIN, C., TAMAIN, P., BUFFERAND, H., CIRAOLO, G., FEDORCZAK, N., GALASSI, D., GHENDRIH, P., AND NACE, N. Turbulent heat transport in TOKAM3X edge plasma simulations. *Contrib. Plasma Phys. 58*, 6-8 (2018), 484–489.

[17] BAUDOIN, C., TAMAIN, P., CIRAOLO, G., FUTTERSACK, R., GALLO, A., GHENDRIH, P., MARANDET, Y., NACE, N., AND NORSCINI, C. On the effect of electron temperature fluctuations on turbulent heat transport in the edge plasma of tokamaks. *Contrib. Plasma Phys. 56*, 6-8 (2016), 563–568.

[18] BERGER, J., BERNARDO, J., AND SUN, D. The formal definition of reference priors. *Ann. Statist. 37*, 2 (2009), 905–938.

[19] BERGER, J., BERNARDO, J., AND SUN, D. Overall objective priors. *Bayesian Anal. 10*, 1 (2015), 189–221.

[20]  BERK, H. L., COHEN, R., RYUTOV, D. D., TSIDULKO, Y. A., AND
      XU, X. Electron temperature gradient induced instability in tokamak
      scrape-off layers. *Nucl. Fusion 33*, 2 (1993), 263.

[21]  BERK, H. L., RYUTOV, D. D., AND TSIDULKO, Y. A. Temperature-
      gradient instability induced by conducting end walls. *Phys. Fluids B 3*, 6
      (1991), 1346–1354.

[22]  BERNARDO, J. Reference posterior distributions for bayesian inference.
      *J. R. Statist. Soc. B 41*, 2 (1979), 113–128.

[23]  BIGLARI, H., DIAMOND, P., AND TERRY, P. Influence of sheared poloidal
      rotation on edge turbulence. *Phys. Fluids B: Plasma Physics 2*, 1 (1990),
      1–4.

[24]  BIJLOOS, G. *Lagrangian dispersion modeling in a horizontally
      homogeneous meteorology for efficient data assimilation design.* PhD
      thesis, KU Leuven, 2022. available at https://lirias.kuleuven.be/3675191.

[25]  BISAI, N., AND KAW, P. Role of ion temperature on scrape-off layer
      plasma turbulence. *Phys. Plasmas 20*, 4 (2013), 042509.

[26]  BISKAMP, D. *Magnetohydrodynamics Turbulence.* Cambridge University
      Press, 2003.

[27]  BOFFETTA, G., AND MAZZINO, A. Incompressible rayleigh–taylor
      turbulence. *Annu. Rev. Fluid Mech. 49*, 1 (2017), 119–143.

[28]  BOLSTAD, W. M., AND CURRAN, J. *Introduction to Bayesian Statistics
      3rd ed.* John Wiley & Sons, Ltd, Hoboken, New Jersey, 2017.

[29]  BONNIN, X., DEKEYSER, W., PITTS, R., COSTER, D., VOSKOBOYNIKOV,
      S., AND WIESEN, S. Presentation of the new SOLPS-ITER code package
      for tokamak plasma edge modelling. *Plasma and Fusion Res. 11* (2016),
      1403102.

[30]  BOURDELLE, C., CITRIN, J., BAIOCCHI, B., CASATI, A., COTTIER, P.,
      GARBET, X., IMBEAUX, F., AND JET CONTRIBUTORS. Core turbulent
      transport in tokamak plasmas: bridging theory and experiment with
      QuaLiKiz. *Plasma Phys. Controlled Fusion 58*, 1 (2016), 014036.

[31]  BOURDELLE, C., GARBET, X., IMBEAUX, F., CASATI, A., DUBUIT, N.,
      GUIRLET, R., AND PARISOT, T. A new gyrokinetic quasilinear transport
      model applied to particle transport in tokamak plasmas. *Phys. Plasmas
      14*, 11 (2007), 112501.

[32] BRAGINSKII, S. Drift-ordered fluid equations for modelling collisional edge plasma. *Reviews of Plasma Physics 1* (1965), 205–311.

[33] BUFFERAND, H., BUCALOSSI, J., CIRAOLO, G., FALCHETTO, G., GALLO, A., GHENDRIH, P., RIVALS, N., TAMAIN, P., YANG, H., GIORGIANI, G., SCHWANDER, F., d'ABUSCO, M. S., SERRE, E., MARANDET, Y., RAGHUNATHAN, M., THE WEST TEAM, AND THE JET TEAM. Progress in edge plasma turbulence modelling—hierarchy of models from 2D transport application to 3D fluid simulations in realistic tokamak geometry. *Nucl. Fusion 61*, 11 (2021), 116052.

[34] BUFFERAND, H., CIRAOLO, G., GHENDRIH, P., MARANDET, Y., BUCALOSSI, J., COLIN, C., FEDORCZAK, N., GALASSI, D., GUNN, J., LEYBROS, R., SERRE, E., AND TAMAIN, P. Interchange turbulence model for the edge plasma in SOLEDGE2D-EIRENE. *Contrib. Plasma Phys. 56*, 6-8 (2016), 555–562.

[35] BUFFERAND, H., CIRAOLO, G., MARANDET, Y., BUCALOSSI, J., GHENDRIH, P., GUNN, J., MELLET, N., TAMAIN, P., LEYBROS, R., AND FEDORCZAK, N. Numerical modelling for divertor design of the west device with a focus on plasma–wall interactions. *Nucl. Fusion 55*, 5 (2015), 053025.

[36] CAMARGO, S., BISKAMP, D., AND SCOTT, B. Resistive drift-wave turbulence. *Phys. Plasmas 2*, 1 (1995), 48–62.

[37] CANUTO, V. M. Compressible turbulence. *Astrophys. J. 482*, 2 (1997), 827–851.

[38] CARLI, S., DEKEYSER, W., BLOMMAERT, M., COOSEMANS, R., VAN UYTVEN, W., AND BAELMANS, M. Bayesian maximum a posteriori-estimation of $\kappa$ turbulence model parameters using algorithmic differentiation in SOLPS-ITER. *Contrib. Plasma Phys.* (2022), e202100184.

[39] CARLI, S., DEKEYSER, W., COOSEMANS, R., DEJARNAC, R., KOMM, M., DIMITROVA, M., ADÁMEK, J., BÍLKOVÁ, P., AND BÖHM, P. Interchange-turbulence-based radial transport model for SOLPS-ITER: A COMPASS case study. *Contrib. Plasma Phys. 60*, 5-6 (2020), e201900155.

[40] CHEUNG, S., OLIVER, T., PRUDENCIO, E., PRUDHOMME, S., AND MOSER, R. Bayesian uncertainty analysis with applications to turbulence modeling. *Reliab. Eng. Syst. Saf. 96*, 9 (2011), 1137–1149.

[41] CHIB, S., AND JELIAZKOV, I. Marginal likelihood from the metropolis–hastings output. *J. Am. Stat. Assoc. 96*, 453 (2001), 270–281.

[42] CITRIN, J., BRETON, S., FELICI, F., IMBEAUX, F., ANIEL, T., ARTAUD, J., BAIOCCHI, B., BOURDELLE, C., CAMENEN, Y., AND GARCIA, J. Real-time capable first principle based modelling of tokamak turbulent transport. *Nucl. Fusion 55*, 9 (2015), 092001.

[43] COEN, S. Development and validation of rans-models for plasma edge simulations of tokamaks. Master's thesis, KU Leuven, 2018. available through Lirias: 0455596_54377855.

[44] COOSEMANS, R., DEKEYSER, W., AND BAELMANS, M. A new mean-field plasma edge transport model based on turbulent kinetic energy and enstrophy. *Contrib. Plasma Phys. 60*, 5-6 (2020), e201900156.

[45] COOSEMANS, R., DEKEYSER, W., AND BAELMANS, M. Bayesian analysis of turbulent transport coefficients in 2D interchange dominated ExB turbulence involving flow shear. *J. Phys.: Conf. Ser. 1785* (2021), 012001.

[46] COOSEMANS, R., DEKEYSER, W., AND BAELMANS, M. Turbulent kinetic energy in 2D isothermal interchange-dominated scrape-off layer ExB drift turbulence: Governing equation and relation to particle transport. *Phys. Plasmas 28*, 1 (2021), 012302.

[47] COOSEMANS, R., DEKEYSER, W., AND BAELMANS, M. A self-consistent mean-field model for turbulent particle and heat transport in 2D interchange-dominated electrostatic exb turbulence in a sheath-limited scrape-off layer. *accepted form publication in Contrib. Plasma Phys.* (2022), e202100193.

[48] COWLEY, S. Hot fusion. *Phys. World 23*, 10 (2010), 46–51.

[49] DE WOLF, R. Bayesian approach to parameter estimation and model validation for nuclear fusion reactor edge turbulence modelling. Master's thesis, KU Leuven, 2020. available through Lirias: 0706107_55418536.

[50] DE WOLF, R., COOSEMANS, R., DEKEYSER, W., AND BAELMANS, M. Bayesian approach to parameter estimation and model validation for nuclear fusion reactor mean-field edge turbulence modelling. *Nucl. Fusion 61*, 4 (2021), 046048.

[51] DEKEYSER, W. Overview of turbulence models for the edge plasma. technical report. 13 October 2017.

[52] DEKEYSER, W. *Optimal Plasma Edge Configurations for Next-Step Fusion Reactors.* PhD thesis, KU Leuven, 2014. available at https://lirias.kuleuven.be/handle/123456789/431573.

[53] Dekeyser, W., Bonnin, X., Lisgo, S. W., Pitts, R., Brunner, D., LaBombard, B., and Terry, J. SOLPS-ITER modeling of the Alcator C-Mod divertor plasma. *Plasma and Fusion Res. 11* (2016), 1403103.

[54] Dekeyser, W., Coosemans, R., Carli, S., and Baelmans, M. A self-consistent k-model for anomalous transport due to electrostatic exb drift turbulence in the scrape-off layer and implementation in SOLPS-ITER. *submitted to Contrib. Plasma Phys.* (202X).

[55] Dekeyser, W., Reiter, D., and Baelmans, M. Divertor target shape optimization in realistic edge plasma geometry. *Nucl. Fusion 54*, 7 (2014), 073022.

[56] Diamond, P. H., Hasegawa, A., and Mima, K. Vorticity dynamics, drift wave turbulence, and zonal flows: a look back and a look ahead. *Plasma Phys. Controlled Fusion 53*, 12 (2011), 124001.

[57] Diamond, P. H., Itoh, S.-I., and Itoh, K. *Modern Plasma Physics: Volume 1, Physical Kinetics of Turbulent Plasmas.* Cambridge University Press, 2010.

[58] Diamond, P. H., Itoh, S.-I., Itoh, K., and Hahm, T. S. Zonal flows in plasma—a review. *Plasma Phys. Controlled Fusion 47*, 5 (2005), R35–R161.

[59] Dif-Pradalier, G., Diamond, P., Grandgirard, V., Sarazin, Y., Abiteboul, J., Garbet, X., Ghendrih, P., Strugarek, A., Ku, S., and Chang, C. On the validity of the local diffusive paradigm in turbulent plasma transport. *Phys. Rev. E 82*, 2 (2010), 025401(R).

[60] Dose, V., Neuhauser, J., Kurzan, B., Murmann, H., Salzmann, H., and the ASDEX Upgrade Team. Tokamak edge profile analysis employing bayesian statistics. *Nucl. Fusion 41*, 11 (2001), 1671.

[61] D'Ippolito, D. A., Myra, J. R., and Zweben, S. J. Convective transport by intermittent blob-filaments: Comparison of theory and experiment. *Phys. Plasmas 18*, 6 (2011), 060501.

[62] Edeling, W., P.Cinnella, R.P.Dwight, and H.Bijl. Bayesian estimates of parameter variability in the $k - \epsilon$ turbulence model. *J. Comput. Phys. 258* (2014), 73–94.

[63] Eich, T., Manz, P., and the ASDEX Upgrade team. The separatrix operational space of ASDEX Upgrade due to interchange-drift-Alfvén turbulence. *Nucl. Fusion 61*, 8 (2021), 086017.

[64] FAN, D., MARANDET, Y., TAMAIN, P., BUFFERAND, H., CIRAOLO, G., GHENDRIH, P., AND SERRE, E. Effect of turbulent fluctuations on neutral particles transport with the TOKAM3X-EIRENE turbulence code. *Nucl. Mater. Energy 18* (2019), 105–110.

[65] FEDORCZAK, N., GALLO, A., TAMAIN, P., BUFFERAND, H., CIRAOLO, G., AND GHENDRIH, P. On the dynamics of blobs in scrape-off layer plasma: Model validation from two-dimensional simulations and experiments in tore supra. *Contrib. Plasma Phys. 58*, 6-8 (2018), 471–477.

[66] FEDORCZAK, N., GUNN, J., GHENDRIH, P., CIRAOLO, G., BUFFERAND, H., ISOARDI, L., AND TAMAIN, P. Experimental investigation on the poloidal extent of the turbulent radial flux in tokamak scrape-off layer. *J. Nucl. Mater. 415*, 1 (2011), S467–S470.

[67] FEDORCZAK, N., J.P.GUNN, NACE, N., GALLO, A., BAUDOIN, C., BUFFERAND, H., CIRAOLO, G., EICH, T., GHENDRIH, P., AND P.TAMAIN. Width of turbulent sol in circular plasmas: A theoretical model validated on experiments in tore supra tokamak. *Nucl. Mater. Energy 12* (2017), 838–843.

[68] FEDORCZAK, N., PERET, M., BUFFERAND, H., CIRAOLO, G., GHENDRIH, P., AND TAMAIN, P. A spectral filament model for turbulent transport and scrape off layer width in circular geometry. *Nucl. Mater. Energy 19* (2018), 433–439.

[69] FONG, E., AND HOLMES, C. On the marginal likelihood and cross-validation. *Biometrika 107*, 2 (2020), 489–496.

[70] FRIEL, N., AND WYSE, J. Estimating the evidence - a review. *Stat. Neerl. 66*, 3 (2012), 288–308.

[71] FUNDAMENSKI, W. *Power Exhaust In Fusion Plasmas.* Cambridge University Press, 2010.

[72] GALASSI, D., CIRAOLO, G., TAMAIN, P., BUFFERAND, H., GHENDRIH, P., NACE, N., AND SERRE, E. Tokamak edge plasma turbulence interaction with magnetic x-point in 3d global simulations. *Fluids 4*, 1 (2019), 50.

[73] GARBET, X. Introduction to turbulent transport in fusion plasmas / Introduction au transport turbulent dans les plasmas de fusion. *Comptes Rendus Physique 7*, 6 (2006), 573–583.

[74] GARCIA, O., BIAN, N., AND FUNDAMENSKI, W. Radial interchange motions of plasma filaments. *Phys. Plasmas 13*, 8 (2006), 082309.

[75] Garcia, O., Horacek, J., Pitts, R., Nielsen, A., Fundamenski, W., Naulin, V., and Rasmussen, J. Fluctuations and transport in the TCV scrape-off layer. *Phys. Plasmas 47*, 7 (2007), 667.

[76] Garcia, O., Naulin, V., Nielsen, A., and Rasmussen, J. Turbulence simulations of blob formation and radial propagation in toroidally magnetized plasmas. *Phys. Scr. T122* (2006), 89–103.

[77] Gelman, A., Roberts, G., and Gilks, W. *Bayesian Statistics.* Oxford University Press, New York, 1996.

[78] Ghendrih, P., Ciraolo, G., Larmande, Y., Sarazin, Y., Tamain, P., Beyer, P., Chiavassa, G., Darmet, G., Garbet, X., and Grandgirard, V. Shearing effects on density burst propagation in sol plasmas. *J. Nucl. Mater. 390-391* (2009), 425–427.

[79] Giacomin, M., and Ricci, P. Investigation of turbulent transport regimes in the tokamak edge by using two-fluid simulations. *J. Plasma Phys. 86*, 5 (2020), 905860502.

[80] Goedbloed, H., Keppens, R., and Poedts, S. *Magnetohydrodynamics of Laboratory and Astrophysical Plasmas.* Cambridge University Press, 2019.

[81] Goldston, R. Heuristic drift-based model of the power scrape-off width in low-gas-puff H-mode tokamaks. *Nucl. Fusion 52*, 1 (2012), 013009.

[82] Goldston, R., and Rutherford, P. *Introduction to Plasma Physics.* Institute of Physics Publishing, Bristol and Philadelphia, 1995.

[83] Gracias, W. Simulating the tokamak edge. internal presentation. 16 June 2020.

[84] Guiasu, S., and Shenitzer, A. The principle of maximum entropy. *The mathematical intelligencer 7*, 1 (1985), 42–48.

[85] Gunn, J., Boucher, C., Dionne, M., Ďuran, I., Fuchs, V., Loarer, T., Nanobashvili, I., Pánek, R., Pascal, J.-Y., Saint-Laurent, F., Stöckel, J., Van Rompuy, T., Zagórski, R., Adámek, J., Bucalossi, J., Dejarnac, R., Devynck, P., Hertout, P., Hron, M., Lebrun, G., Moreau, P., Rimini, F., Sarkissian, A., and Van Oost, G. Evidence for a poloidally localized enhancement of radial transport in the scrape-off layer of the tore supra tokamak. *J. Nucl. Mater. 363-365* (2007), 484–490.

[86] GÖRLER, T., LAPILLONNE, X., BRUNNER, S., DANNERT, T., JENKO, F., MERZ, F., AND TOLD, D. The global version of the gyrokinetic turbulence code gene. *J. Comput. Phys 230*, 18 (2011), 7053–7071.

[87] HAARIO, H., SAKSMAN, E., AND TAMMINEN, J. An adaptive metropolis algorithm. *Bernoulli 7*, 2 (2001), 223–242.

[88] HAHM, T., AND BURRELL, K. Flow shear induced fluctuation suppression in finite aspect ratio shaped tokamak plasma. *Phys. Plasmas 2*, 5 (1995), 1648.

[89] HALPERN, F., RICCI, P., JOLLIET, S., LOIZU, J., AND MOSETTO, A. Theory of the scrape-off layer width in inner-wall limited tokamak plasmas. *Nucl. Fusion 54*, 4 (2014), 043003.

[90] HALPERN, F., RICCI, P., S.JOLLIET, LOIZU, J., J.MORALES, A.MOSETTO, F.MUSIL, F.RIVA, AND AN C. WERSAL, T. T. The GBS code for tokamak scrape-off layer simulations. *J. Comput. Phys. 315* (2016), 388–408.

[91] HAN, C., AND CARLIN, B. MCMC methods for computing Bayes factors: A comparative review. *J. Am. Stat. Assoc. 96*, 455 (2000), 1122–1132.

[92] HASEGAWA, A., AND WAKATANI, M. Plasma edge turbulence. *Phys. Rev. Lett. 50*, 9 (1983), 682–686.

[93] HELD, M., WIESENBERGER, M., KUBE, R., AND KENDL, A. Non-oberbeck–boussinesq zonal flow generation. *Nucl. Fusion 58*, 10 (2018), 104001.

[94] HORTON, W. Drift waves and transport. *Rev. Mod. Phys. 71*, 3 (1999), 735.

[95] HORTON, W., KIM, J., ASP, E., HOANG, T., WATANABE, T., AND SUGAMA, H. Drift wave turbulence. *AIP Conference Proceedings 1013*, 1 (2008).

[96] JEFFREYS, H. *Theory of Probability 3rd ed.* Oxford Classic Texts, Oxford, England, 1961.

[97] JIANG, G.-S., AND SHU, C.-W. Efficient implementation of weighted eno schemes. *J. Comput. Phys. 126*, 0130 (1996), 202–228.

[98] KENNEDY, M., AND O'HAGAN, A. Bayesian calibration of computer models. *J. R. Statist. Soc. B 63*, 3 (2001), 425–464.

[99] Kim, J.-W., Coster, D., Neuhauser, J., Schneider, R., and the ASDEX Upgrade Team. ASDEX-Upgrade edge transport scalings from the two-dimensional interpretative code B2.5-I. *J. Nucl. Mater. 290-293* (2001), 644–647.

[100] Knuth, K., Habeck, M., Malakar, N., Mubeen, A., and Placek, B. Bayesian evidence and model selection. *Digit. Signal Process. 47* (2015), 50–67.

[101] Krasheninnikov, S., D'Ippolito, D., and Myra, J. Recent theoretical progress in understanding coherent structures in edge and sol turbulence. *J. Plasma Phys. 74*, 5 (2008), 679–717.

[102] Kukushkin, A., Pacher, H., Kotov, V., Pacher, G., and Reiter, D. Finalizing the ITER divertor design: The key role of solps modeling. *Fusion Eng. Des. 86*, 12 (2012), 2865–2873.

[103] LaBombard, B., Umansky, M., Boivin, R., Goetz, J., Hughes, J., Lipschultz, B., Mossessian, D., Pitcher, C., Terry, J., and Alcator Group. Cross-field plasma transport and main-chamber recycling in diverted plasmas on Alcator C-Mod. *Nucl. Fusion 40*, 12 (2000), 2041–2060.

[104] Li, H., Fu, Y., Li, J., and W., Z. Machine learning of turbulent transport in fusion plasmas with neural network. *Plasma Sci. Technol. 23*, 11 (2021), 115102.

[105] Madsen, J., Garcia, O., Larsen, J., Naulin, V., Nielsen, A., and Rasmussen, J. The influence of finite larmor radius effects on the radial interchange motions of plasma filaments. *Phys. Plasmas 18*, 11 (2011), 112504.

[106] Manz, P., Carralero, D., Birkenmeier, G., Müller, H., Müller, S., Fuchert, G., Scott, B., and Stroth, U. Filament velocity scaling laws for warm ions. *Phys. Plasmas 20*, 10 (2013), 102307.

[107] Manz, P., Hufnagel, C., Zito, A., Carralero, D., Griener, M., Lunt, T., Pan, O., Passoni, M., Tal, B., Wischmeier, M., Wolfrum, E., and the ASDEX Upgrade Team. The diffusion limit of ballistic transport in the scrape-off layer. *Phys. Plasmas 27*, 2 (2020), 022506.

[108] Manz, P., Xu, M., Fedorczak, N., Thakur, S., and Tynan, G. Spatial redistribution of turbulent and mean kinetic energy. *Phys. Plasmas 19*, 1 (2012), 012309.

[109] MARANDET, Y., NACE, N., VALENTINUZZI, M., TAMAIN, P., BUFFERAND, H., CIRAOLO, G., GENESIO, P., AND MELLET, N. Assessment of the effects of scrape-off layer fluctuations on first wall sputtering with the TOKAM-2D turbulence code. *Plasma Phys. Control. Fusion 58*, 11 (2016), 114001.

[110] MARTÍN, M., TAYLOR, E., WU, M., AND WEIRS, V. A bandwidth-optimized weno scheme for the effective direct numerical simulation of compressible turbulence. *J. Comput. Phys. 220*, 1 (2006), 270–289.

[111] MENEGHINI, O., SMITH, S., SNYDER, P., STAEBLER, G., CANDY, J., BELLI, E., LAO, L., KOSTUK, M., LUCE, T., AND LUDA, T. Self-consistent core-pedestal transport simulations with neural network accelerated models. *Nucl. Fusion 57*, 8 (2017), 086034.

[112] METROPOLIS, N., ROSENBLUTH, A., ROSENBLUTH, M., TELLER, A., AND TELLER, E. Equation of state calculations by fast computing machines. *J. Chem. Phys. 21*, 6 (1953), 1087–1092.

[113] MIKI, K., DIAMOND, P. H., GÜRCAN, Ö. D., TYNAN, G., ESTRADA, T., SCHMITZ, L., AND XU, G. Spatio-temporal evolution of the $L \to I \to H$ transition. *Phys. Plasmas 19*, 9 (2012), 092306.

[114] MOSETTO, A., HALPERN, F., JOLLIET, S., LOIZU, J., AND RICCI, P. Turbulent regimes in the tokamak scrape-off layer. *Phys. Plasmas 20*, 9 (2013), 092308.

[115] MYRA, J., D'IPPOLITO, D., RUSSELL, D., UMANSKY, M., AND BAVER, D. Analytical and numerical study of the transverse kelvin–helmholtz instability in tokamak edge plasmas. *J. Plasma Phys. 82*, 2 (2016), 905820210.

[116] NACE, N. *Dynamics of driven and spontaneous transport barriers in the edge plasma of tokamaks*. PhD thesis, Aix-Marseille University, 2018. available at http://www.theses.fr/2018AIXM0101.

[117] NAULIN, V. Turbulent transport and the plasma edge. *J. Nucl. Mater. 363–365* (2007), 24–31.

[118] NESPOLI, F., BUFFERAND, H., VALENTINUZZI, M., FEDORCZAK, N., CIRAOLO, G., SERRE, E., MARANDET, Y., MAURIZIO, R., OLIVEIRA, H. D., LABIT, B., KOMM, M., FAITSCH, M., AND ELMORE, S. Application of a two-fluid two-point model to SolEdge2D-EIRENE simulations of TCV H-mode plasma. *Nucl. Mater. Energy 18* (2019), 29–34.

[119] NIELSEN, A., RASMUSSEN, J. J., MADSEN, J., XU, G., NAULIN, V., OLSEN, J., LØITEN, M., HANSEN, S., YAN, N., TOPHØJ, L., AND WAN, B. Numerical simulations of blobs with ion dynamics. *Plasma Phys. Contr. Fusion 59*, 2 (2017), 025012.

[120] NISHIMURA, Y., COSTER, D., KIM, J., AND SCOTT, B. Coupling of perpendicular transport in turbulence and divertor codes. *Contrib. Plasma Phys. 42*, 2-4 (2002), 379–383.

[121] PAPADIMITRIOU, D., AND PAPADIMITRIOU, C. Bayesian uncertainty quantification of turbulence models based on high-order adjoint. *Comput Fluids 120* (2015), 82–97.

[122] PERET, M., FEDORCZAK, N., TAMAIN, P., GHENDRIH, P., VERMARE, L., TORE SUPRA TEAM, AND WEST TEAM. A spectral model for interchange transport in tokamak scrape-off layers. *Nucl. Fusion 61*, 4 (2021), 046045.

[123] PITTS, R., BONNIN, X., ESCOURBIAC, F., FRERICHS, H., GUNN, J., HIRAI, T., KUKUSHKIN, A., KAVEEVA, E., MILLER, M., MOULTON, D., ROZHANSKY, V., SENICHENKOV, I., SYTOVA, E., SCHMITZ, O., STANGEBY, P., TEMMERMAN, G., VESELOVA, I., AND WIESEN, S. Physics basis for the first ITER tungsten divertor. *Nucl. Mater. Energy 20* (2019), 100696.

[124] PITTS, R., BUTTERY, R., AND PINCHES, S. Fusion: the way ahead. *Phys. World 19*, 3 (2006), 20–26.

[125] POLITZER, P., AUSTIN, M., GILMORE, M., MCKEE, G., RHODES, T., YU, C., DOYLE, E., EVANS, T., AND MOYERE, R. Characterization of avalanche-like events in a confined plasma. *Phys. Plasmas 9*, 5 (2002), 1962–1969.

[126] POPE, S. *Turbulent Flows.* Cambridge University Press, Cambridge, 2015.

[127] RAMOS, J. General expression of the gyroviscous force. *Phys. Plasmas 12*, 11 (2005), 112301.

[128] REIMOLD, F., WISCHMEIER, M., BERNERT, M., POTZEL, S., COSTER, D., BONNIN, X., REITER, D., MEISL, G., KALLENBACH, A., AHO-MANTILA, L., STROTH, U., AND THE ASDEX UPGRADE TEAM. Experimental studies and modeling of complete H-mode divertor detachment in ASDEX Upgrade. *J. Nucl. Mater. 463* (2015), 128–134.

[129] REITER, D. Progress in two-dimensional plasma edge modelling. *J. Nucl. Mater. 196-198* (1992), 80–89.

[130] REITER, D., BAELMANS, M., AND BÖRNER, P. The EIRENE and B2-EIRENE codes. *Fusion Sci. Technol. 47*, 2 (2005), 172–186.

[131] RIBEIRO, T., AND SCOTT, B. Tokamak turbulence computations on closed and open magnetic flux surfaces. *Plasma Phys. Contr. Fus. 47*, 10 (2005), 1657–1679.

[132] RICCI, P., HALPERN, F., JOLLIET, S., LOIZU, J., MOSETTO, A., FASOLI, A., FURNO, I., AND THEILER, C. Simulation of plasma turbulence in scrape-off layer conditions: the GBS code, simulation results and code validation. *Plasma Phys. Controlled Fusion 54*, 12 (2012), 124047.

[133] RICCI, P., AND ROGERS, B. Plasma turbulence in the scrape-off layer of tokamak devices. *Phys. Plasmas 20*, 1 (2013), 010702.

[134] RISTORCELLI, J., AND CLARK, T. Rayleigh–Taylor turbulence: self-similar analysis and direct numerical simulations. *J. Fluid Mech. 507* (2004), 213–253.

[135] ROGERS, B., AND DORLAND, W. Noncurvature-driven modes in a transport barrier. *Phys. Plasmas 12*, 6 (2005), 062511.

[136] ROGNLIEN, T., RYUTOV, D., MATTOR, N., AND PORTER, G. Two-dimensional electric fields and drifts near the magnetic separatrix in divertor tokamaks. *Phys. Plasmas 6*, 5 (1999), 1851–1857.

[137] ROY, C., AND OBERKAMPF, W. A comprehensive framework for verification, validation, and uncertainty quantification in scientific computing. *Comput. Methods Appl. Mech. Engrg. 200*, 25-28 (2011), 2131–2144.

[138] ROZHANSKY, V., VOSKOBOYNIKOV, S., KAVEEVA, E., COSTER, D., AND SCHNEIDER, R. Simulation of tokamak edge plasma including self-consistent electric fields. *Nucl. Fusion 41*, 4 (2001), 387–401.

[139] RUSSELL, D., D'IPPOLITO, D., MYRA, J., CANIK, J., GRAY, T., AND ZWEBEN, S. Modeling the effect of lithium-induced pedestal profiles on scrape-off-layer turbulence and the heat flux width. *Phys. Plasmas 22*, 9 (2015), 092311.

[140] RUSSELL, D., MYRA, J., AND STOTLER, D. A reduced model of neutral-plasma interactions in the edge and scrape-off-layer: Verification comparisons with kinetic monte carlo simulations. *Phys. Plasmas 26*, 2 (2019), 022304.

[141] SARAZIN, Y., AND GHENDRIH, P. Intermittent particle transport in two-dimensional edge turbulence. *Phys. Plasmas 5*, 12 (1998), 4214–4228.

[142] SCHNEIDER, R., BONNIN, X., BORRASS, K., COSTER, D.,
      KASTELEWICZ, H., REITER, D., ROZHANSKY, V., AND BRAAMS, B.
      Plasma edge physics with B2-Eirene. *Contr. Plasma Phys. 46*, 1-2 (2006),
      3–191.

[143] SCOTT, B. The character of transport caused by ExB drift turbulence.
      *Phys. Plasmas 10*, 4 (2003), 963.

[144] SCOTT, B. The geodesic transfer effect on zonal flows in tokamak edge
      turbulence. *Phys. Lett. A 320*, 1 (2003), 53–62.

[145] SCOTT, B. Drift wave versus interchange turbulence in tokamak geometry:
      Linear versus nonlinear mode structure. *Phys. Plasmas 12*, 6 (2005),
      062314.

[146] SCOTT, B. Energetics of the interaction between electromagnetic ExB
      turbulence and zonal flows. *New J. Phys. 7* (2005), 92.

[147] SCOTT, B. Tokamak edge turbulence: background theory and
      computation. *Plasma Phys. Control. Fusion 49*, 7 (2007), S25–S41.

[148] SELLKE, T., BAYARRI, M., AND BERGER, J. Calibration of p-values for
      precise null hypotheses. *ISDS Discussion Paper 99-13 55*, 1 (1999).

[149] SIMAKOV, A., AND CATTO, P. Drift-ordered fluid equations for modelling
      collisional edge plasma. *Contrib. Plasma Phys. 44*, 1-3 (2004), 83–94.

[150] SIMONINI, R., CORRIGAN, G., RADFORD, G., SPENCE, J., AND TARONI,
      A. Models and numerics in the multi-fluid 2-D edge plasma code
      EDGE2D/U. *Contrib. Plasma Phys. 34*, 2-3 (2018), 368–373.

[151] SINGH, R., AND DIAMOND, P. When does turbulence spreading matter?
      *Phys. Plasmas 27*, 4 (2020), 042308.

[152] SIVIA, D., DAVID, W., KNIGHT, K., AND GULL, S. An introduction
      to bayesian model selection. *Phys. D: Nonlinear Phenom. 66*, 1-2 (1993),
      234–242.

[153] STANGEBY, P. *The Plasma Boundary of Magnetic Fusion Devices.* IoP
      Publishing, 2000.

[154] STEGMEIR, A., ROSS, A., BODY, T., FRANCISQUEZ, M., ZHOLOBENKO,
      W., COSTER, D., MAJ, O., MANZ, P., JENKO, F., ROGERS, B., AND
      KANG, K. Global turbulence simulations of the tokamak edge region
      with GRILLIX. *Phys. Plasmas 26*, 5 (2019), 052517.

[155] SUGAMA, H., AND WAKATANI, M. Statistical analysis of anomalous transport in resistive interchange turbulence. *J. Phys. Soc. Jpn. 61*, 9 (1992), 3166–3177.

[156] SYVERSVEEN, A. Noninformative bayesian priors. Interpretation and problems with construction and applications. *Preprint Statistics 3* (1998), 11.

[157] TAMAIN, P., BUFFERAND, H., CIRAOLO, G., COLIN, C., GALASSI, D., GHENDRIH, P., SCHWANDER, F., AND SERRE, E. The TOKAM3X code for edge turbulence fluid simulations of tokamak plasmas in versatile magnetic geometries. *J. Comput. Phys. 321* (2016), 606–623.

[158] TERRY, J., ZWEBEN, S., HALLATSCHEK, K., LABOMBARD, B., MAQUEDA, R., BAI, B., BOSWELL, C., GREENWALD, M., KOPON, D., NEVINS, W., PITCHER, C., ROGERS, B., STOTLER, D., AND XU, X. Observations of the turbulence in the scrape-off-layer of alcator c-mod and comparisons with simulation. *Phys. Plasmas 10*, 5 (2003), 1739.

[159] THRYSØEA, A., LØITEN, M., MADSEN, J., NAULIN, V., NIELSEN, A., AND RASMUSSEN, J. J. Plasma particle sources due to interactions with neutrals in a turbulent scrape-off layer of a toroidally confined plasma. *Phys. Plasmas 25*, 3 (2018), 032307.

[160] TRAN, T., KIM, S., JHANG, H., AND KIM, J. Turbulence characteristics, energy equipartition, and zonal flow generation in coupled drift wave-parallel velocity gradient driven turbulence. *Plasma Phys. Contr. Fusion 61*, 6 (2019), 065002.

[161] TROTTA, R. Bayes in the sky: Bayesian inference and model selection in cosmology. *Contemp. Phys. 49*, 2 (2008), 71–104.

[162] TSAI, S., PERKINS, F., AND STIX, T. The principle of maximum entropy. *Phys. Fluids 13*, 8 (1970), 2108–2114.

[163] WAGNER, F., BECKER, G., BEHRINGER, K., CAMPBELL, D., EBERHAGEN, A., ENGELHARDT, W., FUSSMANN, G., GEHRE, O., GERNHARDT, J., GIERKE, G., HAAS, G., HUANG, M., KARGER, F., KEILHACKER, M., KLÜUBER, O., KORNHERR, M., LACKNER, K., LISITANO, G., LISTER, G., MAYER, H., MEISEL, D., MÜLLER, E., MURMANN, H., NIEDERMEYER, H., POSCHENRIEDER, W., RAPP, H., RÖHR, H., SCHNEIDER, F., SILLER, G., SPETH, E., STÄBLER, A., STEUER, K., VENUS, G., VOLLMER, O., AND YÜ, Z. Regime of improved confinement and high beta in neutral-beam-heated divertor discharges of the ASDEX tokamak. *Phys. Rev. Lett. 49*, 19 (1982), 1408–1412.

[164] WEILAND, J. *Stability and Transport in Magnetic Confinement Systems.* Springer, New York, 2012.

[165] WESSON, J. *Tokamaks 3rd ed.* Oxford: Clarendon Press, 2004.

[166] WIESEN, S. EDGE2D/EIRENE code interface report. ITC Project Report. 30 June 2006, available at www.eirene.de/e2deir_report_30jun06.pdf.

[167] WIESEN, S., REITER, D., V.KOTOV, BAELMANS, M., DEKEYSER, W., KUKUSHKIN, A., LISGO, S., PITTS, R., ROZHANSKY, V., SAIBENE, G., VESELOVA, I., AND VOSKOBOYNIKOV, S. The new SOLPS-ITER code package. *J. Nucl. Mater. 463* (2015), 480–484.

[168] XIAO, H., AND CINNELLA, P. Quantification of model uncertainty in rans simulations: A review. *Prog. Aerosp. Sci. 108* (2019), 1–31.

[169] YAKHOT, V. Universal law of enstrophy decay in two-dimensional large-reynolds-number turbulence. *Phys. Rev. Lett. 93*, 1 (2004), 014502.

[170] YU, G., KRASHENINNIKOV, S., AND GUZDAR, P. Two-dimensional modelling of blob dynamics in tokamak edge plasmas. *Phys. Plasmas 13*, 4 (2006), 042508.

[171] ZHANG, D., CHEN, Y., XU, X., AND XIA, T. Self-consistent simulation of transport and turbulence in tokamak edge plasma by coupling SOLPS-ITER and BOUT++. *Phys. Plasmas 26*, 1 (2019), 012508.

[172] ZHOLOBENKO, W., STEGMEIR, A., GRIENER, M., CONWAY, G., BODY, T., COSTER, D., JENKO, F., AND THE ASDEX UPGRADE TEAM. The role of neutral gas in validated global edge turbulence simulations. *Nucl. Fusion 61*, 11 (2021), 116015.

# Curriculum Vitae

Reinart Andreas Jan Coosemans
°9/8/1994

**Education**

2017-2022 PhD researcher at the Department of Mechanical Engineering, KU Leuven, Belgium.

2015-2017 Master in Mechanical Engineering, KU Leuven, Belgium.

2012-2015 Bachelor in Mechanical-Chemical Engineering, KU Leuven, Belgium.

**Grants**

Research Foundation Flanders (FWO) Fellow, individual four-year Strategic Basic Research grant.

**Experience**

Teaching assistant at Department of Mechanical Engineering, KU Leuven

- Tutor of four Master in Engineering theses (KU Leuven) in edge plasma modeling
- Thermodynamics (2018-2021)
- Energy conversion machines and systems (2018-2020)
- Planning didactical load within TME division (2018-2021)

# List of publications

**Articles in internationally reviewed academic journals**

1. Dekeyser, W., Coosemans, R., Carli, S., Baelmans, M. A self-consistent k-model for anomalous transport due to electrostatic ExB drift turbulence in the scrape-off layer and implementation in SOLPS-ITER. Contributions to Plasma Physics, (2022) e202100190.

2. Coosemans, R., Dekeyser, W., Baelmans, M. A self-consistent mean-field model for turbulent particle and heat transport in 2D anisothermal interchange-dominated ExB turbulence in the scrape-off layer. Contributions to Plasma Physics, (2022), e202100193.

3. Carli, S., Dekeyser, W., Blommaert, M., Coosemans, R., Van Uytven, W., Baelmans, M. Bayesian maximum a posteriori-estimation of $\kappa$ turbulence model parameters using algorithmic differentiation in SOLPS-ITER. Contributions to Plasma Physics, (2022), e202100184.

4. De Wolf, R., Coosemans, R., Dekeyser, W., Baelmans, M. Bayesian approach to parameter estimation and model validation for nuclear fusion reactor mean-field edge turbulence modelling. Nuclear Fusion, 61 (2021), 046048.

5. Coosemans, R., Dekeyser, W., Baelmans, M. Bayesian analysis of turbulent transport coefficients in 2D interchange dominated ExB turbulence involving flow shear. Journal of Physics: Conference Series, 1785 (2021), 012001.

6. Coosemans, R., Dekeyser, W., Baelmans, M. Turbulent kinetic energy in 2D isothermal interchange-dominated scrape-off layer ExB drift turbulence: Governing equation and relation to particle transport. Physics of Plasmas, 28 (2021), 012302.

7. Carli, S., Dekeyser, W., Coosemans, R., Dejarnac, R., Komm, M., Dimitrova, M., Adámek, J., Bílková, P., Böhm, P. Interchange-turbulence-based radial transport model for SOLPS-ITER: A COMPASS case study. Contributions to Plasma Physics, 60 (2020), e201900155.

8. Coosemans, R., Dekeyser, W., Baelmans, M. A new mean-field plasma edge transport model based on turbulent kinetic energy and enstrophy. Contributions to Plasma Physics, 60 (2020), e201900156.

**Talks and posters presented at international scientific conferences, meetings, and symposia**

1. Coosemans, R., Dekeyser, W., Baelmans, M. Anisothermal mean-field model for 2D ExB drift turbulence in the SOL (presentation). 18th International Workshop on Plasma Edge Theory in Fusion Devices, virtual, 13-15 September 2021.

2. Coosemans, R., Dekeyser, W., Baelmans, M. Influence of the diamagnetic drift contribution on the turbulent kinetic energy balance in isothermal interchange-dominated ExB turbulence in the scrape-off layer (poster). Joint EU-US Transport Task Force Meeting, virtual, 6-10 September 2021.

3. Coosemans, R., Dekeyser, W., Baelmans, M. Bayesian analysis of turbulent transport coefficients in 2D interchange dominated ExB turbulence involving flow shear (poster). Joint Varenna-Lausanne International Workshop on the Theory of Fusion Plasmas, virtual, 12-16 October 2020.

4. Coosemans, R., Dekeyser, W., Baelmans, M. New mean-field plasma edge transport models based on turbulent kinetic energy and enstrophy (presentation). 17th International Workshop on Plasma Edge Theory in Fusion Devices, University of California San Diego, La Jolla, CA, USA, 19-21 August 2019.

FACULTY OF ENGINEERING SCIENCE
DEPARTMENT OF MECHANICAL ENGINEERING
THERMAL FLUIDS ENGINEERING
Celestijnenlaan 300 box 2421
B-3001 Leuven
reinart.coosemans@kuleuven.be
http://www.mech.kuleuven.be/en/tme/research/thermal